THE UNIVERSITY *of* EDINBURGH

ERUPTION DYNAMICS WITHIN AN EMERGENT SUBGLACIAL SETTING: A CASE STUDY OF THE 2004 ERUPTION OF GRÍMSVÖTN VOLCANO, ICELAND

A DISSERTATION SUBMITTED TO THE COLLEGE OF SCIENCE AND ENGINEERING AT THE UNIVERSITY OF EDINBURGH IN FULFILLMENT OF REQUIREMENTS FOR THE DEGREE OF DOCTOR OF PHILOSOPHY.

BY

TANYA CHANTAL JUDE-ETON

SUPERVISORS:

THORVALDUR THORDARSON AND GODFREY FITTON (UNIVERSITY OF EDINBURGH)

MAGNUS T. GUDMUNDSSON (UNIVERSITY OF ICELAND)

PHYSICAL VOLCANOLOGY

SCHOOL OF GEOSCIENCES

THE UNIVERSITY OF EDINBURGH

I, Tanya Chantal Jude-Eton, declare the following:

(a) that this thesis has been composed by myself, the candidate;

(b) that the incorporated work is entirely my own with any contribution from others clearly indicated; and

(c) that this work has not been submitted for any other degree or professional qualification.

ACKNOWLEDGEMENTS

I would like to first acknowledge my family and the many friends who supported me, who made me laugh, who accompanied me on some crazy adventures, who simply hung out, and yet, who also knew when to let go and allow me to go off on my own.

To my mother and father – two people more different in character and lifestyle I could never imagine to meet. Yet, in your very different ways you both instilled in me a unique set of values which proved invaluable to completing a PhD: independence, stubbornness, a questioning nature and willingness to challenge the status quo. To Mamma especially, a lifetime of encouragement really made a difference! Thank you. Steve and Lorraine – thank you for always backing me up and for making me laugh. I have been lucky to have had you both.

Rafael and Connor. You guys spent four years as semi-PhD-orphans and rode so many waves of change. You were patient and good and kind and unfailingly happy to see me every morning. Yet despite the inconvenience that it imposed on you, you both always agreed that I had the most awesome and cool job. Thank you!

To Aunty Bev, Shirley and Allen, who more than once looked after and spoiled the kids so that I could go into the field or take some time to myself. Your time and affection and the sense of stability that you provided were very much appreciated. Thank you.

Daddy Austin, you were never able to see this dream fully realised. But the night before you died I dreamed of you, and you reassured me then that you looked upon this enterprise with approval. Thank you.

To my closest friends: Gillian, Tom, Caroline, Rhian, Edi, Lez, Lora, Becky and Mark: you've definitely seen me at my worst and you've pulled me back from the brink of many small disasters and one or two (or twenty) monumental wobblies. But I like to think that was balanced by the fact that, with you, I always felt my best. I'll never forget

your cuddles, your jokes, your poetry, camping out with you on hilltops, playing on beaches, dancing with you, eating with you and above all the abundant laughter. Thank you ☺

* * * * *

This project was largely funded by RANNÍS, the Icelandic Science Foundation. In Iceland, if you have an idea or a goal, people are prepared to help you make it happen – whether that be simply getting from A to B (even if A IS at the bottom of an active rift and B IS in the interior of the glacial highlands!) or pushing the very frontiers of science…

Significant financial support was also provided by the Graduate Organisation (GO) of the School of Geosciences at the University of Edinburgh. Following the collapse of the Icelandic banks in 2008 the GO were swift and decisive in providing the financial support needed to bring the Grímsvötn project (along with my PhD) to completion. I thank Helena Sim, Sue Rigby, Rosie Mac, Pete Nienow and Wyn Williams not only for their network of tangible support and practical assistance, but also for the reassurance that they provided when money and time grew thin. Thank you.

I had plenty of help in the field from Katy (2007 was a very good year because of you!), Helena and from JÖRFÍ, the Icelandic Glaciological Society. Björn, Eiríkur, Hlinur, Einar Ragnar, Hrafnhildur, Halfdan, Anna, Magnus Halfgrims. all worked with me directly and I thank you for your strong arms, quick thinking and ready humour. Likewise, in the lab I could not have done without the technical support and insight gained from talking to Nic Odling (XRF) and Chris Hayward (EMP). Furthermore, I am grateful to and it was a pleasure to work alongside Ann Mennim in the wet chemistry lab and Mike Hall, thin section technician.

Guðmunda and Anna saved me several hours of torture by helping to sieve a portion of my samples and Mark Naylor, Christopher Hamilton and Ciaran Beggan all helped with making software work for me and with evaluating my work from some entirely novel analytical perspectives.

Finally, I would like to acknowledge a profound respect for and gratitude to my academic supervisors, Thor, Magnus and Godfrey, who provided the initial framework of the Grímsvötn 2004 project and guided my efforts thereafter. For all of your time, your brain-power and the joys of working in the field, THANK YOU.

ABSTRACT

The November 2004 explosive eruption of Grímsvötn volcano, Iceland (G2004) commenced as a subglacial event within the interior of the Vatnajökull ice cap before breaking through the ice cover to generate a 6-10 km high eruption column. This produced a tephra apron extending >50 km across the ice surface northwards from the eruption site, incorporating 0.047 km^3 (DRE) of plagioclase-bearing, sparsely porphyritic, basaltic tephra. This study focuses on quantifying the key eruption parameters and evaluating the stratigraphy, grain size and geochemical characteristics of the proximal facies of the subaerial deposit with a level of detail and precision that has never previously been possible for a modern glacio-volcanic event.

The G2004 deposit consists of a finely layered sequence which is subdivided into seven units (A-G) on the basis of differences in texture, grain size and componentry and the presence of sharp contacts between the layers. It is poorly sorted and fine-grained with a median clast diameter of 1.5 Φ. The grain size characteristics and clast morphologies are indicative of intense phreatomagmatic fragmentation, despite a significant component of highly vesicular juvenile glass. A wide range in thicknesses and geometries of depositional units reflects variations in intensity and style of activity.

Units C and E account for 80% of the total deposit volume, including the entire distal portion, and are interpreted to represent a mixture of (i) a widely dispersed component that fell from the upper margins of a strongly inclined (~45°) 6-10 km high plume and (ii) a locally dispersed (<3 km from source) component originating from (1) pyroclastic density currents generated by shallow explosions and tephra jets and (2) sedimentation from the jet region and lower convective column margins. The other units are only locally dispersed around the vent. A significant proportion of fine material was deposited in the near-vent region due to particle aggregation processes. The bulk of the G2004 deposit is therefore identified as the product of continuous incremental deposition during the passage of a single quasi-steady current supplied by a sustained explosive phreatomagmatic eruption, with a variable contribution of material from concurrent tephra fallout.

Major oxide, trace element and volatile composition of the G2004 tephra were analysed and compared with that of the G1998 and Laki events. Results indicate that the G2004 magma originated within a shallow-level, compositionally stratified chamber and was discharged through an independent plumbing system. The parent magmas for each of these three Grímsvötn events were produced by different degrees of partial melting within a similar lower-crust or mantle source, but are not related by fractional crystallization or magma mixing. Despite episodic intense vesiculation, the G2004 magma was fragmented at very shallow levels by almost exclusively phreatomagmatic mechanisms – the effect of which was to arrest the degassing process such that only 75% of the potential magmatic sulphur budget escaped to the atmosphere.

TABLE OF CONTENTS

LIST OF FIGURES

CHAPTER 2

CHAPTER 3

CHAPTER 4

CHAPTER 5

CHAPTER 6

CHAPTER 7

CHAPTER 9

LIST OF TABLES

CHAPTER 2

CHAPTER 3

CHAPTER 4

CHAPTER 5

CHAPTER 6

CHAPTER 7

CHAPTER 8

CHAPTER 1:

INTRODUCTION

1.1 BACKGROUND AND JUSTIFICATION FOR STUDY

Phreatomagmatic eruptions are both frequent and widespread, occurring wherever magma interacts explosively with external water at or near the Earth's surface. Consequently, phreatomagmatic eruptions feature strongly in volcanically active shallow submarine, littoral, lacustrine and glacial environments.

Previous studies of exposed Quaternary subglacial volcanic constructs (e.g. Bemmelen and Rutten, 1955; Einarsson, 1960; Jones, 1969; 1970; Kjartansson, 1943; 1966; and Matthews, 1947) have demonstrated that table mountains (i.e. "tuyas" and hyaloclastite ridges (i.e. "tindar") are characteristic morphological structures resulting from volcanism in glacial environments. These structures are typified by well-defined lithofacies associations, which reflect environment-induced changes in eruption style and behaviour (see section 2.2.2).

Nowhere are these phenomena more evident than in Iceland, where the historical as well as the geological records show that more than three quarters of all post-glacial (i.e. Holocene) eruptions have been explosive (Larsen and Eiríksson, 2007; Thordarson and Höskuldsson, 2008). Among these explosive events, over 75% have taken place in a subglacial environment. The Grímsvötn central volcano, located in the west-central part of Vatnajökull glacier dominates the event record with, on average, one eruption every ten years (Larsen *et al*., 1998; Larsen, 2002).

Within the glacial environment, however, the preservation potential for deposits is exceedingly low. Unconsolidated hyaloclastite is subject to rapid remobilisation by subsequent glacial, fluvial and aeolian processes (Bemmelen and Rutten, 1955; Jones, 1969; Werner and Schminke, 1999). Consequently, studies based on exposed ancient

subglacial formations are unable to describe and account for the proximal and medial supraglacial deposits of emergent subglacial eruptions (i.e. the tephra apron deposited

on top of glacial ice and beyond the limits of the hyaloclastite tuff cone during at the start of the sub-aerial phase of activity). The focus of this study is therefore the pristine proximal and medial subglacial-subaerial sequence of the 2004 eruption at Grímsvötn, which is not normally preserved intact in the geologic record. This study is the first ever detailed characterisation of the tephra apron produced by the main subaerial explosive phase of an initially subglacial basaltic explosive eruption.

The opportunity to study such an unique and rarely seen tephra sequence was made possible by the swift response of the Icelandic civil defence and the hazard monitoring community at the Iceland Meteorological Office (IMO) and the Institute of Earth Sciences at the University of Iceland (IES), whose monitoring efforts and on-site surveillance ensured comprehensive documentation of the event, and by the Icelandic Research Council (RANNÍS), who provided the financial support for investigations of both the vent complex and tephra deposited onto the ice. Our on-site field campaign focused its efforts on deformation, seismic and gravity measurements, as well as documenting whole-deposit dispersal, internal stratigraphy of the tephra pile, distribution and attributes of individual tephra units and comprehensive sampling of the deposits for laboratory measurements and for experiments on physical and chemical attributes of the deposits. Collectively, these data sets have enabled us to tie together syn- and post-eruption measurements and observations, thus allowing an all-inclusive reconstruction of the sequence of events, characterisation of individual eruption phases and their transportation and depositional mechanisms and quantitative assessments of shallow conduit processes.

1.2 STUDY AIMS

The aim of this PhD study is to evaluate deposit stratigraphy and quantify conduit and expulsion processes from the supraglacial deposits of a basaltic, emergent subglacial, phreatomagmatic eruption, using the 2004 event at Grímsvötn as a case study. This will provide the first ever detailed characterisation of the tephra apron

produced by the main subaerial explosive phase of an initially subglacial basaltic explosive eruption.

1.3 STUDY OBJECTIVES

The core of this dissertation is comprised of a series of papers addressing the following research questions, which focus on particular aspects of the 2004 Grímsvötn eruption (hereafter referred to as G2004):

(1) How can the nature of explosive emergent subglacial basaltic eruptions be described in terms of the observed shifts in style of activity and in deposit characteristics?

(2) What are the dominant mechanisms of magma fragmentation, and what is the relative contribution of exsolving and expanding magmatic gas to these processes compared with that of external water?

(3) What are the characteristic transport regimes and depositional processes involved in the emplacement of the subaerial phases of small emergent subglacial eruptions?

(5) What are the implications of measured chemical compositions of the tephra for magma storage and ascent in the Grímsvötn system?

1.4 STUDY APPROACH AND COLLABORATORS

This PhD study is an integral component of a larger, multidisciplinary research project designed to characterise and quantify eruption styles and fragmentation mechanisms during the G2004 eruption through detailed field and laboratory analysis of the tephra. The Grímsvötn 2004 research team was led by Magnús T. Gudmundsson at the University of Iceland. Collaborators included: Karl Gunnarsson, Gudrun Larsen, Þórdís Högnadóttir and Björn Oddsson (University of Iceland); Bernd Zimanowski (University of Würzburg); Pierrofrancisco Dellino (University of Bari); Thorvaldur

Thordarson and myself (University of Edinburgh). The wider project goals outside of my PhD objectives (previously outlined in section 1.2) included:

i. An MSc. study by Björn Oddsson (2007), which documented transportation of mass during the G2004 eruption through analysis of plume height and duration and ground sampling. Oddsson compared these data with existing models of mass transport / plume height.
ii. Determination of energy fluxes during the G2004 eruption (Gudmundsson *et al*., 2009).
iii. Direct measurement of the viscosity and thermal conductivity of G2004 melt and experimental simulation of water-melt interactions (work to be completed by B. Zimanowski).
iv. Comparison of natural tephra clasts with experimental clasts by SEM (work to be completed by P. Dellino).

I recorded detailed stratigraphic logs through the proximal tephra pile at appropriate spacing for accurate determination of the dispersal and volume of individual tephra beds. These are provided in Appendix I. In addition, a suite of samples were collected for volcanological and geochemical laboratory studies. This provided the raw data for analysis of:

(a) Macro and fine-scale deposit characteristics and tephra dispersal.

(b) Whole-layer grain-size distributions - to enable the assessment of fragmentation versus transportation and depositional regimes.

(c) Clast morphology - to evaluate the relative roles of brittle vs. hydrodynamic fragmentation during magma disintegration.

(d) Whole-rock major oxide and trace element concentrations – to quantify magma petrogenesis and shallow-level plumbing.

(e) Glass and phenocryst compositions along with post- and pre-eruption volatile contents – to evaluate magma degassing and conduit dynamics.

In this way I was able to meet my PhD objectives while contributing directly to the wider project aims. This study also provides a stratigraphic framework for the remaining aspects of the parent study.

1.5 Dissertation Structure

The dissertation has been organised around a core of six scientific papers (Chaps. 3-8), each addressing one or more of the research questions posed in section 1.2. These are bracketed by a literature review (Chap. 2) and a final discursive chapter which synthesises the conclusions of this work (Chap. 9).

In chapter 2 the principal concepts of explosive phreatomagmatic volcanism are introduced, emphasising its occurrence within the subglacial environment. A background to the Grímsvötn volcanic system is also provided.

Chapter 3 describes the dispersal characteristics and deposit architecture of the G2004 succession. This provides the first ever published comprehensive description of the stratigraphy and dispersal characteristics of the tephra apron associated with a contemporary basaltic emergent subglacial eruption. In this chapter I tie the deposit stratigraphy to visual observations and instrumental records to provide a fully-

interpreted reconstruction of G2004 activity. As such, this paper provides the necessary context for the remaining chapters, which target specific aspects of this explosive event. Chapter 3 is currently in press in the Bulletin of Volcanology.

In chapter 4 the method of Bonadonna and Houghton (2005) is utilised to reconstruct total-unit and total-deposit grain-size distributions for the G2004 eruption. The total grain-size distribution is a critical input parameter for volcanic ash transport and dispersion (VATD) models, which are used in hazard mitigation strategies.

Chapter 5 is focused on comparing unit and total layer grain-size distributions in conjunction with analysis of clast morphologies in order to discern the dominant fragmentation regimes, and how these are related to changes in style of activity. Chapters 4 and 5 combined have been submitted as a research paper to the Journal of Volcanology.

Chapter 6 examines the depositional structures and textures of units C and E in detail, which correspond to the sustained main phases of the 2004 eruption. I use these observations to build an argument for deposition principally by a mechanism of progressive aggradation during a period of sustained activity resulting from countless discrete, but closely spaced, phreatomagmatic explosions.

Chapter 7 presents the results of a high-resolution whole rock major and trace element study of the 1998 and 2004 proximal tephra successions. It shows how the composition of the magma changes with time during the 2004 event, and places this finding in context with respect to previous eruptions and previous studies. This chapter also examines the implications of the chemical stratigraphy for our understanding of the Grímsvötn magmatic system.

Chapter 8 presents an analysis of the major and volatile (S, F, Cl) element compositions of glass (i.e. melt) in the 2004 tephra in order to assess the evolution of the melt prior to and during the eruption, including evaluation of its pre- and post-eruption volatile contents. This data is then used to discuss the role of degassing in disintegrating magma in nominally phreatomagmatic events and to calculate sulphur release to the atmosphere.

Where required, presentation of extensive data tables or methodology, along with any other supplementary information, is provided in appendices at the end of this document.

In the final chapter, I synthesise the results and discussion of the entire PhD study to provide an integrated discussion of the eruption dynamics of a small basaltic emergent subglacial eruption. Chapter 9 also places the study results into a wider context in the field of volcanology and points out directions for future work.

CHAPTER 2:

LITERATURE REVIEW

PART 1 – GENERAL CONSIDERATIONS

2.1 BASALTIC EXPLOSIVE VOLCANISM

In a global context, the most common mode of basaltic volcanism is the production of pillow lavas at mid-ocean ridges (Basaltic Volcanism Study Project, 1981). In terrestrial settings, basaltic volcanoes are predominantly characterised by effusive activity. Explosive activity is generally confined to Hawaiian-style lava- or Strombolian fire-fountain activity (Simkin and Siebert, 1994). Fountain activity typically expels ejecta to heights of less than 500 m, rarely having an impact more than a few kilometres from the vent (Chester *et al*., 1985, Simkin and Siebert, 1994, Barberi *et al*., 1995). By contrast, highly explosive eruptions are the norm in chemically more evolved systems (Carey and Sigurdsson, 1989). Compared to their silicic counterparts, basaltic magmas have higher liquidus and eruption temperatures, and lower viscosities. Coupled with basalt's lower initial volatile concentrations, these factors mean that gases are able to readily exsolve. Consequently, gases are often decoupled from the melt during magma ascent (Sparks *et al*., 1994).

Nevertheless, several examples of violent explosive activity have now been documented for basaltic volcanoes. These include sub-Plinian (e.g. Fuego 1973-74; Rose *et al*., 2006; and Shishaldin 1999; Caplan-Auerbach and McNutt, 2003) and Plinian eruptions (e.g. Tarawera 1886 and Etna 122 BC; Coltelli *et al*., 1998; Houghton *et al*., 2004; Sable *et al*., 2006) along with large phreatomagmatic events (e.g. Coombs Hills, Antarctica; White and McClintock, 2001).

During an eruption, the factors which control the rate of magma ascent, fragmentation and expulsion include intrinsic properties, such as melt composition,

pre- and syn-eruptive volatile contents, crystal content, temperature and viscosity, along with external factors such as the dimensions of the conduit and vent, confining pressure and accessibility of interaction with external water.

Deep within the conduit, eruptions are driven by the formation and growth rate of gas bubbles (Sparks *et al*., 1978; Wilson and Head, 1981). Magmatic H_2O plays the dominant role in eruption dynamics, although CO_2 exsolution may be more important at depth (Allard *et al*., 2005). Theoretically, a closed system of degassing is necessary for magma to accelerate sufficiently to drive a powerful, explosive eruption. In this scenario, gas bubbles are mechanically coupled with the melt and cannot escape; the exsolution and expansion of gas therefore accelerates the mixtures upwards as bubble overpressure increases (Cashman *et al*., 2000; Jaupart, 1996). Fragmentation is assumed to take place when the volume fraction of bubbles reaches a threshold value (theoretically 0.75; Sparks *et al*., 1994), or when the bubble overpressure is sufficiently large to rupture bubble walls by exceeding the tensile strength of the surrounding melt (Alidibirov, 1994, Zhang, 1999), or when the strain rate exceeds the tensile strength of the magma, driving the melt through the brittle-ductile transition (Dingwell, 1996; Papale, 1999). The zone of interaction between magma and water often occurs in the relatively shallow conduit or vent regions. Therefore deep magma ascent processes within phreatomagmatic events are generally likely to be similar to those of magmatic eruptions. This is not true for all systems, however. Activity at Vesuvius, for example, is one notable exception (Barberi *et al*., 1989).

Iceland's unique climate and geography provide diverse environmental circumstances that allow for explosive interaction of water and magma – an abundance of accessible groundwater, seawater and glacial ice results in frequent and widespread explosive phreatomagmatic eruptions. Here, although basaltic volcanism dominates, the balance of eruption styles is strongly skewed towards the explosive. Thordarson and Larsen (2007) catalogued volcanism in Iceland in historic time (i.e. since settlement of the island in 870 AD). They found that of 159 individual eruptions (identified by their products), 124 were explosive. If unverified explosive events are included the tally increases to 205 eruptions, of which 170 were explosive. Furthermore, Thordarson and Höskuldsson (2008) showed that there have been 2400

individual eruptions in Iceland in the post-glacial period. Among these, effusive activity accounts for approximately 500 events; the remainder consist of explosive, subglacial, mafic eruptions.

2.1.1 PHREATOMAGMATIC VOLCANISM

On Earth, phreatomagmatism is a globally significant phenomenon. The importance of this end-member style of volcanic activity derives from the fact that a very large proportion (>70%) of Earth's surface is covered by water (Holden, 2010). In addition, groundwater is abundant in most regions of the globe. Phreatomagmatic activity is therefore an intrinsic aspect of volcanism on this planet and occurs with high frequency in a diverse number of settings.

Many phreatomagmatic events are characterised by intense explosive activity (Thorarinsson *et al*., 1964; Houghton and Nairn, 1991), the generation of particularly fine-grained tephra (Walker and Croasdale, 1972) and the formation of pyroclastic density currents (PDCs) from collapsing fountains (Moore *et al*., 1966a; Moore *et al*., 1966b; Waters and Fisher, 1971). Transitions in eruption style between wet eruption columns and cold, relatively dense PDCs (termed "base surges" by these authors) have been observed in many historical phreatomagmatic eruptions. These are largely attributed to changes in the amount of external water interacting with the eruptive mixture.

While phreatomagmatic eruption phases are most frequently distinguished by features such as a more steam or water-laden plume, and finer grained products than those of their purely magmatic counterparts, the principal mode of fragmentation in such events can vary from passive quenching and granulation of magma to large-scale thermohydraulic explosions, according to the relative proportions of magma and water available (e.g. Wohletz, 1983; 1986; Heiken and Wohletz, 1991). The juvenile (glass) population among phreatomagmatic tephra consists of a number of classifiable clast types/shapes, which are indicative of fragmentation (e.g. angular, fractured edges) and

transportation (e.g. pitted outer surfaces) history (e.g. Heiken and Wohletz, 1985; Zimanowski *et al*., 1991; Büttner *et al*., 1999; Dellino *et al*., 2001).

When ascending magma encounters water at the Earth's surface or high within the volcanic conduit, the resulting array of observed eruption styles and fragmentation mechanism reflects the variety of circumstances in which a phreatomagmatic interaction may occur. Specifically, these include phreatic, lacustrine, littoral, submarine and subglacial environments.

2.1.2 "TYPE" EXAMPLES OF SMALL VOLUME BASALTIC PHREATOMAGMATIC ERUPTIONS

2.1.2.1 SURTSEY, ICELAND, 1963-1967

The 1963 eruption of Surtsey was the first extensively observed and documented basaltic, phreatomagmatic, submarine to emergent event. This small eruption off the southwest coast of Iceland dramatically illustrated the explosive influence of water on magma that may have otherwise behaved effusively, or in only a mildly explosive fashion (Fig. 2.1). The following review is based principally upon the accounts of Sigurdur Thorarinsson (1964, 1967, 1974), but also includes detail from later summaries by Thordarson (2000), Thordarson and Sigmarsson (2008) and White and Houghton (2000).

During the Surtsey event material issued from five clusters of vents along a 6 km northeast trending submarine ridge, whereby more than 10^9 m^3 of magma was erupted over approximately 1300 days (Thordarson and Sigmarsson, 2008). As the volcanic edifice built up from the sea floor, volcanic activity passed through submarine and emergent eruption phases before transgressing into an extended period of lava effusion. A description of the two key stages of development and their resulting deposits is given below:

Figure 2.1: Stock images of the 1963-4 Surtsey eruption. (A) Tephra jetting and water-rich plume; (B) “Rooster-tail” (also “cypressoidal” or “finger”) jets; (C) Simultaneous continuous uprush (left and back), tephra jets (front), and steam plume (right); (D) Continuous uprush activity with associated tephra fallout.

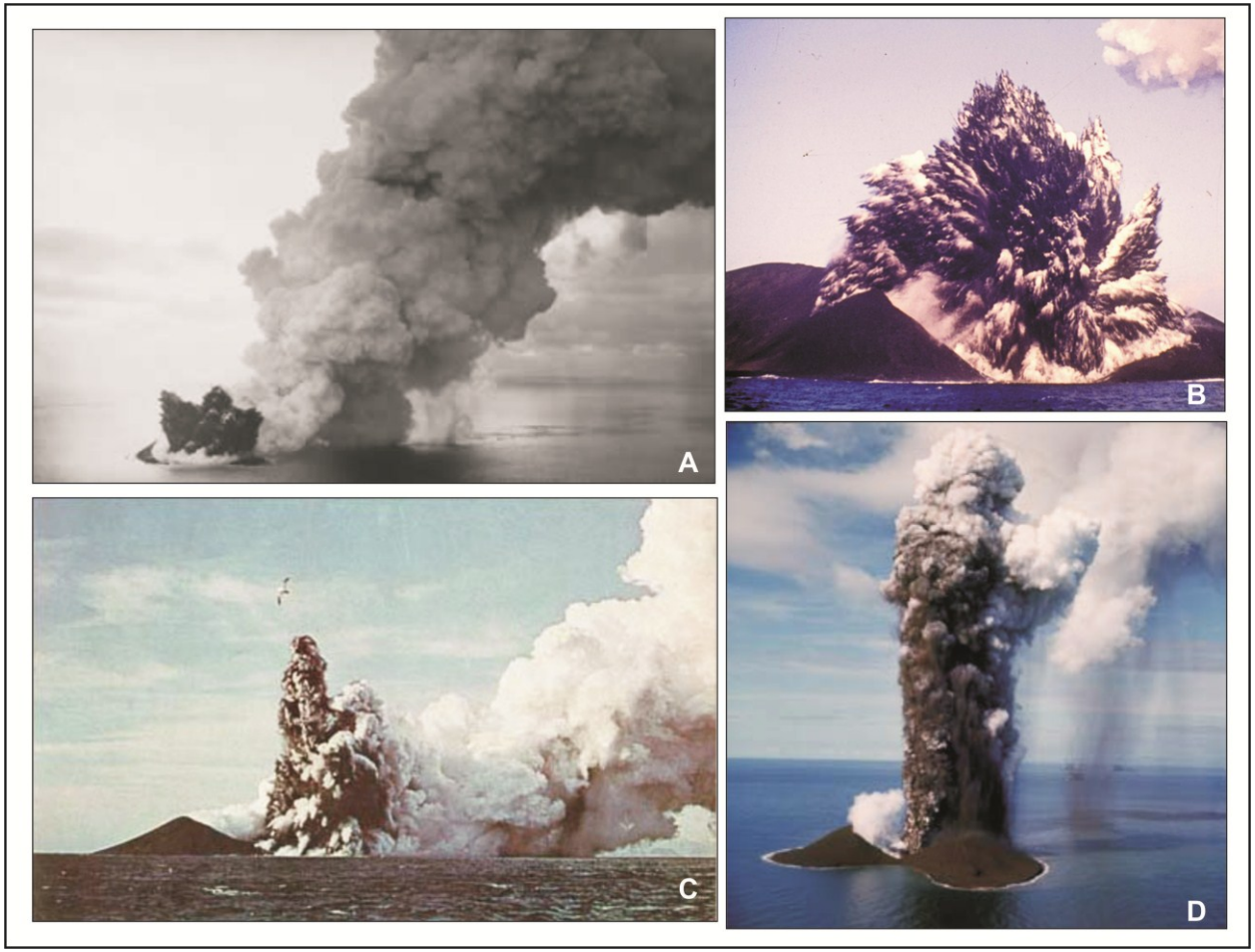

Stage 1 – Subaqueous Explosions

Surtsey's eruption began at 130 m below sea level, progressing unnoticed until the volcano had built up to approximately 10 m below the water surface. On November 14th 1963, eruption columns were established above the surface of the water, quickly reaching heights of up to 200 m. By the next morning, Surtsey had emerged from the sea and was in near-constant eruption (e.g. Thordarson and Sigmarsson, 2008 and references therein). Early jetting activity was fully subaqueous, producing turbulent and dilute gravity flows. Consequently, at this stage deposition took place largely from traction under unsteady flow conditions. Occasional deposition of more massive beds resulted from the ejection of vent slurry, or the collapse of particularly concentrated tephra jets. Later, the most vigorous tephra jets were able to clear the water surface, while those that did not have sufficient momentum to breach still contributed steam to feed a vapour column rising through the water and above its surface (White and Houghton, 2000).

Stage 2 – Emergence from the Sea

Once Surtsey had constructed an edifice above sea-level, two distinct styles of activity were observed. Activity from a flooded vent resulted in the ejection of "rooster-tail jets". These are tephra-steam-water laden sub-horizontal to vertical jets that are accompanied by the expulsion of ballistics. Tephra is observed to be deposited from the jet via a combination of fall and current motions – i.e. the concept of 'inclined fall'. Tephra jets were often produced at time scales on the order of several bursts per minute, but also occurred in isolation at widely and irregularly spaced intervals. Frequently, these occurred in increasingly close succession approaching the onset of continuous uprush episodes. These tephra jets were the principal contributors to construction of the tephra cone. Tephra ramparts (or tephra cone constructs) were then observed to block the passage of sea water resulting in continuous uprush activity. When this happened, relatively stable, water-rich and tephra-laden eruption columns were established, rising several kilometres into the atmosphere. This style of activity is referred to as "continuous uprush" by Thorarinsson (1967).

Surtseyan deposits typically feature a clast population that spans a range of particle sizes – from micrometres to metres, with a high proportion (>50 wt. %) of

juvenile ash. In addition, they contain a range of juvenile clast types, including blocky and platy glass shards, variably vesicular (range 2-90 %) sideromelane glass and tachylite (i.e. cryptocrystalline) fragments, moss-like and drop-like clasts, along with lesser amount of crystal fragments and blocky accidental non-juveniles (Kokelaar, 1983; 1986; Wohletz and Sheridan, 1983). This varied assortment of products reflects the intense energy with which magma is disintegrated, as well as tracking the physical properties of the magma (fluid through to brittle) and the range of kinetic mechanisms driving fragmentation (e.g. quenching and thermal granulation and recurring vapour film growth-collapse events) (Wohletz, 1986).

Both the rooster-tail and continuous uprush styles of activity disperse tephra by mechanisms of pyroclastic fall, surge and flow, often simultaneously. In the 1963-67 Surtsey eruption >85% of the erupted tephra was deposited within 1.5 km of the source vents, building a steep-sided and stratified pyroclastic edifice rising ~260 m above the seafloor. A typical Surtseyan edifice consists of numerous centimetres to metres thick beds with lenticular geometry. On the steeper parts of the edifice beds dip away from the vent at 30-40° angles. However this shallows rapidly over a relatively short distances to sub-horizontal (1-3°) layering at the foot of the tuff cone. The bulk of the deposits produced by emergent Surtseyan eruptions accumulate in close proximity to the vent primarily as a consequence of the premature fallout of ash-grade particles resulting from the combined effects of high tephra load, condensation of steam in the eruptive mixture, and relatively short run-out distances (1-5 km) of associated PDCs. Tephra fallout associated with continuous uprush activity tends to be more widely dispersed. However, deposit thicknesses of >1 cm still seldom extends beyond 30 km from source (Thordarson, 2000).

Figure 2.2: Interpretative cartoon of a typical Surtseyan-style eruptive phase in the 1957-58 Capelinhos eruption. Strong local winds disperse the tephra preferentially in one direction. Simultaneous action of PDC and tephra fall generates hybrid deposits in the proximal regions of the tuff cone. Occasional long-range PDCs reach distances of 1-2 km from the vent. The bulk of magma is fragmented hydrodynamically as a result of its interaction with sea water. However, parts of the centre of the column are envisaged to be isolated from contact with water, and therefore continue to vesiculate during transport upwards. In distal regions falling tephra may be impacted by the wind to produce fall deposits with a strong component of lateral motion. Modified from Cole *et al*. (2001).

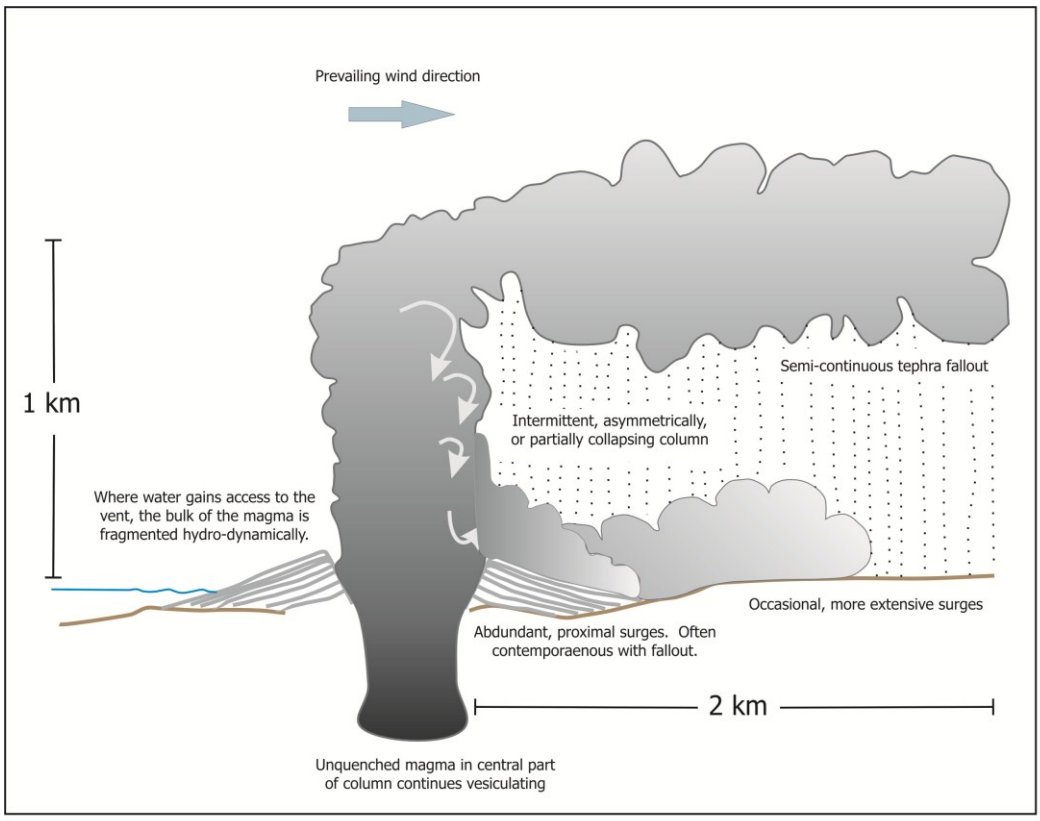

2.1.2.2 Capelinhos, Azores, 1957-58

The 1957-58 eruption of Capelinhos volcano in the Azores is considered to be a classic Surtseyan event, in which rising basaltic magma interacted explosively with sea-water (i.e. Branco *et al*., 1959; Zbyszewski and da Veiga, 1959; Fig. 2.2). During this eruption, three tuff cones were formed. The first two were destroyed during the eruption itself; however the final cone, formed in 1958, remains. Unlike at Surtsey, the remaining portion is accessible, and well-exposed sections exist in wave-cut cliffs, permitting a more detailed investigation of its subaerial deposits. Furthermore, because the Capelinhos eruption occurred immediately adjacent to Faial Island, some of the more distal products have also been preserved.

The Capelinhos eruption began 70 m below sea level, where initially four vents were active, aligned on a west-northwest/east-southeast trending fissure. Phreatomagmatic activity occurred in three main periods during which activity occurred in short but relatively continuous bursts (i.e. eruptive phases), separated by periods of repose which typically lasted for several hours (Cole *et al*., 2001).

Contemporary accounts of the eruption (Branco *et al*., 1959; Zbyszewski and da Veiga, 1959) documented the frequent occurrence of "rooster-tail" tephra jets, alternating with sustained continuous uprush style columns, sometimes >1 km in height. According to Branco *et al*. (1959), effusive and explosive magmatic activity, first occurred as early as December 17th 1957. On several occasions between January and March 1958 simultaneous lava-fountaining (i.e. magmatic) and phreatomagmatic activity was observed. This shows that phreatomagmatic activity did not simply die out and become replaced by fully magmatic activity as the volcanic edifice built up above sea level. Instead, activity rapidly oscillated between the two styles. Tuff cones were constructed during all three periods of phreatomagmatic activity, each forming in a progressively eastward direction.

In May 1958, phreatomagmatic activity at Capelinhos was replaced by predominantly Hawaiian activity (i.e. lava fountaining) punctuated by discrete Strombolian-style explosions, as by that time the sea water was effectively excluded

from the vent. In late May, and in August 1958, lavas were erupted from the main vent as well as subsidiary vents in the flanks of the tuff cone (Cole *et al*., 2001).

A brief summary of the five lithofacies identified by Cole *et al*. (2001) within the Capelinhos deposit is given below for the purposes of later comparison with the Grímsvötn 2004 succession:

Lithofacies I - Even thickness beds with laterally continuous internal stratigraphy; interpreted as fallout.

Lithofacies II - Beds with internally discontinuous lenses and sand wave structures, which increase in abundance toward the outer margins of the tuff cone; interpreted as having been deposited by PDCs.

Lithofacies III - Mantle-bedded deposits with laterally discontinuous internal stratigraphy; interpreted to have been formed by hybrid processes where fallout of tephra occurred simultaneously with PDCs. In the outer flanks of the tuff cone, this unit grades laterally into lithofacies I-type fallout beds.

Lithofacies IV - Alternating beds of coarse ash aggregates and non-aggregated fine ash. These are particularly well developed in distal regions. This lithofacies in interpreted to have formed partly by fallout, however alternating beds also occur which are plastered against obstacles, indicating an origin from wet PDCs.

Lithofacies V - Scoria lapilli beds; interpreted as fallout from Hawaiian-style lava-fountaining.

Cole *et al*. (2001) found a wide range of pyroclast vesicularities within the Capelinhos deposit (30-70%). They interpreted this to mean that both phreatomagmatic and magmatic volatile-driven fragmentation mechanisms were operating simultaneously during nominally "Surtseyan"-style activity. The predominance of poorly vesicular, blocky clasts was attributed to magma quenching by direct contact with water or a water/tephra-slurry (Kokelaar, 1983; 1986), while magma that did not "see" water was therefore not quenched and may have continued to vesiculate within the eruption column.

2.1.2.3 Comparison of the Surtsey and Capelinhos events

There is striking similarity between the 1957-1958 Capelinhos eruption and the emergent phase at Surtsey. Both rooster-tail jets and continuous uprush columns were frequently observed at both locations, in addition to the occurrence of simultaneous magmatic and phreatomagmatic volcanism (Thorarinsson, 1964). Intermittent rooster-tail jet activity is related to higher water to magma ratios than continuous uprush activity (Wohletz and McQueen 1984; Kokelaar 1983, 1986; Moore 1985, 1987; Sohn and Chough 1992).

Similar to the patterns observed at Surtsey, continuous-uprush activity at Capelinhos produced predominantly fall deposits. Approximately 87% of beds 400 m from the vent were formed by fallout processes (Cole *et al*., 2001). PDCs occurred concurrently with fallout during approximately half of this time. This is consistent with studies of tuff cones and tuff rings, which show that tuff cones are formed mainly by fallout processes, whereas tuff rings are the product of more abundant PDCs (Sheridan and Wohletz, 1983; Sohn, 1996). Deposits of Capelinhos tephra more than 1 km from the vent are abundant on the eastern point of Faial island. Representative distal sections are composed of numerous thin beds and laminae in intervals up to several metres thick, recording much of the phreatomagmatic activity that occurred during this event. The presence of tephra plastered against obstacles up to 2 km away from the vent indicates that there were occasional, longer run-out PDCs (Cole *et al*., 2001).

Like at Surtsey, the Capelinhos deposits demonstrate the complex interplay between deposition by pyroclastic density currents versus fallout. The most proximal deposits show evidence for simultaneous deposition by fallout and PDCs. However, at distances of >1km from the vent it is difficult to distinguish between fall and PDC deposits. Tephra transported within a decelerating, low-velocity PDC may experience minimal traction, inhibiting the formation of cross-layering. In this case layers of even thickness may form, which resemble those of fall deposits. Conversely, weak plumes, formed during relatively small explosive eruptions such as this, are strongly affected by the wind. Tephra falling from a strongly inclined plume or a tephra "jet" may be deposited in a similar manner to that of low-velocity PDCs (Sparks *et al*., 1997).

2.2 SUBGLACIAL VOLCANISM IN ICELAND

Subglacial eruptions are issued from a vent situated beneath a mountain glacier or ice sheet (Smellie, 2000). Subglacially constructed landforms are conspicuous features within Iceland's volcanic zones and eruptions continue to frequently occur beneath present-day glaciers (e.g. Kjartansson, 1960; Sæmundsson, 1980; Gudmundsson, 2005). At present, ~20% of Iceland's active volcanoes are covered by ice (Jakobsson and Gudmundsson, 2008). This includes many of the country's most active central volcanoes, such as Grímsvötn and Katla (Fig. 2.3). Historically, more than 50% of all eruptions have taken place within glaciers, mostly in the western part of Vatnajökull (i.e. Grímsvötn and Bárðarbunga) and in Mýrdalsjökull (Katla) (Larsen, 2002).

Eruptions under ice exhibit similar characteristics to subaqueous eruptions in terms of the style of volcanic activity (Jakobsson and Gudmundsson, 2008). However, the interaction of magma with water or ice has a major effect on the style of volcanic activity and the morphology of resulting landforms. Traditionally, subglacial eruptions are classified according to whether they occur beneath ice that is either "thick" or "thin" (e.g. Smellie, 2000). However, this is an over-simplification. It is really the pre-eruption glacier structure (i.e. densification and proportion of impermeable ice) that determines the hydraulic evolution of a subglacial eruption (Smellie, 2002). Previous authors have used the term "thin ice" to refer to ice that is generally <150 m thick, and is permeable (Smellie *et al*, 1993; Smellie and Skilling, 1994), whereas "thick ice" refers to ice that is >150 m thick and largely impermeable. The permeability difference between so-called "thin" and "thick" glaciers is the critical factor. During eruptions beneath thin ice melt-water and volcanic debris are able to readily escape – either by flowing along the bedrock-glacier interface (Nye, 1976; Björnsson, 1988) or over the glacier surface (Jónsson, 1982). Conversely, during eruptions under thick ice, the overburden pressure around the vent traps melt-water in a subglacial vault (Björnsson, 1975; 1988) - albeit that the creation of a subglacial lake may also be coincident with basal leakage and water overflowing at the surface (Smellie, 2000).

Figure 2.3: Extent of exposures of subglacial volcanic rocks of late Pleistocene age (0.01-0.78 Ma) in presently non-glaciated regions of Iceland (grey shading). WVZ: Western Volcanic Zone; EVZ: Eastern Volcanic Zone, NVZ: Northern Volcanic Zone, SVZ: Snæfellness Volcanic Zone, ÖVZ: Öræfajökull Volcanic Zone. From Jakobsson and Gudmundsson (2008).

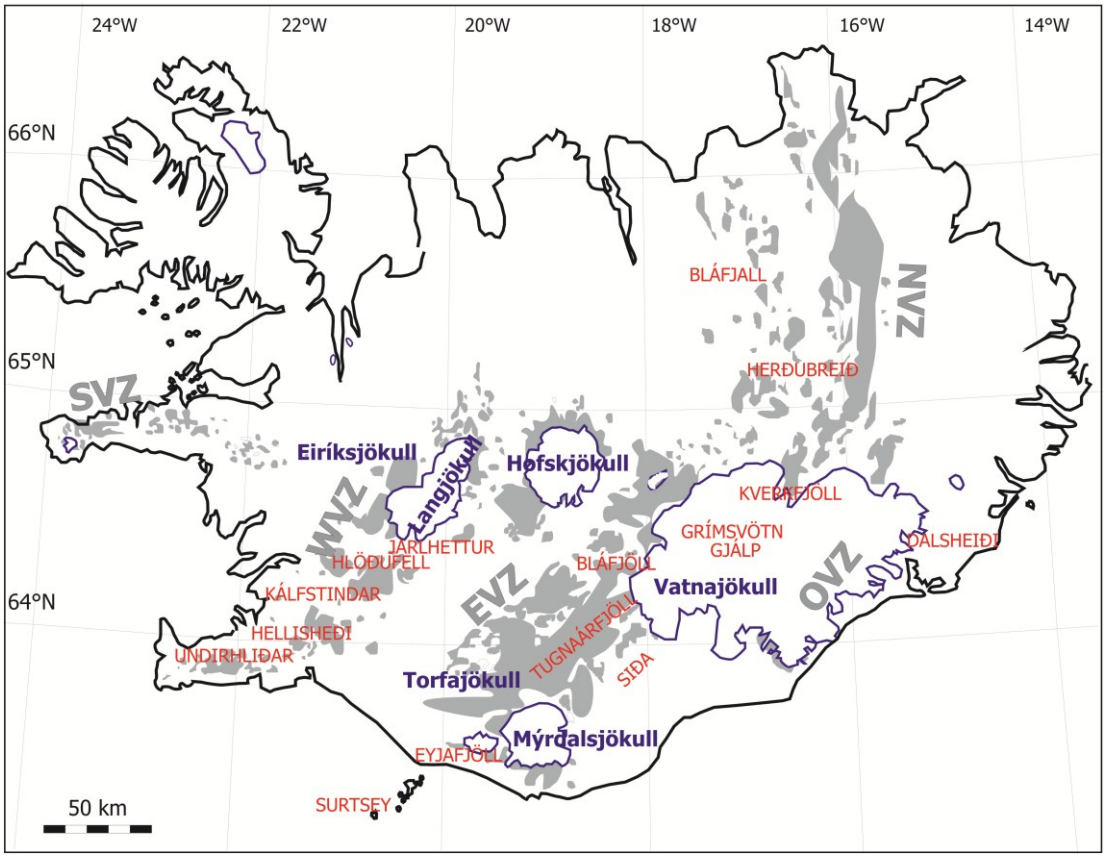

2.2.1 GLACIER HYDRAULICS

Glacier hydraulics exert fundamental controls on the nature of subglacial eruptive sequences. A simple classification is made based upon temperature distribution: temperate (wet-based) glaciers are at the pressure melting temperature throughout their thickness (except in a thin surface layer), while polar glaciers are well below freezing point and are frozen to their beds (Hooke, 2005). This distinction is critical, because in temperate glaciers water can migrate, which has consequences for the course of events in a subglacial eruption (Björnsson, 1988).

Most glaciers are crudely stratified, comprising an uppermost permeable layer (snow, firn, and fractured ice) overlying permeable, unfractured ice (Hooke, 2005). The hydraulic gradient (and thus direction of melt-water flow) in a glacier is controlled by the slope of the glacier surface, rather than that of the glacier bed (Björnsson, 1988). During an eruption, ice above and around the vent is melted, creating a depression in the ice surface. This distortion in the local hydraulic gradient causes melt-water to flow in towards the vent where, for "thick" glaciers, it is contained by an encircling ice barrier in a water filled vault. If melting penetrates right through to the surface, a lake is formed. The water level within the vault depends on a balance between rates of ice melting versus basal leakage. Eventually, if the water becomes deep enough, the surrounding ice barrier is floated and the vault drains (Björnsson, 2003; Gudmundsson and Björnsson, 1991; Jakobsson and Gudmundsson, 2008). The dynamic effects of subglacial hydraulics will therefore have considerable impact on the availability and accessibility of external water.

At Grímsvötn, there is a complex interplay between jökulhlaup release and volcanism (Björnsson, 1974, 2003). In some instances, jökulhlaups occur with no associated eruption. In other cases, such as the 2004 event, geothermal activity causes melt-water to accumulate within the Grímsvötn lake (Guðmundsson and Björnsson, 1991; Guðmundsson *et al*., 1995). The subsequent volcanic eruption is then thought to be triggered by depressurisation associated with the discharge of this accumulated mass of water (Vogfjörð *et al*., 2005). Conversely, the 1996 jökulhlaup occurred five weeks after the Gjálp eruption, as the water from ice melting during and after this event

drained into the Grímsvötn subglacial lake and accumulated there before breaching the ice barrier (Guðmundsson *et al*., 1997).

2.2.2 LITHOSTRATIGRAPHIC UNITS AND EDIFICE MORPHOLOGY

This section establishes the link between classical subglacial lithofacies and eruption style. This lithofacies suite reflects a decrease in confining pressure over time as the volcanic edifice grows vertically within a melt-water lake (e.g. Jones, 1969; Skilling, 1994; Werner *et al*, 1996). Confinement by ice, along with changes in the water level throughout the course of the eruption due to melt-water drainage creates morphological features which are diagnostic of the subglacial environment (e.g. Smellie, 2000; 2006; Gudmundsson *et al*., 2004). At large hydrostatic pressures effusive activity dominates, while at lower pressures this transitions to explosive interaction (e.g. Wohletz, 1986; White *et al*., 2000; Chapman *et al*., 2000). Drainage of the melt-water lake (either supra- or subglacially) may result in lava flows unconformably overlying these fragmented deposits, signalling an abrupt change in eruption conditions (Smellie, 2000). Eruptions beneath thin ice generate a distinct set of lithofacies from those beneath thick ice as a consequence both of the different mechanical properties of the glacier, but also because of the differences in confining pressure and the availability of external water.

A typical subglacial sequence in Iceland will consist of one or more of the following lithostratigraphic units (Fig. 2.4):

Basal Pillow Lavas: The lowest (i.e. first formed) lithofacies consist of pillow lavas inferred to represent an initial subglacial effusive phase of activity. At this stage, the confining pressure of the ice or water within the subglacial vault is sufficiently high to suppress explosive interactions between magma and water (Zimanowski and Büttner, 2003). Individual pillows are commonly 0.5-1.0 m-wide (e.g. Höskuldsson *et al*., 2006), and they increase in porosity with increasing height in the edifice (Jakobsson and Gudmundsson, 2008). Pillow lavas may be locally absent from subglacial sequences (e.g. Schopka *et al*., 2006; Jakobsson and Gudmundsson, 2008), however thicknesses of

up to 280 m have been reported for basal pillow sequences in the Western Volcanic Zone (WVZ; Jones, 1970). Pillows scarcely form in eruptions beneath thin ice.

Hyaloclastites: The basal pillow lavas are typically overlain by a volcaniclastic ("hyaloclastite") sequence produced by explosive water-to-magma interactions, and typified by a complex association of sub-facies ranging from massive hyaloclastite breccia through variably structured lapilli-tuffs to well-bedded tuffs. Within impermeable glaciers much of the vertical growth of the edifice at this stage takes place during subaqueous or subaerial Surtseyan-style activity as magma erupts through a water-filled "cauldron" within the ice. Eruptions that cease before subaerial emergence form steep-sided ridges predominately composed of palagonitised tuff and breccia. Diagnostic landforms are either hyaloclastite ridges (fissure eruption) or hyaloclastite mounds (circular vents) (Thordarson and Höskuldsson, 2002; Thordarson and Larsen, 2007; Jakobsson and Gudmundsson, 2008).

Lavas: Continued construction of the volcanic edifice results in full emergence of the vent, whereby access to external water is restricted by the build-up of tephra ramparts. Consequently, effusive activity commences and lava shields are formed, which cap the subglacial edifice. Flow-foot breccias are created where lava flows into the water surrounding the volcanic edifice (Smellie, 2000; Jakobsson and Gudmundsson, 2008).

Figure 2.4: Simplified cross-sections of a tindar and a tuya-type morphological structure. From Jakobsson and Gudmundsson (2008).

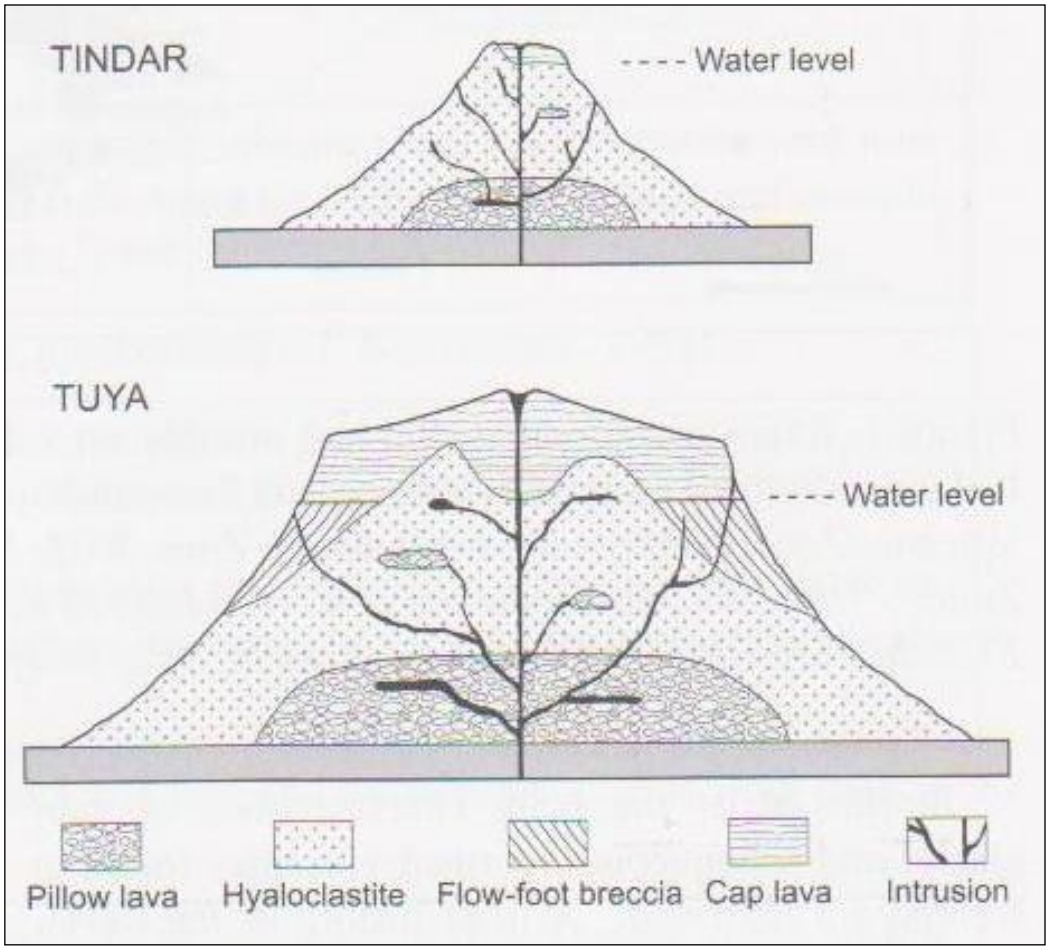

2.2.2 THE MÓBERG FORMATION

The Móberg Formation is a chronostratigraphic unit local to Iceland, which encompasses all strata formed from the Brunhes geomagnetic epoch up to the end of the Pleistocene (i.e. 0.01-0.78 Ma, Kjartansson, 1943; 1960; 1966; Einarsson, 1994). Pjetursson (1905) was the first to show that the Móberg Formation – including the móberg ridges and 'stapar' (tuyas) was Quaternary in age, while its volcanic origin was first demonstrated by Tyrell and Peacock (1927). The Móberg Formation consists of sequences of pillow lavas, hyaloclastites and cap lavas which make up a number of subglacially-constructed mountains. It covers approximately 11,200 km^2 of the portions of the volcanic zones which are not presently covered by ice (Jakobsson and Gudmundsson, 2008).

Kjartansson (1943, 1960, 1966) recognised that the Móberg mountains fall into two morphological types each with similar characteristic lithofacies associations – móberg ridges (later to become known as tindars (Skilling, 1994)), and tuyas (or table mountains). Later work (e.g. Bergh and Sigvaldason, 1991) identified a third morphological type – the móberg sheet.

Hyaloclastite Ridges (a.k.a. Tindars): The word "tindar" (singular = tindur) in Icelandic refers to a cluster or a row of pointy and steep-sided peaks rising up from a mountain range. This term was adopted by Jones (1970) when referring to the common móberg ridge constructs. These are the subglacial equivalent of Holocene fissure vent systems. These eruptions commence with activity along particular fissure segments but subsequently concentrate to a row of craters (Wylie *et al*., 1999). The length of each hyaloclastite ridge is usually more than double its width (i.e. they are high aspect ratio formations) (Jakobsson and Gudmundsson, 2008).

The largest tindar formations feature pillow lavas overlain by hyaloclastite (e.g. Kálfstindar, SW-Iceland; Jones, 1970). However, in many of the smaller tindar formations pillow lavas are absent (e.g. Helgafell, SW-Iceland; Schopka *et al*., 2006). In some cases, tindar formations are made up of pillow lavas exclusively (e.g. Kverkfjöll, central Iceland; Höskuldsson *et al*., 2006). Apparently, in the latter case hydrostatic pressure was sufficient to inhibit explosive magma-water interactions for the entire

duration of the eruption (or, in other words, the eruption ceased before attaining the explosive phase). In examples where pillow lavas are absent, it can be assumed that activity was explosive from onset (i.e. hydrostatic pressure was never sufficient to inhibit explosive interaction). Some tindars in the WVZ feature thin lava caps (e.g. Brekknafjöll; Jakobsson and Gudmundsson, 2008).

Tuyas (a.k.a. Table Mountains or Stapi): Tuyas tend to have a single crater and are often monogenetic eruptions e.g. Eiríksjökull, which is the largest monogenetic volcano identified in Iceland (Jakobsson and Gudmundsson, 2008). However, some examples are known to have a more complex eruptive history e.g. Herðubreið in the NVZ, which Werner *et al*. (1996) show to consist of a lower unit, erupted in a lacustrine environment with little evidence for ice contact, and an upper unit erupted within a thick glacier. It is likely that tuya-forming eruptions were longer lived and of considerably larger volume than tindar-forming fissure events (Jakobsson and Gudmundsson, 2008). Not all tuyas, however, reach the stage of restricted access of water to the vent, and thus a lava cap. Moreover, in the WVZ there are documented examples of tuyas which are constructed purely of pillow lavas (Jakobsson and Johnsson, 2008).

Móberg Sheets: Low aspect ratio, high volume layers of pillow lava and hyaloclastite often with columnar jointing at the base, and overlying tillite in some regions, have been described by a number of workers (e.g. Walker and Blake, 1966; Bergh and Sigvaldason, 1991; Vilmundardóttir *et al*., 2000; Smellie, 2008). These are inferred to have formed by high discharge fissure eruptions under thick ice or by lava flowing under a valley glacier (Jakobsson and Gudmundsson, 2008).

A glossary of terms related to subglacial volcanism is provided in Table 2.1 because of the large number of synonyms in use in the literature of this field.

Table 2.1: Glossary of terms related to eruptions under glaciers.

TERM	DEFINITION
Emergent subglacial volcanism	General term which refers to eruptions and products which have broken through the ice surface to the atmosphere or occur within the ice. Synonym: "Intraglacial" (Jakobsson and Guðmundsson, 2008).
Flow-foot breccia	Sediments that have been deposited as the lava front advances into water (Jones, 1969). Synonyms: "Foreset breccia" (Jakobsson, 1978), "Lava-fed delta" (Skilling, 1994).
Hyaloclastite	Volcaniclastic deposit formed by fragmentation by both explosive magma-water interactions and passive granulation of glassy lava rinds (Fisher and Schminke, 1984). Refers to both consolidated and unconsolidated deposits.
Hyaloclastite Ridge	A linear, often serrated, ridge comprised of hyaloclastite and/or pillow lavas, occasionally capped by lava (Chapman *et al*., 2000). May consist of a series of small peaks. Synonym: "Tindar" (Jones, 1969), "Móberg Ridge" (Kjartansson, 1960).
Móberg	Consolidated mafic to intermediate hyaloclastite (Kjartansson, 1943).
Móberg sheet	A horizontal to sub-horizontal lying layer of hyaloclastite with isolated pillows and pillow fragments, usually with columnar jointed basalt at the base (Walker and Blake, 1966; Loughlin, 2002).
Palagonite	Hydrothermally altered mafic to intermediate volcanic glass (Peacock, 1926; Stroncik and Schminke, 2002).
Passage Zone	The transition zone between a subaerial lava and its subaqueous flow-foot breccia (Jones, 1969).
Tuya	A sub-rectangular or circular, flat-topped mountain comprised of hyaloclastite and/or pillow lava, usually capped by lava (Matthews, 1947). Synonyms: "Stapi" (Kjartansson, 1943), "Table Mountain" (Bemmelen and Rutten, 1955).
Subglacial volcanism	Volcanic processes occurring under the ice (or at the ice-bedrock interface) without direct contact with the atmosphere (Jakobsson and Guðmundsson, 2008).

2.3 PHREATOMAGMATIC FRAGMENTATION

2.3.1 THE PHYSICS OF PHREATOMAGMATISM

Magmas have large heat capacities and are erupted at high temperatures – thus they are a tremendous source of thermal energy. If rising magma encounters ground or surface water at hydrostatic pressures lower than the critical pressure for water (i.e. ~22 MPa, Wohletz and Zimanowski, 2000), then the rapid conversion of water to steam can generate explosions, which fragment the magma. Where confining or hydrostatic pressure exceeds the critical value for water, an explosive interaction will theoretically not take place since the phase transition from water to steam is suppressed. Controls on the conditions by which explosive activity results from magma-water interaction include: the ratio of water mass to magma mass, the dynamic interaction between the magma and water, and also the manner in which the interaction is geometrically confined.

Sustained phreatomagmatic activity has been compared to industrial explosions known as fuel-coolant interactions (Peckover *et al*., 1973; Board and Hall, 1975). Fuel-coolant explosions occur when two fluids are mixed whereby the temperature of one fluid (fuel) greatly exceeds the boiling point of the other (coolant). Thus, the cooler liquid is rapidly vaporised, resulting in an explosion. Wohletz (1986) applied this industrial analogue to volcanic systems, proposing a model for phreatomagmatic explosions (or volcanic MFCI; molten fuel-coolant interactions) in which explosions are generated in a cyclic fashion on timescales on the order of microseconds (Fig. 2.5). MFCI is commonly described in four phases (Morrissey *et al*. 2000; Wohletz and Zimanowski, 2000):

(1) Hydrodynamic mixing;

(2) Trigger;

(3) Fine fragmentation;

(4) Vaporisation and expansion.

At low hydrostatic pressure, the heat transfer across the magma-water interface is limited by the formation of insulating vapour films. This is known to physicists as the "Leidenfrost phenomenon", which is most applicable where liquid (water) droplets are placed on a hot plate. In nature, the steam film only forms where the water is in contact with 'hot' red-glowing liquid magma (i.e. at expansion cracks in the quenched outer skin), but is absent from surfaces that have already formed a coherent crust or skin because the heat transfer across this colder interface is too slow to form and maintain the 'steam film'. This effect can be witnessed on video footage from Hawaii of submarine pillow-forming lavas.

If the energy provided by flow processes is sufficient, explosive "pre-mixes" of water and melt can form (Wohletz and McQueen, 1984; Zimanowski, 1998). A trigger in the form of a seismic shockwave, or simply spontaneous local vapour film collapse will result in rapid and complete breakdown of all the vapour films within this premix. This leads to strong thermal and mechanical coupling in the mixture – i.e. both the heat flux from magma to water, as well as the speed of sound in the premix, increase by 1-2 orders of magnitude in just a few microseconds (Büttner and Zimanowski, 1998).

If low energy (<10 J) shock waves pass through a magma-water premix, then the vapour films collapse quasi-coherently, and direct contact between the magma and water can occur without being separated by the vapour phase (Zimanowski *et al*., 1991; Zimanowski *et al*., 1995). Since the two liquids are now hydraulically coupled, the transfer of heat from magma to water increases by 1-2 orders of magnitude (Fielder *et al*., 1980). This initiates an intense fine fragmentation process, which in turn results in a rapid increase in the surface area (i.e. by enlarging the interface of direct contact between magma and water). The processes are thus coupled in a positive feedback system (Zimanowski *et al*., 1995). As the heat flux from magma to water increases, the water becomes superheated and vaporises. The expanding steam may now drive a sustained volcanic eruption, along with further fragmentation, by disrupting magma that has not yet been involved in the interaction (Wohletz *et al*., 1989, Lorenz *et al*., 1994).

Figure 2.5: Cartoon showing the mechanism of fragmentation by MFCI in phreatomagmatic explosions. Top: Cross-section of a planar Taylor instability at the interface between magma (black) and a collapsing vapour film. Bottom: One complete cycle of instability growth and fragmentation. The oscillation of the vapour film transmits momentum to the magma surface such that it becomes distorted into waves (i.e. instabilities defined by their wavelength (λ) and amplitude (η)). These instabilities break up into individual fragments. Those that are smaller than some critical size (λ_{crit}) will not break up into discrete fragments. Vapour film production, collapse, and fragmentation occur in a cyclic fashion. After Wohletz (1986).

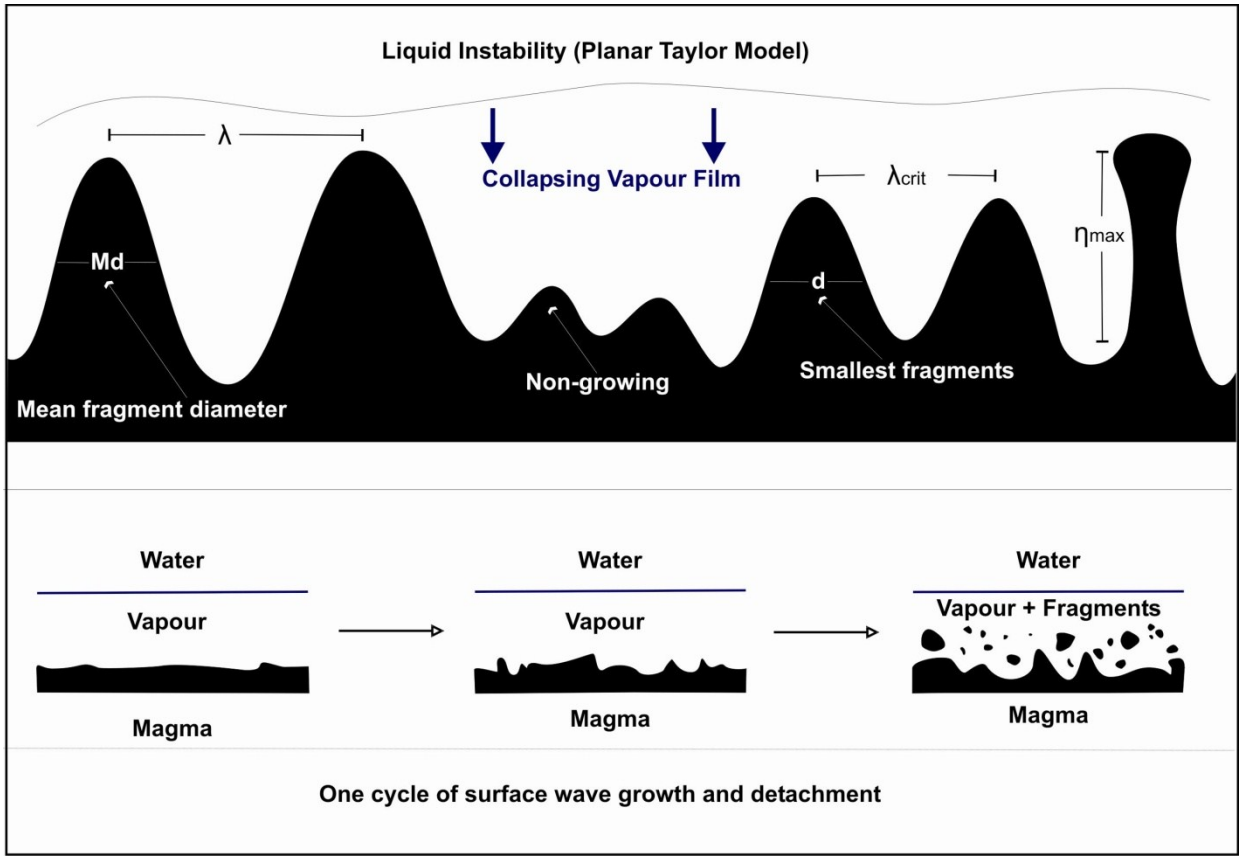

2.3.1.2 EXPERIMENTAL WORK

Since direct observation of volcanic MFCI is not possible, experimental studies have been conducted, with the goals of evaluating the conditions under which phreatomagmatism may occur and identifying fragmentation processes with respect to their products. Wohletz and colleagues pioneered this work (e.g. Wohletz, 1983, 1986; Wohletz *et al*., 1995) using a metal (thermite) melt to approximate magma. These experiments yielded insight into the conditions for maximum efficiency of thermal energy transfer. This occurs when the mass ratio of water to magma is 0.3 (Wohletz, 1986; Kokelaar, 1986). Later studies by Zimanowski and co-workers (e.g. Zimanowski, 1998; Zimanowski *et al*., 1997; 2003; Grunewald *et al*., 2007) experiment with the addition of water to re-melted natural volcanic samples to further explore the properties and kinetics of magma-water interaction in a range of compositions and primary conditions. These studies establish quantitative relationships between particle size distributions and (i) fragmentation and eruption mechanisms and (ii) the rate of energy transfer.

2.3.2 TEPHRA MORPHOLOGY AND ASSOCIATED FRAGMENTATION PROCESSES

Fragmentation of magma and country rock during a volcanic eruption generates particles collectively referred to as “pyroclasts” or “tephra”. Fragmentation can generate a range of particle sizes from several metres to only micrometres in diameter. A summary of terminology applied to these volcanic products, according to their size, is given by Table 2.2. The components of tephra are usually divided into three classes: free crystals, juvenile glass and non-juveniles.

The texture and shape of juvenile pyroclasts reflects the processes of magma fragmentation, transportation and deposition. Heiken and Wohletz (1985) have assembled a collection of SEM (scanning electron microscope) photographs of tephra for various magma compositions, and from a number of different eruptions styles.

Juvenile fragments produced in a phreatomagmatic event have a distinctive morphology. The principal effects of interaction with water are to (i) inhibit or arrest the process of vesiculation, (ii) promote quenching, and (iii) cause thermal fracturing. Consequently, the dominant signature of phreatomagmatic fragmentation noted in both natural and experimental ash-sized clasts is the production of blocky, poorly vesicular fragments, which frequently display hydrothermal fractures (Wohletz, 1983; Heiken and Wohletz, 1985; Triglia *et al*., 2007). It is important to note, however, that while scaled experiments have provided great insight into the fundamental processes of phreatomagmatic explosions, during real volcanic events there are many additional processes which influence the shape and distribution patterns of pyroclasts, which cannot necessarily be accounted for in the laboratory. For instance: magma degassing and resulting variations in vesicularity; crystallisation and chemical heterogeneities in the magma reservoir; particle coalescence and the formation of aggregates; transport and deposition processes; syn- or post-eruptive chemical alteration.

The generalisation that phreatomagmatic deposits are comprised of clasts that are blocky and poorly vesicular does not hold true in Iceland. This is partly because the experiments involve volatile poor (non-vesiculating) melts. In many Icelandic phreatomagmatic deposits the clasts may be characterized by brittle fracture surfaces and roughly equant dimensions, but they are commonly moderately to highly vesicular. Poorly vesicular clasts are present but usually represent only a portion of the mode.

Table 2.2: Size terminology for volcanic ejecta. Adapted from Wentworth (1922) and Fisher (1961).

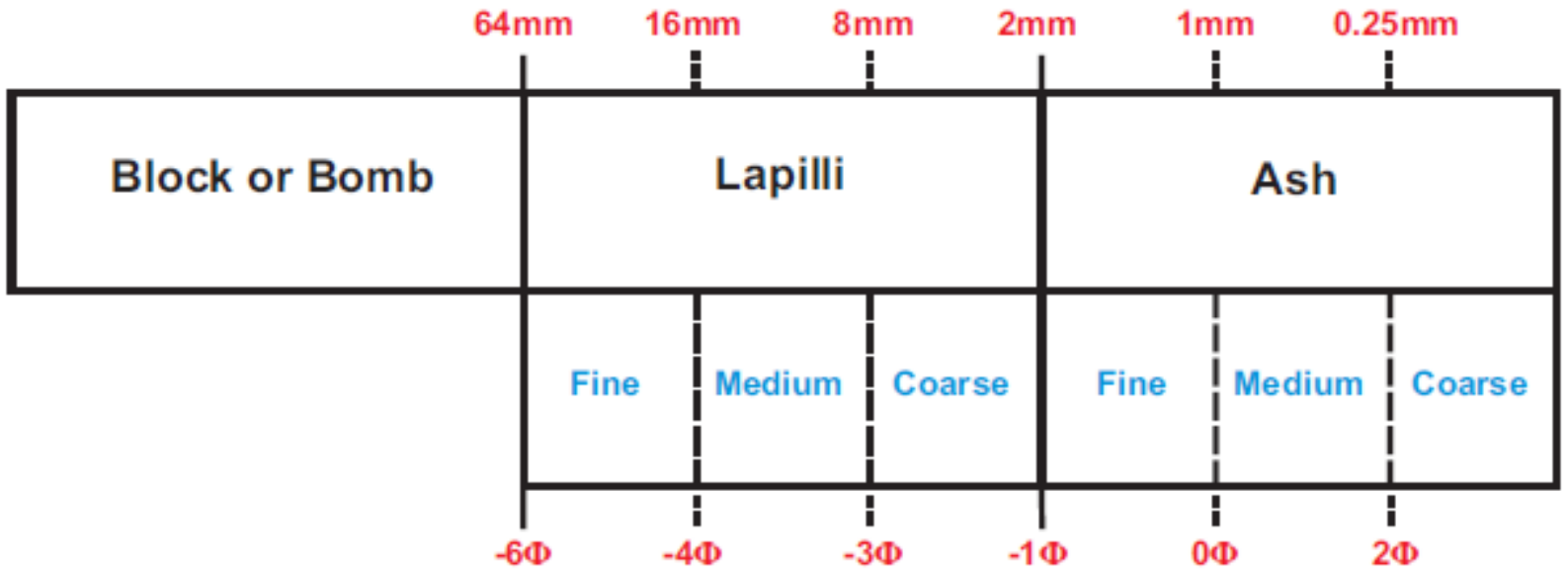

* Note that the "fine" and "coarse" size fractions are frequently further subdivided to denote "*very* coarse" and "*very* fine" material.

2.3.3 CHANGES IN ERUPTION STYLE AND THE INFLUENCE OF CHANGING EXTERNAL CONDITIONS

Changes in the style and/or intensity of a volcanic eruption may occur as a result of changes in the magma supply rate or conduit flow regime (Pinkerton and Stevenson, 1992; Hess and Dingwell, 1996; and Manga *et al*., 1998), or as a result of shifts in external factors. The style and intensity of a volcanic eruption are greatly influenced by conditions at the vent, and in the shallow conduit during the final stages of magma ascent (e.g. Wilson *et al*., 1980; Sheridan and Wohletz, 1983; Barberi *et al*., 1989; Bertagnini *et al*., 1991; and Papale, 1999). The two most important categories of factors at this stage of an eruption are (i) the geometry and changing dimensions of the vent and shallow conduit (Wilson *et al*., 1980), and (ii) the potential for magma to interact with external water (Kokelaar, 1986; Wohletz, 1986; Büttner and Zimanowski, 1998; White and Houghton, 2000). Vent widening is common during large, sustained eruptions. It is often coupled with an increase in the mass discharge rate and a decrease in the exit velocity of the gas-particle mixture, which is critical to the development of a buoyant plume (Wilson *et al*., 1978). It is also clear that external factors, such as accessibility of surface or near-surface water to the vent and the resulting magma to water mass ratio, are important factors (Wohletz, 1983; 1986). Abrupt, or even steadily changing, shifts in this ratio can lead to dramatic changes in the eruption style and intensity, plume development, and pyroclast fragmentation and transportation.

These changes can take place over time-scales ranging from minutes to hours, weeks, or months. Many eruptions involve multiple, reversible changes in eruption style and intensity. Nonetheless, reversible shifts between phreatomagmatic/magmatic activity and buoyant/collapsing columns remain poorly understood.

2.4 PYROCLASTIC TRANSPORT AND DEPOSITION

2.4.1 SEDIMENTATION BY VOLCANIC PLUMES

Terms such as "plume", "column" and eruption "cloud" are often used interchangeably in the literature. However, these words more strictly refer to specific components of an explosive volcanic eruption, which behave in dynamically different fashions. An eruption column, sensu stricto represents the vertical to sub-vertical column incorporating the jet thrust region, convective column and the umbrella cloud up to the level of neutral buoyancy. The eruption cloud, s.s., refers to the steam and ash-laden cloud which is dispersed away from the eruption site by atmospheric currents. The whole system may be referred to as a volcanic plume. This encompasses both the eruption column and the cloud. Therefore the maximum column height and the maximum plume height are not necessarily the same, which has implications for the results of mass discharge calculations and dispersal models.

The majority of published studies of volcanic eruption plumes are based on Plinian eruptions. The geometry of these strong plumes is divided into three areas, according to the particle transport regime (Fig. 2.6). Within the conduit, bubble-rich magma is fragmented to produce a suspension of clasts, supported by expanding gas. As the mixture approaches the vent, its vertical momentum is driven by decompression (Kaminski and Jaupart, 1997). The gas-clast mixture exits the vent at the speed of sound for that particular mixture (Woods and Bower, 1995). For the first 0.5-4 km of its ascent, the erupting mixture travels as a relatively dense, momentum-driven jet (Sparks, 1986; Sparks *et al*., 1997). Models of the jet region suggest that turbulent eddies along its margins entrain air while dispensing with coarse particles (Bursik *et al*., 1992). Consequently, the plume expands and becomes buoyant and the transportation mode grades into a buoyancy-driven convective region. The plume rises until it reaches a level of neutral buoyancy in the atmosphere, where it begins to spread laterally (or in a direction governed by atmospheric conditions such as wind speed and direction); this is known as the "umbrella" region of the plume (Sparks *et al*., 1997). The umbrella region is typically modelled as a gravity current, with provisions for advection by wind (Carey and Sparks, 1986; Bursik *et al*., 1992; Sparks *et al*., 1992;

Koyaguchi, 1994; Bonadonna *et al*., 1998). The size, density and shape of a clast determine how far it can be carried before it is released.

Bursik *et al*. (1992) tie theoretical models of plume sedimentation with data from the Fogo A deposit in the Cape Verde islands, by proposing that tephra transport by eruption columns can be divided into four main categories of dynamic behaviour, which are dependent on grain-size:

(1) The largest clasts travel ballistically, and their motion is only weakly influenced by flow in the column. These clasts leave the column in the lower jet region, their range controlled by ejection angle and muzzle velocity (Walker, 1972). Their distribution, therefore, will be independent of column height.

(2) Clasts 2-10 cm in diameter can be lofted high within eruption columns, so their maximum range is a sensitive indicator of column height (Carey and Sparks, 1986). In the Fogo deposit, these clasts show a continual decrease in accumulation with distance from the vent, indicating that their fallout is not controlled by flow in the umbrella cloud (Bursik *et al*., 1992). Instead, these clasts are continually lost from the margins of the gas thrust and convective regions, with only a few clasts transported to the very top of the column (and therefore reaching the maximum range). This is consistent with a theoretical model of sedimentation from the margins of the plume (Sparks *et al*., 1992).

(3) Clasts with diameters in the 0.05-2 cm range are preferentially transported to the top of the Plinian column. The coarsest clasts exhibit behaviour transitional to those described in group 2 (above) – they fall out from the corner segment of the plume where the vertical support of the column is lost as the flow moves into the umbrella region. The decrease of mass accumulation with distance fits a Gaussian distribution in which the exponential coefficient is dependent on grain-size and flow rate. This is consistent with a simple theory of sedimentation from a turbulent gravity current. Turbulence within the current thoroughly mixes the clast population, but particles fall out at the base.

Figure 2.6: Cartoon (i.e. not to scale) illustrating the principal features of a magmatic volcanic plume, and the principal mechanisms of sedimentation from each region. Bubble-rich magma is converted to a highly turbulent mixture of gas and magma fragments in the fragmentation region, above which the mixture accelerates and is discharged from the vent at high velocity. In the jet region, particle motion is dominated by initial vertical momentum (muzzle velocity), and jet density>atmosphere. Tephra is transported along a modified ballistic trajectory (1). In the convective region, the plume rises by buoyant convection as plume density<atmosphere. In this region, tephra is lost from turbulent eddies at the plume margins (2). H_b refers to the level of neutral buoyancy – the height at which the plume density is equal to that of the atmosphere. The umbrella region is located above this. In the umbrella region, the plume spreads laterally as a gravity current, and sedimentation is consistent with fallout from the base of a well-mixed, turbulent current (3). H refers to the maximum plume height. Modified from Bursik *et al*., 1992.

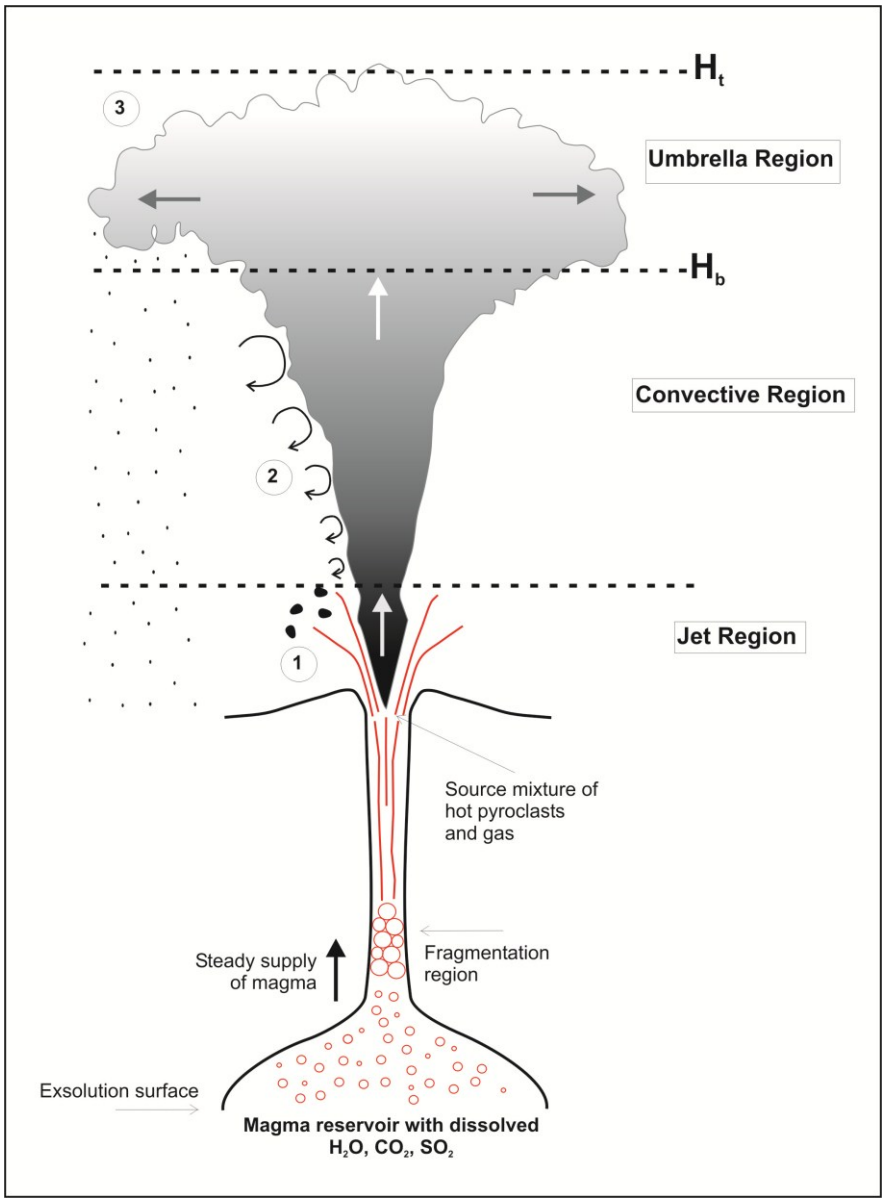

(4) The Bursik model mentions the fines population (particles <0.5 mm), but is not able to take their effects into full account. They are not present in the example (Fogo A) deposit, leading the authors to suggest they were elutriated and blown away, dispersed widely by atmospheric currents. In this case, atmospheric diffusion models such as those of Susuki (1993) and Armienti (1988) may better account for particle transport.

It is important to recognise that the specific grain-size associations for the four categories are dependent upon the eruption intensity and column height, and that these categories will be gradational rather than absolute. Nevertheless, much of the deposition of tephra from eruption columns can be understood by simple treatment of sedimentation from the margins of the turbulent plume, and from the horizontal, turbulent umbrella cloud.

In many cases, part or all of the erupting mixture does not become buoyant as it rises in the gas thrust region. In this instance, the mixture runs out of kinetic energy and collapses as a fountain, generating PDCs. Numerical models indicate that high exit velocities, high gas contents, and narrow vents favour convective columns, while low exit velocities, low gas contents, and wide vents are more likely to result in collapsing fountains (Sparks *et al*., 1997).

2.4.1.2 "WET" PLUMES

Thus far, I have examined the case of plume generation in essentially "dry" eruptions, where the ash is produced generally by exsolution of volatiles within the magma. The addition of large quantities of external water to an erupting magma has important effects on plume dynamics, whether that water enters in the source region, or in the atmosphere. In one scenario, as the external water is heated by the magma and vaporises, the initial density of the mixture falls, promoting the development of a buoyant plume. If the mass of incorporated surface water is small (<10%), the density and temperature of the erupting mixture decreases and therefore a buoyant plume can develop at lower exit velocities (Koyaguchi and Woods, 1996). Numerical models (Koyaguchi and Woods, 1996; Mastin, 2007) demonstrate that increasing the

proportion of external water within an eruptive mixture results in an increase in the plume height attained for a given mass flux of magma.

Mastin (2007) shows that for small eruptions (defined as those producing a plume ≤ 5 km in height, or with a VEI (volcanic explosivity index) value of ≤ 2), the empirical best-fit relationship between eruption rate and plume height (Sparks *et al*., 1997) underestimates plume heights relative to the eruption rate (or, conversely, overestimates the discharge relative to plume height). This is because, as the Plumeria model (Mastin, 2007) demonstrates, atmospheric conditions have a greater influence on small volcanic plumes than they do on larger ones. In a moist atmosphere, small plumes are likely to be buoyed up, thereby attaining greater elevations.

However, the presence of external water also cools the eruptive mixture, which may suppress buoyant plume formation (Sparks *et al*., 1997; Morrissey *et al*., 2000; White and Houghton, 2000). Thus, numerical studies show that magma-water interaction affects plume dynamics dramatically, but that this effect varies according to the magma to water ratio and the resulting density and temperature of the pyroclastic mixture. Mechanisms and conditions for plume formation, particle transport and sedimentation within wet plumes remain poorly constrained, and uncertainty in factors such as: the nature and timing of magma-water interaction, fluctuations in the magma to water ratio, and the state of water at the time of contact limit the applicability of these models (Woods, 1993; Koyaguchi and Woods, 1996).

Models of wet eruption plumes also emphasise the delicate balance between establishing a buoyant plume versus column collapse for eruptions involving external water. This frequently results in sporadic partial column collapse, accounting for the observation of cold, wet PDCs associated with phreatomagmatism (Sparks *et al*., 1997). PDCs have shorter dispersal distances than laterally spreading plumes, which creates in enhanced proximal sedimentation.

The factor which contributes the greatest uncertainty in models of tephra dispersal and sedimentation is the lack of quantitative information that exists on rates and modes of particle aggregation within the plume (e.g. Textor *et al*., 2006).

Aggregates of volcanic particles fall into three principal categories: dry aggregates, accretionary lapilli, and mud rain. The abundance of each sub-type is a function of the amount of water available during aggregation (Gilbert and Lane, 1994; Schumacher and Schminke, 1995; Sparks *et al*., 1997). Particle aggregation principally occurs when particles collide with one another due to gravitational settling within the plume. However, the number of collisions is enhanced by turbulent conditions and electrostatic attraction (Textor *et al*., 2006). In some cases once the particles have collided, electrostatic van-der-Waals forces are sufficient to bind them together. However, if water is available much stronger bonds are formed. Furthermore, the presence of dissolved salts cements particles together (Gilbert and Lane, 1994). Freezing of coalesced particles that are held together by water also results in more durable aggregates.

Calculations of settling rates of volcanic particles based on the particle Reynolds number (Bonadonna *et al*., 1998) show that large particles (>50 μm diameter) rapidly fall out of the volcanic plume at rates of 0.8 km/hr. By contrast, particles which are < 1 μm in diameter fall at rates of 0.0003 km/hr and therefore can reside in the atmosphere for several years after the eruption. However, as Bluth and Rose (2004) point out, observed rates of removal of fine ash decrease rapidly over the first 1-2 days after an eruption, which cannot be explained by theoretical particle settling rates. Thus the influence of particle aggregation is to remove ash from the atmosphere more rapidly than would otherwise take place, thereby depositing material closer to the source.

2.4.2 LATERAL TRANSPORT IN THE CONTEXT OF PHREATOMAGMATIC VOLCANISM

Pyroclastic density currents (PDCs) are an almost ubiquitous feature of phreatomagmatic eruptions because of the inherently unstable nature of columns produced in these events. The potential enhanced density of the mixture of steam, water and magma fragments, along with temporal and spatial heterogeneities, means that PDCs may be produced as discrete events following fountain or column collapse (e.g. Phase C2 Askja 1875, Carey *et al*., 2008; Pinatubo 1991, Rosi *et al*., 2001), or may

occur simultaneously with a sustained buoyant plume that is only partially collapsing (e.g. Phase C1 Askja 1875, Carey *et al*., 2008; Taupo, Wilson and Walker, 1985).

These currents have been divided into two end-members: pyroclastic flows and pyroclastic surges (Carey, 1991; Fig. 2.7). The term "pyroclastic flow" is associated with a high particle concentration (>10 vol. %) current, which moves under the influence of gravity. These are considered to have a sharp or well-defined interface between the high concentration "basal avalanche" and the overlying dilute, turbulent surge clouds (Sparks, 1976). "Pyroclastic surge" indicates a dilute (0.1-1 vol. %), highly turbulent current which contains no abrupt phase transitions, although there may be a vertical gradient of particle concentration (Valentine, 1987). In many cases, PDCs are accompanied by a co-ignimbrite plume – a secondary plume formed by the convective rise of ash above a moving pyroclastic current. This may entrain enough air to become sufficiently buoyant to detach and continue moving independently of the original current (Druitt, 1998). It is largely accepted that all variants of PDC form a continuum between these two end-members (Valentine, 1987; Sparks *et al*., 1997; Wilson and Houghton, 2000).

Figure 2.7: (Top) Schematic cross-section through end-member concentrated (flow) and dilute (surge) density currents to indicate their relative density and velocity structure. Surges show a gradual downward increase in density due to sedimentation, and a decrease in mean velocity due to ground friction. Flows, by contrast, are concentrated in their basal regions with rapid decreases in concentration and velocity across an upper interface to the over-riding cloud. (Middle) Schematic diagram showing typical characteristics of end-member pyroclastic deposit types. Flow deposits are valley-filling, poorly bedded to non-bedded, poorly sorted and contain rounded juvenile clasts. Surge deposits contain non-mantling beds which thicken into topographic lows. They feature cross-stratification, pinch and swell bedding and scoured contacts, are moderately sorted and contain juvenile clasts with a degree of rounding. (Bottom) Schematic diagram showing the effect of fluctuating particle concentration with time on depositional processes and deposit characteristics. All modified from Wilson and Houghton (2000).

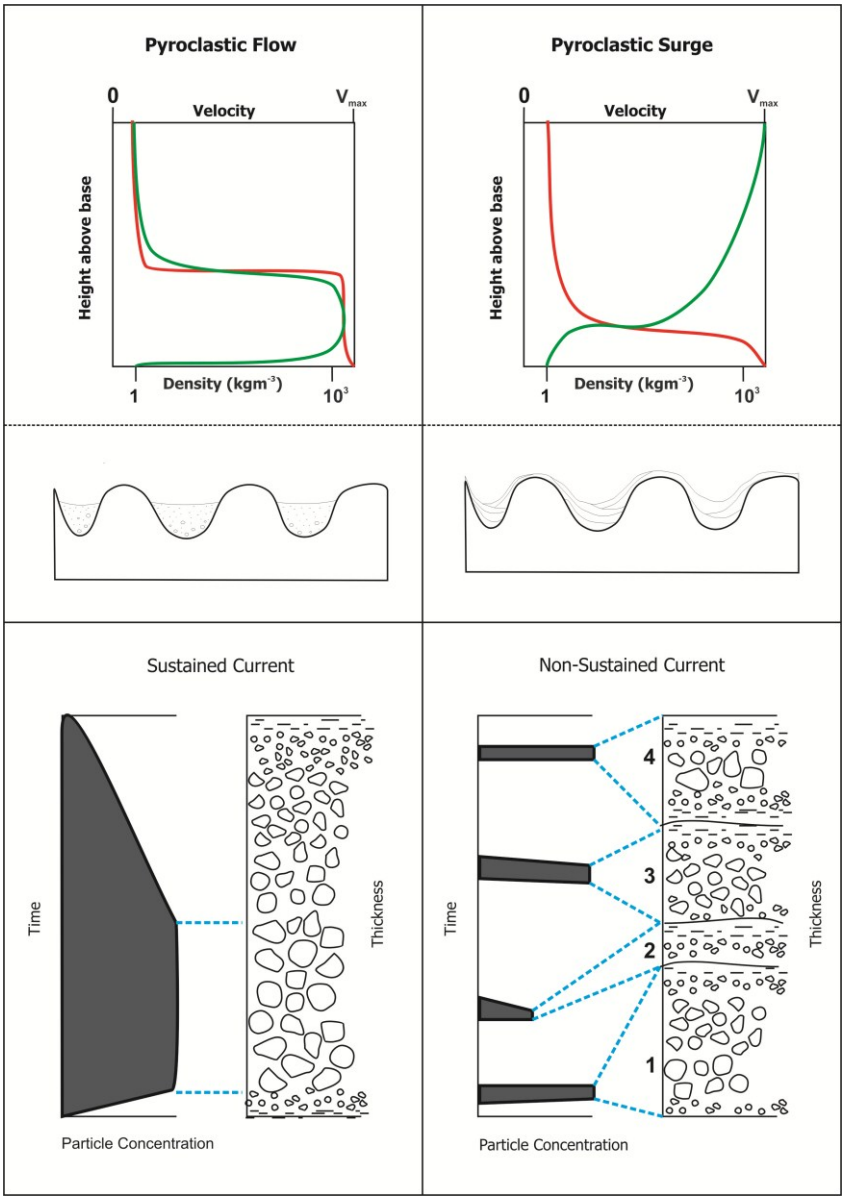

2.4.2.1 GENERATION OF PYROCLASTIC DENSITY CURRENTS

A – Fountain Collapse

PDCs are principally observed to be fed by collapsing fountains of the erupting mixture of tephra, magmatic gas and entrained air, as a consequence of the eruption failing to entrain sufficient air to become buoyant. Nairn and Self (1978) illustrate the key processes of PDC formation based on a time series of photographs taken during the 1975 eruption of Ngauruhoe volcano, New Zealand:

(1) After the initial explosion, a dense slug of gas and ejecta is observed expanding from the crater;

(2) The slug continues to expand, ballistic blocks are decoupled, and the external regions of the slug display structures indicative of turbulence and the entrainment of atmospheric gases;

(3) The external parts of the developing column begin to ascend buoyantly, while material is seen to fall on the upper flanks of the volcano from the column interior; (4) The column interior collapses and PDCs are formed, while the exterior of the slug has formed an ascending convective column. This entire sequence can take less than thirty seconds to develop (Nairn and Self, 1978). Collapsing fountains may be the result of single discrete explosions, or may be continuously fed by explosive discharge (e.g. Rowley *et al*., 1981; Hoblitt, 1986).

B - Collapse of column margins

Alternative mechanisms of generating gravity currents, such as dilute gravity flows from the plume edge, have been modelled in the laboratory (Carey *et al*., 1988). These are considered to result from the re-entrainment, at the margins of the plume, of tephra falling out from the corner and umbrella regions. If, instead of entraining air volcanic particles are taken up, the plume margins will fail to become buoyant and dilute gravity currents will spread radially from the vent. Observational evidence for this mechanism of PDC formation is given by the 1979 eruption of Soufrière in St Vincent (Sparks and Wilson, 1982).

C - Asymmetric collapse

Directed flows are known to occur as a result of directed blasts in lava dome formation (e.g. Bezymianny, 1956; Mount St Helens, 1980). However, Carey *et al*. (1988) found that asymmetric collapse can form eruption plumes, without involving a directed explosion. In experiments, this occurred when the bulk density of the erupting mixture was almost equivalent to the ambient conditions, resulting in a more dilute buoyant plume forming above the vent.

D - Whole column collapse

Considering that the instantaneous proportion of tephra in a column is a very small fraction of the total tephra production of a sustained eruption, the sudden cessation of magma supply, thereby resulting in column collapse, is not a plausible mechanism for the generation of PDCs. The resulting currents would be very dilute, of small volume and quite cool, generating drifting ash current and only thin layered deposits (Sparks *et al*., 1997).

2.4.2.2 Deposition Regimes

A simplified diagram of the structure, behaviour, and depositional characteristics of pyroclastic flows versus surges is given in Fig. 2.7. There are four fundamental controls on the deposition of pyroclastic deposits (Wilson and Houghton, 2000):

Clast trajectory: Ranging from vertical to horizontal, and of particular interest when considering the effects of fallout from an inclined plume as compared to purely lateral or vertical transport. Only vertically-directed plumes have been studied in sufficient detail to understand their effect on tephra dispersal and deposition (Bursik, 1998).

The degree of particle cohesion: Increased particle cohesion results in more rapid deposition, the premature (more proximal) deposition of fine particles that have clumped together, and also allows deposition upon larger slope angle (Wilson and Houghton, 2000).

The time-scale of fluctuations in particle concentration with time: This controls whether the resulting deposit will be a single graded bed, or a succession of beds with varying characteristics (Branney and Kokelaar, 1992).

The concentration and density of particles in the current: In dilute PDCs, material is transported primarily by turbulent suspension, with a minor population of coarser clasts moving as a saltating/sliding traction carpet. By contrast, while turbulence may be present in a comparatively concentrated PDC (i.e. end-member "flow"), it is not the principal mechanism of particle support. In simple terms, a PDC consists of two particle populations: those which are not supported by turbulence and settle rapidly to the base of the current, and those which are carried in suspension (albeit to different degrees). The current therefore rapidly becomes stratified in terms of particle concentration and bulk density (Valentine, 1987).

Druitt (1998) suggests that there are three principal regimes of sedimentation from PDCs, which likely grade into one another as the current travels away from the vent:

Traction sedimentation: Particles saltate, roll, or slide along the bed before coming to a rest. This results in planar, wavy or cross-stratified deposits (Fig. 2.8).
Suspension sedimentation: Particles are deposited directly from suspension with little or no late-stage traction. This results in unstratified deposits, although these may be normally or inversely graded.
Underflow formation: Rather than immediately forming deposits, settling particles remobilise into highly concentrated underflows which decouple from the suspension current and drain into topographic lows as a result of gravitational forces. Deposition, therefore, takes place from the underflow rather than directly from the suspension current.

2.4.2.3 MODELS OF END-MEMBER PYROCLASTIC "SURGES"

It is widely accepted that pyroclastic surges become progressively more dilute with distance from source. This occurs due to a combination of sedimentation, decompression, and air entrainment (Sohn and Chough, 1989; Druitt, 1992). However, an alternative model proposed by Wohletz and Sheridan (1979) suggests that surge clouds deflate progressively during transport, eventually being reduced to thin, dense bedloads. The latter model is likely to be more applicable to "wet surges" (i.e. those which have a temperature of less than 100°C such that steam condenses to form a three-phase suspension of particles, liquid water and gas) due to their lower temperature and the effects of particle cohesion (Druitt, 1998).

Figure 2.8: The formation of cross-beds by traction sedimentation within a pyroclastic density current.

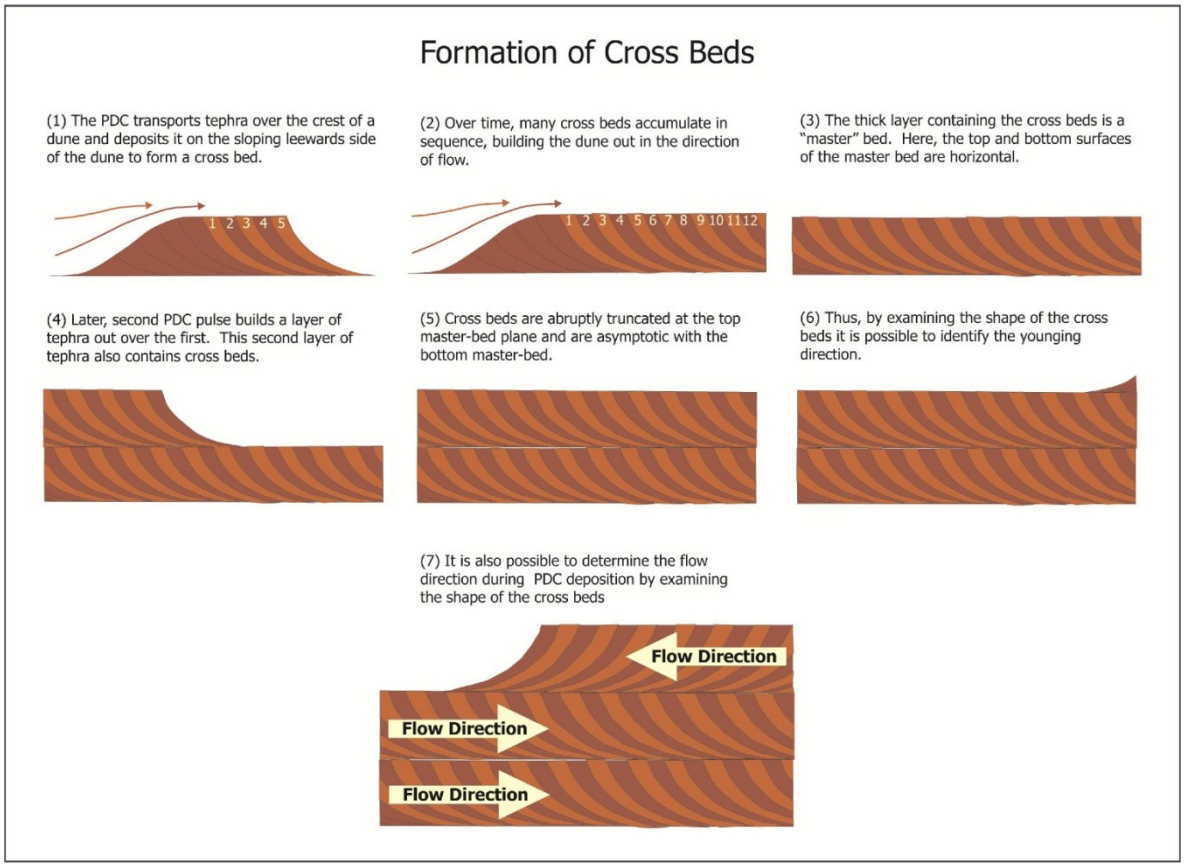

PART 2 – BACKGROUND TO GRÍMSVÖTN VOLCANIC SYSTEM

2.5 GEOLOGIC SETTING AND ICELANDIC VOLCANISM

The island of Iceland rises above sea level in a region of over-thickened oceanic crust known as the Iceland Basalt Plateau (IBP), situated at the junction between the northern end of the Mid-Atlantic Ridge (MAR) and the Greenland-Iceland-Faroe Ridge (Fig. 2.10). The Iceland Basalt Plateau rises more than 3000 m above the surrounding sea floor, with total crustal thicknesses in this region ranging from 10-40 km (Gudmundsson, 2000; Thordarson and Larsen, 2007). Although the oldest exposed rocks on Iceland date to 14-16 Ma (Moorbath *et al*., 1968; Watkins and Walker, 1977), IBP construction is thought to have commenced around 24 Ma (Sæmundsson, 1978; 1979; Jóhannesson, 1980). The volcanic output along this spreading boundary between the North American and Eurasian plates is augmented by the presence of the Icelandic plume, centred beneath north-west Vatnajökull (Gudmundsson, 2000; Lawver and Müller, 1994, Wolfe *et al*., 1997). The Iceland mantle plume has been active for 65 million years (Saunders *et al*., 1997), during which time it has formed the North Atlantic Igneous Province (NAIP) - estimated to be at least 1.3×10^6 km^2 in area and 6.6×10^6 km^3 in volume (Eldholm and Grue, 1994).

The present distribution of active volcanism in Iceland is a product of the superposition of the spreading plate boundary over the Iceland mantle plume. The neovolcanic zones – discrete 15-50 km-wide belts of active faulting and volcanism - are the surface expressions of this interaction (Sæmundsson, 1980; Jóhannesson, 1980, Gudmundsson, 2000). The most prominent belt of activity is the axial volcanic zone, the region of active spreading and crustal growth that follows the plate boundary almost diagonally across Iceland from Reykjanes in the southwest to Öxarfjörður in the north (Fig. 2.10). The principal structures within the axial zone are the West (WVZ) and North (NVZ) Volcanic Zones, which are bridged by the Mid-Iceland Belt (MIB), and extend to the Mid-Atlantic Ridge system via the Reykjanes Volcanic Zone (RVZ) in the south and the Tjörnes acture Zone (TFZ) in the north. The axial volcanic zone is typified by tholeiitic magmatism.

Figure 2.9: Tectonic map of Iceland and the North Atlantic from Thordarson and Larsen (2007). Iceland is an elevated plateau in the middle of the North Atlantic, situated at the junction between the Reykjanes and Kolbeinsey Ridge segments. The Mid-Atlantic Ridge axis is shown by a heavy solid line; elements of the North Atlantic basalt plateau are shaded black, and their submarine equivalents are dark grey. The position of the Iceland mantle plume from 65 million years to the present day is tracked by a white line.

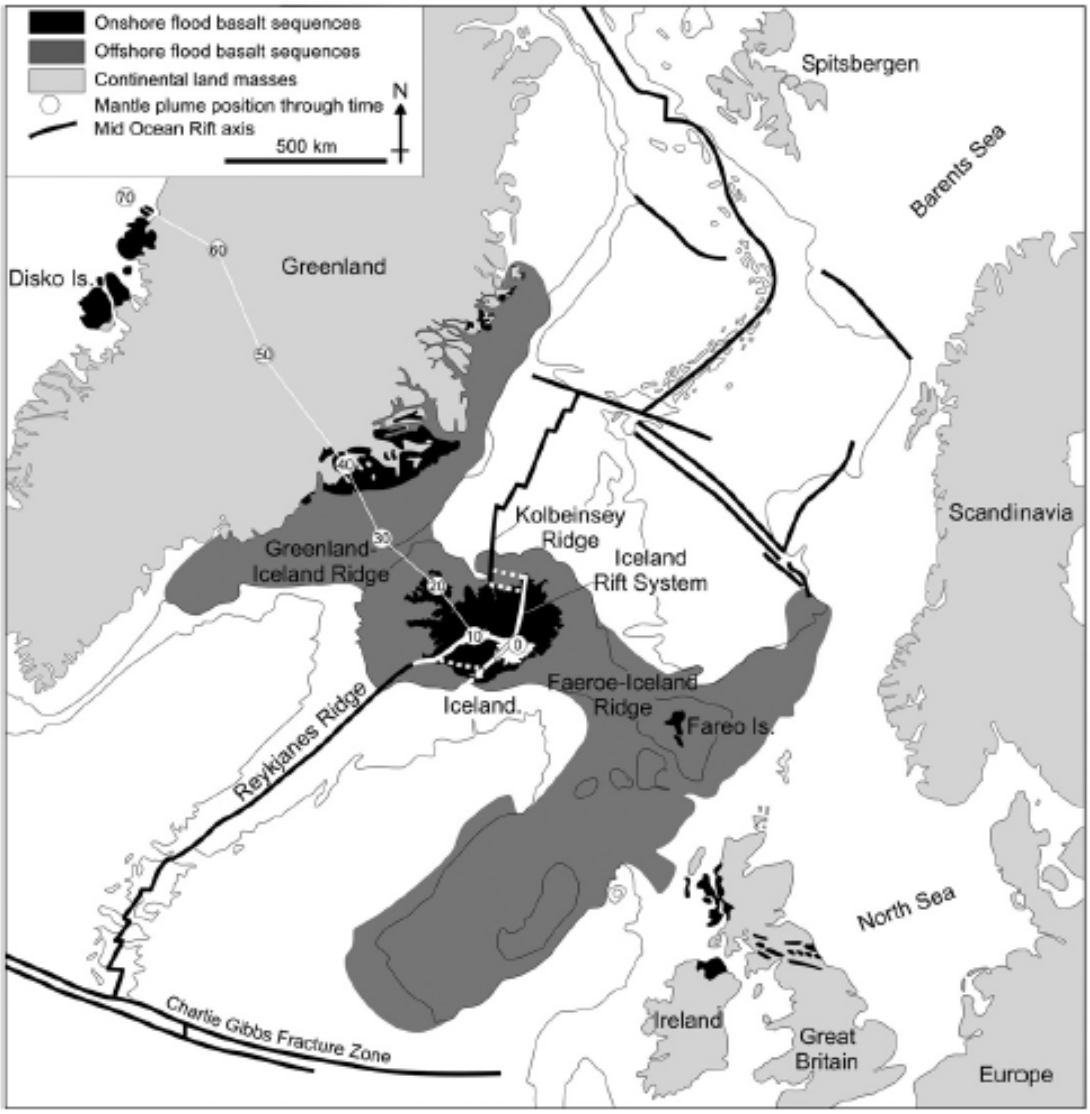

Figure 2.10: The principal elements of the geology of Iceland. The distribution of the major geological subdivisions are shown, along with the principal fault structures, volcanic zones and belts. RR: Reykjanes Ridge; RVB: Reykjanes Volcanic Belt; SISZ: South Iceland Seismic Zone; WVZ: West Volcanic Zone; MIB: Mid-Iceland Belt; EVZ: East Volcanic Zone; NVZ: North Volcanic Zone; TFZ: Tjörnes Fracture Zone; KR: Kolbeinsey Ridge; ÖVB, Öræfi Volcanic Belt; SVB: Snæfellsnes Volcanic Belt. From Thordarson and Höskuldsson (2002).

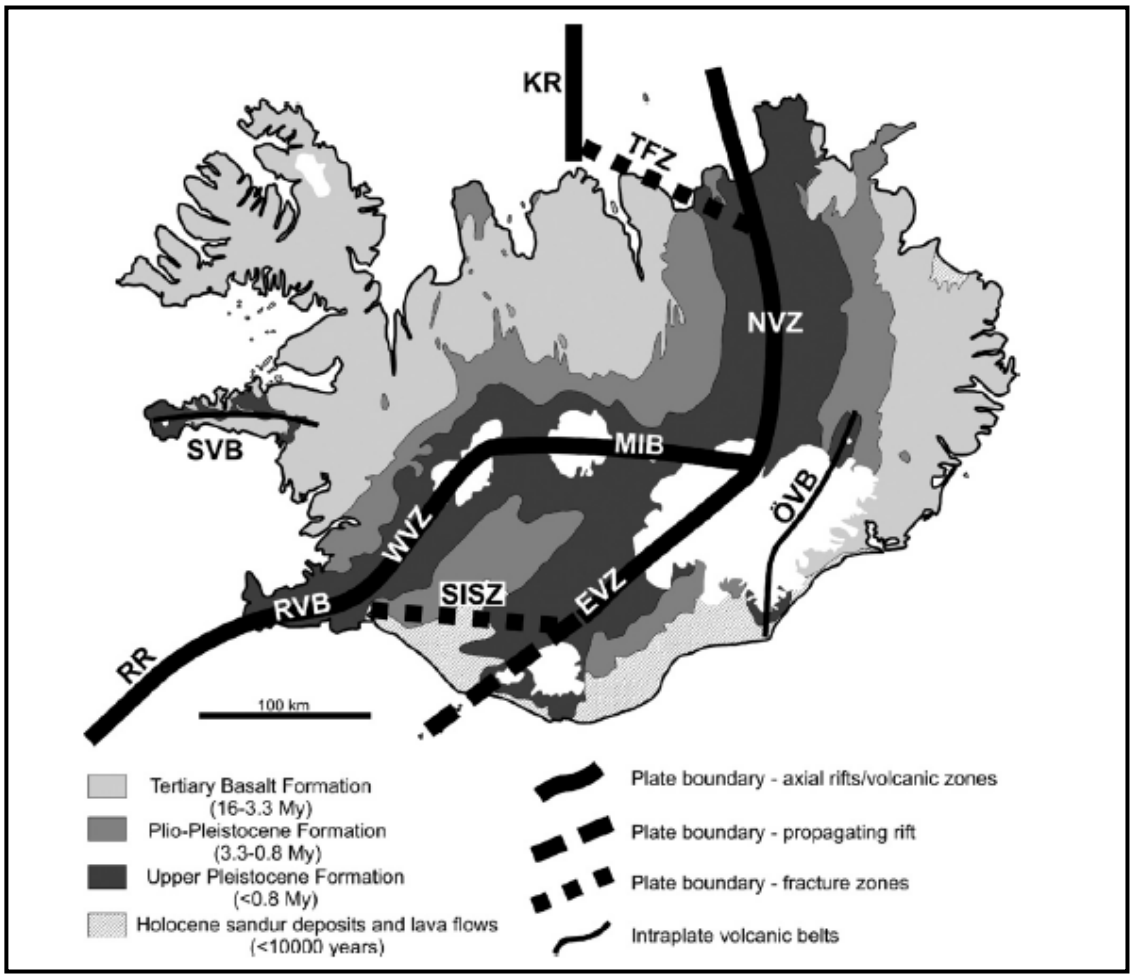

The Eastern Volcanic Zone (EVZ) is a burgeoning axial rift, which will eventually take over from the WVZ (Thordarson and Larsen, 2007) as volcanism propagates through pre-existing crust to the southwest. In the northeast, the EVZ is dominated by tholeiitic magmatism, but the currently propagating southwest segment is characterised by mildly alkalic magmas. The EVZ, which is 60-70 km wide and trends roughly N45°E, underlies the western part of Vatnajökull. Vatnajökull, the largest glacier in Iceland, has an area of 8100 km^2, with a mean thickness of 380 m (Björnsson and Pálsson, 2008). The western Vatnajökull region is the most volcanically active in Iceland (Larsen *et al*., 1998) with about 100 known eruptions over the last 1000 years (Thordarson and Larsen, 2007). Products of EVZ and NVZ volcanism during the Holocene can be traced to specific volcanic systems on the basis of their distinct chemical signature (e.g. Larsen, 1981; Óladóttir, 2009).

In addition to volcanism along spreading margins, there are two active intraplate volcanic belts in Iceland, both of which erupt mildly alkalic magma compositions. The Öræfi Volcanic Belt, situated to the east of the current plate margins, largely underlying eastern Vatnajökull may represent an embryonic rift (Thordarson and Höskuldsson, 2002). By contrast, the Snæfellnes Volcanic Belt in west Iceland is an old rift zone which was reactivated about 2 million years ago and is currently propagating to the east-southeast (Thordarson and Larsen, 2007).

Among the volcanic zones there are 30 active volcanic systems, which are characterised by a conspicuous volcano-tectonic architecture. Each volcanic system features either a fissure swarm system, a central volcano, or both (Fig. 2.11). Some volcanic systems can have two fissure swarms (or axial rift zones). Fissure swarms are linear structures 5-20 km wide and 50-200 km long, generally aligned sub-parallel to the axis of the host volcanic zone. Where a central volcano is present, it is the focal point of eruptive activity, and as such forms the largest structure within the system (e.g. Jakobsson *et al*., 1978, Gudmundsson, 2000). Away from the hotspot locus, volcanism in Iceland is closely linked to tectonic activity. Spreading takes place in distinct rifting episodes that are generally confined to a single volcanic system. Such volcanic episodes can last for several

years to decades, during which time the entire system is activated (Sigurdsson and Sparks, 1979, Björnsson *et al*., 1979, Brandsdóttir and Einarsson, 1979).

The bulk of eruptions in western Vatnajökull throughout the Holocene have taken place on the Grímsvötn or Bárðarbunga volcanic systems (Óladóttir, 2009). These eruptions broadly consist of two types: infrequent and large eruptions on the fissure swarms, including the major eruptions on the swarms southwest of the glacier (Vatnaöldur 871, Veiðivötn 1480, Laki 1783-84; Larsen, 1984; Thordarson and Self, 1993), and frequent, much smaller phreatomagmatic eruptions on fissures within, or on the flanks of, Grímsvötn and, to a smaller extent, Bárðarbunga. Since the central volcanoes are ice-covered, eruptions often lead to ice melting and jökulhlaups. Records of jökulhlaups from Grímsvötn exist from the 14th century onwards (Thorarinsson, 1974).

Figure 2.11: Distribution of active volcanic systems among volcanic zones and belts in Iceland as depicted by Jóhannesson and Sæmundsson (1998). Reykjanes Volcanic Zone: (1) Reykjanes–Svartsengi, (2) Krýsuvík, (3) Brennisteinsfjöll; West Volcanic Zone: (4) Hengill, (5) Hrómundartindur, (6) Grímsnes, (7) Geysir, (8) Prestahnjúkur, (9) Langjökull; Mid-Iceland Belt: (10) Hofsjökull, (11) Tungnafellsjökull; East Volcanic Zone: (12) Vestmannaeyjar, (13) Eyjafjallajökull, (14) Katla, (15) Tindfjöll, (16) Hekla–Vatnafjöll, (17) Torfajökull, (18) Bárðarbunga–Veiðivötn, (19) Grímsvötn; North Volcanic Zone: (20) Kverkfjöll, (21) Askja, (22) Fremrinámur, (23) Krafla, (24) Þeistareykir; Öræfajökull Volcanic Belt: (25) Öræfajökull, (26) Esjufjöll, (27) Snæfell; Snæfellsnes Volcanic Belt: (28) Ljósufjöll, (29) Helgrindur, (30) Snæfellsjökull. The large open circle indicates the approximate centre of the Iceland mantle plume/anomaly as depicted by Wolfe *et al*. (1997). From Thordarson and Larsen (2007).

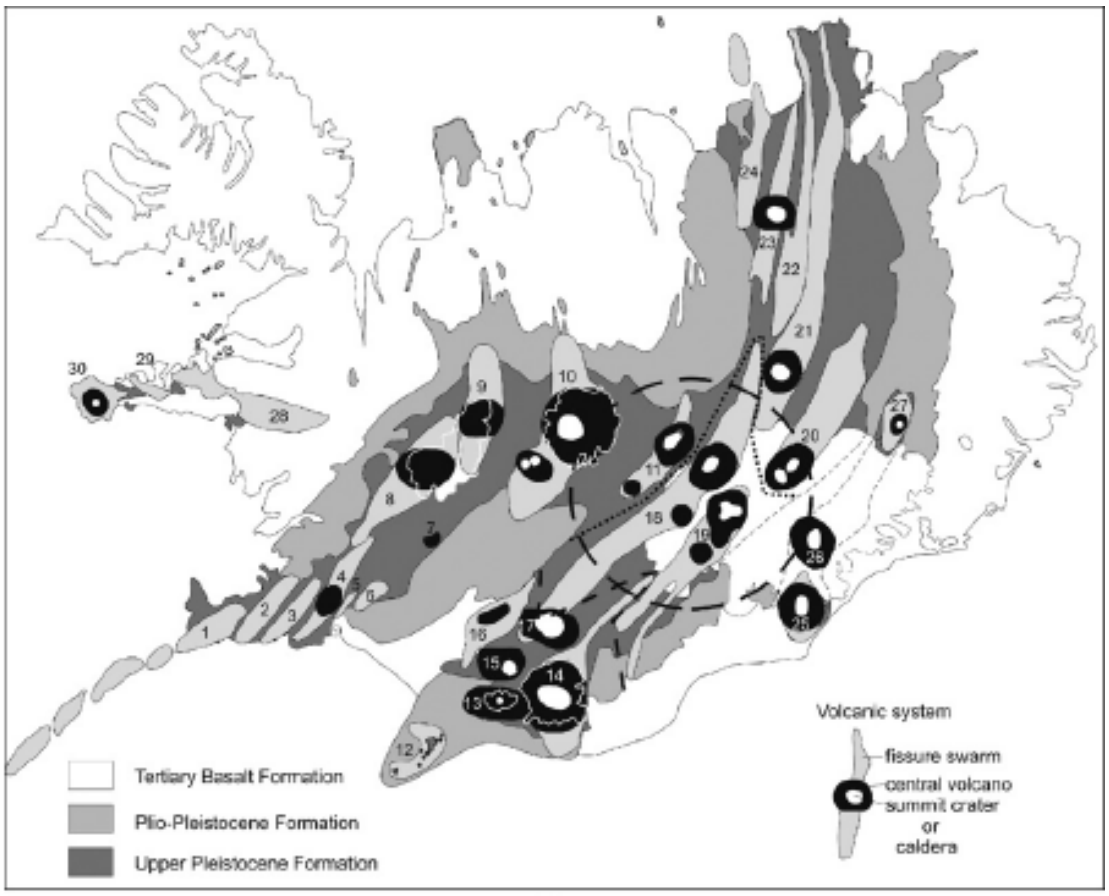

2.6 GEOGRAPHY AND GEOMETRY OF GRÍMSVÖTN VOLCANIC SYSTEM

The Grímsvötn system is almost 100 km long, with the Grímsvötn central volcano located near its northern end and the Þórðarhyrna central volcano 20 km farther to the south-west (Fig. 2.12). The Grímsvötn fissure swarm extends more than 60 km to the south-west of the Grímsvötn caldera to the 1783-84 Laki eruption site, located on the ice-free part of the fissure swarm. As a consequence of its location above the point of juxtaposition of the mid-Atlantic rift with the inferred Icelandic hot-spot, Grímsvötn has the highest eruption frequency of all Icelandic volcanoes, and ranks second in terms of volume of products (Larsen, 2002; Thordarson and Larsen, 2007) - highlighting the relative importance of explosive basaltic tephra fallout compared to predominantly effusive activity in the historical and geologic records of this region. There have been over 70 confirmed eruptions on the Grímsvötn system in the past 1100 years (Larsen, 1998). Furthermore, the occurrence of four eruptions in the past twenty years has been taken as an indication that Grímsvötn volcano has entered a new phase of high activity (Larsen, 2002; Sturkell, 2006). Grímsvötn also comprises one of the most powerful geothermal areas on earth, with an estimated heat output of 2000-4000 MW (Björnsson and Gudmundsson, 1993).

The Grímsvötn central volcano is 15-20 km in diameter and rises to over 1700 m a.s.l. Its base is located at about 1000 m elevation (Björnsson, 1988). This central volcano contains three nested calderas in the south (21 km^2), east (17 km^2) and north (11 km^2) (Fig. 2.13). The structure of Grímsvötn has been studied via a combined gravity and magnetic survey (Gudmundsson and Milsom, 1997) and a teleseismic study (Alfaro *et al*., 2007). These studies attained similar results concerning the upper crustal structure. The south caldera is underlain by low density, low seismic velocity material that extends down to approximately 2 km depth. This is partly attributed to caldera fill and partly to the disruption of incompetent rocks by subsidence during caldera collapse.

Rock exposures in Grímsvötn are limited to the basaltic hyaloclastites making up the 200-300 m high upper part of the southern caldera fault. Hundreds of dykes are

exposed in the caldera wall, commonly with thicknesses on the order of 1 m or less. However, in the wall at Grímsfjall some very prominent dykes are several metres thick. In the south-western caldera wall these trend WSW-ENE. Pillow lavas are largely absent in the exposed walls, while consolidated hyaloclastite dominates. The age of caldera collapse is unknown, but the caldera fault is fresh and the absence of gullies and cirques suggests limited glacial erosion. Known eruption sites are all aligned along the southern and south-western sides of the caldera fault, where several hillocks and mounds are found under the ice cover. The southern caldera fault is also the locus of intense geothermal activity. This explains its youthful appearance and suggests that the fault is the result of piece-meal caldera collapse which took place over an extended period of time, rather than a sudden collapse following a single large-scale event.

Chemical analysis of tephra from historical Grímsvötn eruptions have shown that the composition of erupted magma is a uniform evolved quartz tholeiite - with the exception of 1996 Gjálp eruptions which produced basaltic icelandite magma (e.g. Jakobsson, 1979; Steinthorsson, 1982; Grönvold and Jóhannesson, 1984; Steinthorsson *et al*., 2000; Sigmarsson *et al*., 2000).

Figure 2.12: Simplified tectonic map showing Iceland's volcanic zones (dark grey), the location of the spreading axis between the Eurasian and North American plates (light grey), the inferred mantle plume and study area location. Grímsvötn caldera is depicted as a red polygon and the centre of the Iceland hotspot is marked by a yellow circle. The black box indicates the location shown in more detail in Figure 2.12. The location and orientation of the Laki fissure (an event that occurred between 1784-85 on the Grímsvötn fissure swarm) is shown by a red line on the map and the extent of the lava flows (>14 km^3) is given by a black polygon. Modified from Thordarson and Höskuldsson (2002).

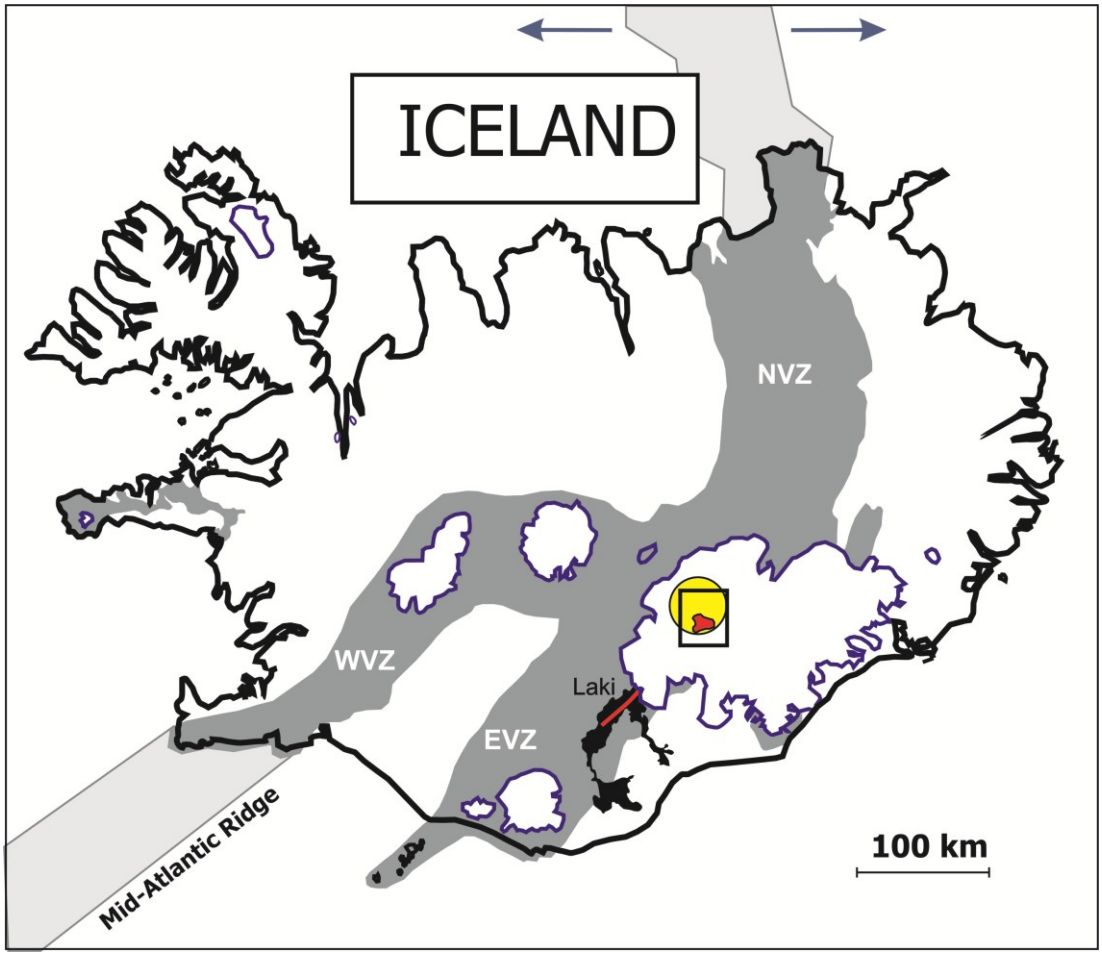

2.6.1 THE GRÍMSVÖTN MAGMA CHAMBER

The energetic geothermal system at Grímsvötn and the close association of lake drainage with eruption triggering has been used by previous workers to indicate the presence of a shallow level magma chamber beneath Grímsvötn (Björnsson *et al*., 1982). GPS measurements of the volcano prior to, and after the 1998 and 2004 events, were fitted to a Mogi model with an inferred point source beneath the centre of the main caldera, indicating a source depth of at least 1.6 km (Sturkell *et al*., 2006). These findings support the results of Alfaro *et al*. (2007) who, on the basis of S-wave shadows and P-wave delays, inferred a magma chamber at around 4 km depth under the caldera. In the period between 2004 and 2011, GPS measurements taken at fixed points around the caldera have been inferred to reflect sustained inflation of the magma chamber - similar to that observed during the period 1999-2004 (Sturkell *et al*., 2006). This culminated in an eruption in May 2011. Other long term precursors to the 1998 and 2004 eruptions included increased seismicity and geothermal activity in the 1-2 years prior to the eruptions. Seismicity and deformation at Grímsvötn prior to the 2011 eruption indicated a shallow magma source, which is consistent with the longer term inflation trends prior to this event (O. Sigmarsson, personal communication, 2011).

2.6.2 GEOTHERMAL ACTIVITY

Geothermal activity at Grímsvötn is manifested most obviously in the 10-12 km wide and 200 m deep surface ice depression centred on the Grímsvötn caldera (Fig. 2.13). However the majority of the thermal output is focused around the south caldera fault segment. The high rate of heat transfer melts the overlying ice and the melt-water flows into the Grímsvötn subglacial lake. It is capped by a floating ice cover which has the characteristics of an ice shelf (i.e. its interior is flat and floats in hydrostatic equilibrium, with an abrupt change in surface slope at the margins; Gudmundsson *et al*., 1995). To the south and west, the lake is bounded by the caldera walls, while on the remaining sides it is contained by the pressure of the ice surrounding the depression. This barrier is termed

the ice "dam". The lake gradually expands towards the north and northeast until it is drained by jökulhlaups every 4-6 years (Gudmundsson *et al*., 1995). The jökulhlaups occur at lake level that is much lower than that required to float the confining ice dam. In fact, at the start of most jökulhlaups, the pressure supplied by the ice overburden exceeds the subglacial water pressure (Björnsson, 1988). Björnsson (1988) suggested that jökulhlaups may be released due to weaknesses in the ice dam due to basal ice movement. The jökulhlaups do not drain the lake entirely as they usually terminate abruptly once the lake level has fallen by around 100 m (Gudmundsson, 1995).

In recent years, the ice dam seal at Grímsvötn has been leaky, partly due to damage caused by the large 1996 jökulhlaup, but also as a result of increased geothermal activity along an east-west line through the ice dam (Gudmundsson *et al*., 2002; 2004). As a consequence, the subglacial lake has, for most of the period since 1998, been only a few square kilometres in area and the lake level quite low. This contrasts sharply with conditions prior to 1996, when the lake reached 15-20 km^2 in size before jökulhlaup onset (M. T. Gudmundsson, personal communication, 2008). The mechanism of jökulhlaup release from Grímsvötn and their general characteristics have been previously described by Björnsson (1974, 1988, and 1992).

Within the Grímsvötn caldera, there are several smaller ice cauldrons, which are principally located along the caldera faults. These depressions, the surface expressions of subglacial geothermal hot-springs, are generally 20-50 m deep. Most of these cauldrons do not store water underneath them as the melt water flows semi-continuously into the subglacial caldera lake at Grímsvötn (Gudmundsson *et al*., 1995). Fluctuations in geothermal activity are manifested in the increase or decline in the volume of these ice cauldrons (Björnsson and Gudmundsson, 1993).

Figure 2.13: Detailed map of the Grímsvötn caldera, including the vent locations for some recent eruptions. (M. T. Gudmundsson).

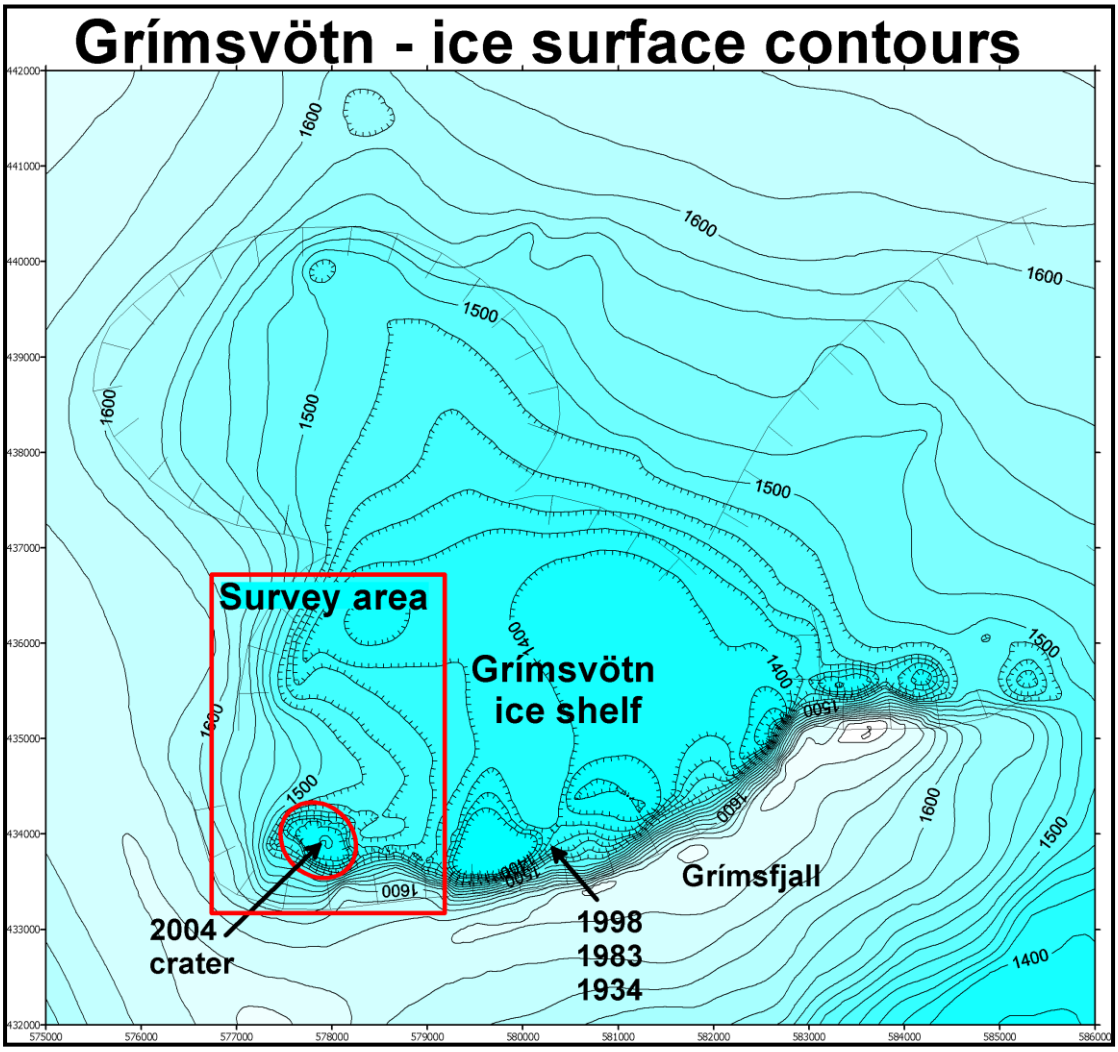

2.6.3 VOLCANO MONITORING

Despite Grímsvötn's remote location, significant hazards may be posed in the event of an eruption due to the generation of jökulhlaups. In addition, eruption plumes may pose a hazard for air traffic in the North-Atlantic. Consequently, characterization and anticipation of events at this volcano is a priority.

The two small peaks on the Grímsfjall ridge, where the caldera wall is exposed above the ice, are named Svíahnúkur Eystri and Svíahnúkur Vestri (Fig. 2.13) in reference to the Swedish expedition that re-discovered Grímsvötn in 1936. Svíahnúkur Eystri is an ENE-WSW trending ridge and its peak is made up of a consolidated cross-bedded tephra deposit which is rich in accretionary lapilli. A group of Icelandic Glaciological Society (JÖRFÍ) huts are located on Svíahnúkur Eystri, near the eastern end of the caldera wall. Considerable geothermal activity is associated with the ridge - especially on the hill Saltari, about 300m to the west of the huts. Geothermal energy has melted ice caves in the shallow glacier on both sides of the hill. Energy from steam within shallow drill holes is harnessed to generate electricity for the huts, one of which houses scientific monitoring instruments, such as a seismometer and a continuously recording GPS station. An automated weather station is installed adjacent to the hut. Beyond Grímsvötn, there is an extensive national seismic and geodetic seismic network across Iceland which is managed under the remit of the Icelandic Meteorological Office. Consequently GPS and tilt measurements are also taken from several other nunataks nearby.

2.7 ERUPTIONS AT GRÍMSVÖTN

The explosive interaction of magma and external water (or ice) places important controls on the style of eruption at Grímsvötn. In historical time, most Grímsvötn eruptions have been relatively small (0.01-0.1 km^3 DRE; Thorarinsson, 1974; Gudmundsson and Björnsson, 1993; Gudmundsson, 2005) and large-scale fallout of tephra seldom occurs outside Vatnajökull. Most eruptions occur within the Grímsvötn caldera, along the southern caldera fault, where the ice is 50-200 m thick (Fig. 2.13). Sometimes eruptions break through the ice cover almost instantly as magma reaches the glacier bed, such as in the 1934 and 1998 eruptions (Gudmundsson, 2005), but the 2004 eruption took about an hour to melt its way through 150-200 m of ice in the southwest corner of the caldera.

In general, eruptions at Grímsvötn melt several-hundred-metre-wide openings (i.e. cauldrons) in the ice cover directly above the active vents. If the eruption becomes subaerial, tephra is deposited on the surrounding ice, but in most cases these do not survive as landforms. The tephra deposited onto the ice surface tends to have a blanket-like morphology, although cone-like structures often form within the cauldrons during late-stage activity. The most intense explosive phase of Grímsvötn eruptions, therefore, create a structurally heterogeneous cauldron fill in addition to more widespread tephra blanket on the ice which is not preserved. This phase is therefore represented in the geologic record by a chaotic hyaloclastite horizon that normally sits below the tuff cone-like horizon in the móberg ridges and stapar. Time-sequence information from this phase is completely lost because no systematic stratigraphy is preserved. Retreating ice walls and the collapse of unstable piles of volcanic ejecta may generate turbidity currents, leading to the accumulation of volcaniclastic deposits at the bottom of the Grímsvötn Lake.

The volume of ice melted during a typical caldera eruption at Grímsvötn is usually limited. For example, in each of the 1998 and 2004 eruptions, only 0.1 km^3 of ice was melted. Neither of these eruptions caused major jökulhlaups. Some of the eruptions in Grímsvötn (1934, 2004, several early 20th century and 19th century eruptions) are

triggered by depressurisation effects on the caldera floor as it is unloaded by a falling lake level during drainage by periodic jökulhlaups (Thorarinsson, 1953; Gudmundsson, 2005).

2.7.1 HOLOCENE ACTIVITY

Grímsvötn has been the most active volcanic system in Iceland throughout the Holocene with, on average, seven eruptions per century (Óladóttir, 2009), erupting a total of 50–55 km^3 of magma. If the volume of the 9.9-10.5 ka Saksunarvatn and associated tephra layers, which have been traced to the Grímsvötn system, are included the total Holocene magma volume increases by 15 km^3. Of this total, approximately 25 km^3 was erupted on the ice-free portions of the system, of which 15.1 km^3 was extruded from the Laki fissures in 1783–1784 (Jakobsson, 1979; Thordarson *et al*., 2003; Thordarson and Larsen, 2007).

The rate of activity has, however, been variable through time. In a recent study, Óladóttir (2009) attributed 36 tephra layers to Grímsvötn for each of the periods 8-7 ka and 6-5 ka, 56 eruptions from 7-6 ka, 140 eruptions in the period 2-1 ka, and 84 eruptions within the last millennium - values consistent with those obtained by previous studies (e.g. Thordarson and Larsen, 2007; Larsen and Eiriksson, 2008) which have identified 81 Grímsvötn layers dating to the last 1000 years.

Activity on the Grímsvötn system therefore peaked at 7-6 ka, and again between 2-1 ka. The extended lull in volcanic activity that took place between 5 and 2 ka is known as the "mid-Holocene low". The timing of this period of relative quiescence could be related to either periodicity in magma upwelling from the underlying hotspot, to tectonic controls, or to environmental factors - such as the extent of ice cover. This effect also observed for several other volcanic systems in the vicinity (Óladóttir, 2009).

Historical observations note that many Grímsvötn eruptions do not break though the ice cover or do not produce widespread fall layers (Thorarinsson, 1974; Gudmundsson and Björnsson, 1993; Gudmundsson, 2005). Where widespread fallout has occurred, tephra layers are not always preserved in soil sections. Hence it is important to recognise

that the calculated event frequency values provided above must be considered minimum estimates, especially with regards to the older time intervals.

Although there is some overlap in composition, major element data are generally sufficient to distinguish Grímsvötn products from those of other volcanic systems in the Vatnajökull region (Jakobsson, 1979; Larsen, 1981). Known Grímsvötn products are quartz-normative tholeiitic basalts which fall into two compositional groups (Óladóttir, 2009). Magmatic evolution in group GI is controlled solely by clinopyroxene (CPX) fractionation. Group GII is depleted in Sr and its composition reveals the influence of contamination by an evolved basaltic crustal component in addition to the effects of crystal fractionation. According to Óladóttir (2009), chemical trends through the Holocene indicate that Grímsvötn rapidly evolved from a simple plumbing system whereby magma travelled directly to the surface from a deep source, to the development of a sill and dyke complex. During periods of relatively low activity, such as at ~3.3-1.9 ka, activity was restricted to eruptions from a small magma chamber only. During periods of peak activity, such as between 1.7 and 1 ka, the entire sill and dyke complex is thought to have been reactivated along a direct conduit to the deep source.

2.7.2 THE 1783-85 SKAFTÁR FIRES (LAKI ERUPTION)

The most significant eruption from the Grímsvötn system in historical time was a two-year-long volcano-tectonic episode which featured intense earthquake activity and eruptions at both the Grímsvötn central volcano and the Laki fissures (Thordarson and Self, 1993; Thordarson *et al*., 2003b). This eruption produced the second largest flood basalt of historical time (after Eldgjá, 934-940 AD; Larsen, 2000; Thordarson *et al*., 2001). The social and environmental impact of the Laki eruption had disastrous and far-reaching consequences both in Iceland and over much of the northern hemisphere (Steinthorsson, 1992; Wood, 1992; Thordarson *et al*., 1996; Thordarson and Self, 2001, 2003).

The 1783–1785 activity featured at least fourteen eruption phases. Among these, ten were associated with the eight-month-long Laki eruption, as a 27 km-long fissure opened progressively from the southwest to the northeast (Thordarson and Self, 1993; Thordarson *et al*., 2003b). Four of the eruption phases on the Laki fissures were accompanied by concurrent explosive eruptions at the Grímsvötn central volcano. Each episode of activity on the fissure system commenced with an earthquake swarm of increasing intensity followed by a relatively short-lived phreatomagmatic or subplinian phase and culminated in Hawaiian-style fire fountaining and lava effusion. The explosive activity at the start of each episode was largely related to the interaction of the ascending magma with ground or surface waters. The final four phases of activity were confined to Grímsvötn exclusively. No tephra layers associated with these latter phases have ever been identified, thus contemporary observations provide the only evidence of activity at Grímsvötn between 1783 and 1785 (Thordarson *et al*., 2003). The simultaneous activity at Laki and Grímsvötn central volcano suggests that these eruptions were part of a major volcano-tectonic episode affecting all parts of the volcanic system. The Laki eruption was followed by a 38-year-long repose interval - there were no eruptions on the Grímsvötn system between 1785 and 1823 (Thordarson and Self, 1993).

The Laki magma is an evolved quartz tholeiite basalt, containing up to 9 vol. % plagioclase, clinopyroxene and olivine glomerocrysts and microphenocrysts, which are in equilibrium with the erupted magma (Grönvold and Jóhanesson, 1984; Métrich *et al*., 1991). The Laki tephra and lava show very limited spatial and temporal compositional variation in major and trace element concentrations (Grönvold and Jóhannesson, 1984; Métrich *et al*., 1991; Sigmarsson *et al*., 1991; Thordarson *et al*., 1996; Passmore, 2009). This apparent compositional homogeneity is remarkable considering the very large magma volume.

2.7.3 20TH CENTURY ACTIVITY

Grímsvötn has been the most active volcanic system in Iceland during the historical period, as well as in pre-historic time (Larsen *et al*., 1998; Larsen, 2002). In fact, 34% of confirmed Icelandic eruptions since 870 AD can be attributed to the Grímsvötn system (Thordarson and Larsen, 2007). Among these, all except the Laki eruption took place on the ice covered part of the system, predominantly within the Grímsvötn caldera (Thorarinsson, 1974; Gudmundsson and Björnsson, 1991). Furthermore, since 1200 AD only one fifth of historical Grímsvötn eruptions have deposited tephra outside of the Vatnajökull ice cap and Iceland's interior highlands (Larsen and Eiríksson, 2008).

There have been ten confirmed eruptions from Grímsvötn since 1900 (in 1903, 1922, 1934, 1938, 1983, 1996, 1998, 2004 and 2011). Among these, all but the 2011 eruption have been rather small events (i.e. VEI ≤ 3), often detected only by unusual seismic activity (Thorarinsson, 1974; Grönvold and Jóhannesson, 1984; Einarsson and Brandsdóttir, 1984; Gudmundsson *et al*., 1997; Larsen *et al*., 1998; Sigmarsson *et al*., 2000). This style of activity appears to be typical, hence our estimates of eruption frequency must be considered minima as eruptions of similar magnitude may have gone unnoticed in the past because of Grímsvötn's remote location. The 2011 event, however, differed from this norm in that it was an order of magnitude more powerful (VEI 4; eruption column 20 km in height) than previous events at Grímsvötn in the last century.

2.7.3.1 GJÁLP AS A SPECIAL CASE

The 1996 Gjálp event is a unique example of a 20th Century eruption that is thought to be derived from the Grímsvötn system yet does not follow the spatial and chemical pattern of the others, and is therefore worthy of mention.

The 1996 eruption site is located between the Grímsvötn and Bárðarbunga calderas, only 10-15 km north of Grímsvötn. The eruption commenced on September 30th and was preceded by 24 hours of seismic activity which originated in the Bárdabunga

caldera then propagated 20 km southwards. Volcanic tremor did not commence until the evening, when the fissure was relatively close to the flanks of Grímsvötn central volcano. Prior to the eruption the ice in this region was 550-750 m thick. Consequently, the eruption did not break through the ice cover to become subaerial until the morning of October 2nd. An estimated 0.45 km^3 D.R.E. of magma was erupted (Gudmundsson *et al*., 2004).

Whole rock chemical analyses show the composition of Gjálp tephra to be Fe-rich basaltic icelandite, a more evolved and crystal-rich (up to 5%) composition than commonly reported at Grímsvötn (Steinthorsson *et al*., 2000). Sigmarsson et al. (2000) demonstrate that the Gjálp magma composition can be produced by ca. 50% fractional crystallisation (approximately 26% plagioclase, 19% clinopyroxene, 4% olivine, and 3% iron-titanium oxides) of a typical Grímsvötn tholeiite, such as the 1998 magma.

The previous eruption located close to the Gjálp site occurred in 1938, and was thought to have originated from the Grímsvötn system. Unfortunately, this was a fully subglacial event, so there are no samples of this magma for chemical analysis. The Gjálp chemistry is, however, similar to that of a tephra layer produced in the Grímsvötn area in 1887 (Steinthorsson *et al*., 2000) but the precise location of the vent of origin of this layer is unknown.

Nevertheless, the available geophysical and chemical data combined with knowledge of the eruption history of this area, strongly suggest that the Gjálp magma originated from the Grímsvötn system. It is likely that fractionation within a subsidiary magma chamber below or near the northern flanks of Grímsvötn volcano produced the observed evolved composition (Sigmarsson *et al*., 2000). The 1996 eruption could then have been triggered by pressure release as the magma chamber was ruptured by a tectonic fracture that propagated southwards from Bárðarbunga. The geochemical evidence therefore conflicts with the concept of lateral migration of magma from the Bárðarbunga system. Furthermore, the style and sequence of seismic activity is more consistent with

initial tectonic fracturing rather than the emplacement of a feeder dyke swarm (Sigmarsson *et al*., 2000). Despite this evidence, the Bárðarbunga-Gjálp-Grímsvötn relationship remains poorly understood. It has even been suggested that the 1996 Gjálp magma belongs to a separate volcanic system, intermediate between Bárðarbunga and Grímsvötn (Steinthorsson *et al*., 2000)

2.8 THE G2004 ERUPTION

A brief summary of the 2004 eruption at Grímsvötn (G2004) is provided here. A more detailed description of G2004 is provided in Chapter 3 of this work. The 1998 eruption at Grímsvötn is also discussed in Chapter 7 and a detailed overview of that event is provided in Appendix V.

Accelerated rates of deformation, along with heightened seismic activity, were recorded prior to the 2004 eruption at Grímsvötn – an event thought to have been triggered by rapid unloading of the volcano induced by a jökulhlaup on October 30th of that year. Consequently, the eruption had been anticipated for several months and it was possible for scientists to alert the civil authorities to the impending eruption at 20:10 on November 1st, based on the observed escalating earthquake frequency trend (Vogfjörð *et al*., 2005).

The start of the eruption was marked by the onset of volcanic tremor - first observed at 21:50 UTM on November 1st, subsequent to the occurrence of a magnitude 2.7 earthquake. In less than an hour, the eruption melted a path through the 200 m thick ice and a ~8-km-high eruption plume became evident on the Veðurstofa Íslands weather radar. The eruption maintained this plume over the following two days, oscillating between altitudes of 6-10 km above the vent. Eruptive activity was also punctuated by the intermittent ejection of "rooster-tail" jets. The extent of tephra dispersal was confined to a sector extending N and NNE from the vent. Of the 5.4×10^{10} kg (0.02 km^3 dense rock

equivalent (DRE)) of magma calculated by Oddsson (2007) to have been ejected, ~50% was deposited within the 800m by 600m wide ice cauldron formed around the vents. More than 95% of all erupted tephra was deposited within Vatnajökull itself, although tephra fallout was detected as far away as the northern coast of Iceland, almost 200 km from the Grímsvötn 2004 crater. The eruption terminated five days later on November 6th, when the last crater explosion was recorded by a nearby seismic station. As such, the 2004 Grímsvötn eruption, can be regarded as typical of small-volume, basaltic, emergent subglacial eruptions in Iceland.

Direct measurements of the water level within the Grímsvötn crater lake are not available for the duration of the G2004 eruption - field mass-balance measurements of ice topography and lake-water levels are taken only once per year.

However, information about the associated jökulhlaup gives us an idea of how much water remained beneath the ice shelf at the time of eruption onset. A jökulhlaup initiated on October 28th in the Skeidará river, which reached its peak flow of over 3000 ms^{-3} on the afternoon of November 2nd. After this, water continued to flow at a diminished rate until early in December 2004. An estimated total of 0.8 km^3 of water was discharged altogether (Vogfjörð *et al*., 2005). Evidence from Berthier *et al*. (2006) indicates that during the 2004 eruption there was an approximately 40 m drop in the level of the ice shelf over Grímsvötn.

CHAPTER 3:

DYNAMICS, STRATIGRAPHY AND PROXIMAL DISPERSAL OF SUPRAGLACIAL TEPHRA DURING THE ICE-CONFINED 2004 ERUPTION AT GRÍMSVÖTN VOLCANO, ICELAND

3.1 INTRODUCTION

Historical records, along with reconstructions from the geological record, demonstrate that three quarters of all eruptions in Iceland in the post-glacial (Holocene) period were explosive (Thordarson and Höskuldsson, 2008; Larsen and Eiríksson, 2008). Of these, in the last 1100 years over 75 % have occurred in a subglacial environment (Larsen, 2002). The Grímsvötn central volcano, located in the west-central part of the Vatnajökull glacier (Fig. 3.1) dominates the event record with, on average, one eruption every ten years (Larsen *et al*., 1998)

A typical subglacial eruptive basaltic sequence beneath thick (>150 m) ice consists of pillow (or other subaqueously emplaced) lavas overlain by hyaloclastite and phreatomagmatic tephra. In some cases, where access to external water becomes restricted, these may eventually be capped by subaerial lava flows (e.g. Jones, 1966; 1970). Little attention has been given to supraglacial deposits of such eruptions. Many studies represent the products of subglacial explosive basaltic eruptions as tuff facies superimposed upon a pillow lava sequence (e.g. Jones, 1966; Skilling, 1994; Smellie, 2000; Jakobsson and Gudmundsson, 2008). No comparable description is available of the tephra apron deposited on top of glacial ice beyond the limits of the tuff cone, i.e. in the proximal and medial regions of the emergent sub-aerial deposit (Fig. 3.2). This is a portion of the products that are not preserved at all in situ implying that the subglacially constructed volcanic edifices preserved in the rock record may in many instances reflect only a part of the overall deposit. However in the study of contemporary eruptions, and for more

complete understanding of deposits and possible effects of past eruptions, such supraglacial deposits should be described and interpreted.

The focus of this study of the 2004 Grímsvötn eruption (hereafter referred to as G2004) is the pristine proximal and medial tephra sequence, which is not normally preserved in the geological record. This study provides vital information for the detailed characterisation of main phase subaerial explosive activity within an emergent subglacial basaltic explosive eruption. The ice cauldron fill within the 2004 crater, capped by a small cone formed during the waning stages of the eruption (Fig. 3.3G, H), is equivalent to the bedded tuff sequences seen to cap classical subglacial successions (Fig. 3.2).

In this study, I describe the temporal evolution of the G2004 eruption in the light of contemporary observations and post-eruption tephra studies by comparing the deposit architecture with the detailed tremor record of the event and visual observations of the eruption. Such a complete study is rarely possible for most glacio-volcanic sequences and so I also assess the eruption in the context of our wider understanding of basaltic phreatomagmatic events, in particular basaltic, explosive, emergent subglacial events.

Figure 3.1: Location map. (A) Map of Iceland showing the location of the Grímsvötn central volcano (in red) and locations of recorded distal tephra fall (1. Möðrudalur; 2. Grímsstaðir; 3. Svartákot; 4. Reykjadalur). (B) Location and geometry of the key features of the Grímsvötn volcanic system in western Vatnajökull. Central volcanoes are outlined with a solid black line, while the fissure system is outlined by a stippled black line (modified after Thordarson and Self, 1993). (C) Ice surface contours within the Grímsvötn caldera showing the vent locations of G2004 and 20th century eruptions. The study area is outlined with a red box.

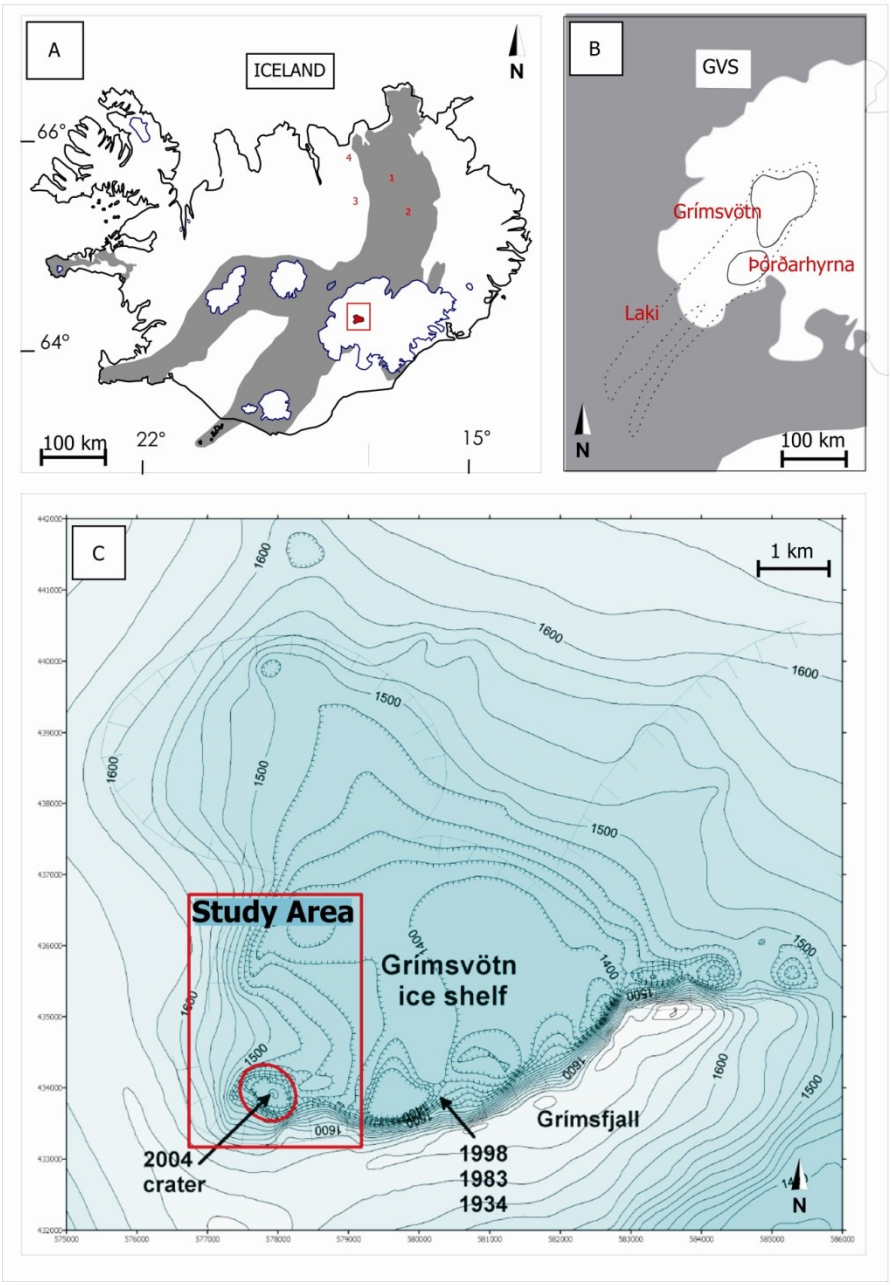

Figure 3.2: Schematic diagram illustrating depositional regions during the emergent/tuff cone stage of emergent subglacial volcanism. Note that the classic sequence described in the literature does not account for the deposition of a tephra apron on the ice surface extending some distance from the vent (highlighted by a red box), which will occur as emergent activity generates a buoyant plume and deposition occurs via direct fallout and pyroclastic density currents. This has been observed during several events, including Capelinhos, 1957; Surtsey, 1963; Gjálp, 1996; G1998, and G2004. In older, exposed subglacial sequences it is likely that there will be little to no remaining trace of this part of the sequence.

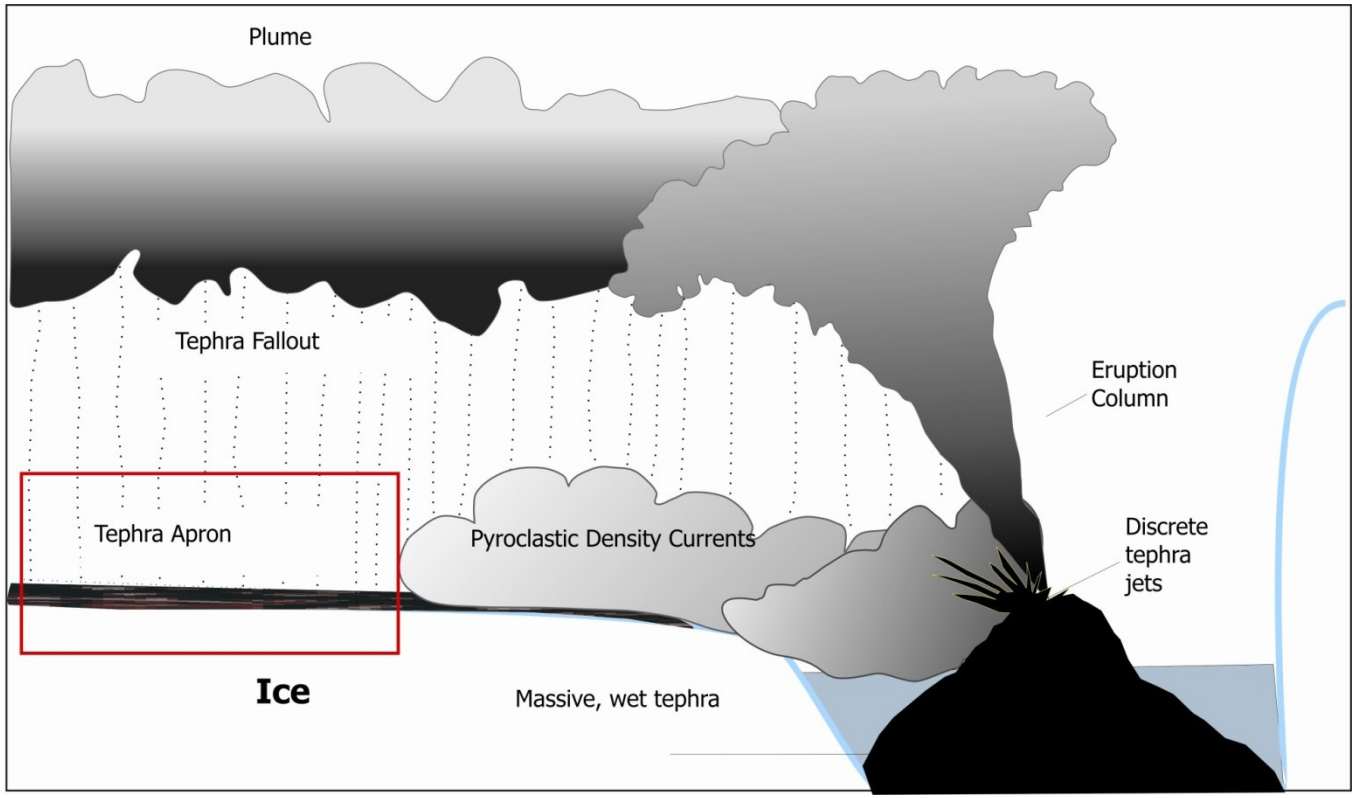

Figure 3.3: Photo time series of activity towards the end of the main phase of the eruption - all pictures (except bottom row) taken 02/11/2004. (A) (15:34) Eruption plume and pyroclastic density currents viewed from the SW. In the light coloured region, the eruption column is rising buoyantly above the vent, while depositing tephra to the north; (B) (15:35) PDCs and plume viewed from the S. Note the narrowly confined and clearly delineated boundary of deposits; (C) (15:38) Pyroclastic fallout viewed from the NE (with respect to the vent). Note that the plume is strongly inclined towards the N, due to strong southerly winds; (D) (15:56) View from the SW. Observe low-level jets emitted from two distinct vents; (E) (15:40) View from the S. Note that the S and W sides of the ice cauldron are confined by steep ice walls; (F) (16:11) From SSW. At this moment, the W vent dominates jet activity. Note also that the deposit has a highly irregular outline close to the vent, which narrows and smoothes out in the more distal region; (G) Aerial view of the tephra apron and late-stage tuff cone at the end of the 2004 eruption on November 6th. A vertical line on the picture, running through the crater, would be oriented approximately SW-NE (top to bottom); (H) Grímsvötn 2004 tuff cone as preserved in August 2005. View towards SSW. Photographs by Magnus Tumí Guðmundsson.

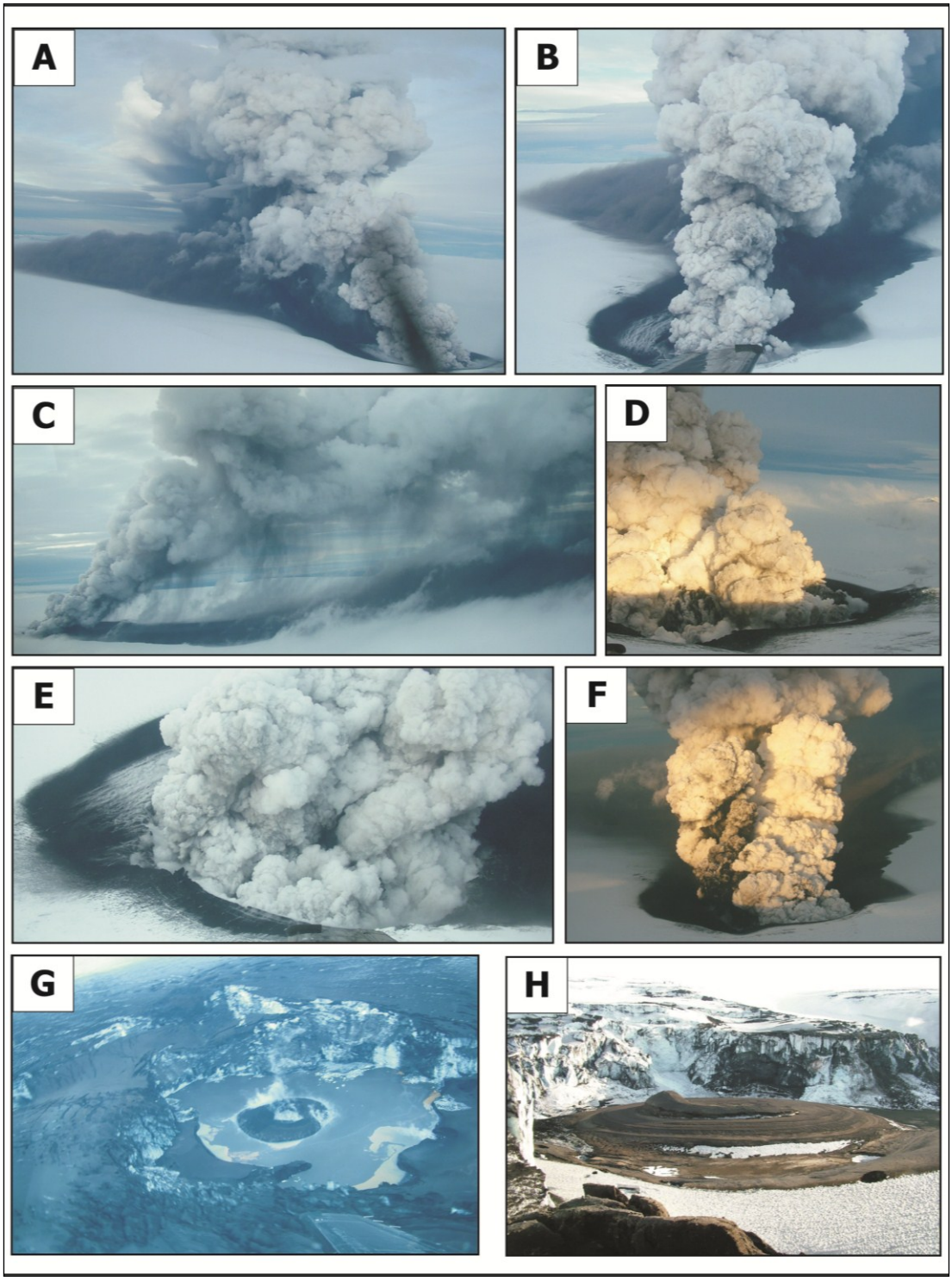
A
B
C
D
E
F
G
H

3.2 STRUCTURE AND SIZE OF GRÍMSVÖTN VOLCANO

The Grímsvötn volcanic system consists of two central volcanoes and an associated fissure system (Fig. 3.1B). Grímsvötn is the dominant of the two and reflects the location of the highest rate of magma supply on the system. Grímsvötn and the smaller Þórðarhyrna central volcano (which is remarkably inactive compared to Grímsvötn) are aligned along a NE-SW trending fissure system (Gudmundsson and Högnadóttir, 2007). Fissure eruptions on the Grímsvötn system include the subglacial Gjálp eruptions in 1938 and 1996 (Gudmundsson *et al*., 2004) and the infamous 1783-85 Laki eruption (Thordarson and Self, 1993).

Grímsvötn contains a 50 km^2 composite caldera at an elevation of 1060-1200 m a.s.l. that consists of three smaller structural domains - the main (or southern), northern and eastern calderas (Sæmundsson, 1982; Gudmundsson, 1989; Gudmundsson and Milsom, 1997). The southern caldera is underlain by low density, low seismic velocity material extending to approximately 2 km depth, which is interpreted as subsided and remobilised clastic material. Gravity and magnetic surveys (Gudmundsson, 1989; Gudmundsson and Milsom, 1997), along with a teleseismic study (Alfaro *et al*., 2007) indicate the existence of shallow magma chamber in the upper crust beneath the volcano.

Grímsvötn is also a very powerful geothermal area, with a heat output of 2000-4000 MW averaged over several decades (Björnsson, 1988; Björnsson and Gudmundsson, 1993). This geothermal activity has created a depression in the ice surface approximately 10 km in diameter, which is, bordered to the south by the steep cliffs marking the southern caldera wall at the Grímsfjall ridge. Ice flows into the depression from the west, north and east. The intense energy release is responsible for the creation and maintenance of subglacial lakes and also affects the extent to which these can be contained by the surrounding ice. Grímsvötn is a renowned locality for jökulhlaups that occur when the level of its subglacial caldera lake reaches sufficient elevation for meltwater to force its way under the glacier, leading to drops of 60-130 m in the lake level and partial draining of the lake. Such jökuhlaups occurred on average once every 4-6 years for most of the 20th century (e.g. Björnsson, 2003).

3.3 ERUPTIONS IN GRÍMSVÖTN

As a consequence of its location beneath the Vatnajökull ice cap, the explosive interaction between magma and external water (or ice) places important controls on the style of eruptions at Grímsvötn. Most eruptions from this volcano occur within the caldera itself, along the southern caldera fault, where the ice is 50-200 m thick. Sometimes eruptions break through the ice cover almost instantly as magma reaches the glacier bed (e.g. the 1998 eruption; Gudmundsson, 2005), but the 2004 eruption took almost half an hour to melt its way through 150-200 m of ice in the southwest corner of the caldera.

In contrast with fissure eruptions under thick ice, as in Gjálp in 1996, melting of ice in a typical Grímsvötn caldera eruption is often quite limited. For example, during each of the 1998 and 2004 eruptions, only 0.1 km^3 of ice was melted. Neither of these eruptions caused major jökulhlaups (glacial outburst floods). Many eruptions (e.g. 2004 and potentially some others in the 19th and early 20th centuries; Albino *et al*., 2010) were triggered by depressurisation by falling lake levels during drainage by periodic jökulhlaups (Thorarinsson, 1953; Gudmundsson, 2005). This supports the existence of a shallow-level magma chamber beneath Grímsvötn. Numerical calculations by Albino *et al*. (2010) confirm that jökulhlaups can trigger eruptions, but only if the underlying magma chamber is already close to failure conditions. That is, where the difference between the tensile strength of the host rocks and the magma pressure at the chamber wall is relatively small.

When eruptions at Grímsvötn are large enough to melt through to the ice surface, the resulting subaerial activity is generally phreatomagmatic in nature as a consequence of large volumes of water provided by melting ice. Eruptions in Grímsvötn are small to moderate in size, with estimated tephra volumes between 0.01 and 0.5 km^3 dense rock equivalent (DRE) (Thorarinsson, 1974; Gudmundsson and Björnsson, 1993; Gudmundsson, 2005; Thordarson and Larsen, 2007) and typically last for several days to a few weeks. An island is usually formed within the ice-confined lake, along with a tephra fan extending onto the icecap downwind from the eruption site. Large-scale

fallout of tephra from these events seldom extends beyond Vatnajökull (Larsen *et al*, 1998; Thordarson and Larsen, 2007; Thordarson and Höskuldsson, 2008).

The higher frequency of Grímsvötn eruptions compared with elsewhere in Iceland, along with the cyclic nature of this activity, can be attributed to the proximity of the volcano to the centre of the Iceland mantle plume (Wolfe *et al*, 1997). Larsen *et al*. (1998) show that in historical time (the past 1100 years) there have been over 70 eruptions attributed to Grímsvötn and that this activity is characterized by 50–80 year-long alternating cycles of high vs. low eruption frequency. Despite Grímsvötn's remote location, significant hazards are posed in the event of an eruption by the generation of jökulhlaups. In addition, the eruption plumes pose a hazard for air traffic in the North Atlantic. In light of the recent (2010) summit eruption at Eyjafjallajökull, which showed that Icelandic explosive emergent subglacial eruptions of small to moderate intensities can produce ash-laden plumes affecting large swathes of Europe (Gudmundsson *et al*., 2010, Schuman *et al*., 2010, Davis *et al*., 2010), the characterization and anticipation of these events is of high priority.

3.4 CHRONOLOGY OF THE 2004 ERUPTION

The G2004 eruption is the best documented volcanic event at Grímsvötn, both in terms of geophysical measurements and visual observations. Visual observation of the eruption progress were made by daily (when weather permitted) inspections of the crater from the air. There are no written records of these observations. However, the eruption photographs used within this chapter were taken during these flights. The event chronology has been previously described by Vogfjörð *et al*. (2005) and Sigmundsson and Gudmundsson (2004).

The Icelandic Meteorological Office (Veðurstofa Íslands, hereafter referred to as IMO) weather radar is located on the Reykjanes Peninsula 260 km away from Grímsvötn. During volcanic eruptions, radar images are acquired every 5 minutes. Due to the distance to the radar station the beam width above Grímsvötn is 4 km and the detected plume altitudes are therefore averaged over this vertical distance. The IMO

also operates a nationwide digital seismic network (SIL) along with a network of continuous GPS stations (ISGPS) to monitor seismic and volcanic activity in Iceland. The instrument records used in this study were collected from these sources (Vogfjörð *et al*., 2005).

The 2004 eruption had been anticipated for several months, as abundant data recording precursory activity at the site were available prior to the event. A jökulhlaup from Grímsvötn commenced on October 28th and by November 1st the water level had fallen by 15 metres. Short term precursors of an eruption were recorded on November 1st in the form of frequent earthquakes. An intense swarm between 20:20 and 21:50 marks the progress of magma to the surface at the glacier bottom. G2004 commenced as a subglacial event located in the southwest corner of the Grímsvötn caldera at 21:50 as estimated from the onset of continuous tremor. Within half an hour it melted through ice almost 200 m thick to become subaerial, forming an approximately 750 m long and 550 m wide ice cauldron over the next two days. The eruption plume was detected by the IMO weather radar at 22:50 UTC and at that time had already risen to 6 km above the vent (a.v.). Over the following four hours, the plume increased to 10 km a.v. (Sigmundsson and Gudmundsson, 2004). The seismic tremor record shows high activity for the first 24 hours, and then a slowly declining tremor amplitude for the next 21 hours, after which it fell to background levels (Fig. 3.4). The record is punctuated by several higher amplitude pulses in the early evening of November 2nd and also the following morning. Visual inspections from aircraft reveal that, at times, two distinct vents were simultaneously active and pyroclastic density currents (PDCs) occurred concurrently with fallout from a high eruption column (Fig. 3.3A, B).

On November 2nd, activity alternated between vigorous continuous uprush and less energetic explosivity, with the plume oscillating between altitudes of 6 to 10 km a.v. (Oddsson, 2007). The ejection of intermittent rooster-tail jets (also known as cypressoidal or tephra finger jets) was also observed, although this formed a minor component of the activity. The terms “continuous uprush” and “rooster-tail jets” were coined by Thorarinsson *et al* (1964) to describe two distinct eruption styles observed in the emergent phases of the 1963-67 Surtsey eruption - each driven by copious

tephra-rich explosions on the time scale of seconds to minutes. Rooster-tail events typify activity where water has ready access to the vent and originate from multiple shallow explosions, each producing vertical to sub-horizontal black tephra jets. Continuous uprush events take place when the vents are completely surrounded by tephra walls, thus restricting the access of water and can last for hours. The continuous uprush events originate from explosions rooted deeper in the vent, which produce 0.5 to 2 km-high vertical black tephra-rich columns (momentum jets) with muzzle velocities >100 m sec^{-1} and maintain convective eruption columns rising as high as 12 km. The continuous uprush events are normally more powerful than the rooster-tail events because of the more favourable water to magma mass ratio.

Figure 3.4: Tremor amplitude (modified from Vogfjörð *et al*., 2005) and corrected IMO radar plume height records (modified from Oddsson, 2007) for the G2004 eruption. Tremor amplitude, plume height, and deposit stratigraphy are correlated to identify the duration and intensity of each unit. On the time-bar at the top of the figure periods of quiescence are represented by white; short, high intensity bursts by black; sustained deposition both tephra fallout and PDCs by dark grey; and low intensity PDC activity by light grey. The start of the eruption, beginning of the subaerial phase, and end time of significant tephra deposition are demarcated by thin green lines

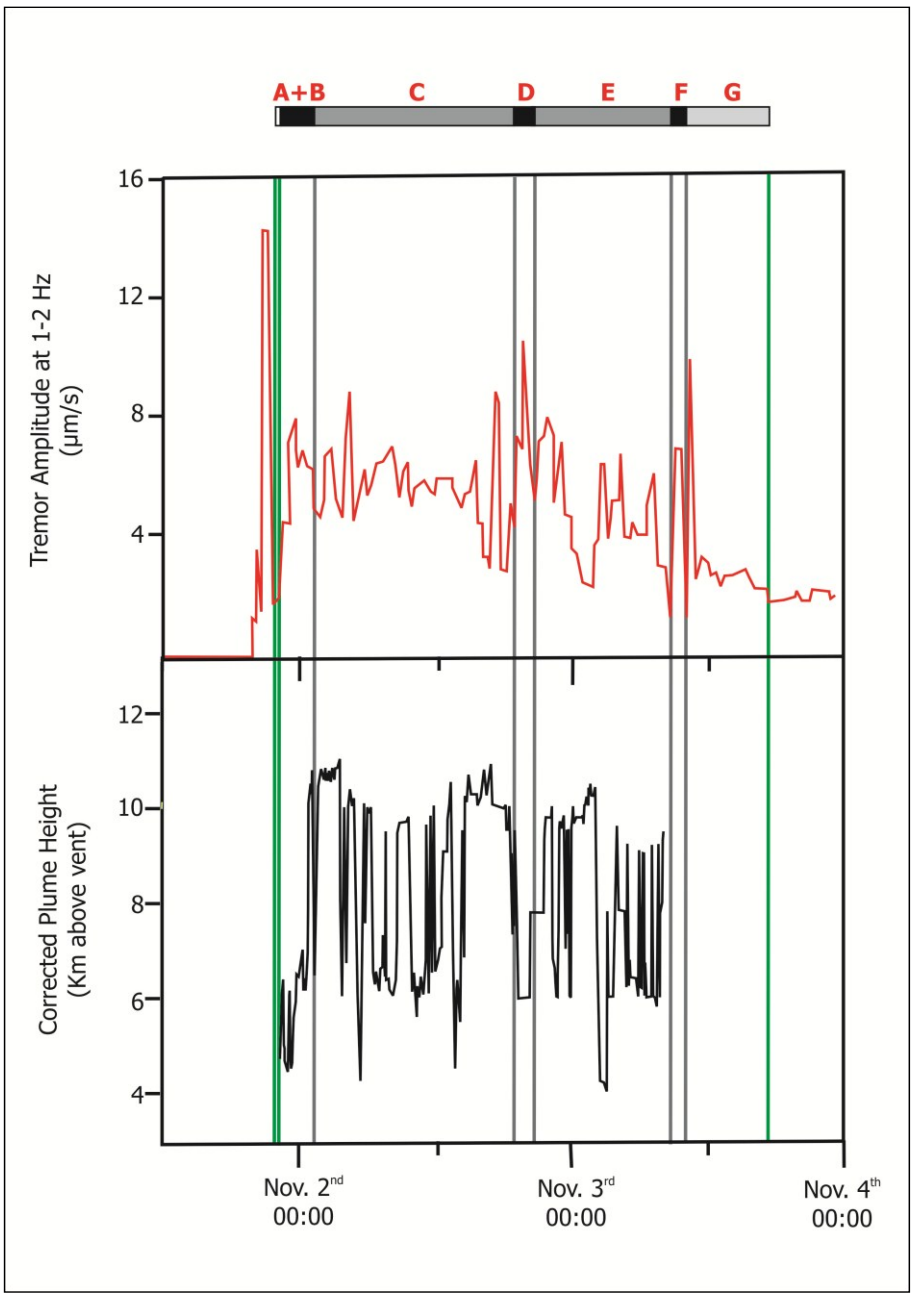

Tphra fall was observed at manned weather stations in northeast Iceland on November 2nd and into November 3rd. The fallout was relatively minor, not forming a continuous layer on the ground and was only observed for limited periods at each station. The fallout was principally towards the north-northeast on November 2nd but towards the north on November 3rd (Oddson, 2007)

The radar cannot detect plumes lower than 4 km a.s.l. (i.e. approximately 2 km above vent) due to the curvature of the earth (Oddsson, 2007). At 08:30 the plume fell out of radar view and the last high amplitude tremor recorded was at 10:54 on November 3rd. Tephra production at this time was minor. On November 4th, activity was minor although a thin blanket extending a few kilometres to the east was formed from a weak plume, which was observed from aircraft to extend 1.5-2 km above the vent. This represents only a fraction of a percent of the total tephra produced. Thus, almost all of the deposits produced by this event are contained within the main, north - directed tephra sector. Tephra fall from the eruption is therefore very well defined, extending north and north-northeast from the vent. From the afternoon of November 3rd, activity was characterised by intermittent phreatomagmatic explosions (Harðardóttir *et al*., 2005; Sigmundsson and Gudmundsson, 2004; Vogfjörð *et al*., 2005). On November 6th the last explosion signal was detected at the Grímsfjall seismic station. By the end of the eruption, a small tephra ring approximately 200 m in diameter had formed within the ice cauldron. The jökulhlaup reached its peak flow of over 3000 ms^{-3} on the afternoon of November 2nd, nevertheless a diminished current persisted until early in December 2004 (Vogfjörð *et al*., 2005).

3.4.1 WEATHER CONDITIONS

Measurements of wind speed and direction, temperature and precipitation were collected every hour from the Jökulheimar weather station which is located approximately 50 km SW of Grímsvötn, off the edge of the Vatnajökull glacier (Table 3.1; data provided courtesy of the IMO). The precipitation recorded at Jökulheimar was low overall – generally less than 0.5 mm/hour. The maximum recorded precipitation

was 4.3 mm for an hour interval during the first subaerial phase of the eruption. However, it is not clear how representative the precipitation at Jökulheimar is likely to be for precipitation within the glacial interior. Over the approximately 45-hour period of the G2004 eruption, the temperature at Jökulheimar oscillated between 0 and 5°C. It is likely that on the glacier temperatures were a few degrees colder than this and that the majority, if not all, precipitation fell as snow or ice. The wind direction over the course of the eruption was variable, oscillating over time intervals of a few hours between southerly and southwesterly. For the first 8 hours of the eruption the wind speed was moderate (i.e. 10-15 ms^{-1}). The wind speed dropped to weak levels (i.e. <10 ms^{-1}) 8-10 hours after eruption onset. It picked up again to moderate levels between 1800 hrs. on November 2nd and 0200 hrs. on November 3rd before gradually dropping off again. Towards the end of the eruption the wind speed was quite low (< 5ms^{-1}).

Table 3.1: Meteorological data from Jökulheimar weather station. Data courtesy of the Icelandic Meteorological Office.

Eruption Unit	Date	Time	Temperature *°C*	Wind Direction *Degrees*	Wind speed *m/s*	Precipitation *mm*
Subglacial	1/11/2004	2100 hrs	5.1	207	14.5	0.0
Unit A + B	1/11/2004	2200 hrs	4.9	201	16.6	0.0
	1/11/2004	2300 hrs	5.1	202	15.3	2.9
	1/11/2004	2400 hrs	5.4	213	15.4	4.3
Unit C	2/11/2004	0100 hrs	5.5	220	15.0	3.7
	2/11/2004	0200 hrs	5.5	224	11.9	2.2
	2/11/2004	0300 hrs	5.2	220	10.4	1.6
	2/11/2004	0400 hrs	5.2	228	10.2	1.1
	2/11/2004	0500 hrs	5.1	230	9.9	0.9
	2/11/2004	0600 hrs	4.5	227	9.8	0.7
	2/11/2004	0700 hrs	4.1	224	10.2	0.2
	2/11/2004	0800 hrs	4.1	229	9.3	0.0
	2/11/2004	0900 hrs	3.5	256	6.4	0.2
	2/11/2004	1000 hrs	2.4	229	3.6	0.1
	2/11/2004	1100 hrs	2.5	224	4.7	0.0
	2/11/2004	1200 hrs	1.9	201	8.1	0.0
	2/11/2004	1300 hrs	2.0	204	8.2	0.0
	2/11/2004	1400 hrs	1.6	191	8.0	0.0
	2/11/2004	1500 hrs	2.0	193	4.0	0.0
	2/11/2004	1600 hrs	2.1	194	5.3	0.0
	2/11/2004	1700 hrs	2.3	198	6.6	0.0
	2/11/2004	1800 hrs	3.8	190	12.0	0.0
Unit D	2/11/2004	1900 hrs	3.4	195	8.8	0.0
	2/11/2004	2000 hrs	4.5	172	15.0	0.3
Unit E	2/11/2004	2100 hrs	4.5	175	13.1	0.0
	2/11/2004	2200 hrs	4.3	186	12.3	0.4
	2/11/2004	2300 hrs	4.0	190	10.9	1.6
	2/11/2004	2400 hrs	4.9	194	13.7	1.5
	3/11/2004	0100 hrs	5.2	200	12.7	1.8
	3/11/2004	0200 hrs	5.1	204	11.4	2.0
	3/11/2004	0300 hrs	3.0	310	4.3	2.2
	3/11/2004	0400 hrs	2.8	197	6.5	2.4
	3/11/2004	0500 hrs	1.9	207	8.1	1.3
	3/11/2004	0600 hrs	0.8	214	6.8	1.3
	3/11/2004	0700 hrs	0.4	228	1.8	0.7
	3/11/2004	0800 hrs	0.7	209	5.2	0.6
	3/11/2004	0900 hrs	0.5	201	6.3	0.2

Eruption Unit	Date	Time	Temperature *°C*	Wind Direction *Degrees*	Wind speed *m/s*	Precipitation *mm*
Unit F	3/11/2004	1000 hrs	0.8	204	6.0	0.0
Unit G	3/11/2004	1100 hrs	1.4	221	4.8	0.2
	3/11/2004	1200 hrs	2.0	163	5.9	0.0
	3/11/2004	1300 hrs	1.1	238	3.1	1.0
	3/11/2004	1400 hrs	1.6	221	4.1	0.4
	3/11/2004	1500 hrs	1.3	262	2.2	0.3
End of Eruption	3/11/2004	1600 hrs	-0.1	328	1.4	0.7

3.5 METHODS

3.5.1 STUDY OF PROXIMAL UNITS

Isopach maps based upon field data were constructed for individual units using ArcGIS. The total deposit thickness is better constrained than that of individual units so the total deposit map was used as a constraint on the sum of individual units. Thinning trends are determined from a semi-log plot of area$^{1/2}$ vs. thickness (after Pyle, 1989). For comparison, the data is also presented in the more traditional form of distance versus thickness plots. As the G2004 tephra does not follow the simple exponential thinning model (see below), I adopt the approach of Houghton *et al*. (2004) and measure average linear thickness half-distance ($t_{1/2}$) for the bulk deposit and its units. The parameter $t_{1/2}$ is defined as the measured distance over which the deposit halves in thickness along any single transect and can be measured in both radial and tangential transects with respect to the vent (Houghton *et al*., 2004).

The deposit volume is obtained by direct integration of the unit and total thickness isopach maps, a method shown to be valid for calculating deposit volume or mass in cases where the tephra blanket is well-preserved and/or samples are collected shortly after the eruption (e.g. Carey and Sparks, 1986; Pyle, 1989; Fierstein and Nathanson, 1992). For the proximal area, where the layer is thick and continuous, direct measurements of thickness were used, while for the distal region mass per unit area values are converted to thickness using the average measured density for the deposit (1190 kg m^{-3}; Oddsson, 2007). The dense rock equivalent (DRE) volume of magma erupted was calculated using a DRE value of 2750 kg m^{-3} (Métrich *et al*., 1991).

3.5.2 BALLISTIC CALCULATIONS

3.5.2.1 THE BALLISTIC DATASET

Ballistic fragments are those which are considered to have been propelled via explosions within the crater directly to their measured resting location. That is, along a ballistic trajectory that has not been modified by the effects of a buoyantly rising plume, atmospheric processes such as wind, or entrained and mobilised by PDCs. Factors which affect the range of a ballistic particle include: the initial velocity with which the fragment was ejected, the angle of ejection, the depth of explosion (and any other changes in altitude between the ejection and landing positions), projectile mass and external ballistic characteristics and influences (e.g. air resistance).

Field measurements of ballistic fragments (blocks/bombs) were taken within sampling circles of increasing radius along two profiles from W-E, and S-N from the crater rim (Fig. 3.5) by Jónas Guðnason in July-August 2007. The two transects extend approximately 1.5 km east and 2.5 km north from the source vents. Measurements of the three maximum orthogonal dimensions of each block were made in situ, with the resting position recorded using handheld GPS to determine ballistic range. In addition, representative samples of each block were taken for later laboratory measurements of block density. Measured and calculated parameters for each sample are given in Table 3.2. Within the 2004 deposit, three non-juvenile blocks types have been identified: (1) Massive - pristine, non-vesicular crystalline lava; (2) Vesicular - pristine, vesicular crystalline lava (no juvenile bombs included); (3) Hyaloclastite - hydrothermally altered, or unaltered, consolidated tuff.

Figure 3.5: Map generated by Garmin MapSource software showing the location of ballistic block or bomb (BOB) sample points (black squares) relative to the G2004 crater (red circle).

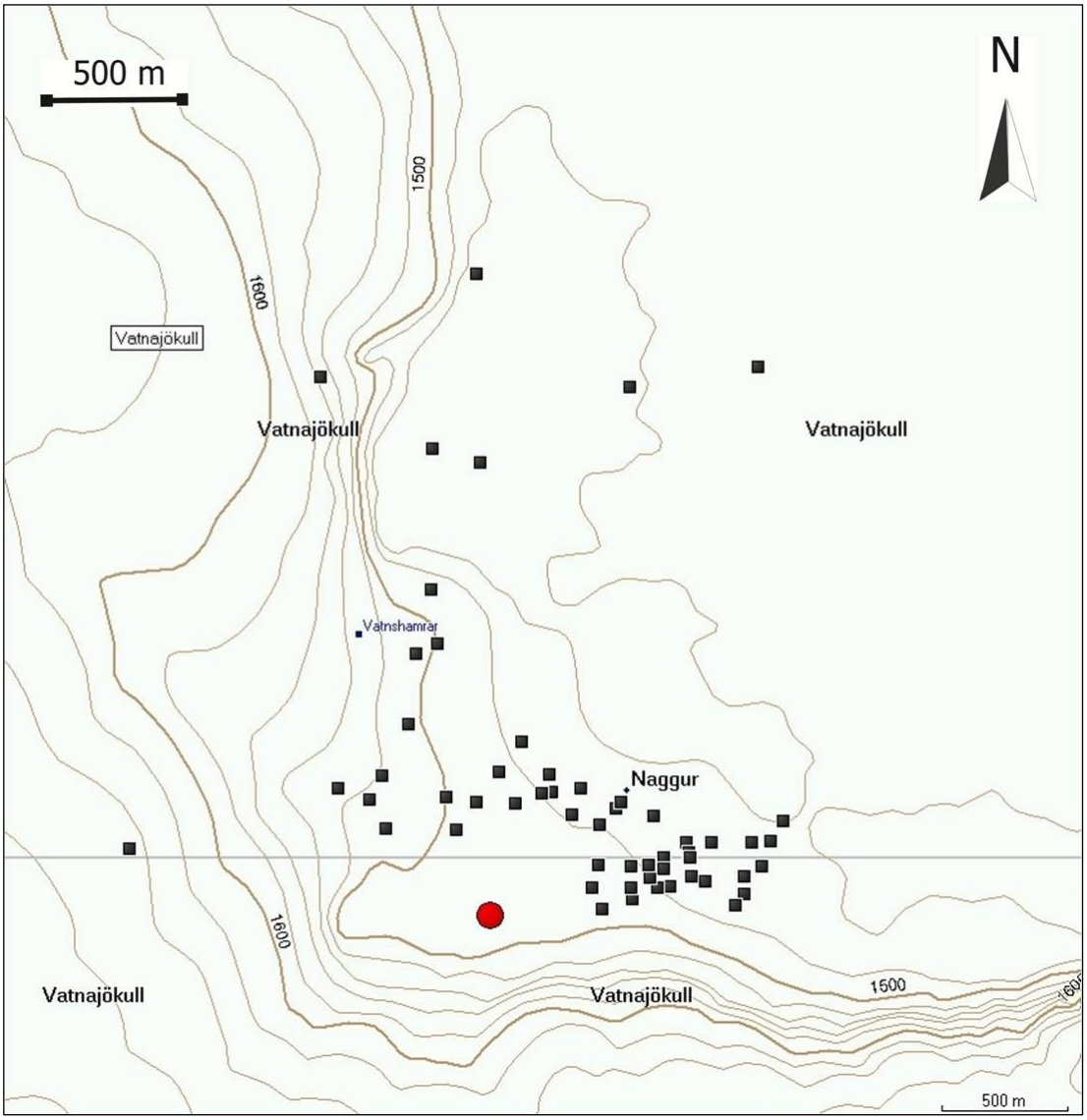

Table 3.2: Locations and measurements for each sample (J. Guðnason), along with calculated parameters i.e. BOB mass; aspect ratio; drag coefficient; and ejection velocity without accounting for at a 60 or 45 degree angle (after Self *et al*, 1980).

Sample #	Distance from vent (m)	x (cm)	y (cm)	z (cm)	Density (g/cm)	Mass (kg)	Aspect Ratio (x/y)	Drag Coefficient	U_0 (m/s) [60°]	U_0 (m/s) [45°]
bob003	994	57	45	40	2.86	146.72	0.702	2.00	129.5	104.4
bob004	1009	50	45	43	2.86	276.71	0.860	1.00	130.5	105.2
bob004	1009	67	60	47	2.86	540.37	0.701	1.00	130.5	105.2
bob004	1009	50	50	45	2.86	321.75	0.900	1.00	130.5	105.2
bob005	1085	75	62	51	2.86	678.25	0.680	1.00	135.3	109.1
bob009	1177	107	70	53	2.86	1135.33	0.495	1.00	140.9	113.6
bob009	1177	60	57	56	2.40	321.75	0.933	1.43	140.9	113.6
bob010	1103	73	70	69	2.10	518.31	0.945	1.43	136.4	110.0
bob010	1103	81	65	58	2.10	448.89	0.716	1.43	136.4	110.0
bob010	1103	68	50	42	2.50	357.00	0.618	1.00	136.4	110.0
bob012	1037	85	70	54	2.86	918.92	0.635	1.00	132.3	106.6
bob012	1037	67	60	42	2.86	386.31	0.627	1.25	132.3	106.6
bob013	982	77	67	60	2.86	885.28	0.779	1.00	128.7	103.8
bob013	982	70	70	65	2.86	819.82	0.929	1.11	128.7	103.8
bob013	982	76	61	60	2.86	477.32	0.789	1.67	128.7	103.8
bob014	846	70	56	54	2.86	423.78	0.771	1.43	119.5	96.3
bob019	729	45	43	40	2.40	167.18	0.889	1.11	110.9	89.4
bob021	822	75	52	43	2.40	281.74	0.573	1.43	117.8	94.9
bob021	822	80	69	50	2.86	710.42	0.625	1.11	117.8	94.9
bob021	822	65	63	47	2.86	330.27	0.723	1.67	117.8	94.9
bob022	798	120	88	85	2.86	2053.71	0.708	1.25	116.1	93.5

Sample #	Distance from vent (m)	x (cm)	y (cm)	z (cm)	Density (g/cm)	Mass (kg)	Aspect Ratio (x/y)	Drag Coefficient	U_0 (m/s) [60°]	U_0 (m/s) [45°]
bob022	798	70	45	42	2.86	227.03	0.600	1.67	116.1	93.5
bob022	798	104	101	90	2.86	1892.61	0.865	1.43	116.1	93.5
bob025	703	86	61	50	2.50	393.45	0.581	1.67	108.9	87.8
bob026	655	52	52	42	2.40	272.56	0.808	1.00	105.1	84.7
bob029	594	59	44	41	2.50	212.87	0.695	1.25	100.1	80.7
bob029	594	82	66	50	2.86	619.13	0.610	1.25	100.1	80.7
bob030	561	72	65	42	2.86	337.30	0.583	1.67	97.3	78.4
bob031	561	55	49	44	2.86	271.31	0.800	1.25	97.3	78.4
bob031	561	51	43	42	2.86	263.42	0.824	1.00	97.3	78.4
bob031	561	233	190	180	2.86	18232.16	0.773	1.25	97.3	78.4
bob031	561	96	83	80	2.86	1276.15	0.833	1.43	97.3	78.4
bob032	452	51	50	40	2.86	204.20	0.784	1.43	87.3	70.4
bob032	452	77	60	60	2.86	713.51	0.779	1.11	87.3	70.4
bob033	420	78	56	52	2.86	649.61	0.667	1.00	84.2	67.9
bob034	506	97	79	49	2.50	657.10	0.505	1.43	92.4	74.5
bob034	506	80	76	44	2.50	535.04	0.550	1.25	92.4	74.5
bob035	458	70	69	48	2.86	464.14	0.686	1.43	87.9	70.9
bob035	458	95	71	66	2.50	890.34	0.695	1.25	87.9	70.9
bob035	458	82	72	60	2.50	708.48	0.732	1.25	87.9	70.9
bob035	458	83	72	50	2.50	448.20	0.602	1.67	87.9	70.9
bob043	466	54	47	43	2.86	312.12	0.796	1.00	88.7	71.5
bob043	466	75	64	52	2.86	713.86	0.693	1.00	88.7	71.5
bob045	484	142	138	86	2.86	3373.88	0.606	1.43	90.4	72.8
bob047	527	85	46	46	2.86	257.20	0.541	2.00	94.3	76.0

3.5.2.2 Analysis of Muzzle (Ejection) Velocity and Ballistic Range

The muzzle velocity of fragments as they are ejected from the vent is related to the kinetic energy of the eruption (Steinberg, 1976). All terms are defined in Table 3.3:

$$E = \frac{x_m 4\pi\rho_(w\text{^}3) g}{2.4(\sin\text{^}3)\theta \sin 2\theta} \qquad [1]$$

The explosive power among eruptions of a similar style or mechanism can therefore be compared by inverse application of the equations of motion for a ballistic trajectory. This calculation takes the effects of air resistance into account, and energy is determined from the measured ranges of large ejected fragments and by calculation of their ballistic coefficients (Steinberg and Lorenz, 1983).

Table 3.3: Definition of terms

Symbol	Description of Symbol	Units
E	Kinetic energy	J
x_m	Horizontal distance travelled by the block/bomb	m
ρ	Block density	kg/m^3
w	Depth of explosion	m
g	Acceleration due to gravity	m/s^2
U_0	Initial (eruptive) velocity of the block/bomb	m/s
θ	Angle of ejection	°
CD	Drag coefficient	-
D	Block/bomb diameter	m
σ	Ballistic coefficient (σ = A/m)	m^2/kg
m	Block/bomb mass	kg
ρa	Density of air	kg/m^3
A	Cross-sectional area of the block/bomb	m^2

From the original sample set of 226 measurements, samples with any axial dimension <40 cm were excluded from further analysis. This value represents a reasonable size threshold, above which a block's flight path may be considered to be unaffected by the wind (Steinberg and Lorenz, 1983). Next, a simple shape factor analysis was performed to identify approximately spherical samples. For each block, the aspect ratio of the minimum and maximum dimensions was calculated. Elongate

blocks (those with values <0.5) were removed from consideration (to allow more realistic calculation of the drag coefficient). The remaining dataset consisted of 45 samples. Assuming approximate sphericity, the drag coefficient was calculated for each sample, according to equation [2], yielding values ranging between 1 and 2.

$$C_D = \frac{2\rho D\sigma}{3} \quad [2]$$

Since there is no analytic solution to the problem of ballistic motion with quadratic drag [3], I arrive at a solution using a finite difference method written in R (Naylor, 2010; Appendix II).

$$x_m = \frac{m}{\rho_a A C_D} \log_e(1 + C_D(u_0\text{^}2)(\sin\text{^}2)\theta \quad [3]$$

The code is validated by application to the data and findings of Self *et al*. (1980). For phreatomagmatic explosions of the 1977 Ukinrek Maars eruption, for blocks >40 cm in diameter, which attained a maximum range of 450 m at a hypothetical ejection angle of 45°, Self *et al*. (1980) calculated muzzle velocities in the range of 86-98 ms^{-1}. Our computed result is 88.16 ms^{-1}, which compares well with the findings of Self *et al*. (1980).

Within the G2004 ballistics dataset there is no correlation between clast dimension/mass and ballistic range. This suggests that aerodynamic drag was not the principal factor controlling the ballistic distribution. Self *et al*. (1980) identify two classes of ballistic distribution: Type 1, whereby block size diminishes with distance from the vent as a consequence of transport in a gas stream from which larger blocks decouple earlier than the smaller ones; and Type 2, whereby block size increases with distance from the vent as a result of direct ejection from phreatomagmatic explosions (i.e. the flight path of large blocks is impeded less by drag effects than that of small blocks).

In most cases of ballistic dispersal, a more complex size distribution is anticipated. In the first instance a single eruption may feature different eruption styles which are likely to generate separate, possibly superimposed, ballistic distributions. Then, a collection of blocks expelled by a single explosion will experience a spectrum of possible ejection angles. Phreatomagmatic eruption phases are characterised by almost continuous explosions in the crater, generating a maintained steam column e.g. Capelinhos, 1957 (Waters and Fisher, 1971); Surtsey, 1963-67 (Thorarinsson, 1974) and are therefore expected to produce block aprons with a complex size distribution, leading to considerable scatter along a representative profile plot.

The maximum observed range for large blocks within the G2004 deposit was 1177 m from the vent. The dimensions of the largest block identified at this location were 107 cm x 70 cm x 53 cm. The application of our ballistic model yields the minimum velocity threshold required for a block of this size to achieve the observed range (Fig. 3.6). It is assumed that there is no change in elevation along the flight path. This is a fair approximation since material was deposited over an essentially flat ice surface. Our calculations show that the G2004 phreatomagmatic explosions expelled non-juvenile blocks at velocities of >130 ms^{-1}; a minimum value that is achieved by assuming a 42˚ ejection angle and that at the time of impact the block had travelled the entire length of its theoretical trajectory (Fig. 3.6).

Figure 3.6: Optimization of launch angle and initial velocity required for $Block_{max}$ to achieve target/observed range (black curve). V_{min} = 129.78 ms^{-1} at a 42 degree launch angle. The red line indicates V_0 if the block is launched at 45 degrees in a vacuum (V_{min} = 107.45 ms^{-1}). The blue line indicates V_0 if the block is launched at 60° in a vacuum (V_{min} = 129.78 ms^{-1}).

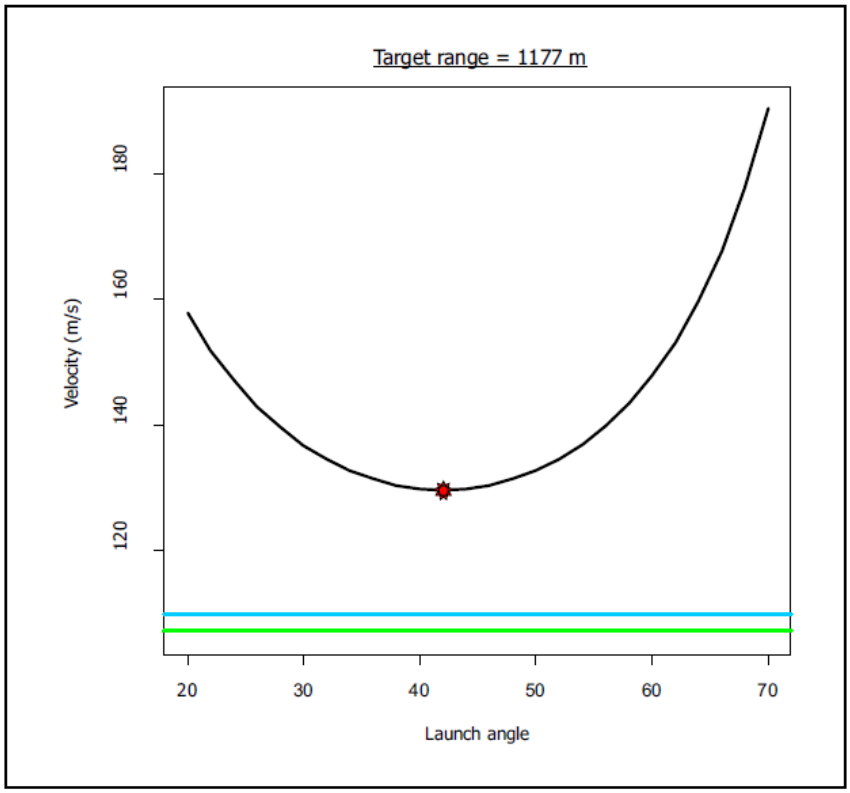

Ejection angles of either 45˚ or 60˚ are commonly used as reference values for volcanic explosions (e.g. Walker *et al.*, 1971; Wilson, 1972; 1980; Steinberg and Steinberg, 1975; Wilson *et al.*, 1978; Self *et al.*, 1980; Steinberg and Lorenz, 1983; Kilgour *et al.*, 2010). In this case, these require muzzle velocities of 130 ms-1 and 148 ms^{-1}, respectively. The theoretical value for the velocity of G2004 explosions, ignoring the effects of aerodynamic drag [4] is 108 ms^{-1}.

$$x_m = \frac{(u_0\text{^}2)(\sin\text{^}2)\theta}{g} \qquad [4]$$

Much of the uncertainty in estimating the muzzle velocity from ballistic blocks is due to the following assumptions: (a) the volume and shape of the block is inferred

from measurements of maximum, medial and minimum length axes, (b) depth of the explosions that expelled the ballistic blocks is assumed to correspond to the vent surface, and (c) the final resting place of the ballistic block represents the full range of its theoretical trajectory. The approximations for drag terms also represent a significant source of error for modal fragment sizes. At a muzzle velocity of 100 ms^{-1}, a fragment with a diameter of approximately 0.5 m, ejected at 45°, achieves a range of 1000 m, in a vacuum. With a drag coefficient of 0.5 (comparable to that experienced by a car moving at speed of >50 $kmhr^{-1}$), that block would only travel 900 m. If the drag coefficient were 2.5 (e.g. for a relatively small, irregularly-shaped, or rough body) the block would achieve a maximum range of only 600 m (Fig. 3.7). Self *et al* (1980) observe that the effect of applying correction for drag to the calculations increases the value for initial velocity by approximately 30%, which is also consistent with our results. The choice of ejection angle actually makes surprisingly little difference to the theoretical trajectory of the fragment. For a fixed range, the difference in computed initial velocity values is less than 20 ms^{-1} for a 15° difference in presumed ejection angle (Fig. 3.7).

Figure 3.7: The effect of drag coefficient on ballistic trajectory at 100m ms^{-1}. Orange line = no drag. C_D = 0.5 - 2.5

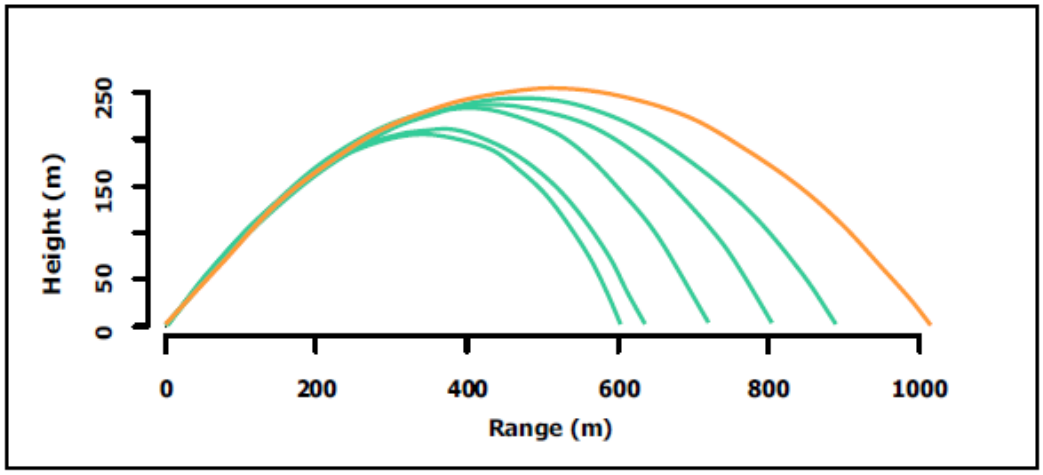

Figure 3.8: Projected trajectories and calculated initial velocities for a block with a hypothetical range of 1177 m, ejected at 45° and 60°, respectively.

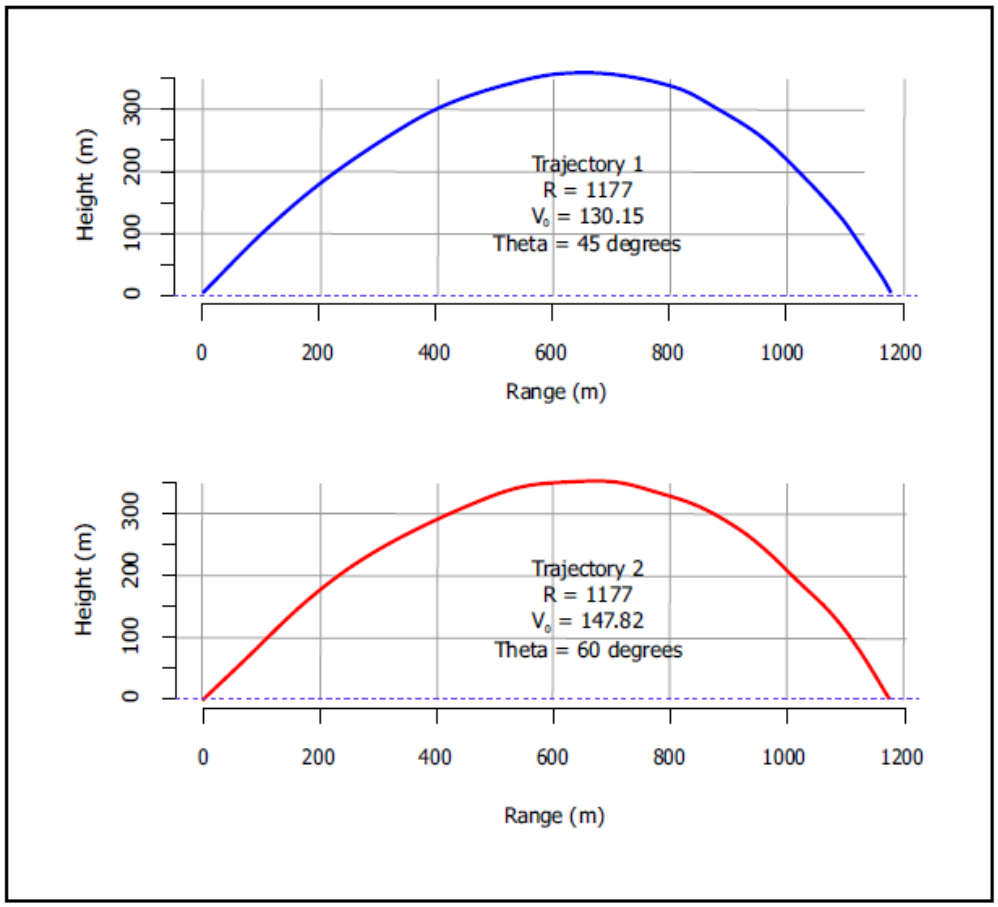

3.5.3 CORRELATION OF ERUPTION UNITS WITH SEISMIC TREMOR AMPLITUDE

The most continuous data record relating to the eruption is that of seismic tremor (Vogfjörd et al. 2005). The parameters that control tremor amplitude are not fully constrained but in many eruptions a correlation has been found between eruption magnitude and tremor magnitude (e.g. McNutt and Nishimura, 2008). Acknowledging that a number of parameters may affect tremor behaviour, I attempt here to correlate the onset of deposition from individual proximal eruption units with spikes in tremor amplitude and corresponding changes in plume altitude. An example would be to correlate a change from a period of sustained combined PDC and fall activity, to a PDC dominated activity with a spike in tremor amplitude and a sudden drop in plume height.

3.6 ERUPTION PARAMETERS

3.6.1 DEPOSIT MASS AND VOLUME

Extensive tephra sampling was undertaken in the summers of 2005 and 2006 on the Vatnajökull glacier and the ice-free region to the north, covering the area of detected tephra fallout (Oddsson, 2007; this study). The tephra blanket in the distal sector was relatively thin (<3 cm) and thus subjected to substantial reworking by ablation, surface runoff and wind in the summer of 2005. However, the proximal to medial sectors of the tephra deposits are situated on the high glacier and thus not affected by these secondary processes induced by the seasonal cycles. However, during this time ice-movement in the proximal to medial sectors induced crevasse formation, which worked to our advantage as it provided perfect profiles through the otherwise undisturbed tephra succession.

The total mass of the deposit is found to be $5.6 \pm 1.0 * 10^{10}$ kg and the measured average bulk density 1190±40 kg/m^3. Seismic refraction measurements show that the tephra pile in the ice cauldron is 70 m thick, containing $2.7 \pm 0.5 * 10^{10}$ kg (Oddson, 2007). The total mass of tephra outside the cauldron (proximal and distal, see below) is $2.9 \pm 0.5 * 10^{10}$ kg. The corresponding volumes are $4.7 \pm 0.8 * 107$ m^3 for the total

deposit, 2.3 ± 0.4 * 10^7 m^3 for the tephra within the ice cauldron and 2.4 ± 0.4 * 10^7 m^3 for the proximal and distal tephra. All values are given as DRE. In this work, I subdivide the tephra into individual units, determine the volume of each and estimate the magma flow rates for individual units and phases (Table 3.4).

Table 3.4: Key eruption parameters for individual units, and the whole deposit.

Unit	Volume (10^6 m^3)	DRE. Volume (10^6 m^3)	Mass (10^9 kg)	Proportion of proximal	Proportion of subaerial	$t_{1/2}$ (m)	Cauldron Mass (10^9 kg)	Distal mass (10^9 kg)	Total mass (10^9 kg)
Subglacial							0.6 ± 0.2	0	0.6 ± 0.2
A	0.59 ± 0.10	0.26 ± 0.03	0.71± 0.09	3.7%	2.4%	490 m		0	
B	1.47 ± 0.17	0.64 ± 0.07	1.76± 0.21	9.4%	6.1%	490 m	4.4 ± 0.8	0	6.9 ± 1.1
C						1.52 km (Avg.)			
						520 m (Prox.)		5.8 ±	
	7.59 ± 0.91	3.31 ± 0.37	9.11± 1.10	47.8%	54.4%	4.5 km (Distal)	17.5 ± 3.0	2.0	32.4 ± 6.1
D	0.88 ± 0.11	0.38 ± 0.04	1.06± 0.13	5.6%	3.7%	290 m	1.0 ± 0.3	0	2.1 ± 0.4
						1.63 km (Avg.)			
						190 m (Prox.)			
						5.96 km		4.2 ±	
E	3.73 ± 0.45	1.63 ± 0.19	4.48± 0.54	23.6%	26.8%	(Distal)	3.5 ± 0.7	1.0	12.2 ± 2.2
F	0.52 ± 0.06	0.23 ± 0.03	0.62±0.11	3.2%	2.1%	190 m	0	0	0.6 ± 0.1
G	1.08 ± 0.13	0.47 ± 0.06	1.30± 0.26	6.9%	4.5%	400 m	0	0	1.3 ± 0.3
Sum of Units (prox.)	1.59 (± 0.19) x 10^7	6.92 (± 0.79) x 10^6	1.90 (± 0.23) x 10^{10}						
Total (Cauldron)	2.3 (± 0.4) x 10^7	1.0 (± 0.2) x 10^7	2.7 (± 0.5) x 10^{10}						48%
Total (Proximal)	1.6 (± 0.2) x 10^7	0.7 (± 0.1) x 10^7	1.9 (± 0.2) x 10^{10}						34%
Total (Distal)	0.8 (± 02) x 10^7	0.4 (± 0.1) x 10^7	1.0 (± 0.3) x 10^{10}						18%
TOTAL	4.7 (± 0.8) x 107	2.1 (± 0.4) x 107	5.6 (± 1.0) x 10^{10}			650 m			

3.6.2 ICE CAULDRON DEVELOPMENT

The development of an ice cauldron was an important part of the eruption since it contains about 50% of the erupted material and its formation accounts for about one third of the total thermal energy released (Gudmundsson *et al.*, 2009). Estimates of its dimensions were made from aerial and ground photos on November 2nd and later in the eruption.

Visual observations of the cauldron at 10:24 and at around 16:00 on November 2nd and later on (e.g. from the ground on November 4th and the air on November 7th) allow its approximate size to be estimated. At 10:24 on November 2nd the length of the cauldron was close to 650 m and the maximum width was around 400 m. At 16:00 it was approximately 700 m long and 500 m wide. The values found on November 7th were 750 m and 550 m, respectively. Assuming that the cauldron was elliptical, these numbers indicate that at 10:24 on November 2nd the cauldron had already reached 63% of its final size and 85% by 16:00. It is likely that by the end of the main activity on November 3rd, the cauldron had reached a size very close to that of November 7th. These numbers can be translated into filling rates, assuming that a 70 m thick pile of pyroclasts accumulated in a cauldron with vertical or subvertical ice walls, i.e. at 10:24 on November 2nd, 63% of the cauldron fill had been formed, 85% at 16:00 and almost 100% by the afternoon of November 3rd. Using a density of 1190 kg m^{-3} for the cauldron fill, a total fill of mass 2.7×10^{10} kg and DRE density of 2750 kg m^{-3}, the filling rates (ms^{-3}) can be calculated and are shown in Fig. 3.9. Two simplified models are shown, both assuming a linearly declining filling rate with time. One model assumes a cauldron filling time of 45 hours (the total duration of identified phases to the north of the vents – see below) and the other only 36 hours (corresponding roughly with the duration of a high eruption plume). The shorter formation time fits better to the observational data and is therefore used to determine the contribution of each unit to filling the ice cauldron (Fig. 3.9).

Figure 3.9: Calculated filling rate of the ice cauldron using a density of 1190 kg m-3 for the cauldron fill, a total fill of mass 2.7x1010 kg, a bulk density of 1190 kg m-3 and DRE density of 2750 kg m-3. Two simplified models are shown, both assuming a linearly declining filling rate with time. The dashed line assumes a cauldron filling time of 45 hours (the total duration of identified phases to the north of the vents), while the solid line assumes 36 hours (the duration of high eruption plume). The curve generated by applying the shorter duration provides a better fit to observations of cauldron size over time.

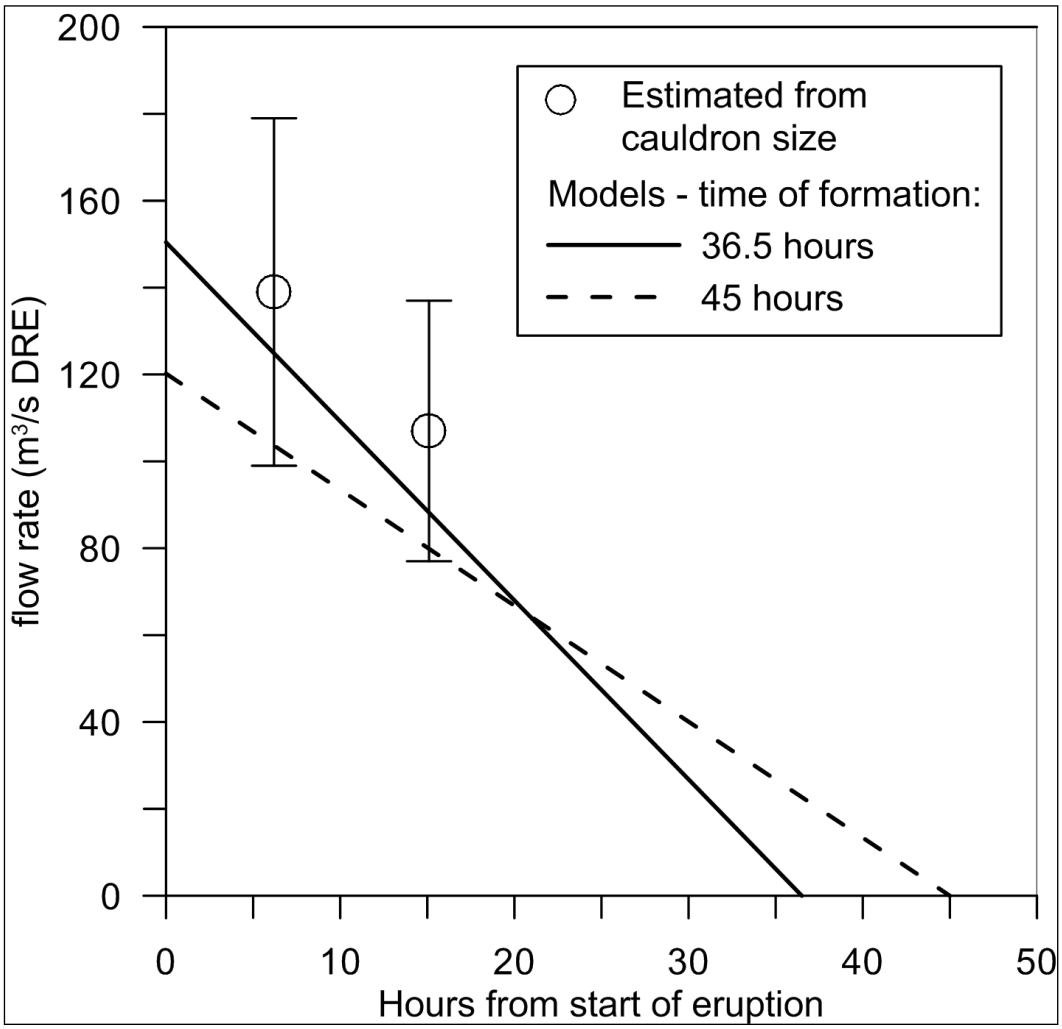

3.6.3 MUZZLE VELOCITY

Within the 2004 deposit, three non-juvenile blocks types have been identified, of which the first category dominates: (1) pristine, non-vesicular crystalline lava; (2) moderately vesicular crystalline lava (no juvenile bombs included); (3) hydrothermally altered, or unaltered, consolidated tuff. The maximum observed range for large blocks within the G2004 deposit was 1180 m from the vent. Over the course of the study (i.e. June 2005-August 2008) GPS locations of key sections and large, distinctive non-juveniles were re-recorded during each field campaign in order to verify that they had not moved due to slumping, sliding, or the movement of the underlying glacier. Recorded locations on each occasion, for each feature, fell within the margins of error for handheld GPS (i.e. 5 m). These measurements confirm that the recorded ranges for large blocks reflect the original rest positions. The dimensions of the largest block identified at this location were 107 x 70 x 53 cm. The application of our ballistic model yields the minimum velocity threshold required for a block of this size to achieve the observed range. It is assumed that there is no change in ground elevation along the flight path. This is a fair approximation since material was deposited over an essentially flat ice surface. Our results show that the G2004 phreatomagmatic explosions resulted in the expulsion of non-juvenile material at velocities of >130 ms^{-1} and that this minimum value is achieved supposing a 42° ejection angle and assuming that, at the time of impact, the block had travelled the entire length of its theoretical trajectory. Ejection angles of either 45° or 60° are commonly used as reference values for volcanic explosions (e.g. Walker *et al*., 1971; Steinberg and Steinberg, 1975; Wilson and Walker, 1987; Self *et al*., 1980; Steinberg and Lorenz, 1983; Kilgour *et al*., 2010). In this case, muzzle velocities are 130 ms^{-1} (45°) and 148 ms^{-1} (60°). The theoretical value for the velocity of G2004 explosions ignoring the effects of aerodynamic drag is 107 ms^{-1}.

3.6.4 PROXIMAL, MEDIAL AND DISTAL REGIONS - DEFINITIONS

The main tephra deposit trends north to north-northeast across the glacier as a result of southerly winds during the eruption. At a distance of 50 km from the eruption site, near the north edge of Vatnajökull, the layer is 30 km wide. The delineation of proximal, medial and distal areas within the deposit is based on the thinning-distance curve generated from the total thickness isopach map (Fig. 3.10A). This simple downwind profile shows that the dominant emplacement mechanism changes with distance from the vent. A clear inflection point is observed at 4.0 km, delineating the distal and medial regions of the deposit. Another occurs at between 1.9 and 2.4 km from source. On either side of these inflection points, the curve is defined by different exponential trends, which form four or more straight line segments on a semi-log thickness distance plot (Fig. 3.10B). Field observations show that the pyroclastic density currents (PDCs) did not extend beyond about 2.3 km run-out distance. Due to over-thickening in the vent area, syn-eruptive remobilisation of tephra and rising lake levels, the area representing the ice cauldron has been removed from the curve.

Figure 3.10: (A) Deposit thinning profile generated from the total thickness isopach map. The deposit is partitioned into proximal, medial and distal regions according to the location of inflection points in the distance-thickness curve. Due to over-thickening in the vent area, syn-eruptive remobilisation of tephra, and rising lake levels, the area representing the ice cauldron has been removed from the curve. A line of best fit for an exponential thinning trend is represented by a blue line and that of the best fit power law trend by a green line. In this case, the power law thinning trend provides the better fit to the deposit profile as also indicated by an R2 value closer to 1. (B) The deposit thinning curve may be defined by changing exponential trends, which form four or more straight line segments on a semi-log thickness-distance plot. Equations of best fit and their corresponding R2 values (indicating goodness of fit) for each segment are displayed at the right.

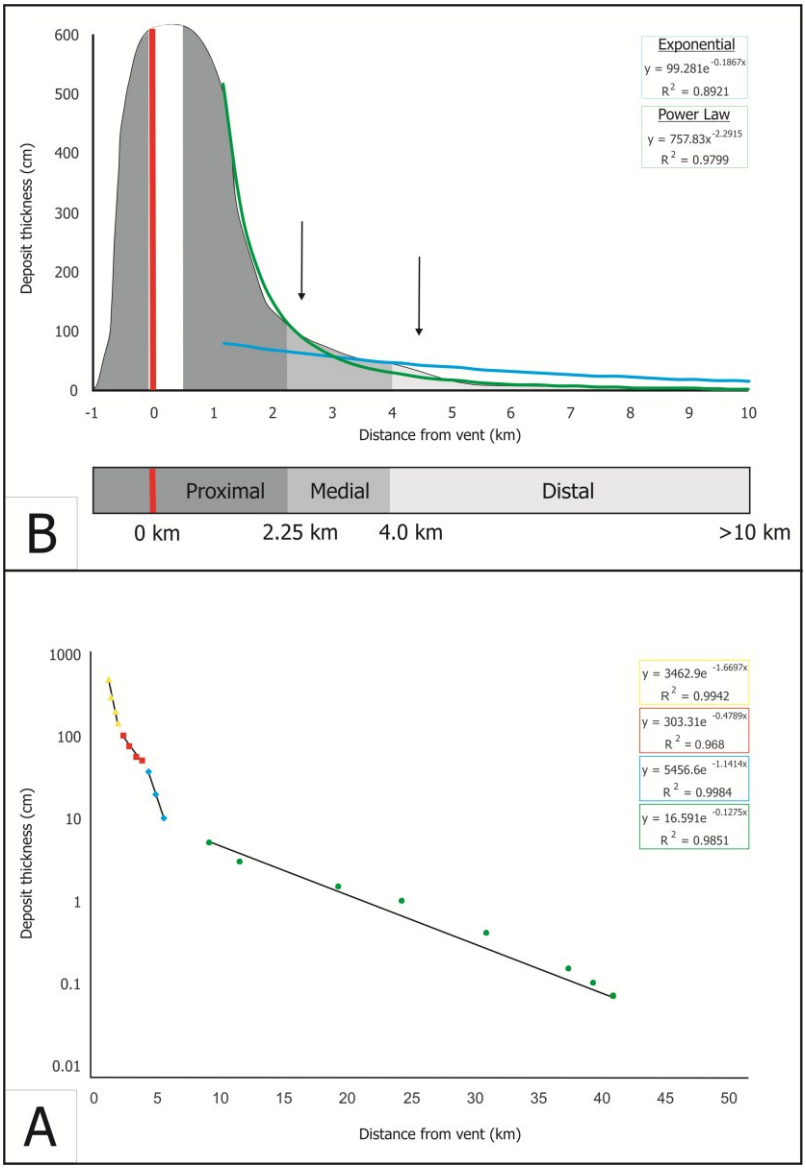

3.7 PROXIMAL-MEDIAL TEPHRA STRATIGRAPHY

A summary of the defined phases of activity and associated unit divisions is presented in Table 3.5. Detailed logging and stratigraphic correlation of 59 vertical sections through the proximal tephra succession to the north of the craters reveals that it consists of a distinctly bedded sequence representing three separate phases of activity. Seven units, labelled A-G on Figs. 3.7 and 3.8, are identified within the proximal to medial sector of the 2004 deposit. Units A and B originated from the eastern vent and were deposited during the initial phase of the eruption, while the second phase was a period of sustained deposition (i.e. units C and E) punctuated by one major short-lived eruptive event (Unit D) and terminated by another (Unit F). At the start of this main phase, both vents were active. However, after the partial column collapse which generated Unit D activity was re-established from the western vent only. The last phase to be deposited to the north of the vents was one of waning activity, during which only one unit (Unit G) was deposited. The latest phase of activity is considered to have issued from the eastern vent. Although minor fallout of tephra occurred to the east and south after November 3rd, the deposits from this late activity form only a very thin (of order 1 mm) layer. They represent only a fraction of a percent of the total deposit and are not considered further here.

Although the terms "pumice" and "scoria" are popularly used to refer to vesicular fragments of felsic and mafic composition respectively, in this manuscript I follow the conventions of Heiken and Wohletz (1985) who use the terms "pumice" and "scoria" to denote textural features of the rock independent of classification by mineralogy or chemistry. According to this nomenclature "pumice" has a lower specific gravity than water (i.e. it floats) because of its higher abundance of small vesicles and thin bubble walls. "Scoria" on the other hand has a higher specific gravity than water (i.e. sinks) and generally contains fewer, larger bubbles with thicker vesicle walls. As a consequence of the transparency of its vesicle walls, pumice of the same composition will generally appear lighter in colour than its scoriacious equivalent. I refer to clasts with > 60 vol. % vesicles as pumice, while clasts in the range of 20-60 vol. % void space are called scoria. Similarly, I

refer to transparent light brown to brown basaltic glass as sideromelane, whereas tachylite is dark brown to black, opaque and in the G2004 deposit contains >10 % micro- or crypto-crystals.

It is also worthwhile to mention here the degree to which the tephra layer has been preserved on the glacier in the months and years following the eruption. Aeolian and water erosion is largely absent at the surface of the accumulation areas of glaciers, allowing for accurate sampling and mapping of tephra layers until they are buried by subsequent snowfall. Eventually, ice flow transports the tephra from the accumulation areas to ablation areas leading to gradual removal of the tephra layer. In Iceland this occurs on a time scale of 100-1000 years (Larsen *et al*. 1998) while in colder, larger and less dynamic glaciers it may be much longer.

Table 3.5: A table linking the key features and interpretations of each depositional unit to the corresponding G2004 eruption phases.

Unit	Dispersal	Key Features and Interpretation	Eruption Phase
A	Extensive. Issued from the E vent, directed N.	Extended fall. Dense, blocky, exclusively juvenile material.	1
B	Issued from the E vent, dispersed in all directions. Irregular outline due to lobe-by-lobe emplacement.	Wet PDCs. Dense, blocky, exclusively juvenile material.	1
C	Extensive, directed N to NNE. Both vents active.	Combined fall and PDC activity. Abundant, distinctive pumice “lenses” and “trains”.	2
D	Issued from both vents, consists of two distinct lobes – one directed to the NNW and one to NE.	Finely laminated, dilute PDCs. Pinch-and-swell morphology. Varying proportions of dense, blocky material and disintegrated pumice. Some non-juveniles.	2
E	Issued from the W vent, directed N. Similar in geometry to Unit C, but more narrowly confined lateral extent.	Combined fall and PDC activity. Higher proportion of pumice ”trains” relative to “lenses” than in Unit C.	2
F	Issued from the W. vent, directed E. Confined to the proximal area.	Directed partial column collapse event. Poorly sorted, non-juvenile-rich, fines abundant.	2
G	Consists of two lobes. May issue from both vents, with eventually only the E. vent continuing to be active towards the end of the eruption.	Pumice-rich, wet, PDCs. Fines abundant. Armoured clasts and accretionary lapilli.	3

3.8 UNIT DESCRIPTIONS AND INTERPRETATION

UNIT A

DESCRIPTION

Unit A is relatively widespread (Fig. 3.11) and is found in every location in which the basal contact of the tephra with the ice is exposed. The Unit A isopachs extend into the medial region of the deposit, while the dispersal axis trends directly northwards and its trace intersects the eastern vent on the 2004 fissure.

In the downwind direction Unit A has a maximum measured thickness of 50 cm at 480 m from source, steadily thinning to <1 cm within 3.5 km of the vent (Fig. 3.13) as it uniformly drapes the ice surface. In the eastern (cross-wind) dispersal area, Unit A is 40 cm thick in the most proximal sections, thinning to less than 0.5 cm 2 km further to the east. The deposit forms two straight-line segments on the semi-log dispersal diagram (Fig. 3.14), whereby the distal segment (2.5 to 3.5 km from source) is steeper than the proximal segment. The average $t_{1/2}$ over this interval is 490 m.

Unit A stands out among the G2004 tephra units because it is massive and jet black in colour, consisting entirely of poorly vesicular, occasionally tachylitic, blocky, juvenile material. Non-juveniles and highly vesicular fragments are entirely absent. Close to the vent, Unit A clasts range from fine ash to fine lapilli (Fig. 3.15), with a median of coarse ash sized fragments (Md_Φ = 0.80). The median grain-size decreases to medium ash (Md_Φ = 1.10) beyond a distance of 1.2 km from source. This layer is poorly sorted overall (σ_Φ = 2.35). In almost all cases it is accompanied by a very thin (millimetre to sub-millimetre) continuous layer of tan brown, very fine ash at the ice contact (Fig. 3.16A). Close to the vent, Unit A is also capped by a very fine, tan coloured ash layer.

UNIT B

DESCRIPTION

Unit B issued from the eastern vent and was dispersed primarily towards the north and north-east. The deposit has an irregular outline and features a series of at least four radial lobes with dispersal axis orientations ranging from north-northwest to east-northeast (Fig. 3.11). Individual lobes have maximum run-out distances of approximately 3.5 km and are thus largely confined to proximal regions.

Although Unit B shows minor inconsistencies in lateral thicknesses when plotted on a dispersal diagram, features such as localised over-thickening and pinch and swell morphology are not evident on the outcrop scale. Within the proximal area, the $t_{1/2}$ value of Unit B is identical to that of Unit A (490 m).

Units A and B are remarkably similar in composition and in terms of clast morphology, but differ vastly in terms of structure and internal fabric (Fig. 3.16A, B). Unit B is cross-bedded, consisting of a minimum of five, 3.5-5 cm thick, reverse-graded sets (from 0.5 Φ at the bottom to -1 Φ at the top), which are capped by laminae of fine ash (Md_{Φ} = 2.5-3). The thickness of fine laminae increases slightly towards the top of the deposit (from 1 mm near bottom to 3 mm at top). Representative dimensions of the coarser cross-beds are 56cm long x 3cm thick, while medium ash layers are 3.5 to 5 cm thick and alternate with the coarse layers. The median grain-size of the entire unit is 1.3 Φ. Within sets Unit B appears moderately to well sorted, however the calculated bulk sorting parameter (σ_{Φ} = 2.40) reveals that it is actually rather poorly sorted overall (Fig. 3.15). Unit B is distinctively black in colour, although the finer layers appear grey. Components are identical to Unit A beneath – homogenous, poorly vesicular, blocky tachylite to sideromelane fragments devoid of non-juveniles, free crystals and pumice shards.

Figure 3.11: Total deposit (modified from Oddsson (2007)) and unit isopach maps. Units A, B, D, F, and G are largely confined to the proximal dispersal region, while Units C and E extend to the glacier limits and account for distal tephra fall. The dispersal axes of fFall-dominated units (C and E) appear to be controlled by the moderate southerly winds acting throughout the eruption, while the PDC lobes are distributed according to geometric factors such as the vent of origin and regions of localised jet instability in the eruption column. Tephra dispersal was also confined by the presence of the 300 m high caldera wall directly to the south of the cauldron. Measured sample locations are indicated by red dots in the first panel.

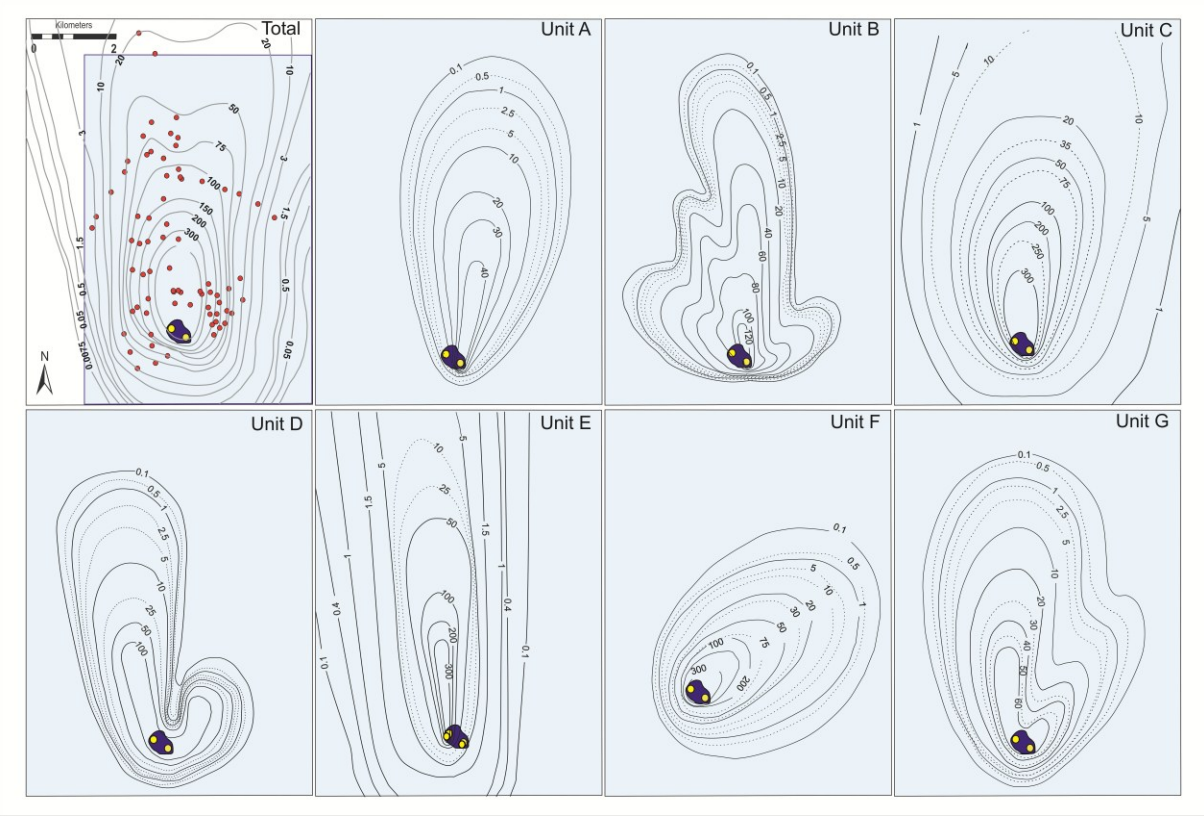

INTERPRETATION OF UNIT A AND B DEPOSITS

Units A and B together represent the first sub-aerial phase of deposition and their similarity in terms of components and dispersal as well as close stratigraphic association indicates a common origin. The consistent dispersal pattern of Unit A, its uniformly decreasing thickness and absence of internal structure indicate that it is a fall deposit. On a plot of median diameter vs. sorting (Fig. 3.15) Unit A samples fall just outside of the sorting field defined by Walker and Croasdale (1972) for fall deposits. This is likely to be a consequence partly of the phreatomagmatic origin of this unit and also of the unusually close proximity of sampling to the vent as all the other characteristics of this unit point to a fall origin. The low $t_{1/2}$ value is consistent with dispersal by moderately explosive activity and thickness data are more consistent with a linear, rather than exponential, thinning trend. By contrast, Unit B has a highly irregular outline forming distinct lobes within the deposit, which reflect emplacement along variable dispersal axes. A simple downwind profile of the Unit B deposit exhibits a hummocky pattern (Fig. 3.13). Areas of localised over-thickening and pinch and swell morphology, characteristic of dilute (low-concentration) PDCs, are evident from this plot. This, coupled with the internal characteristics (inverse grading and finely bedded cross-stratification), indicates emplacement by dilute and closely spaced PDC pulses. The increasing thickness of fine ash partings higher in the stratigraphy is consistent with decreased frequency of PDC pulses at the close of the first phase of subaerial activity.

A key feature of these two units is their exceptionally low vesicularity compared to the rest of the deposit, which may indicate that the magma which produced them was outgassed prior to fragmentation. The fact that Unit A is massive and always precedes its accompanying PDC (Unit B) is a strong indication of fallout from a single phreatomagmatic explosion. Furthermore, the identical $t_{1/2}$ values indicate that the two units were of similar intensity. The smaller volume of Unit A (3.7% of the proximal part of deposit) compared to that of Unit B (9.4 %) thus implies that Unit A was of shorter duration than Unit B (Sable *et al.*, 2006). Tephra fall would have been continuous and heavy, but of short duration, associated with the opening of the ice cauldron on the evening of November 1st.

The average sulphur content of the groundmass hovers around 800 ppm for all units (except the pumice, for which it is 688 ppm), which implies that the degree of degassing (using 1670 ppm as representative value for undegassed melt inclusions) is in the range of 50-53 % for all units, on average (Table 3.6). The data therefore shows that there is no significant difference in the degassing of units A and B compared to later units (Fig. 3.17) and also that the melt represented by the ash fraction was only partly degassed at the point of disintegration. However, units A and B are the only ones that are dominated by partially degassed clasts of low to very low vesicularity - the rest is formed by disintegration of moderately to highly vesicular magma. This implies that the initial batch that rose to the surface lost its vesicles before being disintegrated. The most logical explanation is that the gas existed as a separate phase which rose ahead of the magma.

Figure 3.12: Representative stratigraphy of the G2004 deposit at locality TT01. Typical unit thicknesses, grain-size characteristics, average glass composition, and average deposit density are shown for this location which is approximately 550 m north-east of the vent.

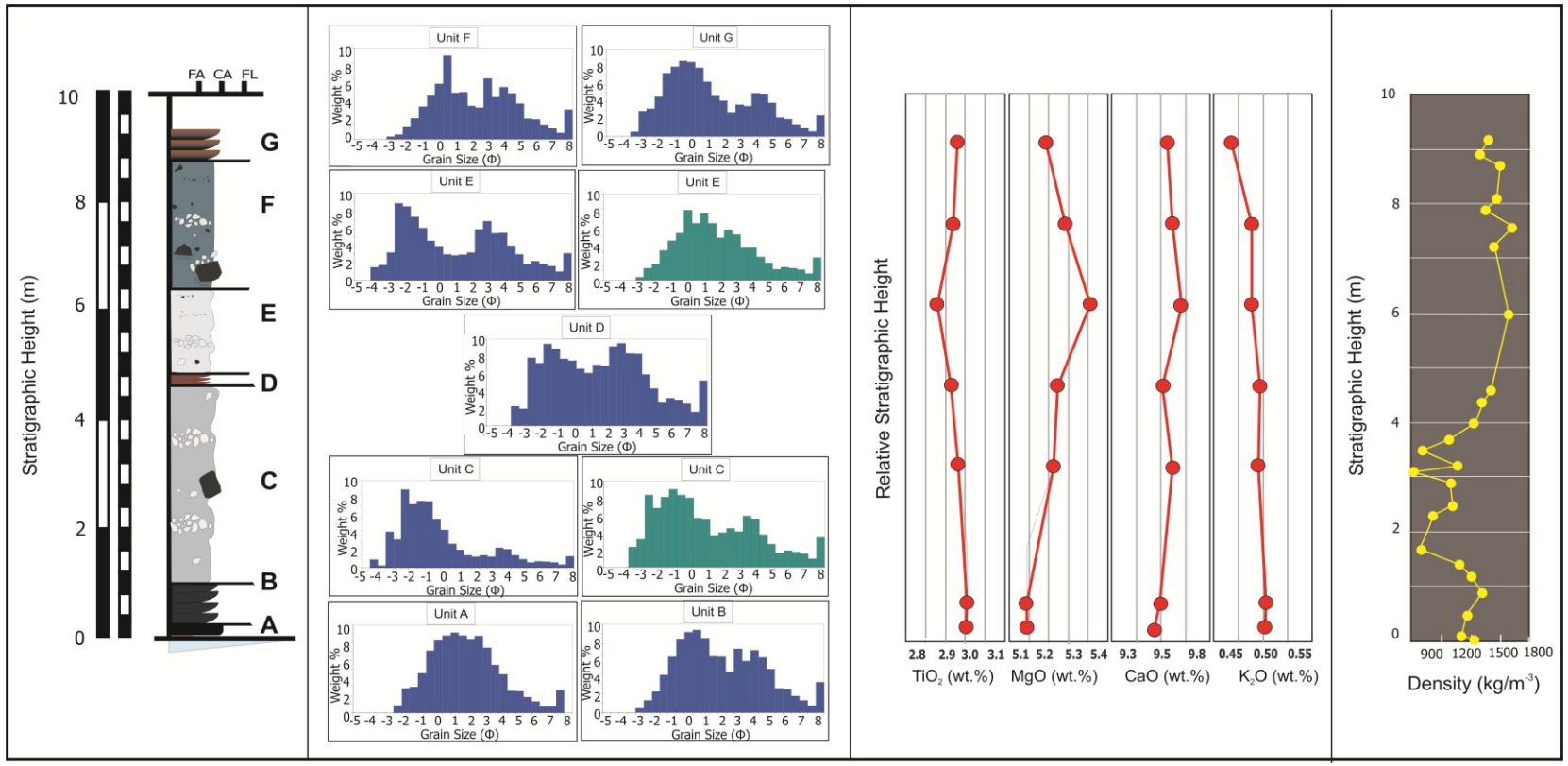

Table 3.6: Average glass compositions (electron microprobe) for individual units and a representative melt inclusion. N = number of analyses

	SiO_2	TiO_2	Al_2O_3	FeO	MnO	MgO	CaO	Na_2O	K_2O	P_2O_5	S (ppm)	Cl (ppm)	% S loss	n
Unit A	50.01	3.00	13.11	14.01	0.24	5.09	9.43	2.90	0.50	0.34	837	182	50	26
Unit B	50.08	3.01	13.06	13.79	0.23	5.09	9.49	2.91	0.51	0.35	831	180	50	72
Unit C	50.00	2.97	13.16	13.73	0.31	5.23	9.62	2.91	0.49	0.33	780	175	53	121
Unit D	50.20	2.93	13.24	13.64	0.23	5.25	9.52	2.96	0.49	0.33	802	181	52	29
Unit E	49.97	2.86	13.21	13.50	0.23	5.41	9.71	2.90	0.48	0.32	818	177	51	69
Unit F	50.05	2.94	13.29	13.62	0.23	5.28	9.62	2.86	0.48	0.32	842	171	50	32
Unit G	49.63	2.96	13.04	13.78	0.23	5.19	9.57	2.90	0.44	0.33	823	174	51	34
Pumice Lens	50.27	3.20	12.88	14.35	0.24	4.84	9.28	2.94	0.54	0.35	688	188	59	43
Melt Inclusion	48.49	4.22	10.39	19.51	0.29	3.83	7.90	2.53	0.81	0.61	1670	438	-	14

Figure 3.13: Median diameter vs. sorting characteristics of grain-size samples from each depositional unit compared to observed fields for known end-member pyroclastic fall, flow, and surge deposits after Walker and Croasdale (1972).

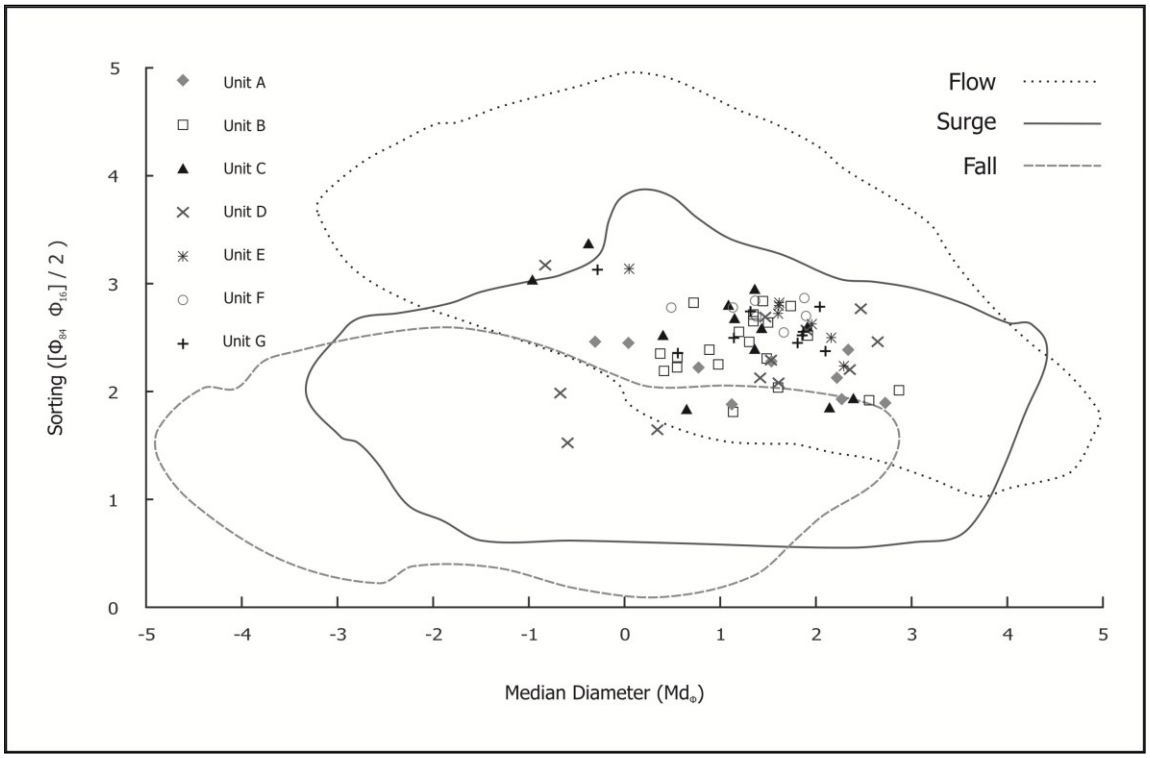

Figure 3.14: Simple downwind thinning profiles by unit.

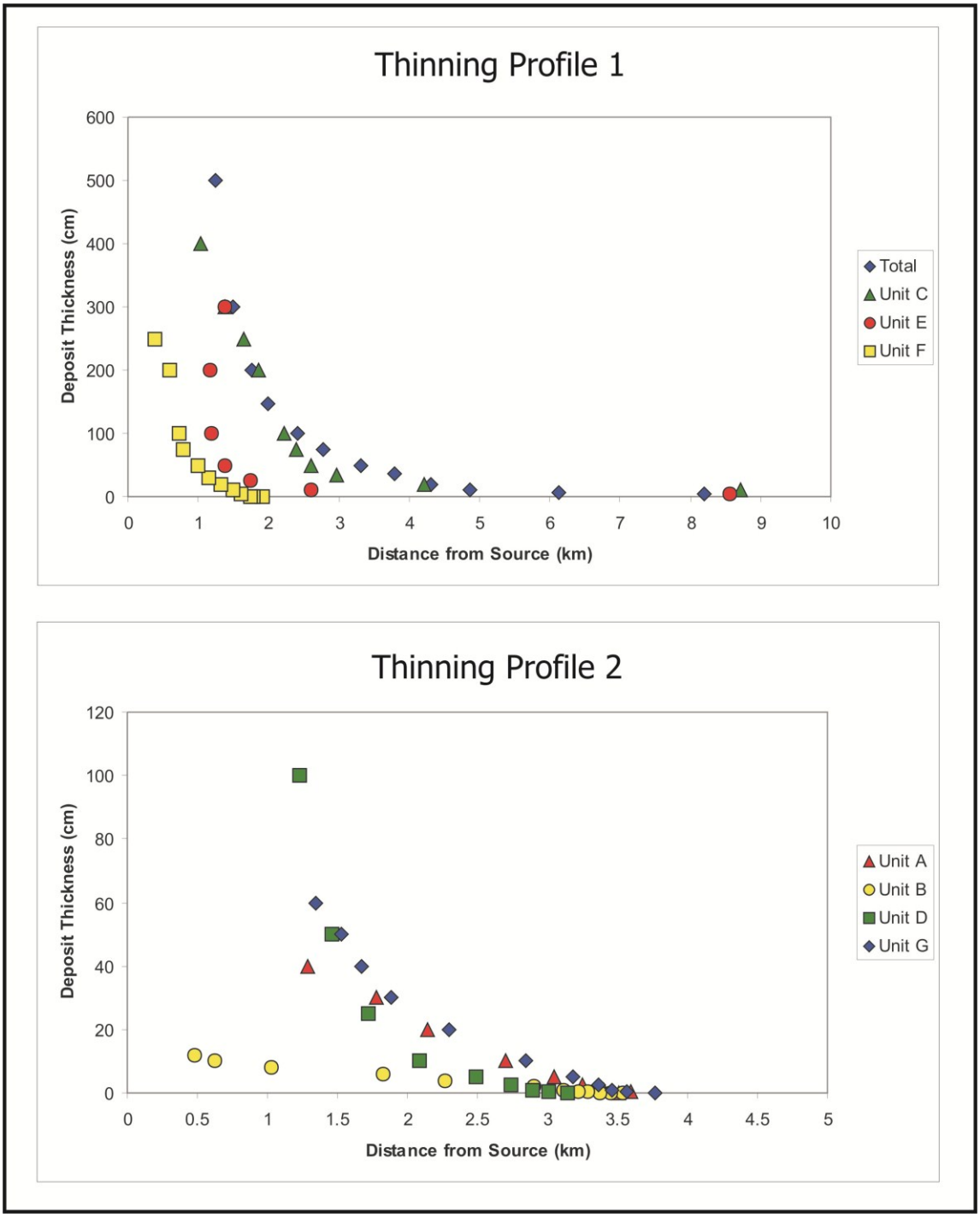

Figure 3.15: Thickness vs. square root of area by unit (after Pyle 1989).

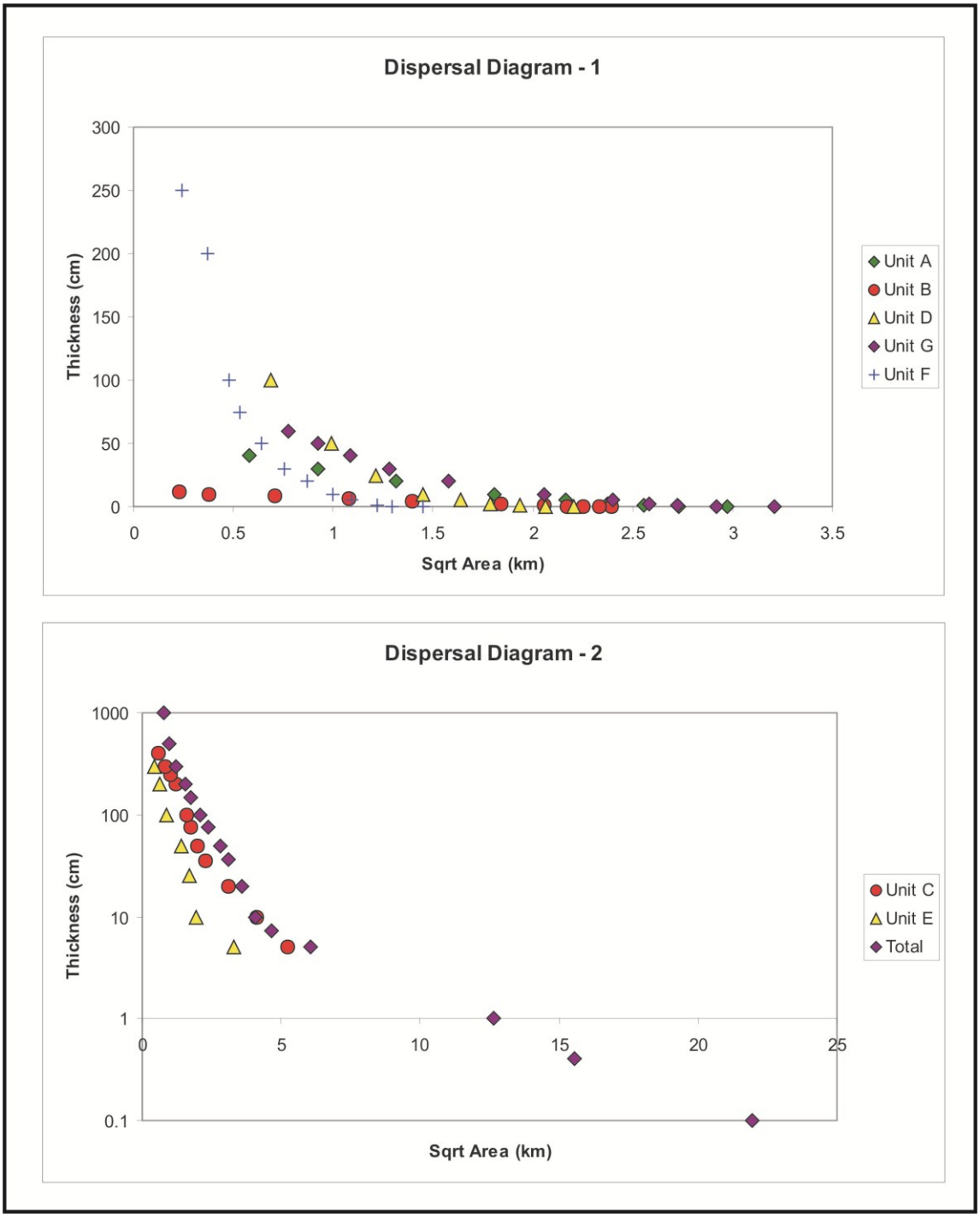

UNIT C

DESCRIPTION

Unit C is the most widespread eruption unit (Fig. 3.11), deposited during the main phase of the eruption and accounting for over half the total subaerial deposit (48% of proximal, two thirds of distal). It is present in every section of the principal dispersal areas, while its eastern margin has been traced by field observations. The isopachs constructed from field data agree with visual observations on the afternoon of November 2nd indicating that the eastern and western vents were simultaneously active when this unit was deposited. It is inferred that tephra deposited in the distal regions of the deposit are temporally correlated to Unit C.

Unit C is up to 5 m thick in proximal sections and lateral thickness measurements are quite consistent. There is an inflection point in the thinning profile for this unit at 3 km from source (Fig. 3.14). Around this mark, the average $t_{1/2}$ value changes from 520 m to 4.5 km. This change in thinning rate occurs in a region comparable to the run-out distance of associated PDCs.

Unit C features several repeated packages displaying indistinct discordant bedding, highlighted by numerous single-clast thick pumice trains. These packages are relatively poorly sorted, but are diffusely layered on a decimetre scale. Certain horizons within the unit exhibit reverse-grading and display more distinct patterns of alternating dominantly coarse and dominantly fine layers. However, these occur on a sporadic basis. Indistinctly cross-bedded structures are highlighted by the occurrence of single-clast thick, attenuated or discontinuous horizons of broken and slightly abraded fine to medium lapilli pumice clasts, which I refer to as “pumice trains”. The crudely layered regions of this deposit lack distinct fine ash partings. The pumice lapilli clasts found in lenses usually are between 60–80% vesicularity and are equant with glassy, quenched rinds and commonly cracked outer surfaces. Vesicle size generally increases closer to the centre of the clast. These are extremely fragile and often crumble along hydrofracture surfaces when handled. These are dominantly in the medium to coarse lapilli size interval but range up to 10 cm in diameter. By contrast, the trains tend to contain fragments of such pumice clasts, which are sub-angular, partially abraded and do not have continuous quenched surfaces.

The most distinctive feature of Unit C is the presence of numerous pumice lenses (Fig. 3.16C) which are variably continuous over tens to hundreds of centimetres, with maximum thicknesses of 30 cm. Outstanding features of the pumice lenses are that: (a) they are fines-poor pumice lapilli deposits within a clast-supported framework, (b) they consist primarily of intact (complete and unbroken) basalt pumice clasts (clots or bombs), which due to their extremely delicate nature could not have survived intact within a turbulent density current, (c) the lenses have a flat based geometry with truncated tops and sides, suggesting that they have been subjected to erosion by laterally moving currents, (d) they are massive or normally graded and (e) maximum clast size decreases with distance from source. In many cases, pumice trains are formed in association with (above or in front of) the pumice lenses.

The grain-size distribution of Unit C contains a number of sub-populations of grain-size modes. These include (i) pumice clasts in the -4 Φ to -5 Φ fractions, which are largely confined to pumice lenses and trains; (ii) moderately vesicular (50-70 %) clasts in the -2 to -1 Φ fractions, which are concentrated in "coarse" sets where cross-layering is evident; and (iii) a bulk matrix of fine ash (> 2.5 Φ).

The fine fraction (<1 mm) within individual flow packages consists largely of bubble wall shards produced by disintegration of vesicular magma (Fig. 3.18). This size fraction can contain up to 30 % dense (<40 % vesicularity) material and < 1 % of non-juvenile fragments. Again, free crystals are virtually non-existent. Angular and abraded pumice fragments also make up >90 % of the lapilli size fractions in the bulk deposit, with the remainder consisting of a mixture of non-juveniles and dense juvenile material.

INTERPRETATION

The indistinct bedding and poor sorting of Unit C, along with reverse-grading in places, suggests deposition from a relatively dense, particle-rich gravity current. The lack of fine ash partings and total inundation of the study area by this unit indicate sustained deposition that lasted for many hours. The fact that many pumice lapilli are hydrofractured and possibly cracked by impact, yet remain coherent until handled supports an interpretation of deposition by fall. It stands to reason that the pieces would

have been unlikely to stay together had they been transported within a laterally moving current (consider the-shell of a boiled egg that is cracked when dropped on the ground compared to one that is cracked on the ground and then pushed along – the latter would become disaggregated, whereas the former would not so much). Indeed, the pumice lapilli in lenses are not abraded as one would expect from such delicate clasts had they been transported any considerable distance by traction or had experienced significant grain-to-grain collisions. Besides, the textural features of the beds support a fall origin even without this deductive reasoning: Pumice lenses stand out from the background features of Unit C. The morphology (flat bases, truncated tops and sides and attenuated clasts) and internal characteristics (massive to normal-graded, clast supported, fines-poor, clasts with quenched rinds) of the pumice lenses, along with their context within the deposit are clearly inconsistent with transport dominated by lateral flow and so these are interpreted as remnants of concurrent pumice lapilli fall layers which have been modified to a degree by erosion by subsequent PDC pulses.

Calder *et al*. (2000) interpret pumice-rich horizons within the 1993 Lascar volcano, Chile ignimbrite as low-density segregations within a concentrated flow, which detached and moved to the margins and distal parts of the flow. This interpretation is supported by reverse grading within pumice horizons and a strong negative correlation between maximum pumice and maximum non-juvenile size with distance from the vent. However, in the G2004 deposit the evidence for pumice occurring as low-density segregations within a stratified flow does not hold. In fact, evidence to the reverse is indicated: pumice horizons are massive or normally graded, maximum pumice size decreases with distance from vent and there is no relationship to the dispersal characteristics of the non-juveniles, all of which lend support to our interpretation of pumice-rich horizons within the G2004 deposit as intercalated fall layers. What is more, in several well-known studies of emergent tuff cone deposits similar deposits are also described which are interpreted to have developed as a result of hybrid fall and flow processes. Cole *et al*. (2001) describe lapilli horizons of regular thickness and widespread dispersal indicative of dominance by a fall signature. In this case beds are defined by coarse clast rich lenses which are up to 4 cm thick and 10-150 cm long. In earlier work, Sohn and Chough (1989) describe well-sorted lapilli tuff facies which are clast-supported and fines depleted and maintain thickness

down-current in the Suwolbong tuff ring. These are interpreted as a "dry" phreatomagmatic fall deposit interspersed with stratified tuff units which are interpreted to result from tractional flow, as they occasionally develop cross-beds down current. This provides evidence for concurrent, or at least rapidly alternating, deposition by both fall and flow in well-established tuff cone sequences. Chough and Sohn (1990) also describe proximal to distal facies variations of Songaksan - an emergent tuff ring on the Cheju Island, Korea. They show that near vent dilute PDCs are turbulent, dense and highly mixed, producing scour-fill bedded tuff. At some distance from the vent, as capacity decreases, it may become density stratified forming graded deposits. Eventually the flow may undergo dilution as a result of loss of sediment load and mixing with ambient air, which produces stratified and dune bedded deposits. According to this model it is unlikely that the extremely proximal units described here would have yet undergone extensive density stratification to produce the pumice lenses.

The changes in thinning rate within the proximal area can be attributed to variability in run-out distances and dispersal axes of PDC pulses and their variable contribution to the deposit at a given location. Within the medial to distal regions of the deposit the curve progressively shallows. The inflection point at 3.5 km for unit C is consistent with a shift in the depositional regime. The dominant emplacement mechanism for this unit changes from PDC to pyroclastic fall, at or beyond the 2.5-3.5 km mark, which accounts for the transition from a low/moderate to a widespread dispersal pattern. I therefore interpret Unit C to have formed by a process of progressive aggradation from multiple, closely-spaced PDCs, along with contemporaneous intermittent or shower-like pumice lapilli fallout. Visual observations of episodic showers from the plume at the same time as persistent ground-hugging density currents by observers during Unit C deposition also lend support to this argument.

Figure 3.16: Deposit photo panel. (A) Units A and B (boundary with Unit C marked by brown line). Note that Unit A is black and massive, while Unit B is lighter in colour and bedding is highlighted by light brown fine ash horizons; (B) Units B, C, and D (unit C is bounded by white lines). At this locality (G1) Unit C is relatively thin (<60 cm) and is dominated by a pumice-rich horizon (light brown clasts); (C) Pumice lens within Unit C (outlined); (D) Unit G. Note the abundance of fine lapilli pumice and crude bedding; (E) Fine-scale laminations and low-angle crossbedding within unit D; (F) Unit F (above grey line) Note that even from some distance (>50 m) the abundance of large non-juvenile fragments is apparent within this unit. All photos taken by Tanya Jude-Eton.

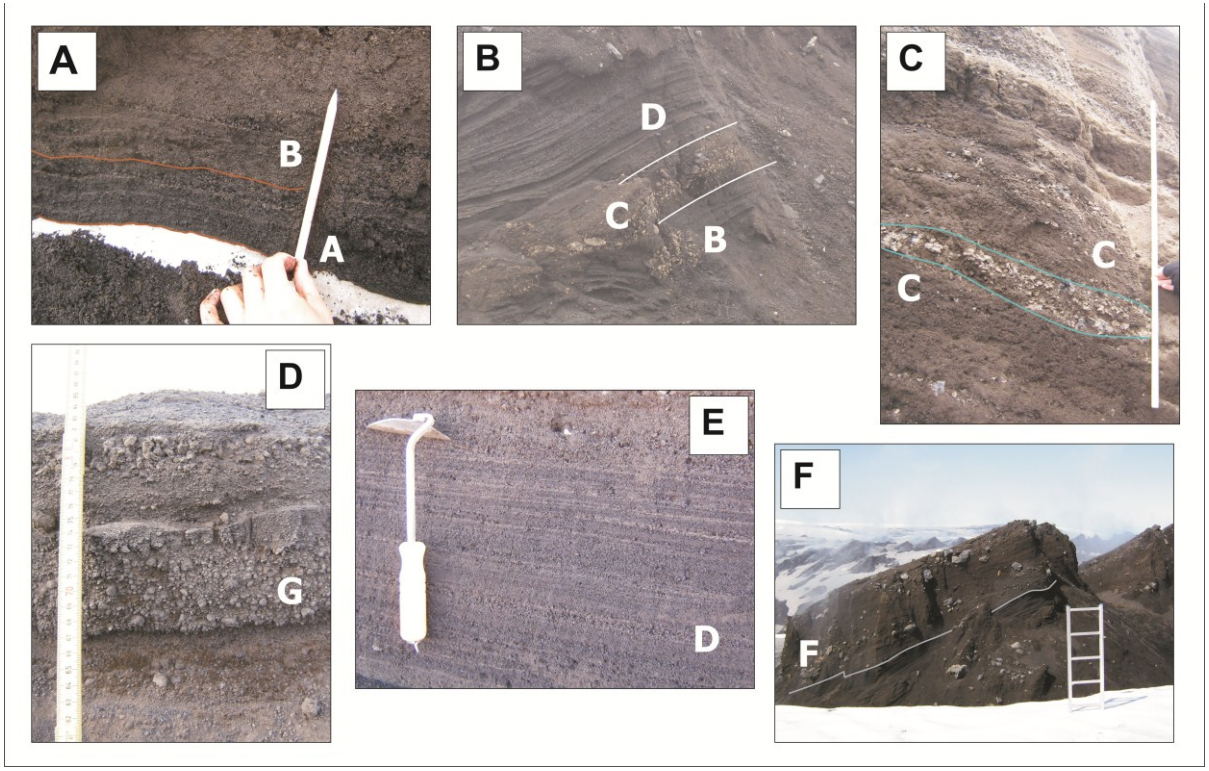

Figure 3.17: A plot to show average sulphur content of groundmass glass for each depositional unit, compared to Ti/Fe ratio (grey circles) via electron microprobe analysis. Representative values for undegassed G2004 melt trapped in plagioclase phenocrysts are also shown (black square).

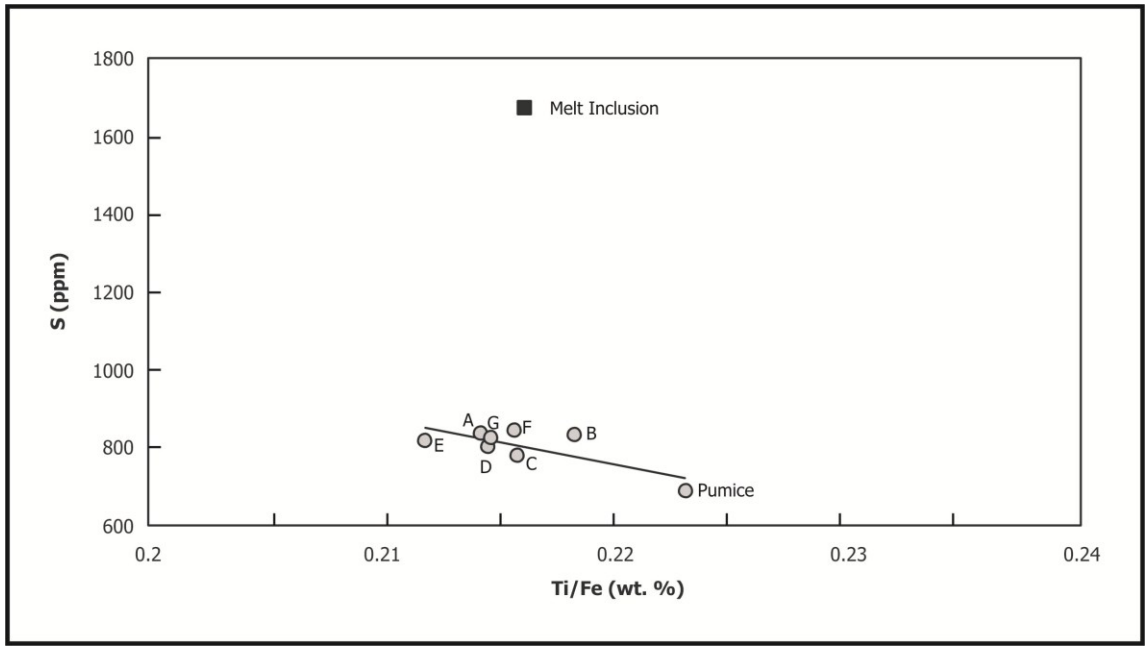

Figure 3.18: Image of tephra clasts from Unit C of the G2004 deposit under the binocular microscope.

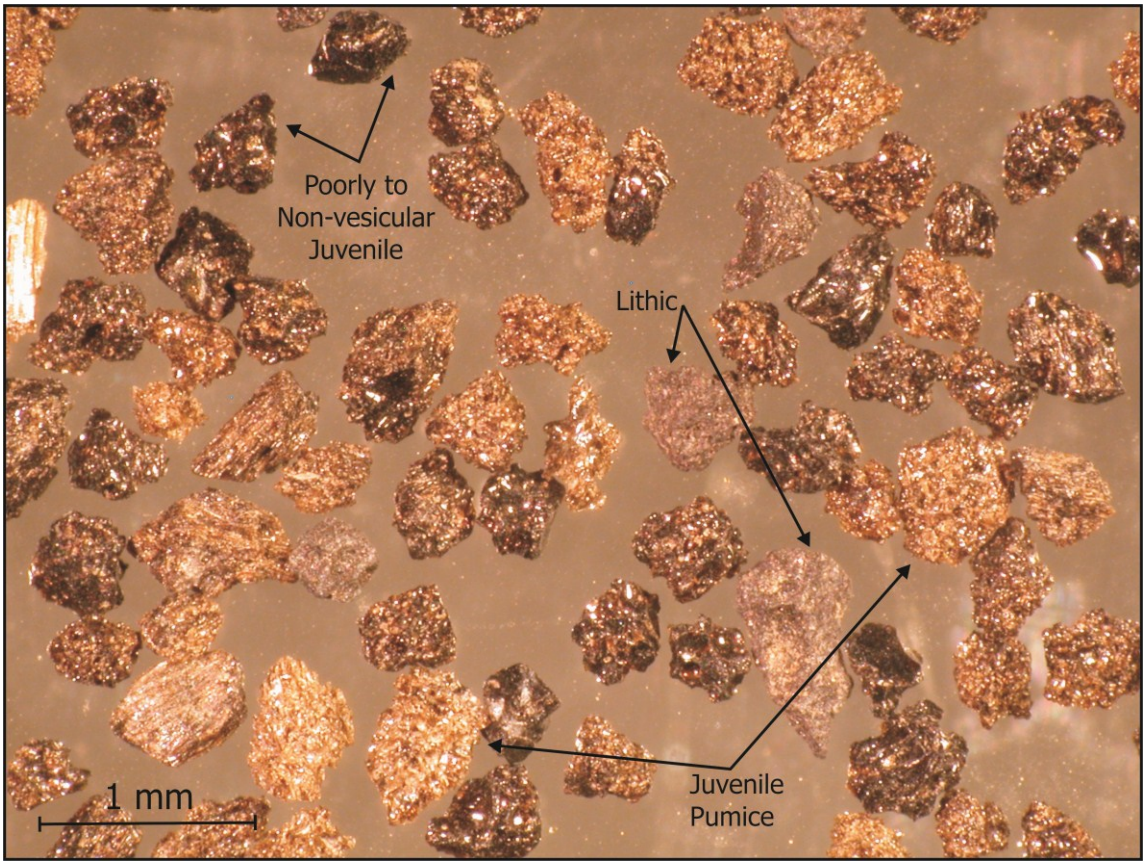

UNIT D

DESCRIPTION

The eruption of Unit D coincides with observations at a time when both vents were simultaneously erupting. This is consistent with Unit D with dispersal characteristics (Fig. 3.11), which indicate that it issued from the both vents and was directed principally northwards. However, as the isopach map shows, it has an irregular outline encompassing two principal lobes with maximum run-out distances of 3.2 km and 2.6 km respectively. Furthermore, the deposit exhibits exaggerated pinch and swell morphology which is apparent at the outcrop scale, but not at the scale of the dispersal diagrams (Fig. 3.14). The unit is locally dispersed within the proximal region, with t1/2 = 290 m.

Unit D is up to 130 cm thick in the most proximal sections, but can exhibit irregular lateral thickness variations. In most locations where Unit D is present it shows a consistent thickness for the extent of the outcrop. Nevertheless, there are numerous instances where the thickness of this unit can vary by 5 to 10 cm within a single section. Examples of this phenomenon include section TS60 (located 360 m NW of the crater), section TT02B (located 550 m NNW of the crater) and section TS80 (located 1100 m north of the crater).

This unit is light to dark brown in overall appearance and consists of many (20 on average) alternating fine and coarse layers ranging from very fine ash to fine lapilli. These are finely inter-bedded on a millimetre to centimetre scale and exhibit very low angle cross bedding (Fig. 3.16E). Individual packets are draped with very fine ash, which is light brown in colour. The deposit is inversely graded.

The grain-size distribution for Unit D is polymodal. Well sorted, fines-depleted packages consist of clasts in the -0.5 to 0.5 Φ size fractions, which are sub-rounded and scoriacious. The finer size fractions are relatively poorly sorted with >90 % of clasts >0 Φ in diameter. Modes occur in this distribution at 0.5 Φ, 2.75 Φ and 3.75 Φ. Progressively finer fractions consist of increasingly larger proportions of poorly vesicular fragments, with average contents of ~90 % scoria, 8 % non-vesicular glass and ~2 % disintegrated vesicular magma.

INTERPRETATION

The observed thickness variations within Unit D are primary. There is no evidence for post- or syn-depositional reworking of the deposit at any outcrop. Undulating bedding cannot, in this case, be a response to substrate topography because tephra was deposited on an essentially flat surface. Undulations are not evident at the ice contact for any section nor are the bottom contacts between Unit D and underlying layers irregular. The pinch and swell morphology evident in this unit is therefore a consequence of emplacement by numerous, directed, small volume PDC pulses.

This is also demonstrated by the fine-scale features of this layer. For example in section TT02B, Unit D varies in thickness between 33 and 41 cm along a 10 m transect and in places internally cross-bedded lobes can be observed to pinch out and overlap one another, separated by 10-20 cm of unstructured fines-rich material bearing medium lapilli sized pumice clasts. A similar effect is observed in section TS60, where a 5-8 cm faintly cross-bedded layer is overlain by 3-7 cm of massive medium to fine ash. Distinct coarse layers are draped by fine material. Likewise, in section TS80, the contact between units D and E is undulating and cross-cuts bedding, suggesting minor erosion by later density currents. In this case, the thickness of Unit D varies by up to 3-4 cm along a 5 m transect.

The spatial distribution of Unit D is not consistent in every region of the deposit. This layer was not deposited in some areas, while in others it may be unexpectedly thin (<10 cm), or unusually thick (> 100 cm). The distinctive fine ash partings draping each set indicate more prolonged time intervals in between pulses than in the higher energy Unit C phase. However, the time available for settling of fine ash above individual traction layers could equally have been extended by the erratic dispersal, meaning that successive pulses were not necessarily emplaced directly on top of one another.

Both the internal characteristics and spatial distribution of Unit D are consistent with deposition by a number of dilute, localised PDCs.

Figure 3.19: Digitised sketches of the variety of Unit D features displayed in several different locations. In section TS60 finely cross-bedded packages are separated by massive medium ash layers. In section TT02B separate cross-bedded lobes can be seen (a) truncating one another and (b) separated by a poorly sorted ash and lapilli horizon. In section TS80 erosive features can be seen.

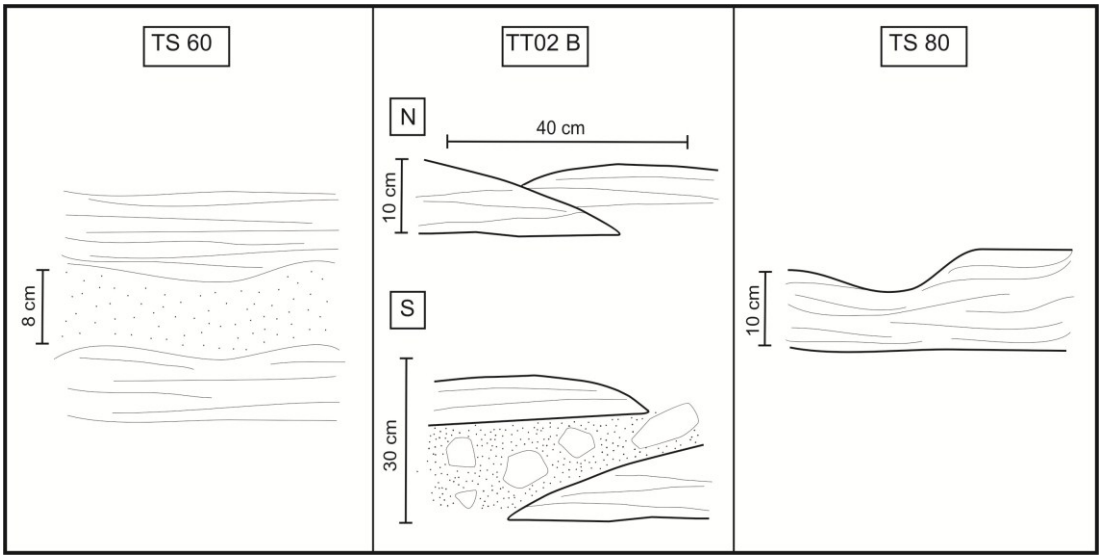

UNIT E

DESCRIPTION

The geometry of the Unit E isopachs (Fig. 3.11) demonstrates that it issued from the western vent and was directed northwards. The geometry of Unit E is similar to and overlaps that of Unit C, but has a more narrowly confined lateral extent. Consequently, it is dominantly confined to the western regions of the study area. The characteristics of this unit plotted on a dispersal diagram look very similar to those of Unit C. Due to their similarity in nature and the lack of a distinct contact, in many sections in this region it is virtually impossible to determine the boundary between units C and E if the Unit D marker layer is not present.

Unit E has a maximum thickness of 265 cm in the most proximal section of the western dispersal area. On a semi-log plot of area$_{1/2}$ vs. thickness (Fig. 3.14) this unit shows a stepwise, decreasing trend consisting of four segments, similar to Unit C. There is

an inflection point in the thinning profile for Unit E at 2 km from source. At this point, the average $t_{1/2}$ value changes from 190 m to 6 km.

The bedding characteristics of Unit E are virtually identical to those of Unit C, differing only in the following: (1) pumice lenses (sensu stricto) are sporadic in Unit E, whereas they are abundant in Unit C. Rather, in Unit E, pumice trains are more abundant, with more attenuated internal architecture; (2) Unit E contains a higher proportion of basaltic non-juvenile fragments and rare hyaloclastite blocks, which are blocky with angular fracture surfaces or columnar jointed (in the case of examples >50 cm across). These tend to be concentrated in specific layers within the deposit or are incorporated into pumice bands.

The top 100-150 cm of Unit E consists of numerous diffusely layered packages, intercalated with pumice lenses and trains. Coherent pumice lenses are up to 10 cm thick and can frequently be traced for more than 3 m in sections oriented along the dispersal axis. Due to their high aspect ratio, such lenses often look like flat layers, but taper towards the edges in long exposures. In the bottom part of the unit, continuous or semi-continuous pumice lenses seldom occur. Instead, layering is highlighted by a number of rather diffuse pumice trains. Despite this geometric distinction in layering, in many places the pumices are intact clasts in the fine lapilli size fraction, rather than fragments broken from a larger clast as in Unit C. Layered packages tend to fine upwards, although the deposit is quite poorly sorted overall.

The Unit E pumice lenses consist of generally “intact” clasts, up to 10 cm in diameter, which range between 60-80 % vesicularity. Abundant 5-10 cm non-juvenile fragments also occur within pumice lenses. These non-juvenile fragments are frequently orange to red in colour due to oxidation or hydrothermal alteration. Although the lenses have the overall appearance of being clast supported, pumice and non-juvenile clasts are fines-coated. The Unit E matrix is dominantly comprised of fine ash, although clasts range from -0.5 to 4 Φ in diameter, with $Md_{\Phi} = 0.75$. Unit E components are similar to those of Unit C, but with a higher proportion (up to 80 %) of fragments with 50-80% vesicularity. In the finer size fractions (-2 Φ and smaller) there are fewer than 2 % non-juveniles.

INTERPRETATION

Unit E is a widespread eruption unit, resulting from a vigorous phase of activity issuing solely from the western vent. The deposit characteristics of Unit E are almost identical to those of Unit C and therefore indicate the same depositional mechanism i.e. combined fall and PDC activity. Together, these two units make up about 80 % of the subaerial deposit and represent the main phase of eruptive activity. The two units show very similar internal characteristics and were both produced by the fallout from the eruption column concurrently with successive flow pulses. A change in thinning rate occurs in a region comparable to the run-out distance of associated PDCs. Consequently, the dominant emplacement mechanism for Unit E changes from PDC to pyroclastic fall at 2.5-3.5 km from source.

Key differences between units E and C, such as the relative abundance of conduit wall fragments ("non-juveniles"), the predominance of pumice train structures over lens structures and the slight differences in dispersal characteristics (particularly $t_{1/2}$ values) suggest that at this time (1) there was less time between successive PDC pulses than earlier in the eruption such that insufficient fall material was able to accumulate to create well defined layers; or (2) a greater proportion of the material deposited was emplaced via PDC activity (as compared to fall) than previously.

UNIT F

DESCRIPTION

The maximum range of Unit F is within 2.5 km of source. The layer is therefore confined exclusively to the proximal area and dominates the small eastern lobe of the deposit. Unit F is dispersed within a sector trending from E to NNE, quite unlike each of the other units from this event. However isopach geometry cannot be used to distinguish which vent this layer originated from as the innermost mapped isopach line encompasses both the eastern and western eruption centres.

Unit F has a maximum thickness of 2.5 m in the most proximal section of the eastern dispersal area and exhibits a very steep, but uniformly linear thinning geometry ($t_{1/2}$ =190 m). There is a clear disjoint in the thinning trend for Unit F at a distance of between 500 m and 700 m from the vent, after which the unit follows a simple pattern of exponential decay (Fig. 3.14).

Unit F is a grey-brown, massive and very poorly sorted layer. The layer broadly coarsens upwards, with 80 % of the abundant (> 3/m^2) ballistic non-juveniles occurring in the top half of the layer. The grain-size distribution is polymodal, with dominant modes ranging from -2 to 4 Φ and, apart from outsize non-juveniles in the top half of the layer, does not vary with stratigraphic height. Fine ash dominates, with 69 % of material falling into size fractions <1 Φ. The fine to medium lapilli size fractions include predominantly pumice clasts (>80 %) in the lower part of the unit. In the upper part, this size fraction is dominated by non-juveniles (up to 60 %). The smaller size classes consist of a roughly equivalent proportion of scoriacious and more vesicular material. The -1 to -2 Φ size fractions contain <5 % non-juvenile fragments and these are not present at all in size classes smaller than -1 Φ. "Bomb sag" structures are frequently present below the larger non-juveniles, many of which also include a pumice tail.

INTERPRETATION

Unit F is massive, very poorly sorted, has limited and directed dispersal and a relatively high abundance of non-juvenile fragments compared to the rest of the deposit. Apart from the inverse grading of large (> 10 cm) non-juveniles the grain-size distribution does not vary within the layer. These characteristics are consistent with en masse deposition via a single highly concentrated PDC.

On the morning of November 3rd changes occurred, as evidenced by a spike in tremor amplitude (Fig. 3.4). Close to this time the plume dropped below radar detection limits. I postulate that the sudden mass-loading caused the eruption column to lose buoyancy and collapse, resulting in deposition from a single, directed, high concentration

pyroclastic current. Material was directed towards NNE and locally interrupted the depositional sequence.

This apparent surge in magma discharge would also account for the numerous non-juvenile clasts found in the block/bomb size fractions of Unit F, which are notably absent from finer fractions. The correlation of non-juvenile abundance with grain-size suggests a connection to either the eruption vigour at that moment, or the intensity of the fragmentation process (Houghton *et al*., 2004). In this case, the relationship clearly does not indicate enhanced fragmentation, but rather that chunks of rock were torn from the conduit walls during this burst in eruption energy.

Figure 3.20: Evidence for particle aggregation within the G2004 deposit. (A) Top surge in Unit G at section TS50. This layer contains abundant coated clasts. White circle highlights an example of a hole left in the deposit where a lapillus has been plucked out and the coating has been preserved. Photo by Tanya Jude-Eton; (B) The pencil points to a non-indurated ash aggregate in unit C. Photo by Thor Thordarson.

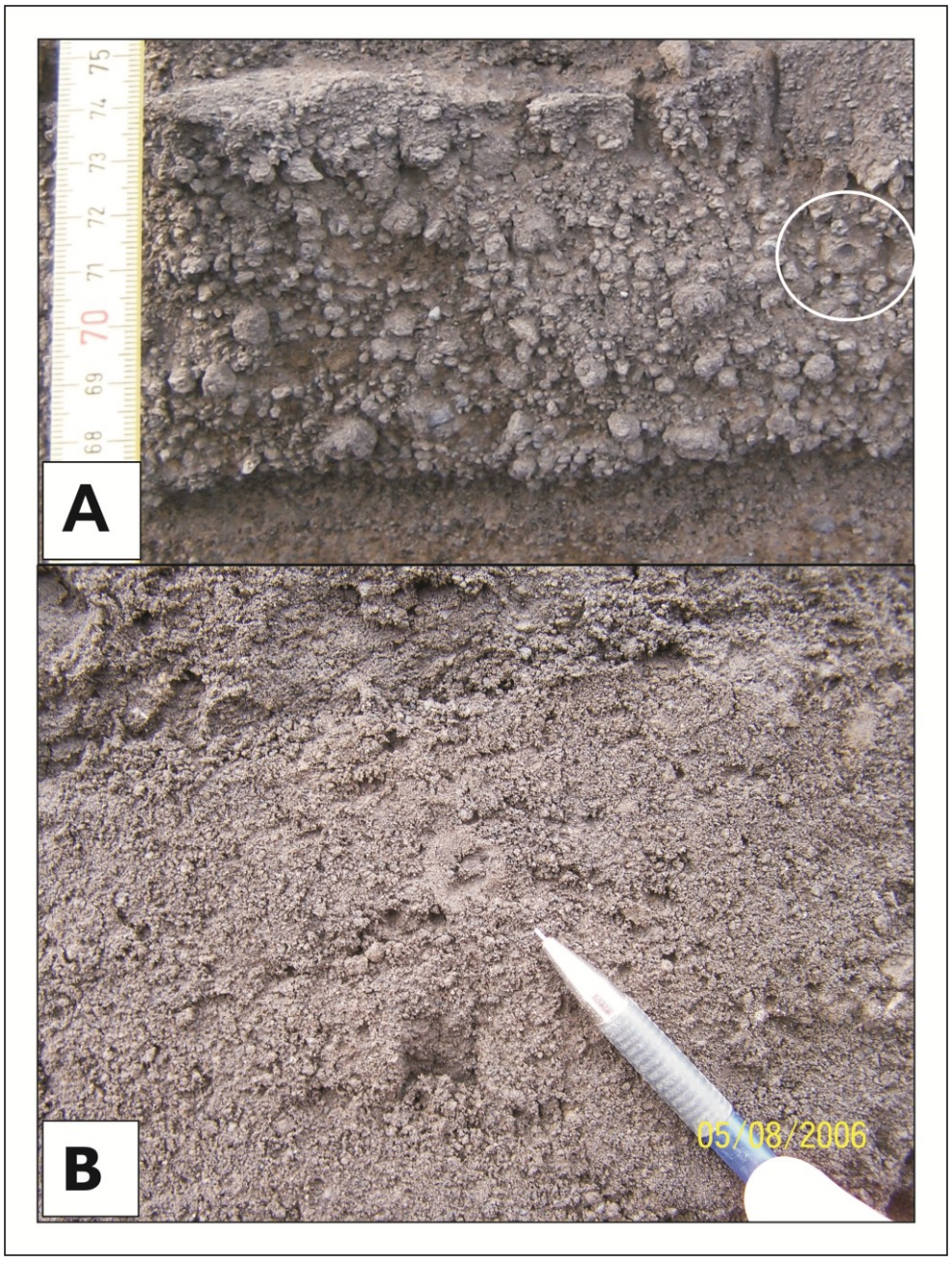

UNIT G

DESCRIPTION

The Unit G isopachs are rather broad, enclosing much of the ice cauldron. It is not clear from this geometry whether material came from the eastern, western, or both vents (Fig. 3.11). However, visual observations indicate that only the eastern vent remained active towards the end of the eruption.

Unit G consists of two distinctive lobes of emplacement which are moderately well-dispersed laterally. Unit G is dominant in the west, but extends to even the most proximal few sections in the east. The unit is largely confined to the proximal area and dies out within 3 km of the vent along the principal dispersal axis (Fig. 3.13). Unit G ranges from 20-50 cm in total thickness and exhibits a relatively shallow thinning rate ($t_{1/2}$ = 400 m).

Unit G variably consists of one to three grey-brown sub-units that exhibit low angle crossbedding. In general, cross-bedded sets coarsen upwards. However, although diffusely layered, the deposit is not well ordered, as clasts belonging to the larger size fractions are not confined to dominantly coarse sets.

In the field, the grain-size of this unit appears bimodal and the deposit is poorly sorted. However, Unit G is notably fines-abundant (over 75 % < 1 mm in diameter), even very close to the crater. The remaining material consists of very coarse ash to fine lapilli. The fine lapilli size class consists of grey, angular non-juveniles and broken juvenile pumice in ratios ranging from 1:1 to 1:2. These are concentrated in pumice-rich horizons towards the top of sets. Clasts coated with fine ash are common in the fine lapilli size fraction, while rare "rim-type" accretionary lapilli (after Schumacher and Schminke, 1995) (Fig. 3.20A) and more common armoured clasts (after Waters and Fisher, 1971) (Fig. 3.20B) are observed in the most proximal G deposits. Occasional non-juvenile blocks 5-20 cm in diameter are also present in this layer. Clasts in the coarse ash to very coarse ash size fractions contain juvenile scoria and pumice in a 60:40 ratio. By contrast, the fine ash fraction consists almost entirely of disintegrated golden pumice. Within all units of the G2004 deposit, the proportion of disintegrated pumice fragments increases with distance

from source relative to that of scoria and non-vesicular glass. In addition, irrespective of vesicularity the vast majority (i.e. >95%) of clasts more than 2.5 Φ in diameter, from all units, exhibit a blocky morphology (cf. Fig. 3.13).

INTERPRETATION

The poorly sorted nature of Unit G, along with the presence of abundant non-juvenile fragments and coated clasts, is diagnostic of wet, phreatomagmatic PDC deposits. The diffuse nature of bedding reflects relatively high particulate concentrations within the current, while reverse grading and segregation of pumice-rich layers towards the top of sets are indicative of a density stratified current. The presence of armoured clasts and accretionary lapilli indicate the presence of up to 15 wt. % condensed water (Gilbert and Lane, 1994; Schumacher and Schminke, 1995).

3.8.1 REFERENCE SECTION TT01

Section TT01 is located approximately 550 m NNE of the centre of the 2004 crater at 64° 24.097' N 17° 22.641' W. I have correlated the stratigraphic variations within different regions of the deposit to yield a comprehensive view of the overall sequence (Fig. 3.21). However, Section TT01 is the only location at which all identified units are present together (Fig. 3.12) and so it lends key support to our interpretation of the event chronology.

At this location Unit A is 40-42 cm thick. The contact between Unit A and the ice below is marked by a <1 mm-thick, continuous layer of tan brown very fine ash. Unit B is 60-62 cm thick, followed by a 69-73 cm Unit C sequence. Unit D is not only present, but exceptionally thick (140-144 cm) at this location. Unit D is directly overlain by Unit E, which is 160-166 cm thick. Anomalously, Section TT01 features a thin (9-12 cm) "D-like" (D') layer between units E and F. This layer is partly eroded and is also marked by ballistic bombardment with associated pumice infill, which is characteristic of the D-F contact in the eastern dispersal area (Unit E is not present in eastern sections). Above the D' layer, Unit F is 138-140 cm thick and is overlain by units G1 (7-9 cm) and G2 (50-55 cm).

The stratigraphic sequence observed at this locality clearly demonstrates that Unit F is a distinct event that occurred some time after, and independently of, the deposition of Unit E, rather than occurring at the end of the C-phase of activity or as a minor episode during the E-phase. The anomalous D' layer is an additional but very localised PDC, presumably issuing from the eastern vent. As the unit isopach maps demonstrate (Fig. 3.11) deposition from PDCs consists of many pulses of activity, which can be separate in both time and space. Consequently units B, D and G all consist of multiple lobes, each with varying axes of dispersal. If I also account for the complexity of the presence of two distinct but closely spaced vents which are alternately or simultaneously active, then it is entirely plausible that Unit D' (closer to the eastern vent) may have been deposited some time after the bulk of the Unit D PDCs in the north, which are likely to have issued from the western vent.

Figure 3.21: Correlation of stratigraphy in the principal direction of dispersal (S-N, top) and along the cross-wind axis (W-E, bottom).

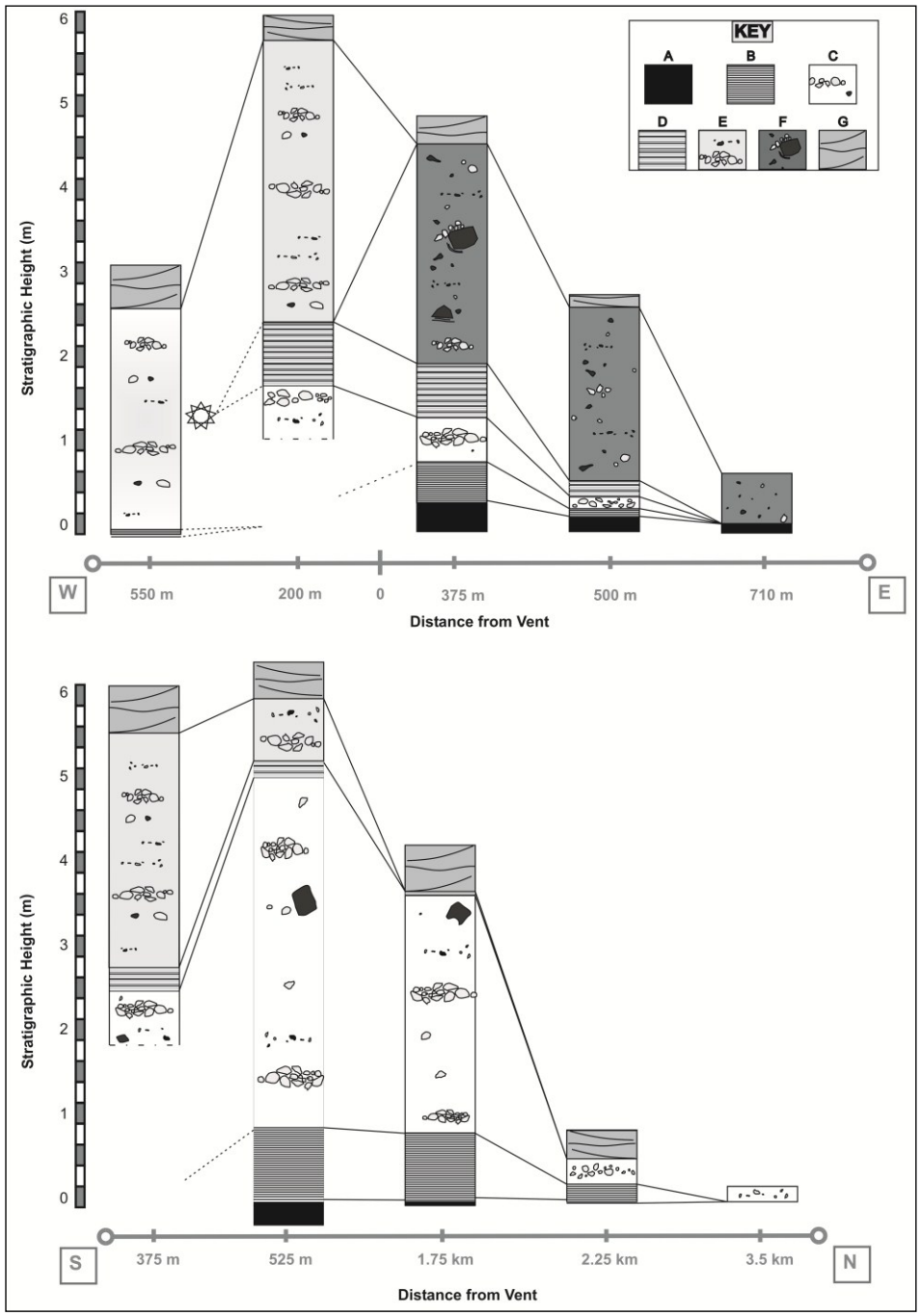

3.9 EVENT RECONSTRUCTION

I present a fully interpreted reconstruction of the G2004 eruption which synthesizes i) visual observations (Fig. 3.3); (ii) instrumental observations (i.e. weather radar for plume detection and seismic records; Fig. 3.4); and (iii) our interpretation of stratigraphic features within the resulting deposit (Figs. 3.8, 3.16). An accompanying conceptual schematic model is provided in Fig. 3.22.

As stated previously, the tremor record is the only record of the eruption with no gaps in data. It is reasonable to expect that large changes in eruption behaviour or vent conditions are reflected in changes in the tremor signal. Although I acknowledge that such connections are tentative without other direct observational data, spikes and sudden changes in tremor are here correlated with the onset of formation of individual units, using the plume record as an additional constraint. On the basis of these timings, an approximate record of magma discharge with time can be constructed.

The seismic record shows the onset of tremor at 21:50 on November 1st, which corresponds to the onset of the subglacial eruption (Fig. 3.22, Panel 1). As shown previously, based on the clast morphology, vesicle abundance and chemistry of Unit A and B tephra the magma in the initial phase was largely outgassed before fragmentation indicating that by the start of the eruption a portion of the magmatic volatiles had decoupled from the melt as it rose through the conduit. This resulted in two-phase (magma-free volatiles) flow within the shallowest part of the conduit upon eruption onset. The escape of magmatic gases may have initiated ice melting, which eventually led to the formation of a subglacial cavity and supplied water for the onset of phreatomagmatic fragmentation. The subglacial phase of the eruption lasted for at least 23 minutes, during which time it melted through the 150-200 m-thick ice cover to the surface. The total thermal energy of the eruption was found to be 7×10^{16} J, of which almost a third was used to melt the ice and a further ten percent to heat the meltwater. Only a few percent of the total energy budget was expended upon fragmenting the magma, while approximately half of the eruption energy sustained the plume (Gudmundsson *et al*., 2009).

Figure 3.22: Schematic diagram depicting the G2004 sequence of events and depositional regime for individual units. The accompanying verbal description for each stage of this diagram is provided in the text.

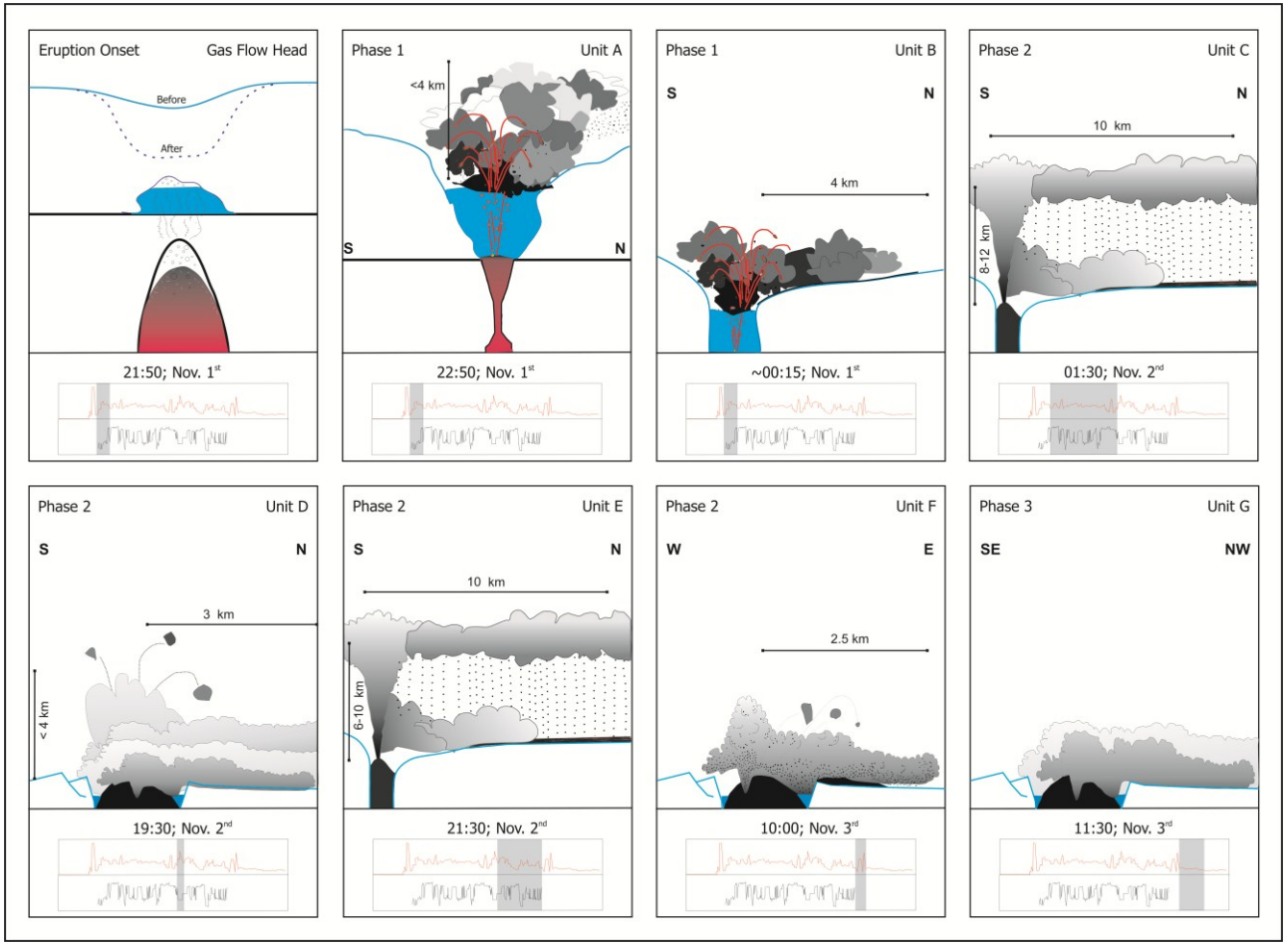

The initial tremor spike at 22:13 is thought to signal the end of a fully subglacial eruption and the onset of Phase 1 which according to this reconstruction lasted for over three hours and includes the deposition of units A and B. The eruption plume was first detected by weather radar 37 minutes later at 22:50 (Fig. 3.4). The first subaerial phase of G2004 commenced with deposition of the almost exclusively proximal phreatomagmatic fall layer (Unit A) with a maximum thickness of 50 cm (Fig. 3.22, Panel 2). The Unit A event was directly followed by emplacement of pulsating PDCs (Unit B), which have a maximum thickness of 80 cm and attain maximum run-out distances of 3-3.5 km. Together, units A and B (Phase 1) total 12 % of the total erupted magma volume. They are paired depositional facies formed by a short lived explosive event generated by the interaction of partly degassed magma and glacial meltwater. The deposition order clearly suggests fallout from a moderately high plume above the eastern vent, followed by PDC emplacement produced by a fountain collapse towards the end of this eruption phase (Fig. 3.22, Panel 3). At the end of Phase 1, there was a momentary lull in the tremor amplitude, after which it rapidly intensified to an oscillating steady state level. The second phase of the G2004 eruption is considered to be the main phase of activity and includes units C, D, E and F.

The period of Unit C deposition is taken to correspond to a period of less-elevated and continuous tremor from 01:27 to 19:32 on November 2nd (Fig. 3.4). This is consistent with the sustained activity indicated by visual observations and deposition by a mechanism of progressive aggradation as inferred from the structural and textural properties of Unit C deposits (Fig. 3.16). Unit C forms 54 % of the total subaerial deposit and the observation of two vigorously active vents is consistent with Unit C isopach geometry (Fig. 3.11). Tephra was deposited by coeval fall and PDC mechanisms (as indicated by deposit characteristics and photographs; Fig. 3.3A, B, F). Continuous uprush style activity dominated, although both visual observations and tremor records show this was punctuated by occasional, higher energy pulses. The photographs in Fig. 3.3, which were taken on the late afternoon of November 2nd, towards the end of Unit C deposition, illustrate a number of these features. They show that both vents were active at the time the photographs were taken, but that western vent became dominant towards the end of Unit

C deposition and the plume became increasingly steam-rich (Fig. 3.22, Panel 4). In the stratigraphic record Unit C is present at every location distinctly overlain in many places by Unit D which exhibits a pinch-and-swell morphology.

The tremor spike which occurred at 19:32 on November 2nd is thought to correspond to the onset of Unit D. The eruption intensity abruptly diminished and there was no significant pause between this and the previous activity. Unit D deposition is thought to have lasted for three hours. During this period the plume stepped down and disappeared below radar detection for 63 minutes (Fig. 3.4). Unit D consists of finely laminated and distinctly cross-bedded PDC packets of limited lateral dispersal within the northeast sector of the tephra blanket, consistent with sedimentation from a very dilute current. This interruption of continuous uprush could be a consequence of a combination of vent migration and an influx of cold water into the vent, which would suppress column buoyancy and account for the relatively low particle density within the Unit D deposit (Fig. 3.22, Panel 5). A rhythmically oscillating tremor phase ensued before the plume picked up again with the onset of Unit E at 21:30 hrs. With the eruption column re-established, a similar style of activity to that of Unit C resumed, but was focused on the western vent and therefore Unit E only occurs in a relatively narrow band towards the western half of the deposit (Fig. 3.21). Unit E deposition lasted for 12 hours and 55 minutes during which time material progressively aggraded by the combined processes of pyroclastic fall and PDC emplacement (Fig. 3.22, Panel 6). This period of rapidly oscillating, sustained activity culminated in a spike in tremor intensity at 09:58 on November 3rd, lasting for only 1 hour and 23 minutes. A possible scenario could be sudden loading of the column corresponding to a short-lived pulse of high magma discharge which caused it to lose buoyancy and collapse towards the east resulting in the deposition of Unit F, a massive, poorly sorted and non-juvenile-rich layer (Fig. 3.16).

The column collapse and emplacement of Unit F were the last events of the main phase of the eruption (Fig. 3.22, Panel 7). After this the eruption column was never fully re-established and tremor amplitude plummeted to a low level. The duration of this final part of deposition towards the north is difficult to determine but I propose that it had come to

an end by 18:16 on November 3rd, when the tremor amplitude drops towards background levels. The stratigraphy indicates that the final pulses of activity during November 3rd resulted in the emplacement of two PDC beds with dispersal axes oriented towards the north and north east. It was in this relatively low energy environment that the Unit G pyroclastic currents were deposited (Fig. 3.22, Panel 8). A minor eruption continued through November 4th with the plume rising 1-2 km over the vent. Aerial inspections on November 5th revealed no additional deposition outside of the ice cauldron. Magmatic activity may have ceased on November 5th, but tremor oscillations continued to be recorded until November 6th and the end of the eruption has been set at this date (Vogfjörd *et al*., 2005; Sigmundsson and Gudmundsson, 2004).

A summary of the timing of onset, duration and termination of each unit is provided in Table 3.7, which is based on time-series analysis of plume height, tremor amplitude and photographs of the eruption.

3.10 TIME BREAKS DURING THE GRÍMSVÖTN ERUPTION

The proximal 2004 succession contains several intercalated PDC deposits (Figs. 3.8, 3.16), all of which are either absent, or represented only by coeval ash fall, in medial and distal sections. The majority of these PDCs are sector-confined and the accompanying variability in proximal fall dispersal (resulting from vent migration and changing wind directions) means that the presence of these distinct PDC beds are not firm indicators of significant time breaks in ash fall. Neither IMO plume height data nor the visual observations on November 3rd indicate any breaks in activity. Furthermore, the tremor record strongly suggests the absence of significant time breaks during the G2004 eruption.

The analysis presented in the previous section indicates that major spikes in amplitude and changes in tremor patterns can be correlated with changes in eruption behaviour. It is possible that more subtle fluctuations in tremor may also reflect short term

variations in eruptive activity during the deposition of individual units. However, without any direct evidence it would be premature to make such correlations.

3.11 MAGMA DISCHARGE

The total duration of the G2004 eruption, as well as the timing for individual units, is constrained by seismic and weather radar records and by visual observations (Vogfjörð, 2005; Oddsson, 2007). Visual observations show that the G2004 eruption lasted at least until November 5th and possibly some magmatic activity persisted until November 6th. According to the event reconstruction presented above, the material erupted later than the afternoon of November 3rd is insignificant in terms of mass and volume of erupted products. Thus, the significant part of the eruption lasted for 45-46 hours (subglacial + units A-G).

Average discharge values for individual eruption units, based on unit size (Table 3.4) and calculated filling rate of ice cauldron (Fig. 3.9) are presented in Table 3.7 and Fig. 3.23. Filling of the cauldron dominates the discharge to start and it is only during deposition of unit D that plume-transported discharge equals the contribution to filling the cauldron. Values derived for the average mass discharge of each unit are broadly consistent with their respective average and maximum tremor amplitudes. The Phase 1 units (A and B) are considered together as they were generated by a continuous phreatomagmatic event and cannot be distinguished from one another on the tremor or the plume records. This first phase of activity was the most intense, with calculated discharge of 218 m^3s^{-1} and peak tremor amplitude of 8 μms^{-1}. The average discharge during Unit C deposition is somewhat less (181 m^3s^{-1}), although the observed oscillations in plume height and possibly also fluctuations in tremor amplitude are consistent with temporal instabilities in the column and pulsating deposition. These may reflect temporal variations in magma supply, but are more likely to relate to variable conditions in the shallow conduit and vent. Unit D deposition is marked by a decline in magma discharge (114 m^3s^{-1}) compared with that of Unit C, especially in the subaerial part. It is possible that the decline in magma discharge

Table 3.7: A summary of the timing of onset, duration, and termination of each unit, based on time-series analysis of plume height, tremor amplitude, and photographs of the eruption.

Unit/Phase	Start time	End time	Duration (hours)	Cauldron (ms^{-3})	Proximal (ms^{-3})	Distal (ms^{-3})	Total (ms^{-3})
Subglacial	1 Nov. 21:50	1 Nov 22:13	0.4	150	0	0	150
A+B	1 Nov. 22:13	2 Nov 01:27	3.2	141	77	0	218
C	2 Nov. 01:27	2 Nov. 19:32	18.1	98	51	32	181
D	2 Nov. 19:32	2 Nov. 21:03	1.9	57	57	0	114
E	2 Nov. 21:03	3 Nov. 09:58	12.9	27	35	32	93
F	3 Nov. 09:58	3 Nov. 11:21	1.4	0	46	0	46
G	3 Nov. 11:21	3 Nov. ~18:15	6.9	0	19	0	19

caused the column to step down, which resulted in a rapid succession of partial collapses generating the Unit D PDCs. Column collapse at this time could also be associated with an influx of water into the vent, which would explain the dilute nature of the deposits, or with a pressure drop in the conduit associated with vent migration. The eruption column is re-established with the onset of Unit E deposition, where activity becomes concentrated on the western vent only. Prior to this, both vents were simultaneously active. The average magma discharge during this time is 93 m^3s^{-1}. This trend of declining average discharge with time over the course of the G2004 eruption is consistent with observations from a number of other basaltic events (e.g. Wadge, 1981).

During Unit C sedimentation, the median tremor amplitude is closer to 6 μms-1 and during formation of Unit D it spikes to 11 μms-1, while for Unit E it oscillates around a value closer to 4 μms^{-1}. The total rate of discharge during Unit C deposition is twice that of Unit E, yet the dispersal trends, style of activity and nature of deposits are remarkably similar for the two units. If I take into account only the mass deposited on the glacier surface (tephra apron) outside of the ice cauldron, this provides us with an apparent discharge of 83 m^3s^{-1} for Unit C and 67 m^3s^{-1} for Unit E. Here the difference in eruption rate and therefore in the amount of energy supplied to the atmosphere by each unit, is less pronounced. Plume height records show that Unit C is characterised by a slightly taller and more stable column than that of Unit E and the stratigraphic record concurs that Unit C contains a larger component of emplacement by tephra fallout. The higher overall $t_{1/2}$ values of Unit C, particularly within the proximal region of deposition, are also consistent with this assessment. In this case, the comparison of "apparent discharge" between the two units is valid because although the actual discharge during Unit C is much greater, the bulk of this material is confined to the ice cauldron and is not dispersed subaerially. The energy from this material largely goes towards ice melting and it should therefore contribute relatively little to the plume. Therefore, despite the considerably larger discharge during Unit C, the deposit characteristics are similar to those of the less energetic Unit E. This shows that the individual dispersal characteristics of Units C and E may be controlled largely by differences in eruption column and plume dynamics rather than by changes in the rate of magma supply.

There is a spike in tremor amplitude associated with the onset of Unit F deposition. This also corresponds to the final collapse of the eruption column. The abrupt increase in tremor amplitude (11 μms^{-1}) is consistent with the interpretation of a vent clearing event at the beginning of this eruption unit, as suggested by the non-juvenile-rich componentry and the presence of large, ballistically emplaced non-juvenile blocks at the base. This change in eruption behaviour is short-lived, however, and ultimately leads to the final column collapse event of the eruption, accounting for the bulk of Unit F deposition. Discharge continues to wane for the remainder of the eruption and a sizable eruption column is never re-established. I have calculated a discharge of 19 m^3s^{-1} for Unit G; but this value is relatively uncertain because of the poor constraints of the absolute end time for the unit. At this stage the eruption is waning, generating relatively low-intensity PDCs.

3.12 SECTORAL PATTERNS OF DISTRIBUTION

The most prominent feature of the G2004 total thickness isopach map is that the deposit is bi-lobate. Tephra deposits exhibiting similar geometry are well known in the literature and mechanisms previously invoked to account for this configuration include: changes of wind direction or intensity with time or with plume height (e.g. Larsen and Thorarinsson, 1978), oscillation in height of the eruption column (e.g. van den Bogaard and Schmincke, 1985), vent migration with time (e.g. Taylor, 1969), oblique orientation of the erupting jet with respect to wind direction (e.g. Sparks *et al*., 1981) and the action of a bifurcating plume (e.g. Ernst *et al*., 1996).

In the case of the G2004 deposit I find that vent migration and sectoral patterns of PDC distribution control the deposit geometry in the proximal area. However, the forked geometry of this deposit also extends into the distal region and, as shown by Oddsson (2007), correlates with timing of tephra fallout in the areas north of Vatnajökull .

Proximal fall and PDC layers show varying degrees of confinement to sectors around the vents. This is manifest both in the lobate distribution patterns of PDC units B, D and G; in the directed nature of Unit F; and in the relatively narrow distribution of

Figure 3.23: Average discharge over time throughout the G2004 eruption, based on unit mass and the calculated filling rate of ice cauldron. The proportion of mass contributed to the subaerial deposit beyond the limits of the ice cauldron is shaded in grey. Filling of the cauldron dominates the discharge to start, and it is only during deposition of unit D that plume-transported discharge equals the filling of the cauldron. Unit designations (bottom) and duration of eruption phases (top) are indicated along the time axis.

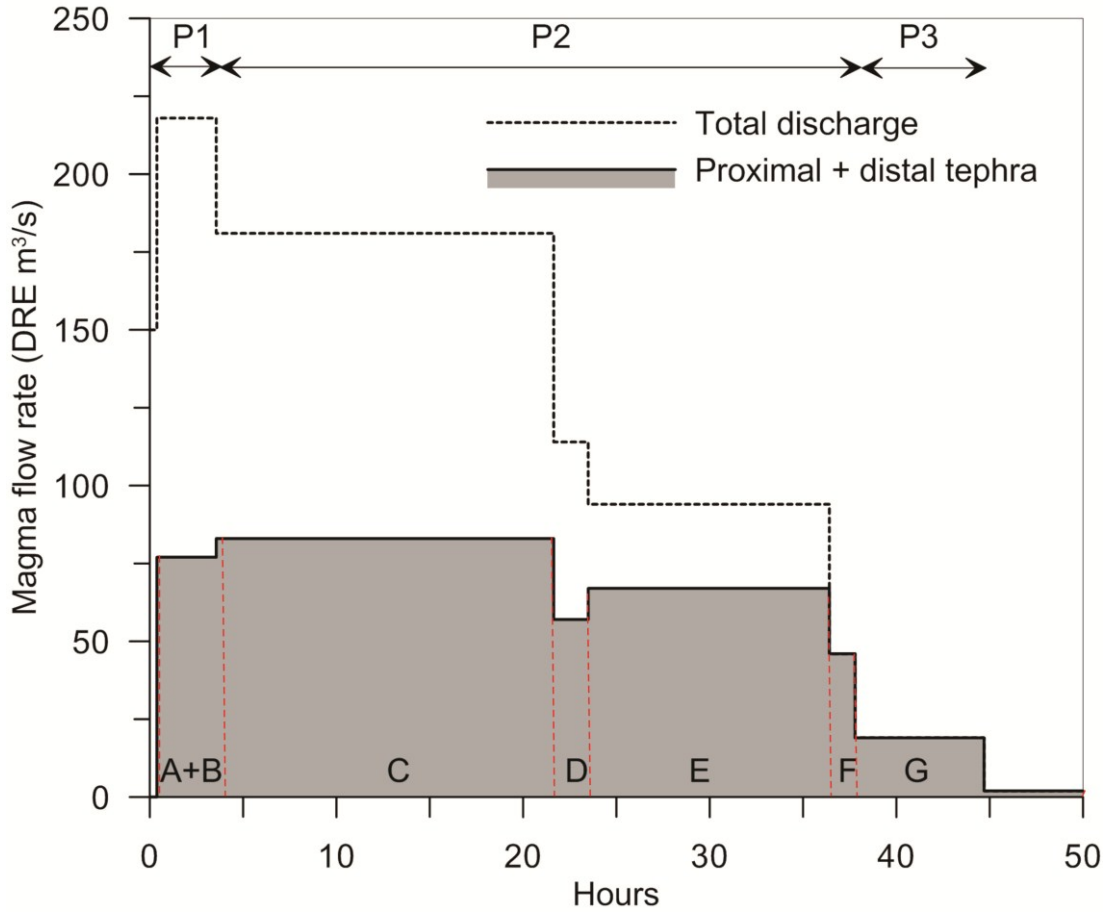

the late fall unit, E (Fig. 3.11). The dispersal axes of fall-dominated units (C and E) appear to be controlled by the south to south-westerly regional wind acting throughout the eruption, while the PDC lobes are distributed according to geometric factors such as the vent of origin and regions of localised jet instability in the eruption column. PDC dispersal was also confined by the presence of the 150 m high caldera wall directly to the south of the crater.

Complete four-dimensional wind field data confirmed by satellite imagery and meteorological recordings are not available for the G2004 eruption. However, contemporary observations and meteorological data from the IMO's Jökulheimar weather station (Table 3.1) confirm that moderate (10-15 ms^{-1}) southerly to southwesterly winds during the main phase of the eruption caused the weak G2004 plume to become inclined towards the north. Suzuki (1983) numerically modelled - tephra transport and deposition using a diffusion-advection equation for horizontal particle motion in a temporally and spatially uniform wind field. He found that when there is no wind the tephra deposit may be circular around the vent while for weak wind velocities (~5ms^{-1}) the plume trace and tephra layers are generally in the shape of an oval in plan view. The dispersal pattern becomes increasingly elongate in the leeward direction with increasing wind speed. At high wind speeds (~30 ms^{-1}) the dispersal distance is greatest and the tephra layer is long and narrow. The narrow and elongate dispersal pattern of the G2004 tephra deposit is consistent with the aspect ratio expected for a moderate wind velocity, as modelled by Suzuki (1983). Suzuki (1983) also found that in the area near the vent the accumulated mass decreases outward at an almost constant rate and the distance from the vent at which the mass decreases sharply depends on the wind velocity. However, the effect of wind velocity on the total area enclosed by the isomass lines is small. Satellite imagery from NASA indicates that the weak G2004 plume did diffuse significantly in the distal regions, but did not bifurcate. Therefore, shifts in wind direction primarily account for the observed bilobate deposition pattern in the distal region.

In the proximal region of dispersal, however, there is little to no direct correlation between unit geometry and wind speed/direction at the time of deposition. In particular, the wind direction appears to have no impact of directions of PDC dispersal. Although the wind direction and speed does impact ash fall dispersal, its effect is mitigated by the effects of particle size distribution and plume height: During

the time that units A and B were deposited, a southerly to southwesterly wind was blowing at an average speed of 15.8 ms^{-1}. These are among the highest wind speeds recorded for the eruption period, yet Unit A is only moderately dispersed (i.e. dies out in the medial deposit sector) and Unit B exhibits a range of dispersal axes rather than being restricted to a north-northeast directed trend. During the time of Unit C deposition the wind was southwesterly with a variable wind speed. For the first 6-8 hours (i.e. until 0600-0800 hrs. on November 2nd) the wind speed is moderate (i.e. 10-15 ms^{-1}). After this it dies down to 5-10 ms^{-1} and doesn't pick up again until the last hour of Unit C deposition (i.e. around 1800 hrs.). Nevertheless, Unit C is one of the two widely dispersed G2004 eruption units. Mild to moderate southerly (average 12 ms^{-1}) winds were acting during the period of Unit D deposition. However, these appear to have had little effect upon the erratic distribution of this unit. Southerly winds continue into the period of Unit E deposition then gradually move towards a southwesterly direction over a 6 hour interval until 0200 hrs. on November 3rd. The wind speed during this time is moderate (average 13 ms^{-1}). After this the wind dies down to an average of 6 ms^{-1} from a west-southwesterly direction. Mild (6 ms^{-1}) south to southwesterly winds continued for the short period of Unit F deposition. However, Unit F was dispersed directly eastward from the vents and was not affected by the action of the wind. Weak (5 ms^{-1}) southerly winds persisted throughout the deposition of Unit G until near the very end of the eruption when the direction changed abruptly to west-northwesterly and the wind speed fell to very light levels (2ms^{-1}).

3.13 SYN-ERUPTIVE RE-WORKING OF THE TEPHRA

Material within the vent is likely to be significantly re-worked due to wall instability, slumping, sub-vertical emplacement of tephra and the presence of abundant water in the crater lake.

In the G2004 deposit outside of the immediate vent area there is little evidence of the following, which would indicate syn-eruptive reworking within the tephra pile: rilling, slumping, faulting, soft-sediment deformation, erosion or truncation of layers,

disturbed bedding. Exceptions to this include: (1) Bomb sag structures beneath some ballistics (especially those which were emplaced at the start of Unit F/end of Unit D); (2) PDC erosion and truncation of lower beds in isolated locations in Unit D packages; (3) Re-working of pumice lapilli fall layers into pumice lenses and trains. The reason that there is so little syn-eruptive disturbance to the tephra pile could be a consequence of the following factors: precipitation was relatively light and due to the cold consisted largely of snow/ice; it was a wet eruption so the material was relatively cohesive but not so wet as to be re-mobilised by the presence of flowing water; winds were only weak to moderate in intensity; deposition took place on a flat or gently sloping surface.

Within the G2004 deposit lapilli-sized lithic fragments have been identified within the in core of vesicular juvenile clasts. However, these are very low in abundance (<0.1%) and no juvenile recycled cores have been identified so there is little evidence within the G2004 deposit to permit estimation of clast recycling within the plume. However, Houghton and Smith (1993) show that data from a Holocene maar deposit in Taupo Volcanic Zone, New Zealand indicates that the first cycle juvenile component of the deposits may be less than one third of that determined by a simple componentry analysis of the proportion of juvenile:lithic:free crystals. This is an important consideration when calculating the energy release of an eruption.

3.14 THINNING GEOMETRY OF PDC VS. FALL UNITS – IMPLICATIONS FOR TRANSPORT AND SEDIMENTATION

By convention, I use semi-log plots of area$^{1/2}$ vs. thickness to evaluate and compare key characteristic of tephra fall deposits (Fig. 3.14). The proximal data for the total deposit, as well as units C and E, adhere to a general trend of increasing slope with increasing proximity to source and the data are only slightly better fitted to a power law relationship than to a series of exponential thinning curves (c.f. Fierstein and Nathanson 1992; Rose 1993; Bonadonna *et al*., 1998). This departure from simple exponential decay reflects the complex interplay between a number of different eruptive regimes and sedimentation processes, along with the influences of plume

height and inclination and water content, on these depositional modes. Many plume-generating eruptions also generate PDCs or deposit material by rooster-tail jetting.

These additional depositional regimes often contribute significant material to the near-vent region, yet I have no comparable dispersal models with which to compare thinning trends among these layers.

Units C and E combined make up approximately 80 % of the volume of material dispersed outside the ice cauldron (Table 3.4). Both visual observations and stratigraphy confirm that fallout from the oscillating 6-10 km high eruption column was the dominant process of particle transport during this time, but that there is also a contribution from successive PDC pulses. Consequently, the dispersal diagrams for these units follow a modified exponential thinning trend. The effects of the PDC component of dispersal is apparent on the semi-log plots of area$^{1/2}$ vs. thickness by forming a "hummocky" or stepped profile, representing occasional regions of localised over-thickening, particularly in the most proximal regions (Figs. 3.9, 3.10).

According to conventional models of plume dispersal, the first inflection point corresponds to the transition between sedimentation from the jet region and column margins to fallout from the umbrella region of the eruption column (e.g. Bonadonna *et al*., 1998). The first inflection point for units C and E is located at 1.9 km and 1.2 km from source, respectively. These values are consistent with expected distances of 1.4-2.4 km to the corner region for a plume that is between 6 and 10 km in height (Bonadonna and Phillips, 2003). However, it is important to recognise that the conventional models derive from an empirical relationship applied to Plinian eruptions. Equivalent models do not yet exist for small basaltic phreatomagmatic eruptions where the relationship between magma discharge, plume height and thinning trends are affected considerably by the action of PDC pulses. Furthermore, particle aggregation resulting in enhanced proximal sedimentation is a common effect in a wet plume environment (e.g. Gilbert and Lane, 1994).

The dispersal diagram constructed using total deposit thickness values (Fig. 3.14) parallels those features highlighted for units C and E. It most closely fits to a power-law trend, but may also be considered to display segmented exponential thinning. Consequently, the deposit as a whole "looks" very much like a fall deposit with

some minor proximal and localised over-thickening due to the influence of PDCs. This is consistent with our observation that PDCs and deposition by ballistic and jet fallout are volumetrically minor (<30 % of the tephra apron), yet significant. It also reveals that the main phase units, for which there is clear field evidence for concurrent deposition by fall and PDC, are dominated by a fall signature. Where thinning trends are plotted for tephra transported exclusively by density currents (i.e. units B, D, F and G) I find that the assumption of an exponential thinning trend is not valid (Figs. 3.9, 3.10). Our comprehensive empirical dataset reveals that the thinning trend of each of the density currents best fits a linear relationship, within the proximal region of deposition. At or near the transition to the medial regions of the deposit (close to the limits of dispersal for these units) the rate of thinning tails off rather than following the abrupt linear trend to zero thickness, presumably as the remaining fine ash drifts and settles. The significance of particle aggregation and the premature deposition of fine ash in the G2004 deposit is evidenced by the predominance of fine ash in proximal sections and the occurrence of numerous examples of coated clasts and accretionary lapilli. Most layers of the G2004 deposit contain between 60-80 wt. % ash less than 1 mm in diameter. Principal modes are usually in the 1 to -1 Φ range and secondary modes occur at 3-4 Φ. The ash was deposited in a notably wet environment and both accretionary lapilli and armoured clasts were observed within the deposit. This demonstrates that (i) the condensed water content within the PDCs is likely to have been 10-20 wt. % (Schumacher and Schminke, 1995) and (ii) that flocculation of fine ash was a significant factor in deposition in the near-source region. Additional factors that may also contribute to the premature deposition of fine material are particle adhesion, as demonstrated by the presence of coated clasts (e.g. Wilson and Head, 2007) and scavenging of fine ash by the condensation of steam within the plume or by atmospheric precipitation (e.g. Rose *et al*., 2008). G2004 took place in the winter and it snowed for part of the eruption. This process may therefore have also contributed to the premature deposition of fines. The G2004 deposit was comprehensively sampled soon after emplacement and there is very little mass beyond the glacier limit. Thus, any significant effect of secondary thickening in the medial regions of the deposit would have been readily identified. The predominance of PDC activity within the proximal area resulted in areas of localised over-thickening, attributed to pinch and swell morphology and lobe-by-lobe emplacement of the PDC deposits, along with the varying

contribution of deposition of fall versus PDC at any given location. However, this is not to be confused with the marked enclaves of anomalous thickness reported in the literature, which result from a decoupling between the near-vent fallout of coarse material from the eruption column and fallout of increasingly fine particles from the advected current or umbrella cloud (Ernst *et al*., 1996). If the cohesion and fallout of fine particles occur as a continuous process, then this could explain the absence of secondary thickening within the G2004 deposit.

The G2004 pyroclastic deposits differ from those produced by dry PDCs in terms of their lithology, bedding characteristics and sedimentary structures (in addition to the observed mechanisms of ejecta dispersal as previously described). Deposits of wet PDCs consist of largely of sideromelane and palagonite ash and lapilli-sized fragments but also incorporate abundant non-juvenile fragments, along with a variable component of accretionary lapilli. By contrast, deposits of dry PDCs consist largely of tachylitic cinders, scoria and pumice, along with juvenile lava fragments and traces of sideromelane ash (Heiken and Wohletz, 1985). Accretionary lapilli are absent from dry pyroclastic deposits. Diagnostic bedform textures for phreatomagmatic facies include near-vent breccias, which grade into sandwave, massive and planar-bedded tephra deposits with distance from the vent (Wohletz, 1983). These are generally fines-rich and very poorly sorted (Walker and Croasdale, 1972) and experience rapid palagonitisation. Dry PDC deposits exhibit similar transitions from bedded sandwave facies to massive and then planar bedding with distance from source. However, these are generally more thinly bedded, exhibit lower primary dips and anticipated to contain a much lower proportion of wall-rock fragments and fine ash (Heiken and Wohletz, 1985). Furthermore, dry PDC deposits are less cohesive than their phreatomagmatic counterparts and are therefore less likely to demonstrate soft sedimentary deformation textures, secondary thickening and the premature deposition of fine ash (Ernst *et al*, 1996). While wet PDCs are commonly dispersed at a low temperature (often <100°C), dry PDCs can achieve temperatures of up to 1000°C (Bryant, 1991). As a consequence, dry PDC deposits may contain clasts with fused outer surfaces and/or may exhibit welding textures (e.g. Sparks *et al*, 1973).

3.15 EMERGENT SUBGLACIAL VERSUS CONVENTIONAL PHREATOMAGMATIC ERUPTIONS

In terms of deposit stratigraphy and the principal mechanisms of fragmentation, this study suggests that the style of deposition is similar to that of other basaltic phreatomagmatic eruptions. The differences lie in the relationship between magma discharge and plume height and tephra dispersal. During the early part of the eruption, the majority of the eruption energy was apparently used to melt ice and to deposit tephra in the ice cauldron. The eruption followed the common pattern of basaltic eruptions from a single magma source of high initial discharge followed by gradual decline. However, as the eruption progressed, ice melting declined, making a proportionally higher fraction of the eruption energy available for plume generation. As a consequence, establishment of the plume was delayed and was significantly subdued relative to total magma flow rate for the first 15-20 hours. This effect diminished in the latter part of the eruption, during deposition of Unit E. Hence, a plume of similar size was maintained for some 30 hours despite a large drop in magma discharge over this period.

3.16 CONCLUSIONS

Both quantitative data and qualitative descriptions for the deposition of explosive products in the emergent, supraglacial environment are virtually non-existent in the literature. This remains a major obstacle to our understanding of eruption drivers, fragmentation regimes and proximal depositional processes for this end-member style of volcanism. Most subglacial eruptions will progress to become subaerial unless they are either of very small volume, or the ice cover is extremely thick. In the G2004 eruption, an appreciable proportion (~50 %) of the mass was deposited over the ice surface forming a tephra apron. In a somewhat larger event it is likely that the contribution to the tephra apron would be all the more pronounced. The tephra apron produced by emergent subglacial eruptions is not at all preserved in the geologic record. Therefore, when I study ancient subglacial volcanic constructs I need to be aware that our interpretations are based on a very incomplete stratigraphic record. Furthermore, I must be doubly cautious in our interpretations of ancient

phreatomagmatic tephra successions in these environments because syn- and post-eruptive remobilisation of deposits is significant.

The rare opportunity afforded by the rapid response to the G2004 event allows us to provide the first comprehensive characterisation of modes of activity and deposit architecture at this type locality for the small, basaltic emergent subglacial end-member style of volcanism. This work directly ties fine stratigraphic detail to visual observations and to seismic tremor and plume height records. It therefore provides a framework for the future interpretation of similar deposits and for event reconstruction in cases where such a wealth of complementary data sets is not available. Accepted models for characterising tephra dispersal often apply only to magmatic, Plinian layers or events or, rarely, to phreatoplinian eruption phases. As such, these are insufficient to describe small and/or wet eruptions, or to calculate volumes and mass discharge for those where transportation via density currents is a significant consideration. This represents the majority of hazardous, explosive events

CHAPTER 4:

GRAIN-SIZE DISTRIBUTION OF THE 2004 ERUPTION AT GRÍMSVÖTN VOLCANO, ICELAND

4.1 INTRODUCTION

The Icelandic tephra record reveals that, in the Holocene period, there have been more than 1450 explosive eruptions of mafic magma from ice-covered volcanoes (Thordarson and Höskuldsson, 2008). This eruption record is dominated by events on the Grímsvötn volcanic system, from which approximately 70% of the tephra layers originate (Óladóttir, 2009). According to Larsen *et al*. (1998), Grímsvötn's eruption frequency ranges from 3-13 eruptions per century at an average of 7-8 eruptions per century. If the 10 Grímsvötn central volcano eruptions that took place during the Laki event (Thordarson and Larsen, 2007) are included in this estimate, then the range is 3-17 eruptions per century (average about 9 per century). In the past 100 years, which roughly corresponds to the period of commercial aviation, there have been 25 confirmed eruptions from ice-capped volcanoes in Iceland (Table 4.1). The high frequency of eruptions, combined with increasingly heavy air traffic over the North Atlantic, presents a significant concern for regional aviation safety. Thus even small-volume eruptions in this region may have far-reaching economic and social consequences, in addition to the localised environmental hazard. Consequently, characterisation of the total grain-size distribution (TGSD) and the nature of the fine ash (i.e. <64 μm) fraction of explosive emergent subglacial eruptions is a high priority.

The TGSD of tephra-fall deposits is an important eruption parameter. By relating particle size to the initial volatile content of the magma and to the processes of magma-water interaction, the TGSD can be used to infer fragmentation mechanism and eruption style (e.g. Houghton and Wilson, 1998; Kaminski and Jaupart, 1998). The magma composition and composition of volatiles are of major importance in determining the dynamics of magma ascent during explosive eruptions (Papale, 1999), which will impact on the fragmentation regime, and thus the grain size distribution at

the point of eruption. In a magmatic eruption (i.e. one where fragmentation of magma is governed by the expansion and acceleration of volatile within the magma), it has been proposed that fragmentation is associated with a gas volume fraction of 0.75 (Sparks, 1977). The point at which this occurs is in turn a function of the initial volatile content of the magma (Dufek and Bergantz, 2005). It has also been proposed that more viscous magma will fragment at lower gas volume fraction (Papale, 1999).

Further to this, the TGSD provides constraints for plume sedimentation models (e.g. Bursik *et al*., 1992; Sparks *et al*., 1992). Upon eruption, the effective amount of continuous gas phase carrying the pyroclasts depends on their GSD. For example, where the pyroclast population is relatively coarse, a significant quantity of magmatic gas remains trapped in bubbles within pyroclasts and therefore does not contribute to the pyroclastic mixture. In this way, for a given mass flux and initial dissolved volatile content, changes in the GSD can have a strong effect on atmospheric column behaviour (Kaminski and Jaupart, 2001).

Finally, the TGSD is a crucial input parameter for tephra dispersal models which predict atmospheric dispersal of tephra, and are used to formulate hazard mitigation plans for potentially vulnerable populations (e.g. Barberi *et al*., 1990; Connor *et al*., 2001; Bonadonna *et al*., 2002).

The 2004 eruption at Grímsvötn volcano, Iceland (hereafter referred to as G2004) is the best-characterised eruption of its type to date (cf. Chap. 3). This eruption, which occurred from Nov 1st-6th 2004, commenced as a subglacial event within the Grímsvötn caldera which lies beneath the interior of the Vatnajökull ice cap. Between Nov 1st to 3rd, an eruption column was maintained at heights between 6-10 km above the vent and tephra was deposited via concurrent plume fallout and pyroclastic density currents, to produce an apron extending >50 km across the ice surface northwards from the eruption site (Fig. 4.1).

A number of factors make the G2004 deposit an exceptional case study for characterising typical grain-size distributions for a basaltic emergent subglacial event. During this event tephra was deposited on an essentially flat ice surface within the accumulation zone of the Vatnajökull glacier. Samples from the distal deposits (> 10 km from source) were collected very shortly after the cessation of activity. In the three years following the eruption samples were collected from the proximal deposit (within

4 km of the vent) in a systematic manner, and in accordance with the internal stratigraphy of the 2004 deposit. This comprehensive data set (mass per unit area values ranging from 2500 to 5 kg m^{-2} for samples collected between 300 m to 30 km downwind from the vent) provides good coverage for all regions of the deposit. Furthermore, detailed stratigraphic control permits a time-sensitive evaluation of the calculated grain-size characteristics within the context of eruption style and tephra dispersal.

This study aims to critically evaluate the grain-size characteristics of the G2004 event, taken here to represent a typical basaltic subglacial eruption in Iceland. I present a reconstructed TGSD for the entire tephra deposit produced by this eruption, as well as for individual tephra units. In this way, it is possible to correlate the tephra grain-size distribution with temporal changes in eruption style. Finally, I consider changes over distance in location-specific grain-size distributions in order to evaluate the relative roles of pyroclastic fall and density currents in subaerial transport and deposition of tephra. This data will aid future studies aimed at modelling the dispersal of fine ash from similar basaltic subglacial eruptions (e.g. future events from Grímsvötn, Katla and other ice-capped central volcanoes within Iceland).

Table 4.1: Recent eruptions from ice-capped volcanoes in Iceland. Data compiled from the online Global Volcanism Project resource (http://www.volcano.si.edu/).

Past 25 Years	
Volcano	Year of Eruption
Eyjafjallajökull	2010
Grímsvötn	1996*, 1998, 2004, 2011
Hekla	1991, 2000
Total: 6 eruptions	
Past 100 Years	
Volcano	Year of Eruption
Bárdarbunga	1910
Eyjafjallajökull	2010
Grímsvötn	1910, 1919, 1922, 1933, 1934 (2), 1938, 1954, 1983, 1996*, 1998, 2004
Hekla	1913, 1947-48, 1970, 1980, 1981, 1991, 2000
Katla	1918
Kverkfjöll	1929, 1959, 1968
Total: 25 eruptions	

* Refers to the subglacial Gjálp eruption, which is considered to have occurred on the Grímsvötn volcanic system (e.g. Gudmundsson and Sigmundsson, 1997; Sigmarsson *et al*., 2000).

Figure 4.1: (Top) Grain-size sample locations on the Vatnajökull glacier (red dots). Red line indicates the estimated margins of tephra dispersal according to Oddsson (2007). (Bottom) Close-up view of sample locations (red dots) within the Grímsvötn caldera (purple box in top panel). The outline of the ice cauldron margins is also shown.

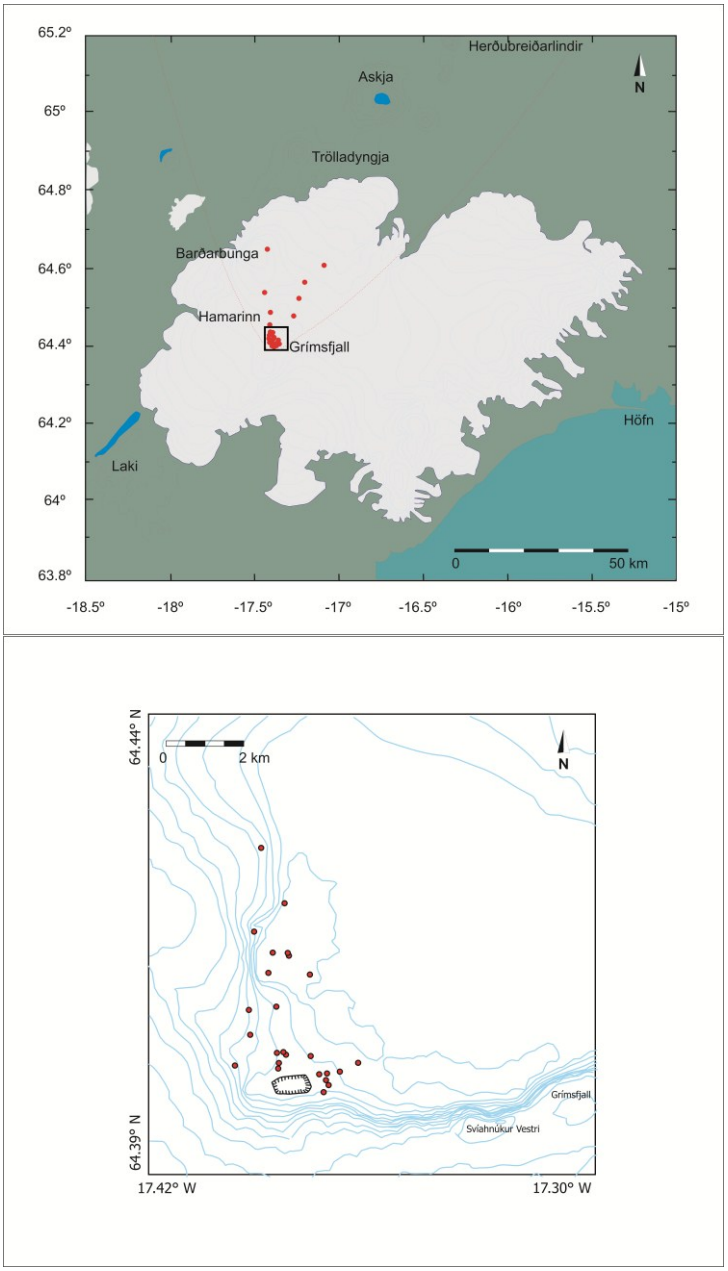

4.2 METHODS

4.2.1 LABORATORY METHODS

Each sample was dried for 24 hours in an oven set to 100˚C, in order to obtain correct, dry masses and to ensure that individual clasts were not adhered to one another by moisture. Samples were then divided into two equal portions according to the "cone and quartering" (or riffle) method of sample reduction. One such portion from each sample was hand-sieved from the -5 to 5 Φ size fractions, in ½ Φ intervals, generating a grain-size distribution in wt. %. The other portion was prepared for laser size analysis. This portion was hand-sieved, to remove all material greater than 0 Φ (1 mm) in diameter. The material <1 mm in diameter was stirred up before 30 ml of the deflocculant sodium hexametaphosphate ($(NaPO_3)_6$) was added to 0.5 g of sample. This mixture was stirred once again and then left, covered, to sit for 24 hours. Just prior to addition to the laser size analyser, each sample was processed in a sonic bath for 10 minutes and stirred once – in order to minimise the effects of particle flocculation.

Particle size analysis was performed using a Beckmann Coulter LS230, with PIDS detector and variable speed fluid module. This instrument measures the volumetric grain-size distribution of a sample by laser diffraction. Light, delivered by a laser, is passed through a chamber containing particles in the 0.04 μm-2000 μm size range which are held in suspension. The light is scattered as it strikes the surface of these particles and this scattered light is captured by a photo-detector array. Instrumental software calculates the particle size distributions by comparing the sample's scattering pattern with an appropriate optical model using a process of mathematical inversion (Mie theory).

Overlapping values of size distribution data generated by the two different methods (i.e. 0-5 Φ) were compared and used to splice the two sets of data together, generating a continuous size distribution from -5 to 10 Φ for each sample. If I assume a constant density for particles across all size bins <1 Φ, then the distributions generated by hand sieving (wt. %) and laser analysis (vol. %) are directly comparable. The assumption of a constant density for all particles across the entire grain-size is an approximation which introduces a marginal degree of error into the calculated overall distribution. Finer particles are likely to be denser than larger particles, particularly as the diameter of such particles approach and fall below the modal vesicle diameter.

Assuming a constant particle density across all size bins is therefore likely to result in an underestimation of the relative mass contribution (wt. %) of fine particles to the overall size distribution. Grain size data is provided in Appendix III.

4.2.2 RECONSTRUCTION OF THE TOTAL LAYER GRAIN-SIZE DISTRIBUTION

4.2.2.1 OVERVIEW

The Voronoi tessellation method of Bonadonna and Houghton (2005) has been demonstrated to provide the best approximation of TGSD compared to previous methods, and is now considered the standard approach (e.g. Bonadonna and Houghton, 2005; Scollo *et al*., 2007; Rose *et al*., 2008; Rose and Durant, 2009; Volentik *et al*., 2010). The Voronoi tessellation function uses Delauney triangulation to divide the tephra deposit into Voronoi cells, which enclose all grid points that are closer to the given sample point than to any other (Fig. 4.2). Each cell is attributed the grain-size distribution measured for its "determinative" point. The TGSD is then calculated as the area-weighted average of all the Voronoi cells over the whole deposit. This calculation was performed in Matlab, using the 'Voronoi_TOTGS' program (Copyright© 2004 C. Bonadonna and G. Marani; freely available online at http://www.ct.ingv.it/Progetti/Iavcei/grain-size.htm). Details of the method are given in Bonadonna and Houghton (2005).

4.2.2.2 SAMPLE LOCATIONS AND ASSIGNATION OF ZERO POINTS:

Sample locations are given in UTM format, plotted in xy space, to construct the Voronoi cells. Input files for the program include the location of sample points, the thickness of the layer at this location and the weight percent values for each clast-size class. It is necessary to also identify a series of zero mass points on the observed edge of the deposit. I have chosen to locate these along the 0.1 cm isopach lines from the unit isopach maps (Chap. 3). Samples from the proximal to medial regions of the deposit (i.e. within 4 km of the vent, Chap. 3) were collected and processed by myself, while "distal" grain-size data is provided by Björn Oddson's master's thesis (2007).

Figure 4.2: Sample locations and constructed Voronoi Tessellation cells for units A-G and the total deposit.

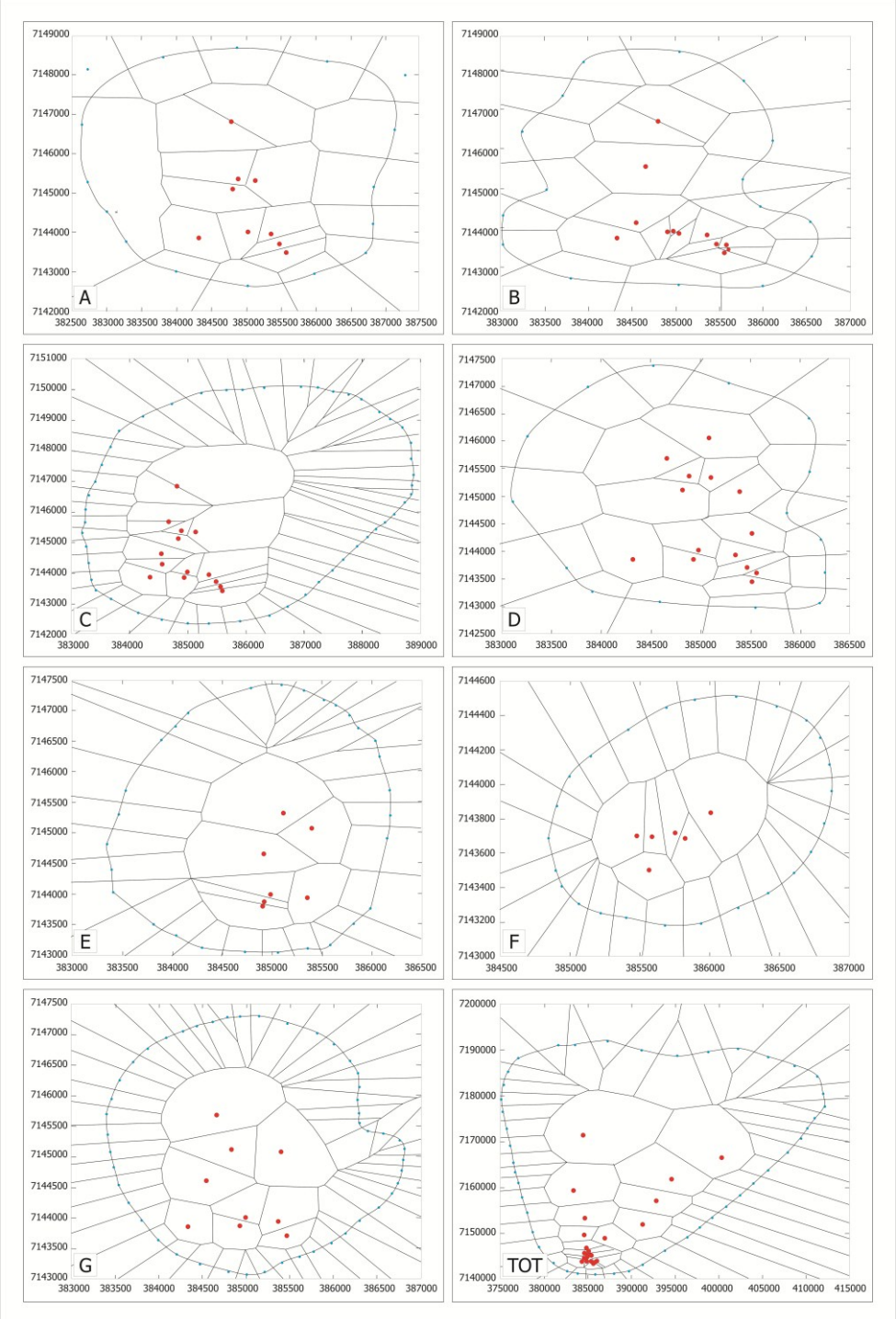

4.2.2.3 Approaches to calculating the total deposit grain-size distribution:

In order to evaluate the effects of a limited data set on the final result, the total grain-size distribution of the G2004 deposit was calculated in three different ways. In the first case (Distribution A), the "total" grain-size distribution was calculated using data from the proximal region of the deposit only (i.e. within 3.5 km from the vent). Then, the distribution was calculated by incorporating all proximal and distal grain-size data (i.e. from 300 m to 30 km from the vent; Distribution B). Finally, the proximal grain-size distribution was calculated in two different ways: (i) by performing a weighted average of the total unit grain-size distributions (Distribution A) which are generated by assigning a Voronoi cell to each sample (the proportion of the mass of the subaerial deposit attributable to each unit is given by Chap. 3) and (ii) by determining the total grain-size distribution at each location (Distribution C), weighted according to layer thickness and assigning a Voronoi cell per section (Fig. 4.2). The latter method uses a more limited data set as not every unit was sampled at each location. Only locations with complete sampling were used to determine distribution C, which is therefore based on fewer Voronoi cells.

Table 4.2: Summary of dispersal parameters and eruption style for each unit of the G2004 deposit, along with variation in proportions of fine and very fine ash.

	Proportion (wt. %) of fine ash (<2 Φ)	Proportion (wt. %) of very fine ash (<4 Φ)	Interpreted style of Activity	Thinning half-distance ($t_{1/2}$)	Duration (hours)
Total Subaerial Deposit	45 %	19 %	Tephra fallout from a high plume with alternating and simultaneous generation of pyroclastic density currents.	650 m (Average)	44.4
Unit A	35 %	12 %	Shower-like fallout generated by a short-lived phreatomagmatic explosion.	490 m (Proximal)	3.2*
Unit B	41 %	14 %	PDC generated towards the end of the short-lived explosion that produced Unit A.	490 m (Proximal)	3.2*
Unit C	43 %	19 %	Sustained deposition by pyroclastic fall from a high eruption column with concurrent PDCs.	1.52 km (Avg.) 520 m (Proximal) 4.5 km (Distal)	18.1
Unit D	40 %	17 %	PDC pulses generated by an interval of column collapse.	290 m (Proximal)	1.9
Unit E	48 %	24 %	Sustained deposition by pyroclastic fall from a high eruption column with concurrent PDCs.	1.63 km (Avg.) 190 m (Proximal) 5.96 km (Distal)	12.9
Unit F	45 %	22 %	PDC generated by directed collapse of eruption column E-ENE.	190 m (Proximal)	1.4
Unit G	43 %	12 %	PDC pulses generated at the vent without an associated eruption column.	400 m (Distal)	6.9

*Duration includes deposition of both A and B – it is not possible to tell definitively when A ended and B began (cf. Chap. 3)

4.3 RESULTS

The subaerial G2004 deposit consists of seven units in the proximal to medial dispersal area (Chap. 3). These eruption units are considered to span three phases of activity: (i) an initial phreatomagmatic burst, which generated shower-like fallout in the proximal to medial regions of the deposit (Unit A) followed by relatively dilute pyroclastic density currents (Unit B); (ii) the main phase of continuous uprush style activity in which an eruption column was maintained for periods of over tens of hours and tephra was deposited by concurrent tephra fallout and pyroclastic density currents (Units C and E, terminated by brief column collapse events represented by Units D and F); and (iii) a waning phase during which wet pyroclastic density currents were issued from the vents without establishing an eruption column at all. Units (C and E) account for approximately 80% of the total deposit, including the entire distal portion. However, although in many cases snowfall layers are intercalated with the tephra, it is not possible to accurately delineate the boundary between units C and E in the distal regions of the deposit. A summary of the activity represented by each eruption unit, along with thinning half distance values and the proportions of fine ash and very fine ash, is provided in Table 4.2.

Individual grain-size distributions are similar across the deposition units in that they are all polymodal, very poorly sorted (σ_Φ = 2.38-2.75) and slightly fines-skewed. Unit A is coarsest overall, with a median diameter of 0.90 Φ and Unit E is the finest with a median diameter of 1.75 Φ. The shapes of the total size distributions of individual units are quite consistent throughout the eruption as the principal and secondary modes for each unit have almost identical locations (i.e. at 0.5 – 1 Φ, 3 Φ and 4 Φ, respectively) with a fine tail extending to less than 1 micron (10 Φ) in diameter (Fig. 4.3). Statistical parameters for the total G2004 grain-size distribution, along with those of individual eruption units are summarized in Table 4.3.

For each unit, the overall shape of the grain-size distribution remains the same regardless of distance from source (Fig. 4.5). However, for units A to F the diameter of the principal mode decreases with distance from source according to a roughly logarithmic thinning trend (Fig. 4.6). The inverse relationship holds for Unit G (Fig.

4.6). This is probably a consequence of enhanced sedimentation of fine material within the very proximal deposit due to particle aggregation processes (see Chap. 3).

Figure 4.3: Near perfect linear correlation in a one-to-one ratio between total grain-size distributions calculated according to three different approaches.

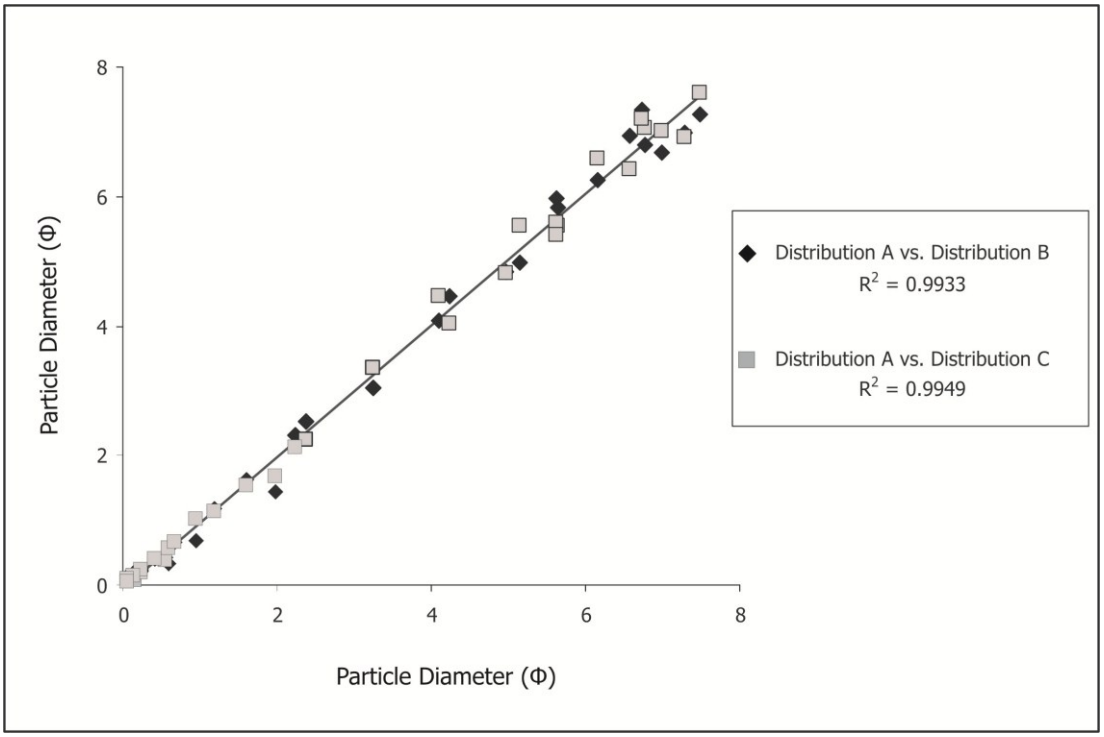

In figure 4.4 the observed fields for end-member pyroclastic fall, flow and "surge" deposits, after Walker and Croasdale (1972), are superimposed onto a plot of median diameter versus sorting for each unit and the total deposit. It demonstrates that the grain-size characteristics remain similar across different phases of the G2004 eruption, and that median diameter vs. sorting values cluster squarely in the area of overlap between end-member pyroclastic surge and end-member pyroclastic flow type deposits. Fig. 4.4 differs from Fig. 3.9 in that each point represents the median diameter and sorting value for the total layer grain-size distribution for each unit. In Fig. 3.9 each point represents the median diameter and sorting value for an individual, site-specific sample, corresponding to each eruption unit at several different localities.

The total grain-size distribution constructed by taking into account all grain-size samples within 30 km of the vent is virtually identical to the total proximal grain-size distribution (Figs. 4.3 and 4.8) except that the amplitude of finer grain-size modes (i.e. 3 Φ and 4 Φ) are enhanced by less than one weight percent. This is partly a consequence of the fact that the distal deposit accounts for only 30% of the mass of the tephra apron and partly due to the considerable overlap between the proximal and distal grain-size characteristics.

Figure 4.4: Total layer grain-size distribution for individual eruption units.

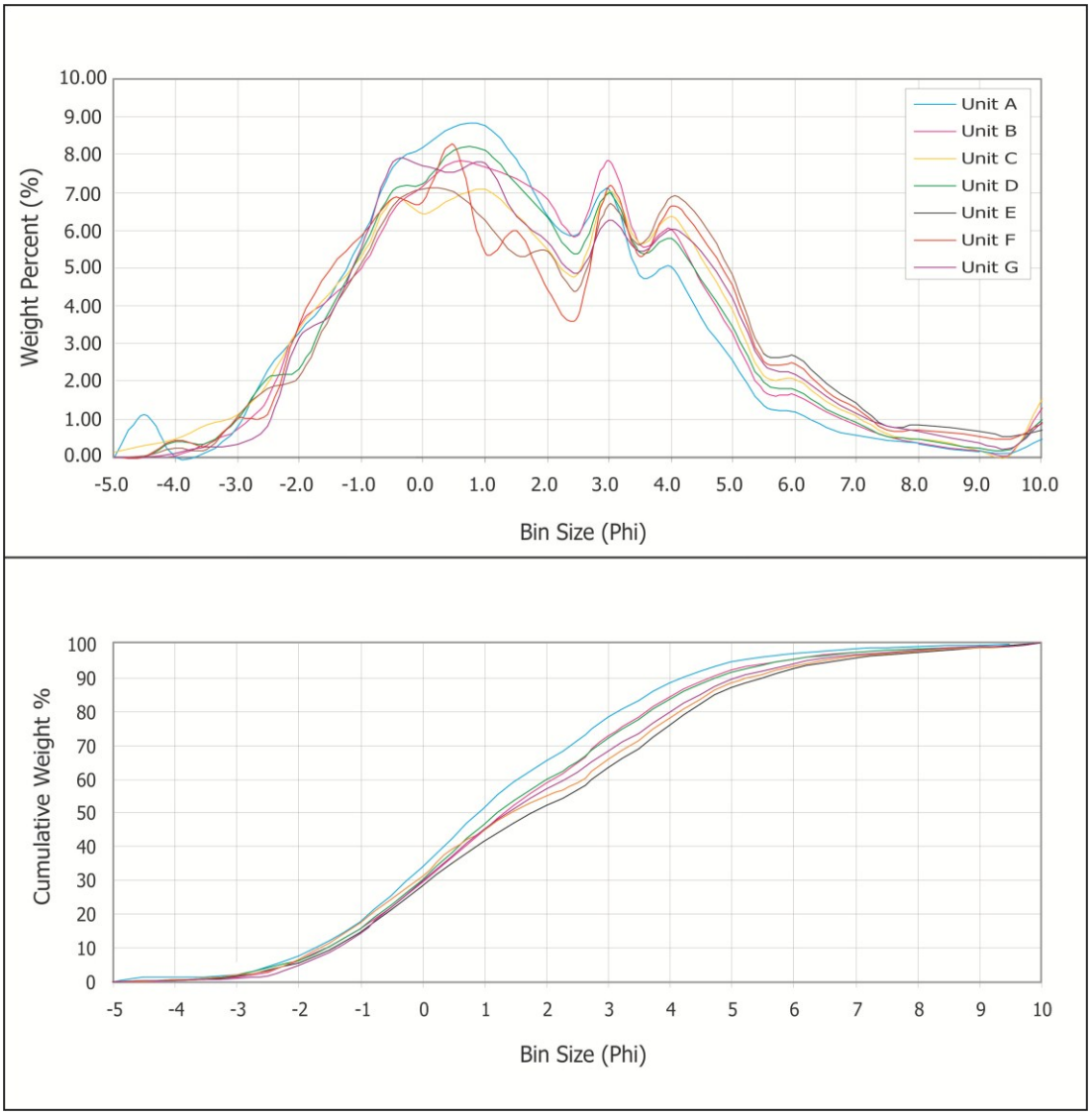

Figure 4.5: Median diameter vs. sorting characteristics of unit and total deposit grain-size reconstructions compared to observed fields for known end-member pyroclastic fall, flow, and surge deposits after Walker and Croasdale (1972).

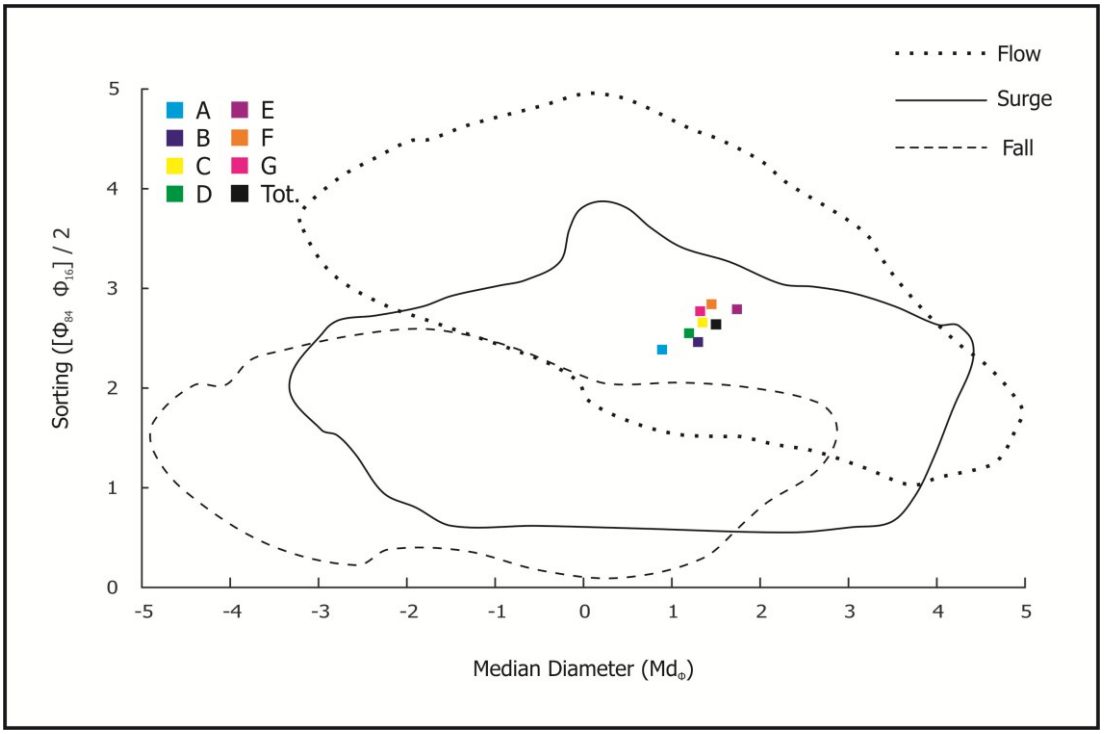

The total grain-size distribution for material in the proximal dispersal region (i.e. <5.5 km from the vent) is trimodal with a median diameter of 1.4 Φ. It is symmetrical but very poorly sorted (σ = 2.6) with Mode 1 located at 0.25 Φ, Mode 2 at 2.75 Φ and Mode 3 at 3.75 Φ. By contrast, the total grain-size distribution for material in the medial-distal dispersal regions (i.e. 5.5-30 km from the vent) is somewhat better sorted and is symmetrical and bimodal in shape. However, even at distance from source, the G2004 tephra is poorly sorted. The medial to distal tephra has a median diameter of 2.5 Φ. Mode 1 is located at 2.75 Φ and Mode 2 is at 1.75 Φ. In the distal region of the deposit, therefore, both the most coarse and the most fine modes represented in the proximal deposit are lost and the secondary mode at 2.75 Φ becomes dominant (Fig. 4.9)

Table 4.3: Statistical grain-size distribution parameters for the G2004 deposit calculated using GRADISTAT® (Blott and Pye, 2001), after Folk and Ward (1957).

	TOTAL DEPOSIT	UNIT A	UNIT B	UNIT C	UNIT D	UNIT E	UNIT F	UNIT G
Median Diameter (Md $_{\Phi}$)	1.50	0.90	1.30	1.35	1.20	1.75	1.45	1.35
Graphic Mean (Mz $_{\Phi}$)	1.58	1.08	1.40	1.47	1.40	1.83	1.60	1.60
Graphic Standard Deviation (σ_{Φ})	2.63 (very poorly sorted)	2.38 (very poorly sorted)	2.40 (very poorly sorted)	2.73 (very poorly sorted)	2.55 (very poorly sorted)	2.74 (very poorly sorted)	2.75 (very poorly sorted)	2.58 (very poorly sorted)
Graphic Skewness	0.05	0.12	0.06	0.06	0.12	0.05	0.08	0.14
Graphic Kurtosis	0.85 (platykurtic)	0.96 (mesokurtic)	0.92 (mesokurtic)	0.90 (mesokurtic)	0.93 (mesokurtic)	0.88 (platykurtic)	0.85 (platykurtic)	0.87 (platykurtic)
Mode 1 (Φ)	2.75	0.75	2.75	0.75	0.75	-0.25	0.25	-0.75
Mode 2 (Φ)	0.25	2.75	0.25	2.75	2.75	3.75	2.75	0.75
Mode 3 (Φ)	3.75	3.75	3.75	-0.25	3.75	2.75	3.75	2.75

Figure 4.6: Changes in grain-size distribution within each unit with varying distance from source. Black bars reflect most proximal section; the next most proximal section is shaded in grey; then white; and finally the most distal section is represented by pink bars. Distance from source is relative as not all units are represented at the same locations.

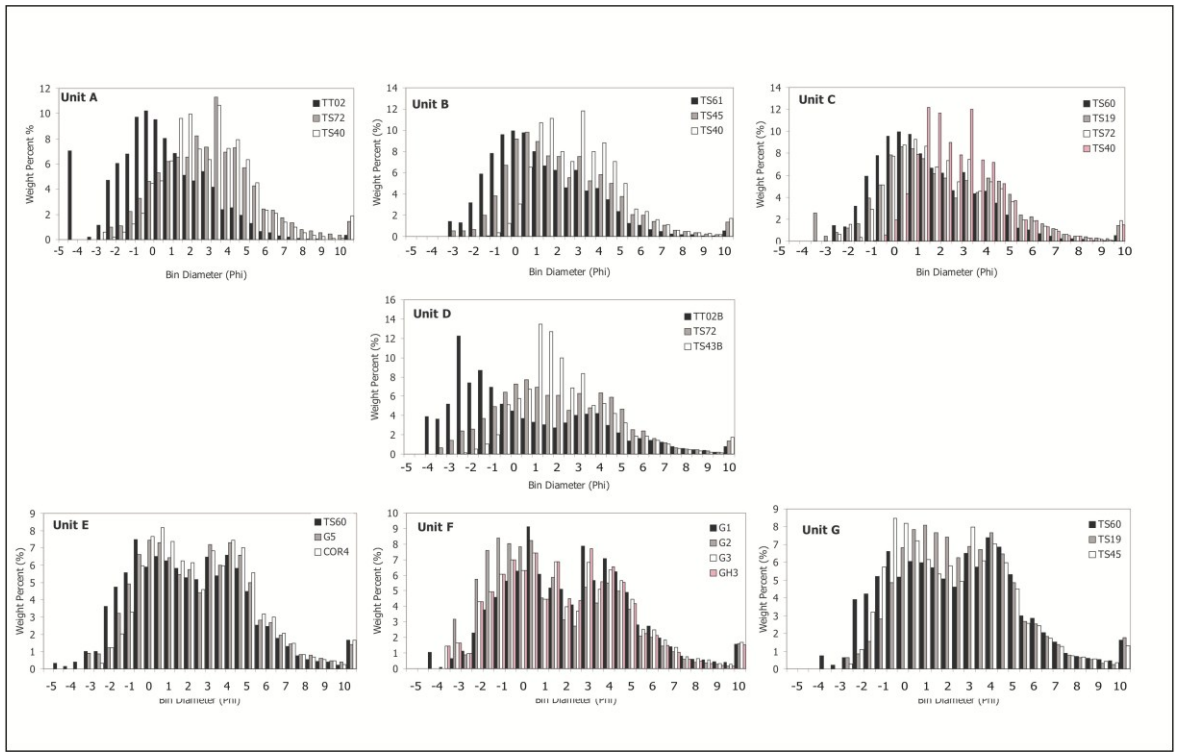

4.4 STATISTICAL ANALYSIS OF GRAIN-SIZE DISTRIBUTIONS

Analysis of grain-size statistics was performed using the GRADISTAT package which runs within Microsoft Excel (Blott and Pye, 2001). This program calculates median and mean diameter, mode, sorting and skewness of each distribution according to both the method of moments and the Folk and Ward graphical parameters (1957). A statistical description of each distribution is provided in the results section of this paper.

Figure 4.7 shows that there is near perfect linear correlation (R^2 = 0.99) between the values within each grain-size interval for the total deposit to that representing the proximal deposit only. Similarly, results generated by the two different approaches (i.e. calculating the total grain-size distribution by combing unit distributions vs. by combining total distributions at each location) are virtually identical (R^2 = 0.99; Fig. 4.7). Pearson's Chi squared test was performed as a further test of the significance of the differences between the proximal vs. total grain-size distribution and the distribution calculated according to the two different methods. At the 95% confidence interval, the differences between each distribution were highly insignificant ($\Delta 2$ (1, N = 31) = 1.00, p = .05).

Figure 4.7: Changes in modal diameter with distance from source for each eruption unit (A-G).

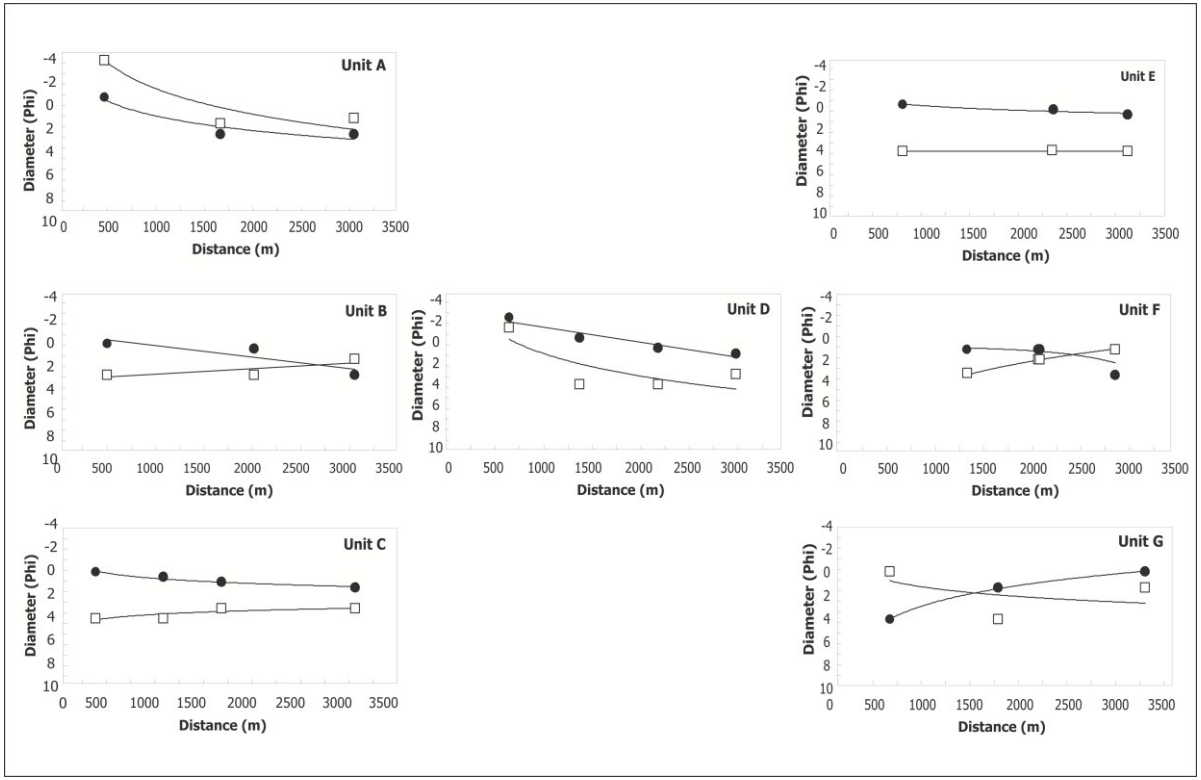

Figure 4.8: Comparison of total grain-size distribution calculated for the G2004 deposit with and without taking medial to distal samples into account

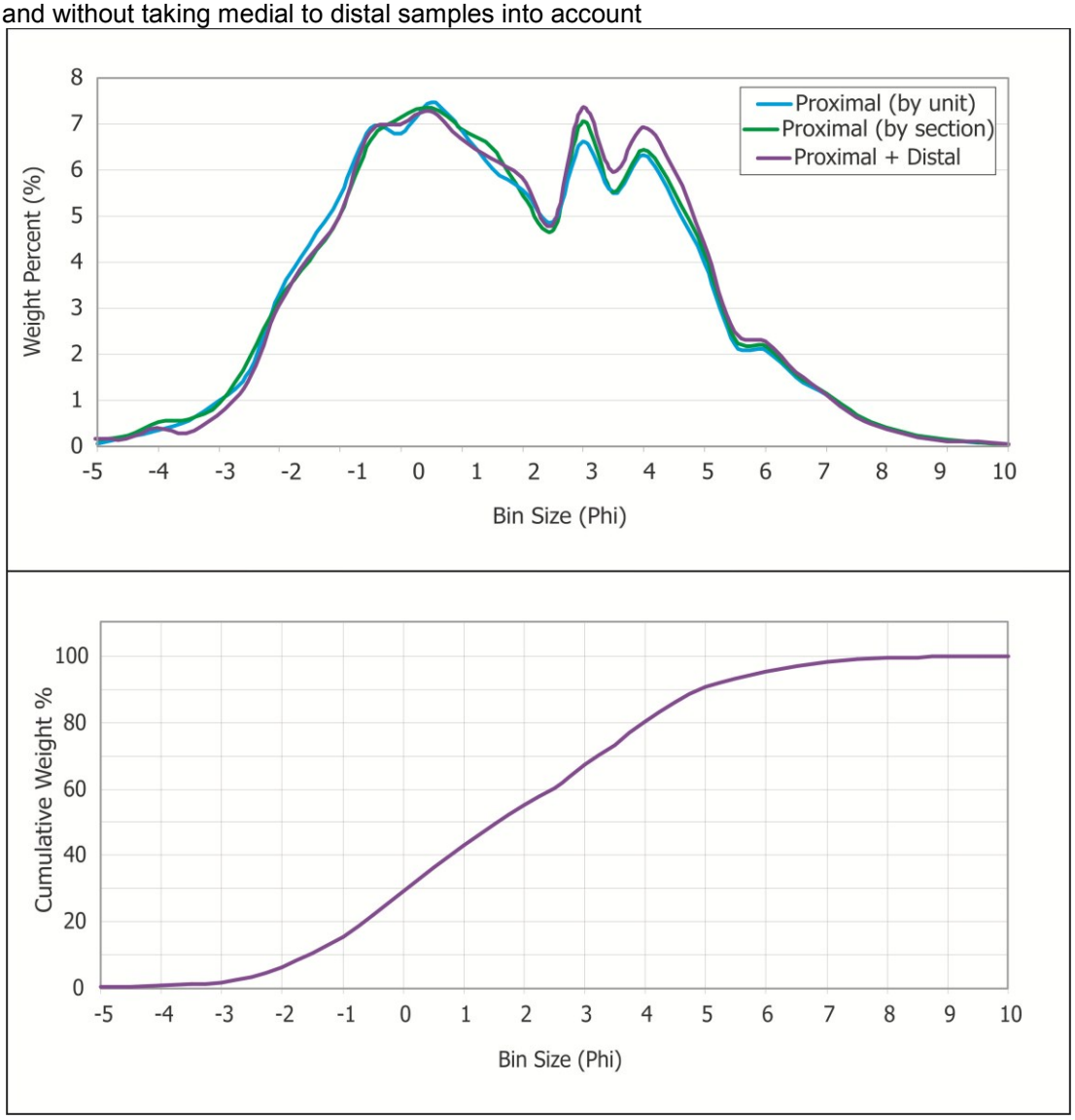

4.5 DISCUSSION

The 2010 eruption of the subglacial Eyjafjallajökull volcano (E2010) caused unexpected and widespread disruption to aviation in Europe for several days. The principal reasons for this disruption were limitations in modelling atmospheric dispersal and removal rates of fine ash as a consequence of poorly defined source parameters for this style of eruption (Larsen *et al*., 2010). However, as demonstrated by Davies *et al*. (2010), such small-volume emergent subglacial events are neither infrequent nor extraordinary occurrences in Iceland. In fact, based on records of eruption history and frequency of events (e.g. Larsen *et al*., 1998) it is realistic to expect that 2-5 eruptions from Iceland's ice-capped volcanoes will occur within the next decade – notably from the large volcanoes of Grímsvötn, Bárðarbunga and Katla.

Both the 2004 and 2011 eruptions at Grímsvötn caused flights to be grounded in Scandinavia and Northern Europe. As Grímsvötn is the most frequently erupting volcano in Iceland and the bulk of Icelandic magmatism is basaltic in composition (Larsen *et al*., 1998), the G2004 event provides a very relevant case study for use in defining appropriate source parameters and typical release scenarios for use in VAAC tephra dispersal models.

Witham *et al*. (2007) used eruption parameters that were available in real time over the course of the G2004 eruption (i.e. vent location, elevation of the crater, and plume heights) to compare a number of VAAC atmospheric dispersion models. They found that the forecasts yielded by each model were in good agreement with one another but highlighted the need for accurately and precisely defined source parameters and appropriate default eruption scenarios to be developed in order to improve tephra dispersal forecasts, for which the uncertainties are rather high. For example, during the G2004 event the error in measured plume heights alone was ± 4 km (Oddsson, 2007). A particular issue highlighted by this study was that existing standard protocols provided no clear choice for grain-size parameterization prior to eruption onset and that such information is difficult to obtain with an eruption already in progress (cf. also Larsen *et al*, 2010). This study of the G2004 deposit places good constraints on the initial grain-size distribution that may be expected from a small-volume, basaltic, emergent subglacial eruption in Iceland - data that has not previously been available for application to atmospheric dispersion models for volcanic ash.

Our results for the subaerially dispersed component of tephra from the subglacial G2004 event reveal that its size distribution is similar to that of basaltic phreatomagmatic eruptions previously described in the literature (cf. Walker, 1980; Self *et al*., 1980; Wohletz, 1983; Houghton and Hackett, 1984; McPhie *et al*., 1990; and Zimanowski *et al*., 2003) in several key ways: the abundance of fine ash (45%) and very poor sorting – even in distal locations (Fig. 4.3) - and transport via a combination of plume fallout and pyroclastic density currents (Cole *et al*., 2001; Houghton *et al*., 2004; Chap. 3). The modal diameter of the G2004 fine ash fraction (i.e. < 64 μm or 4 Φ) is similarly consistent with literature reports that fine ash modes in phreatomagmatic deposits occur in the 4 Φ to 5 Φ interval (e.g. Heiken, 1972; Self and Sparks, 1978; Wohletz, 1983; Dellino *et al*., 1995).

Assessment of the impact of incorporating (or failing to incorporate) the distal tephra deposit in the total layer grain-size reconstruction (see section 4.2.2.4) has implications for assessing the potential error introduced by selecting the 0.1 cm isopach as the deposit boundary. The volume of ash deposited outside of the 0.1 cm isopach is very small compared to that within it. According to Oddson (2007) 95% of the deposit mass was included in the 0.5 kgm^{-2} isomass line which, factored by the measured average deposit density of 1170 kgm^{-3}, corresponds closely with the 0.05 cm isopach. The unaccounted for volume of ash is therefore likely to make very little impact on the reconstructed grain-size distribution, given that taking the entire distal deposit into account (30 % of the overall deposit mass) is shown to make no statistically significant difference. Compared to the proximal (< 5 km from source) distribution, the coarsest mode of the distal (5-30 km from source) distribution is shifted from 1.5 Φ to 2.5 Φ (i.e. the modal diameter halves), the finer mode at 3.5 Φ is greatly augmented and the finest mode at 4.5 Φ is slightly augmented (Fig. 4.9). The expectation therefore, is that if it were possible to incorporate all the material deposited more than 30 km from the vent (along with that which remained aloft in the atmosphere) the effect on the total distribution would be that the modes at 1.5 Φ and 2.5Φ would become marginally smaller, along with a slight increase in the modes at 3.5 Φ and 4.5 Φ.

The principal benefit of looking at the reconstructed total grain-size distribution in comparison to site specific grain-size distributions is that by

recombining data from all regions of the deposit in a representative manner, the transport signature is effectively filtered out of the distribution. In the first instance, this enables us to more accurately assess the proportion of fine ash released at the vent. From a hazard mitigation perspective this is essential for assessing the potential dispersal and concentrations of ash in the atmosphere, where using site-specific results could introduce substantial error as selective removal or concentration of certain size fractions by transport processes will generate modified size distributions that are not representative. Secondly, the influence of sorting by transport processes is to obscure the true nature of the initial fragmentation-generated distribution so the total layer grain-size distribution is of great value to any study which aims to assess magma fragmentation and conduit dynamics (see Chap. 5).

While the high proportion of fine ash within the G2004 deposit can be attributed to enhanced fragmentation via phreatomagmatic mechanisms, the presence of abundant water within the eruption column had a number of effects, all of which contributed to limiting tephra dispersal. In the first instance, the dispersal of fine ash within the atmosphere was limited by relatively low (6-10 km) plume heights (Chap. 3). Secondly, oscillations in energy produced by phreatomagmatic explosions, combined with the presence of water, resulted in a temporally unsteady plume which contributed to the generation of pyroclastic density currents with limited run out distances (compared to a lofted plume) (Chap. 3). Finally, the high moisture content of the plume enabled enhanced aggregation of fine particles. The most frequently identified examples within the G2004 deposit were simple ash clusters. However the deposit also contained abundant coated and armoured clasts along with rare rim-type accretionary lapilli (see Chap. 3) - all contributes to premature fallout of the fine size fractions closer to source (e.g. Gilbert and Lane, 1994; Bonadonna *et al*., 1998; Textor *et al*., 2006; Scollo *et al*., 2007;Volentik, 2010).

Within the G2004 deposit more than half of the tephra removed from the atmosphere via sedimentation within 5 km of the source was less than 500 microns in diameter (Fig. 4.3) - a threshold below which the majority of particles are expected to become incorporated into a range of aggregate types (Lane *et al*., 1993). Particle aggregates have been described from fall (e.g. Cole and Scarpati, 1993), end-member flow (e.g. Schumacher and Schminke, 1991) and end-member surge (e.g. Scolamacchia

et al., 2005) deposits. Particles incorporated into an aggregate have been shown to attain much greater fall velocities than single particles due to their larger dimensions and internal porosity, which allows fluids (usually water) to flow through them (Lane *et al*., 1993). This results in the removal of fine particles from the atmosphere much sooner (or closer to source) than would be expected if they were deposited individually. This effect can have considerable impact on deposit thinning trends. The anticipated deposit geometry for tephra fallout from a high plume is that it will produce a steep proximal segment characterised by exponentially thinning of lapilli to coarse ash size fragments (i.e. >2 mm and with a particle Reynolds number >500), which will grade into a power law thinning trend in the distal sector, where particle dimensions are finer (< 2 mm) and settling behaviour is characterised by Reynolds numbers <0.4 (Bonadonna *et al*., 1998). However, particle aggregation effects result in aberrations from the anticipated trends as more material is deposited closer to source and the exponential thinning relationship may be modified. A prominent example of the unusual thickness trends generated by particle aggregation is the presence of a secondary maximum on a profile of distance versus deposit thickness, such as has been demonstrated at Mount Saint Helen's, USA (Brazier *et al*., 1983) and Fuego, Guatemala (Rose *et al*., 2007).

Figure 4.9: Reconstructed "total" grain-size distribution for the medial to distal region of the G2004 deposit (i.e. 5.5-30 km from source). The proximal "total" grain-size distribution is also shown shaded in grey for comparison.

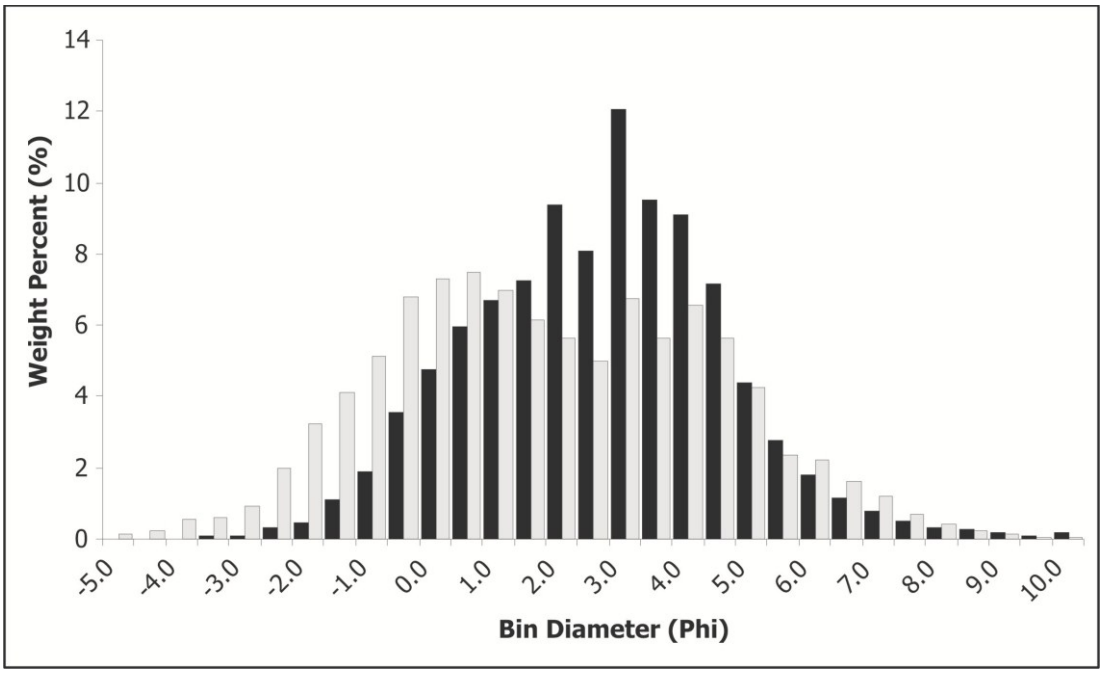

Particle aggregation effects within the G2004 deposit are collectively demonstrated by the high proportion of fine ash found even in the most proximal sections (Fig. 4.6) and the gradual changes in modal diameter with distance from source (Fig. 4.8). The effect of enhanced proximal sedimentation of fine material on the grain-size distribution is particularly apparent in Unit G where the modal diameter actually increases with distance from source (Fig. 4.8) due to the presence of core-type accretionary lapilli in the most proximal sections (i.e. location TS60 and TS19).

The importance of aggregation for premature removal of fine ash was also demonstrated during the E2010 eruption during which syn-eruptive rain and snowfall contributed to flushing fine ash from the plume (Taddeucchi *et al*., 2011). Such enhanced proximal sedimentation of fine material was not anticipated, and this contributed to the extended duration of flight bans imposed by the London VAAC (T. Thordarson, personal communication, May 2011).

The fact that the classic magma discharge-plume height relationship (Sparks *et al*., 1997) overestimates the mass eruption rate relative to plume height for phreatomagmatic eruptions has previously been recognised in the literature (e.g. Witham *et al*., 2007; Larsen and Eirkisson, 2008). This effect has also been noted for

the G2004 event (Oddsson, 2007; Chap. 3). Phreatomagmatic plumes are very rich in steam. Hence the condensation of steam to water (latent heat) will return some of the lost magma heat energy back to the system, enhancing the buoyancy of the mixture and thereby producing plumes that are higher than expected for a given magma discharge (Mastin, 2007). An additional complication is that there is poor consensus as to what researchers define as the volcanic "plume". Whether every component of the system (i.e. the steam and the ash-laden parts of the column and plume) is included, or the tephra-bearing regions only, will impact estimates of mass eruption rate and tephra dispersal since steam-rich plumes will rise higher than the more ash-rich parts. Observations during the E2010 event reveal that the difference in plume height in some cases is on the order of a factor of 2 (Thordarson, personal communication, 2010).

However, in MFCI-driven phreatomagmatic eruptions, a considerable portion of the thermal energy stored in the magma is taken up by the fragmentation process and, in the case of eruptions into a glacial environment, by heating the surroundings (Gudmundsson *et al*., 2010). Hence, the thrust mixture is colder in these eruptions compared to that of magmatic events. This counterbalances the effects of adding latent heat from steam condensation which may result in less heat being available to drive convection, which would make the plume less buoyant. Here the relative abundance of solid material in the erupted mixture - especially a relatively high abundance of "cold" ash is an important factor.

The effects of particle aggregation and particle density within the plume are particularly relevant to phreatomagmatic plumes. Therefore, our understanding of these two factors has significant implications for the application of tephra dispersal models in hazard mitigation and aviation safety in the event of future eruptions of basaltic magma from ice-capped volcanoes in Iceland.

4.6 CONCLUSIONS

Small volume (<1 km^3 DRE) basaltic phreatomagmatic eruptions from the subglacial Grímsvötn central volcano generate a very poorly sorted, polymodal, fines-rich tephra size distribution in which relatively low plume heights, PDC activity and enhanced proximal sedimentation of fine particles as aggregates means that the bulk of the material is deposited close to source (<5 km). Eruptions such as the G2004 event are a common occurrence in Iceland. There have been 27 eruptions from ice-capped volcanoes since 1900 (Table 4.4) and it is anticipated that several more will occur within the upcoming decades. Since comprehensive grain-size data are impossible to attain during an explosive volcanic event, the data provided in this paper is critical for establishing the expected input parameters for incorporation into the default release scenario into VAAC ash dispersal model forecasts for this style of event in an emergency response situation.

Table 4.4 Eruptions from ice-capped volcanoes in Iceland, 1900-2011.

Volcano	Eruption Dates
Bárdarbunga	1902-1903; 1910
Eyjafjallajökull	2010
Grímsvötn	1902-04; 1910; 1919; 1922; 1933; 1934 (x2); 1954; 1983; 1996*; 1998; 2004; 2011
Hekla	1913; 1947-48; 1970; 1980; 1981; 2000
Katla	1918; 2011
Kverkfjöll	1929; 1959; 1968

*The 1996 Gjálp eruption is considered by most to have originated from the Grímsvötn system – however, a relationship between this event and the Bárdarbunga volcano is also implicated.
implicated.between this event and the Bárdarbunga volcano is also

CHAPTER 5

GRAIN-SIZE AND COMPONENT DATA – IMPLICATIONS FOR FRAGMENTATION OF THE G2004 MELT

5.1 INTRODUCTION

It has been demonstrated that there is a fundamental difference between the particle size distributions generated by magmatic versus phreatomagmatic deposits - the latter having a broader, polymodal grain-size distribution which incorporates a much greater abundance of fines (e.g. Self and Sparks, 1978; Walker, 1980, 1981; Barberi *et al*., 1989). This has led to the general conclusion that magma is fragmented much more efficiently in phreatomagmatic eruptions compared to magmatic eruptions. Some workers have credited this difference to a direct outcome of the MFCI (molten fuel-coolant interaction) process which drives phreatomagmatic eruptions (e.g. Wohletz; 1983; Zimanowski, 1998; Büttner *et al*., 1999; Morrissey, 2000). However, until now, sufficient data to generate a whole-deposit grain-size distribution has not been available for any basaltic phreatomagmatic eruption. Site-specific (SGSDs) distributions have been modified (size fractionated) by transport and deposition processes, and therefore are not fully representative of the grain-size populations which are generated by fragmentation of magma within the conduit.

I have reconstructed the total layer grain-size distribution of the total G2004 deposit (TGSD) and that of specific units within it. The sorting effects of transport and deposition have been effectively eliminated because samples from all areas of the deposit are recombined in representative proportions (Bonadonna *et al*., 2005). The resulting particle size distribution is therefore directly related to the intensity, efficiency, and specific mechanisms of magma fragmentation (e.g. Sparks *et al*, 1981; Parfitt, 1998; Zimanowski *et al*., 2003).

Based on comparing the reconstructed TGSD and total unit data with SGSDs, this study aims to address the following: (i) what is the role of magma fragmentation

versus tephra transport in generating the size distributions I observed at individual sites and how do these change as a function of distance from source?

(ii) What were the nature and modes of magma fragmentation within the G2004 eruption?

(iii) Is ash generation in phreatomagmatic eruptions driven by MFCI interactions?

5.2 BACKGROUND

The grain-size characteristics and textural features of basaltic phreatomagmatic deposits have been studied since the early 1970s (e.g. Heiken, 1972; Walker and Croasdale, 1972; Waters and Fisher, 1971). It is widely appreciated that the deposits of Surtseyan, and other explosive mafic phreatomagmatic eruption styles, are distinguished from their purely magmatic counterparts by their finer average grain-size, poor sorting and the variable vesicularity of the fragments. The median diameter of even the most proximal Surtseyan deposits is typically less than 1 mm, whereas those of Strombolian eruptions and Hawaiian lava fountains are on the centimetre scale (Walker, 1971; Walker and Croasdale, 1972; Fisher and Schmincke, 1984). The morphology of clasts produced by phreatomagmatic mechanisms (i.e. dominantly equant and blocky in form) also contrasts with the rounded or elongate droplet and threads and bubble wall morphologies identified within dry, magmatic deposits.

The differences between deposit characteristics of magmatic and phreatomagmatic eruptions reflects a fundamental difference between their respective driving mechanism and fragmentation regimes. The morphology and grain-size characteristics of phreatomagmatic deposits have traditionally been interpreted in the context of discrete vapour explosions (Wohletz, 1983; Zimanowski, 1998; Büttner *et al*., 1999), which stems from observations that many observed Surtseyan-type eruptions eject tephra via a rapid series of intermittent explosions (Moore, 1967; Thorarinsson, 1967). Colgate and Sigurgeirsson (1973) and Peckover *et al*. (1973) suggested that these phenomena were analogous to vapour explosions recognized in industrial settings, commonly referred to as molten fuel coolant interactions (MFCI). MFCIs

involve heat transfer from, and break-up of, a hot melt upon mixing with a cooler, vaporisable liquid.

The role of vapour explosions in phreatomagmatic eruptions has been subsequently investigated by a number of workers (Wohletz and McQueen, 1984; Zimanowski *et al*., 1991; Zimanowski *et al*., 1997a; Büttner and Zimanowski, 1998; Trigila *et al*., 2007). Zimanowski and co-workers generated explosions by shooting a projectile into a crucible of magma into which water had been injected. The explosion trigger mimics a pressure wave which collapses the insulating vapour film (thermal detonation). Thermal detonation occurs over a timescale of milliseconds or less and the following explosion generates powerful shock waves (Zimanowski *et al*., 1997b).

Two primary mechanisms are invoked for fragmentation by phreatomagmatic explosions (Wohletz, 1983):

(1) Where either Rayleigh-Taylor or Kelvin-Helmholtz instabilities form at the melt-water interface, asymmetric film collapse results. This enables water jets to penetrate the melt which produces convolute ("mossy") fragments with high surface areas. Rapid heat transfer is followed by a vapour explosion which generates new areas of contact and/or emits a shock wave, leading to further fragmentation (Fig. 5.1).

(2) The superheated vapour film either collapses or expands explosively, generating stress waves which propagate through the melt. If these exceed the bulk modulus of the melt then it will fracture in a brittle fashion producing blocky, equant fragments (Fig. 5.1).

Figure 5.1: Illustration of magma fragmentation by fluid instabilities and brittle fracture by the passage of shock waves (after Wohletz, 1983).

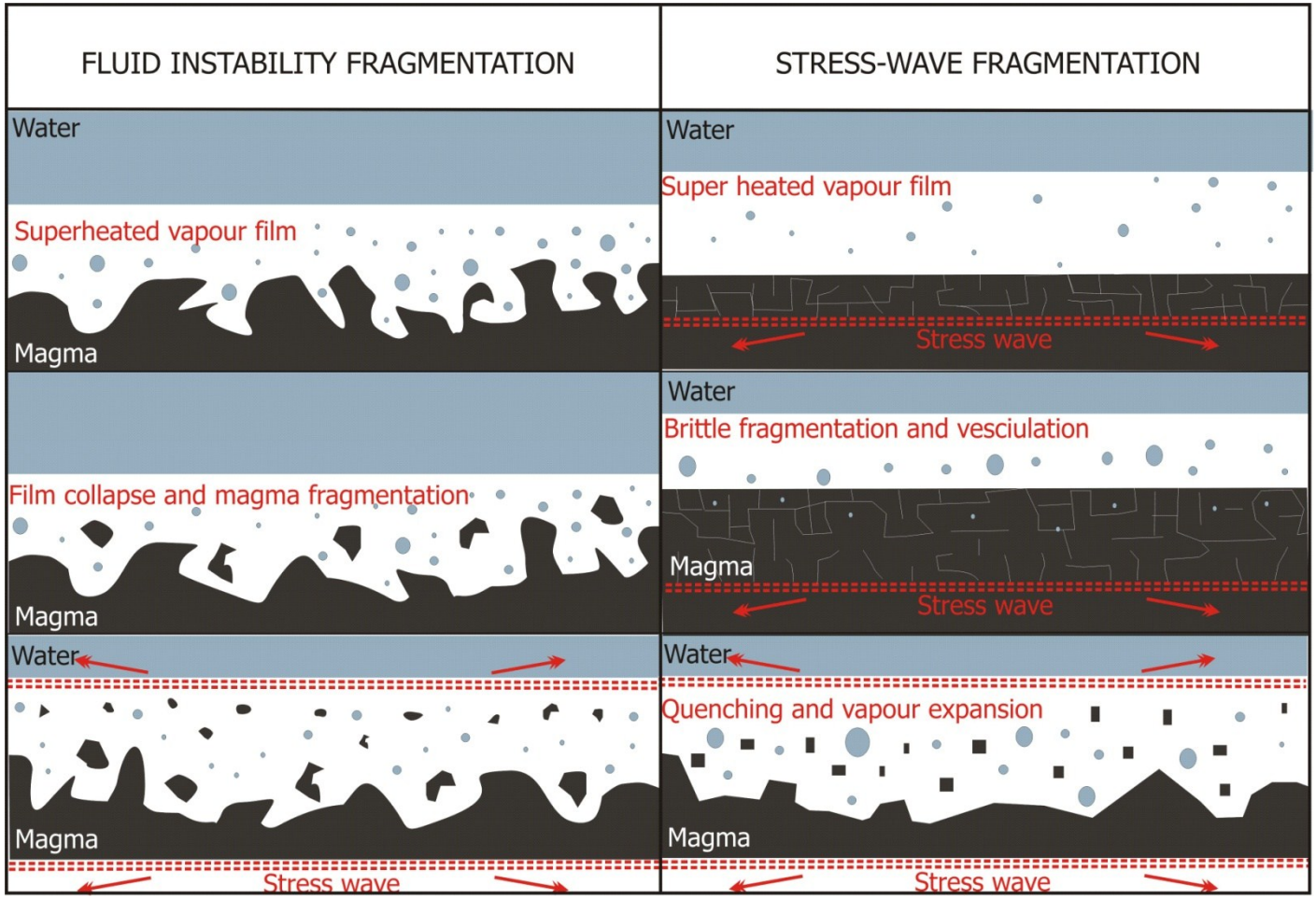

5.3 METHODS

5.3.1 GRANULOMETRIC ANALYSIS

Granulometric analyses of 230 bulk tephra samples were performed using a combination of sieve and coulter counter techniques, which are described in detail in Chapter 4. The size distribution of pumice layers was determined from photographs according to the number density of clasts within a given size range per 100 cm^2. This method is described in detail in Appendix IV.

Inman (1952) parameters are used to express grain-size characteristics: Md_Φ (median diameter = Φ_{50}); σ_Φ (sorting = $[\Phi_{84} - \Phi_{16}]/2$); along with Folk and Ward's (1957) inclusive skewness parameter ($Sk_I = ([\Phi_{16}+\Phi_{84}-2\Phi_{50} / 2(\Phi_{84}-\Phi_{16})] + [\Phi_5+\Phi_{95}-2\Phi_{50} / 2(\Phi_{95}-\Phi_5)])$) and graphic kurtosis ($KG = (\Phi_{95}-\Phi_5)/2.44(\Phi_{75}-\Phi_{25})$). Table 5.1 relates descriptive terms (e.g. lapilli, coarse ash, very fine ash etc.) to specific size intervals.

Table 5.1: Quantification of size terminology used to describe fragmented volcanic ejecta (tephra).

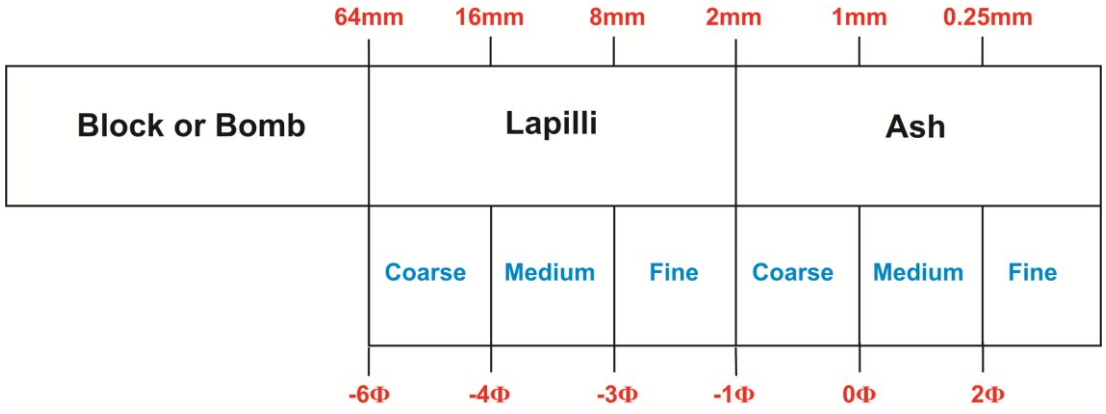

5.2.1.1 Sequential Fragmentation-Transportation (SFT) Analysis

Phreatomagmatic eruptions commonly produce complex, polymodal size distributions (e.g. Houghton *et al*. 2004, Dellino *et al*., 1995). Wohletz *et al*. (1989) posit that complex and polymodal tephra size distributions are the product of a sequential process of fragmentation and transportation, by which the parental magma mass is broken up into increasingly smaller mixtures of daughter particles then sorted according to mass (and fluid dynamic properties, e.g. Bonadonna *et al*., 2002). The sequential fragmentation-transportation (SFT) theory predicts that integration of the results from each step in the sequence will produce a distribution with apparent resemblance to the log normal and Weibull distributions (Wohletz *et al*., 1989; Wohletz and Brown, 1995). Grain size distribution functions derived by SFT analysis fit GSD cureves from pyroclastic deposits better than commonly-used empirical log-normal functions (Wohletx et al., 1989). By inverse application of the SFT theory, fragmentation and transportation mechanisms can therefore be constrained by measurement of grain-size data. SFT analysis and software have been successfully applied in numerous previous studies in order to understand volcanic source materials and their size fractionation by transport (see Wohletz *et al*., 1995; Gomez-Tuenaand Carrasco-Nunez, 1999; Taddeucci and Wohletz, 2001 and Taddeucchi and Palladino, 2002 for recent applications to pyroclastic deposits).

SFT analysis was applied here to measured grain-size distributions from the G2004 deposit in order to simplify complex grain-size distributions into end-member sub-populations. The advantage of this approach is that not only does it pinpoint representative grain-size fractions for component analysis (i.e. the subpopulation modes), but it also permits an assessment of the proportion of the sample that is encompassed by each subpopulation, which in turn allows identification of the fragmentation signature and determination of the efficiency of the fragmentation process (Dellino *et al*., 1995). I used the SFT software (©KWARE; University of California, 2000), which allows a user-interactive discrimination of the subpopulations of a measured size distribution and then describes them in terms of three parameters: weight fraction, mode and dispersion. "Weight fractions" reflects the relative proportion of the total size distribution that is contributed by each subpopulation, "mode" is the modal size represented within each subpopulation distribution and "dispersion" describes the shape of a subpopulation within a grain size distribution in terms of its location, breadth and skewness. The dispersion parameter gives an

indication of the degree of processing (i.e. increasing communition by the fragmentation mechanism or increased sorting by the transport mechanism) undergone by the subpopulation. With increased processing the distribution becomes finer and more peaked (Taddeucchi and Palladino, 2002).

It is possible to assign a maximum of six sub-populations with the mass incorporated into each totalling 100%. For each of the total layer grain size distributions the overall size distribution was deconstructed into individual component subpopulations which were then described in terms of the three SFT parameters. In this analysis, sub-populations are deemed insignificant if they account for less than 5 % of the total mass of the distribution and are not considered further. The location of the mode within each subpopulation is visually identified (manual) and dispersion is adjusted iteratively to find the best fit to the actual data. An advantage of the user-interactive aspect of the program is that it permits manual forcing (within teh mathematical tolerances of the program) where human intelligence is required e.g. where the finest-grained subpopulations may be unreliable due to the truncation of the fine tails of grain-size curves or where the mass fraction incorporated by each subpopulation must be adjusted to compensate for the limitation of decomposition into a maximum of six subpopulations. However disadvantages are that it is time-consuming and fiddly and a fully automated process would not be subject to human error in terms of visual matching of subpopulation modes and dispersion.

5.3.2 CLAST TYPES AND COMPONENTRY

Representative samples of each unit from both a very proximal section (< 600 m from the vent) and one close to the boundary of the proximal dispersal region (2.5-3.5 km from source) were selected for component analysis. For units A, B, C, D, E and G the near-vent samples are taken from sections TT02 and TT02B, which are located < 50 m apart along a single northwest-southeast trending crevasse (535 m and 595 m from the vent, respectively). For units A, B and C the second sample is taken from section TS40 (3.4 km from the vent), at the boundary between the proximal and medial regions of deposit dispersal. However, due to slight variations in the dispersal axes and lateral extents of individual units (as outlined in Chapter 3), the more distal samples of units D, E and G are taken from sections TS43B (2.6 km from the vent), TS48 (1.9 km from the

vent) and TS45 (2.3 km from the vent). A minimum of 200 clasts, selected at random by pouring onto a slide, were analysed in three to four size classes which correspond to grain-size modes.

The mode of any frequency distribution corresponds to the most frequently occurring particle size (i.e. the category containing the highest mass of clasts). The identified modes are based on the reconstructed TGSD and therefore should contain the clast types that typify the dominant magma fragmentation mechanisms. The 0.5 Φ interval is thus chosen as a representative size fraction to compare the components for "near"-proximal and "far"-proximal locations. Clasts were observed and point counted under a binocular microscope. The 3.5 Φ and 4.5 Φ size fractions of one proximal sample from each unit were also evaluated qualitatively using a Philips XL30CP scanning electron microscope (SEM) at the University of Edinburgh. Quantitative measurements were restricted to the coarser (i.e. >2.5 Φ) modes, as analysis of clast morphology within the fine and very fine ash fractions is being conducted as part of a separate study by P. Dellino and co-workers at the University of Bari.

Tephra clasts were initially divided into three categories: non-juvenile (wall rock) fragments, free crystals and juvenile tephra. The proportion of non-juvenile fragments can be related to the eruption intensity, or to the extent of explosive magma-water interaction and to the relative width of the conduit and the stability of its walls (Pittari *et al*., 2008)

Furthermore, in systems where the substrate stratigraphy is well understood, and where there are marked contrasts in the subsurface lithology, non-juvenile composition can be used to constrain the depth of fragmentation. The changing proportion of free crystals within ignimbrite deposits may be indicative of the mass of fine ash that has been removed from the proximal dispersal area and deposited farther afield (Sparks and Walker, 1977).

Juvenile fragments were then classified further according to their vesicle abundance and clast morphology (see Fig. 5.2). Classes of vesicle abundance were arbitrarily defined as either poorly to non-vesicular, moderately vesicular, or highly vesicular (<25%, 25-75%, >75% vesicles by volume, respectively). A significant proportion (~15%) of pumice lapilli approach a reticulitic texture (i.e. >90% vesicles).

However, these are counted under the "highly vesicular" classification and do not form a separate category. Classification of clast shapes and morphologies follows the scheme of Wohletz (1983), who described five dominant clast types produced by phreatomagmatic eruptions. Blocky and equant clasts (Type 1) result from simultaneous brittle fracture and quenching, and are commonly present in fractions >63 microns in diameter. Vesicular and irregular clasts with smooth surfaces (Type 2), found only in the coarser fractions from basaltic eruptions, are formed by turbulent mixing of fragments with water after fracture and before quenching. Moss-like (Type 3) clasts are highly convoluted shapes with high surface area, found in the < 63 micron diameter size fraction of basalts only. Spherical or drop-like forms (Type 4) are produced by surface tension effects and are also found in the finer fraction of basaltic tephra. Plate-like clasts (Type 5) form by nearly simultaneous vesicle burst and fragmentation and are found in the < 63 micron fraction of deposits from vesicular magmas. The term "ragged vesicular" was introduced by Talbot *et al*. (1994) to accommodate clasts that do not fall into any of the previously defined (blocky, platy, quenched and shard/bubble walls) categories. Clasts in this group are predominantly composed of broken vesicle walls that give the edges an irregular, ragged texture. These are inferred to form from the fragmentation of magmatic foam which is in a brittle state. This is most likely to be a consequence of shock wave passage but may also result from large vesicles bursting in a region of heterogeneous vesicle size populations.

Only Type 1, 2 and 5 (after Wohletz, 1983) and "ragged vesicular" (after Talbot *et al*., 1994) juvenile fragments were observed within the G2004 deposit. A description of the identified clast morphologies along with the inferred mechanism of formation is provided in Table 5.2. Since no examples of clast types 3 and 4 could be found in the G2004 tephra, these have not been included in Table 5.2 and are not considered further.

Figure 5.2: Componentry classification flow chart.

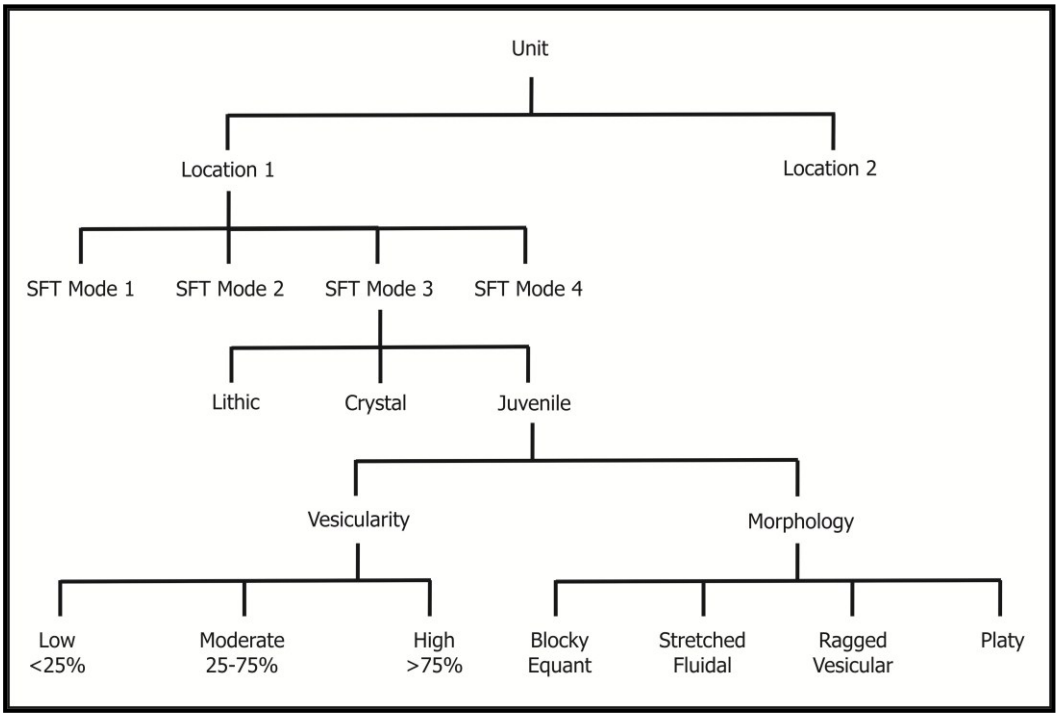

Table 5.2: Classification of diagnostic clast morphologies for phreatomagmatic eruptions from G2004 samples (after Wohletz *et al*., 1983 and Talbot *et al*., 1994).

Blocky		
Exhibit well-developed planar surfaces, often at right angles to one another.	Inferred to result from the brittle fracture of magma.	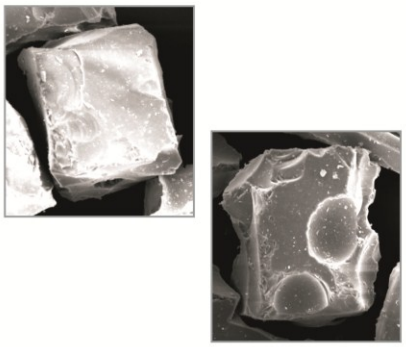
Ropy		
Exhibits smooth, ropy and curved skin texture with deformed internal vesicles.	Evidence of deformation of magma in a fluidal state prior to quenching.	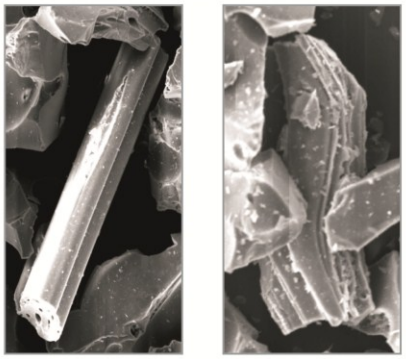
Cuspate		
Exhibit an intersection between 3 or more bubbles and/or the thin, curved remnants of bubble walls.	Remnants of burst vesicles.	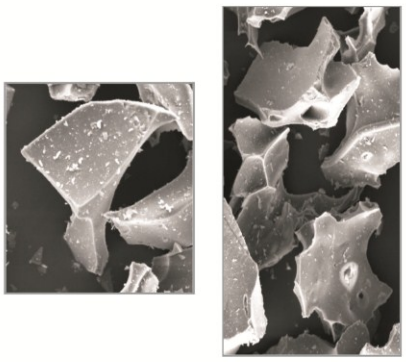
Ragged		
Dominated by broken vesicular walls that give the edges an irregular, ragged texture.	Inferred to result from brittle fracture of a magmatic foam.	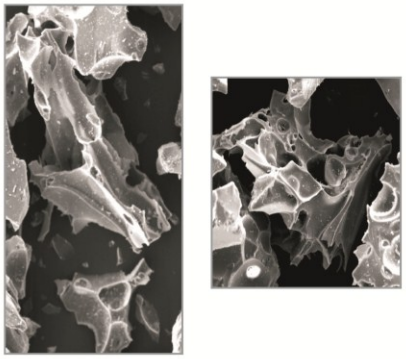

5.3 RESULTS

A detailed description of the G2004 TGSD and total unit grain-size distributions is provided in Chapter 4. However, a summary of key grain-size parameters is reproduced here for easy reference (Table 5.3). In addition, the reconstructed total layer grain-size distributions are provided in Figs. 5.3-5.9. Grain-size data for individual samples is given in Appendices III and IV, while component data is tabulated in Appendix V.

Table 5.3: Summary of grain-size characteristics for the G2004 total deposit, along with individual layers.

	Median Diameter	Sorting	Skewness	Kurtosis
TOTAL	1.5	2.6	0.1	0.9
UNIT A	0.9	2.4	0.1	1.0
UNIT B	1.3	2.5	0.1	0.9
UNIT C	1.4	2.7	0.2	0.9
UNIT D	1.2	2.6	0.1	0.9
UNIT E	1.8	2.8	0.1	0.9
UNIT F	1.5	2.8	0.1	0.9
UNIT G	1.4	2.6	0.2	0.9

5.3.1 SITE-SPECIFIC TEPHRA UNIT GRAIN-SIZE DISTRIBUTIONS

A striking feature in the comparison of all total layer and site-specific grain-size distributions is the salience of the fine ash sub-populations (i.e. those with modes at 3 Φ, 4 Φ and, although it accounts for only a very small portion of the total mass, 6 Φ. In all samples for all units (except Unit F) the finer modes become increasingly prominent with increasing distance from source, and the layer becomes increasingly better sorted. This is consistent with expectations of particle transportation both within a moving, fluid rich current and from a buoyant eruption plume. Comparison of the grain-size distribution for each unit at different locations reveals that most of the variability due to size fractionation with transport arises in size intervals coarser than 2 Φ (250 μm). The coarse spectrum of the deposit, however, accounts for 55 % of the total deposit mass (Chap. 4) so it is essential that these variations be constrained. At this juncture it is important to also recall that this study focuses on the effect of transportation on the grain-size distribution within the proximal deposit sector. Although the contribution of distal ash fall to the total grain-size distribution has already been established to fall

below the 5 % level of significance (Chap. 4) an overview of grain-size parameters for the distal deposit is necessary for understanding the effect of long distance transportation on the size distribution. Data from Oddsson (2007) show that all grain-size samples from the distal region of the G2004 deposit have a poorly sorted (σ_Φ = 1.9), bimodal distribution in which most of the mass is concentrated in the 3 Φ and 4 Φ size fractions. That is, beyond 6 km from source only the salient fine modes remain and most of the material greater than 2 Φ has been removed from the distribution.

In the proximal sector, Unit A – a widespread but small-volume end-member tephra fall layer – is very poorly sorted and forms a complex, polymodal size distribution (Fig. 5.3). The distribution becomes only very slightly better sorted with distance from source (i.e. σ_Φ = 2.5 at TT02 and 2.1 at TS40). With increasing distance from source, the coarse modes (which at all locations represent the bulk of the distribution mass) are shifted from -2 Φ and -1 Φ to 1 Φ and 2 Φ. This represents a decrease of roughly a factor of 8 over approximately 3 km of transport through the atmosphere.

Figure 5.3: Particle size distribution for Unit A for bulk samples at varying distances along the principal dispersal axis, away from source. The reconstructed total layer distribution is also plotted for comparison.

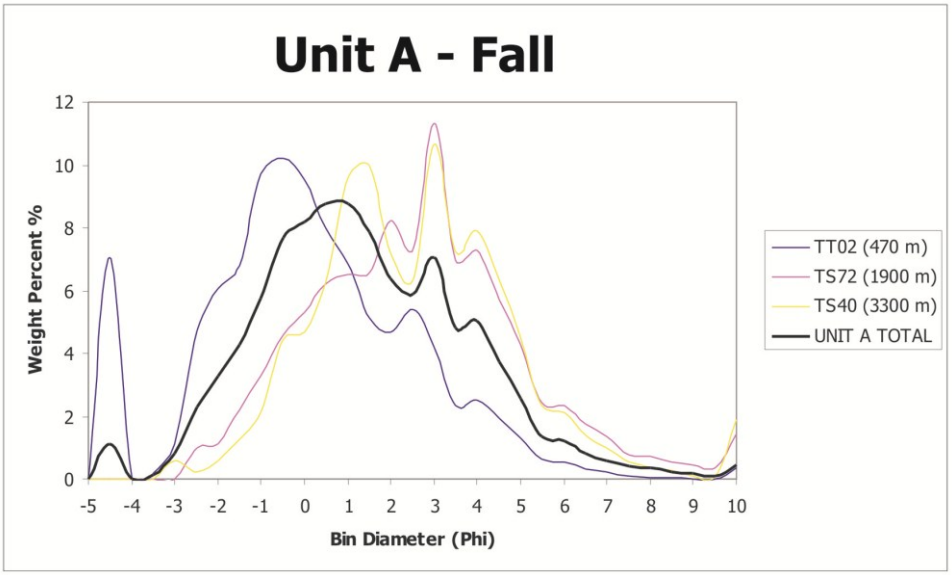

The location-specific tephra size distributions for Units B (Fig. 5.4) and D (Fig 5.5), which represent transport in an end-member pyroclastic surge are similarly complex, polymodal and very poorly sorted. However, for each of these the effects of improved sorting with distance are more pronounced than in Unit A and the rate at which the modal particle size decreases over a 3 km range is much more gentle. Within Unit B there is a threefold decrease in the most abundant particle size, while for Unit D, it is a fourfold decrease. The rate at which the modal diameter decreases with distance from source in the proximal sector is therefore almost double for plume transport compared with transport by PDC. Compared with the fall deposit, in which all size populations are initially represented, and coarser fractions simply fall out with increased distance from source, the pattern of fraction by transport in a PDC is more complex. In the case of Units B and D, within approximately 2 km of the vent the coarse modes tend to migrate to increasingly finer intervals and do not appear to drop out completely until between 2 and 3 km distance (Figs. 5.4 and 5.5).

Figure 5.4: Particle size distribution for Unit B for bulk samples at varying distances along the principal dispersal axis, away from source. The reconstructed total layer distribution is also plotted for comparison.

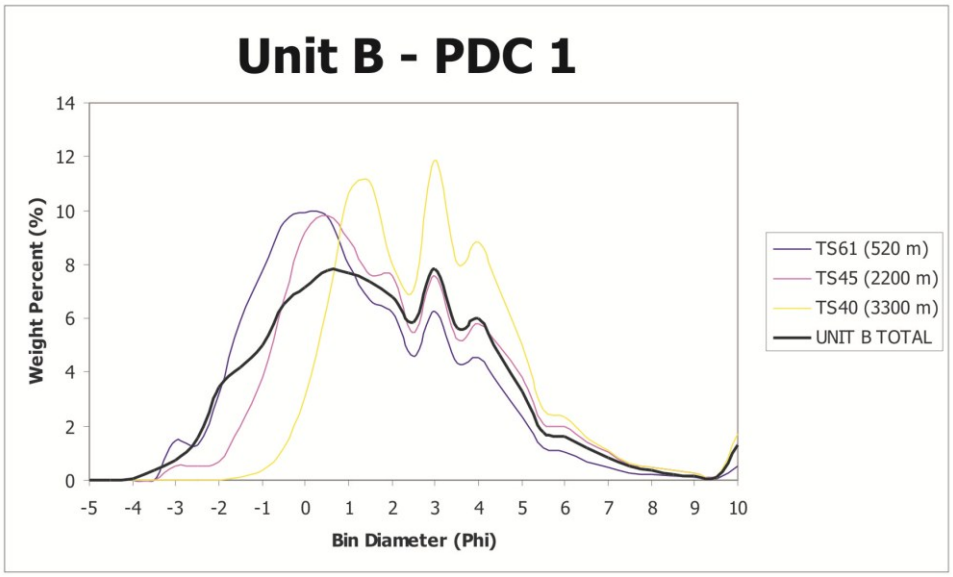

Figure 5.5: Particle size distribution for Unit D for bulk samples at varying distances along the principal dispersal axis, away from source. The reconstructed total layer distribution is also plotted for comparison.

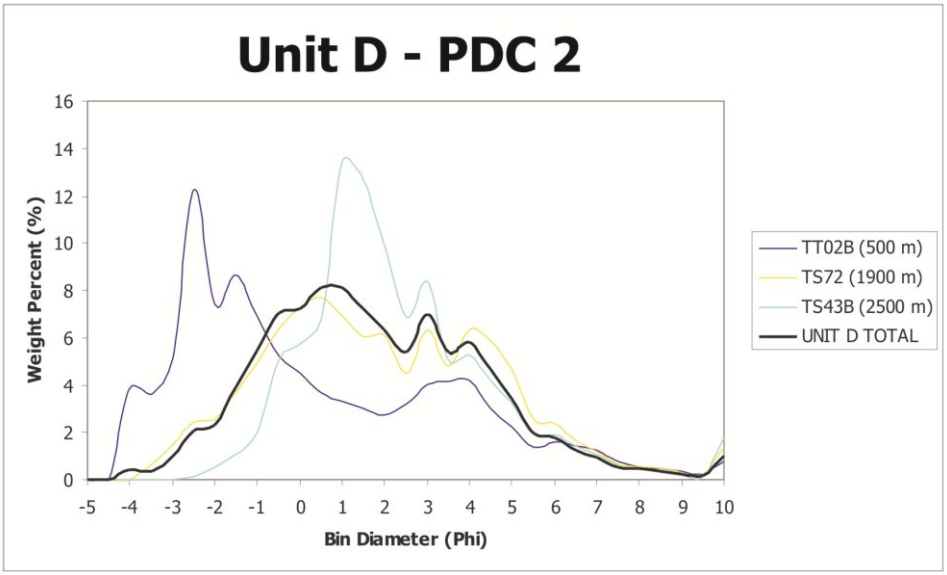

The hybrid main phase units (unit C and E) have very similar grain-size distributions which are modified in the same ways with increasing distance from the vent. In both distributions, the changes with distance from source are relatively gradual compared to both the G2004 fall (Unit A) and PDC (units B and D) deposits. Within the Unit C samples the diameter of the modal size fraction decreases by a factor of 2.5 over ~3 km (Fig. 5.6), while for Unit E the modal diameter halves over ~1.5 km (Fig. 5.7).

Within Unit C there is a marked improvement in distribution sorting with increased distance from source (σ_Φ = 2.8 at TS40 and 2.1 at TS60), while for Unit E the improvement is more subtle (σ_Φ = 2.7 at TS60 and 2.2 at TS48). For both of these hybrid units the changes in particle size distribution with distance are relatively subtle. In Unit C the modal diameter of most samples stays between 0 and 0.5 Φ and there is a secondary mode at 2 Φ. A shift in the distribution does not occur until at least 2 km from source after which the principal mode is shifted to 1.5 Φ and the secondary mode is shifted from 2 Φ to significantly augment the persistent mode at 3 Φ. Unit E proximal samples also have a modal diameter of 0.5 Φ, and an additional secondary mode at 2 Φ. However, the Unit E trends differ from those of Unit C in that the most

proximal sample contains additional coarse modes at -4.5 Φ and -0.5 Φ, which drop out within 1 km from source.

Unit G samples (Fig. 5.8), which are interpreted to be emplaced via PDCs at a time when the eruption plume extended no more than 2 km above the vent exhibits almost identical grain-size patterns to that of Unit E apart from the fact that it contains an additional coarse mode at -1 Φ and none at -4.5 Φ in the most proximal samples.

Figure 5.6: Particle size distribution for Unit C for bulk samples at varying distances along the principal dispersal axis, away from source. The reconstructed total layer distribution is also plotted for comparison.

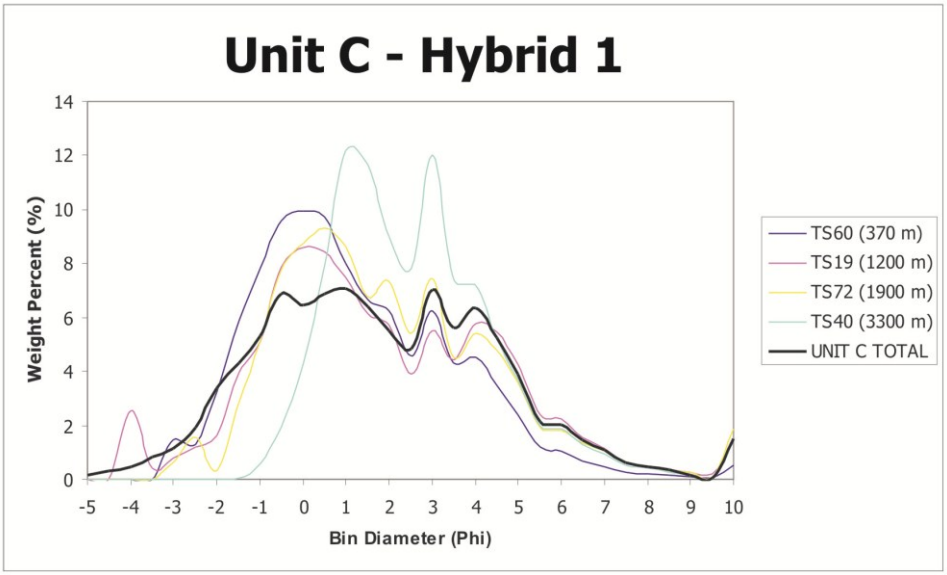

Figure 5.7: Particle size distribution for Unit E for bulk samples at varying distances along the principal dispersal axis, away from source. The reconstructed total layer distribution is also plotted for comparison.

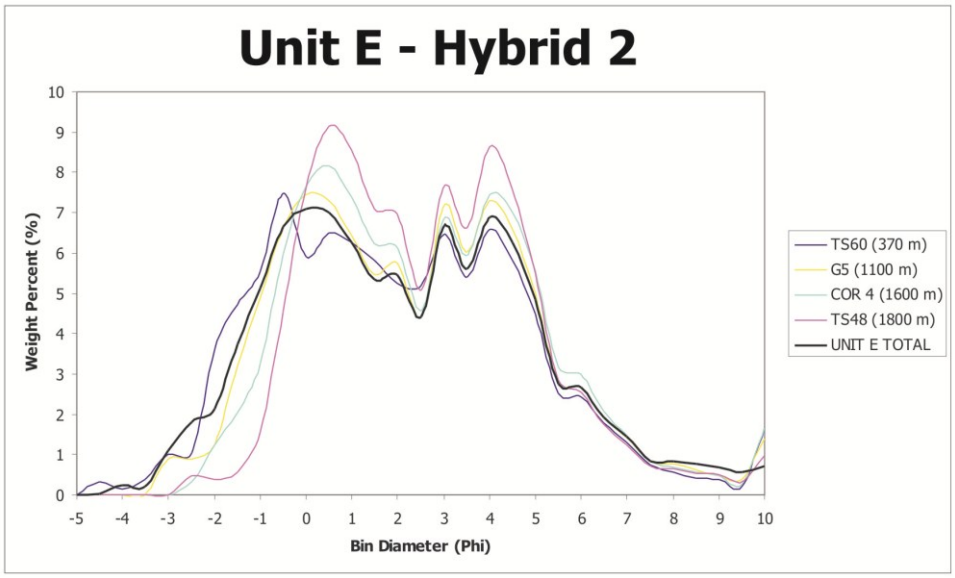

The location-specific grain-size distributions of Unit F (Fig. 5.9) are the most interesting because (i) they show little change with distance from source and (ii) they are very similar to the G2004 total deposit grain-size, despite the fact that they form a very minor proportion of the deposit itself. Unit F samples become no better sorted with distance from the vent although there is some increase in the proportion of fine ash in more distal samples. Unit F is polymodal, with modes at -1 Φ, 0 Φ, 1 Φ, 3 Φ, 4 Φ and 6 Φ in all samples. Some samples also contain very minor coarse modes at -4 and -3 Φ. The fact that there is very little change in grain-size distribution by transport fractionation reflects the emplacement mechanism (high concentration PDC emplaced by en masse freezing) and short run-out distance of this unit (2.5 km), as described in Chapter 3.

Figure 5.8: Particle size distribution for Unit G for bulk samples at varying distances along the principal dispersal axis, away from source. The reconstructed total layer distribution is also plotted for comparison.

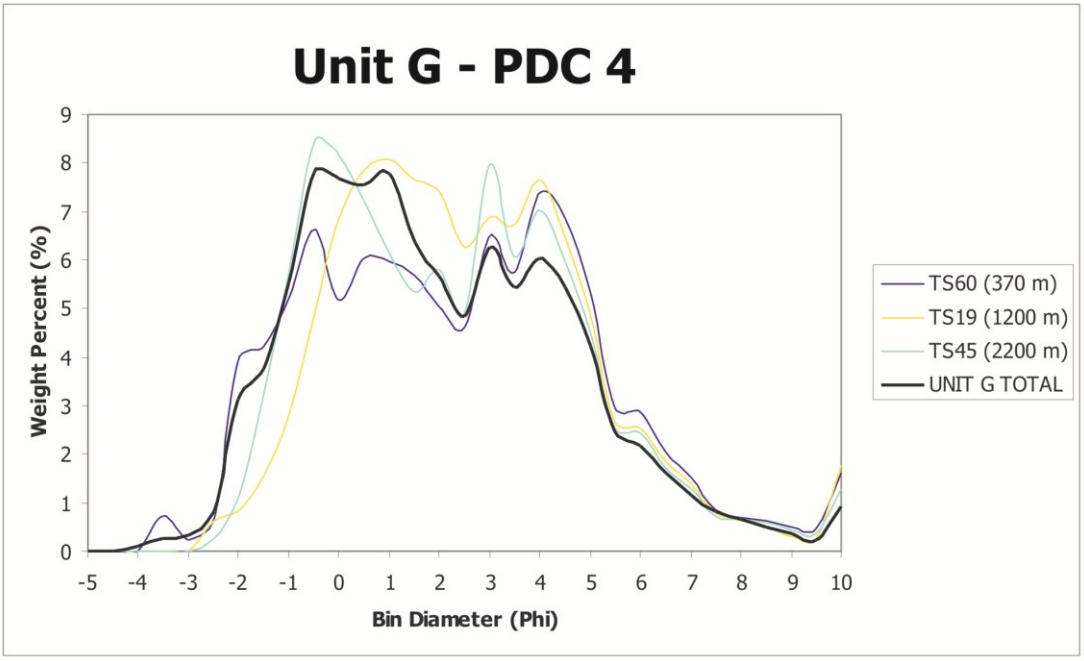

The grain-size distribution of pumice lenses, which are interpreted as relict proximal fall layers intercalated with, and modified by, PDC deposits (see Chaps. 3 and 8) are presented in Fig. 5.10. Pumice lenses are moderately sorted (σ_Φ = 0.8-12), and strongly coarse-skewed. They are all polymodal, but in most cases the bulk of the mass is concentrated within one subpopulation (i.e. the dominant grain-size represented by these pumice layers is -3.5 Φ to -3 Φ (or 8-12 mm; Table 5.1). All of the pumice lenses contain principally clasts with diameters between -3 Φ and -3.5 Φ, along with secondary modes between -4.5 Φ to -5.5 Φ and also at -6.5 Φ. Some lenses contain a very minor subpopulation with modal clast diameters of -2 Φ. With increasing distance from source the pumice lenses become better sorted as the mass becomes concentrated into the principal mode of the distribution.

Figure 5.9: Particle size distribution for Unit F for bulk samples at varying distances along the principal dispersal axis, away from source. The reconstructed total layer distribution is also plotted for comparison.

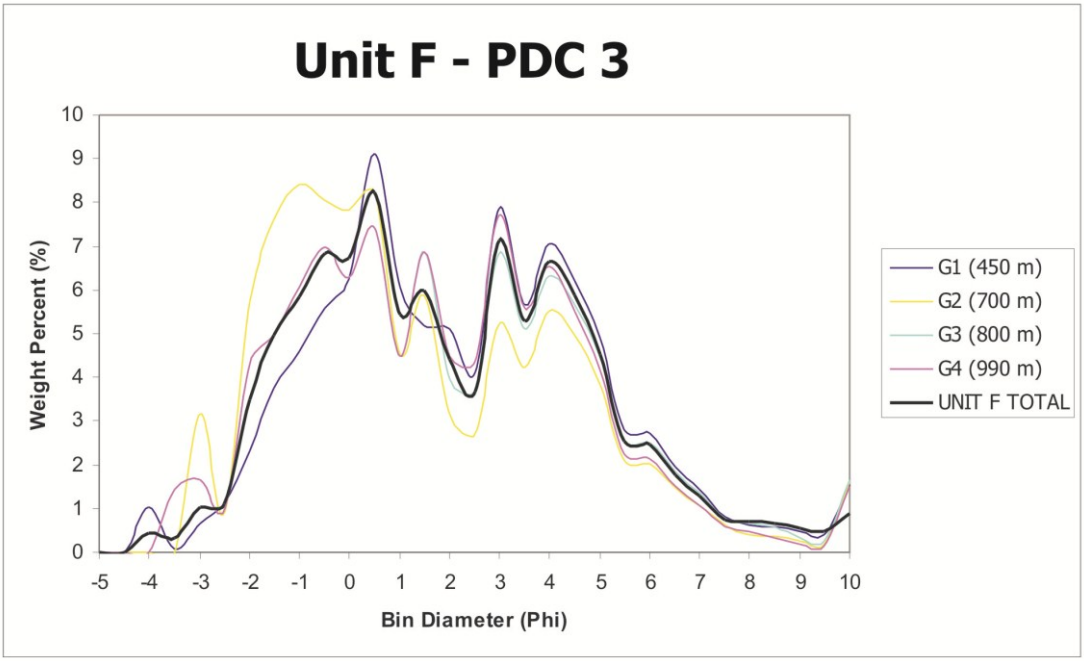

The grain-size distribution of pumice layers is not incorporated into estimates of the G2004 total deposit grain-size distribution for two reasons: (1) because of the extremely delicate nature of the clasts it was not possible to measure their grain-size by traditional sampling and sieving methods and the method of estimating GSD of pumice lenses via image analysis (see Appendix IV) is potentially prone to larger errors; (2) due to their sporadic, and discontinuous nature, along with the fact they occur as discrete horizons floating in the body of units C and E, it was not possible to adequately trace and correlate the dispersal of pumice layers; (3) although visually striking, due to their high vesicularity and sporadic occurrence the pumice lenses likely contribute a very minor proportion to the mass of the deposit.

Figure 5.10: Grain-size distribution of pumice lenses.

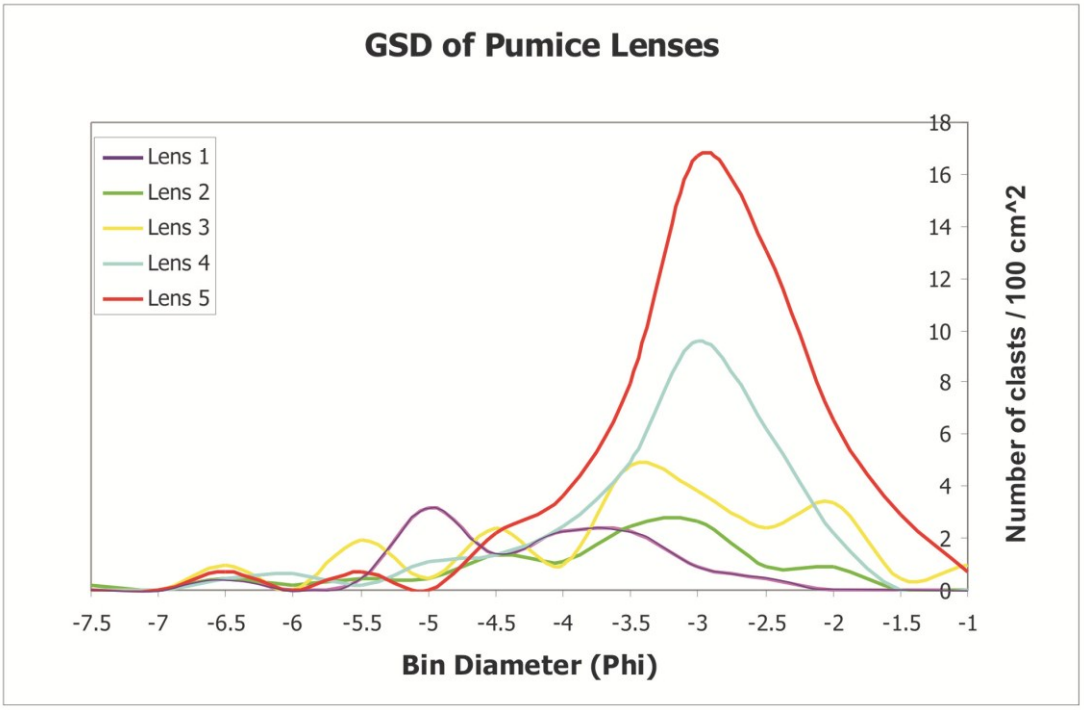

5.3.2 WHOLE DEPOSIT AND TOTAL UNIT GRAIN-SIZE DISTRIBUTIONS

With a median diameter of 0.9 Φ, Unit A is slightly coarser and better sorted (σ_Φ=2.4) than the remaining units, for most of which Md_Φ hovers between 1.2 Φ and 1.5 Φ and σ_Φ from 2.5 to 2.8. The median diameter of Unit E is the finest at 1.8 Φ. Every unit is slightly fines-skewed and has a very poorly sorted, polymodal distribution (Table 5.4 and Figs. 5.3-5.9). Each of the G2004 deposition units shares common modes at -0.5 to -1 Φ, 0.5-1 Φ, 3 Φ and 4 Φ (Figs. 5.3-5.9).

The shape of the total layer distribution is very similar for units A, B and C. For each of these the principal subpopulation has a modal clast diameter of 0.5 Φ or 1 Φ and contains 35-45 % of the total distribution mass. The second subpopulation has a modal diameter at -0.5 Φ or -1 Φ which represents 20-30 % of the distribution mass. Additional sub-populations with modal diameters of 3 Φ and 4 Φ each account for 15-20 % of the distribution mass. Units A, B and C also contain minor sub-populations at 2 Φ and 5 Φ which incorporate 10 % and 5 % of the distribution mass, respectively (Fig. 5.11).

The shape of the total layer grain-size distributions of units D and E are very similar to one another. The location and ranking of modal diameters is the same as for units A-C (i.e. 0.5 Φ > 1 Φ > 3 Φ > 4 Φ) but units D and E both lack the additional minor coarse and fine modes at 2 Φ and 5 Φ (Fig. 5.11).

Units F and G form the most complex grain-size distributions within the G2004 sequence. These two units have all of the major sub-populations in common: -1 Φ, 1 Φ, 3 Φ and 4 Φ. These are the same modal diameters that also crop up in units A-E. However, the mass is distributed in a more diverse and complex manner in units F and G than elsewhere. The total layer grain-size distribution of Unit F features 5 sub-populations (-1 Φ, 0 Φ, 1 Φ, 3 Φ and 4 Φ) across which the mass is relatively evenly distributed (15-22 % in each), along with an additional coarse mode at -2 Φ which incorporates approximately 10 % of the mass. The total layer grain-size distribution of Unit G is similar to that of units A-E in that the modes at -1 Φ and 1 Φ are most prominent (containing 23 % and 27 % of the distribution mass, respectively). However, it also features significant secondary modes at 3 Φ and 4 Φ (16 % and 20 %, respectively). Unlike any of the other unit grain-size distributions, Unit G features additional minor modes at 2 Φ and 6 Φ which account for 7 % and 8 % of the total mass.

As a product of unit distributions, the total grain-size distribution for the G2004 tephra layer is very poorly sorted and platykurtic with a median diameter of 1.5 Φ. The initial particle size population of the G2004 deposit is described by a polymodal, very poorly sorted distribution (σ_Φ=2.6) in which the bulk of the mass is spread between four sub-populations (Table 5.4 and Fig. 5.11). Modal size intervals are: 0.5 Φ (24 wt. %), 4 Φ (23 wt. %), -1 Φ (21 wt. %) and 3 Φ (17 wt. %). Additional minor modes occur at 5.5 Φ (8 wt. %) and 2 Φ (7 wt. %).

Figure 5.11: Deconvolution of unit and total layer grain-size distributions according to SFT theory (Wohletz, 1989).

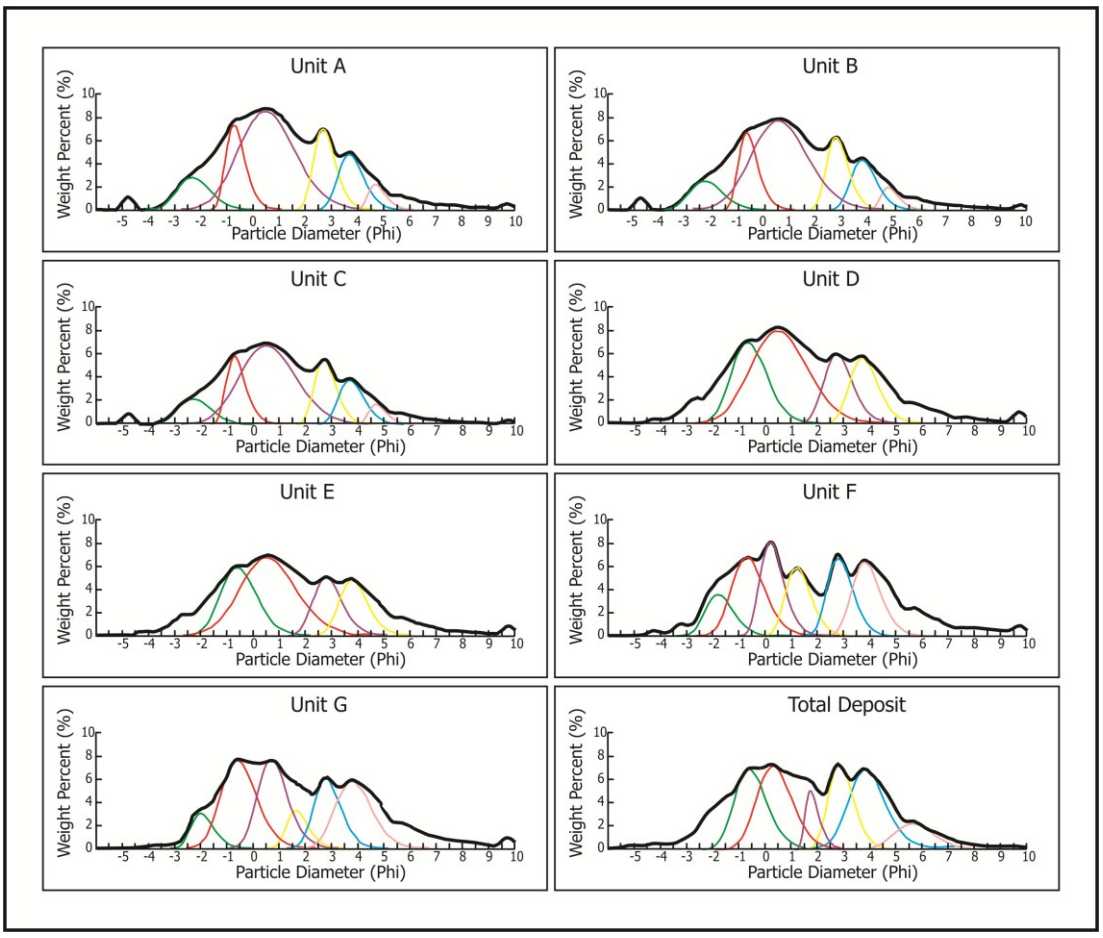

Table 5.4: SFT deconvolution of the measured polymodal grain-size distributions for individual units and the total G2004 deposit.

UNIT A					UNIT B				
Subpop. #	Mode	Dispersion	Shift	Fraction	Subpop. #	Mode	Dispersion	Shift	Fraction
1	-2.3	-0.7	1.11	0.09	1	-2.1	-0.5	0.67	0.09
2	-0.7	0.65	0.37	0.14	2	-0.7	-0.4	0.56	0.13
3	0.5	-0.9	3.33	0.47	3	0.3	-0.7	1.11	0.25
4	2.7	-0.3	0.48	0.15	4	1.7	-0.5	0.67	0.11
5	3.7	-0.5	0.67	0.12	5	2.7	-0.6	0.83	0.22
6	4.7	0.05	0.32	0.04	6	3.8	-0.75	1.33	0.21
UNIT C					UNIT D				
Subpop. #	Mode	Dispersion	Shift	Fraction	Subpop. #	Mode	Dispersion	Shift	Fraction
1	-1.9	-0.75	1.33	0.13	1	-0.6	-0.75	1.33	0.24
2	-0.7	-0.65	0.95	0.20	2	0.5	-0.9	3.33	0.44
3	0.7	-0.87	2.56	0.34	3	2.8	-0.6	0.83	0.17
4	2.8	-0.2	0.42	0.14	4	3.7	-0.6	0.83	0.16
5	3.8	-0.66	0.14	0.19					

Table 5.4 continued: SFT deconvolution of the measured polymodal grain-size distributions for individual units and the total G2004 deposit.

UNIT E					UNIT F				
Subpop. #	Mode	Dispersion	Shift	Fraction	Subpop. #	Mode	Dispersion	Shift	Fraction
1	0.7	-0.95	6.67	0.54	1	-1.8	-0.6	0.83	0.10
2	-0.7	-0.4	0.56	0.21	2	-0.7	-0.7	1.11	0.22
3	2.8	-0.2	0.42	0.13	3	0.2	-0.4	0.56	0.19
4	3.9	-0.7	1.11	0.12	4	1.2	-0.5	0.67	0.15
					5	2.8	-0.51	0.68	0.17
					6	3.8	-0.6	0.83	0.18
UNIT G					TOTAL				
Subpop. #	Mode	Dispersion	Shift	Fraction	Subpop. #	Mode	Dispersion	Shift	Fraction
1	-2.1	-0.35	0.51	0.07	1	-0.7	-0.7	1.11	0.21
2	-0.7	-0.75	1.33	0.27	2	0.3	-0.75	1.33	0.24
3	0.7	-0.65	0.95	0.23	3	1.7	0.85	0.18	0.07
4	1.6	-0.3	0.48	0.07	4	2.8	-0.5	0.67	0.17
5	2.8	-0.55	0.74	0.16	5	3.8	-0.75	1.33	0.23
6	3.8	-0.75	1.33	0.20	6	5.6	-0.8	1.67	0.08

5.3.3 COMPONENTRY

In general, the proportion of blocky and ropy clasts decreases in the finer size fractions, while the proportion of ragged and cuspate clasts increases. However, blocky morphologies make up >75% of identified clast types overall. These trends in clast morphology do not, however, correspond to an increase in clast vesicularity with decreasing grain-size. In fact the reverse is true and, broadly speaking, there is a general increase in clast vesicularity with increasing grain-size. This is likely to be related to the size of vesicles, which are generally larger than 100 microns, so that fragments smaller than these are unlikely to contain numerous intact vesicles. Similarly, the proportion of non-vesicular fragments is inversely related to particle size. There is no clear relationship between size interval and the proportion of moderately vesicular fragments.

Overall, within the G2004 deposit, there is a decrease in non-juvenile abundance and a corresponding increase in the number of free plagioclase crystals within the finer size fractions. The percentage of non-juvenile components in fine lapilli and ash-grade fragments is low (<< 5%). In every unit, the percentage of free crystals is also vanishingly slim (<1 %). This is largely an outcome of the fact that the G2004 magma is strongly aphyric (<0.5 % phenocrysts by volume) and also an artefact of the fact that phenocrysts, where they occur, are rather small (50-100 microns on average) and occur within a glassy or aphanitic groundmass.

Units A and B, which together represent the first phase of the eruption, are the only units in which highly vesicular fragments (i.e. those with >75 % vesicles, by volume) are entirely absent (Fig. 5.12). For Unit A, both the very proximal sample (TT02) and the more distal sample (TS40) consist predominantly of moderately vesicular material – 89 % and 97 %, respectively. Sample TT02 contains 11 % non-vesicular fragments but this component decreases rapidly with distance from source and sample TS40 contains only 3 %. Within Unit B the near-vent sample is dominated by moderately vesicular clasts (81 %), while the more distal sample is dominated by non-vesicular fragments (91 %). The predominant clast morphology in all Unit A and B samples is blocky (Fig. 5.13). However Unit B at section TT02 contains 4 % ropy fragments, while TS40 contains 7 % ragged clasts, a proportion coincident with that of the moderately vesicular clast population (7 %).

Unit C is more crystal-rich and more non-juvenile-rich overall than units A and B. However these components are present in the more distal sample only (3 % and 14 %, respectively). In sample TT02B, the 0.5 Φ size fraction is dominated by moderately vesicular clasts (70 %), but also contains a significant proportion of highly vesicular fragments (29 %). Non-vesicular material is virtually absent. Among these, the blocky morphology dominates (74 %) with an appreciable additional proportion of ragged (16 %) and ropy (10 %) clasts (Fig. 5.13). Among the juvenile glass population from sample TS40 non-vesicular fragments dominate (67 %), with a minor proportion of moderately vesicular material (14 %) and minimal numbers of highly vesicular fragments (2 %). These are almost exclusively blocky in morphology with only 2 % ragged fragments, which again coincides with the proportion of highly vesicular material within that sample. Back-scattered electron (BSE) images of clasts in the 3.5 Φ and 4.5 Φ size fractions are shown in Fig. 5.14 which demonstrates the range in both clast morphology and clast vesicularity within this unit.

Unit D is very similar to units A and B in that virtually all clasts are blocky in the proximal deposit apart from 1 % which have cuspate morphology (corresponding to 1% highly vesicular fragments), and 1 % which have a ropy morphology. However, it differs from units A and B in that the proximal sample is comprised mostly of moderately vesicular fragments (93 %) with a minor proportion of non vesicular material (5 %). The distal sample is largely moderately vesicular (85 %) but also contains 9 % of highly vesicular tephra. The clast morphology in this sample is largely blocky (88 %) but minor quantities of ragged (7 %) and ropy (4 %) clasts are also present, along with a vanishingly small quantity (1 %) of cuspate fragments (Fig. 5.13).

Units E, F and G are all very similar in their represented ranges of clast morphology and vesicularity, which is also close to that of Unit C. The proximal sample contains material which is evenly spread between the categories of moderately vesicular (40 %) and non-vesicular fragments (38 %) with a significant proportion of highly vesicular glass (20 %). Clasts are largely blocky in morphology (74 %), although the sample also contains a significant proportion of ragged (18 %) and cuspate (5 %) forms - associated with the proportion of highly vesicular fragments. There is also a very minor component of ropy fragments (2 %). In the distal sample, however, there are no highly vesicular juvenile glass fragments and so material is divided between

similar proportions of non vesicular and moderately vesicular glass (59 % and 40 % respectively). Among these, clasts are mostly blocky in morphology but there is also a rather large percentage (38 %) of ragged fragments, along with minor cuspate shards (4 %). A BSE image of clasts in the 4.5 Φ size fraction is shown in figure 5.14 depicting the occurrence of a wide range of clast types. This figure also highlights the similarity between Unit C and E components.

Figure 5.12: Second order component classification of the 0.5 Φ fraction of two samples from each unit of the G2004 deposit. Juvenile clasts have been categorised according to blocky, cuspate, ragged and ropy morphologies.

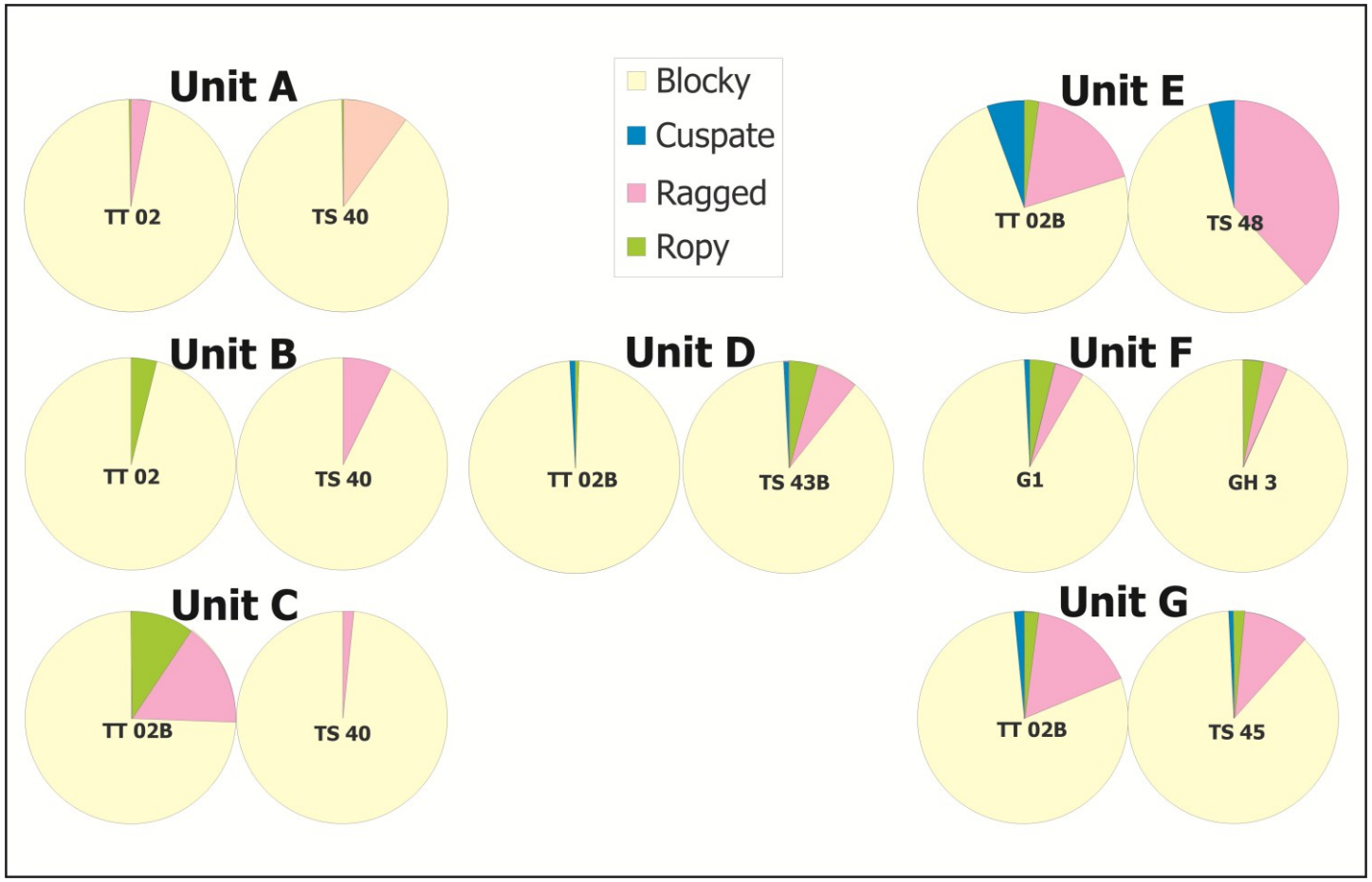

Figure 5.13: First order component classification of the 0.5 Φ fraction of two samples from each unit of the G2004 deposit. Clasts have been divided into proportion of free crystals, non-juveniles (accidental lithics) and highly, moderately and poorly vesicular juvenile fragments.

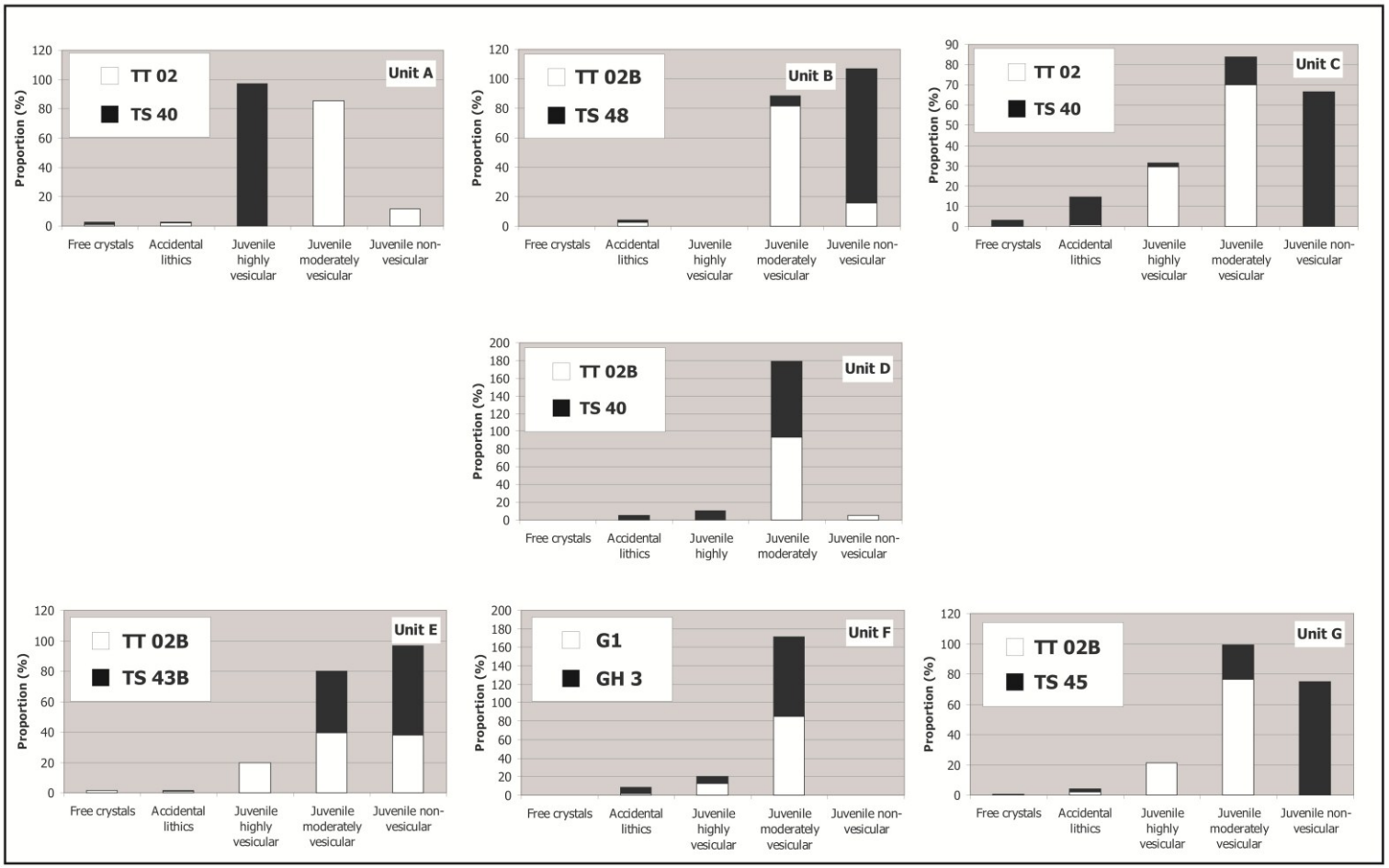

The proximal sample from Unit F consists primarily of moderately vesicular material (85 %) but also contains a significant proportion (13 %) of highly vesicular fragments. Among the juvenile glass there are no non-vesicular clasts and the sample contains no free crystals, and only 2 % of non-juveniles. The tephra is almost all blocky in morphology (91 %) but some ragged (5 %) and ropy (4 %) clasts also occur (Fig. 5.13). A very minor cuspate component also exists within the sample (1 %). In the distal sample Unit F contains 7 % non-juveniles in addition to the juvenile glass. Otherwise, the proportion of moderately and highly vesicular juvenile clasts is similar to that of the proximal sample. Likewise, the clast morphologies follow a similar pattern as within the proximal sample, except that there are no cuspate clasts. Examples of moderately and highly vesicular clast types in the 0 Φ size fraction of Unit F are shown in Fig. 5.16. Despite the difference in their vesicle size populations the external morphology is essentially the same for clasts within both categories.

The proximal Unit G sample is mostly moderately vesicular juvenile glass (77 %) with a significant proportion of highly vesicular material (21 %). It contains only 2 % of non-juveniles and no free crystals (Fig. 5.12). Clast morphology is dominated by blocky clasts (80 %) with a significant proportion of ragged material (17 %) and minor ropy and cuspate clasts. The distribution of components of the distal Unit G samples are similar to the proximal samples, but shifted such that the bulk are non vesicular clasts (75 %), with a small proportion of moderately vesicular fragments (23 %). The morphology is largely blocky (87 %) but ropy, ragged, and minor cuspate fragments are also represented (Fig. 5.13).

Figure 5.14: Back-scattered electron (BSE) image of a field of view of tephra samples from: (A) Unit B, 4.5 Φ; (B) Unit A, 3.5 Φ; (C) Unit B, 3.5 Φ. These images all clearly demonstrate that blocky clast morphologies vastly predominate and the range of clast vesicularity is limited to between 0 and ~30 volume percent.

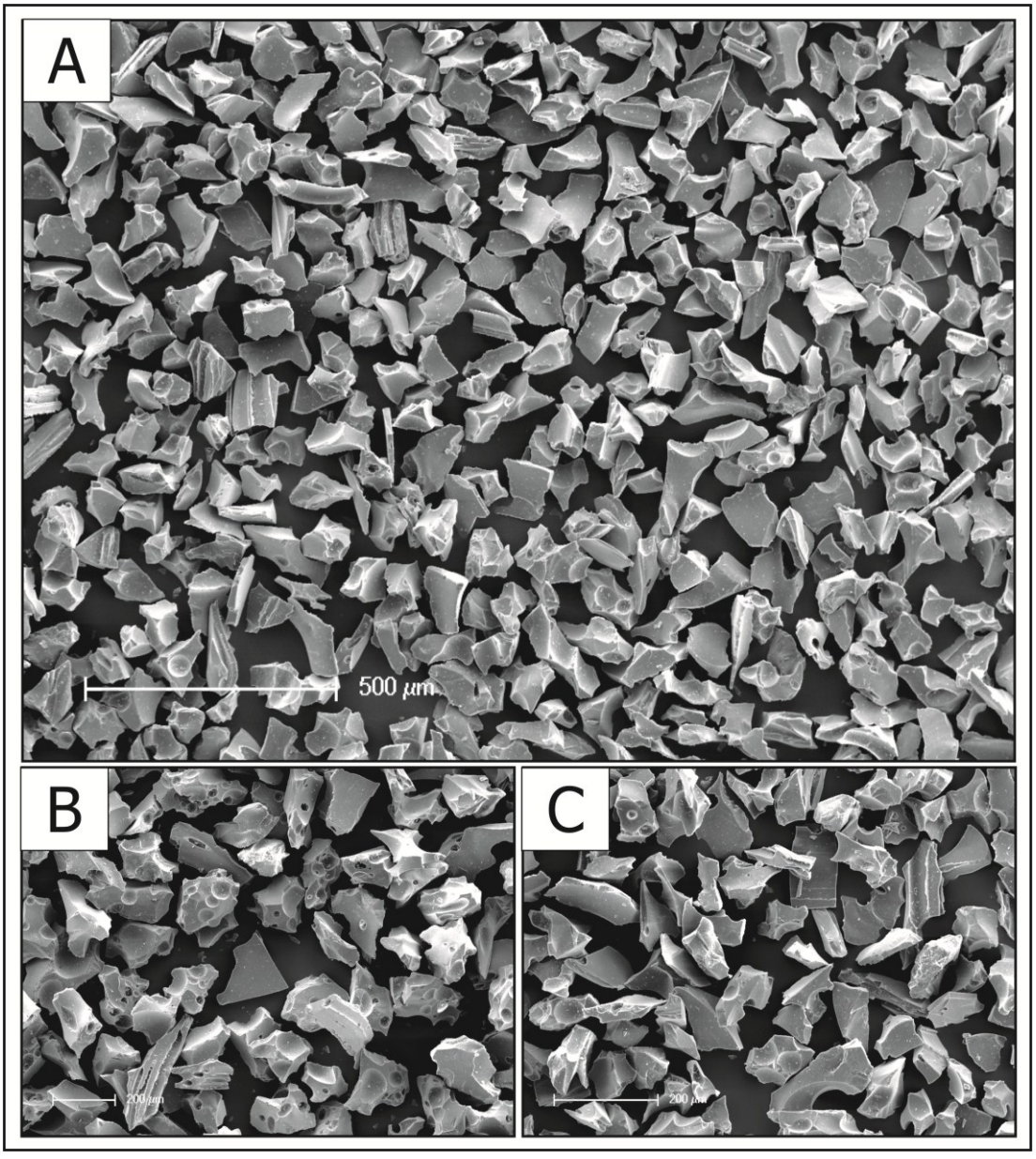

Figure 5.15: Back-scattered electron (BSE) image of a field of view of tephra samples from: (A) Unit C, 3.5 Φ; (B) Unit C, 4.5 Φ; (C) Unit E, 4.5 Φ.

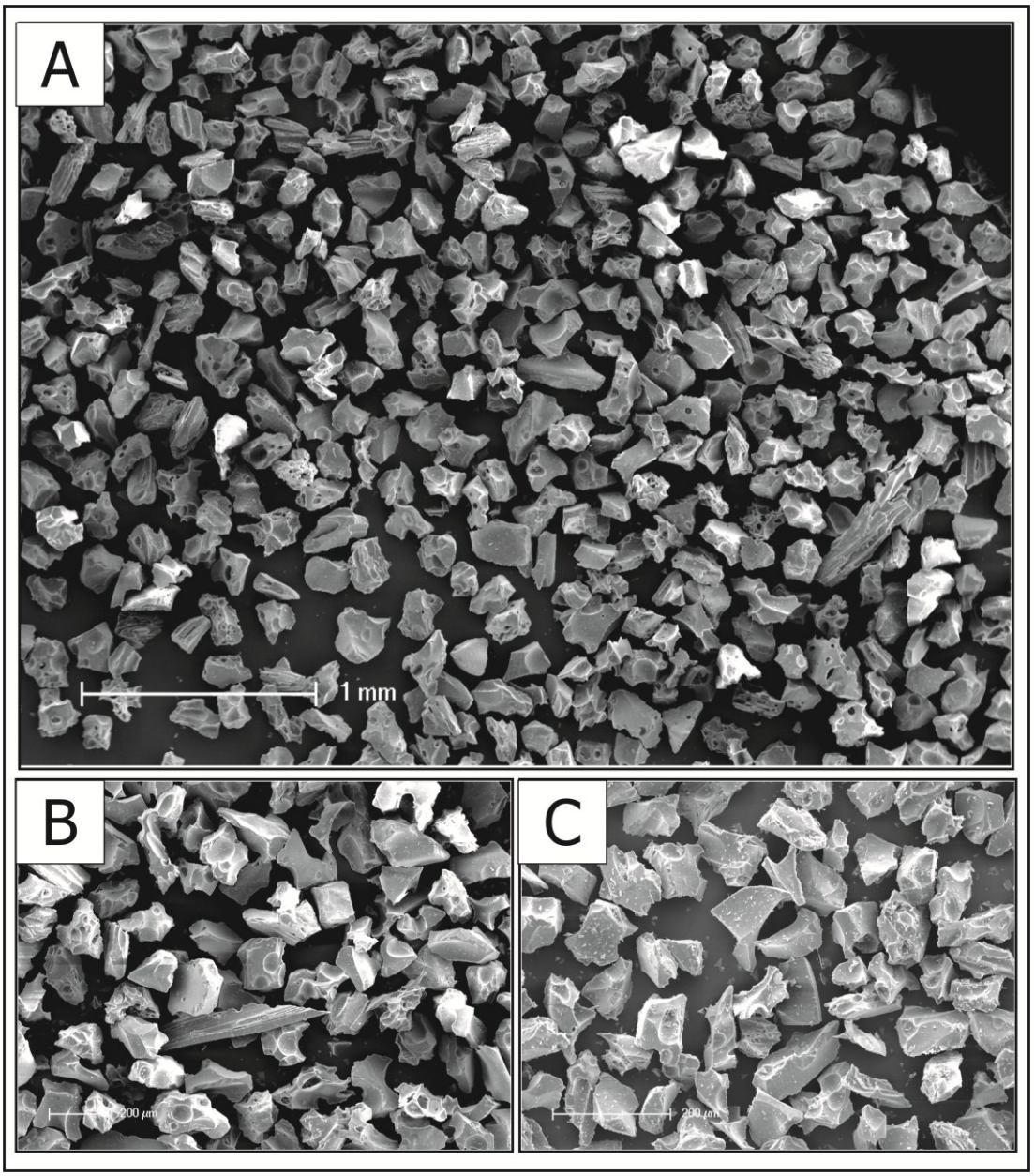

Figure 5.16: Photographs of moderately and highly vesicular clasts in the 0 Φ size fraction from Unit F, under a binocular microscope.

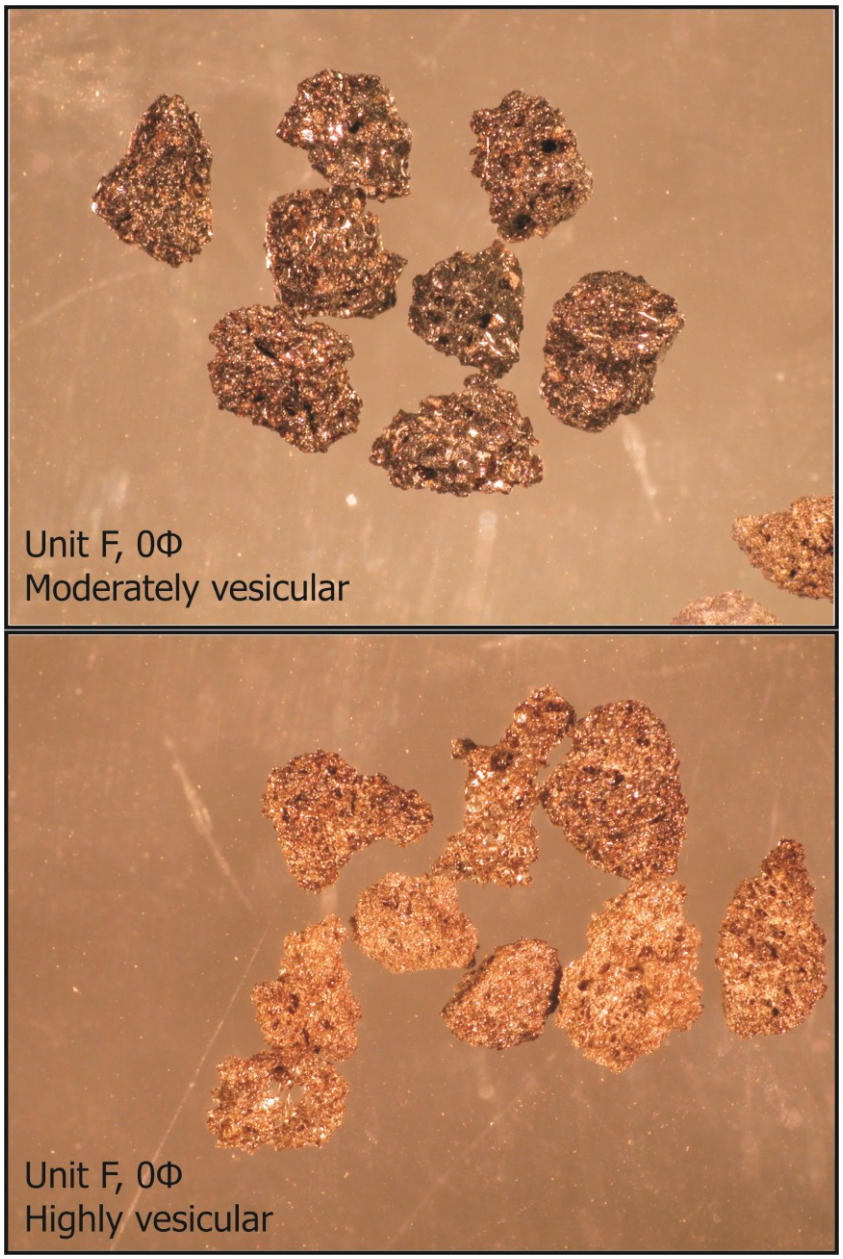

5.4 DISCUSSION

The similarity in the overall pattern of reconstructed total layer grain-size distributions, irrespective of transport and deposition mechanisms, reinforces the assertion that they effectively illustrate the grain-size produced by fragmentation processes. Another factor which lends confidence to the total layer grain-size reconstruction is the similarity between this and the SGSDs for Unit F – a massive layer generated by en-masse freezing of an end-member pyroclastic flow which was generated by column collapse and which had little opportunity to undergo internal size fractionation before abruptly coming to a halt within only 2.5 km of the vent.

One major limitation to this data set however, is the absence of grain-size and component data for the large proportion of erupted material which resides in the ice cauldron. Although phreatomagmatic eruptions are commonly expected to contain a finer spectrum of clast diameters than magmatic eruptions, it is possible that the reconstructed TGSD for the G2004 deposit is artificially fines-skewed because of the inability to access and account for the, presumably coarse, material deposited in the immediate vicinity of the vent. A second caveat is that, while the occurrence of many sporadic pumice trains and lenses interbedded with PDC deposits has been linked to hybrid activity and deposition by fallout from the high plume (Chaps. 3 and 8), it has not been possible to adequately incorporate the size distribution of pumice fall into the total deposit reconstruction (see section 5.3.1). This is a relatively minor setback to our evaluation, however, as the relict pumice layers are considered to constitute a relatively small proportion (i.e. < 5 %) of the overall deposit mass. Nevertheless, these lenses do constitute a unique grain-size population that is not represented in any of the unit GSDs. Therefore, were they incorporated into the TGSD they could constitute a small mode at the coarse end of the spectrum (i.e. around -3 Φ).

The overall consistency in the shape of reconstructed total layer GSDs across all units indicates that, despite their limitations, they refer back to the processes that were involved in disintegrating the tephra before the erupted mixture left the vents. All of the reconstructed distributions are polymodal and the same modes propagate throughout the eruption sequence. The same fragmentation processes were maintained throughout the G2004 eruption and were largely confined to the shallow conduit or vent part of the system. For example, if abrasion during transport and deposition was an important process in generating ash grade fragments, we would

expect to see the fine to very fine ash modes enhanced in the units where PDC emplacement dominated. However, there is nothing in these distributions to indicate that this was a significant process. The same applies to any speculations regarding fragmentation during plume transport and fallout.

The SGSDs have a demonstrated effect of fractionating the tephra such that, at a given location, certain of the original fragmentation modes are enhanced or subdued relative to the others. This effect is particularly prevalent for medial to distal samples in which the coarse modes are no longer represented and the modal diameter is shifted to increasingly finer size fractions. Since it is the medial to distal sector of a phreatomagmatic deposit that is most readily accessible, workers need to be aware of this effect and avoid over-interpretation of this fines-skewed sample population, the modes of which may not be representative of the modal diameter initially produced during magma fragmentation. For example, in the case of G2004, the modal size fraction 4.5 km from the vent is 3 Φ. However, reconstruction of the total deposit size distribution for this event reveals that as the eruption mixture left the vent a quarter of the mass of the eruptive mixture belonged to a subpopulation the modal diameter of which was 1 Φ, and a further 20 % to a subpopulation with a modal diameter of -1 Φ, and so on. The distal sample gives the impression that the process responsible for generating the subpopulation at 3 Φ was dominant, when in reality it accounts for only 17 % of the total deposit mass. This reinforces the importance of whole deposit grain-size reconstructions in evaluating fragmentation in the volcanic conduit.

The G2004 samples are identical in their grain-size characteristics to the products of phreatomagmatic, Surtseyan events in that they are very poorly sorted and fine-grained (Walker 1971; Walker, 1981; Wohletz, 1983). In the reconstructed total layer distribution the signature of transportation is effectively removed because samples from all regions of the deposit are combined in a representative fashion. Therefore the following discussion of grain-size characteristics and componentry addresses fragmentation effects only. These proximal samples show little to no evidence for extensive modification of clast morphology and surface features via transport and deposition processes (such as clast rounding and abrasion, surface alteration etc.). The G2004 juvenile clasts are also similar to those identified within Surtseyan tephras in that samples are typically dominated by blocky forms, even in the

fine and very fine ash size fractions, accompanied in some cases by a significant component of ragged clasts and a variable and very minor component of cuspate and ropy morphologies. The G2004 tephra, however, is conspicuously lacking in the highly fluidal mossy and drop-like morphologies, along with the plate-like clasts associated with hydrovolcanic interactions in basaltic deposits (Wohletz, 1983; Heiken and Wohletz, 1985).

The G2004 pyroclasts formed via a number of mechanisms: (1) The angular, blocky and ragged clast morphologies are attributed to brittle fracture of magma which is quenched and fragmented as a consequence of its interaction with comparatively cold external water, (2) Ropy clasts are interpreted to result from tearing apart viscous yet fluidal magma which has had the opportunity to undergo some turbulent mixing with steam and air prior to finally being quenched and (3) cuspate clasts which signify that a small proportion of the magma fragmented via volatile exsolution and vesicle burst (i.e. magmatic processes).

Phreatomagmatic tephra is commonly assumed to be poorly vesicular because the interaction of magma with water inhibits and then arrests the degassing process (e.g. Thordarson *et al*., 2001; Óladóttir *et al*., 2007; Allen *et al*., 2010). However, in the G2004 case it is apparent from the range in clast vesicularity, accompanied by evidence for fragmentation by predominantly brittle processes, that both magmatic and hydrovolcanic processes occur. That is, the magma was already in the process of vesiculation, then was subsequently shattered by contact with water to produce an even finer and more diverse deposit (e.g. Heiken, 1972). In the total deposit GSD four sub-population modes stand out in terms of the large mass fraction behind them (i.e. together they account for 85 % of the deposit mass) indicating that that they are of prime significance in terms of fragmentation mechanisms. The proportion of material attributable to each is almost equivalent. These are located, in order of mass proportion, at 0.5 Φ, 4 Φ, -1 Φ and 3 Φ. The remaining, lesser, modes reflect processes that precede or are superimposed on the principal modes. Their occurrence at the coarse end of the spectrum at -2 Φ to -3 Φ may be indicative of the modal clast diameter generated by magmatic disintegration. It is noteworthy that the magmatic deposits at Laki also have a median grain-size of this magnitude (e.g. Thordarson and Self, 1993). The secondary mode at -1 Φ is also likely to be attributable to magmatic

fragmentation processes. Component analysis (as discussed below) shows that the remaining sub-populations with modes at 0.5 Φ, 3 Φ and 4 Φ represented the phreatomagmatic components of the G2004 fragmentation scenario. These distributions strongly suggest that the magma went through several modes of sequential fragmentation.

I can envisage two different scenarios by which the plume could come to contain these two sets of grain-size populations originating from different styles of fragmentation: (1) It is possible that because there are two vents active simultaneously, one may be dominated by magmatic fragmentation and the other by phreatomagmatic fragmentation dominates; (2) It is possible that only the outer domains of the rising magma columns come into contact with water, while the centre portion remains isolated from it. Based on the close proximity of the two vents, their geometry and their location within the ice cauldron, the first scenario (i.e. that at one vent there was ready access to water and at one the access was limited) seems improbable. Furthermore, during periods of sustained activity where both vents were simultaneously active, visual evidence confirms that there were intermittent rooster-tail explosions at both vents (see photo panel, Chap. 3). Finally, although evidence for magmatic activity is concentrated in phases where both vents were active, there is a significant contribution of fallout of magmatic clasts within units where dispersal patterns indicate emission from a single vent (i.e. Unit E, when only the western vent was active, and Unit G, when only the eastern vent was active). It is therefore much more likely that both vents were inundated with sufficient water to cause intense phreatomagmatic fragmentation at the column margins, but that this water was not able to effectively mix through the entire mass of the column.

The initial phase of the G2004 eruption (units A and B) consists in large part of low bubble number density fragments with angular, blocky and equant morphologies indicative of the brittle fracture induced by the passage of stress waves through an out-gassed melt (Morrissey, 1990). The observed shift to more vesicular clasts with the onset of Unit C suggests a shift in volatile-magma flow regime which accompanied the sustained explosive eruption. The sulphur content of units A and B is effectively no different that that of any of the later units (C-G). So, the difference in overall vesicularity can only be attributed to out-gassing of the portion of the melt that was

erupted first (Chap. 7). That is, during the initial ascent of the G2004 magma part of the bubble population must have escaped from the top of the magma column before it encountered external water. This could have occurred if the rate of magma ascent was slow enough to allow bubble to rise and escape ahead of it, or could indicate that the there was a short-lived pause in magma ascent (without significant cooling) during which time volatiles were able to escape. Both scenarios strongly indicate that between the ejection of units A/B and Unit C there was a significant increase in the velocity at which magma rose.

However, despite an increase in bubble number densities of individual clasts there is little change overall in the form of the clasts except for a minor increase in the proportion of ragged and cuspate fragments. The changes in magma flow conditions were not accompanied by any change in the fragmentation regime, which was still governed by brittle failure of a quenched melt. This is an interesting observation because it implies that eruption intensity was governed by magmatic/conduit processes rather than by changes in the supply of external water to the shallow vent region. Units C, E, and G contain up to 20 % of microvesicular clasts with high bubble number densities. This is a rather large proportion compared to the products of other basaltic explosive eruptions (Sable, 2006) which suggests that the magma episodically underwent coupled degassing and the development and disruption of a magmatic foam head a result either of rapid decompression or of high ascent rates. Units D and F, each formed by column collapse events, contain 85-95 % moderately vesicular material as magma buoyantly rose to the surface but the magmatic foam component is significantly diminished compared to that within units associated with sustained activity. Variations in the non-juvenile content of pyroclastic deposits may reflect variations in eruption intensity, the degree of involvement of external water, or both (Fisher and Schminke, 1984). Non-juvenile content in the < 0 Φ size fractions throughout the G2004 sequence is generally very low (on the order of 1-2 % only) and only forms a significant component in Unit C (8%, on average). In this case, the increase in non-juvenile content is unlikely to indicate an increase in the involvement of external water as there is no associated major change in clast morphology or abundance of fines that would indicate a difference in magma-water mixing ratios or increased depth of penetration of external water.

Pyroclast morphology is dependent upon the physical properties of the melt and the rate of heat energy release during fragmentation. The dominance of one mechanism over another (e.g. brittle, ductile or viscous deformation) is dependent upon the viscosity, surface tension and yield strength of the magma (Heiken, 1972). Blocky fragments, akin to "Type 1" of Wohletz and Sheridan (1983), are by far the most dominant clast type in the G2004 deposit. The dominance of blocky, equant clast shapes in phreatomagmatic eruptions is due to thermal contraction and shattering of glass whereby brittle fracture occurs before and during quenching (Heiken and Wohletz, 1985). This distribution of components is most similar to those produced by deep-rooted vertical explosions from Surtsey (Morrissey, 1990). Intermittent, shallow and hemispherically expanding rooster-tail explosions, by contrast, produce largely smooth irregular clasts with quenched surfaces, which are not observed to a great degree within the G2004 deposit which indicates that this style of activity formed a very minor component of this eruption. Analogue experiments by Morrissey (1990) show that this type of fracturing is associated with rapid pressurisation of external water to near the critical value, at which point it exists in a saturated to supersaturated liquid state. This pressurisation transgresses into low magnitude shock waves which pass through and shatter the melt. Blocky clasts with curvi-planar surfaces and bisecting vesicle walls, such as those observed in G2004 samples, are considered to be produced in systems where the water/magma mass ratio is between 0.3 and 0.6. This is close to the maximum efficiency value for the conversion of thermal energy from the magma to the mechanical energy of fragmentation (Wohletz, 1983 and Fig. 5.17).

The fact that mossy clasts (which are indicative of viscous tearing and are characteristic of MFCI type interactions) are not present within the G2004 raises the question as to whether ash generation really was driven by an MFCI-type process in this eruption. An outstanding characteristic of the G2004 magma is that it is highly vesiculated prior to the point at which it comes into contact with external water. This is an important feature because (i) the high vesicularity implies that the magma may already be at or past the point of disintegration by expansion of magmatic gases and (ii) foam has much higher yield strength than non-vesicular magma (Pinkerton and Norton, 1995) and thus may interact differently upon contact with external water. For instance, it has not been possible to successfully detonate highly vesicular melt in the course of laboratory experiments on explosive magma-water mixing (Zimanowski *et*

al., 1995) as increases in the melt viscosity and volume fraction of non-condensable gasses tend to suppress detonation (Corradini, 1991). Although in some circumstances thermal detonation associated with vapour film collapse may cause fine phreatomagmatic fragmentation, this may not be the only mechanism. Another possible mechanism is that ash generation is driven directly by quench-induced fracturing of the magmatic foam body - or even of individual foam clasts produced by magmatic disintegration – or even that permeating quench fractures create a network of micro-cracks which weaken the magma sufficiently for expansion or flow-induced stresses to disintegrate the melt further. Clearly further work is needed in order to identify, then either validate or discount, alternative mechanisms for phreatomagmatic fragmentation.

Figure 5.17: Plot of mass ratio of water to magma (R) versus the conversion ratio (the proportion of thermal energy from the magma that is converted to mechanical energy, CR) for varying eruption styles and resultant deposit morphologies. The dark grey area under the curve delineates the range of R and CR expected to correspond to tuff ring formation; the light grey area defines the favourable range of R and CR for tuff cone formation. (After Wohletz, 1983).

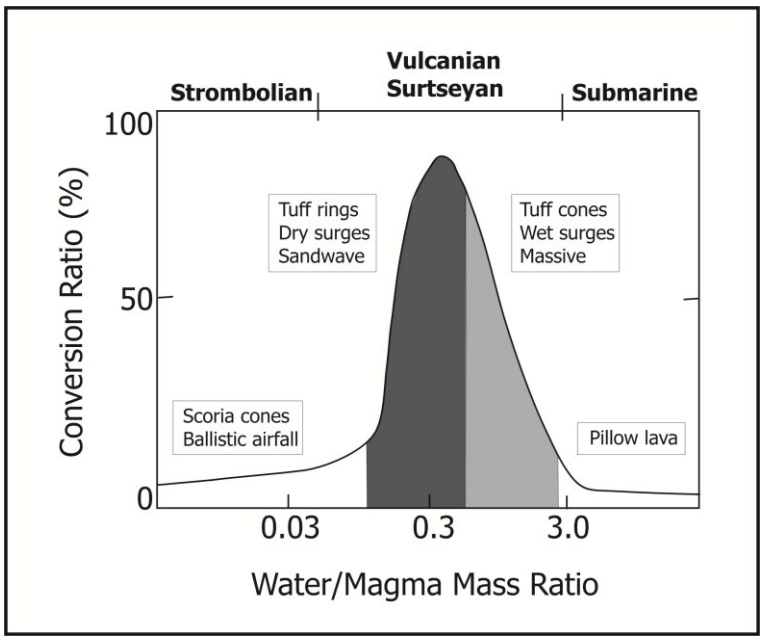

5.6 CONCLUSIONS

The original grain-size distribution produced by fragmentation of magma within the conduit is demonstrated to be increasingly fractionated and modified by transport processes with increasing distance from the vent. This effect is particularly pronounced for air-fall deposits. Reconstruction of the total layer grain-size distribution, however, is shown to reliably reflect only the fragmentation signature.

The persistence of the same modes, median diameters and sorting values across all of the G2004 eruption units, irrespective of transport and deposition mechanism, indicates that a common fragmentation regime was operating over the course of the entire event. The polymodal distribution which incorporates coarse sub-populations with modal diameters associated with dry, magmatic fragmentation as well as fine sub-populations associated with wet, phreatomagmatic fragmentation, indicates a sequential fragmentation process in which a foamy melt, which is either at or beyond the point of fragmentation due to vesicle rupture, is fragmented further by phreatomagmatic mechanisms. The dominant process of phreatomagmatic fragmentation is brittle failure due to shock wave propagation. Mossy, convolute clasts which are diagnostic of MFCI interactions are not observed in the G2004 deposit.

CHAPTER 6:

DIFFUSE STRATIFICATION IN A BASALTIC PHREATOMAGMATIC TEPHRA SEQUENCE: DEPOSITION BY PROGRESSIVE AGGRADATION VIA CONCOMITANT PDCS AND FALL DURING PERIODS OF SUSTAINED EXPLOSIVE ACTIVITY

6.1 INTRODUCTION

The 2004 eruption at Grímsvötn volcano, Iceland (hereafter referred to as G2004) commenced as a subglacial event which rapidly melted through 200 m-thick ice to establish a subaerial eruption column which issued from within a meltwater-filled cauldron in the ice (Chap. 3; Oddsson, 2007; Vogfjörð *et al*., 2005). The 2004 vents were located along the bounding caldera fault in the southwest corner of the Grímsvötn caldera, tucked under the western end of the south caldera wall (Fig. 6.1). The style of activity, deposit architecture and dispersal of this event most closely resemble the subaerial phase of a Surtseyan eruption.

Throughout the main phase of the eruption, activity was dominated by continuous uprush, generating an oscillating 6-10 km-high eruption column that was pushed towards the north-northeast by prevailing southerly winds (Oddsson, 2007). The plume was maintained by numerous discrete but closely-spaced shallow explosions sometimes featuring rooster-tail jets (Sigmundsson and Gudmundsson, 2004). The main phase of the G2004 eruption lasted for approximately 33 hours, during which time erupted material within 4 km of the vent (i.e. the proximal sector) was transported and deposited onto the glacier surface by pyroclastic density currents (PDCs) concurrent with tephra fallout from the high plume, as observed during twice-daily eruption surveillance flights (Chap. 3).

The depositional units (i.e. units C and E) which correspond to phases of continuous uprush style activity have been identified within the G2004 stratigraphy as several-metre-thick diffusely stratified sequences which are highly laterally inconsistent (i.e. it is not possible to correlate individual sub-units on a direct basis between sections situated only 100 m apart, Chap. 3).

Thick sequences characterised by diffuse stratification have also been identified in many other basaltic phreatomagmatic tephra sequences - tuff cone sequences in particular, including Surtsey (Thorarinsson *et al*., 1964), Hrossaborg (Einarsson, 1965), Hverfjall (Lorenz, 1974; Matteson and Höskuldsson, 2010) in Iceland, and elsewhere around the globe (e.g. Faial, Azores, Cole *et al*., 2001; Ichulbong tuff cone, Korea, Sohn and Chough, 1992; Coombs Hills, Antarctica, McClintock and White, 2006). However, despite the fact that workers have provided diverse and case specific interpretations of the mode of emplacement of such sequences, a unified explanation has hitherto evaded us. This is perhaps because previous studies are largely confined to tuff cone structures. This has several key limitations: (a) although they provide a wonderful stratigraphic record, tuff cones are near-vent succession and thus record only the very proximal processes, (b) they are inferred to have high accumulation rates and it is therefore assumed that event distinctions are blurred, (c) the fact that most are emplaced on relatively steep slopes adds complexity to the deposit, (d) the nature of outcrops (i.e. usually on cliff faces) means that close-up examination is often limited to specific vertical sections of short (metres to tens of metres) lateral exposure.

Evaluation of the G2004 deposit provides a unique opportunity to gain new perspectives because (i) it permits examination of the tephra blanket away from the cone succession and (b) the sequence of events and their timing is well constrained through visual observations, seismic data and plume height records. Extensive stratigraphic coverage of the deposit in the proximal sector allows for detailed reconstruction of dispersal characteristics and lateral facies variations within individual units (Chap. 3). Complementary data documents the internal physical and chemical deposit characteristics, including: bulk deposit density (Oddsson, 2007); grain-size distribution and componentry studies (Chaps. 4-5); major and trace element and volatile compositions of the tephra (Chaps. 6-7).

Hence, the purpose of this paper is to characterize the texture (grain-size, clast types and shapes) and depositional structure of the main phase units (C and E), because they provide new insights into modes of tephra emplacement and deposition during sustained phreatomagmatic eruptions and afford a new way of interpreting such tephra sequences.

Figure 6.1: Locations of stratigraphic sections mentioned in the text are shown in relation to their position within the Grímsvötn caldera. The 2004 crater lake is shaded in blue. Inset: map showing the location of Grímsvötn central volcano (red box) and the extent of G2004 tephra dispersal across Iceland (grey shading corresponds to the area within the 0.1 kg m^{-2} isomass line).

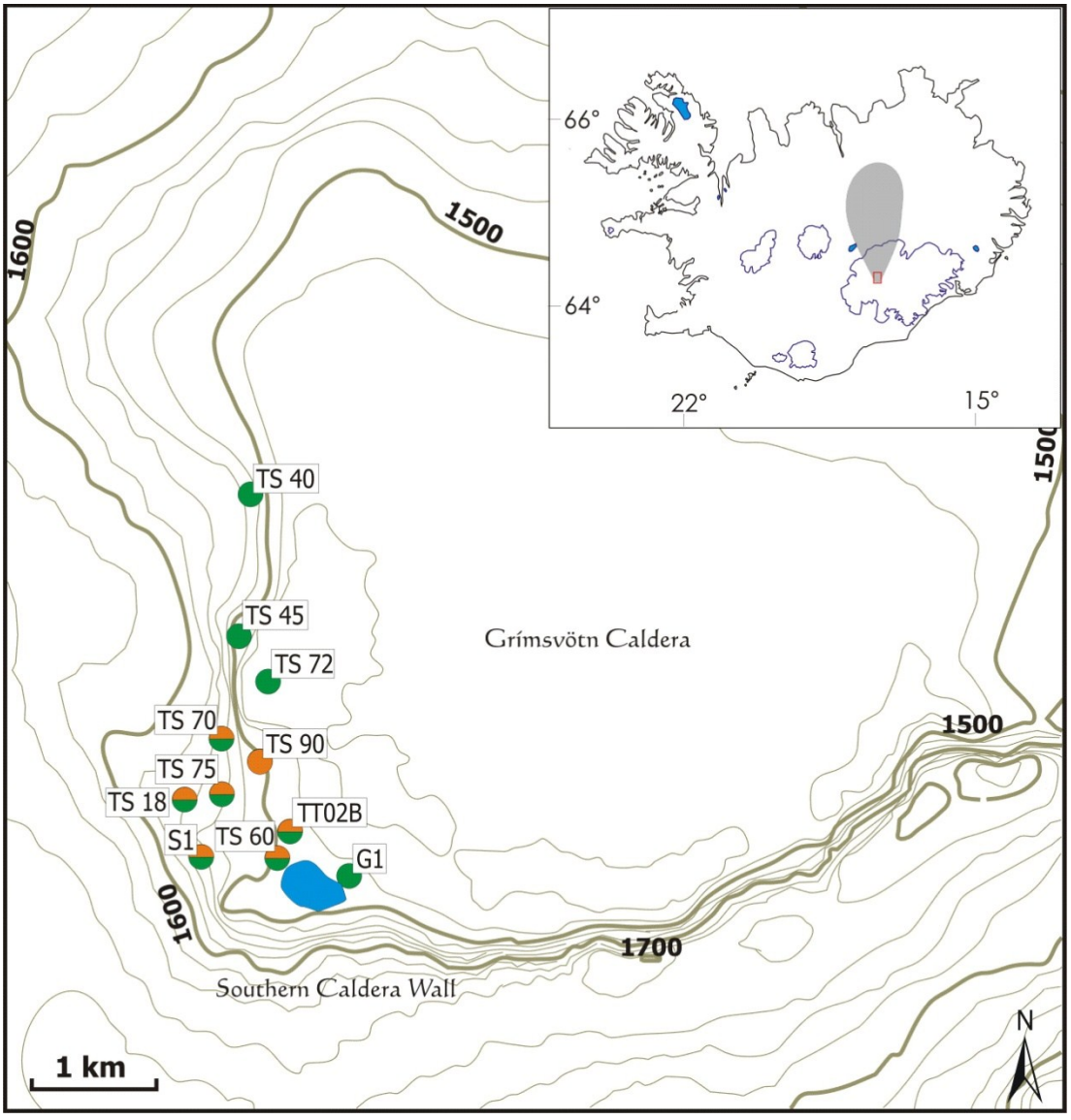

6.2 BACKGROUND

PDC deposits accumulate by rapid succession of surging pulses forming decimetre to metre-thick units, which can be massive, diffusely stratified or distinctly cross-bedded, depending on the depositional regime and solid concentration of the current (Druitt, 1998). Pyroclastic density currents are now considered to represent a continuum of processes between high particle concentration flows and low particle concentration surges (Druitt, 1998). Historically, however, these end-member regimes were considered to result from entirely separate dynamic mechanisms. Consequently, contiguous depositional processes for pyroclastic flows and pyroclastic surges were ruled out.

In his seminal 1966 paper addressing the mechanisms of pyroclastic flow emplacement, Fisher introduced the concept of a "depositional boundary layer" – the transitional deceleration zone situated between the high velocity body of the overriding flow and the stationary ground, which develops due to drag. According to his model, deposition is continuous across the transition zone at the base of the current. Deposits are consequently massive and poorly sorted as particles are deposited together in the reduced velocity zone irrespective of size. Furthermore, deposition is a process which operates continuously through the passage of the current and so the layer gradually thickens (Fisher, 1966).

Sparks (1976) later introduced what is now known as the "en masse freezing" model for PDC deposition. This model postulates that a flow comes to a halt abruptly over its entire depth as it runs out of energy. Consequently, (taking into account post-deposition deflation and compaction) the thickness of the deposit is equivalent to the thickness of the current that produced it and the internal stratigraphy of the deposit reflects the internal organisation of the current itself. Most researchers favoured this model of fluidised en-masse transport and deposition for pyroclastic flows because of the thickness, apparent lack of stratification, and the vertical distribution of non-juvenile versus pumice clasts within pyroclastic flow deposits.

Nevertheless, Fisher expanded his concept of a depositional boundary layer to consideration of end-member surge-type deposits. In his 1990 study of the Mount

Saint Helen's blast deposit, Fisher emphasised the interpretation that surges form by the combined action of a separate transport and deposition system. The regional-scale transport system is considered to be responsible for general trends such as fining and thinning of deposits away from the vent, while the deposition system, at the base of a moving surge, is very local in scale with characteristics determined by the rate of material supplied by the transport system and the influence of local topography. In this sense, emplacement by dilute surges was viewed to take place by an entirely different mechanism than that of concentrated pyroclastic flows.

The concept of a density stratified pyroclastic current which was introduced by Valentine (1987) to describe a density-graded system, irrespective of particle concentration or the presence of density interfaces, built upon these concepts to introduce the premise that pyroclastic flows and surges are end-members in a continuous spectrum of pyroclastic density current, between which all particle concentrations are possible (e.g. Valentine and Giannetti, 1995)

In 1992, Branney and Kokelaar presented evidence controverting the widely accepted notion of ignimbrite emplacement by en-masse deposition. They argued instead that most density currents undergo a process of incremental continuous deposition from the boundary layer, thus expanding on Fisher's (1966) early work and formalising the "progressive aggradation" theory of deposition from pyroclastic density currents. This model accounts for the presence of compositional zoning within flow units (Branney and Kokelaar, 1992; 1997), along with lateral facies variations such as the passage of massive of crudely stratified layers into thinly bedded veneer deposits (e.g. Sohn and Chough, 1989; Druitt, 1992). This theory is further supported by evidence that the duration of emplacement for many large ignimbrite deposits is much longer than the time estimated for a pyroclastic current to travel the length of the deposit (Legros *et al*., 2001), which is inconsistent with a process of en masse freezing.

These new concepts, however, were primarily validated by studies of silicic pyroclastic flows. As a concept traditionally associated with pyroclastic "flow" deposits (i.e. high concentration PDCs) the progressive aggradation theory has yet to be tested against phreatomagmatic tuff sequences, which are typically emplaced by "surges" (i.e. dilute PDCs) which until recently were studied as a separate phenomenon. The theory

that pyroclastic density currents deposit by a mechanism of progressive aggradation from a depositional boundary layer is however, shown to be widely applicable to crudely stratified layers (Branney and Kokelaar, 1992) and is increasingly supported by field observations of both subaerial (e.g. Cole and Scarpati, 1993; Branney and Kokelaar, 1997; Legros *et al*., 2001) and subaqueous (Kokelaar and Busby, 1992; Allen and McPhie, 2009) pyroclastic deposits and indeed deposits formed by non-volcanogenic sedimentation such as turbidity currents (Kneller and Branney, 1995). The application of this concept to field studies of basaltic phreatomagmatic deposits such as those generated by the G2004 eruption continues to direct us towards a more unified theory for mechanisms of PDC emplacement.

6.3 STRATIGRAPHIC CONTEXT OF UNITS C AND E WITHIN THE G2004 ERUPTION

The G2004 eruption consisted of three separate phases of activity, which are distinguished by changes in the observed eruption styles and inferred eruption rates, their diverse deposit structures and components and the presence of clear depositional contacts.

The initial eruptive phase, comprising units A and B, was exclusively phreatomagmatic and commenced with phreatomagmatic ash fall followed by PDCs from a collapsing column (Chap. 3).

The main (second) phase of the G2004 eruption lasted for 33 hours and resulted in the formation of units C-F, which record the bulk (> 80%) of the overall deposit mass. The thinning half distance ($t_{1/2}$) of Unit C is only 520 m in the proximal sector (i.e. within 5 km of the vent). The thinning rate decreases dramatically beyond this point where the average $t_{1/2}$ changes to 4.5 km. Unit E exhibits a similar thinning trend: the proximal $t_{1/2}$ is only 190 m; this increases to 6 km for the distal sector (Chap. 3). Units C and E are the only ones represented in the G2004 distal deposit. Together they represent two periods of semi-continuous deposition over long intervals (12 and

18 hours, respectively) of sustained activity (Chap. 3). By contrast, the units preceding (B and D) and following (Unit F) represent short-lived punctuating events formed by deposition from dilute PDCs (Units B and D) and a concentrated PDC (Unit F). The fact that C and E were formed over such long time periods warrants further examination of their internal structure and texture to assess the nature of their formation.

In the proximal region, units C and E each consist of a sequence of repeated sub-units displaying a range of internal structures from massive to crudely bedded layers, to those which display indistinct and diffuse discordant bedding highlighted by numerous single-clast thick pumice trains (Figs. 6.2 and 6.3). These sub-units are very poorly sorted, exhibit gradational contacts above and below and can be traced laterally for a few metres to tens of metres. These are differentiated on the basis of changes in texture, grain-size distribution and componentry (for which colour is sometimes a good proxy). In some cases boundaries between sub-units can be highlighted by local complexities. For example, where they are terminated upwards by erosional surfaces or horizons of ballistic blocks, pumice lenses, or pumice trains. In the most distal locations and towards the top of the Unit E sequence in more proximal sections, massive or diffusely stratified packages pass into cross-stratified to concordantly bedded packages which are usually inverse-graded and are often capped by distinct fine ash partings up to 1 cm thick.

Units C and E feature a number of sub-units in common, which are clearly identifiable in the field on the basis of differences in the physical properties of the deposit - even though the contacts are diffuse and individual sub-units generally cannot be correlated between sections more than 100 m apart. The sub-units can be grouped into series of lithofacies that exhibit several systematic vertical and horizontal associations.

Figure 6.2a: Stratigraphic log of Unit C packages showing vertical and lateral lithofacies variations in along transects downwind through the central axis. Note that the scale is expanded for section G1 and compressed for section TT02B, compared to the other sections.

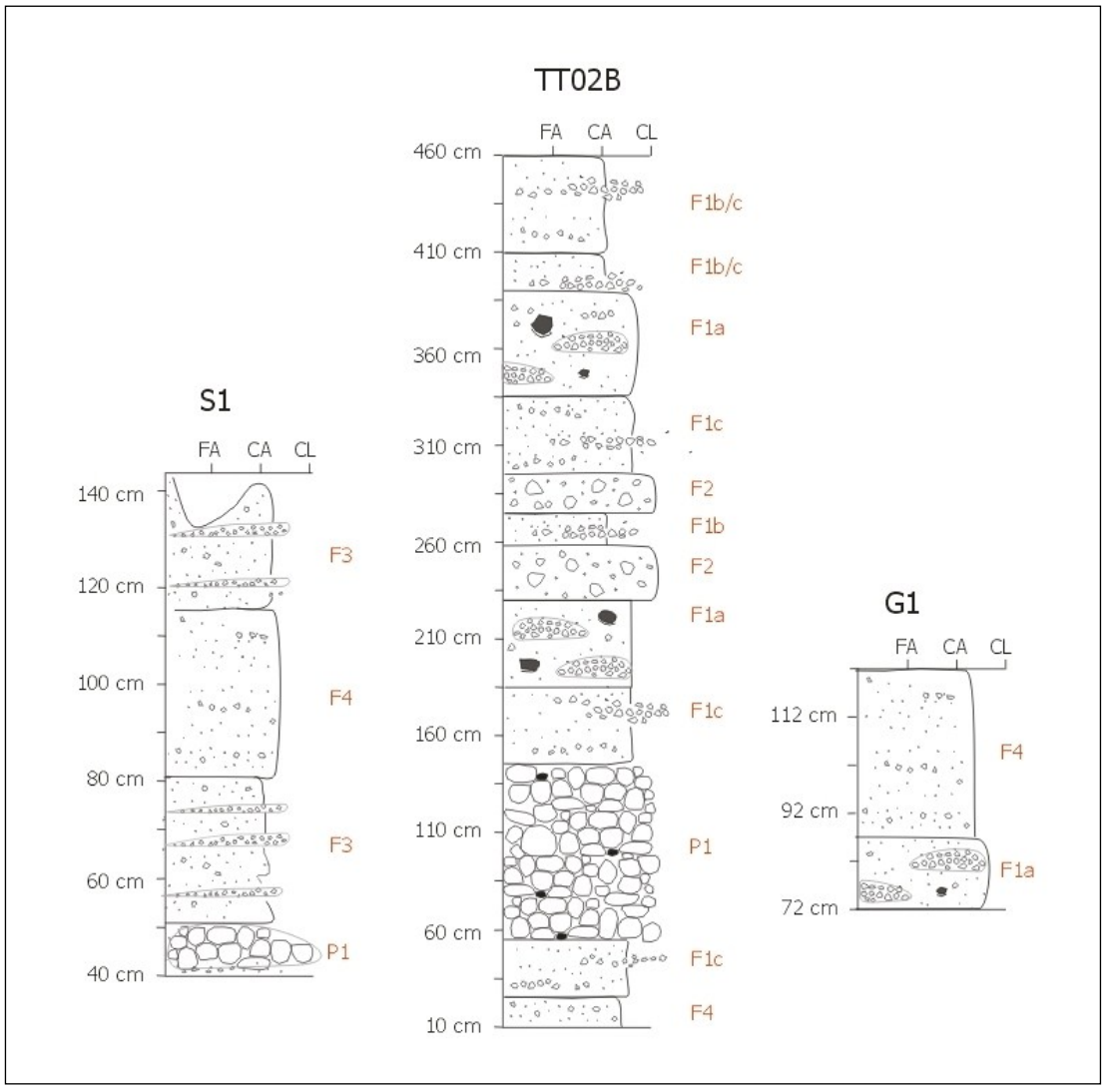

Figure 6.2b: Stratigraphic log of Unit C packages showing vertical and lateral lithofacies variations in along transects in the crosswind direction from west to east. Note that section TS60 is logged from the top down as the full thickness of Unit C is not exposed.

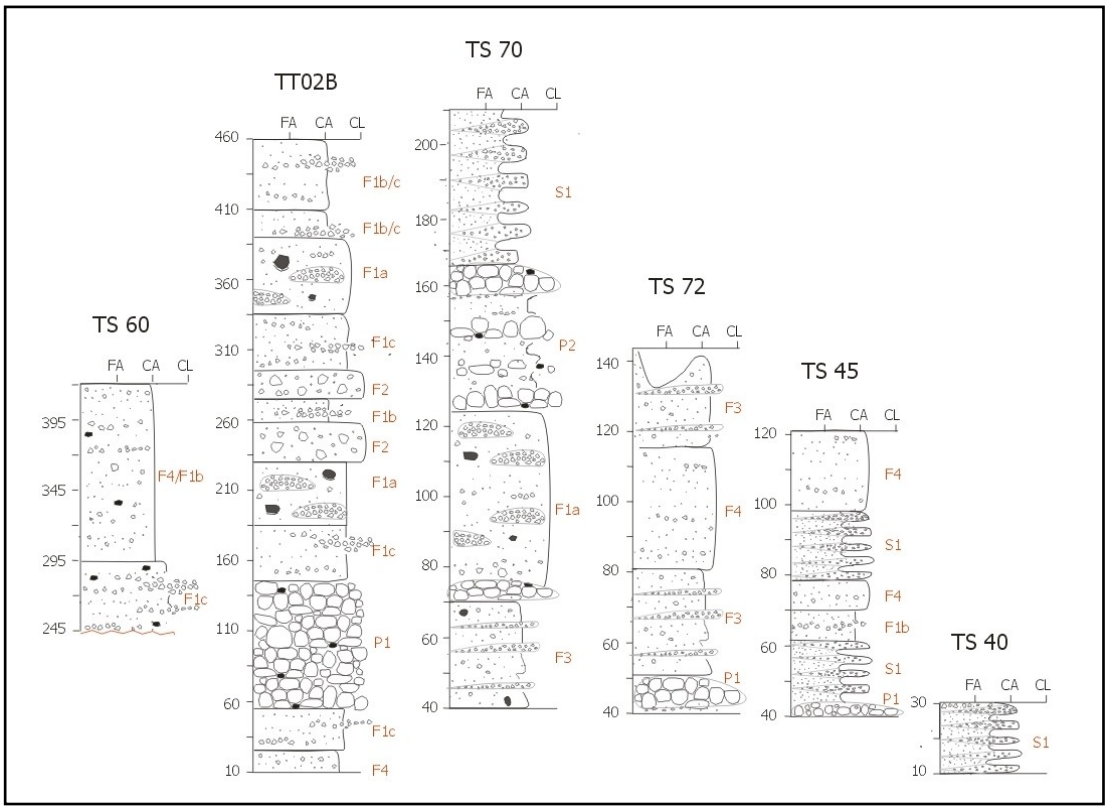

Figure 6.3: Stratigraphic log of Unit E packages showing vertical and lateral lithofacies variations in along downwind transects through the central axis (top) and in the far west of the dispersal area. Note that the scale for section TS60 is compressed relative to that of the other locations.

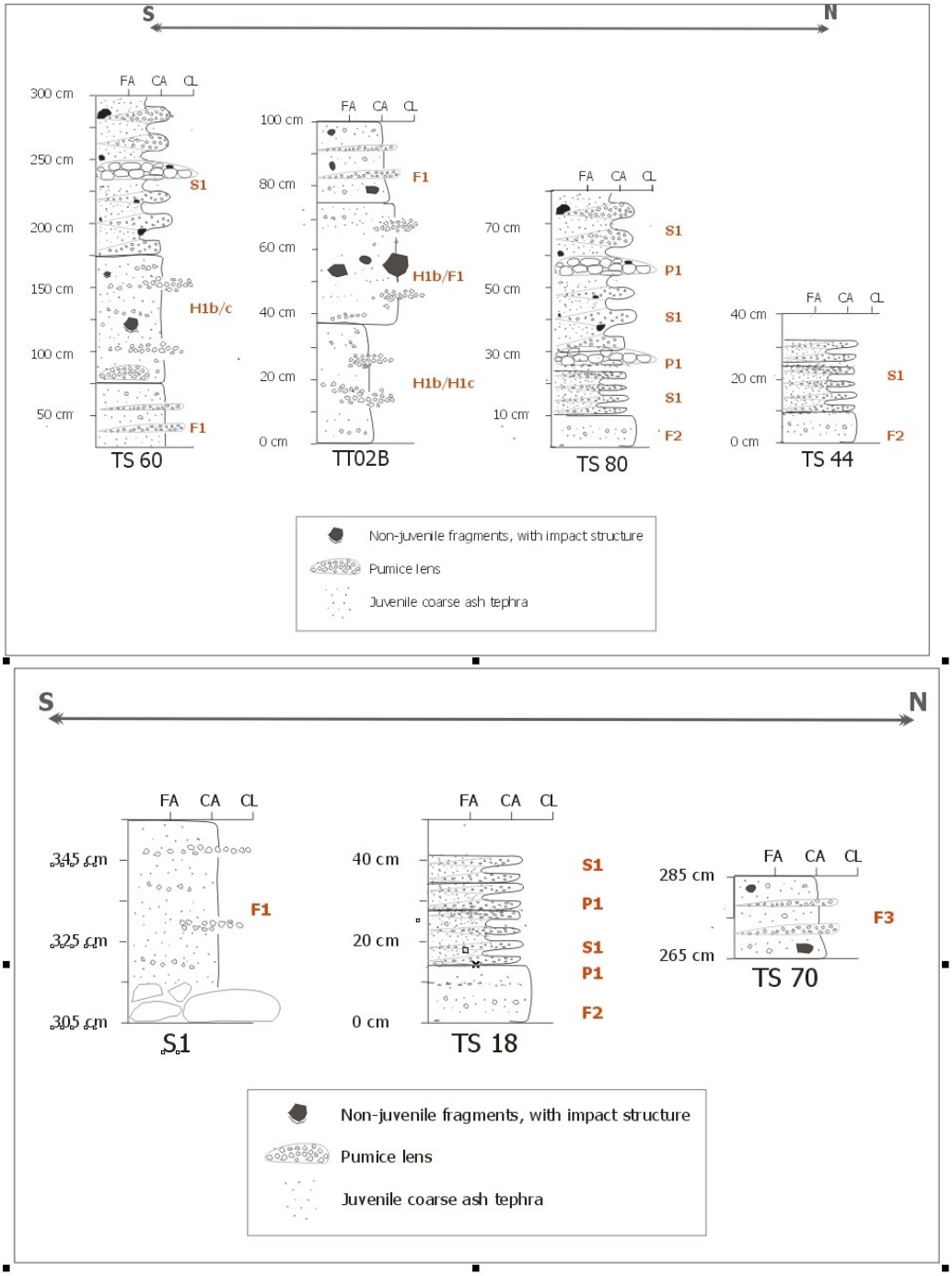

6.4 LITHOFACIES

Units C and E feature two end-member pyroclastic fall and PDC lithofacies, and a number of hybrid lithofacies which fill the spectrum between the two; some are closer to the pure pumice fall in terms of their properties, others are closer to the pure PDC horizons and some represent an approximately 50:50 mixture. In the following section end-member lithofacies types are described and interpreted first, followed by description of interpreted hybrid facies.

LITHOFACIES F1 - CRUDELY STRATIFIED LAPILLI TUFF

DESCRIPTION

Type F1 deposits are grey-brown, massive to crudely cross-bedded, borderline matrix-supported layers which are typically 30 cm thick. Lithofacies F1 consists predominantly of medium to very coarse ash. However, clasts range from fine ash to fine lapilli sized fragments with a dispersed coarse fraction of 2-4 cm clasts and occasional 10-15 mm grey, moderately to highly vesicular basaltic pumice clasts. This lithofacies also features millimetre to centimetre-thick and decimetre to metre-long lenses and trains of very coarse ash to fine lapilli pumice clasts which can be traced for up to ten metres. These lenses sometimes give the impression of planar bedding (Fig. 6.4). Grain-size distributions for F1 packages are bimodal, very poorly sorted (σ_Φ = 3.1) and fine-skewed. The principal mode is located at -2.5 Φ and the secondary mode at 3 Φ (Fig. 6.5). Material in the fine lapilli and coarser size fractions are generally moderately to highly vesicular pumice clasts, while the finer fractions incorporate a range from 30 % vesicularity upwards. Sporadic non-juvenile fragments are generally larger than 5 cm, but usually not more than 15 cm, in diameter.

INTERPRETATION

The bedding characteristics of lithofacies F1 are most consistent with the passage of a high particle concentration PDC, where deposition occurs directly from turbulent suspension and results in massive, poorly sorted beds (cf. Druitt, 1992). However the effects of transient, late-stage traction may be seen where very coarse ash to fine lapilli fragments form diffuse stratification within an ash matrix. Traction

sedimentation indicates a decrease in particle concentration within the density current (e.g. Druitt, 1992; Cole and Scarpati, 1993). However, the predominance of massive horizons and matrix support for pumice clasts denotes rapid particle fallout from the depositional boundary layer. This suggests that traction development was short-lived and incomplete within a quasi-steady flow (cf. Sohn and Chough, 1989; Allen and Cas, 1998).

Figure 6.4: Representative photographs of lithofacies F1 in proximal sections. Note that fine ash predominates, but there is a dispersed coarse fractions which consists of 2-4 cm pumice lapilli.

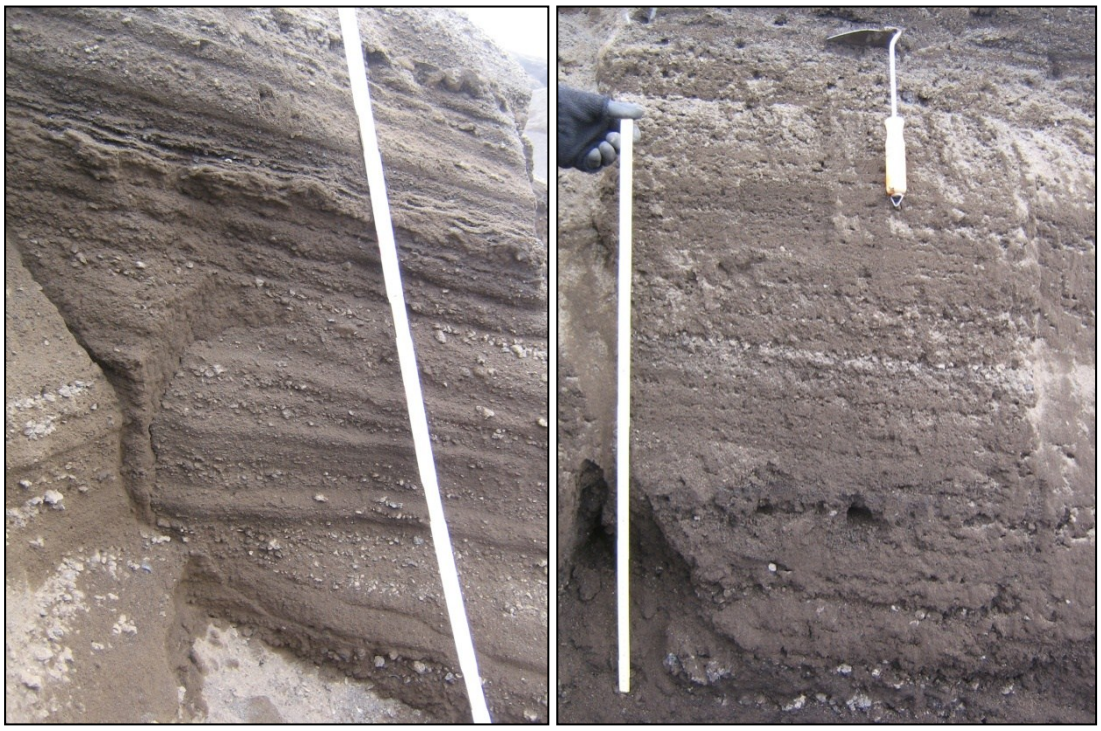

Figure 6.5: Detailed stratigraphic log of Unit E at Section TT02B, accompanied by grain-size distributions for selected subunits.

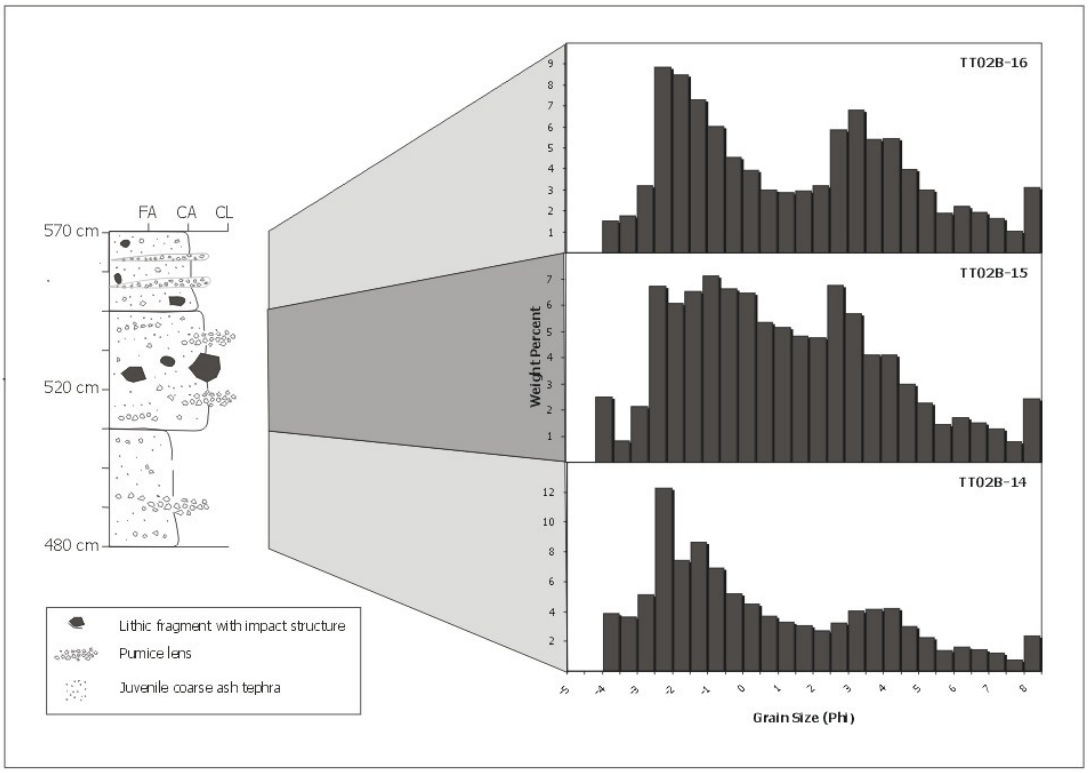

LITHOFACIES F2 - MASSIVE LAPILLI-RICH TUFF

DESCRIPTION

Type F2 layers range between 10-40 cm in thickness and are not found in the most proximal sections. They are brown to greyish brown, massive, matrix-supported and fines-rich (Fig. 6.6). This facies also contains evenly dispersed fine to medium lapilli (2-25 mm) sized blue-black pumice and golden pumice clasts floating in a matrix of poorly to moderately vesicular fine to coarse ash. The coarse components within this lithofacies are often angular pumice fragments with abraded surfaces. Lithofacies F2 is very poorly sorted with an approximately 60:40 ratio of matrix to floating clasts. The grain-size distributions of lithofacies F2 packages are polymodal and fine to very fine-skewed.

INTERPRETATION

The massive nature, poor sorting and lack of internal fabric of this layer are consistent with deposition from a high particle concentration current. Massive beds which occur within dominantly internally stratified deposits have previously been interpreted to reflect suppressed turbulence within either a high particle concentration flow, or in one that is steam-rich, resulting in cohesion and premature deposition of fine material (e.g. Sohn and Chough, 1989; Chough and Sohn, 1990). The evidence of particle abrasion is also consistent with the occurrence of clast-to-clast collisions within a moving current.

Figure 6.6: Photograph of lithofacies F2 in section TS40.

LITHOFACIES S1 - FINELY CROSS-BEDDED TUFF

DESCRIPTION

Type S1 deposits are typically brown-black in colour and are quite distinctly cross-bedded, consisting of usually five or more alternating relatively coarse and relatively fine layers (Fig. 6.7). In proximal locations, the cross-beds are centimetres to decimetres thick and consist of medium to very coarse ash tephra, which are clast-supported and fines-poor with a distinctive coarse base capped by fine ash. In more distal locations individual sets are on the order of 3-6 cm thick and the clast population ranges from fine ash to fine lapilli, consisting predominantly of medium to coarse ash. In these sections, however, the coarse layers are matrix supported consisting of a range from fine to coarse ash (dominantly medium ash). Fine layers appear browner and are dominantly composed of fine ash with up to 25% coarse to very coarse ash. The deposit is moderately sorted within layers. Overall, however, grain-size distributions for S1 packages are bimodal, poorly sorted (σ_Φ= 2.0) and fine-skewed. S1 is the finest lithofacies with the principal mode located at 1 Φ and the secondary mode at 3 Φ (Fig. 6.8). The very coarse ash consists of pumice to moderately vesicular clasts and occasional red, altered non-juveniles, while fine lapilli are grey-golden brown pumice, which are concentrated near the surface.

Figure 6.7: Photograph of section TS18. Lithofacies S1 is highlighted by white lines.

INTERPRETATION

The low-angle cross-stratification of facies S1 suggests deposition from a relatively low particle concentration, turbulent current i.e. end-member type pyroclastic surge. The presence of clast-supported, moderately sorted layers which pinch out on the outcrop scale has previously been interpreted to reflect the occurrence of low particle concentration turbulent eddies within the current from which particles in the depositional boundary layer are transported by traction or even shear-induced grain flow (Sohn and Chough, 1989; Chough and Sohn, 1990; Allen and Cas, 1998). Allen and Cas (1998) interpret bimodality in clast-supported layers to suggest incomplete clast segregation as cohesive, damp ash adhered to lapilli-sized fragments - a process highly applicable to the G2004 deposit. Furthermore, the grain-size characteristics of lithofacies S1 are quite different from those which have been interpreted as end-member fall, end-member "flow" or hybrid processes: it is better

sorted and the modal size fraction is much finer. Finally, the relationship between degree of sorting and median diameter S1 falls squarely within the field defined by Walker (1983) for end-member "surge" deposits (Fig. 6.9).

Figure 6.8: Grain-size distribution of lithofacies S1 from Unit C in section TS40.

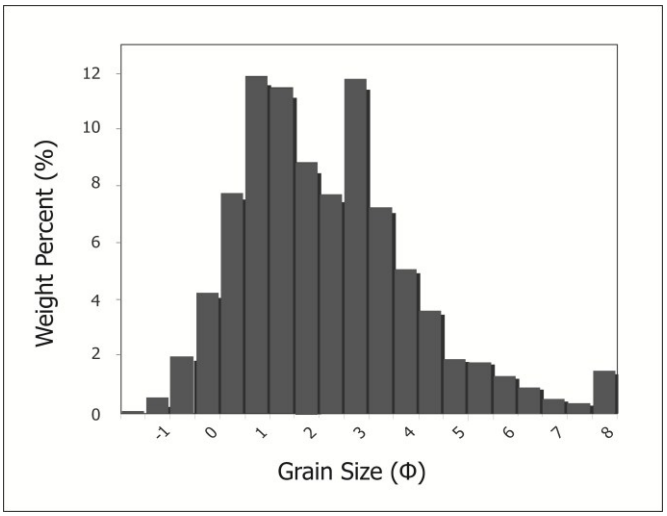

Figure 6.9: Transport regime classification of Unit C and E sub-units and pumice lenses. Diagnostic grain-size fields after (Walker 1983).

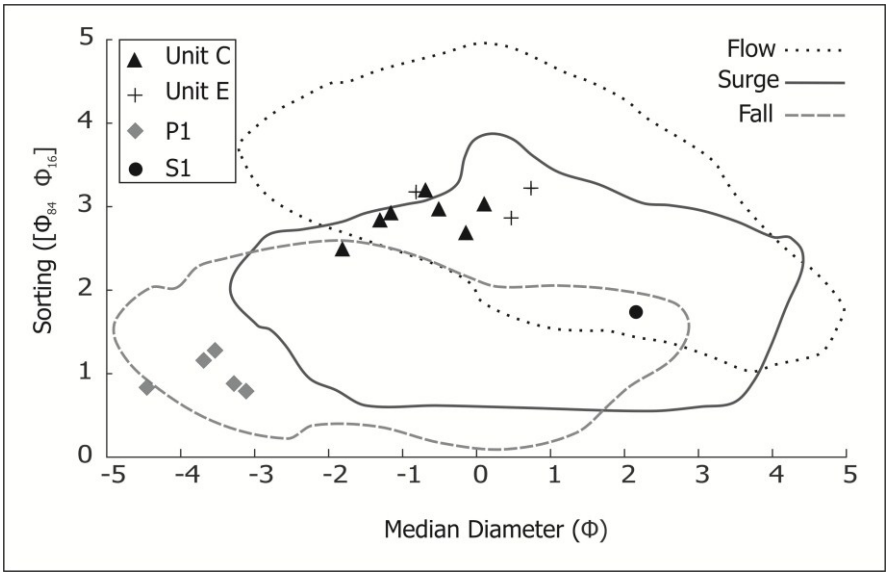

LITHOFACIES P1 - PUMICE LAPILLI LENSES

DESCRIPTION

Coherent pumice lenses are up to 30 cm thick and can frequently be traced for more than 3 m in sections oriented along the dispersal axis. Due to their high aspect ratio, such lenses often look like flat layers, but taper towards the edges in long exposures. Those which are less than 2 m long, by contrast, are distinctly lenticular in shape. Lenses have a flat based geometry with truncated tops and sides. The pumice contained within these lenses are generally equant clasts circumscribed by quenched surfaces, which are up to 10-12 cm in diameter which are usually delicate and highly vesicular golden pumice with blue-black cores, which approach a reticulitic texture. Modal vesicularities for pumice clasts and fragments fall in the range of 60-80 vol. %. Pumice clasts are commonly completely circumscribed by unbroken original surfaces (i.e. ones that have not been modified by transport after fragmentation). Their outer surface is dull (not black and shiny as in magmatic basalt scoria tephra layers). In more proximal locations the lenses also contain frequent non-juvenile fragments that are up to 5-10 cm in diameter and are sometimes red to orange in colour due to hydrothermal alteration. The pumice and non-juvenile clasts are often fines-coated although the lens is clast-supported and fines-depleted overall. Clasts in the interior of the pumice lens are intact pumice bombs which have quenched outer surfaces and are pervasively hydrofractured (Fig. 6.10). These are often larger than 10 cm in diameter and decrease in size towards the edge of the lens. Where the pumice lenses taper out clasts are only 1-2 cm and may consist of broken fragments of equant pumice bombs with quenched surfaces, rather than intact clasts.

Figure 6.10: Close-up photographs of typical massive, clast supported pumice lenses (lithofacies P1).

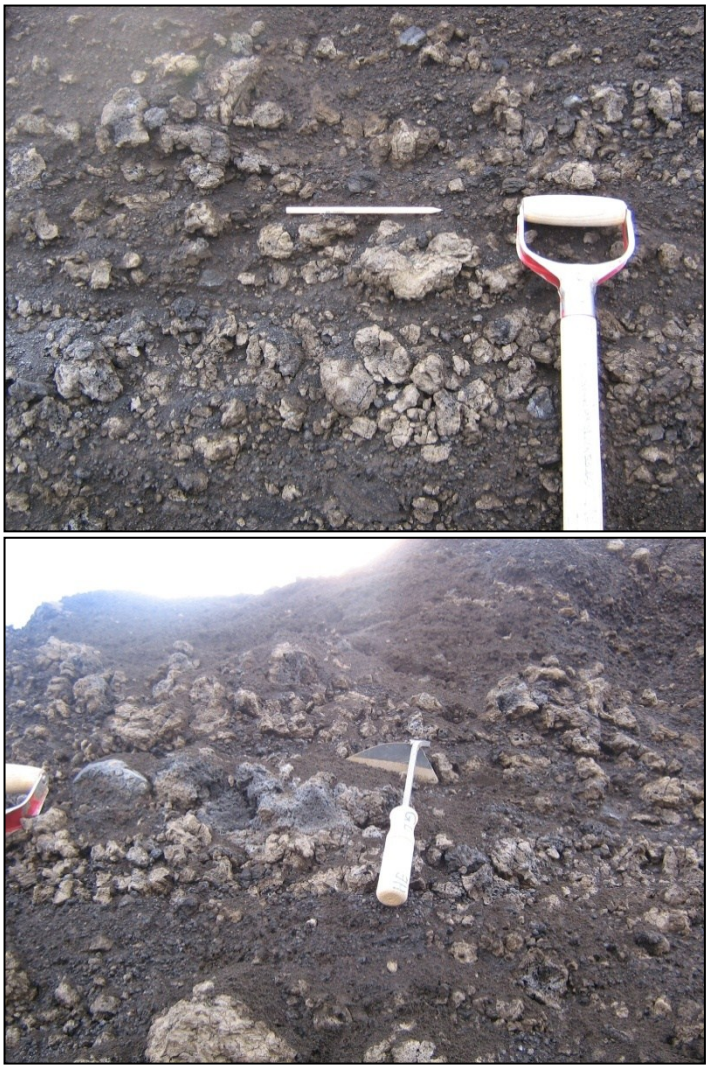

The grain-size distributions for isolated pumice lenses are generally unimodal (Fig. 6.11) as they contain very minor ash-grade fragments, but sometimes feature very minor secondary modes and are moderately sorted. The distributions range from being symmetrical to very coarse skewed (Fig. 6.11). Principal modes are located between -3Φ to -4.5Φ (Table 6.1). Median diameter (Mdφ) and sorting (σφ) values (after Inman, 1952), calculated using the GRADISTAT software package (Blott and Pye, 2001) are plotted against one another to assess how they compare to the characteristic fields for deposits transported via typical end-member fall, flow and surge regimes (after Walker, 1983; Fig. 6.9). All pumice lens parameters fall distinctly within the fall deposit field except for those of Lens 2, which falls just outside of the range observed by Walker (1983). The modal size fraction of Lens 2 is coarser than the boundary of the Walker's pyroclastic fall field but these clasts are clearly not ballistically emplaced clasts and the Md_{Φ}/σ_{Φ} value lies reasonably close to the cluster of values from the other pumice lenses.

Figure 6.11: Examples of typical grain-size distribution for pumice lenses (i.e. lithofacies P1). See Appendix IV for details of method for determining the pumice lens grain-size.

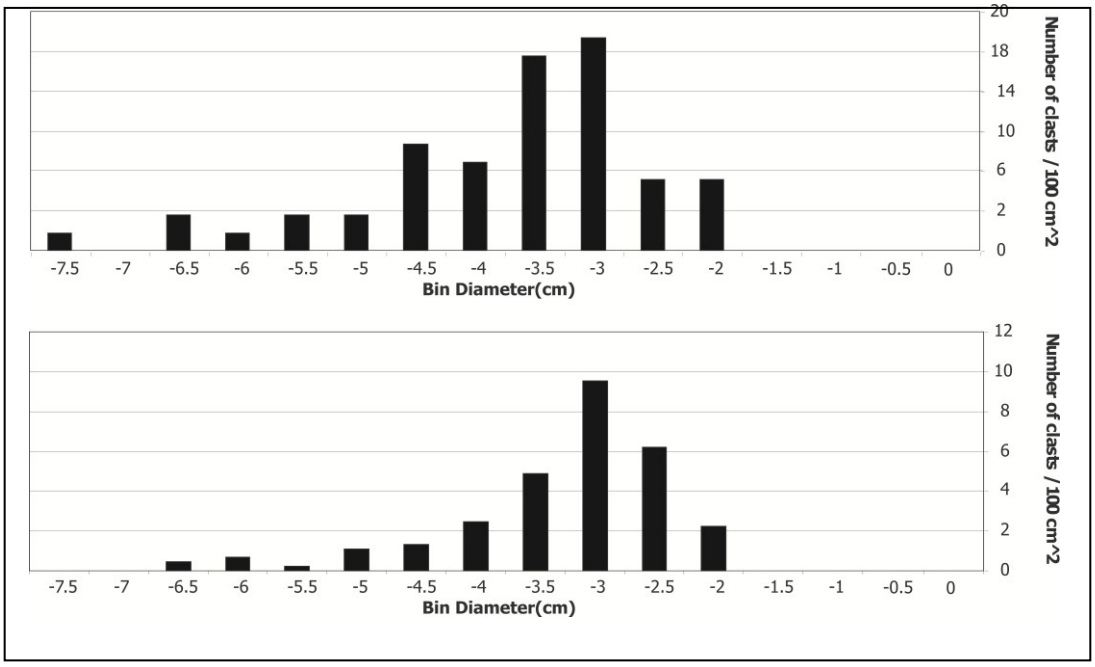

INTERPRETATION

The presence of lithofacies P1 demonstrates that during the G2004 main, continuous uprush phase, part of the magma column consisted of a highly vesiculated foam upon disintegration. From a fragmentation perspective this portion of the foam did not interact to any significant degree with external water, while other parts of the magma column did (cf. Chap. 5). The dull outer surface suggests that these clasts were ejected in a relatively cold gas-particle mixture as opposed to a hot gas-particle mixture (cf. Thordarson *et al*., 1996). The fact that lithofacies P1 consists of intact (equant and not abraded) basalt pumice clots or bombs with quenched outer surfaces which are extremely delicate (these can easily be crushed to dust by hand) shows that these clasts were never exposed to effective clast-to-clast collisions. That is, they were not incorporated into a density current. This is supported by the form of the lenses (flat base and truncated or modified tops and sides) and the fact that ash-grade material is generally absent from the end-member pumice lenses. Grain-size data for these lenses is also unambiguously consistent with the expected distribution resulting from magmatic fall (Fig. 6.9). When the evidence is considered collectively, the only possible explanation for the occurrence of lithofacies P1 is that it is the remnant of basaltic pumice fallout layers resulting from near-magmatic explosions. These layers have later been modified to a degree by erosion by subsequent PDC pulses.

Table 6.1: Grain-size characteristics of Units C and E and of pumice lenses. For units C and E, bulk samples are representative of horizons at increasing stratigraphic height from left to right. Grain-size distributions are plotted according to weight percent for bulk samples (i.e. Units C and E) and by number frequency for those within pumice lenses. Grain-size statistics were calculated using the GRADISTAT program (Blott 2001)).

Unit C							
	TT02B-3c	TT02B-04	TT02B-05	TT02B-08	TT02B-09	TT02B-10	TT02B-11
Md_φ	-1.80	-0.13	-1.17	-0.69	0.11	-1.28	-0.52
σ_φ	2.49	2.67	2.89	3.18	3.01	2.85	2.98
Description	Trimodal, V. poorly sorted, V. fine skewed	Polymodal, V. poorly sorted, V. fine skewed	Trimodal, V. poorly sorted, V. fine skewed	Polymodal, V. poorly sorted, V. fine skewed	Polymodal, V. poorly sorted, V. fine skewed	Polymodal, V. poorly sorted, V. fine skewed	Polymodal, V. poorly sorted, Fine skewed
Unit E							
	TT02B-14	TT02B-15	TT02B-16				
Md_φ	-0.80	0.48	0.73				
σ_φ	3.19	2.93	3.21				
Description	Polymodal, V. poorly sorted, V. fine skewed	Polymodal, V. poorly sorted, Fine skewed	Polymodal, V. poorly sorted, Fine skewed				
Pumice lenses							
	Lens 1	Lens 2	Lens 3	Lens 5	Lens 6		
Md_φ	-3.72	-4.44	-3.51	-3.31	-3.13		
σ_φ	1.15	0.86	1.30	0.88	0.81		
Description	Polymodal, Poorly sorted, V. coarse skewed	Bimodal, Moderately sorted, Symmetrical	Polymodal, Poorly sorted, Coarse skewed	Unimodal, Moderately sorted, Coarse skewed	Unimodal, Moderately sorted, Symmetrical		

LITHOFACIES H1 - DIFFUSELY BEDDED ASH TUFF

DESCRIPTION

Type H1 deposits are brown to grey-brown in colour and packages are up to 50 cm thick. These sub-units form layers which are diffusely bedded on a decimetre scale. The average grain-size is medium ash, but the layers contain a variably dispersed fraction of coarse ash to fine lapilli non-juvenile fragments and juvenile tephra, including sporadic pumice lapilli trains. The H1 packages are polymodal and poorly to very poorly sorted, however the modal size fraction and prominence of each mode vary within each of the three identified sub-types. Type H1b contains fewer non-juvenile fragments than H1a and contains fewer distinct accumulations of pumice within. Type H1c also contains fewer non-juveniles than H1a (Fig. 6.12) and appears slightly more stratified that type H1b, although pumice-rich horizons are more diffuse.

TYPE H1A

Lithofacies H1a exhibits indistinct bedding due to the presence of conspicuous fine to coarse lapilli lenses and trains of basaltic pumice which are typically 10-20 cm thick and less than half a metre long. The layer is matrix-supported, predominantly poorly to moderately vesicular fine to medium ash tephra with a dispersed coarse fraction of very coarse ash to medium lapilli basaltic pumice fragments. Grain-size distributions for H1a packages are bimodal, poorly sorted (σ_Φ=2.2-2.6) and fine-skewed (Fig. 6.13). The modal size fraction is -2.5 Φ. A secondary mode is located at 2.5 to 3 Φ, however this subpopulation accounts for a very minor proportion of the mass compared to the principal mode (Fig. 6.12). H1a deposits contain variable abundances of non-juvenile fragments, or sometimes none at all.

Figure 6.12: (Top) Photograph of a typical lithofacies H1a sub-unit. (Bottom) Photograph of a typical lithofacies H1b sub-unit

TYPE H1B

Type H1b deposits are brown to grey-brown in colour. The layer is borderline matrix-supported to clast-supported and predominantly comprised of poorly to moderately vesicular medium to coarse ash. Lithofacies H1b is fines-rich with sporadic basaltic pumice lapilli trains. Pumice lapilli trains are typically only one or two clasts thick and more than half a metre long (Fig. 6.12). Grain-size distributions for H1b packages are bimodal, poorly to very poorly sorted and fine to very fine-skewed. The principal mode is located between -1.5 Φ and -1 Φ while the secondary mode is fixed at 3 Φ (Fig. 6.13).

TYPE H1C

Type H1c deposits are brown to grey-brown in colour. Numerous basaltic pumice lapilli trains give this facies the appearance of indistinct or crude bedding (Fig. 6.14). The layer is matrix supported and is fines-rich, but also contains a high proportion of fine lapilli tephra, which are predominantly juvenile pumice clasts, making it very poorly sorted. Grain-size distributions for H1c packages are bimodal, poorly to very poorly sorted and fine to very fine-skewed. The principal mode is located at -1.5 Φ. The secondary mode occurs between 3.5 Φ and 4 Φ and is variably more or less pronounced at different stratigraphic intervals (Fig. 6.13).

Figure 6.13: Detailed stratigraphic log of Unit C at Section TT02B, accompanied by grain-size distributions for selected subunits.

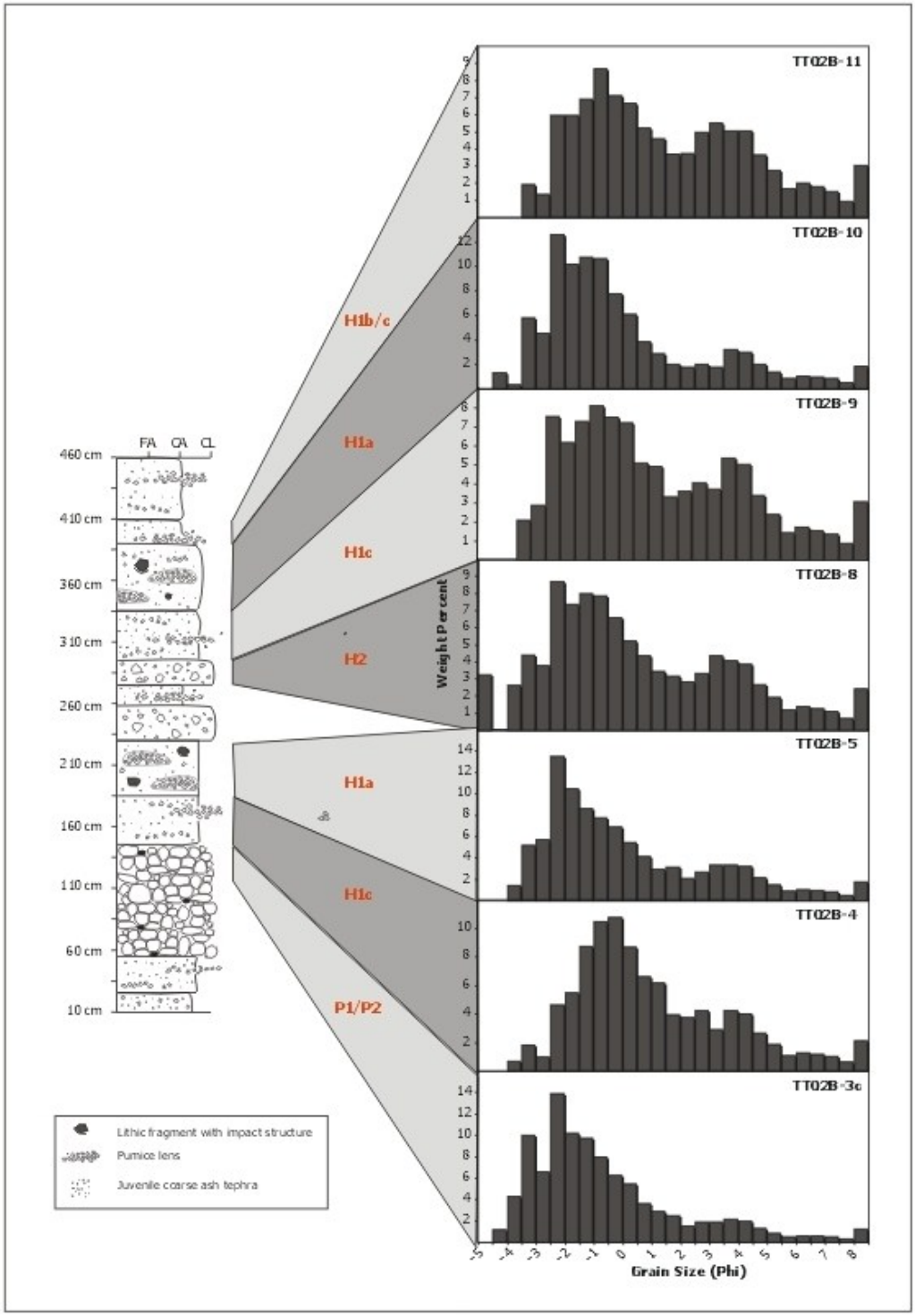

INTERPRETATION

The massive structure of lithofacies H1 punctuated by sporadic accumulations of clast-supported pumice horizons is consistent with hybrid transport processes whereby a variable proportion of material is contributed from an inclined, buoyant plume and attendant PDCs generated from its collapsing column margins. This interpretation is based on the fact that grain-size parameters of each of the type H1 sub-groups fall within the region of overlap between flow and surge deposits, and their internal structures are consistent with deposition from a moderately high particle concentration current with intermediate flow properties. The presence of numerous dispersed pumice trains however is not consistent with deposition from a PDC regime as pumice-rich horizons display similar grain-size properties and internal characteristics to facies P1 (see above). Moreover, observations of the period of continuous uprush during the G2004 event reveal that intervals of deposition via exclusively fall or flow end-members were of relatively short duration compared to that of hybrid activity, whereas lithofacies F1 is the most voluminous sub-unit within the C and E deposit.

Figure 6.14: Photograph of a typical lithofacies H1c sub-unit.

LITHOFACIES H2 – BIMODAL MASSIVE TUFF

DESCRIPTION

Type H2 deposits are brown to blue-black in colour due to differences in the rim vs. core colour of individual pumice clasts within. They form a massive, borderline clast/matrix-supported layer comprised of medium lapilli to coarse lapilli-sized pumice clots floating in a moderately to poorly vesicular fine to medium ash matrix, which is only found in the more proximal sections (Fig. 6.15). Grain-size distributions for H2 packages are polymodal, very poorly sorted (σ_Φ=3.1) and fine to very fine-skewed. The principal mode is located at -2.5 Φ and secondary modes are placed at -1.5 Φ and 3 Φ, respectively (Fig. 6.5). On the Walker plot (Fig. 6.9), F1 layers fall within the characteristic boundary of observed end-member pyroclastic "flow" deposits.

INTERPRETATION

The depositional structure (massive, borderline clast/matrix-supported), lack of fabric, such as normal or inverse grading and grain-size characteristics of lithofacies H2 are consistent with transport within and deposition from a high particle concentration density current in which the depositional boundary layer is undergoing laminar flow. However, the abundance of large fragile pumice clasts, which are neither rounded nor broken and abraded, implies that transport for this component principally involved fallout rather than motion within a vent-generated density current (cf. Allen and Cas, 1998). Lithofacies H2 is only observed in the more proximal sections (Figs. 6.2, 6.3). If we consider these features alongside visual observations noting concurrent plume fallout PDC emplacement it is logical to infer that type H2 deposits result from intermittent fallout of large pumice clots which fell into the body of a PDC but were not carried far from their fallout position. Type H2 is therefore interpreted to result from a hybrid transport process involving deposition by both strongly inclined fall and by pyroclastic flow-type currents.

Figure 6.15: Photographs of borderline matrix/clast-supported lithofacies H2.

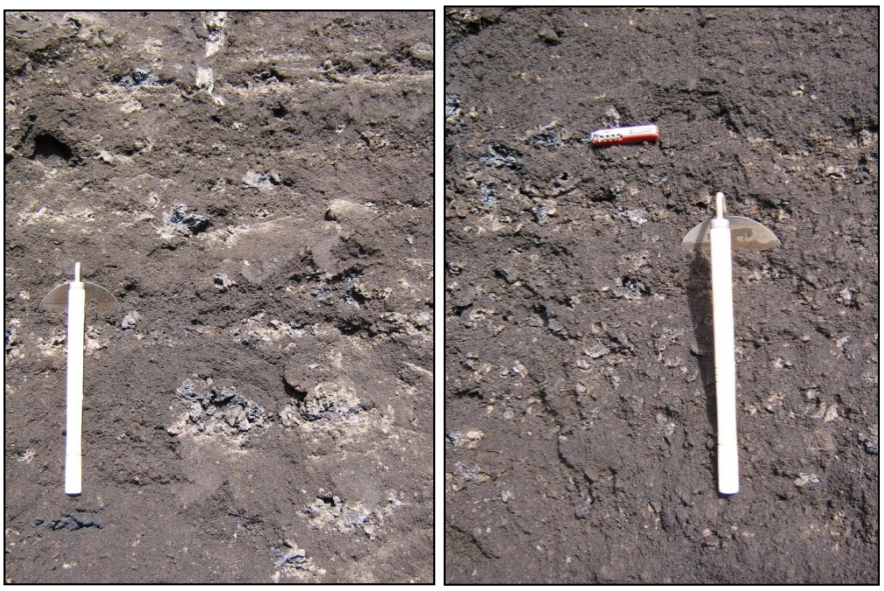

LITHOFACIES P2 - PUMICE LAPILLI TRAINS

DESCRIPTION

Pumice trains are single-clast thick, attenuated or discontinuous horizons of fine to medium lapilli pumice clasts which float within a matrix formed by one of the previously defined lithofacies types (Fig. 6.16). The pumice clasts making up a train are therefore confined to a relatively narrow (5-20 cm) stratigraphic horizon where they are dispersed at 2-10 cm horizontal intervals through the host deposit and have the appearance of diffuse versions of lithofacies P1 which incorporate a substantial proportion of ash-grade material and can be traced for some tens of metres. Lithofacies P2 components are essentially the same as that of lithofacies P1 although the presence of ash coated pumice clasts and foam-armoured non-juvenile fragments is somewhat more conspicuous in the latter (Fig 6.17). In Unit E where pumice trains predominate over lenses, trains chiefly consist of intact pumice clasts with quenched rinds, but in Unit C they are more commonly broken fragments in the fine lapilli size fraction. Lithofacies P2 forms a close association with lithofacies P1 - apart from in the most proximal sections, P2 is always found above or down-current from P1. This relationship is critical to the interpretation of lithofacies type P2.

INTERPRETATION

The similarity in componentry and the close geometric association between lithofacies P1 and P2 implies a common genetic relationship. That is, that both are initially derived from fallout from the high plume. However, the abundance of ash-grade material that is also associated with lithofacies P2 indicates either that the conditions during fallout were different than in P1 fallout, or that the original pumice fall layer from which it is derived has subsequently been modified. Several scenarios are possible: (i) the high plume carries both pumiceous lapilli tephra and moderately vesicular ash, and deposition is promoted by aggregation, such that both size fractions fall out together, (ii) coarse-grained pumice fall as the high plume passes through the co-ash cloud associated with concurrent PDCs and scavenges some of the fine material in the process and (iii) the pumice lapilli is originally deposited as a coarse, fines-depleted, clast-supported layer. Subsequent PDC pulses pluck clasts from at the top and the edges of the fall deposit; the remnant of the fall layer becomes lithofacies P1 while the clasts that are incorporated into the passing current and transported a short distance from the pumice lapilli trains of lithofacies P2.

Figure 6.16: Photograph of a proximal section in the western dispersal area. Pumice trains in units C and E are underscored by white lines. Approximate boundaries of Unit D are outlined in yellow.

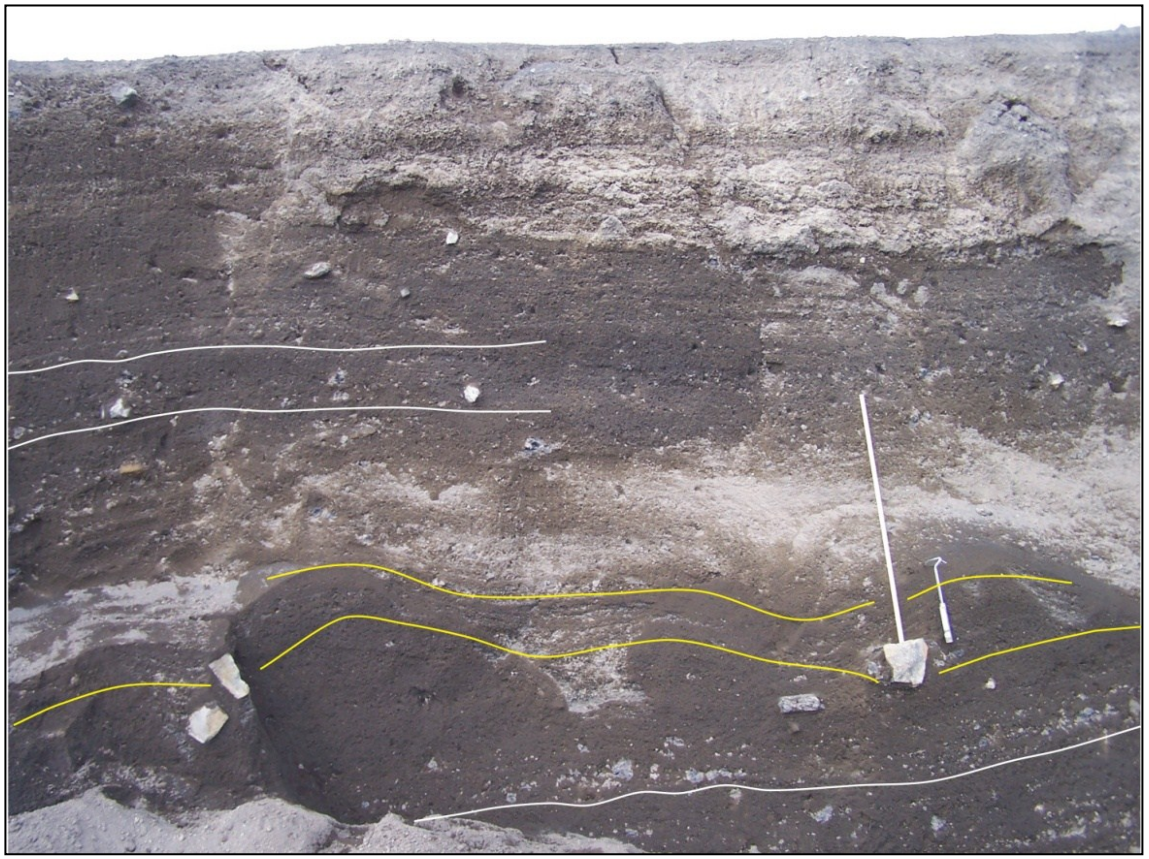

Figure 6.17: Non-juvenile fragments coated in magmatic foam. Photos taken by Thor Thordarson.

6.5 VERTICAL AND LATERAL LITHOFACIES ASSOCIATIONS AND THE SIGNIFICANCE OF THE LENS TRAIN RELATIONSHIP

Transitions between sub-layers are often gradational and thus distinctions between related lithofacies types can be obscure. Nevertheless there are several key vertical and lateral lithofacies associations which recur within Units C and E of the G2004 deposit. Vertical fluctuations between different facies at a single location reflect source conditions such as temporal changes in flow composition and supply rate. Lateral facies variations, by contrast, reflect changes in current dynamics i.e. variations in particle concentration, flow energy, turbulence etc. (Fisher, 1966; Branney and Kokelaar, 1992). Both vertical and lateral facies variations may also reflect the varying contribution to the accumulating deposits from PDCs versus fallout mechanisms. Common spatial and temporal lithofacies associations are depicted schematically in Fig. 6.18.

Figure 6.18: Vertical and lateral lithofacies associations within Units C and E of the G2004 deposit.

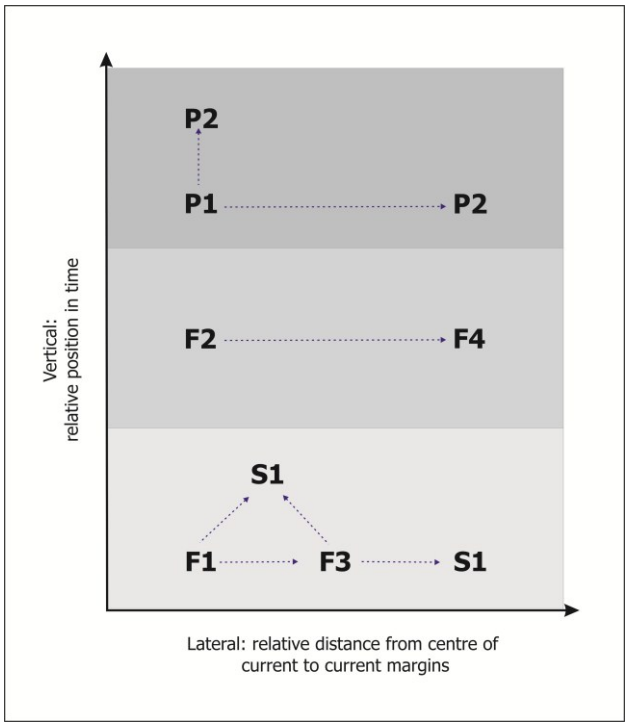

6.4.1 TRANSITION FROM PUMICE LENSES TO PUMICE TRAINS (P1-P2 TYPES)

The pumice lenses (lithofacies P1) and trains (lithofacies P2) occur erratically throughout the deposit and do not form any consistent structural pattern within the context of the remaining five lithofacies. In this sense, despite the fact that they are discontinuous by nature and are finely intercalated with bedded to massive ash layers, they may be considered to each form a unique lithofacies.

In many cases, pumice trains are formed in association with (above or in front of) pumice lenses that have an undulating erosional top surface. Where this occurs the trains consist of a higher proportion of broken pieces of larger pumice clasts relative to intact clasts and it is apparent that they are formed either as pumice clasts are plucked from a pumice layer or lens by an over-riding PDC, or as a pumice lens becomes attenuated by the same mechanism. Thus facies P1 often grades into facies P2 laterally as fall layers are increasingly disturbed by ongoing PDC passage. The vertical P1-P2

association, by the same token, is considered to form by modification of pumice lenses closer to source, which takes place later in time. As Fisher (1966) has pointed out, although stratigraphically higher horizons within a given vertical section are younger than those below, laterally equivalent lithologic zones are not time equivalent as distal sections are younger overall than more proximal sections. Pumice lenses and trains also occur independently of one another, however and so the occurrence of each within a layer can also reflect the intensity and periodicity of fallout, along with spatial variability in plume direction and pre-fallout topography.

The unpredictable nature of the vertical association between lithofacies P1 and all of the other sub-units can also be considered from an eruption perspective as well as that of the deposition process. For example, individual explosions can produce a pumice-laden high plume and an ash-rich PDC. This in turn can produce pumice fall layer that is subsequently overridden by a PDC. This sequence of events predicts a certain pattern (i.e. association) of lithofacies appearance i.e. an end-member pumice lens overlain by ash-rich PDC unit which may contain abraded pumice clasts or trains down-stream. In cases where the pumice lens has been totally removed a sharp gradational contact or fully erosional contact between P1 and any overlying PDC lithofacies can be expected. These relationships are demonstrated in Fig. 6.19.

The lens-train relationship provides key evidence for sustained activity and the interaction of two end-member transport regimes and their consequent depositional modes. The interpretation of pumice lenses and trains as syn-eruptively modified fall layers rather than as rafted pumice within a density stratified current is key to the argument that during the main phase of the G2004 eruption deposits aggraded incrementally from a continuous but unsteady current rather than by the emplacement of successive flows which froze en masse and stacked on top of one another. Intercalated fall horizons within a single flow unit can only occur if there is time for the pumice to fall into or on top of a gradually accumulating deposit by which they are eventually modified and covered. Therefore the thickness and geometry of the fall layers also reflects relative rates of aggradation and the erosive capacity of the density currents (Fig. 6.20).

Rather than occurring as a relatively thick and continuous blanket, fall layers occur as discrete lenses due to any number of factors, including: changes in the particle

size distribution with distance from source, proximity of a given occurrence to the main dispersal axis, changing wind directions, degree of mass loading within the plume, oscillations in plume height, varying partitioning of erupted mass between flow and fall regimes and subsequent modification of thin unconsolidated pumice layers by highly mobile density currents. The alternative to this hypothesis is that pumice lenses are transported via traction or turbulent suspension within a density stratified current from which they are deposited. This scenario is unlikely however because it is inconsistent with structural and textural relationships within the deposit and with the lack of abraded and rounded surfaces among the delicate pumice clasts hosted within lenses and trains. Visual observations of episodic showers from the plume at the same time as persistent ground-hugging density currents by observers during Unit C deposition also lends support to this argument.

Figure 6.19: Flat-based pumice lenses (lithofacies P1) which show evidence for erosion where they are truncated at sides and particles have been remobilised from the top. Photos taken by Thor Thordarson.

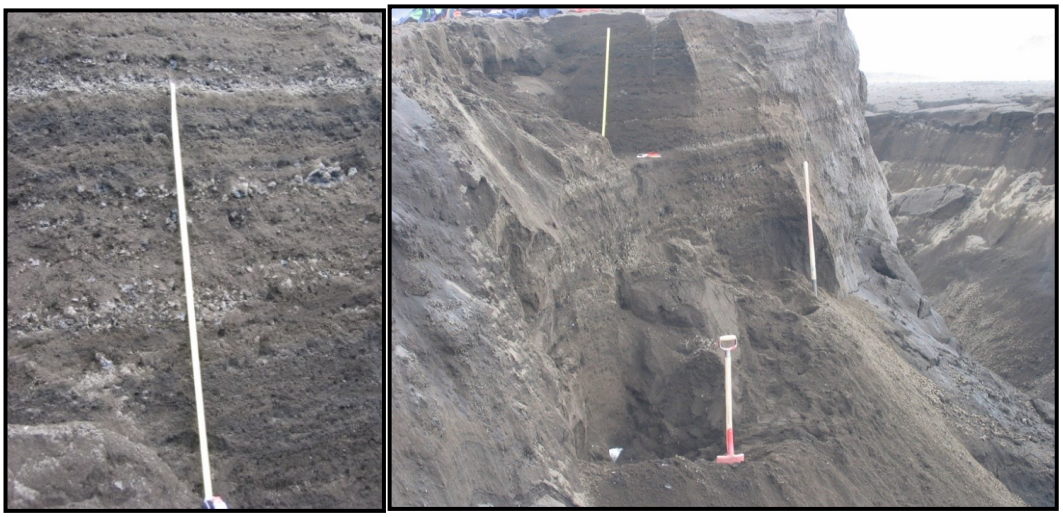

6.5.2 TRANSITION FROM MASSIVE ASH TO CRUDELY STRATIFIED TO FINELY CROSS-LAYERED DEPOSITS (H1-F1-S1 TYPES)

The most complex lithofacies associations are those between H1, F1 and S1 deposit types which form both vertical (temporal) and lateral relationships. Each of these three lithofacies are PDC emplaced deposits which reflect a continuum from end-member "flow" to end-member "surge" characteristics.

LATERAL ASSOCIATION

Time equivalent horizons transition from H1 to F1 to S1 with distance from the vent and towards the deposit margins in the cross-current direction. Thus, a gradual progression into laterally better ordered deposits is identified. This suggests that the sedimentation initially takes place from a relatively high particle concentration current which becomes more turbulent and more dilute down-current as it loses its particle load.

VERTICAL ASSOCIATION

At many locations within the Unit E deposit, facies S1 lies conformably atop lithofacies H1 and F1. This vertical association reflects changes in source conditions and occurs more abruptly than the lateral variations, which reflect changes in current dynamics with gradual energy loss (Fisher, 1966; Branney and Kokelaar, 1992). The rapid transition from thick massive beds, deposited from the main sustained current to thin stratified beds implies a change in either or both of particle concentration and current velocity, such as would occur with waning magma discharge over time.

This interpretation is further supported by the juxtaposition of the H1-F1-S1 association upon the identified vertical relationships between each of these three lithofacies and pumice fall units. Facies H1 displays a far greater degree of interbedding with facies P1 than either facies F1 or S1. Similarly, lithofacies F1 is far more likely to contain intercalated pumice trains (lithofacies P2) than facies S1. Facies S1 is seldom interbedded with either P1 or P2-type deposits except for rare cases where it is underlain by a relatively undisturbed facies P1 layer. This is because, where S1 deposits are associated with waning flow from the vent, the plume is likely to be less energetic and therefore at a lower altitude and less particle-rich, therefore contributing little fall material. Where S1 deposits are associated with flow margins, original pumice fall layers would be finer grained and thinner and are therefore less likely to be

preserved. Facies S1 currents are likely to be less erosive than their H1 or F1 counterparts. Furthermore, pumice scavenged from fall accumulations up-current would probably be so attenuated as to be unrecognisable in distal S1 deposits.

6.5.3 Transition from massive PDC/fall hybrid to massive PDC facies (H2-F2 types)

Facies H2 and F2 are identified within Unit C and are rarely seen in Unit E deposits. These two pumice-rich, massive units are quite similar in appearance but for the fact that facies H2 contains larger and more abundant pumice lapilli clasts and so is borderline matrix/clast-supported. Facies H2 and F2 form a spatial association in which type F2 deposits predominate in more distal sections, or those closer to the deposit margins, while H2 predominates in more proximal sections. Facies H2 is interpreted to have formed by hybrid fall and end-member pyroclastic flow processes, while F2 facies are interpreted to reflect high concentration, laminar flow.

The principal differences between these two deposit types are (i) the proximal-distal decrease in pumice grain-size, which is likely to reflect the shorter residence time of larger clasts within the plume, and (ii) the increasingly matrix-supported framework with distance from source, which is likely to reflect a decreasing volume contribution to the deposit from pumice showers. The fact that facies H2 and F2 are identified principally within Unit C deposits is diagnostic of differences between the currents that produced the two flow units. It is likely that facies H2 and F2 arise only during periods of high discharge and that they reflect higher energy and mass-loading conditions within the eruption column than do facies F1, H1 and S1.

Figure 6.20: Schematic interpretation of pumice lens and train formation. This diagram should be at the end of the data interpretation section - bringing all of the evidence together in a coherent model. Change "local topographic irregularities" to decimetre scale undulations.

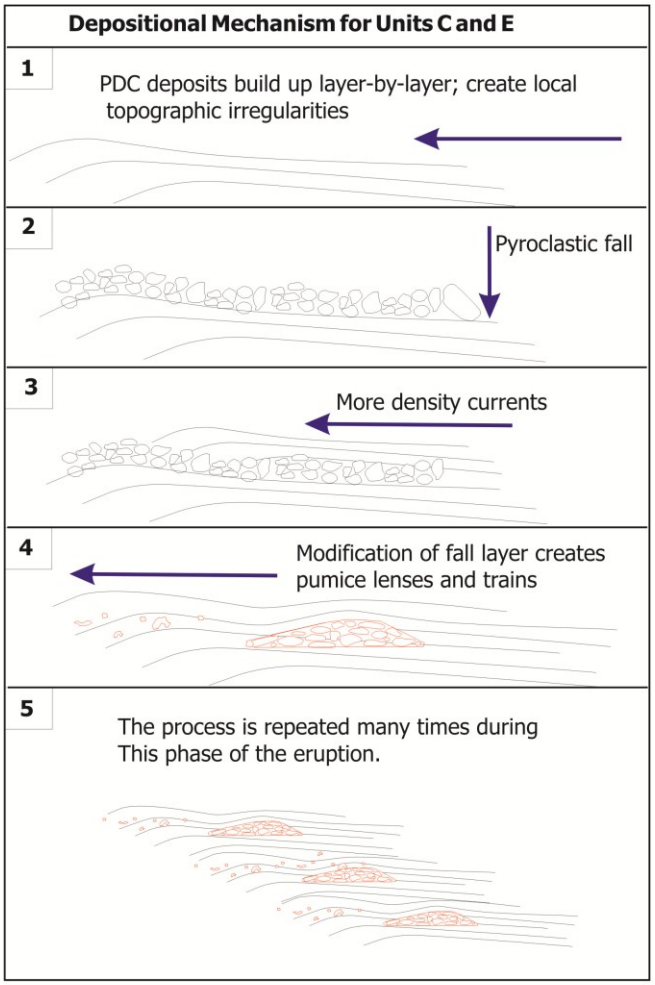

KEY FEATURES OF THE PUMICE DEPOSITS:

- Pumice lenses have a flat based geometry with truncated tops and sides. They are frequently assymetric, having been eroded on the lee side, with clasts "plucked" from the sides and edges.
- They are fines-poor pumice lapilli within a clast-supported framework.
- Larger clasts remain undisturbed in the interior of the lens; these "fine" towards the leading edge.
- They consist primarily of complete and unbroken basalt pumice grains (with quenched and fluidal outer surfaces), which due to their extremely delicate nature (i.e. can easily be crushed to dust by hand) could not have survived intact in a laterally moving flow. These are pervasively hydrofractured causing them to fall apart when removed from the deposit. This is in contrast to the surge material (fine bubble walls, i.e. broken pumice) and the attenuated pumice "trains" which consist of fine lapilli broken pieces of pumice entrained in moving surges. There are no rounded or abraded clasts.

6.6 AGGRADATION OF PHREATOMAGMATIC DEPOSITS WITHIN AN UNSTEADY FLOW REGIME

The timing of eruption and deposition of units C and E is well constrained from seismic and plume height records, as well as by visual observations (Chap. 3). It is therefore possible to calculate average accumulation rates for each unit. A total subaerial mass of 9.11 ± 1.10 $x10^9$ kg within Unit C was erupted over a period of 18 hours and 5 minutes. Unit E contains 4.48 ± 0.54 $x10^9$ kg of material within the subaerial deposit, which was erupted over a 12 hour and 55 minute interval. The average accumulation rate for tephra within the main phase of the eruption was 1.40 x 10^5 kg s^{-1} and 9.63 x 10^4 kg s^{-1} for units C and E, respectively. Similarly, the local deposition rate can also be calculated for different regions of the deposit. For example, at reference section TT02B, located approximately 550 m north of the vent, Unit C is 360 cm thick and Unit D is 160 cm. The average local deposition rate from the C flow-unit in the near-proximal region was therefore 3.3 mm min^{-1}, while for Unit E it was a slightly lower 2.1 mm min^{-1}.

While it is useful to obtain such order of magnitude estimates for accumulation rate as an average over the entire deposit, or for a given location, it is important to recognise that internal stratification reflects changes in flow steadiness over time (e.g. magma supply rate, magma composition, eruption style etc.), while lateral lithofacies changes may also reflect spatial variations in flow evolution (e.g. particle supply rate to the depositional boundary layer, topography, cooling rate and volatile exsolution; Branney and Kokelaar, 1992). In this way a single depositional unit may record successive modes of deposition from an evolving boundary layer. An obvious example of this is that PDC units thin with increasing distance from source. The deposition rate in distal regions is therefore considerably lower than that of the proximal area of the deposit. The changing rate of sedimentation reflects not only the diminishing particle load of the current and its reduced kinetic energy, but also in many cases a change in the depositional regime such as aggradation of the deposit by traction rather than directly from turbulent suspension. Regardless of the disparity in flow steadiness, deposition still takes place incrementally during the passage of a single current.

Reconstruction of the total layer grain-size distributions for each unit within the G2004 deposit reveals that if the effects of sorting by transport are eliminated processes, then the location of the principal modes is the same across each depositional

unit (Chap. 5). This observation points to a common fragmentation mechanism which operated continuously throughout the eruption. Nevertheless, at a fixed location within units C and E while the GSD changes with stratigraphic height indicating temporal variations in the transportation regime, the componentry remains relatively consistent. These observations imply that successive packages within a single flow unit must have been emplaced incrementally on top of one another from a depositional boundary layer which comprises a random mixture of all available components. Therefore the alternating locations of grain-size modes directly reflect trends in current steadiness over time (i.e. parameters such as particle concentration, flow energy etc.) and the variable proportion of material contributed by tephra fallout from the plume.

The process of progressive aggradation accounts for the overall poor sorting of the G2004 deposit and is consistent with the documented accumulation of material from plume fallout simultaneous with an erratically dispersed density current of fluctuating composition and particle concentration. The oscillating, yet systematic, vertical variations in composition, deposit structure and texture, particle size distribution and componentry are dependent upon variations in the chemistry and eruption dynamics at the source and are also best accounted for by the progressive aggradation model. Lateral facies variations within the deposit are dependent primarily upon local rates of energy loss within the current (Fisher, 1966).

6.7 CONCLUSIONS

Contemporary observations of the G2004 eruption reveal that during the 33 hour-long main phase of activity continuous uprush style volcanism, similar to that recorded during emergent Surtseyan-style events, dominated. Seismic records confirm that magma supply during this time was uninterrupted, while radar data establishes that the eruption column was maintained for protracted periods of time. It is therefore demonstrated that each unit reflects the passage of a single, sustained pyroclastic density current or, in the extreme case, a succession of pulses which were so closely spaced that deposition was essentially continuous.

Units C and E, which formed during the main phase of activity and together represent ~80% of the total subaerial deposit, are characterised by: rapid internal gradations between massive and bedded layers; intercalated fall and flow packages which lack distinct contacts. These features of the G2004 deposit require that it formed principally through a gradual and continuous process of incremental deposition from individual currents that were sustained for many hours. This study therefore supports the theory of progressive aggradation as a general mechanism for the formation of a broad spectrum of pyroclastic deposits, including massive to finely laminated sequences produced by small volume end-member style basaltic phreatomagmatic eruptions within a glacial environment.

CHAPTER 7

MAGMA COMPOSITION OF THE TWO LATEST ERUPTIONS FROM GRÍMSVÖTN VOLCANO, ICELAND: IMPLICATIONS FOR MAGMA SOURCE AND PLUMBING

7.1 INTRODUCTION

Grímsvötn boasts a unique geologic setting, as its central volcano (GCV) is located almost directly above the centre of the presumed Icelandic mantle plume (Wolfe *et al*., 1997), where it underlies the North Atlantic mid-ocean ridge system. The Grímsvötn volcanic system (GVS) is the most active system in Iceland with several hundred eruptions in post-glacial times, including the third largest flood lava eruption in Iceland (Laki) and the ~10 ka basaltic explosive eruption that produced the widespread Saksunarvatn tephra (Thordarson *et al*., 2003; Jóhannsdóttir, 2007, Thordarson and Höskuldsson, 2008). Grímsvötn is also one of the two most productive volcanic systems in Iceland, and has erupted ~75 km^3 of magma in post-glacial time (Thordarson and Höskuldsson, 2008). The subglacial GCV, which in historic time has produced on average one basaltic explosive eruption every ten years (Larsen *et al*., 1998), features one of the largest high-temperature geothermal systems in Iceland (Björnsson, 1988) and has produced spectacular jökulhlaups onto Skeidararsandur in the south of Iceland (Björnsson, 2003).

GVS products, irrespective of whether they are erupted on the fissure system or from the central volcano, are characterized by moderately to highly evolved tholeiitic compositions, which many workers take as an indication of low-pressure magma evolution (e.g. Métrich *et al*., 1991; Sigmarsson *et al*., 2000; Kelley and Barton, 2008). The compositional range of post-glacial GVS products is rather narrow when we consider it in the broader spectrum of basaltic volcanism in Iceland. This compositional similarity between Grímsvötn and Laki products, along with apparent chemical homogeneity within and among Grímsvötn eruptions has led to suggestions that all GVS eruptions are derived from and fed by a common magma storage zone and plumbing system. This common source was initially inferred to be the shallow

crustal magma chamber beneath Grímsvötn, an interpretation that was used to underpin the importance of lateral flow in driving basaltic eruptions on the fissure swarm via lateral injection from a shallow crustal chamber beneath the central volcano (e.g. Sigurdsson and Sparks 1978; Métrich *et al*., 1991). The importance of lateral flow for driving the Laki eruption was first disputed by Gudmundsson (1987; 1988) on the basis of structural modelling; then by Sigmarsson *et al*. (1991) on chemical grounds by comparison of trace element chemistry of Laki versus Grímsvötn; and finally by Thordarson and Self (1993) on the basis of physical volcanology.

Our high-resolution sampling of the proximal tephra deposits from the two most recent Grímsvötn eruptions (G1998 and G2004) coupled with high precision whole rock analyses enables a more detailed evaluation of the compositional homo- or heterogeneity of magmas from individual GCV events, with appropriate stratigraphic (i.e. temporal) context, than has previously been possible. The surprising result of this work is to contradict the general belief that magmas from individual Grímsvötn events are compositionally homogeneous. The G1998 and G2004 magmas cover an unexpectedly large range (i.e. one that is much larger than observed in the Laki products). The fact that, in a global context, the compositional range of GVS magmas is rather small (4.7-6.8 wt % MgO) emphasises the requirement for good stratigraphic control combined with high precision analysis. These variations could be fully or partly masked by simple factors such as inter-laboratory biases induced by differences in the procedures, standards, or sampling methods used. This work also highlights the caveats of collecting single grab sample and sampling of distal tephra as such an approach may not detect subtle variations and could introduce an artificial difference between eruptions (depending on what part of the eruption sequence the sample represents). For example, if during the course of an eruption the dispersal direction of tephra emitted from a compositionally zoned magma chamber were to change, the composition of the same layer would be significantly different in different tephra sectors. This is important for petrologic studies as well as chemical fingerprinting of tephra layers.

A well articulated knowledge of the geochemistry and magmatic plumbing of GVS has direct implications for our understanding of the migration of magma through the crust above mantle plumes, and in other volcanic settings characterised by high magma fluxes and steep thermal gradients. In this study I use this new data set to

assess the origin of the G1998 and G2004 magmas, the nature of the plumbing system beneath the Grímsvötn volcano, and the proposed relationship between the genesis of Grímsvötn and Laki magmas.

Table 7.1: Basaltic fissure eruptions in the ice-free part of the Grímsvötn volcanic system (after Thordarson et al., 2003).

Volcanic System	Fissure eruption	Age (B.P.)	Calendar age (AD)	Length (km)	Area (km^2)	Volume (km^3)
Grímsvötn	Laki	217	1873-84	65	599	15.1
Grímsvötn	Lambavatnsgigar	ca. 800				0.01
Grímsvötn	Nupar	ca. 3800		>25	236	7.0
Grímsvötn	Bunuholar-Raudholl	ca. 4000				0.01
Grímsvötn	Halsagigar-Botnar	>5000?				3.0
					Total	25.1

Figure 7.1: (A) Iceland location map with key structural components of the Grímsvötn volcanic system. The area on the blue box is expanded in the lower panel. Location of the inferred Iceland mantle plume is shown by a yellow circle, while the Grímsvötn caldera is shaded in red and aerial extent of Laki lavas in black. (B) Location of Grímsvötn's two central volcanoes and the Laki fissure swarm with respect to the Vatnajökull glacier.

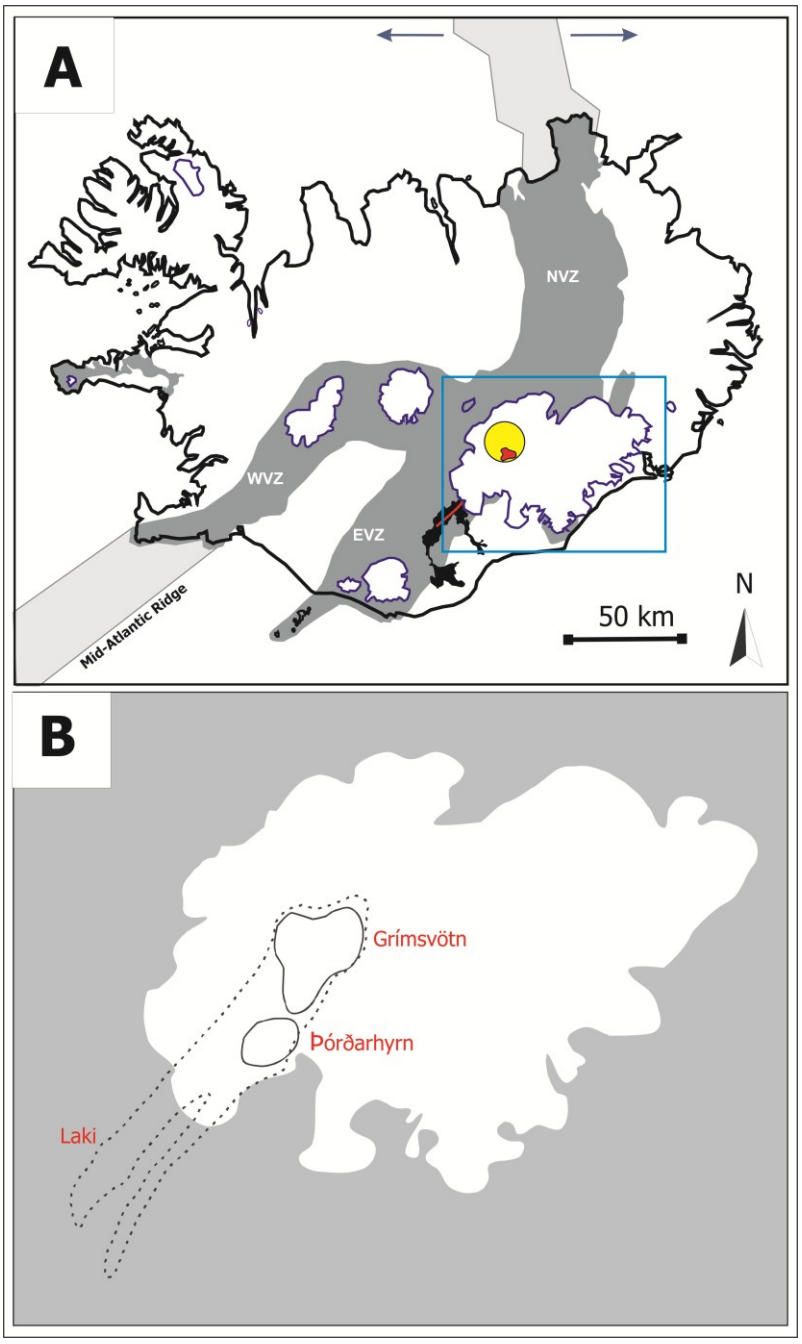

7.2 BACKGROUND TO THE GRÍMSVÖTN VOLCANIC SYSTEM

7.2.1 GEOLOGY AND GEOGRAPHY

The Grímsvötn volcanic system (GVS) is located within Iceland's Eastern Volcanic Zone (EVZ) at the juxtaposition between the Mid-Atlantic Ridge (MAR) and the inferred centre of the Iceland mantle plume (Fig. 7.1a). It is almost 100 km long and the southwestern part, where 1783-84 Laki and other Holocene subaerial fissure vent systems are located, is ice-free and ~60 km long (e.g. Jakobsson, 1979). The northeast sector of the system is beneath the west-central part of the Vatnajökull ice-cap with the Grímsvötn central volcano (GCV) located near its northern end, and the smaller Þórðarhyrna central volcano 20 km farther to the south-west (Fig. 7.1b).

7.2.2 ERUPTION HISTORY

The Grímsvötn central volcano has produced more than 70 eruptions in historical time (i.e. over the last 1100 years) (Larsen *et al*., 1998; Larsen, 2002; Thordarson and Larsen, 2007) and an additional 280 tephra layers are known from prehistoric time (Óladóttir, 2010). Following Jakobsson (1979), there have been five post-glacial fissure eruptions on the ice-free part of the system (Table 7.1), including the 15.1 km^3 D.R.E. (dense rock equivalent) Laki eruption, the second largest historical eruption in Iceland (Thordarson and Self, 1993). The Laki eruption was a part of a major volcano-tectonic episode on the GVS that lasted from May 1783-May 1785 which featured at least 10 eruptions at the GCV in addition to the large fissure eruptions for which it is well known (Thordarson *et al*., 2003).

The total post-glacial magma production on the GVS is estimated at ~85 km^3, of which ~25 km^3 comprises fissure eruptions on the ice-free part of the system (T. Thordarson personal communication, 2010). The remaining volume was erupted by explosive events at the Grímsvötn central volcano. The largest known explosive eruptions from Grímsvötn are in the time period 10.5 – 9.9 ka, comprising a series of six tephra layers, including the 10.2 ka Saksunarvatn tephra, which have a collective volume of >15 km^3 (Jóhannsdóttir, 2007) and form a widespread marker horizon across the North Atlantic (e.g. Davies *et al*., 2010, and references therein).

7.2.3 MAGMATISM

Reported magma compositions from the Grimsvötn-Laki volcanic system are predominantly crystal-poor quartz-normative tholeiitic basalts (Métrich *et al*., 1991; Thordarson *et al*., 1996; Bindeman *et al*., 2006), although olivine tholeiite and icelandite compositions have also been documented (e.g. Jakobsson, 1979; Grönvold and Jóhannesson, 1984; Steinthorsson *et al*., 2000). A TiO_2/FeO vs. K_2O whole rock discrimination diagram, highlighting the known compositional fields for Grímsvötn magmas and tholeiitic basalts from a number of nearby volcanic systems, is shown in Fig. 7.2. It demonstrates that Grímsvötn products can be distinguished from those of other volcanoes largely by major element data alone.

Previous geochemical studies of GVS products show that there are systematic differences between the compositions of magma erupted at the central volcano versus on the fissure system. In general, GCV products contain less MgO and CaO and more K_2O and TiO_2 than fissure products, for a similar range in FeO and Al_2O_3 content (e.g. Fig. 7.3a). Table 7.2 also shows that central volcano eruptions contain higher TiO_2 and K_2O contents and lower MgO contents than fissure eruptions. Furthermore, central volcano magmas are enriched in incompatible (relative to the melt) elements (such as Ba, Sr, Y and Zr) compared to fissure magmas (Table 7.2).

On figure 6.3a, white circles represent literature data from all events on GVS, which incorporates both fissure eruptions and central volcano eruptions. Analyses of fissure magmas contain higher wt. % MgO and lower wt. % K_2O than those of central volcano eruptions. The G2004 event contains less MgO than Laki, but the G1998 range overlaps partially with that of Laki. Nevertheless, the G1998 range is considerably larger than that of Laki and extends to far more evolved compositions. The two largest fissure eruptions on the ice-free part of the Grímsvötn fissure swarm, the Laki and Núpar events (data included under the label "other fissure"), are similar in terms of their major element magma composition. However these are noticeably less evolved than the magmas erupted at the Grímsvötn central volcano in terms of their relative depletion in the incompatible elements Y and Zr (Fig. 7.3b). Conversely, central volcano magmas are enriched in all incompatible trace elements relative to their counterparts from the fissure swarm (Fig. 7.3b).

In addition to the broad-scale differences identified between fissure swarm and central volcano compositions (Table 7.2), there is an apparent trend from less to more evolved compositions with time in the period of most recent activity (last ~230 years) on GVS. During this period the least evolved magma was produced by the 1783-84 Laki eruption and since then, particularly in 20th century, the central volcano eruptions appear to produce progressively more evolved magma with time (Fig. 7.3). This evolutionary trend has been explained by progressive fractional crystallisation of clinopyroxene, olivine and plagioclase from a magma body with Laki-like starting composition, coupled with variable degree of crustal assimilation (e.g. Sigmarsson *et al*. 1991; 2000; Bindeman *et al*. 2006; 2008). However, the current dataset is limited in terms of the total number of analyses (both within individual CV events, and across eruptions), and samples are temporally and spatially patchy. Another limitation is that drawing together data from disparate sources often results in a diffuse spread of data.

Table 7.2: Range of compositions reported in the literature for selected major and trace elements, highlighting differences between fissure swarm and central volcano magmas on the Grímsvötn volcanic system. Data from: Jakobsson (1979); Oskarsson et al. (1982); Steinthorsson (1982); Grönvold (1984); Thordarson et al. (1988); Sigmarsson et al. (1991); Steinthorsson et al. (1995); Thordarson (1995); Thordarson and Miller (unpublished data, 1997); Sigmarsson et al. (2000); Steinthorsson et a.. (2000); Passmore (2009).

	Fissure Swarm Eruptions	***Central Volcano Eruptions***
TiO_2 (wt. %)	2.27 - 2.95	2.42 - 3.07
Al_2O_3 (wt. %)	13.11 - 15.19	13.45 - 14.80
FeO (wt. %)	13.11 - 15.20	13.00 - 15.06
MgO (wt. %)	5.10 - 7.04	4.13 - 5.68
CaO (wt. %)	10.00 - 13.77	13.45 - 14.80
K_2O (wt. %)	0.24 - 0.54	0.40 - 0.55
Ba (ppm)	71 - 99	75 - 109
Sr (ppm)	205 - 225	210 - 242
Y (ppm)	22 - 28	38 - 49
Zr (ppm)	133 - 172	168 - 212

Figure 7.2: Whole rock TiO_2/FeO vs. K_2O diagram highlighting the compositional field for magmas from the Grímsvötn and other nearby tholeiitic volcanic systems. (Data are from: Breddam, 2002; Grönvold 1978; Grönvold, 1984; Hansen and Grönvold, 2000; Hartley, 2010, unpubl. data; Heier, 1966; Jakobsson, 1979; Jónasson, 1994; Óskarsson *et al*., 1982; Schiellerup, 1995; Sigmarsson *et al*., 1991; Sigmarsson *et al*., 2000; Slater *et al*., 1998; Steinthorsson, 1982; Steinthorsson, *et al*., 1995; Steinthorsson *et al*., 2000; Thordarson *et al*., 1988; Thordarson, 1995; Thordarson & Miller, 1997, unpubl. data; Thordarson, 2003; Vilmundardóttir, 1977).

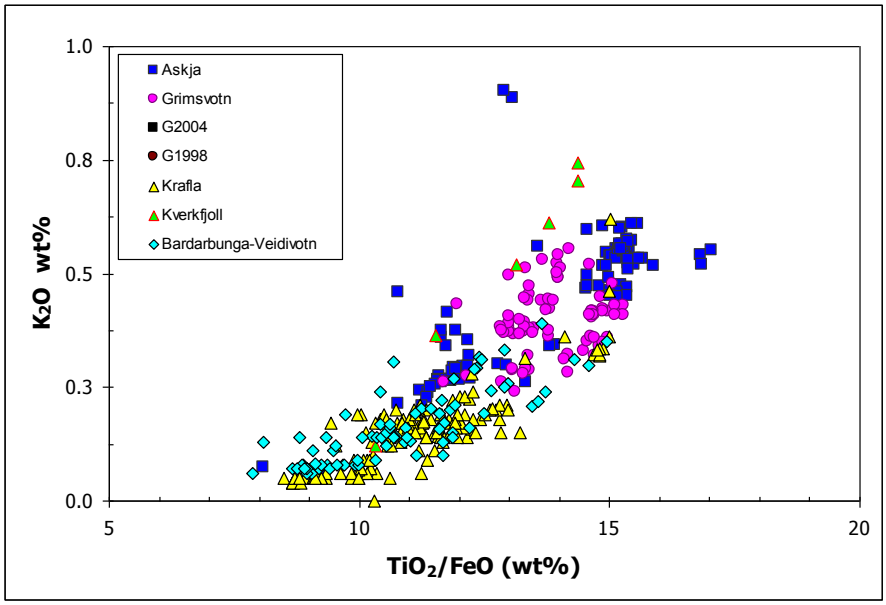

Figure 7.3: Examples of major oxide and trace element co-variation diagrams as depicted by previous geochemical studies of Grímsvötn Volcanic System products. (Data are from: Gronvold, 1984; Jakobsson, 1979; Passmore, 2009; Sigmarsson *et al*., 1991; Steinthorsson, 1982; Steinthorsson, *et al*., 1995; Steinthorsson *et al*., 2000; Thordarson, 1995; Thordarson, unpublished data 1999).

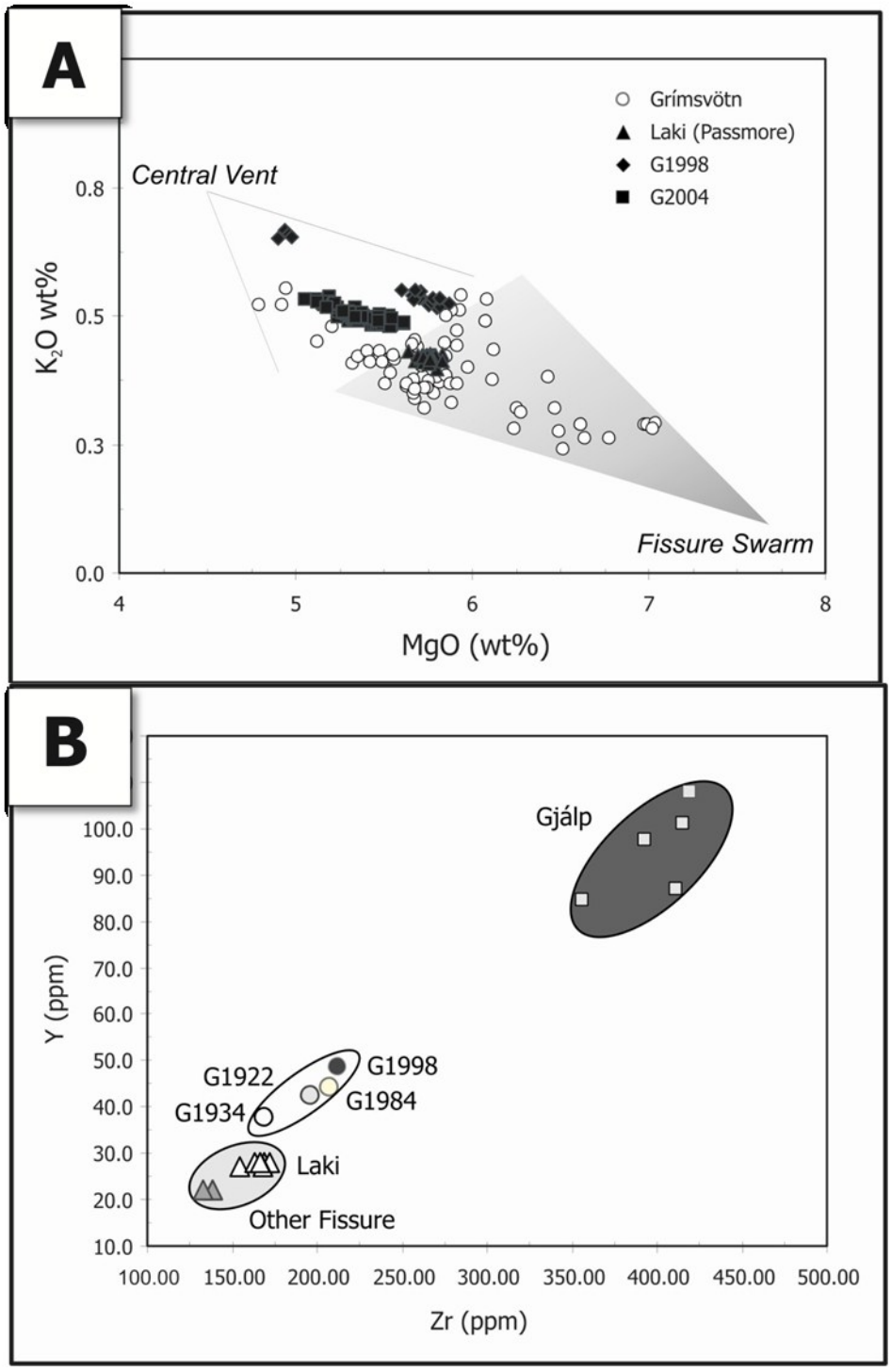

7.2.4 MAGMA PLUMBING

The presence of a shallow-level magma storage zone, with a volume of ~20 km^3 at a depth of 1-4 km beneath the Grímsvötn central volcano, is indicated by gravity and magnetic and teleseismic surveys (Gudmundsson, 1989; Gudmundsson and Milsom, 1997; Alfaro *et al*., 2007). This value independently corroborates early work by Björnsson *et al*. (1982), who calculated that a magma volume of at least 20 km^3 is required to maintain the 5000 MW heat output at Grímsvötn over the 400-year-long record of jökulhlaup observations. These studies also indicate the presence of another melt region at depths of >4 km beneath Grímsvötn (Alfaro *et al*., 2007).

A variety of possible structures for the magma storage and plumbing system beneath the GVS have been postulated based on analyses of magma chemistry (Fig. 7.4). These are largely based on studies of the Laki products and few of these studies include any GCV samples. The oldest models (i.e. Steinthorsson, 1977; and Sigurdsson and Sparks, 1978) interpreted the April 1784 Grímsvötn eruption as an aftermath of Laki, and used that along with similarity in major element composition between Laki products and tephra from 19th – 20th century Grímsvötn eruptions, to propose that the Laki fissures were fed via lateral flow of magma from a shallow crustal magma chamber beneath Grímsvötn. This is a similar mechanism to that proposed by several workers to explain the 1975-84 Krafla volcano-tectonic episodes (e.g. Bjornsson *et al*., 1979; Einarsson and Brandsdóttir, 1980) and so this argument was stimulated by recent observations of the Krafla event.

This hypothesis, however does not account for the fact that the Grímsvötn central volcano erupted in phase with Laki fissure eruptions, and continued to erupt for a total of ten times between 1783-1785 (Thordarson and Self, 1993). The early lateral flow hypothesis also does not account for the fact that magmas from pre- and post-Laki GCV eruptions are always more evolved than the Laki magma.

Métrich *et al*. (1991) attempted to resolve the question of disparity between fissure and central volcano compositions by updating the Sigurdsson and Sparks (1978) hypothesis to propose a stratified magma chamber beneath GCV which fed the Laki eruption via lateral flow from the lower part of the reservoir, with central volcano eruptions tapping the highly evolved upper part of the shallow crustal chamber. This study is based, however, on a hypothetical trend of magma differentiation constructed

from analysis of melt inclusion hosted by olivine and plagioclase phenocrysts from the phreatomagmatic tephra of one episode (episode 4) of the Laki eruption. No Grímsvötn samples were included in the study, and the Fe-Ti compositions anticipated by this model have never been reported for GCV products.

Later studies (e.g. Gudmundsson, 1988; Thordarson and Self, 1993) have disputed the feasibility of the lateral flow hypothesis for the 1783-85 Grímsvötn-Laki volcano-tectonic episode on the basis of physical and chemical aspects of the GVS. Based on field observations of fault and fissure systems in Iceland, Gudmundsson (1988) argues that magma chambers are only able to erupt 5-20% of their melt volume in any one event. Therefore shallow-level magma chambers beneath Icelandic volcanoes are too small to feed large volume fissure eruptions and major fissure eruptions must be erupted directly from larger reservoirs at the crust-mantle boundary. By this calculation, the volume of the magma storage system required to produce the Laki eruption would have to have been on the order of 100 km^3. The volume inferred by geophysical studies for the shallow-level magma chamber at Grímsvötn is much less (only 20 km^3). Gudmundsson (1988) argues that the stress regime imposed by the inflation of such a large reservoir could affect the entire volcanic system, resulting in several eruptions occurring simultaneously on its different components. According to this model the primary magma within a deeper-seated reservoir at the crust-mantle boundary could also be modified by crystal fractionation and crustal contamination processes to produce evolved quartz tholeiite melt compositions (Gudmundsson, 1988).

Thordarson and Self (1993) point out that the central volcano and the Laki fissures erupted synchronously and in phase during the 1783-85 Grímsvötn-Laki volcano-tectonic episode is inconsistent with the lateral flow hypothesis. If the Laki eruption was fed by lateral flow from a 20 km^3 shallow crustal chamber beneath Grímsvötn, the 2000-6000 m^3s^{-1} magma discharge on the Laki fissures must have produced a significant pressure drop in the Grímsvötn chamber. Hence, the chamber pressure would have been insufficient to drive simultaneous eruptions at Grímsvötn. Furthermore, lateral dyke injection and subsequent extrusion of ~15 km^3 of magma by the Laki fissures would have effectively emptied the ~20 km^3 shallow chamber. It is logical to assume that complete or partial draining of the crustal chamber would have resulted in a caldera collapse. In addition, removal of this high-level heat source would

have altered the geothermal regime and modified the established Grímsvötn jökulhlaup frequency for a period of time after the event. There is no evidence for either having taken place (Thorarinsson, 1974; Björnsson, 1988). Furthermore such a large eruption from beneath the Grímsvötn central volcano would require syn-eruption recharge at rates that are one to two orders of magnitude greater than the estimated 1.6 m^3/s magma present-day influx (Bjornsson *et al*., 1982; Thordarson and Self, 1993). Thus, Thordarson and Self (1993) proposed that the best explanation for synchronised activity at Laki and Grímsvötn during the 1783-85 eruption is that magma was supplied directly from a deeper-seated reservoir to the Laki fissures and simultaneously injected into the shallow crustal chamber at Grímsvötn by a large semi-vertical feeder dyke from the deeper reservoir (Fig. 7.4c).

Th and U systematics suggest that the Laki and Grímsvötn magmas share a common source but evolved separately. The two magmas share a common U/Th ratio, but the concentrations of both elements are slightly higher in the Grímsvötn magmas than in the Laki magma (Sigmarsson *et al*., 1991). This is inferred to result from low pressure crystal fractionation of olivine-plagioclase-CPX during magma storage in a shallow-level crustal magma chamber over "short" time frames of months to years. Conversely, the lower U and Th content of the Laki magma, along with the range of measured La/Yb ratios suggests that it came from a larger and deeper reservoir located at the crust-mantle boundary (Sigmarsson *et al*., 1991). Sigmarsson *et al*. (1991) therefore proposed a model which supports the volcano-tectonic model of Gudmundsson (1987; 1995; 2000) with geochemical observations. This invokes the presence of a deep magma reservoir which feeds the fissure swarm eruptions and also recharges the shallow magma chamber beneath GCV (Fig. 7.4c). A later development to this model argues that the shallow magma chamber was last recharged during the Laki event, and that Grímsvötn magmas since then have been produced by fractional crystallization of that batch, becoming increasingly evolved with time (Sigmarsson, 2000). This model is plausible given known physical constraints on the geometry and plumbing of Grímsvötn. However, a continuous fractionation trend over time has yet to be demonstrated for Grímsvötn central volcano products.

The most recent model is that of Bindeman *et al*. (2005; 2008) which, based on oxygen isotopes in crystals and melt inclusions, argues for multiple pulses of magma injection into a complex plumbing network (Fig. 7.4d). The magma composition is

variably affected by crustal assimilation and polybaric crystal fractionation before being re-homogenised as it enters the shallow magma storage region beneath GCV. This model is consistent with thermobarometry calculations which reveal polybaric crystallisation of clinopyroxene as well as with geophysical models of the presence of a shallow "crystal mush" beneath Grímsvötn. However, it remains excessively complicated from a dynamic perspective, requiring small volumes of melt to be separately emplaced in the crust, to crystallise and assimilate crustal material and yet to remain sufficiently hot and mobile to later coalesce and rehomogenize. Furthermore, an avenue or "trigger" (e.g. seismic event) must also be invoked to provide a pathway for coalescence.

Figure 7.4: Sketches (i.e. not to scale) illustrating the key features of proposed models for magma plumbing within the Grímsvötn volcanic system (A) In the models of Steinthorsson (1977) and Sigurdsson and Sparks (1978) both the Laki and the GCV eruptions are fed by the same shallow-level reservoir. (B) This model is expanded by Métrich *et al*. (1991) to show that this reservoir is undergoing fractional crystallisation. The magma feeding central volcano eruptions is extracted from the top of reservoir and is therefore more evolved. (C) Sigmarsson *et al*., (1991, 2000) propose that the Laki eruption was fed by a large, deep reservoir also intermittently replenishes a shallow-level reservoir beneath the central volcano. The shallow-level reservoir also undergoes fractional crystallisation in between injections of magma from below. (D) Bindeman *et al*. (2008) propose that individual magma pulses from the a deep reservoir at the crust-mantle boundary undergo varied paths of storage crystallisation before being re-homogenised in, and erupted from, a shallow-level chamber beneath the central volcano.

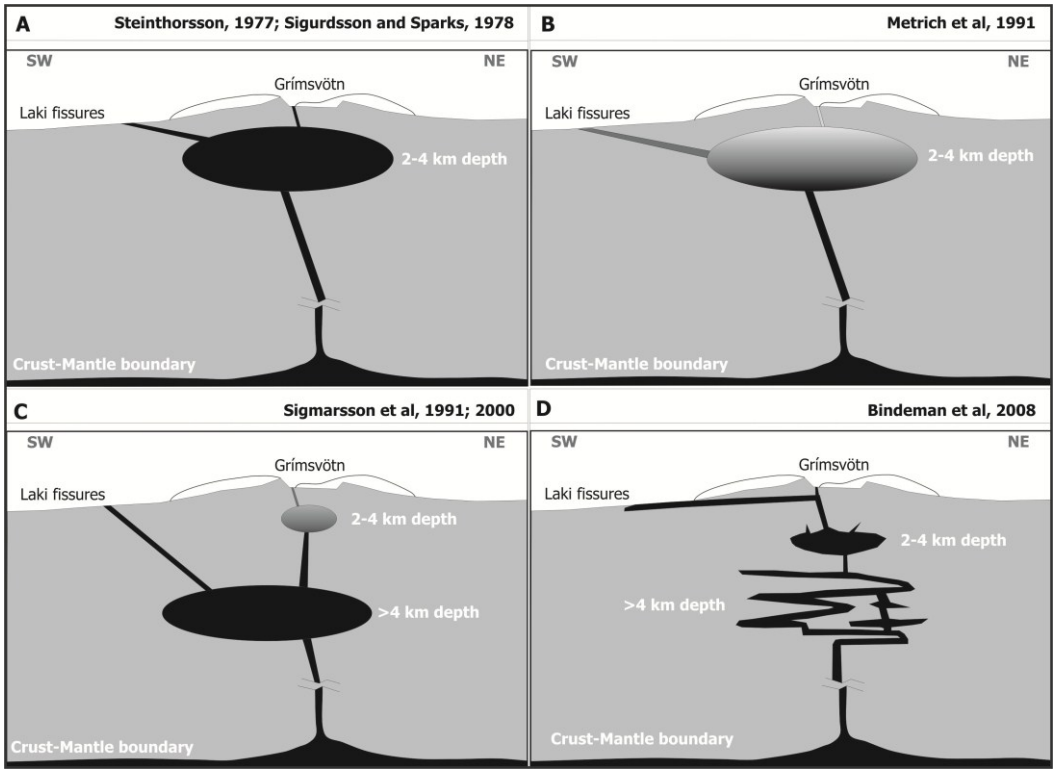

7.3 THE 2004 AND 1998 ERUPTIONS

7.3.1 OVERVIEW OF EVENTS AND DISPERSAL

The Grímsvötn 1998 (G1998) and 2004 (G2004) eruptions both occurred along the southern caldera fault at eruption sites located approximately 2.5 km apart (Fig. 7.5). Both eruptions rapidly became subaerial and established convective eruption columns, depositing tephra over the ice surface. The calculated volume of magma erupted in 2004 (<0.06 km^3, Chap. 3) is of comparable magnitude to volume estimates for the 1998 event (< 0.1 km^3; Alfaro *et al*., 2006). Each eruption was also preceded by vertical and radial inflation of the volcanic edifice, interpreted to reflect magma influx into the shallow crustal magma storage system beneath Grímsvötn (Sturkell *et al*., 2003; E. Sturkell, personal communication, 2007). A description of the stratigraphy and eruption chronology of G1998 is given in Appendix VI, while a detailed account of the dispersal, deposit characteristics and eruption chronology for G2004 is provided in Chapter 3.

7.3.2 SAMPLE LOCATIONS

During the first phases of the 1998 eruption, tephra was deposited towards the south and southeast of the vent onto the Grímsfjall ridge. Later, as the wind direction changed, tephra was deposited northwards within the caldera itself. Samples for whole rock chemical analysis were taken at ten centimetre vertical intervals from one proximal section located centrally within each dispersal sector.

Southerly winds prevailed throughout the 2004 event, such that the bulk of tephra was deposited northwards. Samples for whole rock chemical analysis were taken at five to fifty centimetre intervals from thirteen locations within the proximal region of the deposit. Such a fine sampling interval, focussed on the proximal area of the deposit, ensures that representative samples from each eruptive phase are analysed and places precise time constraints on the data.

Figure 7.5: A view of the Grímsvötn southern caldera wall and the locations of the G1998 and G2004 eruption sites

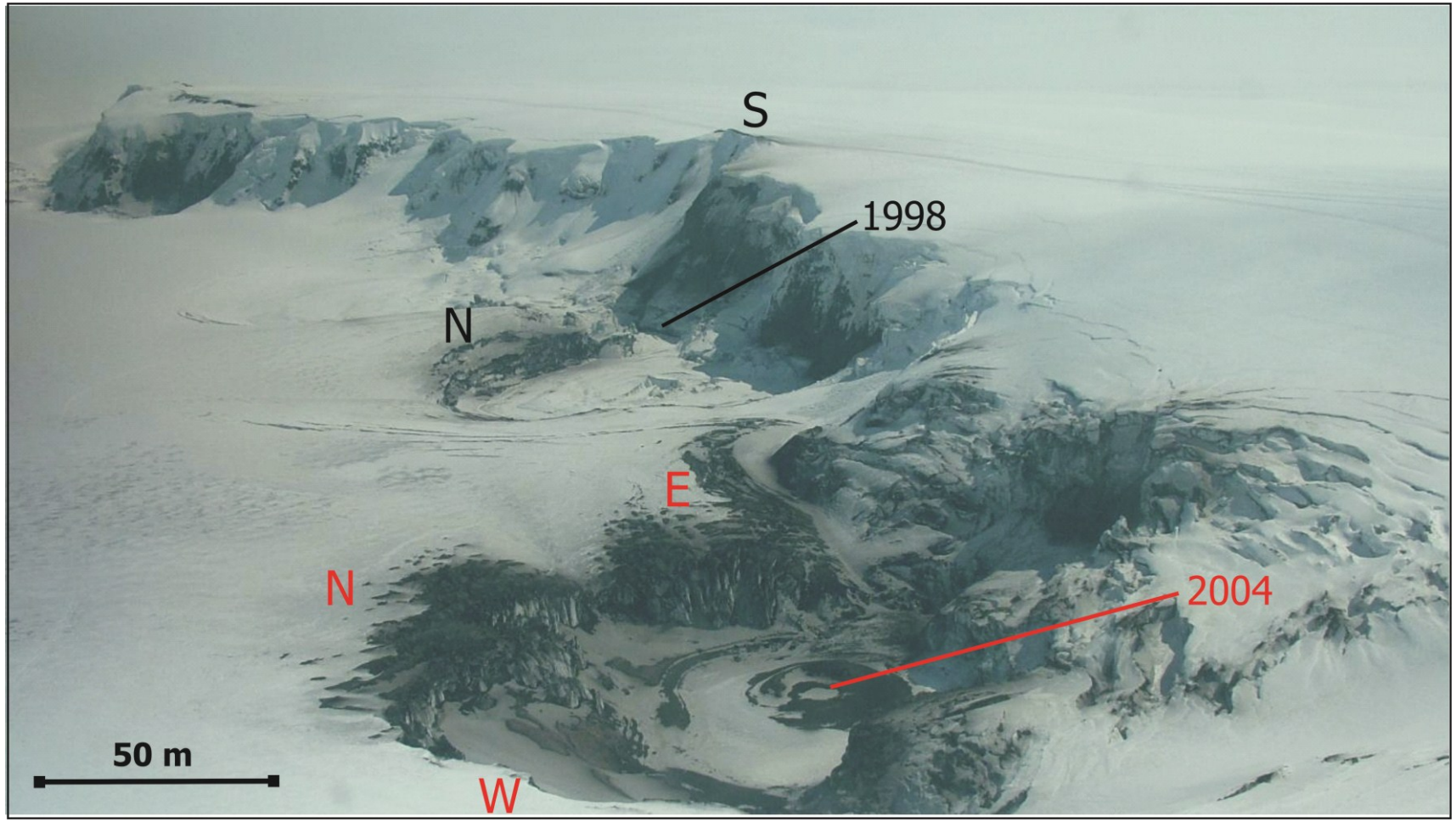

7.4 METHODS

7.4.1 FIELD METHODS AND SAMPLING STRATEGY

When logging, measuring and sampling tephra sections, the sampling was undertaken as the final task in order to ensure that samples are placed in the appropriate stratigraphic context. All sections were sampled starting from the top and working down-section in order to reduce the risk of contamination from overlying tephra layers and tools were cleaned thoroughly in between taking each sample. Representative samples (i.e. those in which an equal amount of material is taken across the entire layer) bulk samples were taken as representative for layers < 50 cm thick, while thicker layers were represented by bulk sub-samples across 20-50 cm intervals of full stratigraphic thickness. By this means it was possible to gather data on both average unit composition and changes over time within large units.

7.4.2 WHOLE ROCK ANALYSIS BY X-RAY FLUORESCENCE

Prior to sieving, samples were oven-dried for 24 hours at 60˚C. For each sample, tephra in the > 125μm size range was hand-picked under a binocular microscope to remove accidental non-juveniles and hydrothermally altered fragments. Samples were then ground to a homogeneous powder in a tungsten carbide TEMA mill (shatter box) and analysed by X-ray fluorescence (XRF) spectrometry using a PANalytical PW2404 wavelength dispersive (WDS) sequential x-ray spectrometer at the University of Edinburgh. Major element concentrations were measured from glass discs, while trace element concentrations were determined from pressed powder pellets. A detailed description of the sample preparation and XRF analysis procedure is given by Fitton *et al*., 1998.

7.4.2.1 ANALYTICAL UNCERTAINTIES

The standard deviation for each element analysed is a product of heterogeneity within the sample itself and of instrumental variability. In order to determine sample homogeneity, five separate glass disks and pressed powder pellets were analysed for each of two randomly selected samples. For major oxide analyses, instrumental precision was assessed by analysing a single glass disk five times consecutively. High precision whole rock analyses of trace element compositions were obtained by

analysing individual samples three times each (Appendix VII). For each element or oxide, error margins are displayed on individual plots as two standard deviations, which represent the combined error attributable to both sample heterogeneity and instrumental precision.

Standards BCR-1, BEN, and BHVO-1, and three Laki samples (Passmore, 2009) were analysed alongside Grímsvötn samples, to confirm the accuracy of these results (Table 7.3).

Table 7.3: Reported and average of measured whole-rock (XRF) major oxide and trace element concentrations in the BHVO-1 and BIR-1 international standards. Number of analyses = n. All analyses from this study fall within the report ranged of standard deviation of literature values. For almost all elements the standard deviation among analyses from this study is significantly lower than those reported in the literature. This is evidence of the high precision of these analyses.

			SiO_2	TiO_2	Al_2O_3	Fe_2O_3	MnO	MgO	CaO	Na_2O	K_2O	P_2O_5	Sum		n
Reported	*BHVO-1*	Mean 1 σ	49.8 0.3	2.75 0.04	13.7 0.2	12.4 0.2	0.17 0.01	7.22 0.07	11.4 0.2	2.3 0.1	0.53 0.01	0.27 0.01	100.53 -		- -
This Study	*BHVO-1*	Mean 1 σ	50.1 0.19	2.72 0.00	13.98 0.09	12.31 0.02	0.17 0.00	7.19 0.02	11.30 0.06	2.28 0.07	0.49 0.03	0.23 0.03	100.22 -		8 -
			Nb	**Zr**	**Y**	**Sr**	**Rb**	**Zn**	**Cu**	**Ni**	**Cr**	**V**	**Ba**	**Sc**	**n**
Reported	*BHVO-1*	Mean 1 σ	18.6 1.8	174 9	26 2	396 1	9.19 0.17	106 9	137 9	118 6	287 15	318 15	133 1.0	31 2	- -
This Study	*BHVO-1*	Mean 1 σ	19.7 0.1	176.4 0.1	27.7 0.1	396.9 0.2	9.2 0.1	102 1.7	135 0.8	116 1.8	296 1.1	313 2.4	132.8 0.9	32.5 0.6	8 -
Reported	*BIR-1*	Mean 1 σ	0.55 0.05	14 0.1	15.6 0.9	109 2	0.2 0.01	72 18	119 8	166 7	391 15	319 18	17 2.0	39.5 0.3	- -
This Study	*BIR-1*	Mean 1 σ	0.5 0.1	13.9 0.1	16.6 0.1	110.0 0.2	0.3 0.1	65.8 0.5	122.6 0.5	149.5 0.6	386 1.3	313 2.2	17 3.0	39.1 0.7	8 -

7.5 PETROGRAPHY

Whole-rock major and trace element compositions and CIPW norm calculations (Appendix VII) of G2004 tephra reveal that the dominant composition is quartz-normative tholeiitic basalt. A wide range of clast vesicularity is observed - from dense, vesicle-free glass to clasts approaching a reticulitic texture (Fig 7.6). Both poorly and highly vesiculated glass coexist in samples from any given stratigraphic level. However, higher proportions of poorly vesicular material are found at the very base of the sequence (see componentry study, Chap. 5). The observed vesicle size population clusters around an average diameter of 80 μm. In general, vesicle diameters range between 30 and 280 μm, although coalescence leads to bubble diameters between 500 μm and 1.6 mm. Highly vesicular samples (>90% vesicles) approaching a reticulite texture exhibit pseudo-hexagonal packing. In this case vesicles are uniformly 200-250 μm in diameter (Fig. 7.6).

The tephra groundmass is dominantly clean, aphyric sideromelane glass. However many samples from units A and B (cf. stratigraphy in Chap. 3) exhibit extensive (75-90%) microlite crystallisation, resulting in a tachylitic groundmass texture (Fig. 7.6). The G2004 tephra is sparsely porphyritic, containing <1% plagioclase phenocrysts in pumice sections and <1% free crystals in tephra >2.5 Φ in diameter (see Chap. 5). Rare examples of feathery pyroxene, olivine phenocrysts and glomerophyric plagioclase can also be found in pumice sections. The plagioclase crystals contain occasional translucent, brown glass (melt) inclusions ranging from <5 to 100 microns in the longest dimension (Fig. 7.6). Among these, the majority fall in the 10 to 80 μm size range and are usually spherical or oblate in shape. Occasional vapour bubbles are also associated with glass inclusions.

Figure 7.6: BSE images of G2004 tephra at a variety of scales. (A) Non-vesicular juvenile glass. (B) Highly vesicular (reticulate) juvenile glass. (C and D) Moderately vesicular juvenile glass and plagioclase phenocrysts. (E and F) Plagioclase phenocrysts in poorly vesicular juvenile glass. (G) Relatively crystalline sample containing plagioclase and Fe-Ti oxides. (H).Tachyltic texture with abundant plagioclase microcrysts.

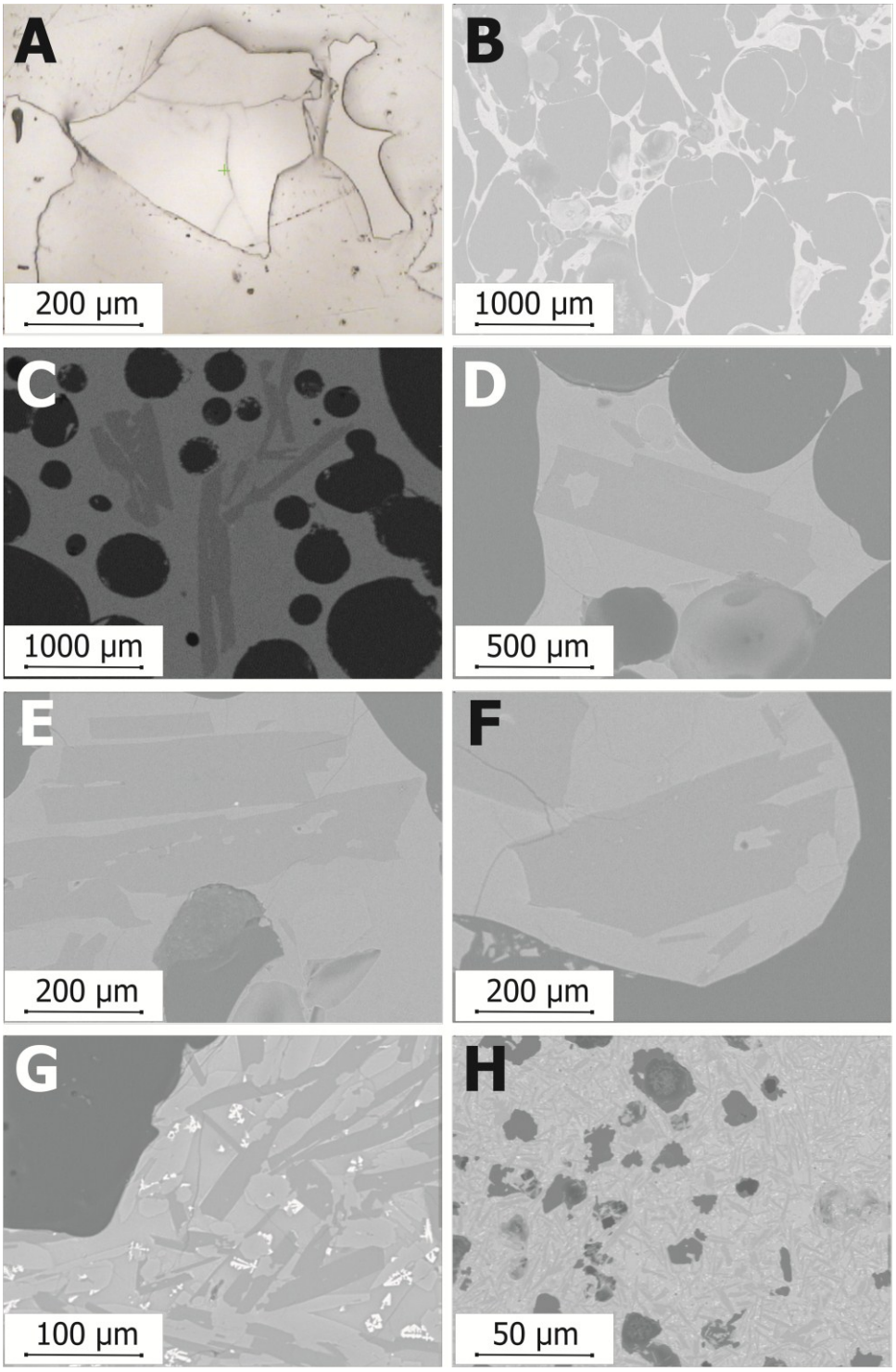

7.6 RESULTS

Eleven whole rock samples of G1998 tephra and sixty-nine samples of G2004 tephra were analysed by XRF to determine major oxide and trace element abundances. Results of major oxide and trace element analyses are given in Appendix VII. Results from whole rock XRF analysis of Laki samples (Passmore, 2009) are also plotted for comparison (Fig. 7.7).

7.6.1 MAJOR ELEMENT DATA

7.6.2.1 CLASSIFICATION OF G1998 AND G2004 PRODUCTS

According to the TAS (total alkalis versus silica) classification of Cox *et al*. (1979), the G1998 tephra samples all fall on the borderline between basalts and basaltic andesites (Fig. 7.8). G2004 samples are largely quartz-normative tholeiitic basalts, but 14 out of 62 analyses exhibit borderline quartz-olivine normative character, and one sample is strongly olivine normative (see CIPW norm calculations, Appendix VIII). On the TAS diagram (Fig. 7.8) G2004 samples plot as relatively evolved basalts.

Figure 7.7: Co-variation of all major oxides with MgO (by weight percent) for whole rock analyses of Laki (lava samples), G1998 (tephra samples) and G2004 (tephra samples) products. G1998 is represented by open diamonds, G2004 by open squares, and Laki by black triangles. Note that for some oxides the points are so densely clustered that they overlap and obscure one another.

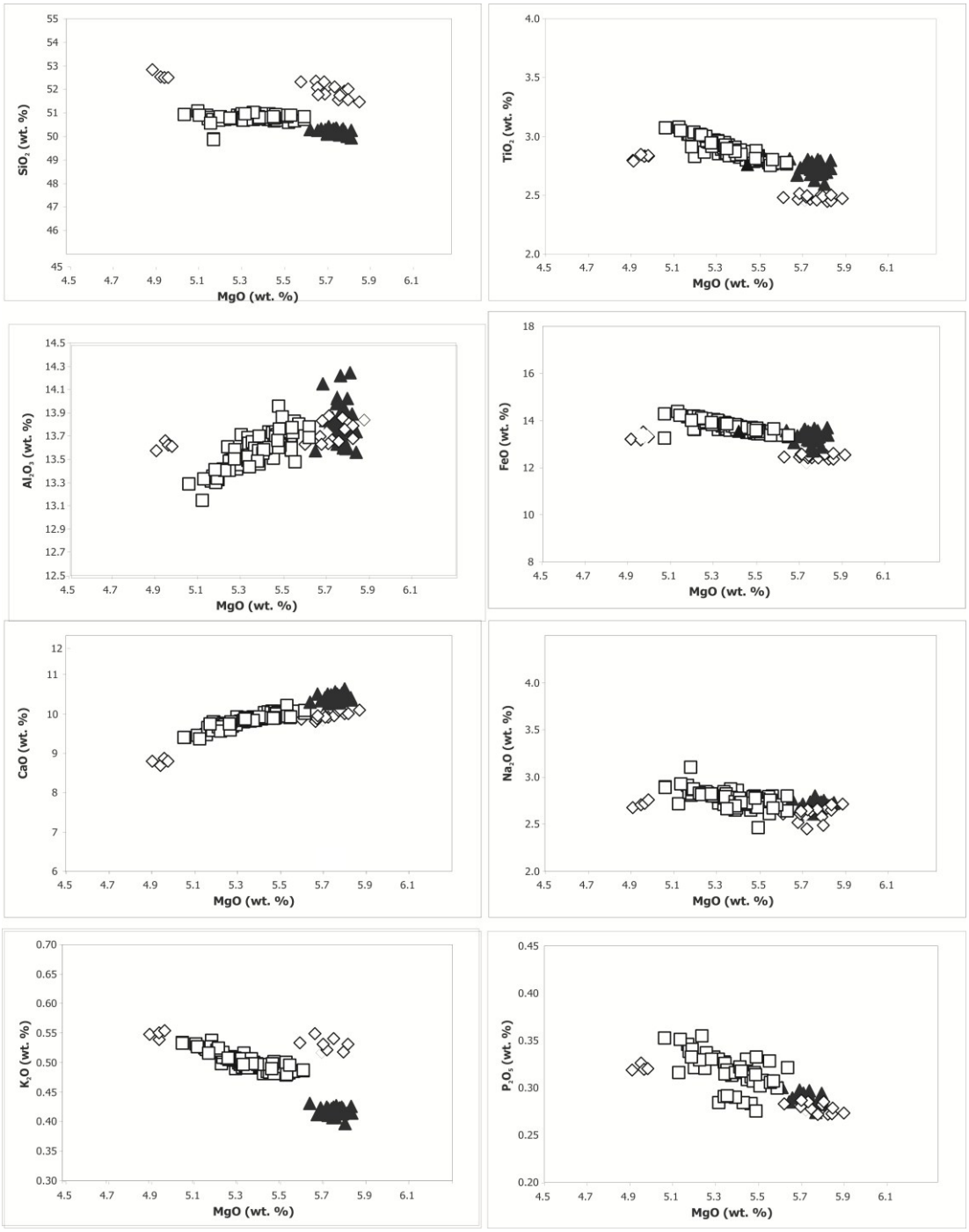

7.6.2.2 COMPOSITIONAL TRENDS

The G1998 and G2004 magmas plot towards the more evolved end of the previously defined Grímsvötn compositional field (Fig. 7.2). Both magmas are generally more K_2O-rich than previously recorded central vent compositions and comparatively lower in MgO, but exhibit a similar range in both FeO and TiO_2 contents. The G1998 and G2004 whole rock data thus generally falls in the established compositional field for the GCV, although extending it to slightly more evolved compositions (Fig. 7.2a).

As shown on Figure 7.7, the products of the G1998, G2004, and Laki eruptions each define distinct clusters and trends on major oxide covariation diagrams. The average and range of compositions for each eruption is given in Table 7.4. The G1998 magma is richer in silica (51.45-52.84 wt. % SiO_2) and alkalis (0.52-0.65 wt. % K_2O) than the G2004 magma (49.86-51.05 wt. % SiO_2; 0.48-0.54 wt. % K_2O), which is in turn more evolved in composition overall than Laki (Fig. 7.7). Within the G1998 and G2004 eruptions there is an inverse correlation between TiO_2 (also FeO) and MgO contents (Fig. 7.7). These trends are offset from one another in that the 2004 magma contains greater abundances of Ti and Fe (2.76-3.08 wt. % TiO_2, and 12.62-14.43 wt. % FeO, respectively) than the 1998 magma (2.45-2.80 wt. % TiO_2; 13.36-14.37 wt.% FeO). Both magmas show strong positive correlation between wt. % CaO and MgO but as before this trend is offset, with the 2004 magma richer in CaO (Fig. 7.7). The K_2O content of the 1998 magma varies little with MgO, while the 2004 magma shows a strong correlation between these two elements, with a shallow negative slope.

As expected, the G1998 and G2004 products exhibit compositions that are comparable to earlier products at the central volcano in terms of degree of evolution. However, it is apparent that none of the other 20th century central vent eruptions (i.e. 1922, 1934, 1984) plot within the narrow fields defined by these two events - evidence that each CV eruption is generated by a separate magma of different composition.

Figure 7.8: Total alkalis vs. silica (TAS) diagram for G1998 (grey diamonds) and G2004 (black squares) products.

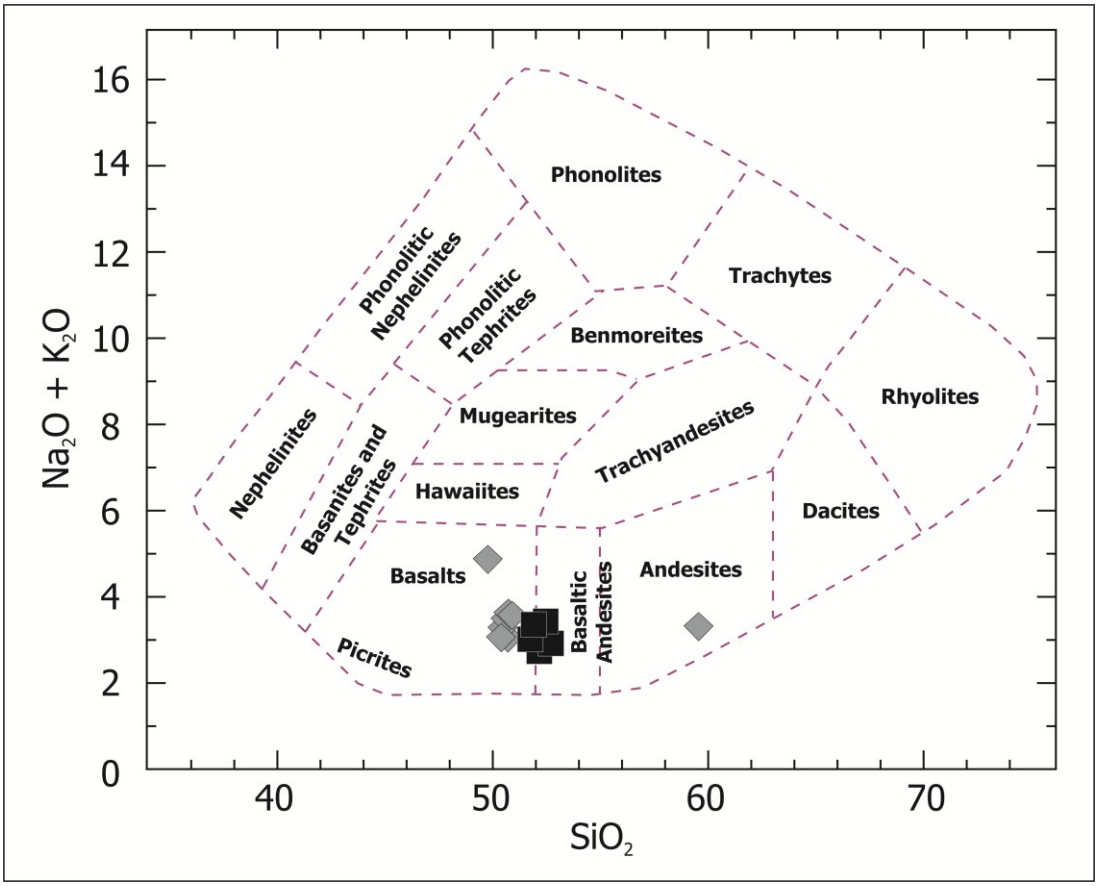

Table 7.4: The average and range of compositions for products of the G1998, G2004 and Laki eruptions. Laki data is from Passmore (2009). Number of analyses = n.

		SiO_2	TiO_2	Al_2O_3	FeOT	MnO	MgO	CaO	Na_2O	K_2O	P_2O_5			n
G1998	*Mean*	52.0	2.5	13.72	12.6	0.21	5.6	9.8	2.62	0.55	0.29			21
	St. Dev.	0.37	0.13	0.09	0.34	0.00	0.30	0.47	0.09	0.05	0.02			-
G2004	*Mean*	49.98	2.84	13.30	13.52	0.23	5.27	9.67	2.74	0.49	0.31			99
	St. Dev.	0.60	0.58	0.27	0.13	0.19	0.26	0.02	0.08	0.01	0.02			-
Laki	*Mean*	50.26	2.85	13.30	13.55	0.23	5.26	2.76	2.76	0.49	0.30			21
	St. Dev.	0.10	0.08	0.58	0.27	0.01	0.13	0.26	0.26	0.02	0.01			-
		Nb	**Zr**	**Y**	**Sr**	**Rb**	**Zn**	**Cu**	**Ni**	**Cr**	**V**	**Ba**	**Sc**	**n**
G1998	*Mean*	21.0	214.7	42.8	221.3	11.3	129.0	95.5	41	53	380	122	39.79	42
	St. Dev.	1.14	15.33	2.33	3.22	1.27	4.98	4.23	2.31	15.53	15.22	10.24	1.00	-
G2004	*Mean*	21.1	204.8	42.4	222.5	9.5	139.3	97.1	37	34	422	102	43.13	70
	St. Dev.	3.68	33.37	7.16	34.05	1.49	4.14	5.17	4.63	14.00	8.11	8.65	0.94	-
Laki (*b)	*Mean*	19.9	184.6	41.0	233.8	7.8	126.6	100.5	40	60	389	90	43	46
	St. Dev.	0.42	3.05	0.67	2.43	0.15	6.03	5.50	2.32	5.00	15.72	1.80	2.00	-

7.6.2 TRACE ELEMENT DATA

The compositional difference between the G1998 and G2004 magmas is further substantiated by differences in their respective trace element abundances. The G1998 tephra spans a relatively broad compositional range for both incompatible (Zr = 203-249 ppm; Nb = 20.1-23.6 ppm; Ba = 112-143 ppm; Sr = 215-224) and compatible elements (Cu = 89-102 ppm; Cr = 18-66 ppm; Ni = 37-44 ppm). However, this range encompasses two distinct compositional groups which lie on a common trend on all covariation diagrams, but are separated by a significant compositional gap (cf. Fig. 7.9). The G2004 tephra spans a similar compositional range to that of G1998 products for melt-incompatible (Zr = 203-233 ppm; Nb = 20.1-24.0 ppm; Ba = 88-127 ppm; Sr = 119-234) and melt-compatible elements (Cu = 84-108 ppm; Cr = 13-70 ppm; Ni = 28-49 ppm). However, the two eruptions form separate trends on all compatible and incompatible element covariation diagrams (Fig. 7.7). With the exception of copper and nickel, there is a strong linear correlation between Mg number (Mg # = 100*([Mg^{2+}]/([Mg^{2+}]+[Fe^{2+}]) and all trace element abundances within the G1998 magma (Fig. 7.9). Trends are considerably less well-defined for G2004 samples, although these also show a general inverse relationship between Mg # and incompatible trace element abundances (Fig. 7.9).

Samples from Laki (Passmore, 2009), Grímsvötn 1998 and Grímsvötn 2004 all define distinct trends on the Zr-Nb, Zr-Y, Sr-Rb, Sr-V, and other trace element covariation diagrams (Fig. 7.10). Each eruption forms Nb/Zr close to 0.1 with near-perfect linear correlation, intersecting the y-axis close to the origin. However, the y-axis intercept is offset for each trend, and they each have significantly different slopes (Fig. 7.10). The G1998 magma forms the shallowest trend (slope = 0.074), while the Laki magma is the most enriched in Nb relative to Zr and therefore forms the steepest trend line (0.13).

Figure 7.9: Trends in melt-incompatible (right column) and melt-compatible (left column) trace element abundances with Mg # in G2004 whole rock samples.

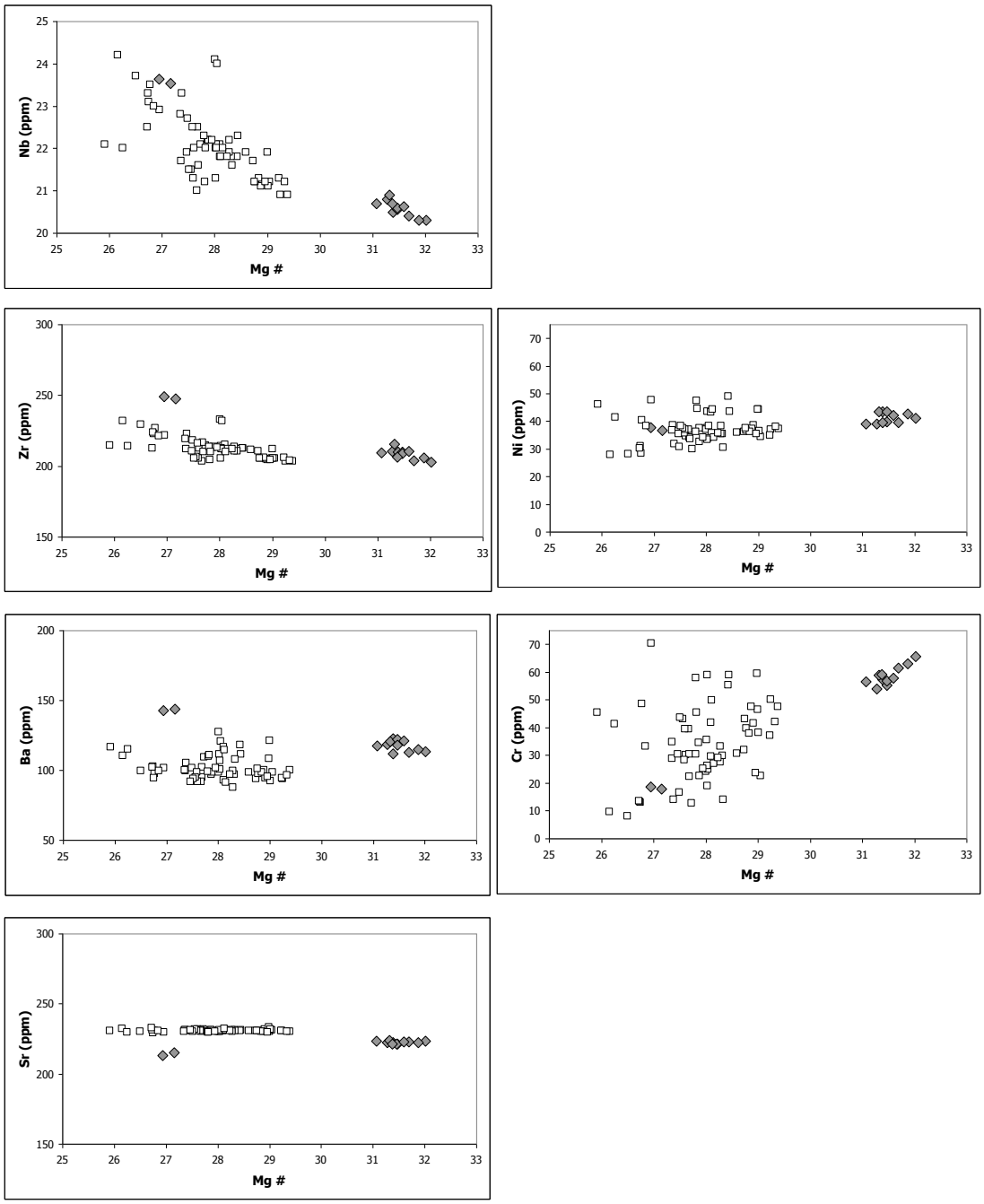

Figure 7.10: Trace element co-variation diagrams for Laki (grey triangles), G1998 (open diamonds) and G2004 (open squares) products. On teh plot of Zr (ppm) vs. Nb (ppm), black circles represent hypothetical Nb and Zr compositions given a further 10% and 25% fractional crystallisation of any mineral in which Nb and Zr are incompatible (olivine, clinopyroxene and plagioclase are all candidates).

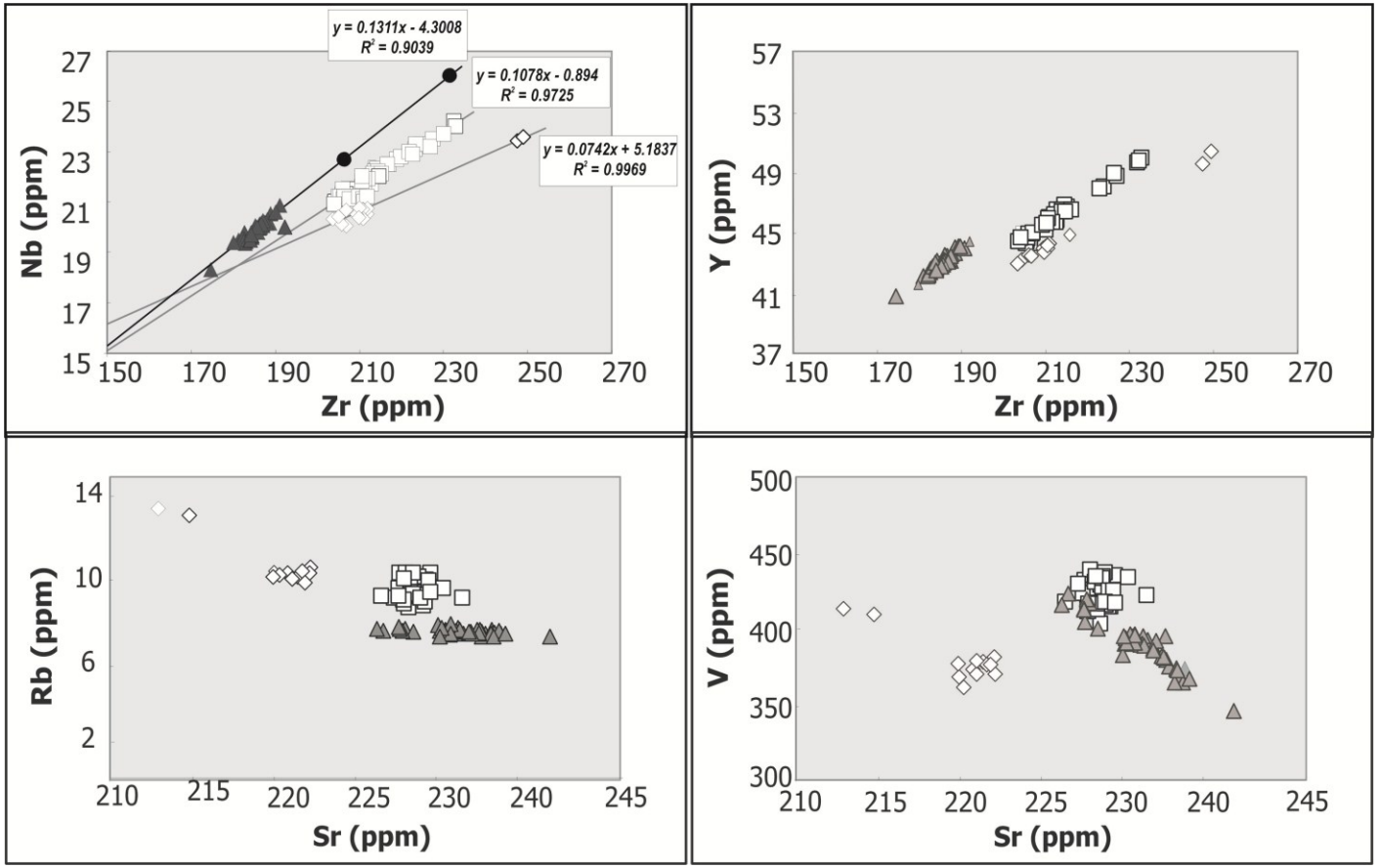

7.6.3 CHEMICAL STRATIGRAPHY WITHIN THE G1998 AND G2004 ERUPTIONS

1998

In the 1998 stratigraphic sequence there is a very clear trend from more to less evolved compositions as the eruption proceeds (Fig. 7.11). However, as noted above, the G1998 eruption products fall into two distinct compositional groups, which occupy different stratigraphic levels. Products of the initial phase of the 1998 eruption (group I compositions) have a relatively low Mg # (27) and low CaO content (8.8 wt. %), and relatively high FeO and K_2O (13.4 and 0.67 wt. %, respectively). The G1998 initial phase is also relatively enriched in incompatible trace elements such as Y (48.3 ppm) and Rb (14.3 ppm).

As we move upwards in the stratigraphic column (Fig. 7.11), there is an abrupt compositional jump to comparatively higher Mg # (31-32) and CaO (9.9 wt. %) values, and correspondingly low FeO (12.6 wt. %), K_2O (0.53 wt. %), accompanied by a marked decline in incompatible trace element contents (e.g. Y = 41.2-42.9 ppm; Rb = 10.4-11.2 ppm). The sampling interval within the G1998 tephra pile is continuous and therefore the polarisation of the deposit into two separate compositional groups may be considered to be real and not an artefact of any gap in the data coverage. In the latter phase (group II compositions) of the 1998 eruption a gently meandering cyclic pattern within the narrow compositional range defined by this group is superimposed upon the overall trend towards less evolved compositions with time (Fig. 7.11). Group I compositions are a volumetrically minor fraction of the G1998 deposit and correspond to only the lowest 16 cm of the most proximal section (see Appendix VI).

2004

The G2004 deposit exhibits more complex compositional zoning than that of the G1998 eruption although on discrimination diagrams the G2004 tephra form a single coherent compositional group (e.g. Figs. 7.6 and 7.8). The changes in composition with stratigraphic height in the G2004 deposit are subtle yet analytically significant, and also accompany major transitions in eruption style (Fig. 7.11 and Chap. 3). Consequently data from individual G2004 eruption units cluster in distinct regions of both major oxide and trace element covariation diagrams (Fig. 7.7).

Comparatively evolved compositions were erupted during phase 1 of the G2004 eruption (i.e. Units A and B – see chapter 3). At this stratigraphic level, Mg # = 27.9, CaO = 9.83 wt. %; FeO = 13.8 wt. %, and K_2O = 0.51 wt. % (see Appendix VII). At the transition between units B and C, there is an abrupt change to somewhat less evolved compositions with a marked decrease in incompatible trace element abundances (i.e. Y falls from 47.7 ppm to 44.1 ppm and Rb from 10.9 ppm to 9.8 ppm). Throughout Unit C, the first deposit of the main phase of the 2004 eruption, there are a number of abrupt shifts in composition (Fig. 7.11), with an overall trend of magma becoming less evolved over time. These cycles are probably related to the timescale of formation and disruption of a magma foam head during vesiculation in the conduit as the most evolved G2004 compositions are associated with large pumice clots and syn-eruptive crystallisation of plagioclase (cf. Chap. 8). With the onset of Unit D, which occurs during a major column collapse event, the composition of the tephra subtly shifts to more primitive compositions, representing the least evolved magma erupted by the 2004 event (CaO = 10.11 wt. %; FeO = 13.40 wt. %, K_2O = 0.48 wt. %; Y = 42.3 ppm; Rb = 9.7 ppm). The onset of another period of sustained deposition (Unit E) is marked by a gradual shift towards slightly more evolved compositions which remain relatively homogenous throughout Unit E deposition. The final column collapse event (Unit F) is marked by another shift towards the more evolved end of the G2004 compositional spectrum. The Unit G compositional cycle commences with a pulse of relatively basic magma which becomes more evolved towards the end of the eruption (Fig. 7.11). Trends in incompatible trace element abundances mirror the stratigraphic variation observed in the major oxide data. Eruption onset is marked by relatively high concentrations of most incompatible trace elements, while the major column collapse event of Unit D is marked by a distinct negative anomaly (Fig. 7.11).

Figure 7.11: Variations in selected major and trace element abundances with relative stratigraphic height for G1998 and G2004 composite sections. Error bars are smaller than the size of the points and are therefore not displayed.

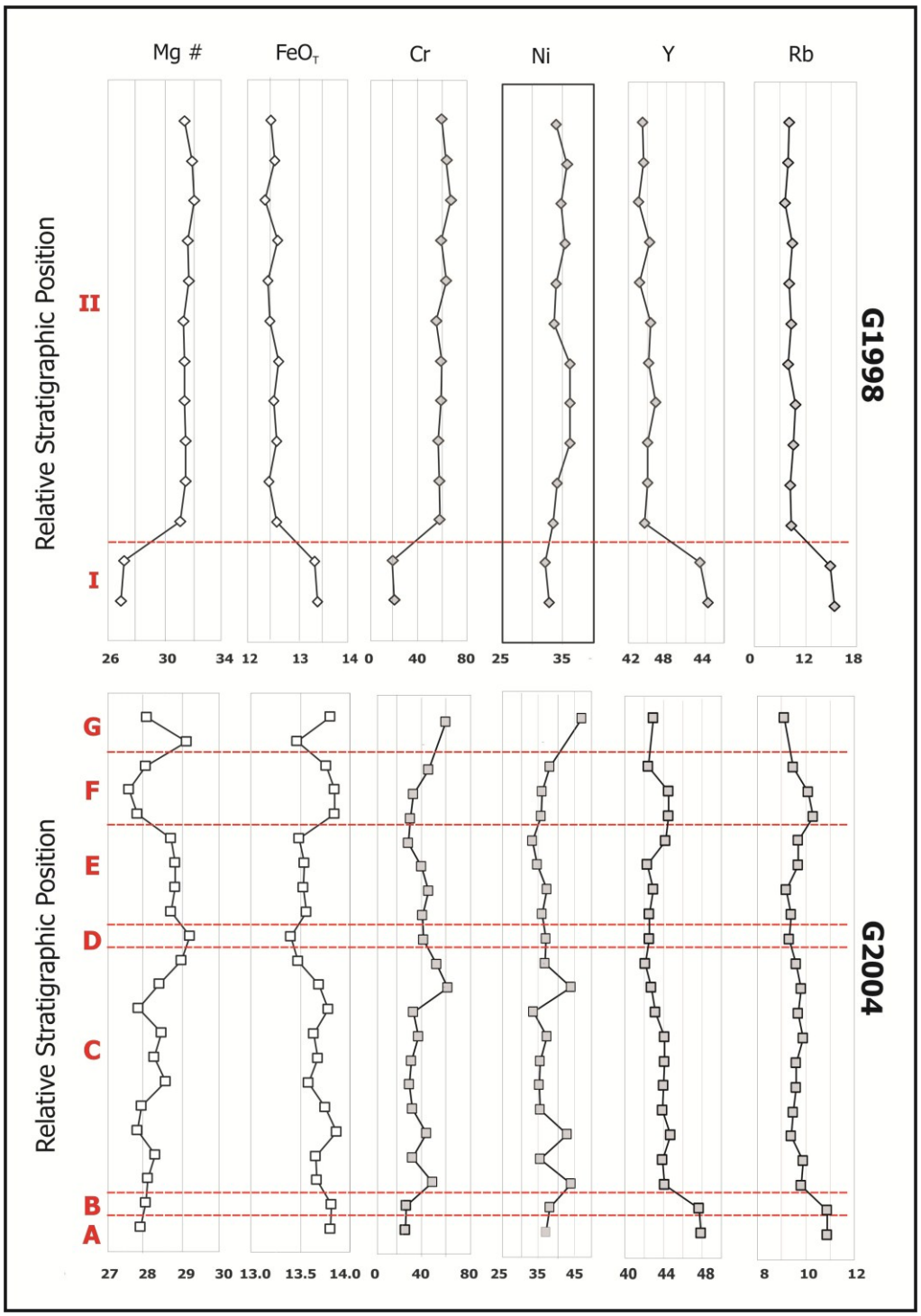

7.7 DISCUSSION

7.7.1 GENETIC RELATIONSHIPS BETWEEN THE LAKI, G1998 AND G2004 MAGMAS – SOURCE EFFECTS

Trace element ratios are sensitive indicators of the genetic relationships among a particular sample suite (e.g. Albarede, 1976; Muenow *et al*., 1991) because of (i) the manner in which they are selectively partitioned between various crystal phases and the melt (unlike the major elements, which are generally abundant in most rock-forming minerals), and (ii) the fact that their concentrations may vary by up to three orders of magnitude (compared with major elements whose concentrations usually vary by a factor of <10). The ratio of the incompatible elements Nb and Zr will not be significantly altered by crystal fractionation of basaltic melts since neither element fits within the crystal lattice of the major crystallising phases (olivine, plagioclase and CPX). However, this ratio is unlikely to remain constant (i.e. a slope close to 1) if magma mixing has taken place (Natland, 2007). Each of the Laki, G1998, and G2004 magmas form separate trends on bivariate plots (Fig. 7.9), indicating that they originate from separate primary magma batches as each trend reflects a different degree of partial melting from a mantle or deep crustal source. Since Nb is somewhat more incompatible than Zr, the shallower slope of the G1998 trend compared to that of the G2004 and Laki eruptions suggests that this magma was generated by a higher degree of melting in the mantle source.

7.7.2 FRACTIONAL CRYSTALLISATION TRENDS

Plagioclase (Plag), Clinopyroxene (CPX), and Olivine (Ol) are major rock-forming minerals in MORBs which have all been identified (albeit in vanishingly small quantities for the latter two phases) in G1998 and G2004 samples. MELTS calculations using Laki whole-rock compositions return a low crystallisation pressure assemblage of plagioclase-olivine-clinopyroxene (Bindeman *et al*., 2006). Consequently, using PETROLOG (Danyushevsky and Plechov, 2011) I have modelled variable crystal fractionation of these three phases at 1 kbar pressure. Starting compositions were selected by taking the highest wt. % MgO analyses from among each of the Laki (Passmore, 2009), G1998 and G2004 datasets. The trends resulting from this projection are plotted in figure 7.12.

On figure 7.12, each eruption forms a separate, but almost parallel crystallisation trend. This indicates that the more recent magmas did not form from the Laki magma as a result of a simple and direct fractional crystallisation process. Indeed, the results indicate separate starting compositions even for the closely spaced G1998 and G2004 events. However, the trends within each erupted magma batch are clearly consistent with fractional crystallisation during a period of shallow magma storage and prior to eruption.

The fact that Sr content is essentially constant in the G1998 analyses (and also in all but the first phase of G2004) along with the fact that plagioclase is the most dominant crystal phase in the samples confirms that the plagioclase crystallization is a very late and shallow level phenomenon (Figs 7.9 and 7.13). Relationships between the elements Ba (largely incompatible in all phases), Sr (compatible in Plag; incompatible in CPX and Ol), Ni (highly compatible in Ol; moderately compatible in CPX; incompatible in Plag), and Sc (compatible in CPX; incompatible in Plag and Ol) are inconclusive, but appear to indicate control by both plagioclase and clinopyroxene crystallisation (Fig. 7.13). This may suggest that crystal fractionation occurred at, or close to, the Plag-CPX cotectic line which buffered the magma composition. Alternatively, it may reflect polybaric fractional crystallisation during magma ascent. In a study based on Laki glass petrology (Kelley and Barton, 2008), polybaric crystallisation was also inferred for the Laki eruption at depths of between 26 and 7 km.

Figure 7.12: Projected trends for variable fractional crystallisation of olivine, clinopyroxene and plagioclase using Laki, G1998 and G2004 most primitive starting compositions.

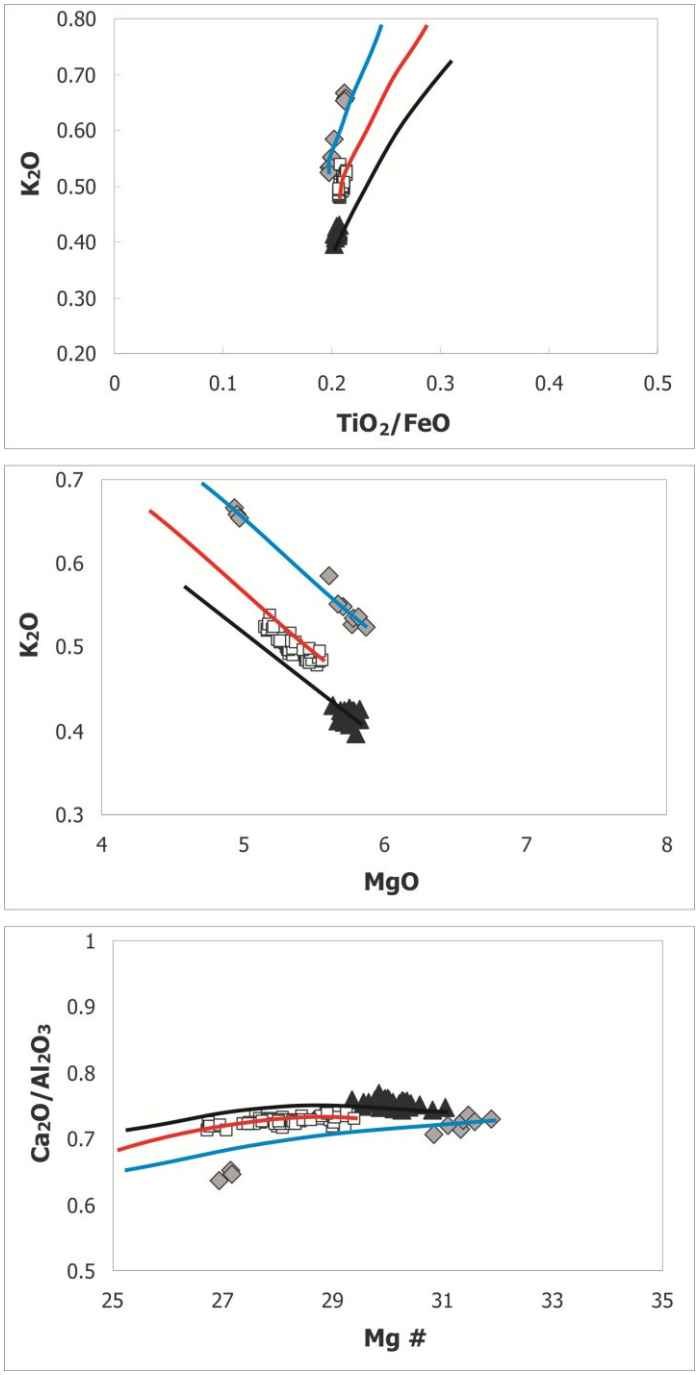

Figure 7.13: Variation Sc (ppm) with Ni (ppm) (top), Sc (ppm) with Al_2O_3 (wt. %) (middle) and variation in Sr (ppm) with Ba (ppm) (bottom) for the G1998 (filled diamonds) and G2004 (open squares) eruptions.

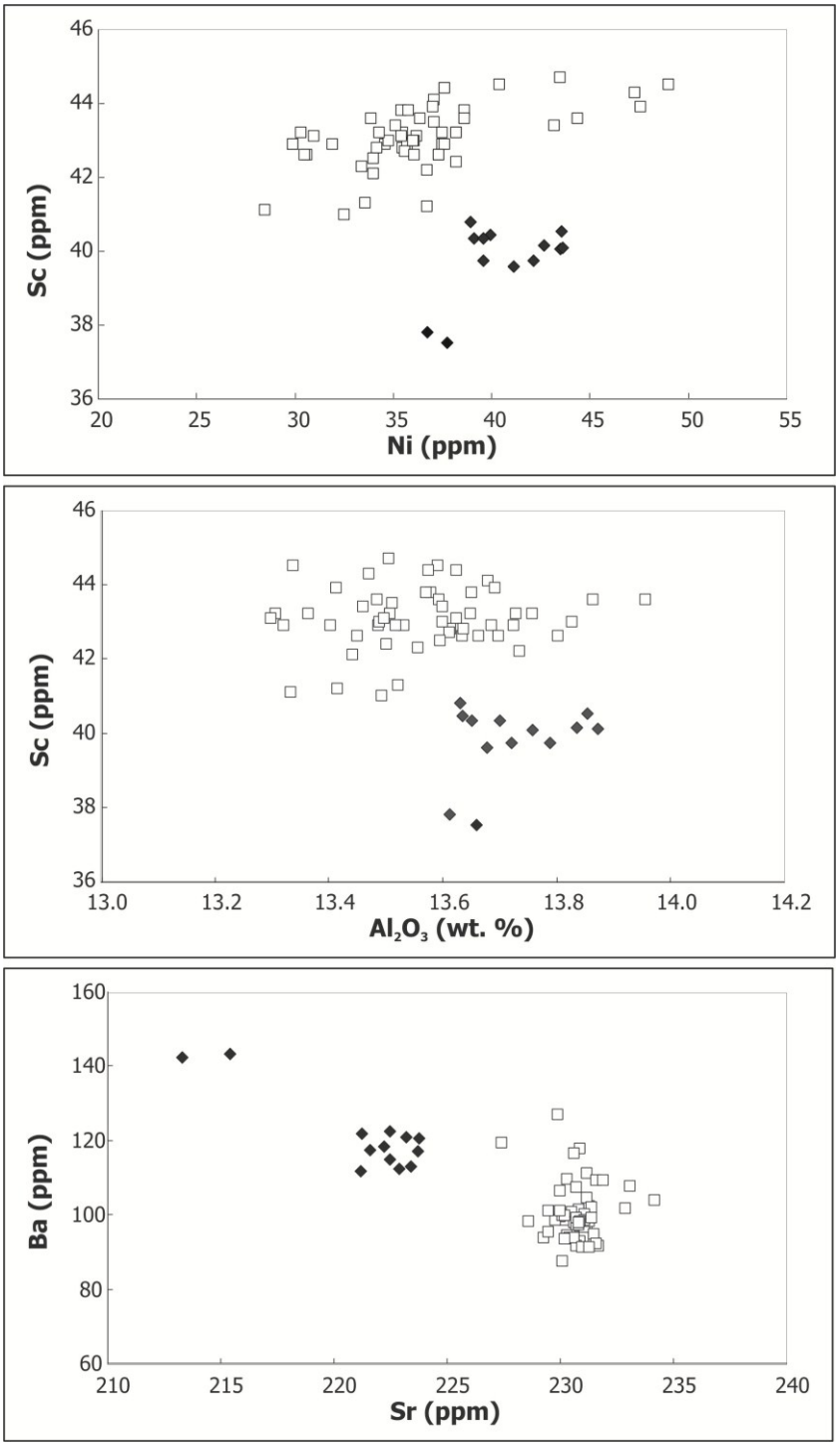

7.7.3 ASSIMILATION OF HYDROTHERMALLY ALTERED CRUST

The most recent models for magma plumbing and evolution beneath Grímsvötn volcanic system (Bindeman *et al.*,2006; 2008) argue for the presence of a high-level magma chamber, tapped by both the Laki fissure eruptions and by subsequent Grímsvötn eruptions. This model is based upon measurements of Laki and Grímsvötn glasses which share low $\delta^{18}O$ values of 3.0 to 3.2‰, compared to normal mantle values of ~5.6‰ $\delta^{18}O$. This discrepancy is explained by the authors as resulting from assimilation of hyaloclastite, which has been altered by glacial meltwater (low $\delta^{18}O$), into a shallow magma chamber.

Although this argument is compelling, the proportion of assimilated material invoked by the authors is rather high (up to 45%; Bindeman *et al*., 2006). Later work by Passmore (2009) questions this analysis on the basis of similarities in measured La/Yb ratios in Laki glass and olivine-hosted melt inclusions. The La/Yb ratio is considered to be very sensitive to contamination by assimilation of foreign material (Passmore, 2009). Furthermore, Passmore (2009) argues that the Icelandic crust has a high geothermal gradient, which restricts the depths to which meteoric waters are able to penetrate. Assimilation of hyaloclastite material, were it to occur, would therefore have to take place at depths of <1-2km beneath the surface.

7.7.4 IMPLICATIONS FOR MAGMATIC PLUMBING BENEATH GRÍMSVÖTN

The data strongly suggest that the two most recent eruptions (G2004 and G1998), although of small volume and closely spaced, are not derived from the same magma batch, nor can they have evolved from a Laki-like magma batch via fractional crystallization. These results imply that the magma plumbing system beneath Grímsvötn is more complex than previously realised. The results identify more than one magma pocket in the shallow crust beneath Grímsvötn, each with its own separate link to a deeper source and distinct pathways by which magma travels to the surface (Fig. 7.14).

Chemical stratigraphy of the G2004 event indicates an ephemeral, compositionally stratified shallow sill undergoing crystal fractionation as the magma resides in a low pressure environment for a relatively short period of time (< 6 years) prior to eruption. The G1998 magma exhibits a similar degree of chemical variation, but it is not clear from the data that this varies systematically over time during the

course of the eruption. The data therefore show that each eruption comes from an individual shallow sill-like body beneath Grímsvötn that begins to form shortly after previous eruption. That is, the 1998 magma batch may have started to establish itself within the shallow magma storage region shortly after the 1984 eruption and similarly the 2004 batch began to accumulate after 1998. This explains the observed inflation patterns, and the seismic and gravity data, along with the chemical trends presented in this study.

These new findings have significant implications for eruption forecasting and for our understanding of the duration and controls on eruption cycles in historical time. Deformation at Grímsvötn is currently modelled from a single Mogi point source (Mogi, 1958), and inflation is interpreted to be a direct response to the influx of fresh magma from depth into a single, centrally located storage chamber (Sturkell *et al*., 2003). In order to take the results of this study into account it will be necessary to redefine the current concept of the mechanisms and timescales of edifice inflation and subsequent eruption cycles at Grímsvötn.

7.8 CONCLUSIONS

Grímsvötn eruption products are not as homogeneous as previously supposed – both within individual, small events, and between eruptions. The suite of analyses presented in this study not only provide new analytical data from the two most recent Grímsvötn eruptions, slightly extending the known compositional range for this volcanic system, but also provides the most comprehensive sampling to date within a single central volcano event. The data suggest that the Grímsvötn and Laki magmas do not share a common parental magma, but rather are sourced from separate batches derived from different degree of partial melting of a homogenous mantle source. These magmas then migrate to the surface via separate pathways and are erupted from small, discrete magma pockets that have evolved separately. It is possible that crustal assimilation may play a significant role in magma evolution at Grímsvötn – a factor which has not been quantified by this study. In either case the results of this study point towards an increasingly complex model for magma storage and ascent beneath this highly active volcanic system.

Figure 7.14: New conceptual model for Grímsvötn magma plumbing and storage. Note that this is a cartoon-style diagram and therefore not to scale.

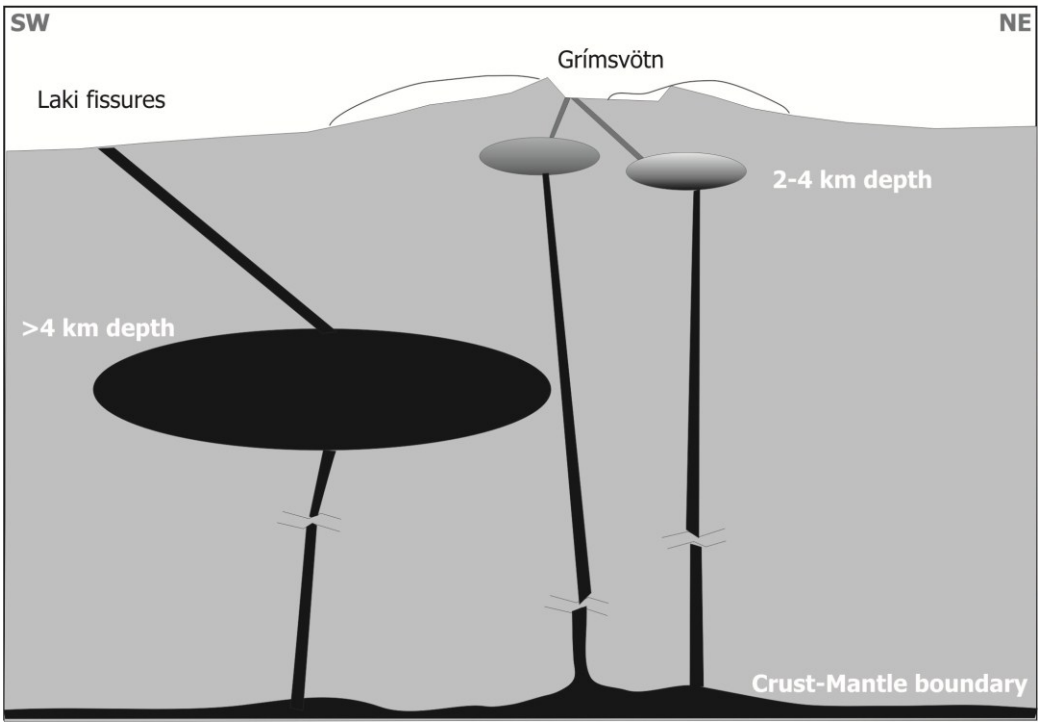

CHAPTER 8

VOLATILE EMISSIONS AND GLASS CHEMISTRY OF THE 2004 ERUPTION AT GRÍMSVÖTN VOLCANO, ICELAND

8.1 INTRODUCTION

Eruptions from ice-capped central volcanoes are a significant end-member style of volcanism in Iceland (Jakobsson and Gudmundsson, 2008; also see chapters 2 and 3, this volume). Among these, Grímsvötn volcano, which lies beneath west-central Vatnajökull, has been the most frequently active in historical time (Larsen *et al*., 1998; Larsen, 2002; Thordarson and Höskuldsson, 2008). Previous geochemical (e.g. Bindeman *et al*., 2006) and geophysical studies (e.g. Alfaro *et al*., 2007; Sturkell *et al*., 2003) infer the presence of a shallow (2-4 km depth) crustal storage chamber beneath the Grímsvötn caldera which is intermittently replenished by mafic magma from below. Furthermore, a link has been made between jökulhlaup (glacial outburst flood) release and the depressurisation-induced triggering of eruptions at Grímsvötn (Gudmundsson *et al*., 1997; Vogfjörð *et al*., 2005; Albino *et al*., 2010). However, due to the remoteness of the eruption site it has not previously been possible to perform any detailed and systematic geochemical study of the nature of the shallow crustal storage system beneath the Grímsvötn central volcano and the individual crystallization and degassing histories within any single event.

This study evaluates major oxide and trace element glass compositions, along with volatile (S, Cl and F) contents and mineral chemistry, of the Grímsvötn 2004 (G2004) products in order to (i) make inferences about the nature of the shallow crustal storage system beneath the Grímsvötn central volcano; (ii) evaluate the impact of conduit processes on eruption style and deposit characteristics; and (iii) quantify SO_2 and Cl release to the atmosphere during a typical small volume, high frequency Grímsvötn eruption and determine the effect of the englacial environment on magma degassing.

8.2 BACKGROUND

Sulphur contributed by volcanic degassing is a significant input to the atmospheric reservoir and plays an important role in the global geochemical cycle (Liu, 2007). The short-term (i.e. 10-20 year) annual estimated volcanic flux of sulphur species into the atmosphere due to small magnitude eruptions is on the order of 0.4 Mt (Pyle at al, 1996). The atmospheric effects of sulphur gases (mainly sulphur dioxide, SO_2) and sulphuric acid (H_2SO_4)) are very well-studied (e.g. McCormick *et al*., 1995; Self *et al*., 2005; Self *et al*., 1981). Thus, determining quantities and mechanisms of S release to the atmosphere is critical to evaluating the environmental impacts of volcanism (Sharma *et al*., 2004; Wallace *et al*., 2002).

At high latitudes, the tropopause is quite low (8-9 km) (Stothers *et al*., 1986; Self *et al*., 1998). This allows relatively small plumes to readily inject SO_2 and other volatiles into the stratosphere, where aerosols have a longer residence time and greater global dispersal than if they are confined to the troposphere alone (Wallace, 2002). In fact, Pyle *et al.* (1996) infer that the eruptive mass required for a volcanic plume to penetrate the tropopause at mid to high latitudes may be as little as $1.3x10^{10}$ kg, emphasising the contribution of small magnitude, high frequency eruptions towards the global volcanogenic sulphur budget. The explosive phases of basaltic fissure eruptions are known to release large amounts of sulphur and other gases into the atmosphere because of the high sulphur yield of basaltic magmas (i.e. 2-4 times that of silicic compositions (Haughton, 1974; Wallace and Carmichael, 1992)) coupled with efficient vent degassing mechanisms (Thordarson *et al*., 1996). The atmospheric loading in these cases, which may be likened to the explosive phases of basaltic englacial eruptions, is essentially instantaneous because volatiles are released by a single event (or series of short explosive events) lasting only several hours to a few days. Values for the total SO_2 contribution by flood lava eruptions are well constrained for several well-known eruptions both outside of Iceland (e.g. Columbia River flood basalts, Thordarson and Self, 1996; Self *et al*., 1996) and within Icelandic rift systems (e.g. Grímsvötn-Laki, Bárðarbunga-Veidvötn and Katla-Eldgjá, Thordarson *et al*., 1996; Thordarson *et al*., 2001; Thordarson *et al*., 2003). In Iceland, however, these account for only half of the magma volume erupted throughout the Holocene. The majority (85 %) of the remainder of magma production was emitted by explosive emergent phases of englacial eruptions at central volcanoes (Larsen *et al*., 1998) which are very different

in style and in pattern to fissure eruptions. It has been inferred that because of their similar compositions, central volcano eruptions possess similar potential sulphur yields to basaltic fissure events. However, until now it has not been possible to estimate the total SO_2 mass loading for these englacial eruptions because of insufficient knowledge of magma degassing and eruption column processes in phreatomagmatic events (Thordarson *et al*., 2003).

Compared to sulphur the influence of halogen degassing from volcanic eruptions on atmospheric chemistry is poorly understood (Self, 2006; Tabazadeh and Turco, 1993). However, both volcanogenic F and Cl (generating HF and HCl in gaseous or aerosol form) have demonstrated detrimental effects on high-altitude ozone concentrations, particularly at high altitudes (e.g. Hunton *et al*., 2005; Prather, 1992). Furthermore, due to its high toxicity, low-level F emissions were shown to have catastrophic local and regional environmental effects during and after the 1784-84 Laki eruption in Iceland (e.g. Fiacco *et al*., 1994).

No direct measurements of SO_2 in the atmosphere were taken during the G2004 eruption. Consequently the petrologic method (Devine *et al*., 1984, Self and King, 1996;) is used to estimate sulphur, chlorine and fluorine degassing via comparison of S and Cl contents in matrix glass with those of melt inclusions hosted in plagioclase phenocrysts (complete data is presented in Appendix XI). Although it often underestimates the mass of sulphur released by eruptions in arc systems (e.g. Wallace, 2001; Sharma *et al*., 2004), the petrologic method has been shown to give reliable results for divergent margin and hot spot basalt eruptions (e.g. Andres *et al*., 1989; Thordarson *et al*., 1996).

Table 8.1: Reported and average of measured (EMP) major element concentrations in the international standards BHVO-2G and Lipari-1. All measured values reported as weight percent.

BHVO-2G		**SiO_2**	**TiO_2**	**Al_2O_3**	**FeO**	**MnO**	**MgO**	**CaO**	**Na_2O**	**K_2O**	**P_2O_5**	**F**	**SO_2**	**Cl**	**Sum**	**n**
Reported		49.30	2.78	13.60	11.30	0.17	7.13	11.40	2.40	0.51	0.27	-	-	-	98.86	-
S.D. (1 σ)		*0.10*	*0.02*	*0.10*	*0.10*	*0.03*	*0.02*	*0.10*	*0.05*	*0.02*	*0.02*	-	-	-	-	-
This study		49.74	2.78	13.57	11.02	0.17	7.24	11.34	2.28	0.51	0.25	0.052	0.008	0.004	98.88	71
S.D. (1 σ)		*0.39*	*0.05*	*0.28*	*0.22*	*0.01*	*0.12*	*0.13*	*0.13*	*0.03*	*0.01*	*0.015*	*0.002*	*0.002*	-	-
Lipari-1		**SiO_2**	**TiO_2**	**Al_2O_3**	**FeO**	**MnO**	**MgO**	**CaO**	**Na_2O**	**K_2O**	**P_2O_5**	**F**	**SO_2**	**Cl**	**Sum**	**n**
Reported		74.35	0.08	12.87	1.51	0.07	0.05	0.74	3.93	5.11	-	-	-	-	98.71	-
S.D. (1 σ)		*0.17*	*0.01*	*0.07*	*0.05*	*0.02*	*0.01*	*0.02*	*0.06*	*0.04*	-	-	-	-	-	-
This study		73.95	0.08	13.03	1.52	0.08	0.04	0.73	4.07	5.09	-	-	-	-	98.59	31
S.D. (1 σ)		*0.37*	*0.01*	*0.27*	*0.12*	*0.03*	*0.01*	*0.03*	*0.11*	*0.10*	-	-	-	-	-	-

8.3 SAMPLING STRATEGY AND ANALYTICAL PROCEDURE

A total of 44 samples, spanning a variety of clast types from different stratigraphic levels, were selected for analysis by electron microprobe. This fine sampling interval, focussed on the proximal area of the deposit, ensured that representative samples from each eruptive phase were analysed. In addition, it places precise time constraints on the data. A full description of the eruptive sequence and deposit stratigraphy of the G2004 eruption is given in Chapter 3.

8.3.1 ELECTRON MICROPROBE (EMP) ANALYSIS

Samples selected for EMP analysis were prepared according to two different methods. Individual clasts ranging between 16-32 mm in diameter and between 60-85% vesicularity taken directly from pumice lenses were impregnated with resin and cut into thin sections. Matrix tephra samples were handpicked from the 125-250 μm size fractions and set in resin plugs which were then sectioned and polished.

Point analyses were performed using a Cameca SX100 at the Grant Institute, School of GeoSciences, University of Edinburgh, UK. This instrument was calibrated against an assortment of natural and synthetic glass and mineral standards. Analyses were conducted using standard WDS techniques under the following conditions: accelerating voltage - 15 kV; beam current - 2nA for major elements (Si, Al, Fe, Mg, Ca, Na, K) and 80 nA for trace elements (Mn, Ti); beam diameter - 5 μm; counting times - 20 s for all elements with the exception of Mn and Ti which were 50 s and 40 s respectively. The total time taken for each analysis was approximately 5 minutes. Analyses of the Lipari and BHVO-2G standards were conducted prior to and at the end of analytical sessions and at regular intervals in between, to mitigate against instrumental drift. ZAF (atomic number, absorption and fluorescence) corrections were applied to the data using XPhi Cameca PeakSight software. For more details on analytical procedure, see Hayward and Thordarson (The Holocene, in review).

8.3.1.2 QUALITY ASSURANCE

Three point analyses of international glass standards were taken at the beginning and end of each analytical session, as well as at three to six hour intervals during sessions of extended duration. In total the Lipari standard was analysed 31

times and BHVO-2G 71 times, yielding narrow compositional ranges (Table 8.1). The results are within the acceptable compositional range for these samples, as reported in the literature.

S, F and Cl measurements were calibrated against a set of known natural and synthetic standards. S is calibrated against a natural barite standard. The instrumental standard deviation is 85 ppm, with a detection limit of 70 ppm. Cl is calibrated against NaCl with a standard deviation of 68 ppm and a 76 ppm detection limit. F is calibrated against a $RbMnF_3$ standard. Measurements of this standard have a standard deviation of 450 ppm, for a detection limit of 510 ppm. As there is such a high level of uncertainty in the F measurements, the results are noted for completeness, but will not be discussed in great detail.

8.4 RESULTS

8.4.1 GROUNDMASS GLASS MAJOR ELEMENT DATA

Glass analyses were performed on two types of tephra – moderately and poorly vesicular ash from all units and lapilli-sized pumice clasts, which are taken from units C and E and the late-stage tuff cone. Results of chemical analyses for individual samples are given in Appendix IX, while a summary of the average and range of compositions for each unit are given here in Table 8.2.

Over the entire range of eruption products there is a significant range in the Mg # (34-43) and K_2O contents (0.37 – 0.63 wt. %; σ = 0.03 wt. %; Fig. 8.1), which are important indices of evolution in basaltic magmas. The pumice clasts form the most evolved group, and are compositionally distinct from the less vesicular samples. While the mean glass composition varies over time, abundances of all major oxides show poor correlation with clast vesicularity – notwithstanding the fact that the higher vesicle abundance (>70 vol. %) associated with selected pumice samples clearly accompanies a more evolved glass composition (Fig. 8.1).

The phreatomagmatic tephra follows a general trend of progressing from the most evolved (lowest median wt. % MgO; highest median wt. % K_2O) to most primitive (highest median wt. % MgO; lowest median wt. % K_2O) compositions for units A through to E, then swinging back to slightly more evolved compositions, closer to the bulk average, for units F and G (Fig. 8.2). The dense clustering of data points confirms a relatively uniform composition within individual units. The phreatomagmatic ash from main-phase unit C shows the most variable major element concentrations which form an array spanning the entire compositional range of the bulk magma and the pumice clasts (Fig. 8.1). Although there is considerable overlap between compositions of different units, they each tend to cluster in specific regions of the major oxide covariation diagrams (e.g. Figs. 8.3 and 8.4). Key differences and similarities are outlined below:

The lowermost units, A and B, are indistinguishable from one another in terms of magnesium and potassium content (Fig. 8.5). With Mg # between 36-41 and K_2O 0.42-0.59 wt. % these are the most evolved units, yet are less evolved than the individual pumice samples (Fig. 8.1). The entire compositional range for both Mg# and

K_2O are represented by Unit C, though most samples cluster near the median values of Mg # = 41 and 0.45 wt. %, respectively. Pumice from units C and E are the most evolved glass samples, with a lower mean Mg # (38) and elevated K_2O (0.54 wt. %) compared to moderately to poorly vesicular clasts from other units. By contrast, Unit D spans a wide compositional range (Mg#: 38-43; K_2O: 0.42-0.56 wt. %), but hardly overlaps with the most evolved pumice compositions. The average composition of Unit D is Mg # = 41, K_2O 0.49 wt. %. Unit E has similar composition to most of the Unit C samples, but it is the least evolved depositional unit, with the highest average Mg# (42) and relatively low K_2O (0.48 wt. %). Unit F is marginally more evolved than the overall average, but clusters close to average values for the bulk deposit. The mean Mg# of Unit F is 41 and mean K_2O is 0.48 wt. %. Unit G also clusters in the central region of the K_2O vs. Mg# plot (Fig. 8.1), overlapping considerably with units A and B, in terms of Mg #, but with a narrower range (Mg#: 40 – 41). Unit G is relatively deficient in K_2O compared to many other samples (average = 0.44 wt. %).

Similarly, on plots of wt. % TiO_2 and wt. % FeO covariation with wt.% MgO (Figs. 8.3 and 8.4) Unit C exhibits the largest range in both TiO_2 and FeO contents (2.8-3.4 wt. % and 13.4-14.7 wt. %, respectively). The mean Ti content of Unit C tephra is 3.0 wt. %, while for Fe it is 13.7 wt. %. Pumice samples are comparatively enriched in both FeO (mean = 14.35 wt. %; range = 13.73-15.26 wt. %) and TiO_2 (mean = 3.2 wt. %; range = 3.0-3.4 wt. %) compared to the bulk deposit average and overlap only with the highest TiO_2 values in the Unit C range. Units A and B overlap with high Unit C values, units D and G with the median to high end of the range and units E and F overlap with the lower and middle values covered by Unit C (Fig. 8.3). The compositional fields of units A and B largely overlap, but A has higher mean FeO (14.0 wt. %) than B (13.8 wt. %) for the same TiO_2 content (3.0 wt. %). These are similar average values to that of Unit C, but with a more restricted range. Unit D has slightly lower median TiO_2 and FeO contents (2.9 wt. % and 13.6 wt. %, respectively) than those of units A, B and C. Unit E is similar in TiO_2 content to Unit D, but has lower median FeO values (13.5 wt. %). Unit F also covers a very restricted range with low Ti content, but an average FeO content (13.6 wt. %) similar to the overall average. Unit G clusters close to the median Ti and Fe compositions. Although small, these compositional differences are significant as they lie outside of analytical error. One standard deviation is only 0.22 wt. % for FeO and 0.05 wt. % for TiO_2.

The average glass compositions for each unit follow the same trends on most major oxide covariation diagrams as the whole rock data. However, these are offset as for most units the whole rock samples contain a higher proportion of K_2O, FeO and MgO than the groundmass glass (Fig. 8.5). The groundmass glass of pumice sample, however, contains less MgO and more FeO than the whole rock. In all cases, except for the pumice samples, there is more TiO_2 in the groundmass glass than the whole rock sample.

The relationship between whole rock and glass Al_2O_3 and Na_2O contents is slightly more complex. The wt. % MgO and wt. % Al_2O_3 forms a shallower positive trend for the glass samples than it does for the whole rock and there is less Al in the glass samples, overall (Fig. 8.6). Similarly, on the MgO vs. Na_2O bivariate plot the glass data displays an almost horizontal (but slightly negatively sloping) trend, while the whole rock data has a steeper negative slope. There is less Na_2O in the whole rock samples than in the groundmass glass (Fig. 8.6).

One key difference between the major element whole rock versus glass trends is that within the glass data pumice analyses always jump to a more evolved composition and extend the compositional range (e.g. Figs. 8.5 and 8.6). By contrast, whole rock pumice data occupy a position close to the Unit C and Unit E averages. That is, in whole rock terms the pumice compositions are no different from those of poorly to moderately vesicular ash within the unit from which they were taken.

Figure 8.1: Mg number vs. K_2O content for groundmass glass of individual tephra clasts from all G2004 units. The field of XRF (whole rock) analyses is shown by a white-shaded ellipse.

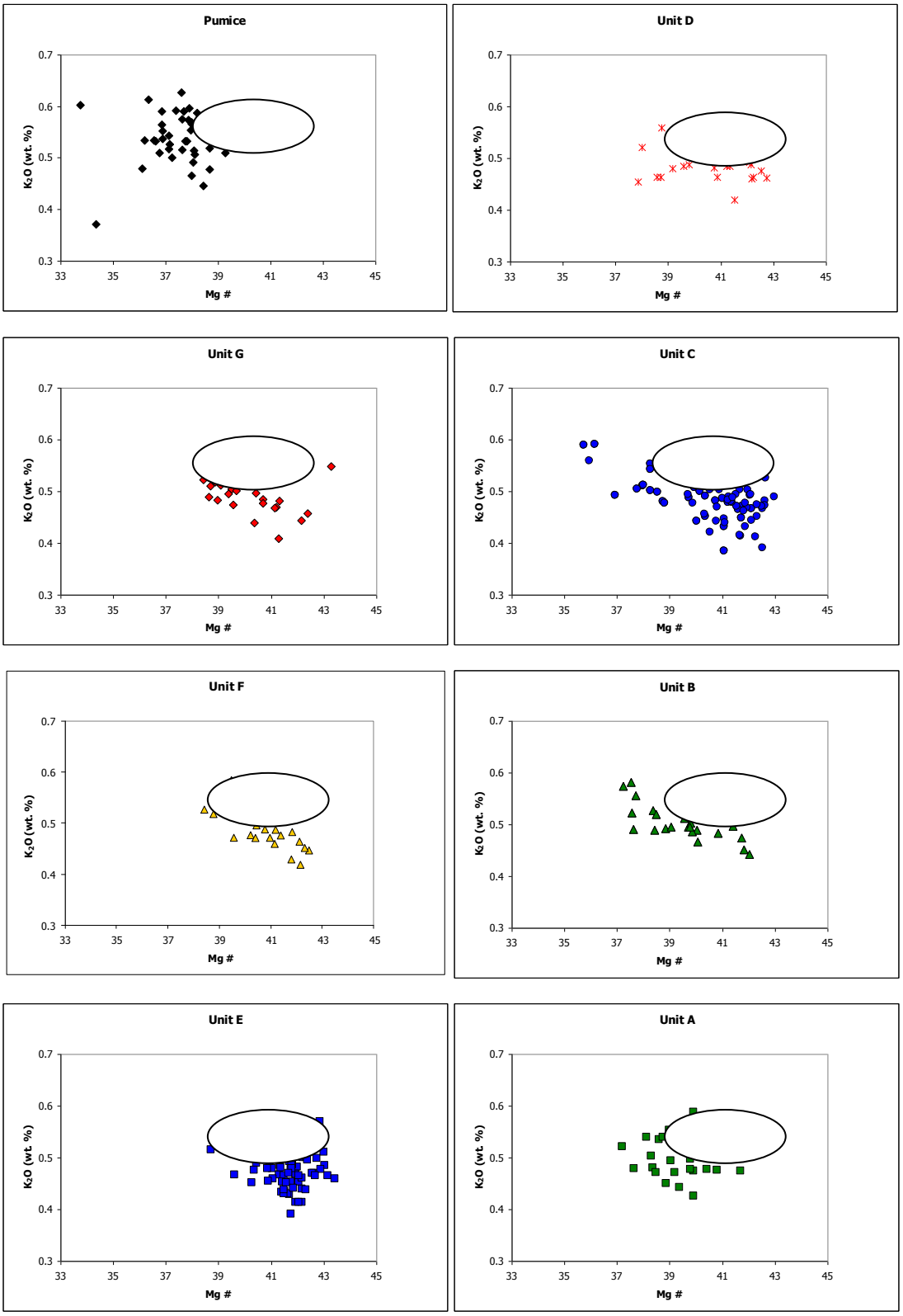

Figure 8.2: Major oxide average glass abundances of weight percent TiO_2, MgO, CaO and K_2O with stratigraphic level. Error bars are smaller than the size of the points and are therefore not visible.

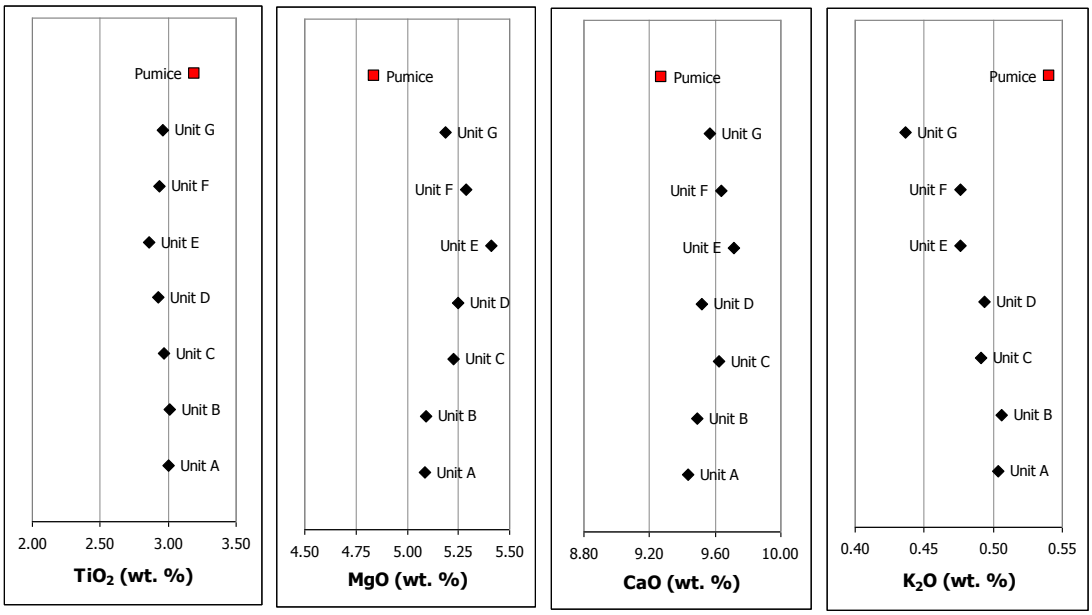

Figure 8.3: MgO vs. TiO_2 content for groundmass glass of individual tephra clasts from all G2004 units.

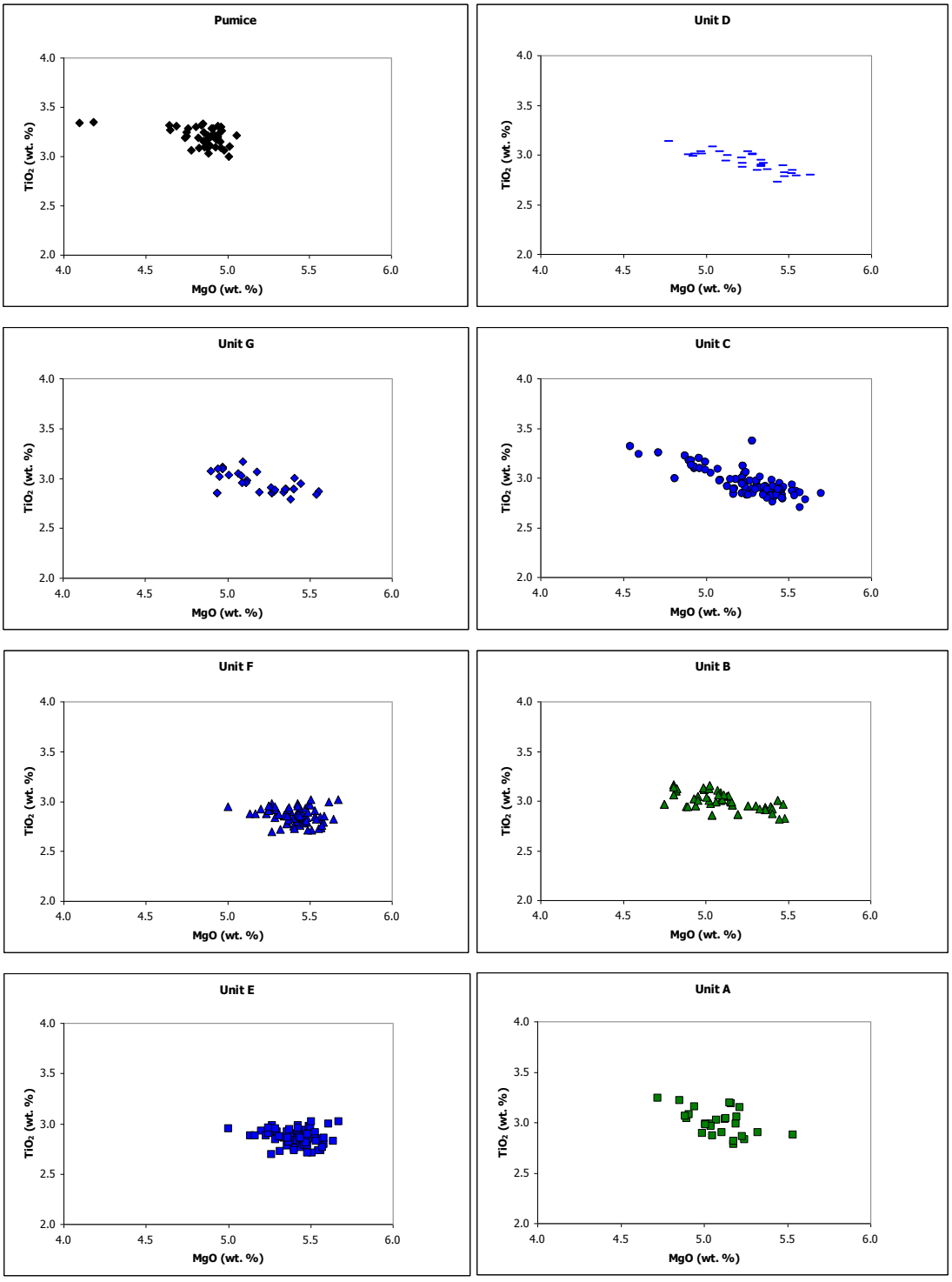

Figure 8.4: MgO vs. FeO content for groundmass glass of individual tephra clasts from all G2004 units.

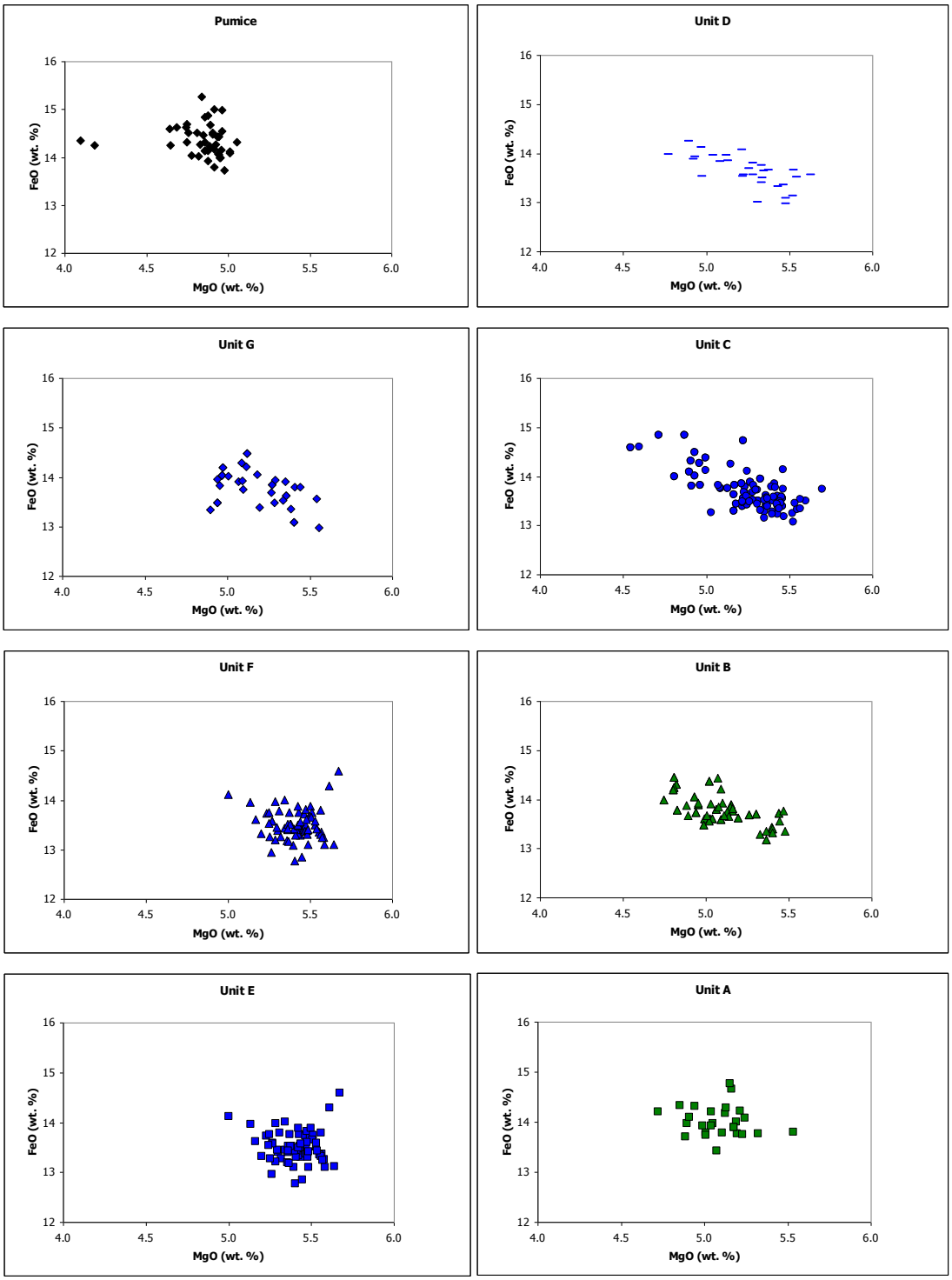

Figure 8.5: (Top) Average unit weight percent TiO_2 versus K_2O for groundmass glass and whole rock analyses. (Bottom) Average unit weight percent MgO vs. TiO_2 for groundmass glass and whole rock analyses.

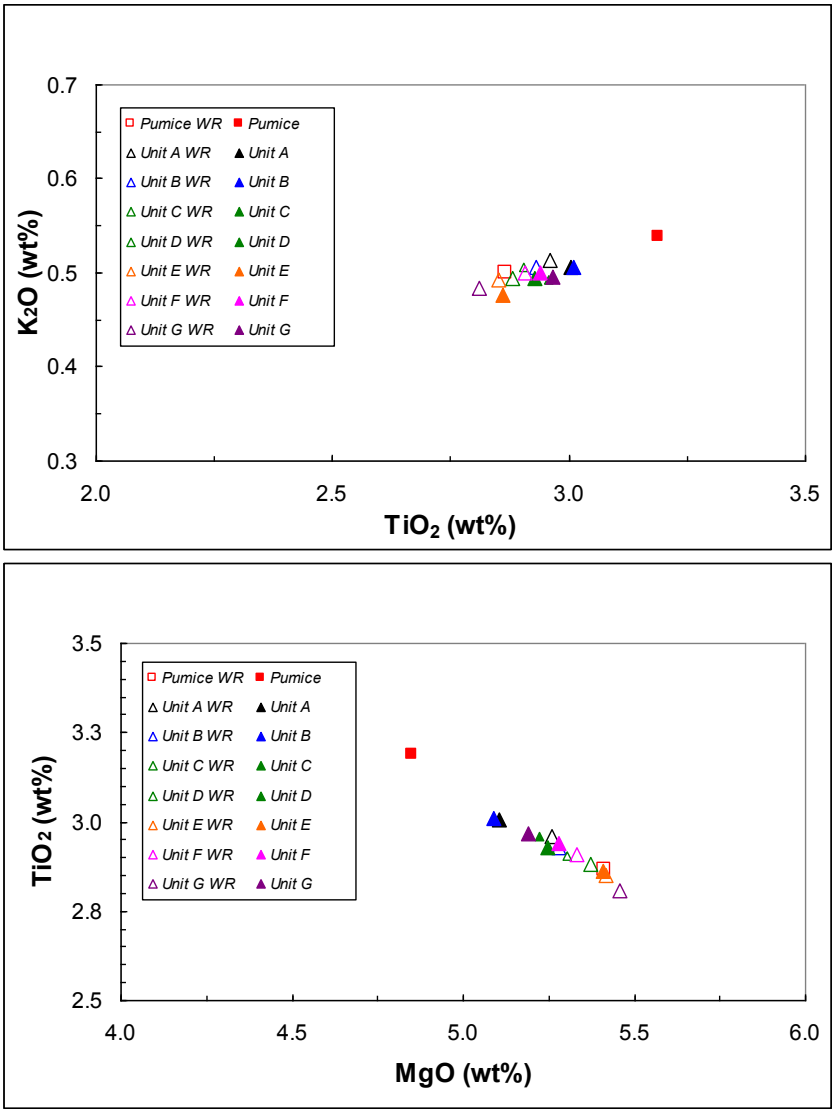

Figure 8.6: (Top) Average unit weight percent MgO versus Al_2O_3 for groundmass glass and whole rock analyses. (Bottom) Average unit weight percent MgO versus Na_2O for groundmass glass and whole rock analyses.

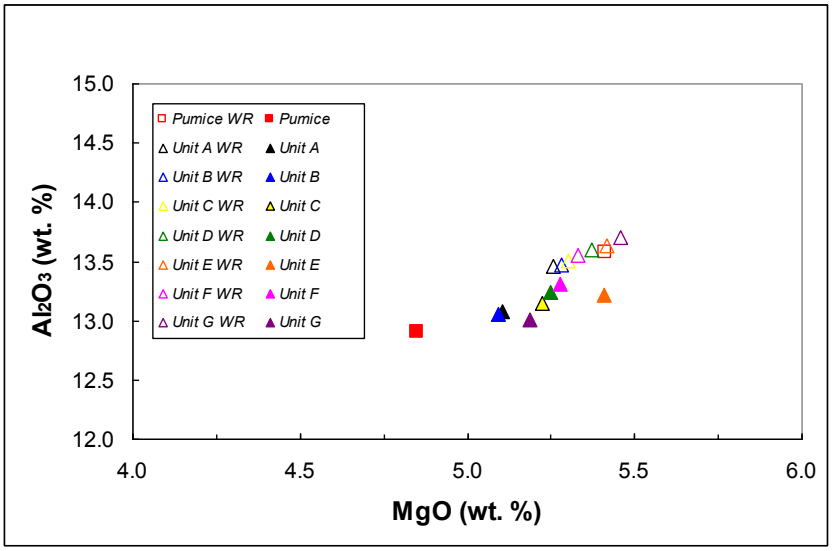

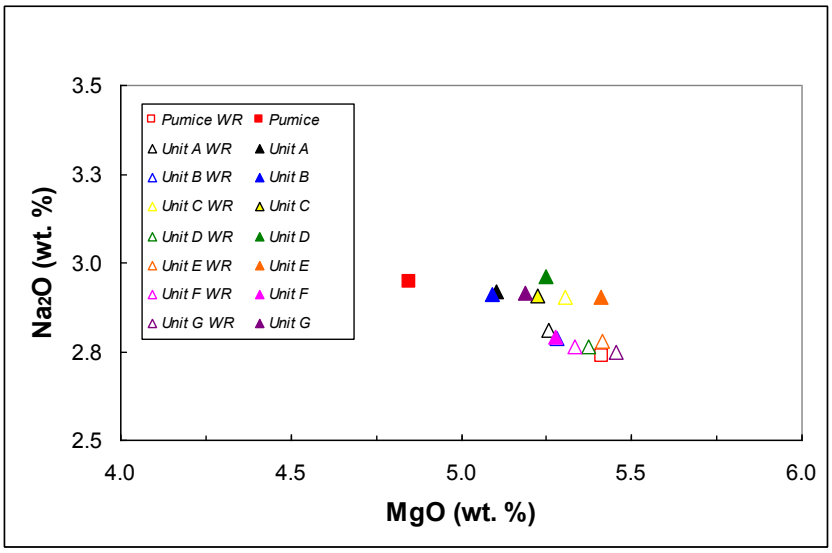

Table 8.2: Average and range of compositions for G2004 glass analyses, by unit

		SiO_2	TiO_2	Al_2O_3	FeO	MnO	MgO	CaO	Na_2O	K_2O	P_2O_5	S (ppm)	F (ppm)	Cl (ppm)	n
Unit A	*Mean*	50.01	3.00	13.11	14.01	0.24	5.09	9.43	2.90	0.50	0.34	837	557	182	26
	Min	49.45	2.79	12.48	13.42	0.22	4.72	8.90	2.29	0.43	0.32	578	193	108	-
	Max	51.08	3.24	13.55	14.77	0.25	5.54	9.83	3.13	0.59	0.37	1018	884	232	-
Unit B	*Mean*	50.08	3.01	13.06	13.79	0.23	5.09	9.49	2.91	0.51	0.35	831	547	180	72
	Min	49.33	2.82	12.68	13.18	0.21	4.75	9.01	2.75	0.42	0.31	643	321	135	-
	Max	51.23	3.17	13.77	14.46	0.26	5.48	9.88	3.11	0.59	0.40	1084	877	229	-
Unit C	*Mean*	49.99	2.96	13.14	13.74	0.31	5.22	9.62	2.91	0.49	0.33	790	538	178	121
	Min	49.00	2.70	12.30	13.07	0.21	4.54	9.00	1.48	0.39	0.29	604	235	118	-
	Max	51.12	3.31	13.80	14.84	0.59	5.70	10.07	3.15	0.59	0.39	1024	901	231	-
Unit D	*Mean*	50.20	2.93	13.24	13.64	0.23	5.25	9.52	2.96	0.49	0.33	802	647	181	29
	Min	49.33	2.72	12.72	12.97	0.21	4.77	9.13	2.75	0.42	0.30	711	366	139	-
	Max	51.07	3.13	13.67	14.24	0.25	5.63	10.02	3.19	0.56	0.38	854	892	214	-
Unit E	*Mean*	49.97	2.86	13.21	13.50	0.23	5.41	9.71	2.90	0.48	0.32	818	617	177	69
	Min	49.00	2.70	12.50	12.77	0.21	5.00	9.23	1.51	0.39	0.28	625	267	99	-
	Max	50.85	3.02	13.90	14.59	0.25	5.67	10.20	3.09	0.57	0.35	1270	968	297	-

		SiO_2	TiO_2	Al_2O_3	FeO	MnO	MgO	CaO	Na_2O	K_2O	P_2O_5	S (ppm)	F (ppm)	Cl (ppm)	n
Unit F	*Mean*	50.09	2.94	13.29	13.63	0.23	5.29	9.64	2.80	0.48	0.32	848	662	171	32
	Min	49.44	2.85	12.91	13.10	0.21	4.84	9.24	0.88	0.23	0.29	741	276	117	-
	Max	51.28	3.07	13.72	14.18	0.24	5.52	10.24	3.15	0.59	0.35	1061	1031	212	-
Unit G	*Mean*	49.63	2.96	13.04	13.78	0.23	5.19	9.57	2.90	0.44	0.33	823	593	174	34
	Min	48.49	2.79	12.65	12.98	0.21	4.90	9.11	2.53	0.22	0.30	700	155	141	-
	Max	50.76	3.17	13.52	14.49	0.25	5.55	9.99	3.18	0.55	0.35	1447	1054	262	-
Pumice	*Mean*	50.27	3.20	12.88	14.35	0.24	4.84	9.28	2.94	0.54	0.35	688	774	188	43
	Min	49.14	3.00	12.28	13.73	0.22	4.10	8.90	0.91	0.37	0.33	428	391	131	-
	Max	51.37	3.35	13.47	15.26	0.27	5.05	9.90	3.35	0.63	0.37	1002	1085	245	-
Groundmass	*Mean*	50.03	2.97	13.12	13.78	0.26	5.19	9.56	2.91	0.49	0.33	1304	599	178	426
Glass	*Min*	48.49	2.70	12.28	12.77	0.21	4.10	8.90	0.88	0.22	0.28	556	155	99	-
Overall	*Max*	51.37	3.35	13.90	15.26	0.59	5.70	10.24	3.35	0.63	0.40	2594	1085	297	-

8.4.2 GROUNDMASS GLASS VOLATILE DATA

There is a wide range in the S content of samples across all units. The highest mean S concentrations are found in units A (837 ppm), B (831 ppm) and F (849 ppm) and the lowest in Unit C (780 ppm). However, the frequency distribution for S content (Fig. 8.7) demonstrates that despite its relatively high average S content, several measurements for Unit A fall in the 600-699 ppm range. Such low S values are not represented in any other group, apart from the pumice.

S concentrations in units D (802 ppm), E (818 ppm) and G (823 ppm) are close to the overall groundmass glass average of 814 ppm. Of all the units, D exhibits the most restricted range of S concentrations (± 72 ppm), while Unit E samples are the most variable (± 323 ppm; Fig. 8.7). The variable, moderate S concentration in the groundmass glass of phreatomagmatic clasts (mean = 811 ppm) contrasts with more uniform, lower S abundances in the pumice clasts (mean = 688 ppm) taken from different stratigraphic levels within units C, E and the tuff cone (Figs. 8.9 and 8.10). The S concentration within the phreatomagmatic ash fraction ranges from approximately 578 to 1270 ppm, but the corresponding compositional range for pumice clasts is only 528 – 1002 ppm (Fig. 8.8). S abundances in the groundmass glass of phreatomagmatic clasts show little to no correlation with degree of vesicularity.

Chlorine abundances of G2004 glass show no correlation with sulphur content (Fig. 8.8). The compositional fields for chlorine content of each unit overlap. Analyses of groundmass glass within pumice clasts are the exception and contain marginally less chlorine and significantly less sulphur.

Figure 8.7: Frequency distribution of sulphur content among analyses of matrix glass from each unit, compared with that of melt inclusions. Frequency values are normalised to 100.

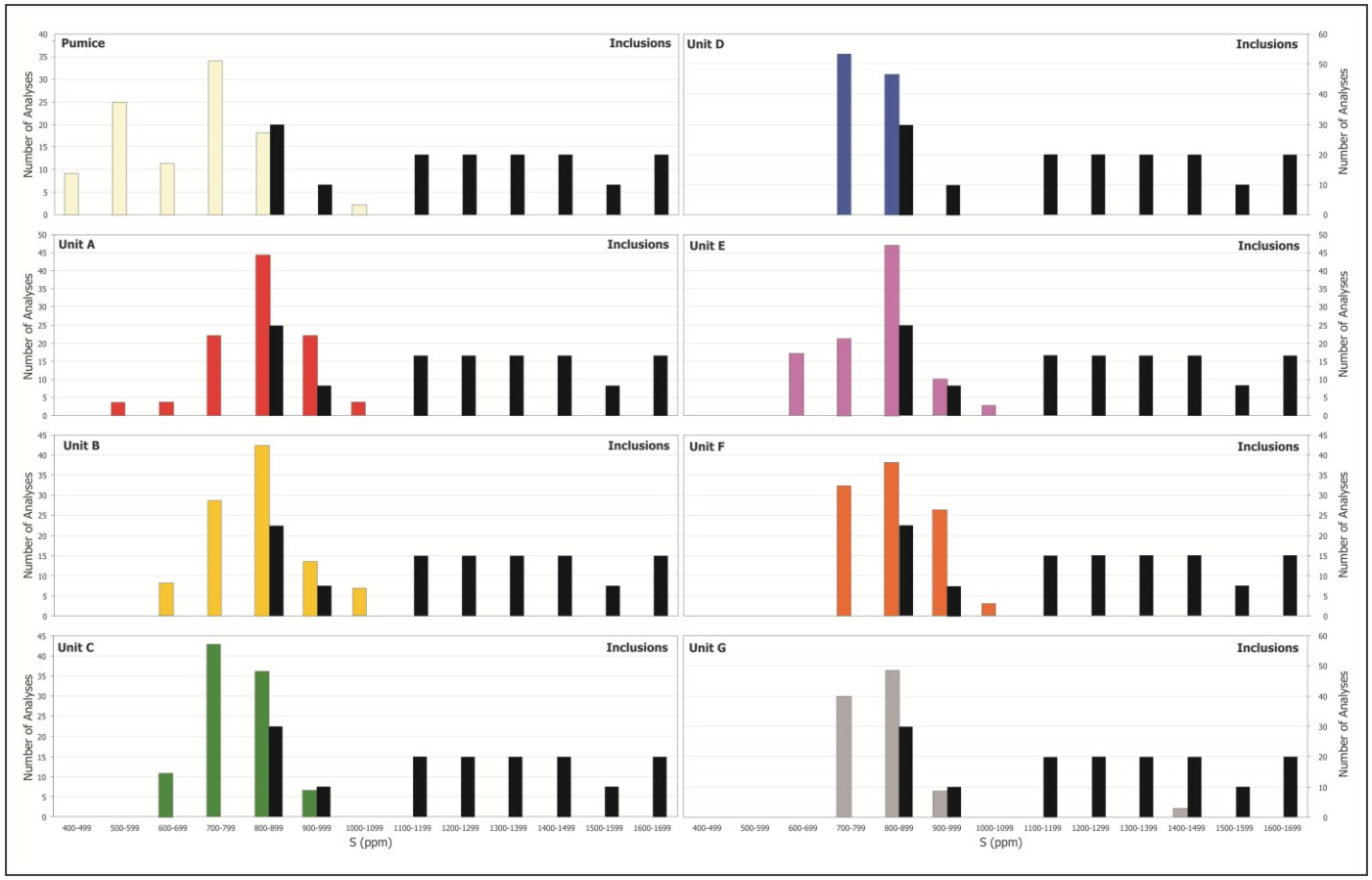

Figure 8.8: Chlorine-Sulphur covariation diagram for G2004 groundmass glass (by unit) and melt inclusions (corrected).

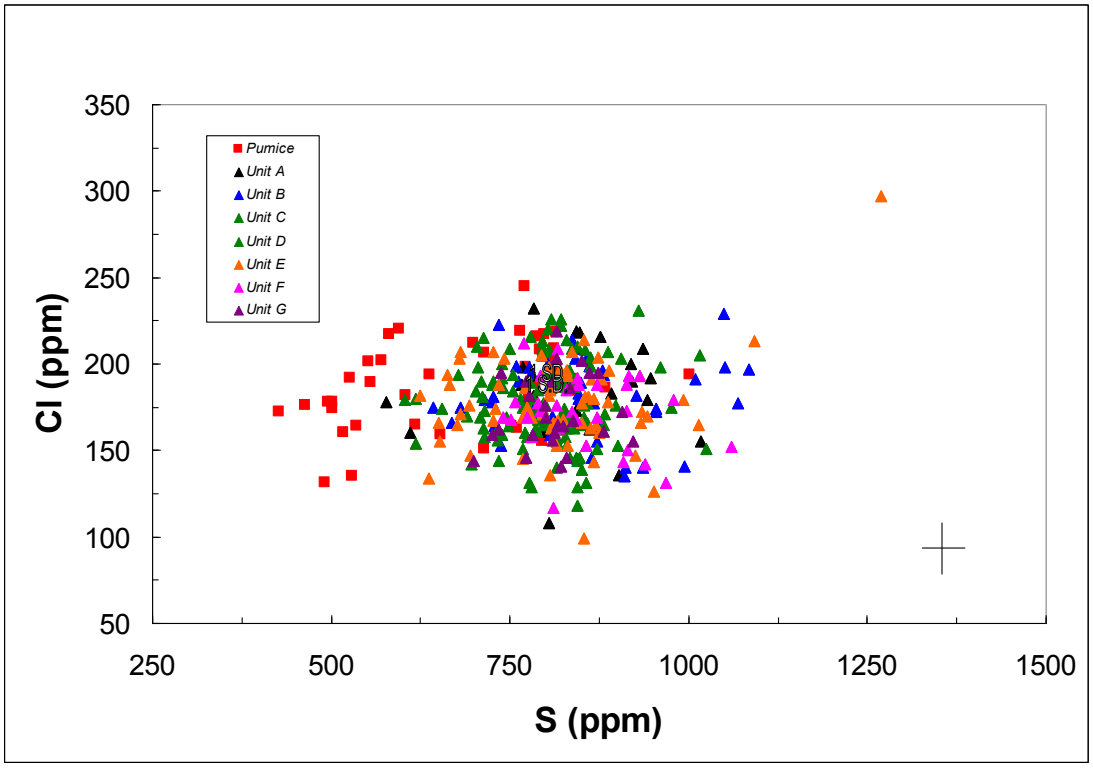

Figure 8.9: Examples of the range of vesicle textures displayed in G2004 pumice. Top: Sample TTB-9A, approaching hexagonal closest packing (> 90% vesicularity). Bottom: Sample F13, spherical bubbles spanning ~2 size populations (60-70% vesicularity).

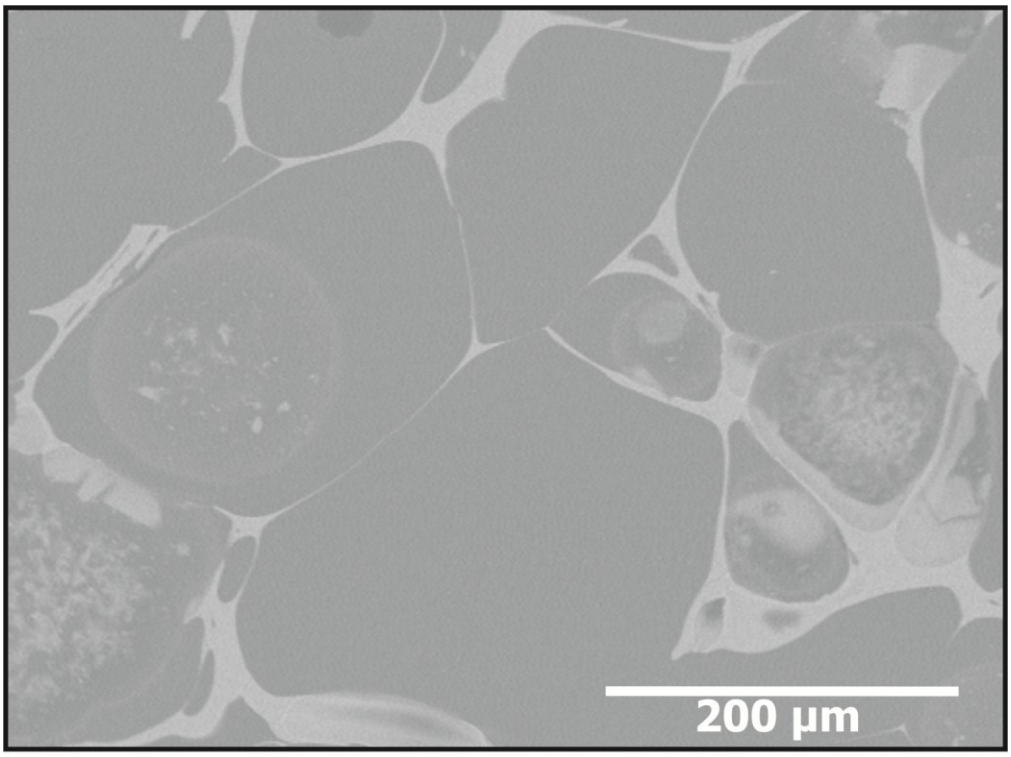

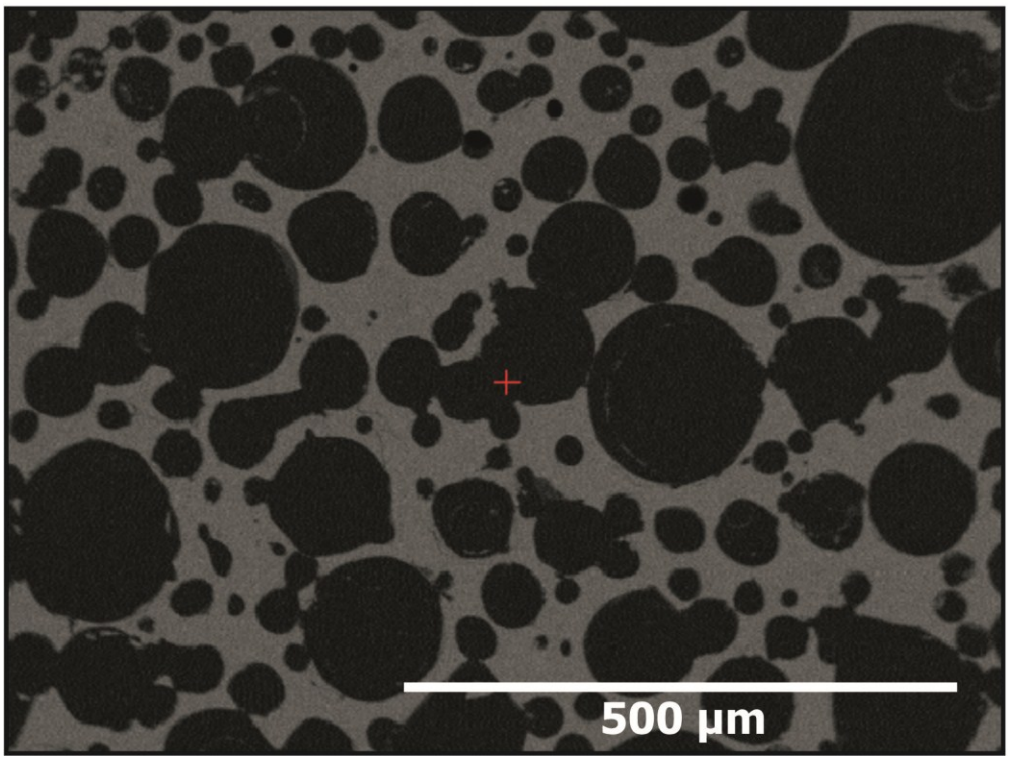

8.4.3 *PHENOCRYST MODES AND COMPOSITIONS*

Measurements of plagioclase phenocryst compositions form an apparent bimodal distribution with two widely spaced modes (Fig.8.6): the largest proportion of measured crystals fall into a low-An (labradorite) compositional group. These range from An_{65} to An_{70} with a modal composition of An_{66}. A smaller, yet significant, number of crystals form the high-An (bytownite) compositional group. These range between An_{76} and An_{84} with a modal composition of An_{82}.

Petrologic modelling using MELTS (Ghiorso and Sack, 1995; Asimow and Ghiorso, 1998) demonstrates that at a temperature of 1200°C and 1 kbar (i.e. lithostatic pressure at 4 km – the inferred depth of the shallow crustal chamber at Grímsvötn according to Björnsson *et al*., 1982; Sturkell *et al*., 2003; Alfaro *et al*., 2007) the low-An phenocryst population is in compositional equilibrium with G2004 groundmass glass (see Appendix X for MELTS modelling results). Low-An crystals exhibit virtually no zonation and are equant to tabular in form (Figs. 8.7 and 8.8). In many cases they are incompletely developed and partly enclose melt embayments, which may be indicative of rapid growth. By comparison the high-An crystals are generally larger than those in the low-An group and exhibit chemical zonation, with difference of up to An_8 between the core and the rim (Table 8.3). Petrologic modelling using MELTS also demonstrates that the melt from which the high-An group crystals grew was more primitive than even the least evolved G2004 and Laki magma compositions. High-An crystals frequently appear broken or with ragged, partly resorbed edges.

This textural assessment, along with the results of petrologic modelling confirm that the measured compositional distribution represents two separate, yet overlapping subpopulations rather than a bimodal, discontinuous continuum of compositions. Nevertheless, the composition of melt inclusion hosted within the high-An crystals fall on, or very close to, the trends observed for G2004 groundmass glass (see section 8.4.4, below) and so this crystal population is considered to be derived from a less evolved precursor to the magma erupted in 2004 (i.e. the same batch) rather than having been inherited from a pre-2004 magma batch or a dyke.

Figure 8.10: Distribution of plagioclase phenocryst compositions

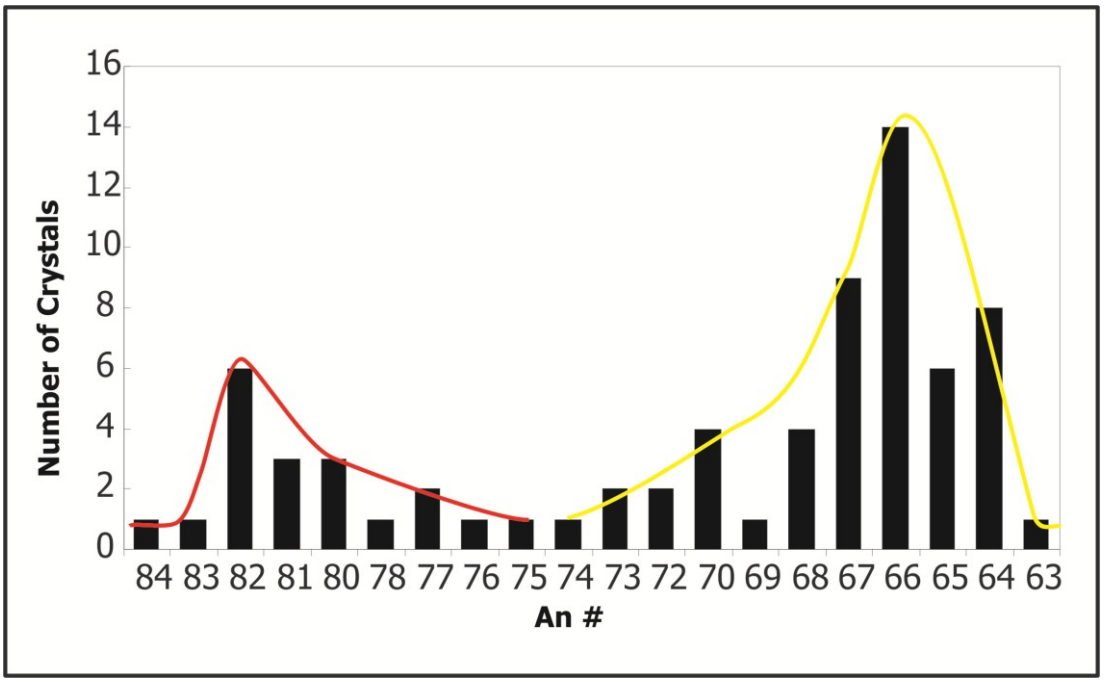

Figure 8.11: (Top) Sample K22, rare plagioclase phenocryst in overall tachylitic sample texture. The hypocrystalline groundmass contains abundant plagioclase microcrysts. (Bottom) Magnification of area within red box above.

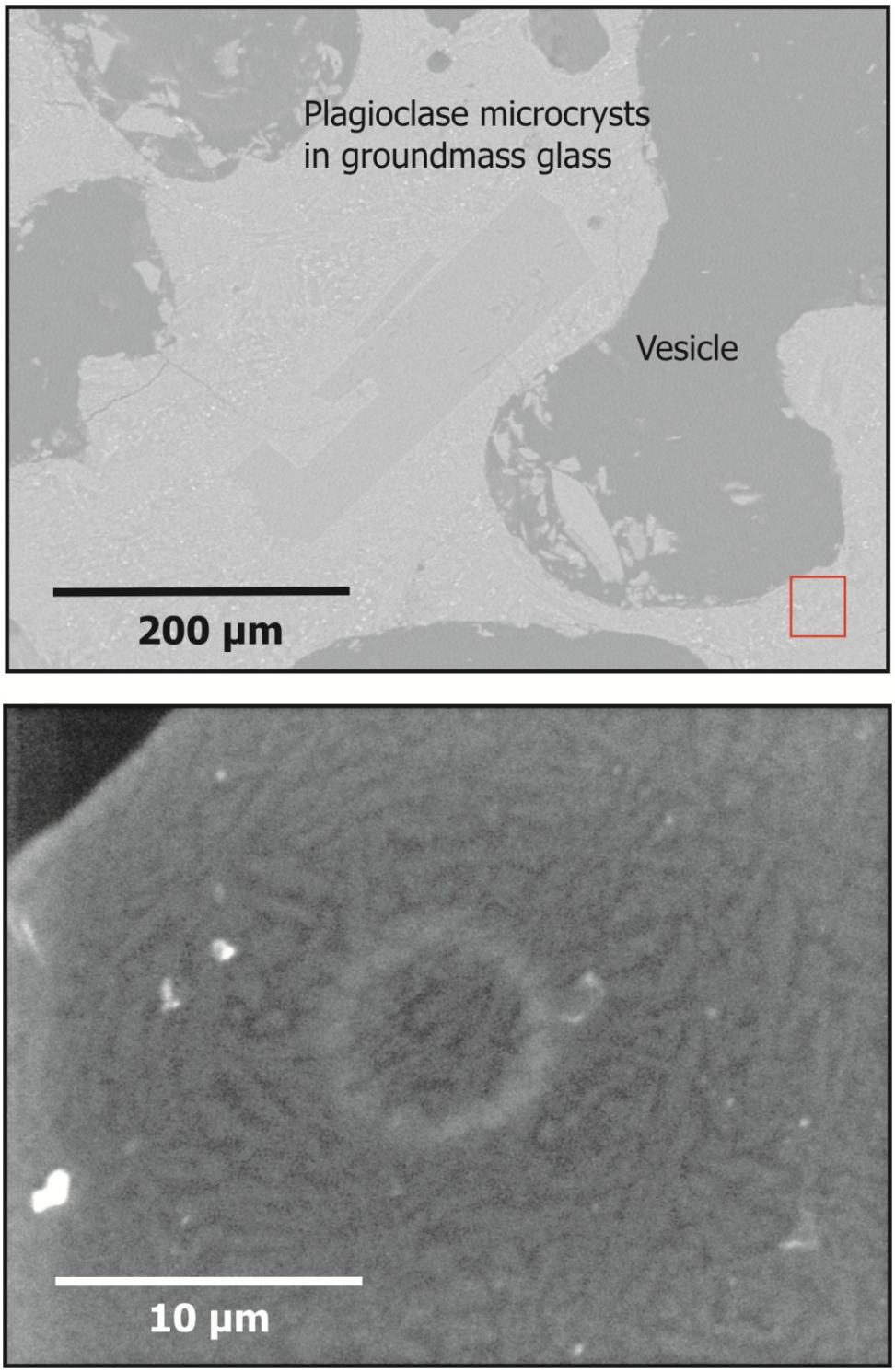

Figure 8.12: Typical plagioclase phenocrysts in G2004 pumice. Top: Sample TS 12-05-47 (An_{80-84}). Plagioclase containing melt inclusions with vapour bubbles. Bottom: Sample TS 12-05-58 (An_{63-64}). This Plagioclase phenocryst is in compositional equilibrium with the G2004 melt, and also contains melt inclusions with associated vapour bubbles. The trapped glass composition is similar to G2004 avg. glass composition. Note also the holohyaline groundmass texture.

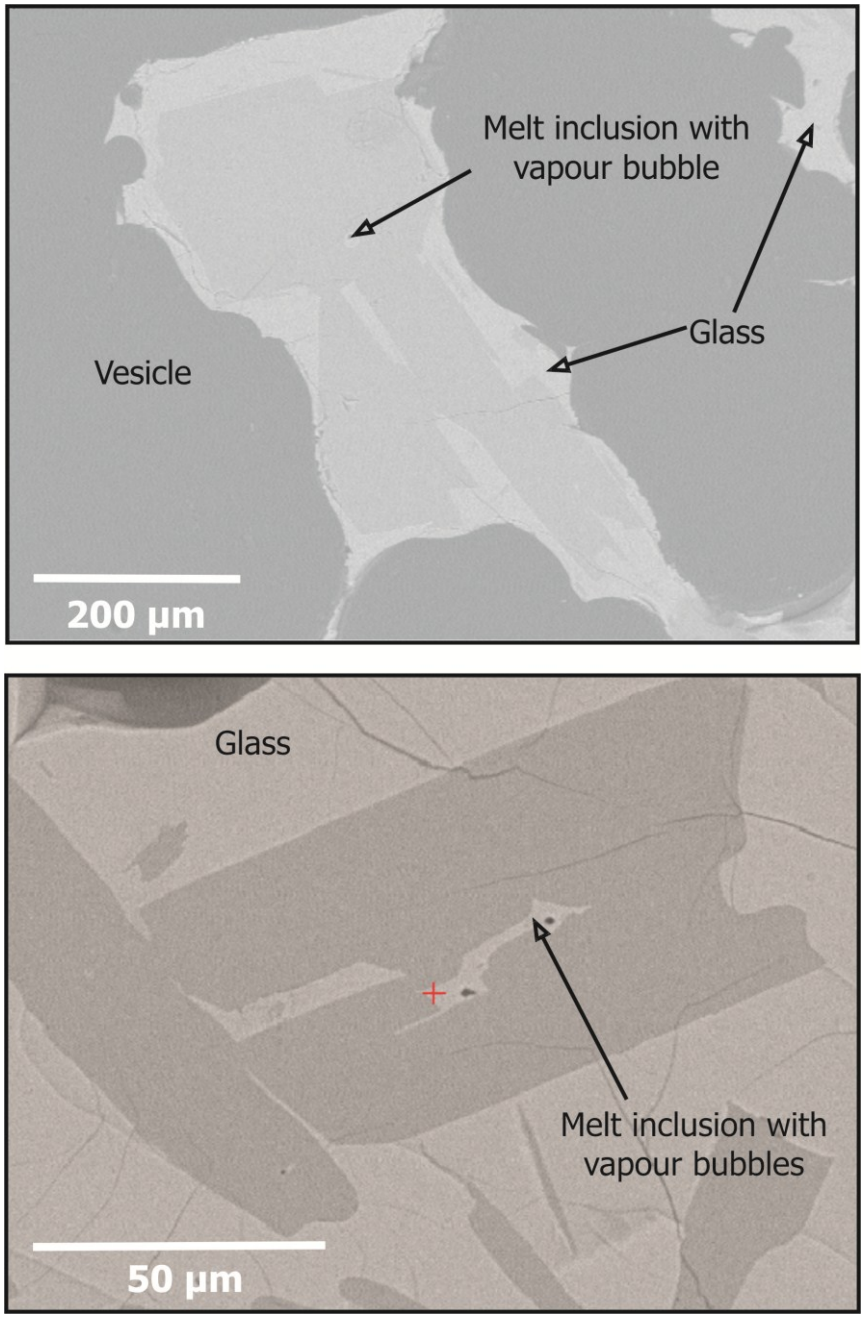

8.4.4 MELT INCLUSION MAJOR ELEMENT AND VOLATILE DATA

Major element compositions of 19 glass inclusions in plagioclase feldspar phenocrysts were measured by EMP to locate un-degassed melt of similar composition to the G2004 magma. The data were divided into three groups on the basis of these results (Table 8.3). Major element abundances of 10 inclusions (Group 1) closely match the average glass composition of the G2004 magma and are considered to be representative of the pre-eruption magma composition. These exhibit restricted ranges of Ti/Fe (0.21-0.23) and Al/Na (4.18-4.59), comparable to those of the G2004 groundmass (0.22-0.23 and 4.25-4.54, respectively). Group 1 Mg numbers and wt. % FeO also span a similar range to that of the G2004 groundmass and follow a linear inverse correlation of similar slope (Fig. 8.13a). The Na_2O and Al_2O_3 contents of Group 1 inclusions are likewise positively correlated, following the same trend as that of the groundmass glass (Fig. 8.13b). However, both the Al_2O_3 (10.9-13.0 wt. %) and Na_2O (2.6-2.9 wt. %) compositional ranges are slightly lower than the measured groundmass range (i.e. 12.7-13.8 wt. % and 2.8-3.1 wt. %, respectively). Within this group S concentrations range from 974 to 1804 ppm, while the Cl concentration is a relatively consistent 174-253 ppm.

Group 2 inclusions (n = 8) are enriched in TiO_2 and FeO and depleted in Al_2O_3 compared to the G2004 average glass composition. Some exhibit higher MgO contents and either lower CaO or Na_2O content than those of Group 1. These differences in major element composition can be accounted for by post-entrapment plagioclase crystallisation of the host. Original volatile abundances are consequently restored (after Métrich *et al.*, 1991) by using the average groundmass glass Al/Na ratio (average: 4.52) as a benchmark for evaluating the extent of crystallisation effects. Corrected volatile abundances yield values that are consistently higher than that of the average G2004 groundmass. The corrected abundance of S in Group 2 inclusions ranges from 1010 to 1633 ppm (mean = 1369 ppm) and Cl from 265 to 511 ppm.

One analysis (Group 3) yielded an anomalous major element composition and was therefore not considered further. This inclusion was enriched in TiO_2, FeO, K_2O and P_2O_5, yet depleted in SiO_2 and Al_2O_3 compared with the average G2004 glass composition. Measured S and F contents were also anomalously high (4470 ppm and 1251 ppm, respectively). S-, Cl- and/or F-bearing mineral phases may have formed

within this inclusion subsequent to the entrapment of a volatile-saturated melt. However, no such minerals were revealed by petrographic examination.

Figure 8.13: (Top) A plot of Mg # versus FeO for G2004 groundmass glass and melt inclusions. (Bottom) A plot of Al_2O_3 versus Na_2O for G2004 groundmass glass and melt inclusions. Black squares represent G2004 groundmass glass (average unit values), blue circles represent Group 1 melt inclusion values and Group 2 melt inclusion analyses are depicted by red diamonds.

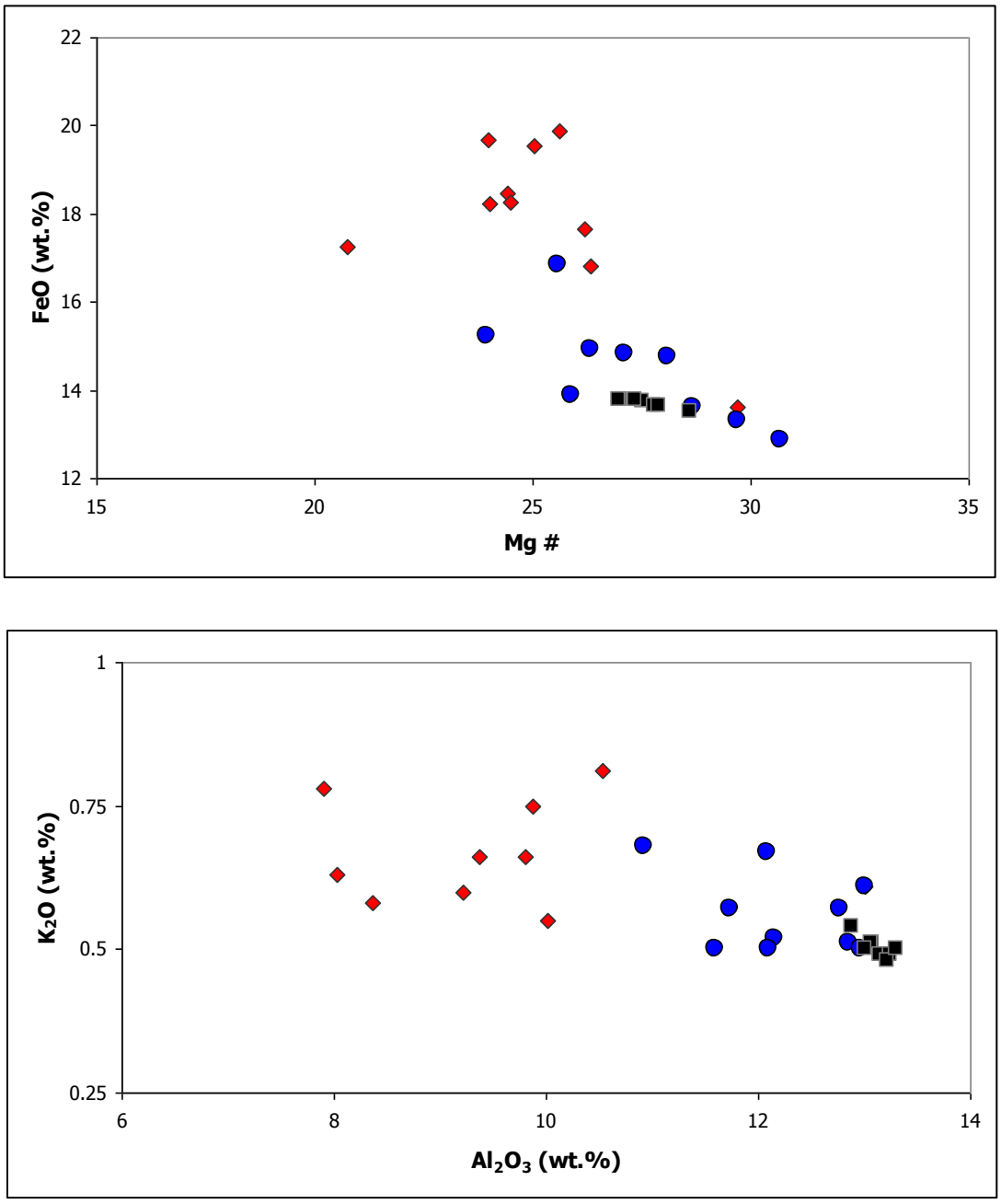

Table 8.3: Major element compositions and volatile concentrations within glass inclusions. Group 2 compositions are reported as corrected values.

	Sample #	Section	SiO_2 (wt. %)	TiO_2 (wt. %)	Al_2O_3 (wt.%)	FeO (wt.%)	MnO (wt.%)	MgO (wt.%)	CaO (wt.%)	Na_2O (wt.%)	K_2O (wt.%)	P_2O_5 (wt.%)	Total	S (corr) (ppm)	F (corr) (ppm)	Cl (corr) (ppm)	An # (host)
Pristine	F13_1_2	G5	50.24	2.90	12.85	12.88	0.22	5.70	9.95	2.80	0.51	0.29	98.73	1490	746	165	75
/Near	F13_1_1	G5	49.50	3.00	12.77	13.30	0.24	5.63	9.53	2.57	0.57	0.30	97.79	1683	694	209	75
Pristine	F13_1_3	G5	50.01	2.99	13.00	13.60	0.24	5.74	9.85	2.43	0.61	0.30	99.18	1804	1061	253	75
(GP1)	F13_1_4	G5	49.82	3.01	12.97	13.87	0.24	5.58	9.84	2.83	0.50	0.32	99.34	1473	500	163	75
	TS12_2_1	TS12	50.20	3.31	12.16	14.92	0.24	5.21	9.60	2.90	0.52	0.35	99.70	1064	382	180	82
	TS12_3_1	TS12	49.57	3.26	12.10	14.76	0.24	5.27	9.50	2.76	0.50	0.33	98.59	1100	570	204	81
	F13_3_3	G5	49.29	3.29	11.73	14.83	0.29	5.79	9.75	2.58	0.57	0.34	98.83	1505	526	232	81
	TS12_3_1	TS12	49.80	3.19	12.08	15.23	0.24	5.66	9.43	2.79	0.67	0.33	99.71	1089	403	174	70
	TS12_4_3	TS12	49.55	3.52	11.60	16.85	0.27	5.31	9.81	2.56	0.50	0.38	100.62	982	775	222	68
	TS12_5_2	TS12	49.36	3.43	10.93	16.13	0.27	5.54	9.49	2.57	0.68	0.35	99.02	974	931	187	-

	Sample #	Section	SiO_2 (wt. %)	TiO_2 (wt. %)	Al_2O_3 (wt.%)	FeO (wt.%)	MnO (wt.%)	MgO (wt.%)	CaO (wt.%)	Na_2O (wt.%)	K_2O (wt.%)	P_2O_5 (wt.%)	Total	S (corr) (ppm)	F (corr) (ppm)	Cl (corr) (ppm)	An # (host)
Affected	TS12_6_1	TS12	48.99	3.55	9.88	17.64	0.28	6.26	9.23	2.21	0.75	0.37	99.49	1271	819	306	76
(GP 2)	T9B_2_1	TT02-B	48.10	3.47	9.37	18.46	0.30	5.96	9.24	1.95	0.66	0.35	98.27	1429	1313	265	-
	TS12_5_4	TS12	47.42	3.80	8.03	19.54	0.30	6.52	9.65	1.61	0.63	0.38	98.28	1633	1069	518	70
	TS12_4_4	TS12	47.64	4.00	8.37	19.89	0.31	6.85	10.10	1.79	0.58	0.42	100.35	1497	1039	417	76
	TS12_3_2	TS12	48.64	3.57	9.22	18.23	0.27	5.76	9.37	2.01	0.60	0.36	98.37	1010	1288	321	68
	TS12_3_4	TS12	48.52	3.79	10.01	18.25	0.27	5.92	9.75	1.99	0.55	0.37	99.67	1099	757	271	68
	TS12_4_5	TS12	48.72	4.06	7.90	19.66	0.31	6.20	9.18	1.83	0.78	0.44	99.47	1427	829	326	81
	TS58_1_4	TS58	48.46	3.99	9.80	17.25	0.29	4.52	10.01	2.09	0.66	0.37	97.84	1418	896	361	64
(GP 3)	TS12_5_3	TS12	49.47	3.61	10.53	16.81	0.27	6.01	9.46	1.32	0.81	0.38	99.05	2540	1891	446	70

8.6 DISCUSSION

8.6.1 INFERENCES FOR SHALLOW CRUSTAL STORAGE AND CONDUIT DYNAMICS

Despite its relatively low abundance in magmas compared with H_2O and CO_2, sulphur degassing from volcanoes is of great significance as it is in itself potentially capable of triggering eruptions and also represents one of the most convenient means of monitoring active systems (Oppenheimer *et al.*, 2011). As magma rises to the surface, the exsolution of its major volatile constituents (i.e. H_2O and CO_2) result in bubble nucleation and growth, this generally determines the dynamics of magma ascent and eruption (Métrich and Wallace, 2008; Sparks, 1978; Tait et al., 1989). Depending on its redox state, the sulphur dissolved in magma may be fractionated into a water-rich phase and/or into sulphur-bearing minerals. Oxidized and water-rich basaltic magmas can therefore hold large quantities of dissolved sulphur (up to 1.5 wt %) dissolved as sulphate up to very low pressures (Jugo *et al*., 2005). Measuring the sulphur composition of volcanic plumes and magmas composition is therefore a good proxy for evaluating the volcanogenic fluxes for other volatiles species, and provides insights into volatile degassing mechanisms during magma ascent (Aiuppa *et al.* 2004).

If the maximum S value yielded by melt inclusion analysis is taken to reflect the original S concentration, then pumice samples exhibit 54 % to 76 % S degassing, while phreatomagmatic ash fragments range from only 40 % up to 68 % S loss. Glass inclusion S values indicate that melt lost 0 % to 40 % of its original sulphur content prior to entrapment. There is little difference in the extent of degassing experienced by products of different units.

The groundmass glass of all tephra types, from all units, spans a wide range of Cl (99-297 ppm; mean = 178 ppm) and F concentrations (185-1055 ppm; mean = 596 ppm). The fluorine and chlorine concentrations show no obvious correlation with vesicularity, or with unit designation. The F concentration of G2004 products is particularly high when compared both to Cl concentrations of the same samples and also to reported values for phreatomagmatic tephra from the Laki eruption (i.e. 220-560 ppm; Thordarson *et al*., 1996). Nevertheless, although high, these concentrations

must reflect a degree of F loss during magma ascent as the range of F concentrations within melt inclusions is 10-35% higher (450 – 1200 ppm).

The compositional differences and similarities between the pumice and fine ash (125-250 μm diameter) samples are of interest because the physical distinction between these two clast types represent differences in degassing history and, arguably, fragmentation mechanism and style of explosive activity (cf. Chapter 5). Furthermore, these two separate clast populations have been deposited by different mechanisms: fallout from a high eruption column in the case of the pumice and predominantly via pyroclastic density currents for the ash particles (see chapters 3 and 6). These differences may reflect compositional heterogeneity in the magma reservoir or changes due to magma evolution during the course of the eruption. Finally, any differences or similarities in magma composition that correspond to differences in eruptive style and/or clast type may have implications for our assessment of the contributions of magmatic gases vs. that of external water to explosive activity.

The phreatomagmatic tephra units are composed of poorly sorted fine ash to lapilli (250 μm to 4 mm) sized fragments consisting of non-vesicular to highly vesicular angular and blocky clasts. Pumice samples are >18 mm fragments taken from selected pumice-rich horizons within units C and E. These are generally 75 - 90% vesicles, by volume (Fig. 8.9). Pumice fragments are also relatively equant and angular, usually derived from larger clots of magmatic foam which have been weakened by pervasive hydrofracturing (see Chapter 6). Vesicle populations within the pumice range from those featuring a single population of 0.5 to 2 mm spherical vesicles, through samples featuring stretched and coalesced vesicles, to those in which the vesicle population has evolved to create a mature polyhedral framework that may be more properly classified as reticulite (Fig.8.9). Unlike the Strombolian pumice clasts previously described from the Laki eruption (Thordarson *et al*., 1996), G2004 pumice samples lack a thin fluidal skin and fused outer surfaces. Instead, they are extensively hydrofractured with quenched rinds. Both phreatomagmatic tephra and broken pumice fragments have angular, sharp edges characteristic of brittle fragmentation surfaces.

The fact that the most evolved glass compositions are found among pumice samples with highly evolved vesicle populations is consistent with our inference, based on whole rock data, of a compositionally stratified magma chamber. The most evolved melt is also the least dense and therefore sits at the top of the magma chamber.

Consequently, it is likely that this portion of the magma batch will be more extensively degassed, resulting in the most evolved vesicle population.

The most compositionally evolved and highly vesicular magma was erupted during the climactic periods of eruption, rather than at the beginning. Given the nature and timing of eruptive events and the relatively small tephra volume, in addition to the differing trends observed for whole rock and glass geochemical data, this would suggest that a portion of the magma evolved chemically within the conduit once the eruption had already begun. Evidence from melt inclusion analyses clearly demonstrates that crystals were continuing to grow in the G2004 magma during and after the onset of vesiculation. The uniformity of crystal sizes and textures, along with plagioclase compositions suggest that that these "late" crystals were formed with the eruption already underway. "Late-stage" degassing induced crystallisation of basaltic magmas is well documented within the literature. This phenomenon was first reported by Lipman and Banks (1985), who found that undercooling of magma due to gas release during the 1984 eruption of Kilauea resulted in an increase in microphenocryst contents from 0.5% to 30% over a matter of days. Experiments by Métrich and Rutherford (1993) and Couch *et al*. (2003) have subsequently demonstrated that degassing-induced crystallisation show that this may take place on time-scales of as little as 4 hours, depending on the rates of decompression and undercooling within the system. More recently, a field-based study by Johnsson *et al*. (2008) found that degassing-induced crystallisation is not only viable, but a significant contributor to crystallisation within basaltic magmas at eruptive timescales.

8.6.2 THE ROLE OF VOLATILE DEGASSING AND ITS IMPLICATIONS FOR ERUPTION DYNAMICS

The average volatile concentrations of melt inclusions are higher than those of groundmass glass, which suggests that the highest values (i.e. S = 1804 ppm; Cl = 518 ppm; and F = 1313 ppm) may be close to the original concentrations of these species prior to eruption onset. However, the variability in volatile concentrations of G2004 inclusions mirrors the degassing trend observed in the groundmass glass of pumice and volcanic ash samples.

The highest S contents are observed in melt inclusions. Most inclusions exhibit 0 to 40 % S loss, with a maximum of 46 % S loss. By contrast, phreatomagmatic tephra

units record a range of moderate to low S concentrations, which are poorly correlated with clast vesicularity. Units A and B have lost a similar amount of sulphur as the other units, but contain a greater frequency of low-S analyses and have significantly lower vesicularity (see Chap. 5). The lowest S concentrations are found in groundmass glass of pumice-reticulite clasts, which have lost up to 76 % of their original sulphur content (Fig. 8.7). This trend reflects the relative timing of crystal growth, degree of degassing and magma fragmentation during the course of this eruption.

Cl loss for all units, including pumice samples varies from 46-79%, around an average of 63%. This is consistent with the results of similar studies on the Laki eruption (Thordarson *et al*., 1996) and of the products of other basaltic fissure eruptions in Iceland (e.g. Thordarson, 1995). There is no relationship between the extent of halogen loss and stratigraphic position or clast type. Similarly, there is no correlation between extent of F or Cl degassing and that of S.

Reported average pre-eruption sulphur concentrations for the Laki magma are 1800 ± 100 ppm (Métrich *et al*., 1991) and 1677 ± 225 ppm (Thordarson *et al*., 1996). The comparable, yet systematically lower, values obtained from G2004 inclusions may be a consequence of the location of this eruption on the volcanic system. The volatile content of trapped melt within central volcano eruption products is far more likely to be diminished as a consequence of open system behaviour during magma residence at shallow crustal levels. The powerful geothermal system within Grímsvötn caldera provides evidence of the mobility of hydrothermal solutions and potentially also for the escape of magmatic gases. Structural features such as faults, dykes and variably consolidated hyaloclastite caldera fill provide further avenues for volatile escape.

The degree of variance in S, F and Cl values for G2004 inclusions cannot be attributed to analytical error alone and may result from a combination of the following factors: (a) small scale compositional heterogeneity in the magma reservoir; (b) variations in the timing of crystal growth and melt entrapment, dominated by late-stage crystal growth from an already partially degassed melt; and (c) in some cases, a fraction of the volatiles may have exsolved from the liquid phase creating a vapour bubble within the inclusions after entrapment (Fig. 8.2). Consequently, the mean S, F and Cl concentrations of G2004 inclusions are likely to be minimum estimates for the quantities of S, F and Cl dissolved in the magma prior to eruption onset. The validity of the argument that crystallisation largely took place within an actively degassing melt

either shortly prior to eruption onset or during ascent in the conduit is confirmed by empirical observations that inclusions with higher sulphur contents tend to be found closer to the crystal core whereas those with partially degassed compositions are more frequently found closer to crystal rims. As previously noted in the petrography section, textural features of many plagioclase crystals are also consistent with rapid, late growth.

Explosive activity at the central volcano is controlled entirely by the interaction of hot magma with external water. Volatile overpressure is not a significant factor as even pumice and reticulite clasts with evolved bubble populations show textural evidence for phreatomagmatic rather than magmatic fragmentation (Chap. 5). I build an argument similar to that presented by Thordarson *et al*. (1996) for the Laki eruption, as follows: During the G2004 event a large fraction of the volatiles that had accumulated near the top of the magma chamber was released at the vent immediately prior to eruption onset, resulting in effective separation of volatiles and melt during magma ascent. Tephra from the initial phase (i.e. units A and B) was largely, but not fully, outgassed prior to fragmentation, and was still in a hot, fluid state. Consequently we observe that a relatively immature vesicle population is preserved within samples from this unit. Within moments of eruption onset, a phreatomagmatic interaction occurred (as evidenced by the timing of the seismic signal, chap. 3, and the exclusively brittle and blocky clast morphologies in samples from these units). By this means the magma was quenched, fragmented and ejected in a rapid transfer of energy whereby the presence of external water provided an additional means of performing "work" (i.e. through the mechanical process of vapour expansion and propulsion). The abundance of highly vesicular clasts in the phreatomagmatic tephra of units C and E demonstrates that vesiculation and foam formation was in progress by the time the magma explosively interacted with water to produce the deposits. Thus the initial two phase flow transitioned into a homogenous flow regime promoting rapid vesiculation and creating a foam head (Cashman and Mangan, 1994). The more evolved composition and vesicle structure of the pumice clasts suggests that these were derived by fragmentation of such a foam layer, presumably at quite shallow conduit levels. This process occurs cyclically and this is why concentrated pumice horizons occur periodically within the deposit among layers of less degassed, finer-grained tephra.

8.7 CONCLUSIONS

High initial sulphur contents (1700-1800 ppm) are not unique to the Laki magma, but a common feature of eruptions from the Grímsvötn system. Trapped melt from magmas which have been stalled in the shallow crust are likely to record lower and more variable S concentrations than those erupted on fissure swarms, as they have had the opportunity to passively degas prior to eruption onset. Furthermore, the S content of groundmass glass and melt inclusions from the G2004 magma, along with those from inherited crystals, reflect a trend of progressive magma degassing during its rise through the crust. This highlights the need for long term monitoring of both passive emissions and eruptive degassing at Grímsvötn.

Prior to or at the point of exit, the G2004 magma was quenched and fragmented such that post-emergence degassing is not considered to be a significant factor. Furthermore, incremental degassing from a leaky shallow crust and the eruption of sparsely porphyritic magmas characterised by late crystal growth connotes that volatile accumulation as a response to crystal growth is not an important causative factor of central volcano eruptions. The observed oscillations in eruption style, along with the occurrence of rhythmic bedding and sporadic pumice-rich fall horizons in the G2004 deposit, reflect cyclic escalation of vesicle growth and frequent switches between homogenous and heterogeneous flow regimes within the conduit during the course of syn-eruptive degassing.

Chapter 3 shows that the wet plume generated by an explosive eruption in the englacial environment is suppressed relative to the height predicted by the empirical mass-column height relationship developed for Plinian eruptions (Carey and Sigurdsson, 1989). In addition, in wet plumes a significant proportion of SO_2, Cl and F may be scavenged early on by adherence to condensing water (e.g. Pyle, 1996; Tabazadeh *et al*., 1993). Both factors lead to a much more limited atmospheric dispersal of magmatic volatile species than previously supposed as (1) the plume is less likely to achieve stratospheric heights for a given mass of magma/magnitude of eruption than theoretically predicted and (2) the concentration of sulphur and halogen compounds in the atmosphere will be considerably diminished if they are washed out of the plume close to source. These factors, coupled with the arrest of degassing

associated with rapid magma quenching, indicates that the contribution of S, F and Cl species to the atmosphere by englacial eruptions (and, by extension, phreatomagmatic eruptions in other environments) is rather limited compared to that of their magmatic and subaerial counterparts.

CHAPTER 9

CONCLUSIONS

9.1 REVIEW OF STUDY AIMS

The rapid response of the Icelandic Meterological Office, University of Iceland and Icelandic Glaciological Society to monitoring the 2004 eruption at Grímsvötn, an ice-covered caldera volcano, afforded a unique research opportunity to describe and evaluate the subaerial component of end-member style glacio-volcanism. Because of its remote glacial environment this type of eruption has rarely been observed in the past and its deposits are seldom preserved in the geologic record for later study.

The key aims of this PhD study were to characterise conduit and expulsion processes, transport regimes and depositional modes in basaltic emergent subglacial phreatomagmatic eruptions, using the 2004 event at Grímsvötn as a case study. This was achieved through detailed documentation of the deposit stratigraphy and dispersal, evaluation of the deposit grain-size distribution and components, along with geochemical analysis of the tephra.

9.2 G2004 ERUPTION MODEL

9.2.1 OVERVIEW

The G2004 eruption occurred between November 1st and 6th 2004, following the release of a jökulhlaup into the river Skeidará on October 30th. It commenced as a subglacial event which rapidly became subaerial and discharged 2.1 x 10^7 m^3 of magma (DRE) at an average rate of 130 m^3s^{-1}, with muzzle velocities of up to 150 ms^{-1}. Approximately 50% of this mass was deposited over the Vatnajökull ice surface forming a tephra apron which consisted of a finely layered sequence. I subdivided this

deposit into seven units (A-G) which are interpreted to represent a mixture of (1) a widely dispersed component that fell from the upper margins of a strongly inclined (~45°) 6-10 km high plume and (2) a locally dispersed (<3 km from source) component originating from (i) PDCs generated by shallow explosions and tephra jets and (ii) sedimentation from the jet region and lower convective column margins. Chemical stratification within the deposit shows that the eruption tapped a single magma batch, progressively extracting magma from the top to the bottom of the shallow reservoir (Fig. 9.1).

9.2.2 SULPHUR DEGASSING

Prior to the onset of eruption the maximum volatile content of the G2004 melt, as recorded by glass inclusions hosted in plagioclase phenocrysts, was 1804 ppm S and 518 ppm Cl. On average, the G2004 glass lost 56 % of its original sulphur content prior to being quenched – a value which is fairly consistent across much of the eruption, except for sporadic horizons of highly vesicular pumice, which had experienced up to 76 % sulphur degassing. Despite experiencing the same sulphur loss as subsequent units, tephra from the first phase of the eruption (units A and B) consist predominantly of non-vesicular tephra fragments while subsequently erupted tephra (C-G) contains high proportions of moderately to highly vesicular clasts. This difference in vesicularity of Phase 1 products compared to Phase 2 and 3 can only be attributed to outgassing, rather than degassing, of the melt. That is, during ascent of the first portion of the G2004 melt, part of the bubble population escaped before the magma encountered external water. One possible explanation is that the ascent rate was slow enough to allow the bubbles to rise faster and escape from the top of the magma column. Another logical idea is that the magma temporary halted its ascent without undergoing significant cooling, thus allowing bubbles to escape. Tephra from units C-G is variably vesicular and ranges from having lost 40-68 % of its original sulphur content. The presence of frozen vesicles with a range of bubble number densities and textures indicates that this magma was fragmented as vesiculation was underway. Highly vesicular fragments (>85 % vesicles) represent a disintegrated magmatic foam head. The observed oscillations in eruption style, along with the occurrence of rhythmic bedding and sporadic pumice-rich fall horizons in the G2004 deposit, reflect cyclic

escalation of vesicle growth and frequent switches between homogenous and heterogeneous flow regimes within the conduit during the magma ascent.

9.2.3. TOTAL LAYER GRAIN-SIZE DISTRIBUTION AND THE ROLES OF PHREATOMAGMATIC VS. MAGMATIC FRAGMENTATION

It has been demonstrated that there is a fundamental difference between grain-size distributions of magmatic versus phreatomagmatic deposits, the latter having a broader grain-size distribution (more poorly sorted) and a far greater abundance of fines. This has led to the general statement that the processes of magma fragmentation are much more efficient in phreatomagmatic eruptions compared to magmatic eruptions. This difference has been accredited to the role of the MFCI process that drives phreatomagmatic eruptions. The issue has largely remained unresolved because it has not previously been possible to obtain a total deposit grain-size distribution for a phreatomagmatic eruption that is not modified by the effects of size fractionation during transport and deposition.

One characteristic of basaltic phreatomagmatic deposits in Iceland that is highlighted by (but not unique to) this study is that the magma is highly vesiculated at the point of interaction with external water (cf. Askja 1875, Surtsey, and others). This is an important observation because it implies that here the magma is already at or past the point of disintegration by the expansion of magmatic gases by the time it encounters external water. Because foam has much higher yield strength than non-vesicular magma it may interact differently upon contact with external water than a non-vesiculated melt. This calls into question the dynamics and driving mechanisms for fragmentation as depicted in the classical MFCI model for phreatomagmatic interaction. How do these dynamics work in highly vesiculated magma or do they even work at all? It is possible that the role of external water in generating ash in this type of eruption is less direct than previously conceived – operating, for example, by quench-induced hydrofracturing of the magmatic foam which weakens the foam structure such that expansion- and flow-induced stresses are sufficient to disintegrate the foam further thus producing the high ash content that typifies phreatomagmatic deposits.

Figure 9.1: Interpretative cartoon depicting the G2004 magma chamber, which has undergone fractional crystallisation and is tapped progressively from the top downwards. Zone 1 is the most evolved composition, which is outgassed and aphyric. Zones 2 and 3 are undergoing varying degrees of vesiculation and carry phenocrysts in minor abundances. The G2004 tuff cone is constructed within a water-filled cauldron in the glacier bed, which is bounded to the south (left in figure) by the sheer southern caldera wall which outcrops from the ice. As they are expunged from the magma chamber tephra sourced from zones 2 and 3 are progressively re-deposited and the G2004 tephra pile accumulates layer-by-layer on the glacier surface. Not to scale.

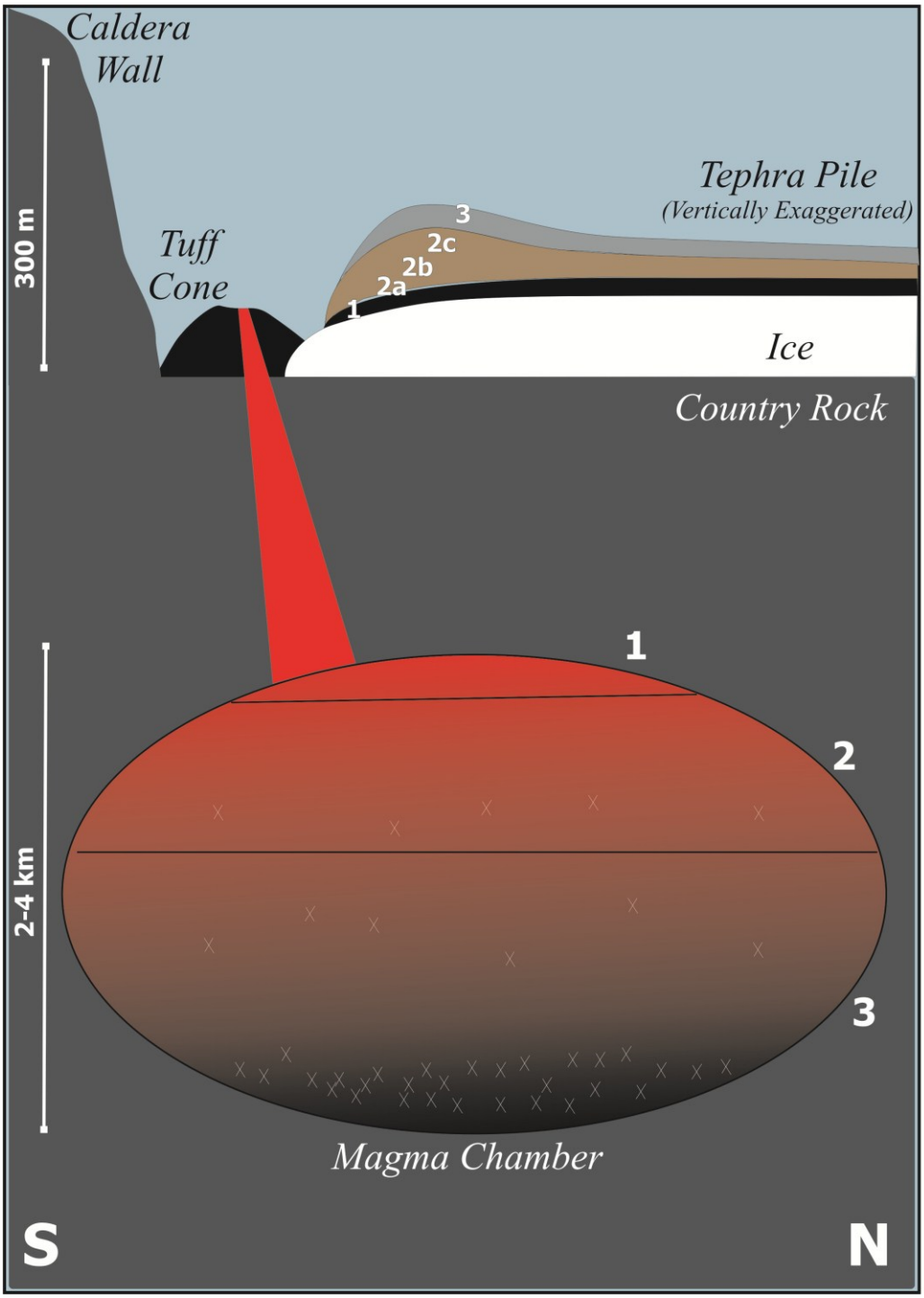

9.2.4 PROGRESSIVE AGGRADATION OF PYROCLASTIC DEPOSITS

An appreciation of common features among the G2004 main phase units and other PDC deposits around the globe extends not just to phreatomagmatic settings, basaltic compositions, or to specifically low versus high particle concentration end-members. Units C and E are identified, on the basis of vertical and lateral lithofacies associations, grain-size, componentry and chemical stratigraphy, as the product of continuous incremental deposition during the passage of a single quasi-steady current supplied by a sustained explosive phreatomagmatic eruption (continuous uprush), which also comprises a variable contribution of material from concurrent tephra fallout. The evidence that many ignimbrite deposits are formed by a process of progressive aggradation is well-established in the literature. However, this concept has not previously been applied to basaltic phreatomagmatic tephra sequences. The recognition that progressive aggradation of pyroclastic deposits operates regardless of such diverse settings and eruptions styles directs us towards a more unified theory for mechanisms of PDC emplacement.

9.2.5 COMPARISON TO EMERGENT SURTSEYAN ERUPTIONS

The purpose of this PhD study is to describe the parts of the tephra deposit produced by emergent submarine and subglacial eruptions that is rarely, if ever, preserved in the geological record. That is, evaluation of the G2004 eruption is almost entirely confined to the 'apron deposits' (plus the very top two metres of the cone, which represents very late stage activity). Therefore, the findings are not always automatically comparable to previous studies of Surtseyan and other phreatomagmatic basaltic events which, because of the preservation and accessibility issue are very strongly biased to observations of tuff cone sequences. In general, the cone may feature depositional units from the rooster-tail events in addition to the near-vent facies of the continuous up-rush and deposits from the punctuating PDC events.

Although there are resemblances between G2004 main phase and the periods of 'continuous up-rush' as described from the Surtsey eruption, the G2004 event lacks the distinctive rooster-tail phases that featured strongly at Surtsey. Weak rooster-tail explosions took place during G2004 but these were superimposed on the sustained activity and did not define specific phases in the eruption, nor reach the level of

intensity observed at Surtsey. Furthermore, the explosive activity at Surtsey lasted for weeks at a time, whereas the entire G2004 event lasted for a few days only. This difference is significant because it may allude to differences in vent conditions between emergent submarine eruptions and those taking place in an ice-confined environment. It may be that the availability and modes of delivery of external water to the vents is different. We know that in the Surtsey eruption the amount and level of external water in the vent varied drastically over short time spans throughout the eruption. At times of continuous up-rush the water level was low and the explosions originated deep inside the vent, whereas at times of rooster-tail explosions the vent was typically full to the brim with external water and the explosions originated at shallower levels. It is possible that the level of standing water in the vents during the G2004 eruption was never sufficiently high to generate rooster-tail jets and if so, this may be a characteristic feature of explosive phases of temperate subglacial eruptions.

Nevertheless, it is very interesting that numerous tuff cones in Iceland (including Surtsey) feature fairly thick units that resemble units C and E of the G2004 deposit in terms of their depositional structures and textures. This aspect of similarity between the two types of sequence suggests that these depositional features are synonymous with periods of continuous up-rush activity.

9.3 DIRECTIONS FOR FUTURE WORK

9.3.1 MAGMA VESICULATION AND DEPTH OF FRAGMENTATION

The G2004 deposit contains clasts with a wide vesicularity range (<5 - >90 vol. %), along with variable degrees of S degassing. Measurements of H_2O and CO_2 in both G2004 groundmass glass and melt inclusions would extend this study to permit consideration of the relative contributions of magmatic and external water in fragmentation, along with placing better controls on the depth of fragmentation within the volcanic conduit and how this changed with time. This can be combined with the other data sources previously evaluated in this PhD study (e.g. grain-size and morphology data) and coupled with a more extensive study of the vesicle size distributions of tephra from different phases of the eruption (via image analysis) in order to better evaluate conduit processes within subglacial phreatomagmatic eruptions.

9.3.2 SYN-ERUPTIVE VS. PASSIVE DEGASSING AT GRÍMSVÖTN

Long-term monitoring of sulphur and carbon dioxide emissions at active volcanoes is a valuable means of tracking magmatic processes and developing early warning systems. For example, COSPEC (correlation spectrometer) measurements taken on the eastern rift at Kilauea volcano, Hawaii show an increase in SO_2 emissions prior to the onset of new eruptions (Chartier *et al*., 1988). At Etna volcano, Italy, tremor increases were correlated with SO_2 flux during intervals of open conduit activity (Caltabiano *et al*., 1994). Rymer *et al*. (2000) have also demonstrated the benefits of integrating measurements of volatile flux with other geophysical parameters in a study which correlated changes in gravity and sulphur flux at Masaya volcano, Nicaragua, relating these to cyclic convective overturn in the magma chamber.

Grímsvötn central volcano is an ideal location for a long term study of volatile emissions, which could be integrated with existing monitoring infrastructure (i.e. seismic stations and tiltmeters). The current high frequency of eruption cycles would enable a comprehensive record of both passive and syn-eruptive degassing to be established through the use of a stationary COSPEC which could be supplemented with

overflights and possible vehicle mounted devices during eruptions. The gathered data would provide greater insight into magmatic processes in this complex system, in addition to aiding characterisation of the heat source driving its powerful geothermal field.

9.3.3 TEPHRA DISPERSAL MODELS AND HAZARD MITIGATION

A number of authors have recognised that phreatomagmatic eruption columns are often enhanced relative to the heights predicted by empirical models relating magma discharge to column height (e.g. Textor *et al*., 2006; Witham *et al*., 2007; Mastin *et al*., 2009), a finding supported by the results of this study. In the aftermath of disruption to European aviation caused by the, G2004, Ejyafjallajökull 2010 and Grímsvötn 2011 subglacial eruptions, studies have again highlighted the need for improved characterisation of glaciovolcanic plumes (e.g. Witham *et al*., 2007; Davies *et al*., 2010). The database compiled by Mastin *et al*. (2009) to collate eruption source parameters makes a significant step in addressing this shortfall. The results of this study will provide a valuable additional entry as this database contains little information for end-member small-volume basaltic phreatomagmatic eruptions. Consequently, there is a need to gather more data regarding column heights and dispersal of small-volume glaciovolcanic and related volcanic events in order to define empirical relationships appropriate to this style of event.

REFERENCES

Aiuppa A, Federico C, Giudice G, Gurierri S, Paonita A, Valenza M (2004) Plume chemistry provides insights into mechanisms of sulphur and halogen degassing in basaltic volcanoes. ESPL 222:469-483

Albino F, Pinel V, Sigmundsson F (2010) Influence of surface load variations on eruption likelihood: application to two Icelandic subglacial volcanoes, Grímsvötn and Katla. Geophysical Journal International 181:1510-1524

Alfaro R, Branðsdóttir B, Rowlands DP, White R S, Gudmundsson, MT (2007) Structure of the Grímsvötn central volcano under the Vatnajökull icecap, Iceland. Geophysical Journal International 168:863-876

Alidibirov M, Dingwell, DB (2000) Three fragmentation mechanisms for highly viscous magma under rapid decompression. Journal of Volcanology and Geothermal Research 100:413-421

Allard P, Burton, M, Mure, F (2005) Spectroscopic evidence for a lava fountain driven by previously accumulated magmatic gas. Nature 433:407–410

Allen SR, Cas RAF (1998) Rhyolitic fallout and pyroclastic density current deposits from a phreatoplinian eruption in the eastern Aegean Sea, Greece. Journal of Volcanology and Geothermal Research 86(1-4):219-251

Allen SR, McPhie, J (2009) Products of neptunian eruptions. Geology 37(7):639-642

Allen SR, Fiske RS, Tamura Y (2010) Effects of water depth on pumice formation in submarine domes at Sumisu, Izu-Bonin arc, western Pacific. Geology 38(5):391-394

Applegarth L, Tuffen H, James MR, Cashman KV, Pinkerton H (2011) Quantifying degassing-driven crystal growth in basaltic lavas. AGU Fall Meeting 2011, Abstract V23H-02

Andres R, Kyle PR, Stokes JB, Rose WI (1989) SO_2 from episode 48A eruption from, Hawaii: sulfur dioxide emissions from the episode 48A East Rift Zone eruption of Kilauea volcano, Hawaii. Bulletin of Volcanology 52:113-117

Armienti P, Innocenti F, Petrini R, Pompilio M, Villari L (1988) Sub-aphyric alkali basalt from Mt. Etna: inferences on the depth and composition of the source magma. Rendiconti Società Italiana di Mineralogia e Petrologia 43:877-891

Asimow P, Ghiorso MS (1998) Algorithmic Modifications Extending MELTS to Calculate Subsolidus Phase Relations. American Mineralogist 83:1127-1131

Barberi F, Cioni R, Rosi M, Santacroce R, Sbrana A, Vecci R (1989) Magmatic and phreatomagmatic phases in explosive eruptions of Vesuvius as deduced by grain-size and component analysis of the pyroclastic deposits. Journal of Volcanology and Geothermal Research 38(3-4):387-307

Barberi F, Macedonio G, Pareschi MT, Santacroce R (1990) Mapping the tephra fallout risk: an example from Vesuvius, Italy. Nature 344(6262):142-144

Barberi F, Coltelli M, Frullani A, Rosi M, Almeida E (1995) Chronology and dispersal characteristics of recently (last 5000 years) erupted tephra of Cotopaxi (Ecuador): implications for long-term eruptive forecasting. Journal of Volcanology and Geothermal Research 69(3-4):217-239

van Bemmelen RW, Rutten MG (1955) Table Mountains of Northern Iceland. E. J. Brill, Leiden, 217 pp

Bergh S, Sigvaldason GE (1991) Pleistocene mass-flow deposits of basaltic hyaloclastites on a shallow submarine shelf, South Iceland. Bulletin of Volcanology 53:596-611

Bertagnini A, Landi P, Santacroce R, Sbrana A (1991) From magmatic to phreatomagmatic activity through the flashing of a shallow depth hydrothermal system: the 1906 eruption of Vesuvius. Bulletin of Volcanology 53: 517-532

Berthier E, Björnsson H, Pálsson F, Feigl KL, Llubes M, Rémy F (2006) The level of the Grímsvötn subglacial lake, Vatnajökull, Iceland, monitored with SPOT5 images. Earth and Planetary Science Letters 243:293-302

Bindeman I, Sigmarsson O, Eiler J (2006) Time constraints on the origin of large volume basalts derived from O-isotope and trace element mineral zoning and U-series disequilibria in the Laki and Grímsvötn volcanic system. Earth and Planetary Science Letters 245(1-2):245-259

Bindeman I, Gurenko A, Sigmarsson O, Chaussidon M (2008) Oxygen isotope heterogeneity and disequilibria of olivine crystals in large volume Holocene basalts from Iceland: Evidence for magmatic digestion and erosion of Pleistocene hyaloclastites. Geochimica et Cosmochimica Acta 72(17):4397-4420

Björnsson H (1974) Explanation of jökulhlaups from Grímsvötn, Vatnajökull, Iceland. Jökull 24:1-26

Björnsson H, Björnsson S, Sigurgeirsson Th (1982) Penetration of water into hot rock boundaries of magma at Grímsvötn. Nature 295:580-581

Björnsson H (1988) Hydrology of ice caps in volcanic regions. Soc. Sci. Isl 45

Björnsson H (1992) Jökulhlaups in Iceland: prediction, characteristics, and simulation. Annals of Glaciology 16:95-106

Björnsson, H (2003) Subglacial lakes and jökulhlaups in Iceland. Global Planetary Change 35:255-271

Björnsson A, Johnsen G, Sigurðsson S, Þorbergsson G, Tryggvason E (1979) Rifting of the plate boundary in North Iceland 1975-1978. Journal of Geophysical Research 84:3029-3038

Björnsson H, Björnsson S, Sigurgeirsson Th (1982) Penetration of water into hot rock boundaries of magma at Grímsvötn. Nature 295:580-581

Björnsson H, Gudmundsson MT (1993) Variations in the thermal output of the subglacial Grímsvötn caldera, Iceland. Geophysical Research Letters 20:2127-2130

Björnsson H, Palsson F (2008) Icelandic glaciers. Jökull 58:365–386.

Blott S, Pye K (2001) GRADISTAT: A grain size distribution and statistics package for the analysis of unconsolidated sediments. Earth Surface Processes and Landforms 26:1237-1248

van den Bogaard P, Schmincke H-U (1985) Laacher See tephra: a widespread isochronous late Quaternary ash layer in Central and Northern Europe. Bulletin of the Geological Society America 96:1554–1571

van den Bogaard C, Dörfler W, Sandgren P, Schmincke H-U (1994) Correlating the Holocene records: Icelandic tephra found in Schleswig-Holstein (Northern Germany). Naturwissenschaften 81(12):554-556

Bonnadonna, C, Ernst, GCJ, Sparks, RSJ (1998) Thickness variations and volume estimates of tephra fall deposits: the importance of particle Reynolds number. Journal of Volcanology and Geothermal Research81:173-187

Bonadonna C, Macedonio G, Sparks RSJ (2002) Numerical modelling of tephra fallout associated with dome collapses and Vulcanian explosions: application to hazard assessment on Montserrat. In: Druitt T, Kokelaar, P (eds.) The Eruption of Soufrière Hills Volcano, Montserrat, from 1995 to 1999. The Geological Society of London pp 517-537

Bonadonna C, Phillips JC (2003) Sedimentation from strong volcanic plumes. Journal of Geophysical Research 108:2340-2368

Bonnadonna C, Houghton BF (2005) Total grain-size distribution and volume of tephra-fall deposits. Bulletin of Volcanology 67:442-456

Brandsdóttir B, Einarsson P (1979) Seismic activity associated with the September 1977 deflation of the Krafla central volcano in North-Eastern Iceland. Journal of Volcanology and Geothermal Research 6:197-212

Branney MJ, Kokelaar P (1992) A reappraisal of ignimbrite emplacement: progressive aggradation and changes from particulate to non-particulate flow during emplacement of high-grade ignimbrite. Bulletin of Volcanology 54:504-520

Branney MJ, Kokelaar P (1997) Giant bed from a sustained catastrophic density current flowing over topography: Acatlan ignimbrite, Mexico. Geology 25(2):115-118

Brazier S, Sparks RSJ, Carey SN, Sigurdsson H, Westgate JA (1983) Bimodal grain size distribution and secondary thickening in airfall ash layers. Nature 301:115-119

Bryant, EA (1991) Natural Hazards. Cambridge University Press, 294 pp

Bursik M, Sparks RSJ, Gilbert JS, Carey SN (1992) Sedimentation of tephra by volcanic plumes: I. Theory and its comparison with a study of the Fogo A plinian deposit, Sao Miguel (Azores). Bulletin of Volcanology 54(4):339-344

Büttner R, Zimanowski B (1998) Physics of thermohydraulic explosions. Physical Review E 57(5):5726-5729

Büttner R, Dellino P, Zimanowski B (1999) Identifying magma-water interaction from the surface features of ash particles. Nature 401:688-690

Calder E, Sparks RSJ, Gardeweg MC (2000) Erosion, transport and segregation of pumice and lithic clasts in pyroclastic flows inferred from ignimbrite at Lascar Volcano, Chile. Journal of Volcanology and Geothermal Research 104:201-235

Caltabiano T, Romano R, Budetta G (1994) SO_2 flux measurements at Mount Etna (Sicily). Journal of Geophysical Research 99(D6):12809-12819

Caplan-Auerbach J, McNutt SR (2003) New insights into the 1999 eruption of Shishaldin volcano, Alaska, based on acoustic data. Bulletin of Volcanology 65(6):405-417

Carey S, Sparks RSJ (1986) Quantitative models of the fallout and dispersal of tephra from volcanic eruption columns. Bulletin of Volcanology 48:109-125

Carey S, Sigurdsson H (1989) The intensity of plinian eruptions. Bulletin of Volcanology 51:28-40

Carey S, Sigurdsson H, Sparks RSJ (1988) Experimental studies of particle-laden plumes. Journal of Geophysical Research 93:15314-15328

Carey S (1991) Transport and deposition of tephra by pyroclastic flows and surges. In: Fisher RVS, G. A. (ed) Sedimentation in Volcanic Settings. Society of Economic Paleontologists and Mineralogists, pp 39-57

Carey R, Houghton BF, Thordarson T (2008) Contrasting styles of welding observed in the proximal Askja 1875 eruption deposits I: Regional welding. Journal of Volcanology and Geothermal Research 171(1-2):1-19

Cashman KV, Sturtevant B, Papale P, Navon O (2000) Magmatic Fragmentation. In: Sigurdsson H, Houghton B, McNutt, SR, Rymer H, Stix J (eds.) Encyclopaedia of Volcanoes. Academic Press, pp 421- 430

de Castello Branco A, Zbyszewski G, Moitixxio de Almeida F, da Veiga Feirreira O (1959) Le volcanisme de L'ile de Faial et l'eruption du Volcan de Capelinhos. Portugal Geological Survey

Chapman MG, Allen CC, Gudmundsson MT, Gulick VG, Jakobsson SP, Luchitta BK, Skilling IP, Waitt RB (2000) Volcanism and ice interactions on Earth and Mars. In: Zibelmann J, Gregg T (eds.) Environmental effects on volcanic eruptions: From deep oceans to deep space. Kluwer Academic/Plenum Publishers, New York

Chartier TA, Rose WI, Stokes JB (1988) Detailed record of SO_2; emissions from Pu'u `O`o between episodes 33 and 34 of the 1983–86 ERZ eruption, Kilauea, Hawaii. Bulletin of Volcanology 50(4):215-228

Chester DK, Guest JE, Kilburn C (1985) Mount Etna: anatomy of a volcano. Springer, London, p 300

Chough S, Sohn YK (1990) Depositional mechanics and sequences of base surges, Songaksan tuff ring, Cheju Island, Korea. Sedimentology 37:1115-1136

Cole P, Scarpati C (1993) A facies interpretation of the eruption and emplacement mechanisms of the upper part of the Neapolitan Yellow Tuff, Campi Flegrei, southern Italy. Bulletin of Volcanology 55:311-326

Cole PD, Guest JE, Duncan AM, Pacheco JM (2001) Capelinhos 1957-1958, Faial, Azores: deposits formed by an emergent surtseyan eruption. Bulletin of Volcanology 63:204-220

Colgate SA, Sigurgeirsson T (1973) Dynamic mixing of water and lava. Nature 244:552-555

Connor C, Hill BE, Winfrey B, Franklin NM, la Femina PC (2001) Estimation of volcanic hazards from tephra fallout. Natural Hazards Review February 2001:33-43

Corradini ML, Taleyarkhan RP (1991) Vapor explosions: A review of experiments for accident analysis. Nuclear Safety 32(3): 337-360

Couch S, Sparks RSJ, Carroll MR (2003) The kinetics of degassing-induced crystallization at Soufrière Hills volcano, Montserrat. J Petrol 44(8):1477-1502

Cox K, Bell JD, Pankhurst RJ (1979) The Interpretation of Igneous Rocks. George Allen and Unwin.

Danyushevsky L (2001) The effect of small amounts of H_2O on crystallisation of mid-ocean ridge and backarc basin magmas. Journal of Volcanology and Geothermal Research 110(3-4):265-280

Danyushevsky L, Plechov P (2011) Petrolog3: Integrated software for modelling crystallization processes. G^3 12: Q07021-53

Davies SM, Larsen G, Wastegård S, Turney CSM, Hall VA, Coyle L, Thordarson T (2010) Widespread dispersal of Icelandic tephra: how does the Eyjafjöll eruption of 2010 compare to past Icelandic events? Journal of Quaternary Science 25(5):605-611

Dellino P, LaVolpe L (1995) Fragmentation versus transportation mechanisms in the pyroclastic sequence of Monte Pilato-Rocche Rosse (Lipari, Italy). Journal of Volcanology and Geothermal Research 64:211-231

Denny M (2008) How the Ocean Works: An Introduction to Oceanography. Princeton University Press, Princeton, NJ

Devine J, Sigurdsson H, Davis AN, Self S (1984) Estimates of sulphur and chlorine yield to the atmosphere from volcanic eruptions and potential climatic effects. Journal of Geophysical Research 89(B7):6309-6325

Dingwell DB, Romano C, Hess KU (1996) The effect of water on the viscosity of a haplogranitic melt under P–T–X- conditions relevant to silicic volcanism. Contributions to Mineralogy and Petrology 124:19-28

Druitt T (1998) Pyroclastic density currents. In: Gilbert J, Sparks RSJ (eds.) The Physics of Explosive Volcanic Eruptions. Geological Society London, pp 145-182

Dufek J, Bergantz, GW (2005) Transient two-dimensional dynamics in the upper conduit of a rhyolite eruption: A comparision of closure models for the granular stress. JVGR 142: 113-132

Einarsson T (1960) Geologie von Heillisheidi (Sudwest Island). Geolog Inst Univ Koln, 55 pp

Einarsson P, Brandsdóttir B (1980) Seismological evidence for lateral magma intrusion during the July 1978 deflation of the Krafla volcano in NE Iceland. Journal of Geophysical Research 47:160-165

Einarsson P, Brandsdóttir B (1984) Seismic activity preceding and during the 1983 volcanic eruption in Grímsvötn, Iceland. Jökull 34:13-23

Einarsson, T (1965) The ring-mountains Hverfjall, Lúdent and Hrossaborg in Northern Iceland. Soc. Sci. Isl. IV

Einarsson T (1994) Geology of Iceland - Rocks and Landscape. Mal og Menning, Reykjavik, p 309

Eldholm O, Grue K (1994) North Atlantic Volcanic Margins: Dimensions and Production Rates. Journal of Geophysical Research 99(B2): 2955-2968

Ernst GGJ, Carey SN, Bursik MI, Sparks RSJ (1996) Sedimentation from turbulent jets and plumes. Journal of Geophysical Research 101:5575–5589

Fiacco RJ, Germani MS, Self S, Palais JM, Withlow S, Grootes PM (1994) Atmospheric aerosol loading and transport interpreted from ash particles and acidity due to the 1783-1784 Laki eruption in the GISP2 ice core. Quaternary Research 42:231-240

Fielder A, Fröhlich G, Müller G, Benz R, Bürger M, Schwalbe W, Unger H (1980) Theoretische und experimentelle Untersuchungen zur Dampfexplosion. p 72

Fierstein J, Nathenson M (1992) Another look at the calculation of fallout tephra volumes. Bulletin of Volcanology 67:350-357.

Fisher R (1961) Proposed classification of volcaniclastic sediments and rocks. Geological Society of America Bulletin 72(9):1409-1414

Fisher R (1966) Mechanism of deposition from pyroclastic flows. American Journal of Science 264:350-363

Fisher R (1990) Transport and deposition of a pyroclastic surge across an area of high relief: the 18 May 1980 eruption of Mount St. Helens Washington. Geological Society of America Bulletin 102:1038-1054

Fisher R, Schminke H-U (1984) Pyroclastic Rocks. Springer Verlag, New York, 472 pp.

Fitton J, Saunders AD, Norry MJ, Hardarson BS, Taylor RN (1997) Thermal and chemical Structure of the Iceland plume. Earth and Planetary Science Letters 153(3-4):197-208

Fitton J, Saunders AD, Larsen LM, Hardarson BS, Norry MJ (1998) Volcanic rocks from the southeast Greenland margin at 63°N: composition, petrogenesis, and mantle sources. In: Saunders A, Larsen HC, Wise SW (eds.) Proceedings of the Ocean Drilling Program, Scientific Results. pp 331-350

Flanagan F (1976) Descriptions and Analysis of Eight New USGS Rock Standards. USGS Bulletin 840:192

Flanagan F (1984) Three USGS mafic rock reference samples, W-2, DNC-1, and BIR-1.USGS Bulletin 1623:54

Folk RL, Ward WC (1957) Brazos River bar [Texas]; a study in the significance of grain size parameters. Journal of Sedimentary Research 27(1):3-26

Ghiorso M, Sack RO (1995) Chemical Mass Transfer in Magmatic Processes. IV. A Revised and Internally Consistent Thermodynamic Model for the Interpolation and extrapolation of Liquid-Solid Equilibria in Magmatic Systems at Elevated Temperatures and Pressures. Contributions to Mineralogy and Petrology 119:197-212

Gilbert JS, Lane SJ (1994) The origin of accretionary lapilli. Bulletin of Volcanology 56:398-411

Gómez-Tuena A, Carrasco-Núnez G (1999) Fragmentation, transport and deposition of a low-grade ignimbrite: The Citlaltépetl Ignimbrite, Eastern México. Bull Volcanol 60:448-464

Grönvold K, Makkipa H (1978) Chemical composition of Krafla lavas 1975–1977, Nordic Volcanological Institute Rep., 78-16, 49 pp., 1978

Grönvold K, Johannesson H (1984) Eruption in Grímsvötn 1983; course of events and chemical studies of the tephra. Jökull 34:1-11

Grönvold K (1984) The petrochemistry of the Laki lava flow. In: Einarsson T, Gudbergsson, GM, Gunnlaugsson, GA, Rafnsson, S, Thorarinsson, S (eds.) Skaftareldur 1783-84: Ritgerdir og Heimildir. Mal og Menning, Reykjavik, pp 49-58

Gudmundsson A (2000) Dynamics of Volcanic Systems in Iceland: Example of Tectonism and Volcanism at Juxtaposed Hot Spot and Mid-Ocean Ridge Systems. Annuals Reviews of Earth and Planetary Science 28:107-140

Gudmundsson A (1988) Effect of tensile stress concentrations around magma chambers on intrusion and extrusion frequencies. Journal of Geophysical Research 35:172-179

Gudmundsson M (1989) The Grímsvötn Caldera, Vatnajökull: Subglacial Topography and Structure of Caldera Infill. Jökull 39:1-20

Gudmundsson M, Björnsson H (1991) Eruptions in Grímsvötn, Vatnajökull, Iceland, 1934-1991. Jökull 41:21-46

Gudmundsson, MT (1989). The Grímsvötn caldera, Vatnajökull: subglacial topography and structure of caldera infill. Jökull 39:1-20

Gudmundsson MT, Björnsson, H (1993) Eruptions in Grímsvötn 1934-1991. Jökull 41:21-46

Gudmundsson MT, Björnsson H, Palsson, F (1995) Changes in jökulhlaup sizes in Grímsvötn, Vatnajökull, Iceland, 1934-91, deduced from in-situ measurements of subglacial lake volume. Journal of Glaciology 41:263-272

Gudmundsson MT, Milsom J (1997) Gravity and magnetic studies of the subglacial Grímsvötn volcano, Iceland: implications for crustal and thermal structure. Journal of Geophysical Research 102:7691-7704

Gudmundsson M, Milsom J (1997) Gravity and magnetic studies of the subglacial Grímsvötn volcano, Iceland: Implications for crustal and thermal structure. Journal of Geophysical Research 102(B4):7691-7704

Gudmundsson MT, Sigmundsson F, Björnsson H (1997) Ice-volcano interaction of the 1996 Gjálp subglacial eruption, Vatnajökull, Iceland. Nature 389:954-957

Gudmundsson MT, Palsson F, Björnsson H, Hognadóttir Th. (2002) The hyaloclastite ridge formed in the subglacial 1996 eruption in Gjalp, Vatnajökull, Iceland: present day shape and future preservation. In: Smellie JL, and Chapman, MG (eds.) Volcano-Ice Interaction on Earth and Mars. Geological Society of London, Special Publications, pp 319-335

Gudmundsson MT, Sigmundsson F, Björnsson H, Högnadóttir Th. (2004) The 1996 eruption at Gjálp, Vatnajökull ice cap, Iceland: efficiency of heat transfer, ice deformation and subglacial water pressure. Bulletin of Volcanology 66:46-65

Gudmundsson MT (2005) Subglacial volcanic activity in Iceland. In Caseldine C, Russell A, Harðardóttir J, Knudsen O Iceland - Modern processes and past environments. Elsevier, 420pp

Gudmundsson MT, Högnadóttir Th. (2007) Volcanic systems and calderas in the Vatnajökull region, central Iceland: constraints on crustal structure from gravity data. Journal of Geodynamics 43:153-169

Gudmundsson MT, Harðardóttir J, Jónsson P, Sigurðsson G, Elefsen SO, Sigfússon B, Gíslason SR (2005) Discharge and Sediment Monitoring of the 2004 glacial Outburst Flood Event (Jökulhlaup) on Skeiðará Sandur Plain, South Iceland. Geophysical Research Abstracts 7:09946

Gudmundsson MT, Zimanowski B, Jude-Eton TC, Oddsson B, Büttner R, Dellino P, Thordarson T, Larsen G (2009) Energy Partitioning in the Phreatomagmatic Basaltic Eruption of Grímsvötn in 2004. AGU Fall Meeting 2009, Abstract V11B-1952

Gudmundsson M, Pedersen R, Vogfjord K, Thorbjarnadottir B, Jakobsdottir S, Roberts MJ (2010) Eruptions of Ejyafjallajokull Volcano, Iceland. EOS 91(21)

Guðnason J (2007) Sprengigos í Jöklum: Grímsvatnagosið 2004 (Explosive eruptions in Glaciers: 2004 Grimsvotn event). Student project final report to Nýsköpunarsjóður Námsmanna (Student Innovation Fund), August 2007, Reykjavik, Iceland: 27p

Hansen H, Grönvold K (2000) Plagioclase ultraphyric basalts in Iceland: the mush of the rift. Journal of Volcanology and Geothermal Research 98(1-4):1-32

Hayward C L, Thordarson T (in review) High spatial resolution electron probe microanalysis of tephras and melt inclusions without beam-induced chemical modifications. The Holocene

Haughton D, Roeder PL, Skinner BJ (1974) Solubility of sulfur in mafic magmas. Economic Geology 69:451-467

Heier KS, Chappell BW, Arriens PA, Morgan JW (1966) The geochemistry of four Icelandic basalts. Norsk geol. tidsskr. 46, 42737

Heiken G (1972) Morphology and Petrography of Volcanic Ashes. Geological Society of America Bulletin 83(7):1961-1988

Heiken G, Wohletz K (1985) Volcanic Ash. University of California Press, Berkeley, p 246

Heiken G, Wohletz K (1991) Fragmentation processes in explosive volcanic eruptions. In: Fisher R, Smith, GA (ed) Sedimentation in volcanic setting. pp 19-26

Hess KU, Dingwell DB (1996) Viscosities of hydrous leucogranitic melts: A non-Arrhenian model. American Mineralogist 81(9-10):1297-1300

Hoblitt RP (1986) Observations of the eruptions of July 22 and August 7, 1980, at Mount St. Helens, Washington. US Geological Survey Professional Paper 1335

Holden J (2010) An Introduction to Physical Geography and Environment Pearson Education Ltd, Harlow, Essex, UK, p 762

Hooke R (2005) Principles of Glacier Mechanics Cambridge University Press, Cambridge, UK

Hoskuldsson A, Sparks RSJ, Carroll MR (2006) Constraints on the dynamics of subglacial basalt eruptions from geological and geochemical observations at Kverkfjoll, NE-Iceland. Bulletin of Volcanology 68:689-701

Houghton BF, Hackett WR (1984) Strombolian and phreatomagmatic deposits of Ohakune craters, Ruapehu, New Zealand: A complex interaction between external water and rising basaltic magma. Journal of Volcanology and Geothermal Research 21(3-4):207-231

Houghton BF, Schmincke H-U (1986) Mixed deposits of simultaneous strombolian and phreatomagmatic volcanism: Rothenberg volcano, east Eifel volcanic field. Journal of Volcanology and Geothermal Research 30(1-2):117-130

Houghton BF, Nairn IA (1991) The 1976–1982 strombolian and phreatomagmatic eruptions of White Island, New Zealand: eruptive and depositional mechanisms at a "wet" volcano. Bulletin of Volcanology 54 25-49

Houghton BF, Smith RT (1993) Recycling of magmatic clasts during explosive eruptions: estimating the true juvenile content of phreatomagmatic volcanic deposits. Bull Volcanol 55(6): 414-420

Houghton BF, Wilson CJN (1998) Fire and water: physical roles of water in large eruptions at Taupo and Okataina calderas. In: Arehart GB, Hulston JR (ed) 9th International Symposium on Water-Rock Interaction. AA Balkema, Rotterdam, Taupo, New Zealand, pp 25-30

Houghton BF, Wilson CJN, Del Carlo P, Coltelli M, Sable JE, Carey R (2004) The influence of conduit processes on changes in style of basaltic Plinian eruptions: Tarawera 1886 and Etna 122 BC. Journal of Volcanology and Geothermal Research137:1-14

Hunton D and 11 others (2005) In-situ aircraft observations of the 2000 Mt. Hekla volcanic cloud: composition and chemical evolution in the Arctic lower stratosphere. Journal of Volcanology and Geothermal Research 145: 23-34

Inman DL (1952) Measures for describing the size distribution of sediments. Journal of Sedimentary Research 22(3):125-145

Jakobsson SP, Shido F (1978) Petrology of the Western Reykjanes Peninsula, Iceland. Journal of Petrology 19(4):669-705

Jakobsson SP (1979) Petrology of recent basalts of the Eastern Volcanic zone, Iceland. Acta Naturalia Islandica 26:1-103

Jakobsson SP, Gudmundsson MT (2008) Subglacial and intraglacial volcanic formations in Iceland. Jökull 58: 179-196.

Jaupart C (1996) Physical models of volcanic eruptions. Chemical Geology 128:217-227

Jónasson K (1994) Rhyolite volcanism in the Krafla central volcano, north-east Iceland. Bulletin of Volcanology 56:516-528

Johannesson H (1980) Stratigraphy and the development of rift zones in West Iceland. Natturufraedingurinn 50:13-31

Johnsson ER, Wallace PJ, Cashman KV, Granados HD, Kent AJR (2008) Magmatic volatile contents and degassing-induced crystallization at Volcán Jorullo, Mexico: implications for melt evolution and the plumbing systems of monogenetic volcanoes. ESPL 269(3-4):478-487

Jones JG (1966) Intraglacial volcanoes of south-west Iceland and their significance in the interpretation of the form of the marine basaltic volcanoes. Nature 212:586-588

Jones JG (1969) Intraglacial volcanoes of the Laugarvatn region, south-west Iceland, I. Quarterly Journal of the Geological Society of London 124:197-211

Jones JG (1970) Intraglacial volcanoes of the Laugarvatn region, southwest Iceland, II. Journal of the Geological Society of London 78:127- 140

Jugo PJ, Luth RW, Richards JP (2005) Experimental data on the speciation of sulfur as a function of oxygen fugacity in basaltic melts. Geochim Cosmoschim Acta 69(2):497-503

Kaminski E, Jaupart C (1997) Expansion and quenching of vesicular magma fragments in Plinian eruptions. Journal of Geophysical Research 102(B6):12187-12203

Kaminski E, Jaupart C (2001) Marginal stability of atmospheric eruption columns and pyroclastic flow generation. JGR 106(B10):21785-21798

Kelley DF, Barton M (2008) Pressures of crystallization of Icelandic magmas. Journal of Petrology 49, 465-492

Kilgour G, and 9 others (2010) The 25 September 2007 eruption of Mount Ruapehu, New Zealand Directed ballistics, surtseyan jets, and ice-slurry lahars. Journal of Volcanology and Geothermal Research191:1-14

Kjartansson G (1943) Jardsaga (Geological History). Arnesingasaga I, Arnesingafelagid, Reykjavik, 250 pp

Kjartansson G (1960) The Moberg Formation. In: Thorarinsson S (ed) Geological Congress 21, Session Excursion Guide A2. Reykjavik, pp 21-28

Kjartansson G (1966) Srtapakenningin og Surtsey Natturufraedingurinn 36, 1-34

Kneller BC, Branney, MJ (1995) Sustained high-density turbidity currents and the deposition of thick massive sands. Sedimentology 42:607-616

Kokelaar BP (1986) Magma-water interactions in subaqueous and emergent basaltic volcanism. Bulletin of Volcanology 48:275-289

Kokelaar P, Busby C (1992) Subaqueous Explosive Eruption and Welding of Pyroclastic Deposits. Science 257(5067):196-201

Koyaguchi T (1994) Grain size variation of tephra derived from volcanic umbrella clouds. Bulletin of Volcanology 56:1-9

Koyaguchi T, Woods AW (1996) On the formation of eruption columns following explosive mixing of magma and surface-water. Journal of Geophysical Research 101(B3):5561-5574

Lane SJ, Gilbert JS, Hilton M (1993) The aerodynamic behaviour of volcanic aggregates. Bulletin of Volcanology 55(7):481-488

Larsen G, Thorarinsson S (1978) H4 and other acid Hekla tephra layers. Jökull 27:28-46

Larsen G (1981) Tephrochronology by microprobe glass analysis. In: Self S and Sparks RSJ (eds.) Tephra studies D. Reidel Publishing Company, Dordrecht, pp 95-102

Larsen G, Gudmundsson MT, Björnsson H (1998) Eight centuries of periodic volcanism at the centre of the Iceland hotspot revealed by glacier tephrostratigraphy. Geology 26: 943-946

Larsen G (2000) Holocene eruptions within the Katla volcanic system, south Iceland: Characteristics and environmental impact. Jökull 49(1-28)

Larsen G (2002) A brief overview of eruptions from ice-covered and ice-capped volcanic systems in Iceland during the past 11 centuries: frequency, periodicity, and implications. Geological Society Special Publication 202: 81-90

Larsen G, Eiríksson J (2007) Late Quaternary terrestrial tephrochronology of Iceland – frequency of explosive eruptions, type and volume of tephra deposits. Journal of Quaternary Science 23(2):109-120

Larsen G, Eiríksson J (2008) Holocene tephra archives and tephrochronology in Iceland - a brief overview. Jökull 58: 229-250

Larsen G, Thordarson T, Hoskuldsson A, Gudmundsson MT, Sverrisdottir G, Oddsson B, Oskarsson BV, Jonsdottir I, Oladottir B, Thorsteinsson T, Hartley ME, Meara R (2010) On-land distribution and modes of deposition of the Eyjafjallajokull 2010 tephra. Abstract V53F-04 presented at 2010 Fall Meeting, AGU, San Francisco

Legros F, Marti J (2001) Formation of inversely graded basal layers in ignimbrites by progressive aggradation. Journal of Volcanology and Geothermal Research 111:25-33

Lipman PW, Banks NG, Rhodes JM (1985) Degassing-induced crystallisation of basaltic magma and effects on lava rheology. Nature 317(17): 604-607

Liu Y, Samaha N-T, Baker DR (2007) Sulfur concentration at sulfide saturation (SCSS) in magmatic silicate melts. Geochimica et Cosmochemica Acta 71:1783-1799

Lorenz V (1974) Vesiculated tuffs and associated features. Sedimentology 21(2):273-291

Lorenz V, Zimanowski B, Frohlich G (1991) Experiments on explosive basic and ultrabasic, ultramafic, and carbonatitic volcanism. In: Meyer H, Leonardos AO (eds.) 5th International Kimberlite Conference in Araxa, Brazil CPRM Special Publications 1/A, Brasilia, Brazil, pp 270-282

Luhr J, Carmichael ISE, Varemkamp JC (1984) The 1982 eruptions of El Chichon Volcano, Chiapas, Mexico: Mineralogy and Petrology of the anhydrite-bearing pumices. Journal of Volcanology and Geothermal Research 23:69-108

Manga M, Castro J, Cashman KV, Loewenberg M (1998) Rheology of bubble-bearing magmas. Journal of Volcanology and Geothermal Research 87:15-28

Mastin L (2007) A user-friendly one-dimensional model for wet volcanic plumes. Geochemistry Geophysics Geosystems Q03014, 27pp

Mastin LG, Guffanti M, Servranck R, Webley P, Barsotti S, Dean K, Durant A, Ewert JW, Neri A, Rose WI, Schneider D, Siebert L, Stunder B, Swanson G, Tupper A, Volentik A, Waythomas CF (2009) A multidisciplinary effort to assign realistic source parameters to models of volcanic ash-cloud transport and dispersion during eruptions. Journal of Volcanology and Geothermal Research 186(1-2):10-21

Mattsson HB, Höskuldsson Á (2011) Contemporaneous phreatomagmatic and effusive activity along the Hverfjall eruptive fissure, north Iceland: Eruption chronology and resulting deposits. Journal of Volcanology and Geothermal Research 201(1-4):241-252

Matthews, WH (1947) "Tuyas", flat-topped volcanoes in northern British Columbia. Americal Journal of Science 245(9):560-570

McClintock M, White J (2006) Large phreatomagmatic vent complex at Coombs Hills, Antarctica: Wet, explosive initiation of flood basalt volcanism in the Ferrar-Karoo LIP. Bulletin of Volcanology 68(3):215-239

McCormick MP, Thomason LW, Trepte CR (1995) Atmospheric impact of the Mt. Pinatubo eruption. Nature 373:399-404

McNutt SR, Nishimura T (2008) Volcanic tremor during eruptions: Temporal characteristics, scaling and constraints on conduit size and processes. Journal of Volcanology and Geothermal Research 178: 10-18.

McPhie J, Walker GPL, Christiansen, RL (1990) Phreatomagmatic and phreatic fall and surge deposits from explosions at Kilauea volcano, Hawaii, 1790 A.D.: Keanakakoi Ash Member. Bulletin of Volcanology 52(334-354)

Métrich N, Sigurdsson H, Meyer PS, Devine JD (1991) The 1783 Lakagigar eruption in Iceland: geochemistry, CO_2 and sulfur degassing. Contributions to Mineralogy and Petrology 107:435-447

Métrich N, Rutherford MJ (1998) Low pressure crystallization paths of H_2O-saturated basaltic hawaiitic melts from Mount Etna: implications for open system degassing of basaltic volcanoes. Geochim Cosmochim Acta 62:1195-1205

Métrich N, Wallace PJ (2008) Volatile Abundances in Basaltic Magmas and Their Degassing Paths Tracked by Melt Inclusions. In: Putirka K, Tepley III, FJ (eds.) Minerals, Inclusions and Volcanic Processes. Mineralogical Society of America, pp 363-402

Michaud V, Clocchiati R, Sbrana S (2000) The Minoan and post-Minoan eruptions, Santorini (Greece), in the light of melt inclusions. Journal of Volcanology and Geothermal Research 99:195-214

Mogi K (1958) Relation between the eruptions of various volcanoes and deformations of the ground surfaces around them. Bull Earth Res Inst 36:99134

Moorbath S, Sigurdsson H, Goodwin R (1968) K-Ar ages of the oldest exposed rocks in Iceland. Earth and Planetary Science Letters 4:197-205

Moore JG (1966a) The 1965 eruption of Taal volcano. Science 151(3713):955-960

Moore JG (1966b) The September 28-30, 1965 eruption of Taal volcano, Philippines. Bulletin of Volcanology 29:75-76

Moore, JG (1967) Base surge in volcanic eruptions. Bulletin of Volcanology 30 (1): 337-363

Moore JG (1985) Structure and eruptive mechanisms at Surtsey Volcano, Iceland. Geology Magazine:649-661

Moore JG (1987) Subsidence of the Hawaiian Islands. In: Decker R, Wright TL, Stauffer PW (eds.) Volcanism in Hawaii. pp 85-107

Morrissey M (1990) Application of results from Fe-Al melt-water explosion experiments to hydrovolcanic eruptions. MSc. Thesis, University of Texas, Arlington, 141 pp

Morrissey M, Zimanowski B, Wohletz K, Büttner R (2000) Phreatomagmatic Fragmentation. In: Sigurdsson H, Houghton B, McNutt SR, Rymer H, Stix J (eds.) Encyclopaedia of Volcanoes. Academic Press.

Nairn I, Self S (1978) Explosive eruptions and pyroclastic avalanches from Ngauruhoe in February, 1975. Journal of Volcanology and Geothermal Research 3:39-60

Natland JH (2007) Nb and the role of magma mixing at the East Pacific Rise and Iceland. Geological Society of America Special Papers 430:413-449

Oddsson B (2007) The Grímsvötn eruption in 2004: dispersal and total mass of tephra and comparison with plume transport models. MSc. Thesis, Institute of Earth Sciences, University of Iceland, Reykjavik 130 pp

Óladóttir B (2009) Holocene eruption history and magmatic evolution of the subglacial Vatnajökull volcanoes, Grímsvötn, Bárdarbunga and Kverkfjöll, Iceland. PhD Dissertation U.F.R. de recherché Scientifique et Technique. Université Blaise Pascal, 395pp

Óladottir B, Thordarson T, Larsen G, Sigmarsson O (2007) Survival of the Myrdalsjokull ice cap through the Holocene thermal maximum: evidence from sulphur contents in Katla tephra layers (Iceland) from the last 8400 years. Annals of Glaciology 45:183-188

Óladóttir B, Sigmarsson O, Larsen G, Thordarson T (2008) Katla volcano, Iceland: magma composition, dynamics and eruption frequency as recorded by Holocene tephra layers. Bulletin of Volcanology 70(4):475-493

Oppenheimer C, Scaillet B, Martin RS (2011) Sulfur degassing from volcanoes: source conditions, surveillance, plume chemistry and earth system impacts. Rev Min Geochem 73(1): 363-421

Óskarsson N, Sigvaldason GE, Steinthorsson S (1982) A Dynamic Model of rift zone petrogenesis and the regional petrology of Iceland. Journal of Petrology 23(1):28-74

Papale P (1999) Numerical simulations of magma ascent along volcanic conduits. Physics and Chemistry of the Earth, Part A: Solid Earth and Geodesy 24(11-12):957-961

Parfitt EA (1998) A study of clast size distribution, ash deposition and fragmentation in a Hawaiian-style volcanic eruption. Journal of Volcanology and Geothermal Research 84:197-208

Passmore E (2009) Feeding large eruptions: crystallisation, mixing and degassing in Icelandic magma chambers. PhD Thesis, Department of GeoSciences. University of Edinburgh, Edinburgh, 363 pp

Peacock MA, Tyrrell GW (1926) The Petrology of Iceland. Transactions of the Royal Society of Edinburgh, 55: 69

Peckover RS, Buchanan, DJ, Ashby, DETF. (1973) Fuel-Coolant Interactions in Submarine Volcanism. Nature 245:307-308

Pinkerton H, Stevenson RJ (1992) Methods of determining the rheological properties of magmas at sub-liquidus temperatures. Journal of Volcanology and Geothermal Research 53(1-4):47-66

Pinkerton H, Norton G (1995) Rheological properties of basaltic lavas at sub-liquidus temperatures: laboratory and field measurements on lavas from Mount Etna. Journal of Volcanology and Geothermal Research 68(4):307-323

Pittari A, Cas RAF, Wolff JA, Nichols HJ, Larson PB, Martí J (2008) Chapter 3: The Use of Lithic Clast Distributions in Pyroclastic Deposits to Understand Pre- and Syn-Caldera Collapse Processes: A Case Study of the Abrigo Ignimbrite, Tenerife, Canary Islands, In: Joachim Gottsmann and Joan Martiacute;, Editor(s), Developments in Volcanology, Elsevier, 2008, Volume 10, Pages 97-142

Prather M (1992) Catastrophic loss of stratospheric ozone in dense volcanic clouds. Journal of Geophysical Research 97:10187-10191

Project BVS (1981) Basaltic Volcanism on the Terrestrial Pts. Pergamon Press, Inc., New York, 1286 pp

Pyle, DM (1989) The thickness, volume and grainsize of tephra fall deposits. Bulletin of Volcanology 51:1-15

Pyle D, Beattie PD, Bluth GJS (1996) Sulphur emissions to the stratosphere from explosive volcanic eruptions. Bulletin of Volcanology 57:663-671

Rose W, Self S, Murrow P, Bonadonna C, Durant A, Ernst G (2008) Nature and significance of small volume fall deposits at composite volcanoes: insights from the October 14, 1974 Fuego eruption, Guatemala. Bulletin of Volcanology 70:1043-1067

Rose W I (1993) Comment on "Another look at the calculation of fallout tephra volumes" by J Fierstein, M Nathenson. Bulletin of Volcanology 55:372-374

Rose W, Self S, Murrow P, Bonadonna C, Durant A, Ernst G (2007) Nature and significance of small volume fall deposits at composite volcanoes: Insights from the October 14, 1974 Fuego eruption, Guatemala. Bulletin of Volcanology 70(9):1043-1067

Rose WI, Durant AJ (2009) Fine ash content of explosive eruptions. Journal of Volcanology and Geothermal Research 186(1-2):32-39

Rosi M, Paladio-Melosantos ML, Di Muro A, Leoni R, Bascolcol, T (2001) Fall vs. Flow activity during the 1991 climactic eruption of Pinatubo volcano (Philippines). Bulletin of Volcanology 62(549-566)

Rowley P, Kuntz MA, Macleod NS (1981) Pyroclastic-flow deposits. In: Mullineaux P, (ed) The 1980 Eruptions of Mount St. Helens, Washington, U.S. Geological Survey Professional Paper. pp 489-512

Rymer H, Cassidy J, Locke CA, Barboza MV, Barquero J, Brenes J, Van der Laat R (2000) Geophysical studies of the recent 15-year eruptive cycle at Poás Volcano, Costa Rica. Journal of Volcanology and Geothermal Research 97(1-4):425-442

Sable JE, Houghton BF, Del Carlo P, Coltelli M (2006) Changing conditions of magma ascent and fragmentation during the Etna 122 BC basaltic Plinian eruption: Evidence from clast microtextures. Journal of Volcanology and Geothermal Research 158:333-354

Saemundsson K (1978) Fissure swarms and central volcanoes of the neovolcanic zones of Iceland. Geol J Spec Iss 10:415-432

Saemundsson K (1980) Outline of the geology of Iceland. Jökull 29:7-28

Saemundsson K (1982) Calderas in the active volcanic belts of Iceland (in Icelandic). Eldur er í Nordri. Sogufelagid, Reykjavik, pp 221-239

Saunders A, Fitton JG, Kerr AC, Norry MJ, Kent RW (1997) The North Atlantic Igneous Province. In: Mahoney J, Coffin MF (eds.) Large Igneous Provinces: Continental, Oceanic, and Planetary Flood Volcanism. Americal Geophysical Union, Washington DC, pp 381-410

Schopka H, Gudmundsson MT, Tuffen H (2006) The formation of Helgafell, a Monogenetic subglacial hyaloclastite ridge: sedimentology, hydrology and volcano-ice interaction. Journal of Volcanology and Geothermal Research152:359-377

Schiellerup H (1995) Generation and equilibration of olivine tholeiites in the northern rift zone of Iceland. A petrogenetic study of the Bláfjall table mountain. Journal of Volcanology and Geothermal Research 65:161-179

Schumacher R, Schmincke H-U (1991) Internal structure and occurrence of accretionary lapilli — a case study at Laacher See Volcano. Bulletin of Volcanology 53(8):612-634

Schumacher R, Schmincke HU (1995) Models for the origin of accretionary lapilli. Bulletin of Volcanology 56:626-639

Schuman U and 32 others (2010) Airborne observations of the Eyjafjalla volcano ash cloud over Europe during air space closure in April and May 2010. Atmospheric Chemistry and Physics Discussions 22131-22218

Scolamacchia T, Macías J, Sheridan M, Hughes S (2005) Morphology of ash aggregates from wet pyroclastic surges of the 1982 eruption of El Chichón Volcano, Mexico. Bulletin of Volcanology 68(2):171-200

Scollo S, del Carlo P, Coltelli M (2007) Tephra fallout of 2001 Etna flank eruption: Analysis of the deposit and plume dispersion. Journal of Volcanology and Geothermal Research 160:147-164

Sheridan MF, Wohletz, KH (1983) Hydrovolcanism: Basic Considerations and Review. Journal of Volcanology and Geothermal Research 17(1-4):1-29

Self S, Sparks R (1978) Characteristics of widespread pyroclastic deposits formed by the interaction of silicic magma and water. Bulletin of Volcanology 41(3):196-212

Self S, Kienle J, Huot JP (1980) Ukinrek Maars, Alaska, II. Deposits and formation of the 1977 craters. Journal of Volcanology and Geothermal Research7:39-65

Self S, Rampino MR, Barbera JJ (1981) The possible effects of large 19th and 20th Century volcanic eruptions on zonal and hemispheric surface temperatures. Journal of Volcanology and Geothermal Research11:41-60

Self S, King AJ (1996) Petrology and sulfur and chlorine emissions of the 1963 eruption of Gunung Agung, Bali, Indonesia. Bulletin of Volcanology 58:263-285

Self S, King AJ (1996) Petrology and sulfur and chlorine emissions of the 1963 eruption of Gunung Agung, Bali, Indonesia. Bulletin of Volcanology 58:263-285

Self S (2005) Effects of volcanic eruptions on the atmosphere and climate. In: Ernst G, Marti, J (ed) In Environmental effects of volcanic activity. Cambridge University Press, Cambridge, UK, pp 152-174

Self S (2006) The effects and consequences of very large explosive volcanic eruptions. Philosophical Transactions of the Royal Society 364:2073-2094

Settle M (1978) Volcanic eruption clouds and the thermal power output of explosive eruptions. Journal of Volcanology and Geothermal Research 3:309-324

Sharma K, Blake S, Self S (2004) SO_2 emissions from basaltic eruptions and the excess sulfur issue. Geophysical Research Letters 31:L13612, 4pp

Sigmarsson O, Condomines M, Grönvold K, Thordarson T (1991) Extreme magma homogeneity in the 1783-84 Lakagigar eruption: origin of a large volume of evolved basalt in Iceland. Geophysical Research Letters 18(12):2229-2232

Sigmarsson O (1996) Short magma chamber residence time at an Icelandic volcano inferred from U-series disequilibria, Nature 382: 440–442

Sigmarsson O, Karlsson HR, Larsen G (2000) The 1996 and 1998 subglacial eruptions beneath the Vatnajökull ice sheet in Iceland: contrasting geochemical and geophysical inferences on magma migration. Bulletin of Volcanology 61:468-476

Sigmundsson F, Gudmundsson MT (2004) The Grímsvötn eruption, November 2004. Jökull 54:139–142

Sigurdsson H (1982) Volcanic pollution and climate: the 1783 Laki eruption. . EOS 63:601-602

Sigurdsson H, Sparks RSJ (1979) An active submarine volcano. Nat Hist 88:38-43

Simkin T, Siebert L (1994) Volcanoes of the World. Geoscience Press, Tuscon, AZ, 349 pp

Skilling, IP (1994) Evolution of an englacial volcano: Brown Bluff, Antarctica. Bulletin of Volcanology 56:573-591

Slater L, Jull M, McKenzie D, Grönvold K (1998) Deglaciation effects on mantle melting under Iceland: Results from the Northern Volcanic Zone. Earth and Planetary Science Letters 164:151-164

Smellie, JL (2000) Subglacial Eruptions. In: Sigurdsson H, Houghton B, McNutt SR, Rymer H, Stix J (eds.) Encyclopaedia of Volcanoes. Academic Press, pp 403-418

Smellie, JL (2006) The relative importance of supraglacial versus subglacial meltwater escape in basaltic subglacial tuya eruptions: an important unresolved conundrum. Earth Science Reviews 74:241-268

Smellie, JL (2008) Basaltic subglacial sheet-like sequences: evidence for two types with different implications for the inferred thickness of associated ice. Earth Science Reviews 88:60-88

Sohn YK, Chough SK (1989) Depositional processes of the Suwolbong tuff ring, Cheju Island (Korea). Sedimentology 36:837-855

Sohn, YK (1996) Hydrovolcanic processes forming basaltic tuff rings and cones on Cheju Island, Korea. Geological Society of America Bulletin 108:1199-1211

Sohn YK, Chough SK (1992) The Ilchulbong tuff cone, Cheju Island, South Korea. Sedimentology 39(4):523-544

Solgevik H, Mattsson HB, Hermelin O (2007) Growth of an emergent tuff cone: fragmentation and depositional processes recorded in the Capelas tuff cone, São Miguel, Azores. Journal of Volcanology and Geothermal Research 159(1):246–266

Sparks RSJ (1976) Grain size variations in ignimbrites and implications for the transport of pyroclastic flows. Sedimentology 23:147-188

Sparks RSJ, Self S, Walker GPL (1973) Products of ignimbrite eruptions. Geology 1(3): 115-118

Sparks RSJ, Sigurdsson H, Wilson L (1977) Magma mixing: a mechanism for triggering acid explosive eruptions. Nature 267:315-318

Sparks RSJ, Wilson L, Hulme G (1978) Theoretical modelling of the generation movement and emplacement of pyroclastic flows by column collapse. Journal of Geophysical Research 83:1727-1739

Sparks RSJ, Wilson L, Sigurdsson H (1981) The pyroclastic deposits of the 1875 eruption of Askja, Iceland. Philosophical Transactions of the Royal Society of London 299:241-273

Sparks RSJ, Wilson L (1982) Explosive volcanic eruptions — V. Observations of plume Dynamics during the 1979 Soufrière eruption, St Vincent. Geophysical Journal of the Royal Astronomical Society 69(2):551-570

Sparks RSJ (1986) The dimensions and dynamics of volcanic eruption columns. Bulletin of Volcanology 48:3-15

Sparks R, Bursik MI, Ablay GJ, Thomas RME, Carey SN (1992) Sedimentation of tephra by volcanic plumes. Part 2: controls on thickness and grain-size variations of tephra fall deposits Bulletin of Volcanology 54(8):685-695

Sparks RSJ, Barclay J, Jaupart C, Mader HM, Phillips JC (1994) Physical aspects of magma degassing I: experimental and theoretical constraints on magma degassing. In: Carroll MR, Holloway, JR (eds.) Volatiles in Magmas. Mineralogical Society of America, Washington, D. C., pp 413-435

Sparks RSJ, Bursik M, Carey S, Gilbert J, Glaze L, Sigurdsson H, Woods A (1997) Volcanic Plumes. J. Wiley and sons, Chichester

Steinberg GS, Lorenz V (1983) External ballistic of volcanic explosions. Bulletin of Volcanology 46:333-348

Steinberg GS, Steinberg AS (1975) On possible causes of volcanic tremor. Journal of Geophysical Research 80:1600-1604

Steinberg G (1976) On the determination of the energy and depth of volcanic explosions. Bulletin of Volcanology 40(2):116-120

Steinthorsson S (1992) Climatic effects of large volcanic eruptions with special reference to the Skaftar Fires of 1783-1785. In: Geirsdóttir A, Helgadóttir GN (eds.) The 20th Nordic Geological Winter Meeting. Reykjavik

Steinthórsson S, Óskarsson N, Sigvaldason GE (1985). Origin of alkali basalts in Iceland: a plate tectonic model. Journal of Geophysical Research 90:10027–10042.

Stothers R (1996) The great dry fog of 1783. Climate Change 32:79-89

Steinthorsson S, Hardarson BS, Ellam RM, Larsen G (2000) Petrochemistry of the Gjalp 1996 subglacial eruption, Vatnajökull, SE Iceland. Journal of Volcanology and Geothermal Research 98:79-90

Sturkell E, Einarsson P, Sigmundsson F, Hreinsdottir S, Geirsson H (2003) Deformation of Grímsvötn volcano, Iceland: 1998 eruption and subsequent inflation. Geophsical Research Letters 30(4):1182

Sturkell E (2006) Volcano geodesy and magma dynamics in Iceland. Journal of Volcanology and Geothermal Research 150:14-34

Sutton A, Elias T, Gerlach TM, Stokes JB (2001) Implications for eruptive processes as indicated by sulfur dioxide emissions from Kilauea Volcano, Hawai'i, 1979-1997. Journal of Volcanology and Geothermal Research 108:283-302

Suzuki T (1983) A theoretical model for the dispersion of tephra. In: Yokoyama D, (ed) Arc Volcanism: Physics and Tectonics. TERRAPUB (Terra Scientific Publishing Company), Tokyo

Tabazadeh A, Turco RP (1993) Stratospheric Chlorine Injection by Volcanic Eruptions: HCI Scavenging and Implications for Ozone. Science 260(5111):1082-1086

Taddeucci J, Wohletz KH (2001) Temporal evolution of the Minoan eruption (Santorini, Greece), as recorded by its Plinian fall and interlayered ash flow deposits. Journal of Volcanology and Geothermal Research 109: 301-319

Taddeucci J, Palladino DM (2002) Particle size-density relationships in pyroclastic deposits: inferences for emplacement processes. Bull Volcanol 64: 273-284S

Taddeucci J, Scarlato P, Montanaro C, Cimarelli C, Del Bello E, Freda C, Andronico D, Gudmundsson MT, Dingwell DB (2011). Aggregation-dominated ash settling from the Eyjafjallajökull volcanic cloud illuminated by field and laboratory high-speed imaging. Geology 39(9):891-894

Tait S, Jaupart C, Vergniolle S (1989) Pressure, gas content and eruption periodicity of a shallow, crystallising magma chamber. ESPL 92(1):107-123

Talbot J, Self S, Wilson CJN (1994) Dilute gravity current and rain-flushed ash deposits in the 1.8 ka Hatepe Plinian deposit, Taupo, New Zealand Bulletin of Volcanology 56(6-7):538-551

Taylor, PS (1969) Soluble material on volcanic ash. Dartmouth College, NH, USA, MSc Thesis: 77pp

Textor C, Graf HF, Herzog M, Oberhuber JM, Rose WI, Ernst GGJ (2006) Volcanic particle aggregation in explosive eruption columns. Part I: Parameterization of the microphysics of hydrometeors and ash. Journal of Volcanology and Geothermal Research150:359-377

Thorarinsson, S (1953) Some new aspects of the Grímsvötn problem. Journal of Glaciology 2:267-274

Thorarinsson, S (1964) Surtsey: the new island in the Atlantic. Viking Press, New York: 63pp

Thorarinsson, S (1967) Surtsey, the new island in the North Atlantic. Viking Press, New York

Thorarinsson, S (1974) Votnin Strið. Menningarsjodur, Reykjavík: 254pp

Thordarson T, Self S (1988) Old map helps to interpret Icelandic eruptions. EOS 69 (8): 86

Thordarson T (1995) Volatile release and atmospheric effects of basaltic fissure eruptions. PhD Dissertation, University of Hawaii, Manoa

Thordarson T, Self S (1993) The Laki (Skaftár Fires) and Grímsvötn eruptions in 1783–1785. Bulletin of Volcanology 55:233-263

Thordarson T, Self S (1996) Sulphur, chlorine and flourine degassing and atmospheric loading by the Roza eruption, Columibia River Basalt group, Washington, USA. Journal of Volcanology and Geothermal Research 74:49-73

Thordarson T, Larsen G (2007) Volcanism in Iceland in historical time: eruption styles and eruptive history. Journal of Geodynamics 43:118-152

Thordarson T, Self S, Óskarsson N, Hulsebosch T (1996) Sulfur, chlorine and fluorine degassing and atmospheric loading by the 1783-1784 AD Laki (Skaftár Fires) eruption in Iceland. Bulletin of Volcanology 58:205-225

Thordarson T (2000) Morphology and structure of the AD 1963-67 Surtsey lava flow field: Results from preliminary observations. Surtsey Research Progress Report XI: 125-142

Thordarson T, Miller DJ, Larsen G, Self S, Sigurdsson H (2001) New estimates of sulfur degassing and atmospheric mass-loading by the 934 AD Eldgjá eruption, Iceland. Journal of Volcanology and Geothermal Research 108(1-4):33-54

Thordarson T, Hoskuldsson A (2002) Iceland. Terra, 200 pp

Thordarson T, Self S, Miller DJ, Larsen G, Vilmundardottir EG (2003a) Sulphur release from flood lava eruptions in the Veidivotn, Grimsvotn and Katla volcanic systems, Iceland. Geological Society of London Special Publication 213:103-121

Thordarson T, Larsen G, Steinthorsson S, Self S (2003b) The 1783-85 Laki-Grímsvötn eruptions II: Appraisal based on contemporary accounts. Jökull 53:11-48

Thordarson T, Larsen G (2007) Volcanism in Iceland in historical time: Volcano types, eruption styles and eruptive history. Journal of Geodynamics 43(1):118-152

Thordarson T, Höskuldsson Á (2008) Postglacial volcanism in Iceland. Jökull 58:197-228

Thordarson T, Sigmarson O (2008) Effusive activity in the 1963-67 Surtsey eruption, Iceland: flow emplacement and growth of small lava shields. In: Self S, Rowland S, Hoskuldsson A (eds.) Studies in Volcanology: The legacy of George Walker. Geological Society of London Special Publication

Triglia R, Battaglia M, Manga M (2007) An experimental facility for investigating hydromagmatic eruptions at high pressure and high temperature, and the importance of magma texture for magma-water interaction. Bulletin of Volcanology 69(4):365-372

Tyrrell and Peacock (1927) The petrology of Iceland. Transactions of the Royal Society of Edinburgh.

Tryggvason E (1986) Multiple magma reservoirs in a rift zone volcano: Ground deformation and magma transport during the September 1984 eruption of Krafla, Iceland. Journal of Volcanology and Geothermal Research 28:1-44

Valentine, GA (1987) Stratified flow in pyroclastic surges. Bulletin of Volcanology 49:616-630

Valentine GA, Giannetti B (1995) Single pyroclastic beds deposited by simultaneous fallout and surge processes: Roccamonfina volcano, Italy. Journal of Volcanology and Geothermal Research 64(1-2):129-137

Vilmundardóttir E, Snorrason SP, Larsen G (2000) Geological map of subglacial volcanic area southwest of Vatnajökull icecap, Iceland. In: Orkustofnum and Landsvirkjun, Reyjavik

Vogfjörð, KS and 17 others (2005) Forecasting and monitoring a subglacial eruption in Iceland. EOS 86:245-248

Volentik ACM, Bonadonna C, Connor CB, Connor LJ, Rosi M (2010) Modeling tephra dispersal in absence of wind: Insights from the climactic phase of the 2450 BP Plinian eruption of Pululagua volcano (Ecuador). Journal of Volcanology and Geothermal Research 193(1-2):117-136

Wadge G (1981) The variation of magma discharge during basaltic eruptions. Journal of Volcanology and Geothermal Research11:139-168

Walker GPL (1980) The Taupo pumice: Product of the most powerful known (ultraplinian) eruption? Journal of Volcanology and Geothermal Research 8(1):69-94

Walker GPL (1983) Ignimbrite types and ignimbrite problems. Journal of Volcanology and Geothermal Research17:65-88

Walker GPL, Blake DH (1966) The formation of a palagonite breccia mass beneath a valley glacier in Iceland. Quarterly Journal of the Geological Society of London 122:45-61

Walker, GPL, Wilson, L, Bowell, ELG (1971) Explosive volcanic eruptions I. The rate of fall of pyroclasts. Geophys J Royal Astronom Soc 22:377-383

Walker, GPL, Croasdale, R. (1972) Characteristics of some basaltic pyroclasts. Bulletin of Volcanology (35):303-317

Walker, GPL (1981) Plinian eruptions and their products. Bulletin of Volcanology 44:223-240

Walker GPL (1981) Generation and dispersal of fine ash and dust by volcanic eruptions. Journal of Volcanology and Geothermal Research 11(1):81-92

Walker GPL (1983) Ignimbrite types and ignimbrite problems. Journal of Volcanology and Geothermal Research17:65-88

Wallace P, Carmichael ISE (1992) Sulfur in basaltic magmas. Geochemica et Cosmochimica Acta 56:1863-1874

Wallace P (2001) Volcanic SO_2 emissions and the abundance and distribution of exsolved gas in magma bodies. Journal of Volcanology and Geothermal Research 108:85-106

Wallace P (2002) Volatiles in Submarine Basaltic Glasses from the Northern Kerguelen Plateau (ODP Site 1140): Implications for Source Region Compositions, Magmatic Processes and Plateau Subsidence. Journal of Petrology 43(7):1311-1326

Wallace P (2005) Volatiles in subduction zone magmas, concentrations and fluxes based on melt inclusion and volcanic gas data. Journal of Volcanology and Geothermal Research140:217-240

Waters AC, Fisher RV (1971) Base surges and their deposits: Capelinhos and Taal volcanoes. Journal of Geophysical Research 76:5596-5614

Watkins ND, Walker GPL (1977) Magnetostratigraphy of eastern Iceland. American Journal of Science 277(5):513-584

Werner R, Schminke, H-U, Sigvaldason, GE (1996) A new model for the evolution of table mountains: volcanological and petrological evidence from Herdubreid and Herdubreidartogl volcanoes, Iceland. Geol. Rundsch. 85:390-397

Werner R, Schmincke H-U, (1999) Englacial vs. lacustrine origin of volcanic table mountains: evidence from Iceland. Bulletin of Volcanology 60: 335–354

Wilson L (1972) Explosive Volcanic Eruptions-II The Atmospheric Trajectories of Pyroclasts. Geophysical Journal of the Royal Astronomical Society 30(4):381-392

Westrich H, Gerlach TM (1992) Magmatic gas source for the stratospheric SO_2 cloud from the June 15, 1991, eruption of Mount Pinatubo. Geology 20:867-870

Wilson L (1972) Explosive Volcanic Eruptions-II The Atmospheric Trajectories of Pyroclasts. Geophysical Journal of the Royal Astronomical Society 30(4):381-392

Wilson L, Sparks RSJ, Huang TC, Watkins ND (1978) The Control of Volcanic Column Heights by Eruption Energetics and Dynamics. Journal of Geophysical Research 83(B4):1826-1836

Wilson L (1980) Relationships between pressure, volatile content and ejecta velocity in three types of volcanic explosion. Journal of Volcanology and Geothermal Research 8(2-4):297-313

Wilson L, Walker GPL (1987) Explosive volcanic eruptions VI. Ejecta dispersal in plinian eruptions: the control of eruption conditions and atmospheric properties. Geophysical Journal of the Royal Astronomical Society 89: 657–679

Wilson L, Head JW (2007) Explosive volcanic eruptions on Mars: tephra and accretionary lapilli formation, dispersal and recognition in the geologic record. Journal of Volcanology and Geothermal Research163:83-97

Witham C, Hort MC, Potts R, Servranck R, Husson P, Bonnardot F (2007) Comparison of VAAC atmospheric dispersion models using the 1 November 2004 Grimsvotn eruption. Meteorological Applications 14:27-38

White JDL, Houghton, B (2000) Surtseyan and Related Phreatomagmatic Eruptions. In: Sigurdsson H, Houghton B, McNutt SR, Rymer H, Stix, J (eds.) Encyclopaedia of Volcanoes. Academic Press, pp 497-511

White JDL, McClintock MK (2001) Immense vent complex marks flood-basalt eruption in a wet, failed rift: Coombs Hills, Antarctica. Geology 29(10):935-938

Wilson L, Sparks RSJ, Huang TC, Watkins ND (1978) The Control of Volcanic Column Heights by Eruption Energetics and Dynamics. Journal of Geophysical Research 83(B4):1826-1836

Wilson L, Sparks RSJ, Walker GPL (1980) Explosive volcanic eruptions IV. The control of magma properties and conduit geometry on eruption column behaviour. Geophysical Journal of the Royal Astronomical Society 63(1):117–148

Wilson L (1980) Relationships between pressure, volatile content and ejecta velocity in three types of volcanic explosion. Journal of Volcanology and Geothermal Research 8(2-4):297-313

Wilson L (1980) Relationships between pressure, volatile content and ejecta velocity in three types of volcanic explosion. Journal of Volcanology and Geothermal Research 8(2-4):297-313

Wilson L, Head JW (1981) Ascent and eruption of basaltic magma on the Earth and Moon. Journal of Geophysical Research 86:2971-3001

Wohletz KH (1983) Mechanisms of hydrovolcanic pyroclast formation: grain size, scanning electron microscopy and experimental studies. Journal of Volcanology and Geothermal Research 17(1-4):31-63

Wohletz KH (1986) Explosive magma-water interactions: Thermodynamics, explosion mechanisms, and field studies. Bulletin of Volcanology 48(5):245-264

Wohletz KH, Sheridan MF (1983) Hydrovolcanic explosions II. Evolution of basaltic tuff rings and tuff cones. American Journal of Science 283:385-413

Wohletz K, Sheridan MF, Brown WK (1989) Particle Size Distributions and the Sequential Fragmentation/Transport Theory Applied to Volcanic Ash. Journal of Geophysical Research 94(B11):15703-15721

Wohletz K, McQueen RG (1984) Experimental studies of hydromagmatic volcanism. pp 158-169

Wohletz KH, Brown, W (1995) Particulate size distributions and sequential fragmentation/transport theory. Las Alamos National Laboratory, submitted toNSF/JSPS AMIGO-IMI Seminar, Santa Barbara, CA, June 8-13, 1995

Wohletz KH, McQueen RG, Morrissey M (1995) Experimental study of hydrovolcanism by fuel-coolant interaction analogues. Las Alamos National Laboratory, submitted to NSF/JSPS AMIGO-IMI Seminar, Santa Barbara, CA, June 8-13, 1995

Wohletz KH, Orsi G, de Vita S (1995) Eruptive mechanisms of the Neapolitan Yellow Tuff interpreted from stratigraphic, chemical and granulometric data. Journal of Volcanology and Geothermal Research 67:263-290

Wohletz KH, Zimanowski B (2000) Physics of phreatomagmatism, Part I: explosion physics. Terra Nostra 6:515-523

Wolfe CJ, Bjarnason IT, VanDecar JC, Solomon SC (1997) Seismic structure of the Iceland mantle plume. Nature 385:245–247

Wolff JA, Turbeville BN (1994) Comment on "A reappraisal of ignimbrite emplacement: progressive aggradation and particulate to non-particulate flow transitions during emplacement of high-grade ignimbrite" by MJ Branney and P Kokelaar. Bulletin of Volcanology 56:134-137

Wood C (1992) Climatic effects of the 1783 Laki eruption. In: Harrington CR (ed) The year without a summer? Canadian Museum of Nature, Ottawa, pp 58-77

Woods A, Bower, SM (1995) The decompression of volcanic jets in a crater during explosive volcanic eruptions. ESPL 131:189-205

Woods AW (1993) A model of the plumes above basaltic fissure eruptions. Geophysical Research Letters 20(12):1115-1118

Wright J, Walker GPL (1981) Eruption, transport and deposition of ignimbrite: a case study from Mexico. Journal of Volcanology and Geothermal Research9:111-131

Wylie J, Helfrich KR, Dade B, Lister JR, Salzig JF (1999) Flow localization in fissure eruptions. Bulletin of Volcanology 60:432-440

Zanon V, Pacheco J, Pimentel A (2009) Growth and evolution of an emergent tuff cone: considerations from structural geology, geomorphology and facies analysis of São Roquevolcano, São Miguel (Azores). Journal of Volcanology and Geothermal Research 180:277-291

Zapata J and 11 others (1997) SO_2 fluxes from Galeras Volcano, Colombia, 1989-1995: Progressive degassing and conduit obstruction of a Decade Volcano. Journal of Volcanology and Geothermal Research 77:195-208

Zbyszewski G et al (1959) Le volcanisme de L'ile de Faial et l'eruption du Volcan de Capelinhos Rapport de la Deuxieme mission Geologique. In: Serv Geol Port Mem pp 29–55

Zhang YX (1999) A criterion for the fragmentation of bubbly magma based on brittle failure theory. Nature 402:648-650

Zimanowski B, Fröhlich G, Lorenz V (1995) Experiments on vapour explosions by interaction of water with silicate melts. Nuclear Engineering and Design 155:335-343

Zimanowski B, Büttner R, Lorenz V, Hafele H (1997a) Fragmentation of basaltic melt in the course of explosive volcanism. Journal of Geophysical Research 102(B1):803-814

Zimanowski B, Büttner R, Lorenz V (1997b) Premixing of magma and water in MFCI experiments. Bulletin of Volcanology 58:491-495

Zimanowski B, Büttner R (1998) Physics of thermohydraulic explosions. Physical Review 57(5):5726-5729

Zimanowski B, Wohletz KH, Dellino P, Büttner R (2003) The volcanic ash problem. Journal of Volcanology and Geothermal Research 122:1-5

Zimanowski B, Fröhlich G, Lorenz V (1991) Quantitative experiments on phreatomagmatic explosions. Journal of Volcanology and Geothermal Research 48(3-4):341-358

APPENDIX I

STRATIGRAPHIC LOGS AND FIELD NOTES

Figure A1.1: Location of measured sections within the Grímsvötn caldera.

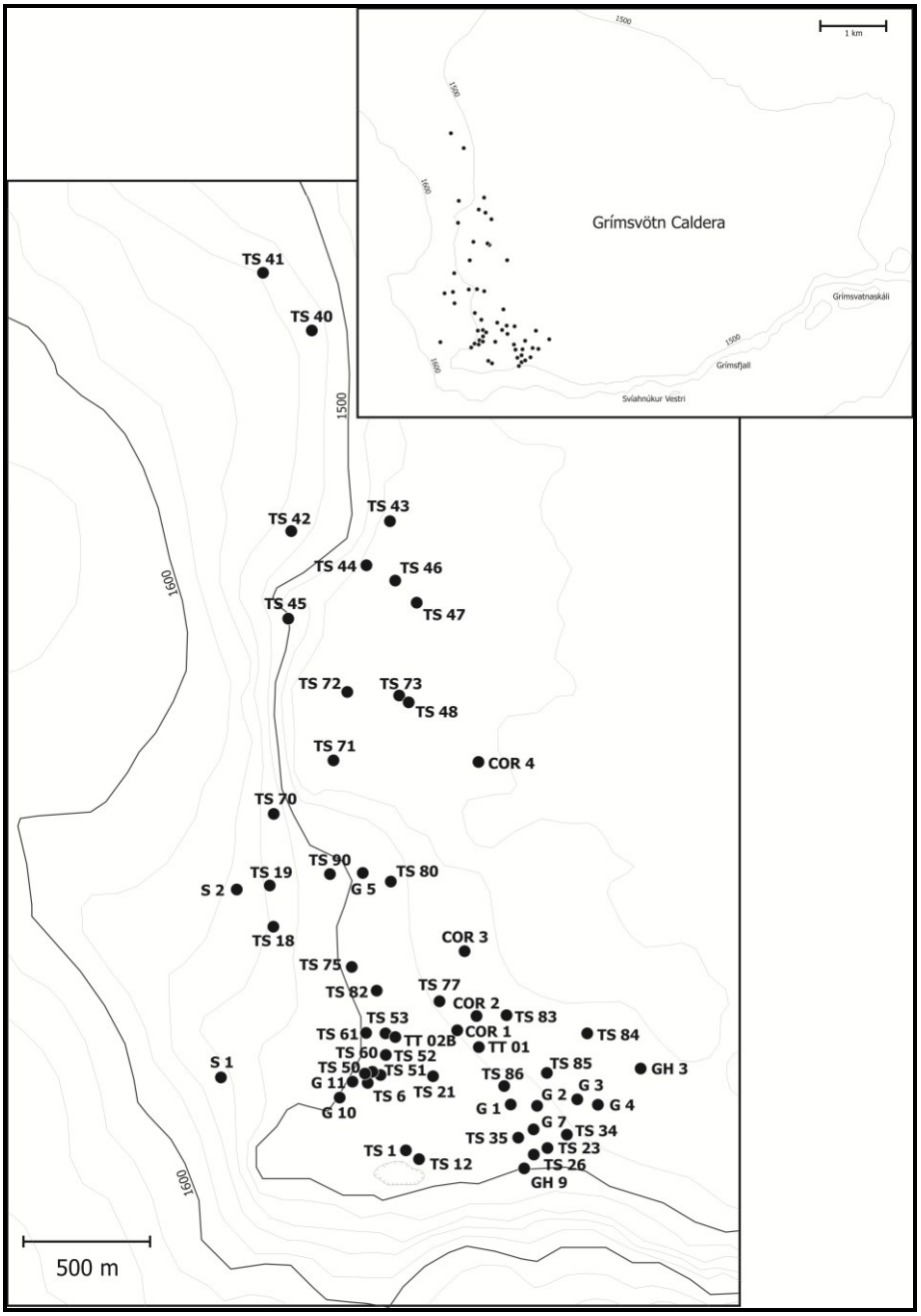

Table A1.2: Section names, along with locations (as recorded by handheld GPS) and total thickness data.

Locality	Position	Thickness (cm)	Distance from Vent (m)
TT01	64˚ 24.112' N; 17˚ 22.705' W	720	549
TT02	64˚ 24.129' N; 17˚ 23.118' W	>430	510
TT02B	64˚ 24.141' N; 17˚ 23.169' W	645	566
S1	64˚ 24.043' N;17˚ 23.985' W	353	831
S2	64˚ 24.447' N;17˚ 23.912' W	295	1300
G1	64˚ 23.983' N; 17˚ 22.550' W	468	467
G2	64˚ 23.983' N; 17˚ 22.417' W	263	724
G3	64˚ 23.996' N; 17˚ 22.222' W	85	731
GH3	64˚ 24.067' N; 17˚ 21.900' W	55	1000
G4	64˚ 23.986' N; 17˚ 22.115' W	77	785
G5	64˚ 24.483' N; 17˚ 23.283' W	>460	1200
G7	64˚ 23.933' N; 17˚ 22.433' W	260	513
GH9	64˚ 23.850' N; 17˚ 22.483' W	209	452
G10	64˚ 24.000' N; 17˚ 23.400' W	>480	376
G11	64˚ 24.033' N; 17˚ 23.333' W	>274	386
TS1	64˚ 23.877' N; 17˚ 23.062' W	>220	6
TS6	64˚ 24.030' N; 17˚ 23.257' W	>810	351
TS12	64˚ 23.871' N; 17˚ 23.008' W	>115	5
TS18	64˚ 24.369' N; 17˚ 23.722' W	240	926
TS19	64˚ 24.459' N; 17˚ 23.750' W	200	1200
TS21	64˚ 24.047' N; 17˚ 22.935' W	>180	347
TS23	64˚ 23.893' N; 17˚ 22.365' W	180	578
TS26	64˚ 23.878' N; 17˚ 22.433' W	196	490
TS34	64˚ 23.920' N; 17˚ 22.262' W	95	634
TS35	64˚ 23.915' N; 17˚ 22.512' W	402	440
TS40	64˚ 25.654' N; 17˚ 23.538' W	30	3500
TS41	64˚ 25.766' N; 17˚ 23.782 W	25	3700

Locality	Position	Thickness (cm)	Distance from Vent (m)
TS44	64˚ 25.143' N; 17˚ 23.259' W	77	2400
TS45	64˚ 25.031' N; 17˚ 23.653' W	100	2300
TS46	64˚ 25.114' N; 17˚ 23.116' W	84	2400
TS47	64˚25.064' N; 17˚ 23.016' W	80	2200
TS48	64˚ 24.851 N;17˚ 23.060' W	204	1900
TS50	64˚ 24.050' N; 17˚ 23.259' W	>40	395
TS51	64˚ 24.050' N; 17˚ 23.200' W	>400	375
TS52	64˚ 24.093' N; 17˚ 23.169' W	>300	452
TS53	64˚ 24.133' N; 17˚ 23.258' W	>250	541
TS60	64˚ 24.058' N; 17˚ 23.239' W	>395	389
TS61	64˚ 24.140' N; 17˚ 23.268' W	125	539
TS70	64˚ 24.612' N; 17˚23.720' W	285	1500
TS71	64˚ 24.728' N; 17˚23.423' W	410	1600
TS72	64˚ 24.874' N; 17˚ 23.353' W	183	1900

G1; 468 cm
64° 23.983' N; 17° 22.550' W
31/07/2006 (TJ)

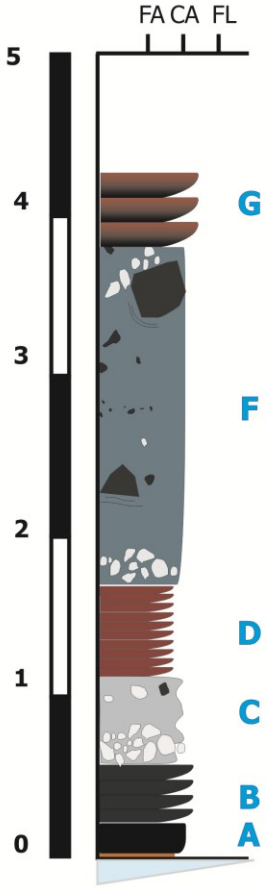

Unit G
This unit is 30cm thick. The overall colour of the deposits is brown, with black lapilli fragments and blue-grey bombs. At the base of the unit cross bedding can be observed well-sorted lenses of fine pumice lapilli (80%) are interbedded with medium ash layers (with less than 5% coarse ash and fine lapilli). These range from 2 to 6 cm thick, with the thickest beds at the top of this section of the unit. The crossbeds have a large length range. They are up to 25cm long near the bottom and form almost continuous layers near the top. Between 7 and 15cm from the top of the unit a layer of medium to fine ash is present. It is well-sorted with less than 5% coarse ash and fine lapilli. Within the top 7 cm of the unit the deposits consist of poorly sorted medium ash to coarse lapilli.
Maximum lithic:
4 x 4 x 3 cm.

Unit F
This unit varies in thickness from 196 to 256cm. It is very poorly sorted and consists of a predominantly medium ash matrix in which many ballistic fragments are embedded. The full range of grain sizes are represented in this unit. The ash is brown in colour, while the ballistics are a blue-grey "andesity" colour. There is a broad coarsening upwards within the unit, and 95% of the large ballistics are in the top 1.5m. The fine to medium lapilli fraction is dominated by pumices clasts (80%) in the lower part of the unit. In the upper part of the unit this fraction is dominated by lithics (60%). Bomb sags are present below the larger bombs (indicating decoupling from the main plume).
Maximum lithics:
A 64 x 38 x 25 cm
B 64 x 37 x 29 cm
C 60 x 35 x 26 cm

Unit D
The exposure is uniformly 50cm thick and is light to dark brown in overall appearance and consists of many (20 or so) alternating fine and coarse layers ranging from very fine ash to fine lapilli (surge deposits?). These are finely interbedded on a mm to cm scale, and exhibit low angle cross bedding. Individual packets are draped with very fine ash, which is light brown in colour. The medium ash is darker brown in colour. Fine lapilli are concentrated in fines depleted packages which are well-sorted. The fine lapilli are sub-rounded and scoreacious.

Unit C
This is a greyish brown, clast supported, pumice-rich layer, 14cm thick. The matrix is predominantly medium ash but contain almost 25% fine to coarse lapilli (grains >2cm make up less than 5% altogether). The pumice is golden brown in colour with dark blue iridescent centres. The maximum pumice clast is 34cm long and 8cm thick. The pumice is very crumbly. The pumice layer is discontinuous and forms a very uneven boundary with the underlying unit. Overlain by two packages which are separated by a poorly distinct contact.
The lower unit is 18cm thick, and the upper 22cm. The lower unit consists of poorly sorted fine ash to fine lapilli, which is dark brown to black in colour. The dominant grain size is medium ash (60%). The upper unit also consist of dominantly medium ash, but is better sorted than the lower part. The maximum clast is 6mm fine lapilli. Also, the upper unit contains a smaller proportion of fine material than the unit below.

Unit B
The unit is generally black in colour although ash layers are greyer. The unit is uniformly 43cm thick. The unit consists of a minimum of five coarse ash to medium lapilli layers interbedded with layers of fine to medium ash and capped by laminae of fine to very fine ash which are grey to tan in colour. These layers are normally graded and well sorted. The thickness of fine laminae increase slightly towards the top of the deposit (from 1mm near bottom to 3mm at top). Representative dimensions of the coarser lenses are 56cm long x 3cm thick, while the medium ash layers are 3.5 to 5cm thick and occur in between the coarse layers. These have been interpreted as surge packets. Note also that there is an uneven, "steeped" contact between this unit and the one above.
Components as in unit A.

Unit A
Dark brown to black with trains of lighter material (these are much finer grained). Tan coloured very fine ash layer at the base (1-2mm). This unit is also capped by a tan coloured fine ash layer. The layer is continuous and ~ 30cm thick almost uniformly. The unit is massive with occasional, pockets of light coloured fine material (up to 3cm across and 1cm thick). No internal bedding is visible. The unit consists of medium ash to fine lapilli sized fragments coarsening upwards. The dominant grain size overall is medium ash. Near the base, coarse ash account for approximately 10% of clasts, while fine lapilli account for 5%. Closer to the top fine lapilli continue to account for approximately 5% of clasts, but the proportion of coarse ash is closer to 20%. This layer is well sorted. The fine lapilli fraction consists largely of sub angular scoria. Componenet are exclusively blocky, poorly vesicular juvenile material.

G2; 263 cm
64° 23.983' N; 17° 22.417' W
02/08/2006 (TJ)

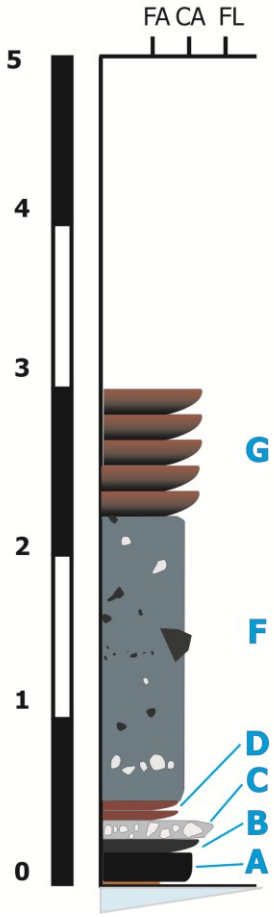

Unit G
This layer is variable in thickness between 10 and 20cm. It consists of 75% brown, medium ash matrix, and 25% coarse ash to fine lapilli. The fine lapilli are pumiceaous, light brown, and subangular. The coarse ash consists of black, angular scoria fragments as well as pumice. Note, however that there is a surficial lack of medium and coarse pumice. Rare lithic bombs can be found, mostly on the surface. The lithics make up less than 1% of this layer, and some have visible crystals within (plagioclase?). There is no apparent structure or fabric to the layer, although overall it is moderately well-sorted and matrix supported

Unit F
This is a 200cm thick, massive layer with a brown, predominantly medium ash matrix. The lower 125cm contains 80% medium ash. The remainder consists of clast ranging from coarse ash to bombs in size. The bombs make up less than 5% and are lithic fragments. The lapilli size fraction contains pumice, scoria and lithics. On the whole this part of the unit is very poorly sorted. The top 75cm contains approximately 20% bombs, which are grey, angular lithics and often have bomb sags beneath. Some have associated pumice trains. The matrix (brown, medium ash) makes up 60%, and 20% of this section consists of fragments in the size range coarse ash to coarse lapilli. Towards the bottom of this lithic-rich layer there are pumice trains with no associated bombs. These are up to 1.5m long and 10cm thick.
Bombs:
- 10 x 6 x 4 cm
- 10 x 10 x 12 cm

Unit C
Here, unit C has a maximum thickness of 10cm and forms a discontinuous pumice-rich lens, approximately 50cm in length. The matrix is black and consists predominantly of medium ash with 5% subrounded fine scoria lapilli. Pumice clasts are found in the size range medium to coarse lapilli. These are also subrounded and are light golden brown in colour on the outside surfaces with grey-blue iridescent interiors. The unit is matrix supported, comprising up to 30% pumice clasts.
Overlain by black to brown alternating layers. The black layers consist of medium ash to fine lapilli and coarsen upwards. These coarser layers contain lenses of fine lapilli towards the top, which have a maximum thickness of 2cm and maximum length of 38cm. The grains in the coarse layers are subrounded, moderately well sorted microvesicular black scoria clasts. The light brown layers consist of very fine to fine ash.

Unit B
The unit is 6cm thick and alternates between black and brown coloured layers. The unit consists of 3 crossbedded layer alternation between fine and coarse ash. The fine ash layers are 1mm thick and brown, while the coarse ash layers are black and up to 1cm thick. The coarse layers consist of well sorted medium to coarse ash comprising subrounded to subangular clasts. The "fine" layers consist of fine to very fine ash.

Unit A
This unit is 12-15cm thick, and black in colour. At the ice contact there is a tan coloured very fine ash continuous layer less than 1mm thick. The rest of the unit is massive and very well sorted, with grain sizes in the range of fine to coarse ash, but dominated by the finer fraction.

G3; 85 cm
64° 23.996' N; 17° 22.222' W
02/08/2006 (TJ)

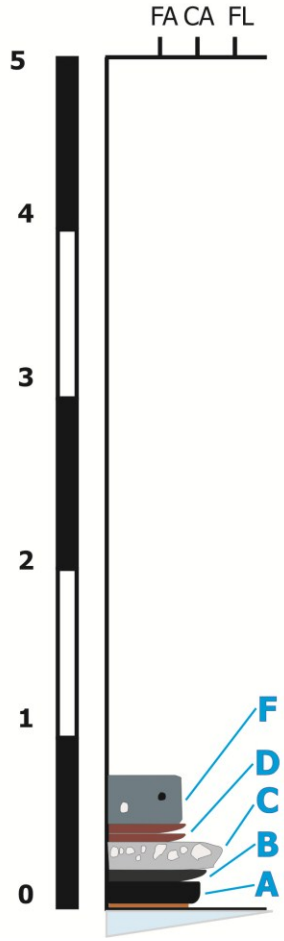

Unit F
Surge deposits (?). These are cross-bedded with 3 coarse lenses 4cm apart. The grain size in the coarse lenses consists of medium to coarse ash with <5% fine lapilli. The lapilli are subangular to subrounded black scoria. There is very little variation among the coarse lenses. The finer layers consist of fine to medium ash with 1-2% fine pumice lapilli. The unit is black in colour overall. Both the coarse and fine layers are continuous for over a metre despite being cross-bedded.

Unit D
This is a matrix supported unit. The fine to coarse ash matrix comprises 60-70% of this segment. The remainder is composed of pumice, scoria and lithic fragments from fine lapilli to bomb sized. The unit is massive, and poorly sorted.

Unit C
A lens of pumice-rich material between 8 and 12 cm in thickness. The matrix consists of fine to coarse ash (75%), 5% fine scoria and pumice lapilli, and 20% coarse pumice lapilli. Lenses of pumice are approximately 20cm across and 5cm thick. The pumice has a reddish golden brown exterior with grey shiny interiors. The pumice lenses are discontinuous and offset from one another. This layer also contains a decoupled lithic fragment with an impact structure beneath and an associated pumice train occupying the entire thickness if the layer.

Unit B
This segment is black and contains discontinuous crossbedding with alternating coarse and fine lenses, coarsening upwards. At the base the layers are 1-2cm thick, while towards the top the coarse lens are up to 4cm thick. The finer layers are uniformly 1cm thick. These are made up of fine to medium ash with 5% coarse ash near the top. Towards the bottom, the coarse ash is missing. Coarse layers at the base consist of medium to coarse ash with 10% fine, black, subrounded, well sorted, scoria lapilli. At the top the coarse lenses consist of up to 40% scoria lapilli.

Unit A
This unit is 3cm thick with a 1mm layer of tan coloured very fine ash at the base. The layer is black in colour and consists of well sorted medium to coarse ash overall, interbedded with some discontinuous tan layers of very fine ash which are less than a mm thick. The boundary with the overlying layer is very poorly defined.

G4; 566 cm
64° 24.067' N; 17° 21.900' W
02/08/2006 (TJ)

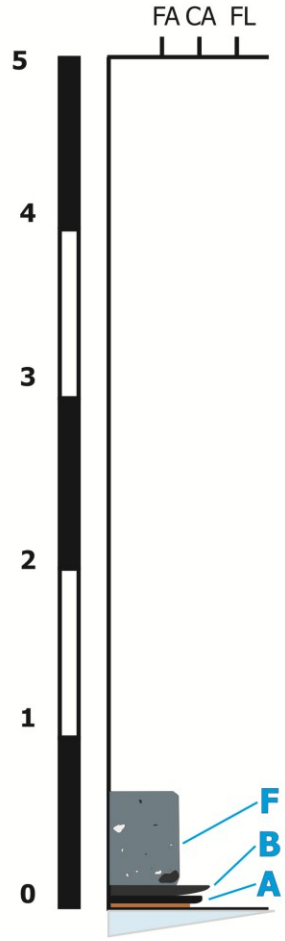

Unit F?
Next 67 cm
This segment is brown overall, and poorly sorted, but shows some reverse grading. It includes occasional, discontinuous pumice lenses up to 40cm in length, with a maximum thickness of 15cm. The individual pumice fragments are up to 8cm long with a light brown exterior and blue-grey interior. The matrix of this unit consists of medium to coarse ash and makes up 70-80% of this segment. Fragments that are medium lapilli sized and larger are concentrated in the top 20cm (up to 20%). These tend to consist mostly of lithic fragments. There are fewer large bombs here than in previous sections, although the maximum sizes remain similar. These have traces of medium to fine pumice lapilli lag.
Representative Lithics:
- 22 x 20 x 5 cm
- 19 x 13 x 6 cm
- 20 x 17 x 7 cm
- 19 x 16 x 11 cm
- 20 x 20 x 15cm
Big Blocks:
- 78 x 26 x 75 cm

Unit C, or part of F?
Next 8 cm
This is a brown layer medium to coarse ash overall. It contains up to 25% fines black subrounded to subangular scoria lapilli and occasional (!) fine pumice lapilli (possibly incorporated from the layer above?).

Unit A
The layer ranges between 2 3 cm thick. At the base, there is a layer of tan coloured, very fine ash which is less than an mm thick. The layer is massive with no distinct structure and consists of black, fine to medium ash.

G5; >460 cm
64° 24.483' N; 17° 23.283' W
04/08/2006 (TJ)

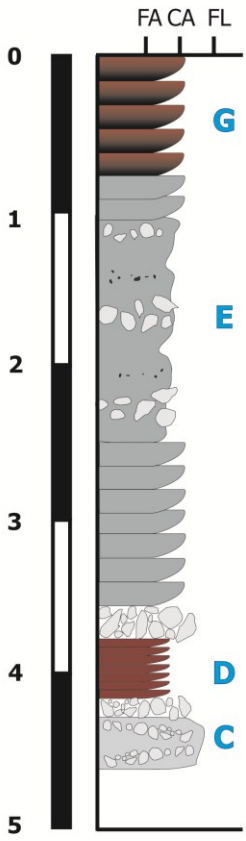

Bottom >35cm
This segment is brown to black in colour and is crudely layered. The layers are ~5cm thick - boundaries between the layers are not very distinct. "Coarser" layers consist of coarse ash to fine lapilli (10%). 70% of the lapilli are black scoria and the remainder are golden brown pumice. The finer layers consist of medium to coarse ash with 5% black scoria lapilli. These layers are brown in overall appearance.
75 cm layer containing "sub layers"
Bottom 50 cm of this 75cm unit
Black, medium ash to coarse lapilli. The layer is dominantly medium ash 90%. Of the fine lapilli fraction, 90% are golden brown pumice and 10% black scoria. This layer contains 4 distinct pumice trains, which are clast supported. The matrix of these trains contains 40 % black medium ash, 48% fine lapilli, 10% medium lapilli, and 2% coarse lapilli. It is not clear whether these pumice trains are continuous bands of very variable thickness of many discrete lenses.
Top 25cm of this 75cm segment
Here we see alternating fines-rich and fines-poor layers of ~5cm thickness. The coarse layers are 20% dark brown coarse ash, 55% fine scoria lapilli, 20% medium scoria lapilli, and 5% coarse pumice lapilli. The medium lapilli are blocky, while the fine lapilli are more shard like. Both are black in colour. The fine layers make up 2/3 of this part of the deposit and consist of 80% medium to coarse ash and 20% fine lapilli, both of which are angular black scoria fragments.

Next 15-20 cm
This is a clast supported pumice layer with a brown-black coarse ash matrix. The pumice is in the fine to coarse lapilli size range and is angular and broken up, with quenched rims and 2-3mm sized vesicles in the core.

Next 30cm This is a black layer with distinctive tectonic offsets with respect to the layers above. It is crudely bedded, showing possible cross-bedding and consists of alternating coarse and fine layers (up to 5cm thick). The fine layers consist of coarse ash (95%) and fine lapilli (5%), and are black in colour. The fine lapilli are black, scoria clasts that are sub rounded and blocky. The coarse layer consists of coarse ash (50%) to medium lapilli (5%). The ash is brown while the medium lapilli consist of golden brown angular pumice. The fine lapilli are dark grey, blocky, angular scoria. There is one large grey lithic bomb (22 x 22 x 13 cm) in the layer and associated bomb sag. The bomb is angular.
"Unit" approximately 178cm

Next 3-10 cm
This layer is brown and well sorted. Clasts are in the size range coarse ash to fine lapilli (10%). The fine lapilli are platy and shard-like black scoria.

Next 20 cm
Laterally discontinuous pumice lens, approximately 3m in length and up to 10cm thick. The lens is clast supported. Pumice clasts range from fine to medium lapilli in size, but are dominantly fine lapilli. They are golden brown in colour with dark grey cores. The matrix make sup 10% of the lens and consists of black, medium ash.

Next 20cm
This is a crossbedded unit. The crossbeds are 2-5cm thick and appear to be inversely graded overall (it is difficult to tell as there is considerable variability). Towards the top the fine units are dark brown and consist of medium ash to fine lapilli (25%). The fine lapilli are black, platy scoria. The coarser layers consist of 20% coarse ash and 70% fine lapilli, and 10% medium lapilli. The lapilli are black, sub-rounded scoria, with <5% golden brown pumice.

Next 20cm
Pumice lens as before

Next 35cm
This is a crudely layered unit, which possibly contain slow angle crossbedding. The layers are 2-3cm thick, and consist of fine golden brown pumice lapilli interbedded with layers that consist of 90% coarse ash and 10% fine scoria lapilli. The scoria and black, subangular and occasionally platy (<1%).

Next 20cm (max thickness)
Pumice lens as before
Next 5-10cm
Well sorted fine to medium black ash.
Next 20cm (max thickness)
Pumice lens as before
Top 45cm (within 178cm layer)
This section is crudely bedded and crudely coarsens upwards. It is matrix supported throughout. The matrix is fine to medium ash, although at the base there is 5% fine lapilli, which are angular black scoria. (Note: this is reminiscent of unit D in section G1). Towards the top there is up to 20% coarse ash/fine lapilli. At the upper contact, the boundary is sinusoidal (dune like structures?). Also a bomb is present, which is 10 x 10 cm in cross section. It is weathered on the surface but is probably grey basaltic andesite which has fallen in to the layer.

Top 95cm alternating black and brown layers, crudely layered, grain size changes according to different layers...

Next 6-15cm
This is a continuous layer of jet black, well sorted coarse ash to fine lapilli. It exhibits low angle cross bedding. The fine lapilli are slightly glassy (5%) scoria clasts and are generally confined to the coarser lenses. These coarser lenses have a maximum thickness of 5cm and a maximum length of 20cm. Tan brown, fine to very fine grained ash laminae occur randomly.
This layer is capped by a 1-3mm tan coloured fine ash layer.
Then, this is overlain by a <1cm thick subrounded to subangular coarse layer which consists of 80% fine lapilli in a medium to coarse ash matrix. The fine lapilli are scoria.

G7; 260 cm
64° 23.933' N; 17° 22.433' W
05/08/2006 (TJ)

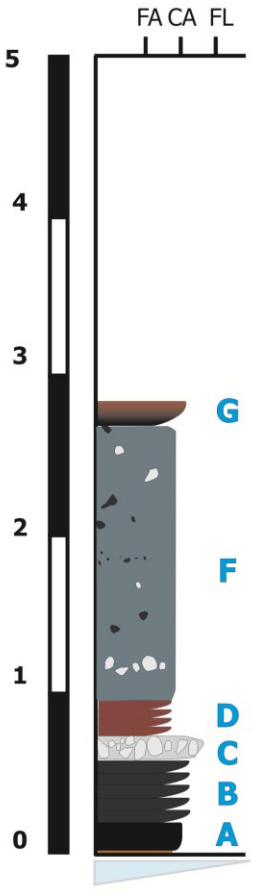

Units A and B (40-58cm total)

Unit A
This unit is 13-16 cm thick. The unit is massive and consists predominantly of coarse ash to very coarse ash, with particles in the range from fine ash to medium lapilli. The typical upper end of clast size is 6-8mm. Occasional juvenile and lithic fragments occur in the size range 15 to 25mm. The unit is moderately sorted; clast supported, and fines poor. Dominant clast population is black, blocky and platy, non to moderately vesicular juvenile clasts, with <5% lava lithics up to 25mm. There is no pumice present. Occasional fusiform clasts can be found. At the base of the layer there us a 15cm juvenile bomb. At the very base is a sub mm layer of very fine grained brown fine ash laminae.

Next 5 -16cm
This section is black in colour and consists of medium ash sized particles on average, with a size range of fine ash to fine lapilli. The maximum clast is 7-8mm, although clasts of this size are rare. As a whole, this section is moderately sorted, clast supported and fines poor. This section displays low angle cross bedding, with individual beds 0.52 cm thick and 15-50cm in length. Each cross bed is normally graded, with very coarse ash at the base up to medium ash with very fine ash caps. They are well sorted and clast supported. The very top of each unit is capped by an mm thick fine ash layer. The componentry is black, blocky, moderately to non-vesicular (as in the unit below), with a similar lithic population to the unit below. There are a few red oxidised lava lithics.

Next 15- 26 cm
This is a black, massive layer of generally very coarse ash, although the clast size ranges from fine ash to medium lapilli. The maximum clasts are 10-12mm in size. This layer is clast supported, moderately poorly sorted, and fines poor. The componentry is similar to the bottom, massive layer but with more moderately vesicular clasts. Normal lava lithics are present along with hydrothermally altered and red oxidised scoria. The lithics are smaller than before with a maximum length of 13mm. There is more red oxidized scoria than lava lithics. At the top there is a 1.5-2 cm thick horizon of fine to medium ash capped by laminae of grey-brown very fine ash.

Next 5cm
This layer is black and consists mostly of fine to medium ash, although particle size ranges from very fine ash to coarse ash, except for the top 0.5 to 1.5 cm where it is coarser (mostly medium to coarse ash, with a range from fine ash to very coarse ash). There are occasional fine lapilli clasts (10mm). Overall this section of the deposit is clast supported and fines poor. This part of the unit is crossbedded, with individual crossbeds 3-15mm thick, and 15-50cm long. These are low angle crossbeds, and each is normally graded as below. Individual layers of the crossbeds are well-sorted. The lower 3 to 4 cm of this section contains most of the crossbedded sets, which are finely graded. The finer beds consist of medium/coarse ash to fine ash, while their coarser counterparts are composed of very coarse ash to fine ash.

C/D Package, 9-20cm (variation mostly in C)
This part of the deposit is greyish-brown in colour (apart from the pumice lenses and trains) and is massive. It consists mainly of fine to medium ash, ranging from very fine ash to fine lapilli. The largest clasts are 10-15mm pumice, although these are more typically 5-6mm in length. The layer is very poorly sorted, fines-rich and matrix-supported. The coarse fraction consist of very coarse ash to fine lapilli and is composed of a mixture of black, blocky, non to moderately vesicular lavas and brown pumices. The clasts are typically coated with fine ash and so it is difficult to tell the lithic proportion (probably <1%). The layer has distinctive pumice lenses and trains around 3-5cm above the base to 10-13cm above the base. The lenses are between 4-7cm thick, and 50-100cm long, and consist of medium to coarse lapilli, well-sorted, clast supported, fines poor individual pumice clasts coated by fines (especially on top). These are entirely highly finely vesicular brown pumice sometimes with silvery-grey cores with 1-3mm large vesicles. At the same horizon there are 1-2 grain thick trains of pumices up to 50cm long. Above the pumice lenses there are 0.5cm thick and 1-2cm long trains of lapilli clasts, usually pumice (incipient structure?).

D
This unit is 2-3cm thick. The contact between C and D is a sharp transition, although not exactly a bedding plane. The unit goes from brown to black to brown to grey, and is massive, mostly medium to coarse ash, with a size range from fine ash to very coarse ash. Maximum clasts are approximately 4mm. It is moderately sorted, clast supported, with a moderate amount of fines. The coarse ash to very coarse ash is dominantly black, blocky, platy, and non to moderately vesicular material with rare brown basalt pumice.

E
This unit is 15-19cm thick and is grey-black to grey-brown in colour, and consists of medium to very coarse ash on average. It is moderately sorted; generally clast supported and fines poor, with grain size in the range fine ash to fine lapilli. The maximum grains are between 7 and 9mm. The layer contains distinctive crossbeds. Individual sets are 10 50 cm long and 1-2.5 cm thick. The cross beds are normally graded from very coarse ash or fine lapilli to medium ash. At the top they are capped by a 2-5mm fine ash horizon. Occasionally these are capped in turn by sub mm laminae of brown very fine ash. Individual ash beds are very well to well sorted. The lower coarse part is devoid of fine ash. It is clast supported and dominated by black, blocky, poorly to moderately vesicular clasts. Platy fragments occur to a lesser extent. The fine ash fragment is dominated by curls of basaltic pumice (i.e. like broken vesicles). This layer is devoid of lithics or very lithic poor.

Unit F

G10; >480 cm
64° 24.000' N; 17° 23.400' W
09/08/2006 (TJ)

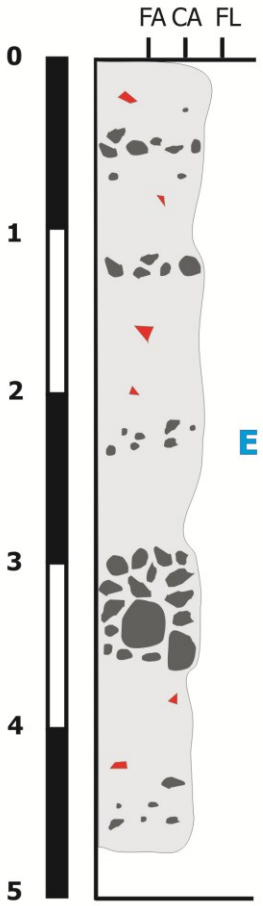

Top 150 cm
This section is massive and brown in colour. There is no apparent grading or structure and it is poorly sorted. Lots of semi-continuous to discontinuous pumice lenses occur throughout. Pumice clasts are up to 15cm maximum length. Grain sizes occur in the range fine ash to medium lapilli, although the section consists mostly of coarse ash. Occasional red lithics are present. The lapilli are very blocky and angular and consist of poor to moderately vesicular scoria and pumice. The bottom 50cm of this segment contains approximately 3 somewhat continuous pumice layers 10cm apart, approximately 1 grain (5-10cm) thick.

Next 75cm
As above, but also some fusiform scoria (twisty) with big bubbles in the middle (10 x 5cm). Maximum pumice clast is 22cm long.

Next 95cm
As before, except the bottom 50cm of this part consists of stacks of pumice.

Next 160cm
Again, more or less the same as before, but with lots of yellow-orange hydrothermally altered clasts, 1-8cm long. Large pumice clasts occur sporadically throughout. Overall, this section has a finer matrix (fine to medium ash), with pockets of fine ash. The deposit is very well sorted.

Bottom 10cm
This section of the deposit is black, well-sorted and relatively well indurated. It consists mainly of medium ash, but clasts range in size from fine ash to fine lapilli (<5% scoria lapilli). The deposit is cut by yellow-orange veins (hydrothermal alteration?).

G11; >274 cm
64° 24.033' N; 17° 23.333' W
09/08/2006X (TJ)

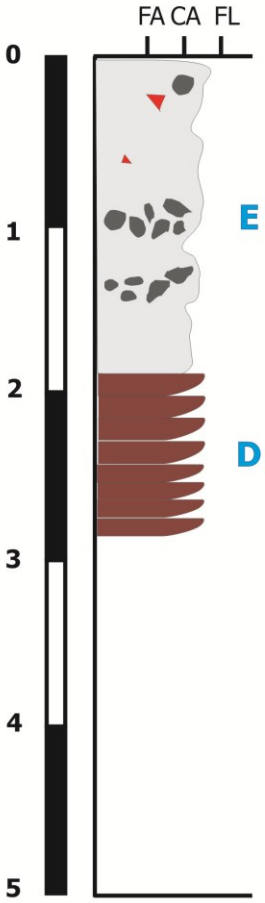

Exposed base to 95cm ("surge 1"?)
This segment of the section is crossbedded, with alternating brown fine layers (fine ash) and coarser black layers (mostly coarse ash, but ranging between medium ash and fine lapilli). Within individual corssbed sets the deposit is well sorted. This segment also contains many randomly interspersed big (5-10cm) pumice and scoria clasts. The deposit is most pumice rich at the base, although there are occasional pumice-rich horizons throughout. The crossbeds become less distionct towards the base (it becomes sort of massive), and this segment may be broadly coarsening upwards.

Next 33cm
Pumice horizon: This is brown, and mostly clast supported (apart from a 10cm thick layer of "matrix" in the middle). The pumice is semi-continous (80cm long), with a fine ash matrix.

Next 15-20cm
"surge 2"
This unit is crossbedded, and consists of predominantly fine to medium ash with lenses of fine lapilli.

Next 4cm
Well sorted, massive, medium brown coloured medium ash to fine lapilli.

Next 22cm
Faint structure

GH3; 55 cm
64° 24.141' N; 17° 23.169' W
03/08/2006 (TJ)

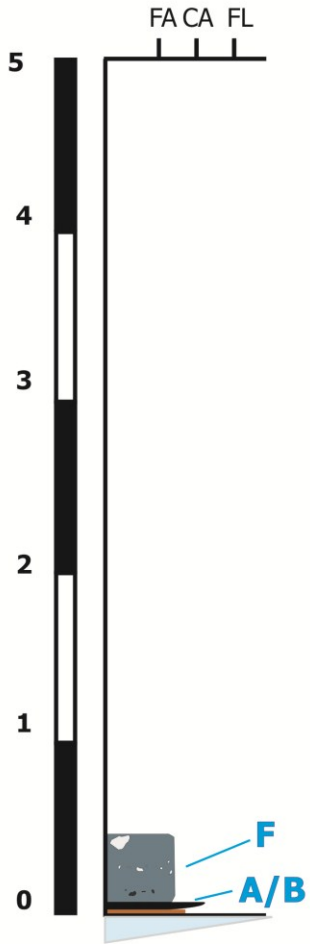

This section is 45-55cm thick in total. At the base there is a trace of brown (not tan) very fine ash.
This is overlain by 2-5mm of black fine to medium ash (Unit A?)
This is overlain by 3-5cm of crossbedded, alternating black coarse/ brown fine sets. The coarse sets contain fine ash to fine lapilli. The lapilli consist of black poorly vesicular scoria. The fine layer aare composed of fine to medium ash.
The remainder of the section is massive with (perhaps) some very indistince bedding. It is brown overall and clasts are in the size range fine to medium ash with 1% fine lapilli. The lapilli are black scoria.
The top 8cm consists of the same matrix as lower down, and is matrix supported, but contains 5% or fewer lithics.
Maximum clasts:
10x6x5 cm, 13x9x7 cm, 6x5x3 cm, 8x5x4 cm, and 7x5x4 cm

GH9; 209 cm
64° 23.850' N; 17° 22.483' W
07/08/2006 (TJ)

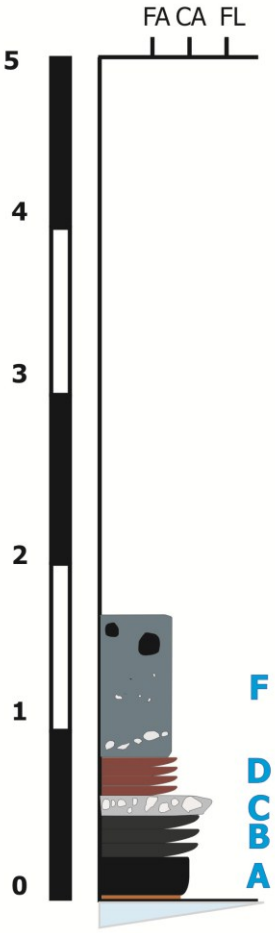

Unit F
This unit is more than 105cm thick. It is massive (as before) and consist of medium ash to small bombs. It is brown in colour overall and contains fewer bombs than in previous localities. The maximum lithic is 47x40x29cm. The boundary between E and F is fairly indistinct but seems to be marked by pumice trains which are 1-2 grains thick, 12cm long. This layer has a predominantly medium ash matrix, and is matrix supported. The largest blocks are very near the surface, while sporadic pumice trains are mostly confined to the base of the unit.

Unit D
This unit is 27-32cm thick. The clasts in this unit range from medium ash to fine lapilli, predominantly consisting of coarse ash. The crossbedding is much less distinct that in previous sections. Individual layers are well-sorted within the layer and alternate between coarse and fine. The coarse layers consist of coarse ash to fine lapilli (70:30). The fine lapilli are black, blocky scoria and are poorly to moderately vesicular. The fine layers consist of medium ash with up to 5% coarse ash/fine lapilli. (same componentry). Occasional lithic fragments are present, with a characteristic size of 15x8.5x7 cm.

Unit C
At the base of C or top of B there is a laterally discontinous lens (20 x 3cm) of black fine to medium lapilli. This is poorly to moderately vesicular scoria, which is often platy and shard-like.
This layer consist of many clast supported pumice lenses in a poorly sorted matrix (40%) of brown medium ash to fine lapilli (10%). The fine lapilli are moderately vesicular black scoria and golden brown pumice. The maximum length of the pumice lenses is 90cm. The maxiumum lithic in this layer is 13x10x07cm, and is a vesicular dark grey basaltic clast with vesicles sizes of 1-5mm.

Unit B
This unit is 42cm thick and is brown-black in colour. Grains occur in the size range from medium ash to fine lapilli, with coarse ash dominating. The unit contain indistinct crossbeds, which appear to be fining upwards. The fine lapilli are predominantly blocky to shard-like in morphology, and consist of poor to moderately vesicular black scoria. The top 3-5cm consist of medium to very fine ash, fining upwards. The layer is brown in colour and has a stepped boundary with the layer above.

Unit A
This layer is 25cm thick and consists of a black unit that is well sorted and consists of clasts in the size range medium ash to fine lapilli, with coarse ash dominating. There is a sub-millimeter tan very fine ash layer at the base. The unit is massive, broadly coarsening upwards. The fine lapilli are poorly to moderately vesicular black scoria, which are generally

TS1; >220 cm
64° 23.877' N; 17° 23.062' W
05/06/2007 (TJ)

TS12; >115 cm
64° 23.871' N; 17° 23.008' W
05/06/2007 (TJ)

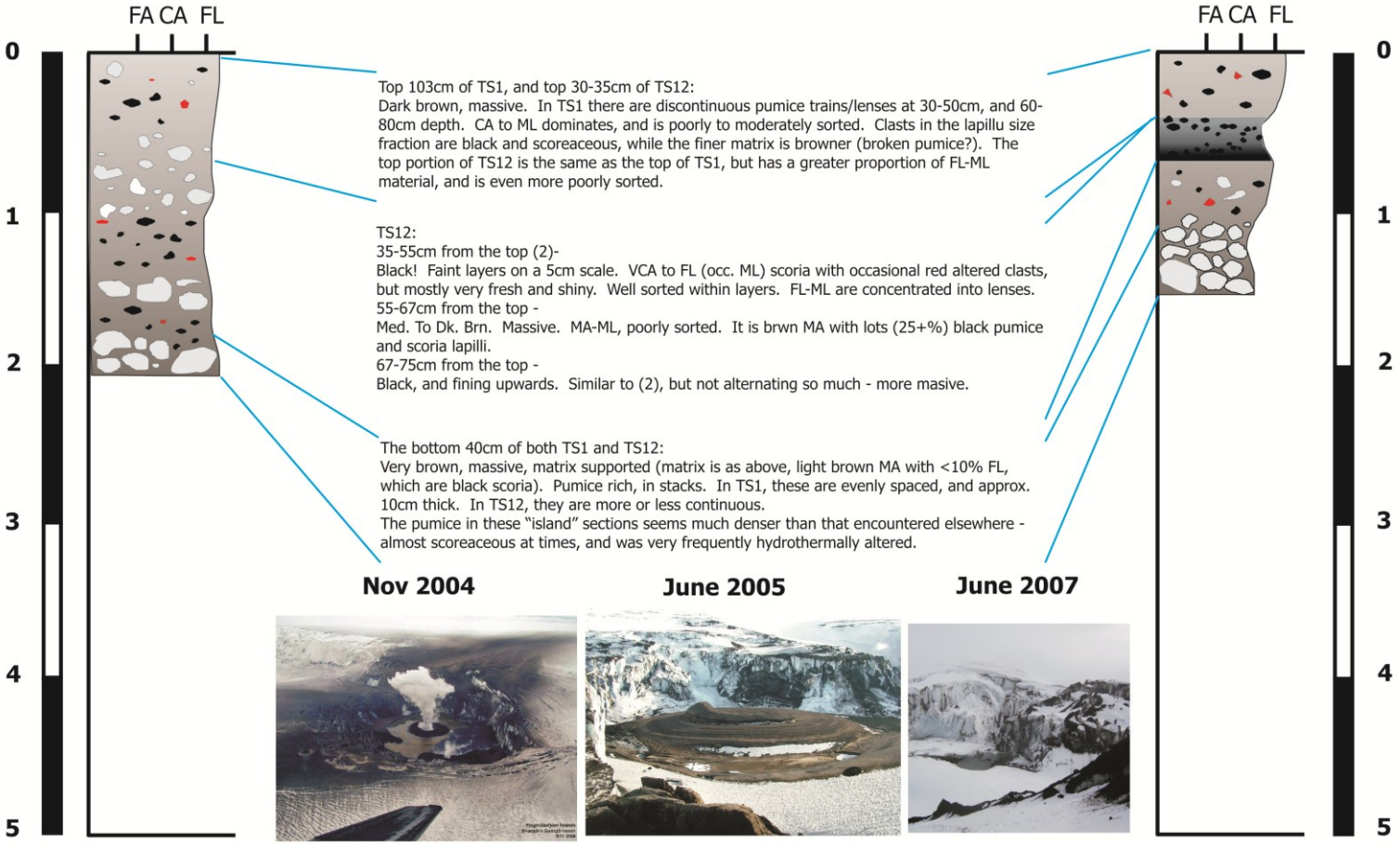

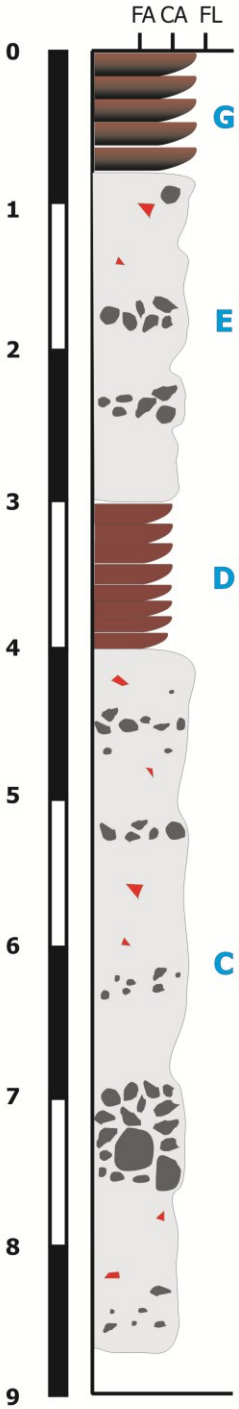

TS6; >810 cm
64° 24.030' N; 17° 23.257' W
04/06/2007 (TJ)

Top-down
(1) Black, faintly cross-bedded. Some coarser lenses (medium ash with 25% fine lapilli scoria). Average is medium medium to coarse ash. Occasional bombs and pumice (<10 cm).
(2) Top 70 cm. Pumice clasts up to 14x9 cm. These are blusish black and scorieaciuos. Deformed below a big bomb. Blue black scoria with a golden pumice rind. Medium ash to fine lapilli matrix, very coarse ash dominant. Armoured lapilli and red altered lapilli are present. Red ones approx. 5 per square metre. A few (5%) very large (1-5 cm) pumice clasts and 25? Matrix supported. To bottom (124 cm total): more Golden pumice towards the bottom (<10 cm on average), 60% matrix, 40% pumice. Contains a bomb 48 x 24 cm.
(3)Next 35 cm: Black overall, more or less massive but perhaps faintly crossbedded. Medium ash to fine lapilli, dominantly black coarse ash scoria, but also fine to medium lapilli pumice. The pumice appear to be concentrated in little layers/trains 1 grain thick and a few cm long, perhaps giving the impression of being crossbedded. Moderately sorted, lots of orange-red clasts.
Next 61 cm: at 42 cm start to have definite layers. As before, looks somewhat less massive with alternating ~2 cm thick, continuous over ~10 cm fine and coarse lenses. Coarse are coarse ash to medium lapilli, fine are medium ash. Quite well sorted within lenses.
(4) At 42 cm there is a coarse almost continuous layer that is 5cm thick. Then a fine layer (5 cm; medium to coarse ash), then 7cm coarse layer (80% pumice 0.5- 1cm in diameter). * This bit is confusing check graphic log*
(5) 104 cm: Relatively uniform from last distinct pumice layer to the next. Black, moderately well-sorted, predominantly medium ash with one large (10x6 cm) black scoria fragments and occasional fine to medium lapilli golden pumice. Some medium lapilli are altered red clasts approximately 5/m2.
(6) 19-34 cm: Brown medium ash with occasional pumice (fine lapilli) cross-layers, semi-continuous, average is medium ash. Range is medium ash to medium lapilli.
(7) Next 48 cm: same as in layer 5.
(8) Next 124 cm: Brown, layered, pumice bombs at top (dark black scoria to golden pumice), clasts up to 15 cm long matrix supported ma, moderately sorted ma to fine lapilli. 36 cm to first 1-2cm layer of very coarse ash, then 1-2mm tan vfa. Starting to freeze, hard to pick out structures. 2-3 cm brown medium ash then the same again.
24 cm to next very pumice-rich part as before in layer 2. Stacks of pumice fine lapilli to large bombs. 25-30% is medium ash matrix. This part of the section is quite hard compacted and frozen.
(9) Next 55 cm: Black, more or less massive, perhaps vaguely bedded (crossbeds or lenses) but very indistinct. Medium ash to fine lapilli, medium ash dominates. Moderately well-sorted. Occasional pumice near bottom. On a decimetre scale there are up to 5 coarse trains of fine lapilli. Mostly dense, black juvenile material. Occasional golden pumice (more of the same for 8 cm more).
(10) Next 20 cm: back to pumice-rich layers as before. Black to golden scoria to pumice in a medium ash matrix. Matrix supported.
(11) 23 cm as above, relatively massive, black medium ash to fine lapilli.
(12) Next 104 cm: 42 cm to top of 1st pumice stack, pretty massive, perhaps faintly layered with a coarse lens near the bottom.
To bottom: (810 cm) pumice stacks as before but more obviously layered on a decimetre scale.

TS18; 240 cm
64° 24.369' N; 17° 23.722' W
07/06/2006 (TJ)

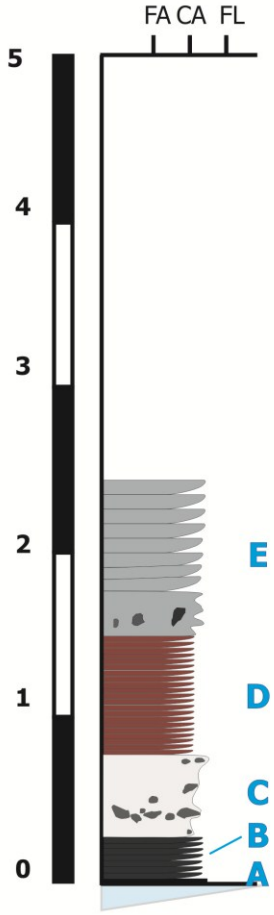

Unit E
8 cm dark brown, massive, very well sorted, fine to medum ash.
8 cm, black, fairly well-sorted medium ash to fine lapilli (<5%) massive.
Top 60-70 cm layer brown to black, crossbedded, approximately 6 alternating coarse and fine layers. Coarse layers are 1-4 cm thick, fine layers are 5-16 cm thick. Well sorted within layers. Fine layers are fine to coarse ash, coarse layers are <90% fine lapilli black scoria and occasional golden pumice. Near the top are occasional 10 cm golden pumice.

Unit D
Brown unit. 75 cm. Many indistinct layers, approx 5 cm scale, alternating between relatively fine and relatively pumice-rich coarse horizons. Composition of the coarser bits is the same as the bulk composition of the fine. Fine to coarse ash predominates, fine, gluey due to wetness. Pumice up to 9cm across are predominantly less than 5cm. Golden pumice and also black scoria clasts approx. 5 cm. less than 5% black scoria, occasional red, altered fine lapilli.

Unit C
10 cm. Medium to coarse ash. Near the top are medium coarse ash with up with 50% fine lapilli. Dark brown, contact with unit below is relatively indistinct. 2cm thick coarse lens 4 cm abve the bottom. Overall this layer in fining upwards medium ash to fine lapilli at the bottom.
7 cm thick black massive fine to medium ash with occasional (< 5%) fine lapilli scoria clasts.
42 cm. Faintly layered on a decimetre scale, near the bottom it is pretty massive, moderately to poorly sorted. Range From fine ash to coarse lapilli, average medium ash. 5-10 %
Pumice. Top 0.5 cm is lighter brown fine ash.

Unit B
17-20 cm, low angle crossbedding. Well sorted within layers. Coarse layers are 2 cm thick and consist of medium ash to fine lapilli. Fine layers are 3-4 cm thick and consist of Medium ash with less than 5% coarse ash.

Unit A
1 cm very black medium to coarse ash comprised of poorly vesicular blocky fragments. 1mm light brown fine ash at the Very bottom.

TS19; 200 cm
64° 24.459' N; 17° 23.750' W
07/06/2007 (TJ)

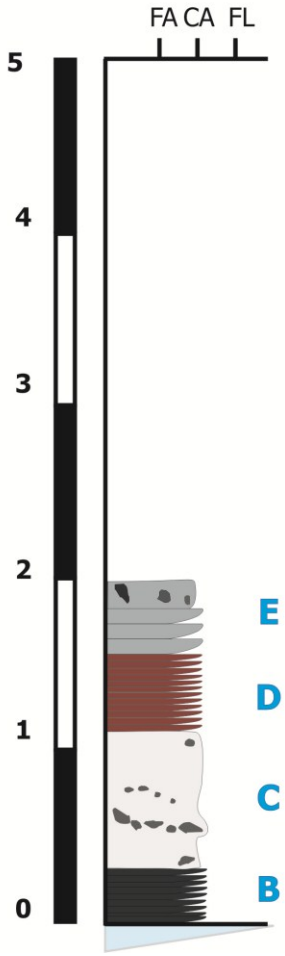

Unit E
Top 15 cm: Brown, massive, poorly sorted fine ash to fine lapilli (50/50). Occasional angular medium lapilli lithic fragments. Juvenile fine lapilli are pumice.

Unit D
45 cm: layered, lighter brown than previous, more than ten layers which are alternating coarse and fine. Fine layers are medium ash to fine lapilli, coarse are medium ash to medium lapilli. Lots of pumice clasts <5 cm scattered throughout. 3/10 cm2.

Unit C
25 cm. Clast supported pumice layer, continuous, bluish grey and golden brown pumice (individual clasts). Max 5-10 cm. Lithic 15x12x8 cm. Virtually no matrix to speak of. What is there is brown, coarse ash, which could be crushed pumice.
15-20 cm. Layered unit. Top 4 cm brown, well sorted medium ash, 3 layers 1-3 cm thick. All well-sorted medium ash. Slightly coarser layer has >15% fine lapilli pumice there are brownish 4-6 cm finer layers at the top and bottom.
35-40 cm: pumice layer as before, but larger proportion of matrix (<30%)., quite a few red and orange altered lithics (10/10 cm2).

Unit B
20-22 cm. Layered unit. Alternating black-brown on a loosely 5 cm scale. Black layers are medium to coarse ash

TS21; >180 cm
64° 24.047' N; 17° 22.935' W
08/06/2007 (TJ)

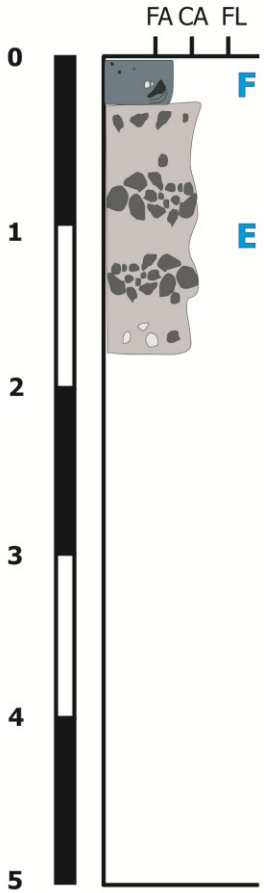

Unit F
18-25 cm. Brown, massive, relatively poorly sorted medium ash to coarse lapilli. 80-90% medium ash. Lapilli are Pumice fragments, quite a few lithics i.e. >15/50 cm^2.

Unit E
Pumice stacks. Alternates between matrix and clast-supported horizons on a 20 cm scale. Predominantly matrix supported. Matrix is the same as in 1. Pumice have a grey core and Golden brown exteriors. Some are quite big, up to 40x 20 cm.

Ts23; 180 cm
64° 23.893' N; 17° 22.365' W
08/06/2007 (TJ)

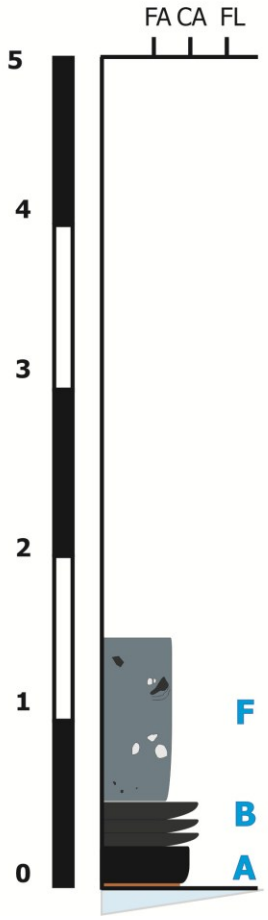

Unit F
Top 95-100 cm like layer F previously. Brown, massive, poorly sorted, fine to medium ash matrix, contains a range of pumice and lithicsin the fine lapilli and larger size fractions.

Unit B
Next 27-33 cm: Brown, crossbedded, fning upwards, medium ash to fine lapilli range all over, greater proportion of Oarse ash and fine lapilli in coarse sets and near bottom.

Unit A
Another 42 cm to the bottom of the section, a but frozen in places so it is difficult to evaluate the layering etc. The top of this 42 cm segment is capped by a 1-2 mm very fine ash. Several laminae in the top 3-5 cm. The stuff in between is black, well-sorted medium to coarse ash. 8 cm to the next vfa laminae. In between is coarse ash to fine lapilli, indistinctly layered.
The rest of it is very hard to tell because it is frozen. But it looks like black medium ash to fine lapilli scoria, and looks relatively massive athough the slightly larger fragments may be concentrated in discontinuous lenses and layers giving it a slightly cross-bedded air.

Ts26/25/30 Composite; 196 cm
64° 23.878' N; 17° 22.433' W
09/06/2007 (TJ)

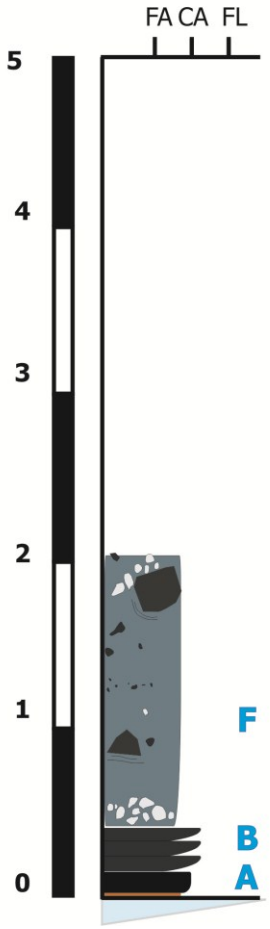

Unit F
150 cm brown, massive, poorly sorted, lithic rich. Larger bombs are concentrated at the very top and base of the unit. Matrix supported. A considerably amount of golden pumice, often associated with lithics max lithic = 23x38X30 cm. quite a few red altered lithics matrix is brown fine to medium ash range in this layer is fine ash to bombs. Lithics and golden pumice are fine lapilli and larger. Less juvenile black scoria than other components.

Unit B
27 cm dark brown more or less massive, perhaps faintly crossbedded (only really appears that way when deformed by bomb) possible reverse grading. * Go back to notebook for more detail of structures along section.*

Unit A
Bottom 5 cm is well sorted medium to coarse ash with fine lapilli. Top is medium ash to fine lapilli reverse graded higher proportion of fine lapilli at top. Dense black scoria, well sorted.

Ts34; 95 cm
64° 23.920' N; 17° 22.262' W
09/06/2007 (TJ)

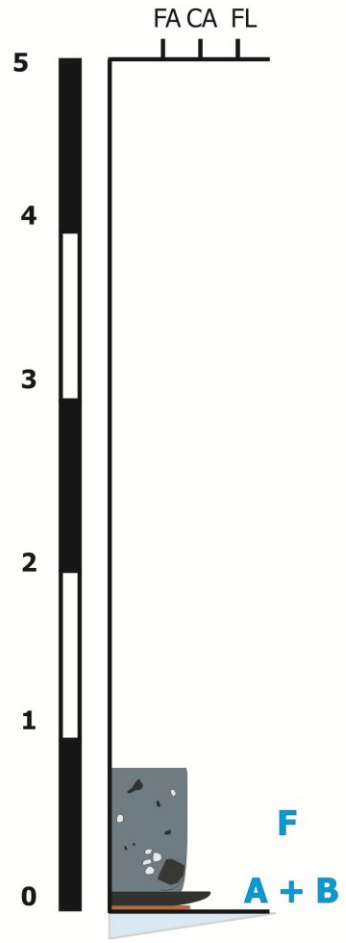

Unit F
75 cm: like unit F previously but with some additional structure near the bottom.
Bottom 30 cm is crossbedded, 15-20 cm into this bottom 30 cm is a pumice train. Brown, pumice train is only semi-continuous, matrix supported, golden pumice. 5-10 cm clasts and smaller fragments. At least 5 coarse layers which are medium ash to fine lapilli (60%) black scoria no more than 3 cm thick and over 30 cm long. Fine are fine ash to fine lapilli. Less than 10% fine lapilli 3-5 cm thick. Different unit at the pumice boundary?
Fallen lithic more than ½ m in diameter can't dislodge to measure properly.

Unit B
10-12 cm. Lots of layers, crossbedding, black to brown, 5 very fine ash tan brown laminae 1.5-3 cm apart. Fining upwards. Medium ash to fine lapilli in coarse layers near bottom, fine ash to coarse ash near top, sets like in previous sections with normal graded sets.

Unit A
0.5-1 cm. Very black, fine to coarse ash, massive. 1mm tan very fine ash at bottom.

Ts35; 402 cm
64° 23.915' N; 17° 22.512' W
09/06/2007 (TJ)

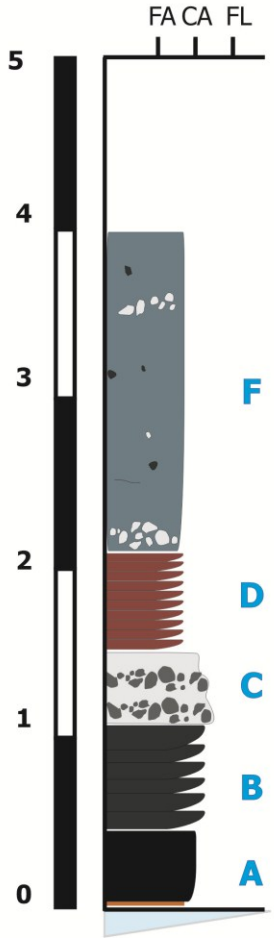

Unit F
190 cm: Massive, very poorly sorted, brown matrix, matrix supported, matrix is medium ash to fine lapilli. Contains all components (pumice, scoria, lithics), lots of bombs and sporadic pumice lenses, some semi-continuous, others associated with bombs. Possibly some faint cross-bedded structure within the bottom 40 cm of this unit.

Unit D
60 cm: bounded at top and bottom by pumice. Layered. Approx 10 packages coarsening upwards, mm-thick tan brown, brown very fine ash at base of each package. Pumice layer is pretty continuous.

Unit C
28-45: Variable thickness, mostly around 30 cm. Where it gets to 45 cm it may be overthickened in a slumped bit. Pumice, a few lithic fragments in with the pumice as well. Matrix supported. Matrix is medum ash to fine lapilli dark brown scoria. Pumice is fine lapilli and upwards in size. Biggest clast are 10 cm but these are rare. Pumice and mostly golden at rinds and bluish in interior.

Unit B
57-60 cm: There is no distinct boundary with unit below, seems to grade in. layered/crossbedded approximately 8 packages normal grading. Tan very fine ash laminae in between each set. Look almost same as ones on top. Well sorted with in layers coarse and fine layers approximately 1-2 cm thick each. Fine are medium coarse ash, coarse are coarse ash to fine lapilli, mostly fine lapilli.

Unit A
50 60 cm: Black, massive, (maybe feint structure near top), occasional pockets of brown very fine ash. Scoria. Very coarse ash to fine lapilli, mostly very coarse ash. At very bottom of section next to ice contact there is a mm thick layer of tan very fine ash.

Ts40; 30 cm
64° 25.654' N; 17° 23.538' W
22/07/2007 (TJ)

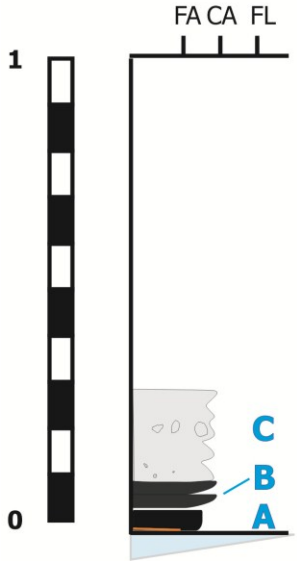

Unit C
20cm. Brown black. Layered. Range = FA-FL. Avg. = MA-CA. Very well sorted within layers. 5 alternating, relatively coarse and fine layers 4-6 cm thick. FL are grey/golden brown pumice, concentrated at surface, in bottom layer, and 3rd layer from the bottom. Coarse layers are matrix supported. 80-90% matrix. Fa-Ca, predominantly MA. Fine layers are browner, FA-CA (range), predominantly FA. But somewhat bimodal with 25% CA to VCA pumice, border line scoria. Occasional red altered lithics.

Unit B
Very well sorted. 6cm black. 5mm at base is very black MA to CA. more or less massive but possibly, finely cross bedded. The rest is MA to CA. Very CA is occasional and this is concentrated into lenses. No more than 5mm thick, continuous only over 2cm.

Unit A
4cm. Brown FA-MA. Massive, possible fining upwards? Capped by 5mm lighter brown finer ash. Very well sorted. At ice contact trace of very fine ash present.

Ts41; 25 cm
64° 25.776' N; 17° 23.782’ W
22/07/2007 (TJ)

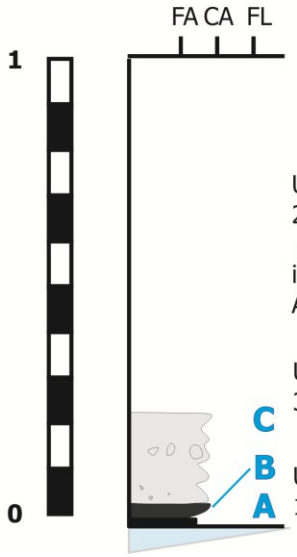

Unit C
21 cm. Brown.
Approx. 6 alternating fine and coarse layers, however these are less distinct than in the previous section. Bottom layer is 3-4 cm, pumice-rich, fine to medium ash. Layers above are 2-4 cm.
As in TS 40.

Unit B
3 cm. Black, massive, fine to coarse ash. Predominantly fine ash. Coarse ash consists of moderately vesicular scoria.

Unit A
1cm. Black, massive, fine to medium ash. Predominantly fine ash. Frozen. Lacks v. fine ash layer at the base.

Ts42; 61 cm
64° 25.218' N; 17° 23.634' W
22/07/2007 (TJ)

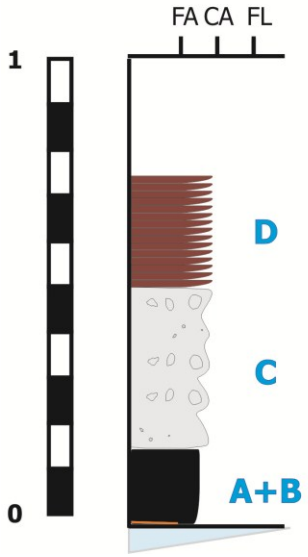

Unit D
25-27 cm. Low angle cross-bedded unit consisting of approx. 10 alternating coarse and fine sets. Range: fine to coarse ash. Dominantly medium ash with up to 5% fine lapilli, which is concentrated in coarser sets.

Unit C+E
35 cm. Layered. Looks similar to top layered unit in TS 40; TS 41. Alternating relatively coarse and relatively fine layers. Fine layers are graded from fine ash to coarse ash. Pumice bands occur are at 0-6 cm; 10-15 cm; 32-35 cm from top of unit.

Unit A+B
14 cm. Black. Fine ash to coarse ash. Massive, possibly coarsening upwards. Blacker at the top.

Ts43; 52 cm
64° 25.243' N; 17° 23.141' W
22/07/2007 (TJ)

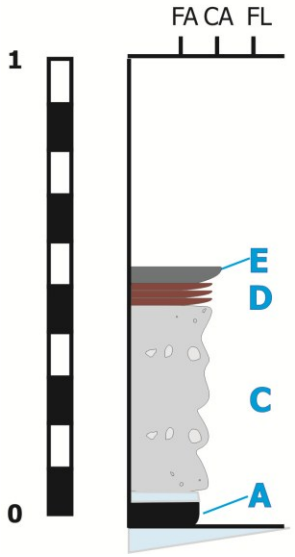

Unit E
5-7 cm. Brown. Very indistinctly cross-bedded. Medium ash to fine lapilli. Fining upwards. Very small-scale

Unit D
5-7 cm. Black, finely cross-bedded. Medium ash to fine lapilli. Fine lapilli are predominantly pumice, but a sig. Proportion are also juvenile black scoria. Medium ash is dark brown and looks like disintegrated pumice. Consists of alternating coarse and fine layers. It is relatively well-sorted within layers, but the layering is somewhat diffuse.

Unit C
40 cm. Brown to black. Layered sequence. The colour transition from brown to black occurs at 23 cm from the base of this unit. The lower part of this unit is diffusely cross-bedded with fine lapilli lenses and trains throughout within a matrix of black, medium to very coarse ash. From 23-38 cm above the base of the unit is grey-brown with abundant and more continuous pumice lenses. Max clasts are up to 5 cm in diameter. Avg.: 0.5-1 cm. The lenses are clast supported and continuous for up to 25 cm. The matrix is dominantly medium ash which looks like disintegrated pumice, but also contains fine lapilli scoria.

Unit A
3-6 cm. Black, Coarse to v. coarse ash. Well-sorted, massive. There is snowfall between this unit (A) and that

Ts44; 77 cm
64° 25.143' N; 17° 23.259' W
23/07/2007 (TJ)

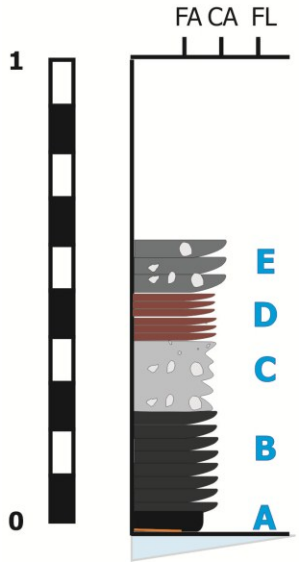

Unit E
6-8 cm. Pumice layer, as before, but matrix is less well-sorted. Consists of medium ash to fine lapilli. Avg, pumice clasts are slightly larger (2-5 cm).
Then 25 cm. Brown to black. Distinctly layered. 7 alternating coarse and fine sets displaying low-angle cross-bedding. Well-sorted within sets. Fine layers are browner fine to very coarse ash. Predominantly fine to medium ash. Coarse sets have the same grain size range but are dominantly medium ash with up to 5% fine lapilli. Fine lapilli are dense black scoria. Occasional red altered lithics in the coarse ash fraction. Coarse layers are continuous over 40 cm and up to 1 cm thick. Fine layers are up to 3 cm thick.

Unit D
10 cm. More distinctive surge-type deposit but structure is obscured because the section is frozen. Sets are continuous over 20cm with up to 2 cm maximum thickness. Well-sorted within sets. Medium ash to fine lapilli overall, but dominantly medium to coarse ash.

Unit C
10-15 cm. Pumice-rich. Continuous layer. Max. pumice clasts are 8 x 6 cm, although these are rare. Avg. pumice are fine lapilli up to 1cm in diamter. This layer also contains occasional red, altered lithics in the coarse ash to fine lapilli size fractions. Occasional fine to medium lapilli angular lithic fractions. Layer is matrix supported. Matrix is well-sorted medium ash.

Unit B
20-23 cm. Dark brown. Low angle cross-bedding. Structure is hard to make out as it is frozen. Fine to coarse ash, dominantly medium ash. Well-sorted.

Unit A
4 cm. Black, massive, fine to coarse ash. Dominantly medium to coarse ash. Well-sorted. Juvenile scoria.

Ts45; 100 cm
64° 25.031' N; 17° 23.653' W
23/07/2007 (TJ)

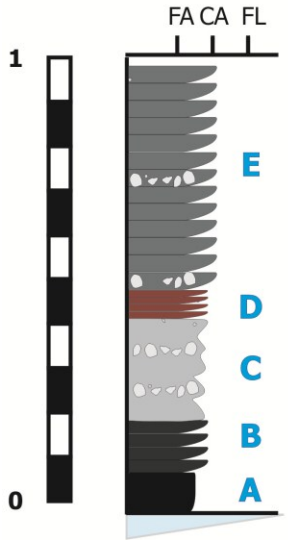

Unit E
6-8 cm. Black. Matrix supported (85%), pumice-rich. Matrix is medium to coarse ash. Pumice is avg. 1-5 cm in diameter.
Then 45 cm. Layered. Top 25 cm is massive, dominantly medium ash with <5% coarse ash. Then 25-40cm of distinct surges comprised of more than 5 cross-layers. Coarse layers consist of very coarse ash to fine lapilli scoria and pumice. Occasional red lithics. Finer layers are the same but with a higher proportion of fine and medium ash (80%). Coarse layers contain only 60-70% fine and medium ash. Well sorted within layers.

Unit D
7 cm. Dark brown. Indistinctly cross-bedded. Very well-sorted. Medium ash with <5% very coarse ash to fine lapilli. These are concentrated into lenses that are 0.5 cm thick and 5-8 cm long.

Unit C
22 cm. Layered unit. Relatively poorly sorted overall. Bottom 7 cm is very pumice-rich as before. Pumice are fine lapilli in size. Range: 0.5-10 cm. Avg.: 1 cm. Matrix supported. 5 coarse layers with intercalated fines-rich packages. Medium ash to fine lapilli. Fine lapilli are blue to golden brown pumice which are concentrated in coarse layers.

Unit B
10-15 cm. Similar to previous but significantly coarser. Medium ash to fine lapilli. Dominantly coarse ash. Blacker in colour than previous examples.

Unit A
8 cm. A layer. Probably medium ash. Frozen.

Ts46; 84 cm
64° 25.114' N; 17° 23.116' W
23/07/2007 (TJ)

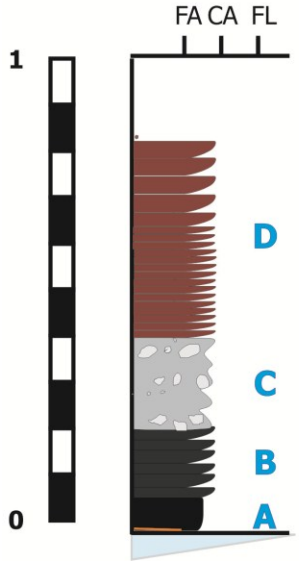

Unit D
43 cm. Surges. Almost the same as TS 45. Brown and very distinctly layered near the base. The layer is darker and more massive near the top. Same sequence of layers as in the last section and same components and size distribution.

Unit C
17-20 cm. Matrix-supported, pumice-rich layer. As seen previously. Pumice is variable in size between 1-8 cm. The matrix is very dark brown, medium ash. Fairly well-sorted.

Unit B
15 cm. Dark brown. Faintly cross-bedded. Medium to coarse ash. Individual are less than 0.5 cm thick. As in previous sections.

Unit A
5 cm

Ts47; 80 cm
64°25.064' N; 17° 23.016' W
23/07/2007 (TJ)

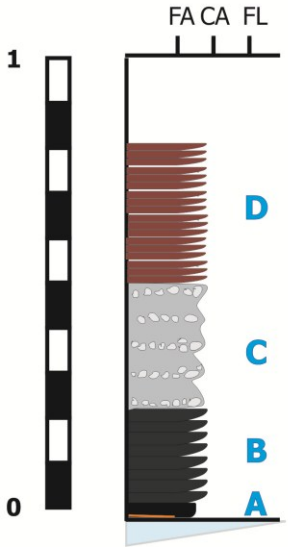

33 cm. Brown, layered. Alternating coarse and fine layers. Banded in appearance between lighter and darker brown. It becomes more massive in the top 15 cm, however layering is present throughout. There are up to 10 coarse bands which are 1-2 cm thick. They consist of a medium ash matrix with 60% black, fine lapilli scoria. Fine layers are 6-10 cm fine to medium ash. Very well-sorted within layers. Pumice and fine lapilli seem rounded.

30 cm. Layered on a decimetre-scale. Cross-bedded. Pumice-rich, but not like the pumice layer seen before. More like a surge with discrete pumice-rich lenses. The layer contains 5 pumice lenses, which are 3-5 cm thick. Continuous over 35-45 cm. These are matrix-supported. The matrix is fine to medium ash with up to 50% fine to medium lapilli pumice . The pumice are relatively dense, almost scoria. The largest pumice is 5x4 cm, but clasts of this size are rare. The layer is black overall but grey-brown within the pumice lenses.

20 cm. Typical B-layer, but with a pumice lense 5 cm from the base. Frozen. Quite black.

2-3 cm. Typical A-layer. Sub-mm, continuous brown very fine ash at the ice contact. Medium to coarse ash, massive, very well-sorted.

Ts48; 204 cm
64° 24.851 N;17° 23.060' W
23/07/2007 (TJ)

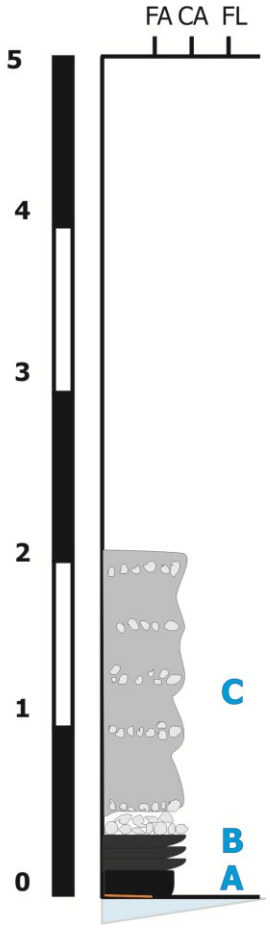

Unit C
8 cm. Pumice band. Continuous layer. Frozen. 60% pumice in a medium to coarse ash matrix. Matrix supported. Matrix consists of black, angular, dense scoria. Pumice are up to 5 cm across but more commonly 1-2 cm. Pumice are blue in centre with a golden brown rind.
Then 50 cm. Dark brown. Finely layered, relatively well-sorted within layers. Fining upwards overall. Coarse layers are 1 cm thick near the base and consist of fine ash to fine lapilli with at least 30% fine lapilli. Near the top coarse layers are less distinct. Fine layers are fine to medium ash with a higher proportion of fine material near the top.
Then 130 cm. Surges interbedded with three almost continuous pumice layers. There is a transition in colour at 84 cm from the top from dark brown/black to just dark brown. Possibly fining upwards overall, and definitely fining upwards within sets. The pumice layers occur at 0-14 cm; 30-40 cm; 60-63 cm from the base of this unit. The unit displays low angle cross-bedding and is well sorted within horizons. The bulk of the deposit is medium ash to fine lapilli, predominantly medium ash. Fine lapilli is concentrated in coarse layers 1 cm thick. Fine layers are

Unit B
15 cm. Quite frozen. Brown to black and indistinctly cross-bedded. Fine to coarse ash, predominantly medium ash.

Unit A
10 cm. Black, with 1-3 mm tan brown vfa at ice contact. Medium to coarse ash, very well-sorted, predominantly coarse ash. Dense juvenile scoria.

Ts50; >40 cm
64° 24.050' N; 17° 23.259' W
23/07/2007 (TJ)

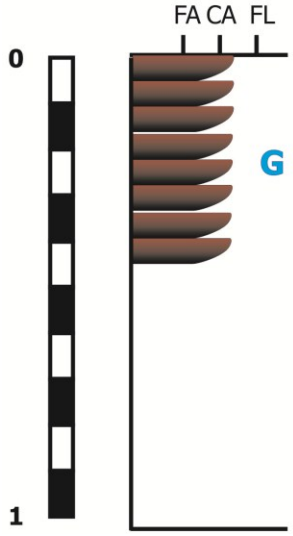

Unit G
Top 20 cm. Finely layered surge, similar to what is seen at the top of more distal sections. Brown, with an abundance of fine ash despite its proximity to the crater. Contains 5-10% fine lapilli. Ranges from highly vesicular golden brown pumice to blue, denser pumice. Occcasional red, altered lithics in fine lapilli fraction. Frequent coated lapilli clasts, but not armoured or accretionary.
Next 20+ cm. Different layer, same componentry as above. Less well-ordered than the layer above with even more diffuse cross-bedding, if at all.

Ts51; >400 cm
64° 23.877' N; 17° 23.062' W
24/07/2007 (TJ)

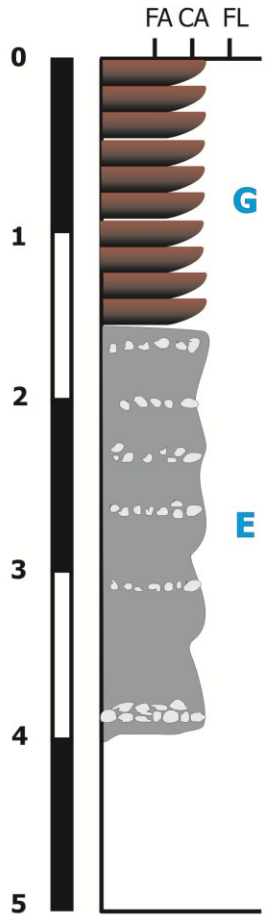

(1) 25 cm
(2) 50 cm
(3) 40 cm
All brown surge units.
Abundance of fines (brown disintegrated pumice). Below this is a darker brown unit (probably also a surge) These surge units are made up of many fine layers. They are quite poorly sorted with abundant lithics, including many altered/oxidised examples. Lower down in TS 51 we encounter pumice-rich units. This is not a continuous enough section to evaluate whether these are lenses or continuous layers. The top of this part is ~165 cm from the top of the section. There are at least two distinct units. The top 70 cm is distinctly layered. In the bottom 1m+ the structure is less distinct and the pumice are in diffuse trains rather than distinct lenses or layers. Pumice horizons in the top are clast-supported (dominantly), whereas below is borderline matrix/clast-supported (pockets of each throughout).

Ts53; >250 cm
64° 24.133' N; 17° 23.258' W
24/07/2007 (TJ)

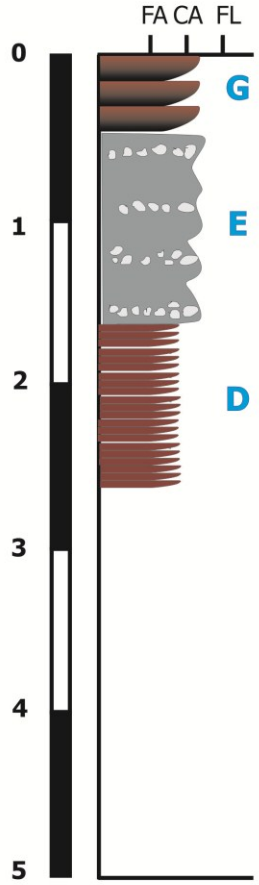

* Section a bit slumped, deformed, and uneven*
Logged from top-down.

Unit G
22-40 cm. Brown, finely crossbedded. Crossbedding is indistinct, relatively diffuse. Fine ash to fine lapilli. Predominantly fine to medium ash looks like disintegrated pumice. Fine lapilli are less than 10% and consist predominantly of pumice. NB this layer is a little out of reach! Log best you can, no lithics seen. Coarse to very coarse ash 5-10%. These tend to be shiny, black, juvenile scoria. Looking at this layer elsewhere lithics are seen mostly near the surface.

Unit E
80-90 cm. Again, this layer is deformed, in some places by slumping and in others by ballistic impact. So, it has variable thickness which is not primary. Numerous cross-bedded surge layers. Interbedded with pumice lenses and trains. Possible that this is two units with a gradational contact so I will describe them separately.
Top 40-45 cm: Very pumice-rich. Pumice occur in discrete horizons as lenses or trains. At the top contact with unit 1 there's a very clear, clast-supported pumice horizon, very clearly lensiodal in shape. The max thickness of this lense is 10cm. Pumice in the lense appears to be a mixture of complete and fragmented clasts and although the lens is clast supported individual clasts are fines coated. Below this, pumice occurs as numerous, i.e. >20 trains Pumice in these trains are fine to medium lapilli and fragments appear broken. The layer is brown, matrix is brown medium ash which looks like disintegrated pumice. The rest of this unit is fairly distinctly cross-bedded. Although crosslayers are somewhat diffuse and cannot be divided into alternating fine and coarse layers. Pretty much as above, but with a higher proportion of coarse ash in which blocky juvenile scoria dominates and fine lapilli pumice. This part of the layer lacks poumice trains and lenses. There is a very sharp contact between this and the layer below.

Unit D
>115 cm. Quite slumped. Contact with layer above is irregular. From 105 cm down is frozen. Inferred D layer. Very distinctive cross-layers with alternating coarse and fine sets, darker brown to black. The alternating coarse and fine sets are very variable in thickness from ~2cm to 8 cm each. The coarse layers are massive, black, coarse ash to fine lapilli. Abundant juvenile scoria, very occasional pumice. Fine layers are dark brown to black medium to coarse ash. Mixture between black, juvenile scoria, which is shiny and angular, and disintegrated pumice. In some places, the layering is on a finer scale. With 5-8cm, coarsening upwards layers which are capped by fine ash.

Ts60; >395 cm
64° 24.058' N; 17° 23.239' W
25/07/2007 (TJ)

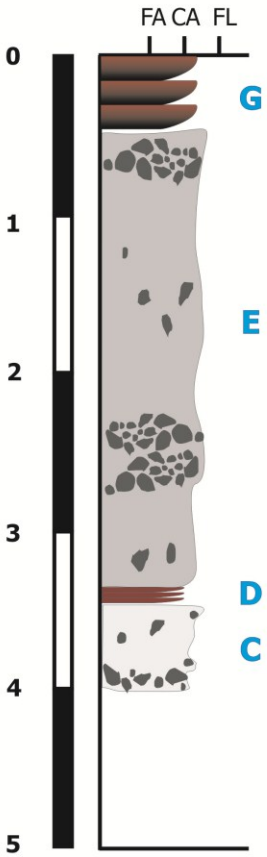

Top down.
Top 15 cm. Diffuse layering, low angle cross-beds, grey in appearance, especially when fines have been winnowed at surface. Relatively poorly sorted. Grain size appears bimodal. 80-90% fine ash, which is brown and looks like disintegrated pumice. Remaining 10-20% of fine lapilli are grey, angular lithics and juvenile pumice in almost equal proportion. Although the layer is crossbedded, the fine lapilli are not obviously confined within coarse sets. 30 cm. Another diffuse surge packet. Browner than above. Very poorly sorted with a few lithics and pumice 5-10 cm. Occasional bombs. Diffusely layered crossbedded, mostly fine ash as before, but now with up to 10% very coarse ash which are predominantly juvenile scoria. Coated clasts can be seen in these top two layers, a described in photograph yesterday. Occasional red altered lithics. Again, although diffuse, crossbedding is apparent. Material is not concentrated into coarse and fine sets or lenses. Abundance of fines is remarkable, given proximity to crater.
Proportion of lithic fragments outweighs that of pumice by at least a factor of two. Compare notes and pictures of this with those taken from nearby localities yesterday.
Top part (i.e. to 160 cm from top) numerous surge packages with intercalated pumice layers and trains. Dark brown. Greyer appearance where pumice predominates. The first coherent pumice lens has 10cm max thickness and can be traced for more than 3m. It appears to taper towards the edges. The pumice in these lenses are generally whole clasTs up to 10cm in diameter and range from blueish somewhat dense borderline scoria to golden pumice. There are also frequent lithics in the pumice lenses that are 5-10 cm sometimes orange-red altered. The pumice and lithic clasts are fines-coated although the lens has the overall appearance of being clast-supported.
All of this unit feels more competent than the 1st two unts and this is particularly the case clos to the bottom of the next unit. This unit has many alternating black and brown surge layers. Pumice trains, mostly clastsin the fine lapilli size fraction. They sometimes seem to occur as disrete but diffuse sets mixed into the brown finer layers.Concentrated near the contact with the black coraser layer below. These seem to be fining upwards within sets with black very coarse ash and fine lapilli near base fining upwards to coarse ash with a brown layer of fine ash to fine lapilli on top. This layer is relatively poorly sorted. Coarse ash to fine lapilli in coarase lenses of black juvenile scoria wherae in the finer lenses lapilli range from scoria to pumice. Frequent red, altered lithics and orange altered lithics. Scoria coarse ash and lapilli are frequently subangular. Very banded appearance.
As above, but less banded in appearance and browner overall. Diffuse pumice trains throughout. Pumice clasts are larger on the whole, occasionally 30 cm, more commonly 5-10 cm. xbed still present, but diffuse. Less ordered, normal grading notseen. Pumice lapilli are present throughout, but they don't seem to follow any ordered pattern in relation to the cross-bedding. Large pumice are in clast-suported pockets. These are generally whole clasts, but more diffuse parts of trains tend to be more broken clasts. Surges/matrix have similar componentry to previously. The fine-medium ash looks more like disintegrated pumice than ever.
40 cm. Very competent. Feels hard when scraping. Black. Crossbedded. Cannot be easily distinguished between coarse and fine lenses, more diffuse. Approximately 5
pumice trains which are 1 clast thick. Clasts are 3-5 cm on average, continuous over only 20-30 cm. Coarser than surges above, ranges from medium ash to fine lapilli, dominantly coarse ash with up to 30% fine lapilli. Fine lapilli and coarse ash are black, subangular to subrounded juvenile dense scoria. Very rare pumice dispersed through surges and confined to trains. Occasional coarse ash and red, altered lithics. Otherwise, virtually no lithic content. Quite poorly sorted overall. Bottom 5 cm is a slightly more massive region with a slightly higher proportion of medium ash. It looks like disintegrated pumice whereas elsewhere looks like it consists of more dense, juvenile material.
Very similar to unit above, but with a distinct contact between the two. Somewhat browner in appearance and cross-layers are even less distinct than previously. Unlike
the previous layer there are abundant lithics from coarse ash to coarse lapilli which are frequently orange and red altered. In the bottom 20 cm we start to see pumice trains
again, similar to unit 4. Dark brown darker in colour than unit 4, finer overall than
unit 5.

Ts61; 125 cm
64° 24.140' N; 17° 23.268' W
26/07/2007 (TJ)

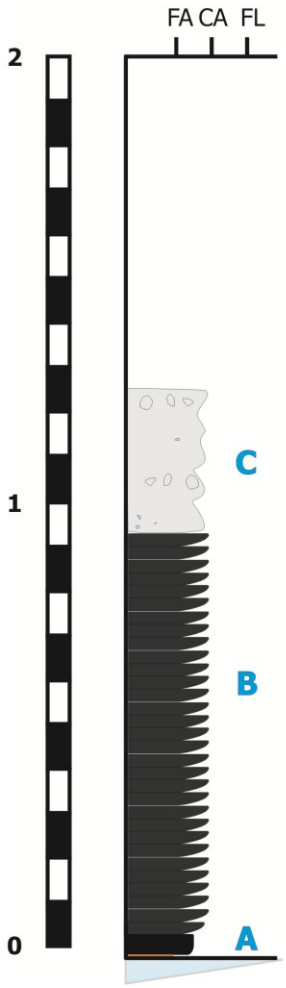

The whole section is very irregular and quite slumped. The bottom contact with the ice is irregular. There are several bomb sag features which have subsequently been filled in by the A-layer.

Unit C
35 cm: very indistinctly layered pumice rich. Pumice occurs in trains or highly localised, clast supported horizons. Not more than 1m long and a few grains thick. Grain size of pumice ranges from FL up to about 10cm very pumice rich horizons may be associated with bombs. This layer is predominantly medium ash looks like disintegrated pumice. Contains abundant lithic fragments which are from fine to coarse lapilli and very occasional scoria lapilli. Coated clasts are not uncommon. Somewhat poorly sorted. When scraped, shows the remains of lithics in the 10cm size range which had fines coating up to 2-3 mm thick.

Unit B
90 cm: dark brown to black, crossbedded, very many alternating fine and coarse layers. Abundance of juvenile material, very similar to A. Medum ash to fine lapilli. Well-sorted within layers. Fine lapilli often subangular, shiny, black, poorly vesicular material.

Unit A
6 cm: Black, massive. Very coarse ash to fine lapilli, well sorted, purely dense, juvenile material. Why is there no lithic population in this layer. From trace to up to 4 mm of tan brown, very fine ash at the ice contact. Highly discontinuous traces of the same at the contact with the B-layer, but this is very localised.

Ts70; 285 cm
64° 24.612' N; 17°23.720' W
30/07/2007 (TJ)

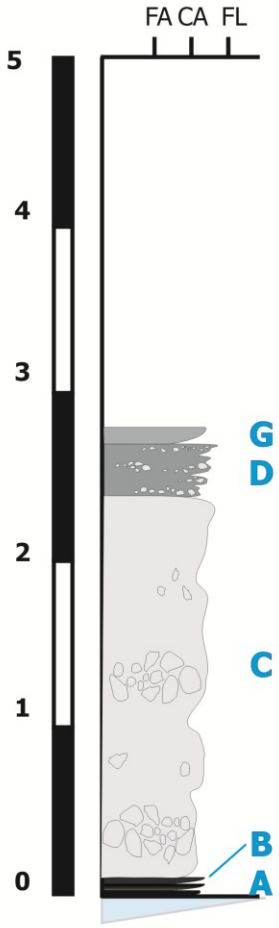

Unit G
8 cm This unit is largely similar to the underlying unit, but with a distinct contact between the two. Appears greyer in colour, especially where winnowed out on a wind-blown surface due to more pumice.

Unit E
18 cm Crossbedded, very poorly sorted, from fine ash to fine lapilli. The fine ash is light brown disintegrated pumice. FL exhibits a considerable range of componentry. Predominantly pumice but also abundant lithic fragments and black scoria. Layers look quite distinctive in both clean and windblown surface. However, material of a given size fraction is not concentrated into discrete horizons so somewhat diffuse. Hard to tell because sets are so diffuse, but it appears that every 2-3 cm they are capped by a 0.5 cm fine layer. This is particularly evident at the top of the unit, bordering the contact with the unit above.

Unit C.
260 cm. Brown to black very indistinctly crossbedded with many intercalated pumice-rich horizons. Pumice-rich horizons vary between clast-supported lenses and matrix supported trains. Pumice are broken fragments in the fine lapilli sized fraction. Next 55 cm at the top of this segment the first stacked pumice trains come in. In between, a typical c layer crossbedded surge layers of alternating black-brown bands. These are medium to very coarse ash, predominantly coarse ash. The fine ash fraction could be disintegrated pumice, but not dominantly. A significant proportion, practically most of it is black, juvenile scoria.
Next 40 cm stacked pumice trains, 1 clast thick, on average. Clasts range from 0.5 cm to 8 cm. Occasional pumice bombs up to 15cm with the exception of the very largest clasts, pumice in both the trains and the lenses consists of broken fragments. Intact clasts tend not to have fused outer surfaces. The very top of this 40 cm is a discrete pumice lense which can be traced laterally for up to 2 m. It is no more than 10-15 cm thick. Lenses are very obviously lensoidal in shape.
Top 40-45 cm of Unit C is distinctly surge-like in appearance. Numerous alternating coarse and fine crosslayers. Lighter grey-brown in colour because of abundance of pumice. Individual sets have a total thickness of 8 cm on average. These are coarsening upwards and consist firstly of 2-3 cm layer of light brown fine to coarse ash. Looks like disintegrated pumice. Then there is a darker 2cm layer which consist of medium ash to fine lapilli. Higher proportion of black scoria, occasional red altered lithics, still predominantly pumice. All capped by a very pumice rice predominantly FL.

Unit B
4.5 cm. Black, trace of tan vfa at contact with A layer. Crossbedded. Fine ash to coarse ash with up to 5% fine lapilli which are concentrated in coarse lenses. Components are entirely black, poorly vesicular, juvenile clasts.

Unit A
3-5 mm. Contact with layer above is relatively indistinct. Mm-sub mm tan vfa layer present at the ice contact. Massive, black, fine to medium ash. 1% coarse ash, which is juvenile, dense, black scoria.

Ts71; 410 cm
64° 24.728' N; 17°23.423' W
30/07/2007 (TJ)

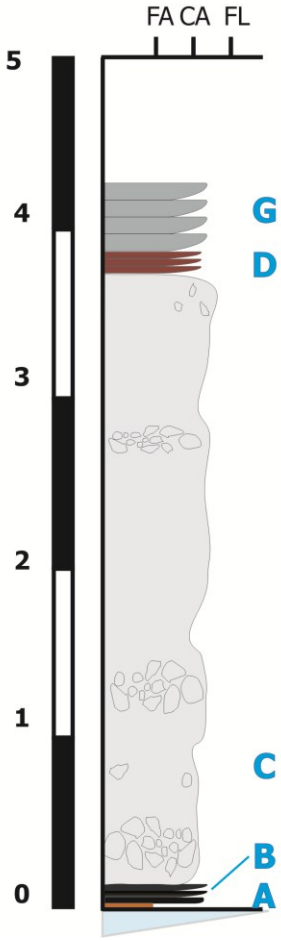

Unit G
Uneven contact with layer below. 23-30cm. Brown to black. Distinctly crossbedded. Relatively well organized between coarse and fine. Although boundaries are more diffuse than sharp. Range FA to fL. MA and FA are brown, disintegrated pumice. FL are also pumice. CA to VCA fraction dominated by scoria and glass.

Unit D
Probable D unit is present from 50-57cm from the top of the section. It varies wildly in thickness. Pinches and swells on a very small scale.

Unit C
83cm. This unit looks dark brown to black compared to lighter brown above. Numerous distinct cross layers, sporadic pumice clasts occurring individually, these are on the order of 1cm in diameter. These range from continuous massive layers up to 8cm thick to coarser lenses which generally can't be traced for more than 50cm. These have a maximum thickness of 2cm. Pumice in FL sized fraction is concentrated in coarse lenses. But these are matrix supported. Coarse lenses contain up to 10% pumice in the fine fraction, but are dominantly scoria. FA to CA, dense black scoria. I am having difficulty assigning this layer a unit with respect to marker beds because it has considerably more pumice than usual for B layer, but unlike C packages it lacks accidental lithics and crossbedding is more distinct and a significant proportion of dense, juvenile material.

Unit B
3-3.5cm. Crossbedded. Black. Exclusively dense juvenile material. FA to CA.

Unit A
0.5-1cm undulating. Black, massive. 1mm brown VFA present at ice contact. At the top of this unit there are traces of discontinuous VFA. It is black MA, well sorted.

Ts72; 183 cm
64° 24.874' N; 17° 23.353' W
31/07/2007 (TJ)

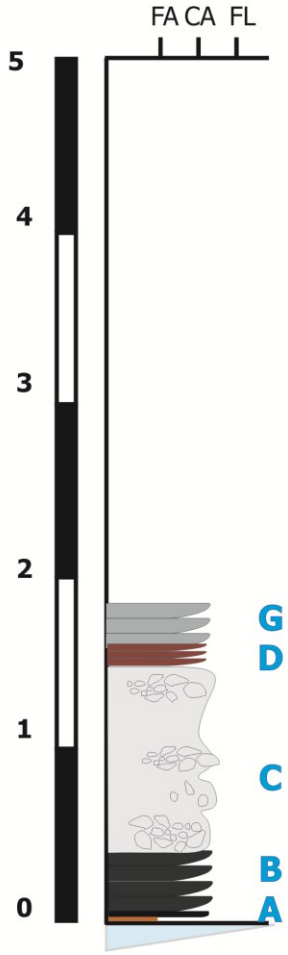

Unit G
Top 11cm. Grey brown indistinctly x-bedded. Mod poorly sorted. FL 5%. Fa looks like disintegrated pumice. VCA 5-10% angular, blocky dense juvenile material. Diff size fractions do not appear to be concentrated into different layers. Although top 7cm is a distinct well-sorted FA layer. Beneath which is single clast thick 2mm CA layer.
Bottom 13 cm. Another brown, indistinctly bedded unit. Perhaps somewhat more distinctly layered than above. Same componentry as before but with several pumice trains which are fine lapilli sized fragments one clast thick. Highly discontinuous, sharp contact with unit below.

Unit D
Up to 13 cm. But very variable thickness on a local scale. Pinch and swell morphology. Possibly several overlapping lobes on a 5m scale. Indistinct boundary between these.
Bottom contact is slightly undulating an in places the top contact shows relatively sharp dips that are truncated by the layer above. Black, distinctly layered, coarsening upwards within sets. Browner, finer material in bottom 0.5-1cm. The coarsening upwards trend is not as distinct as in previous sections

Unit C
Up to 107 cm. Variable thickness (possibly because partly eroded by above). Brown to black, numerous pumice trains interacalated with indictictly bedded surge units.
Pumice lense only occurs at the very bottom. Distinctly lensoidal in shape. Rraced for apprix 2 m, max thickness is 10-12 cm. Clasts in the interior of the pumice lens are larger than 10cm in diameter which are complete pumice bombs. They decrease in size towrads the edge. Where the pumice lenses tape out the are only 1-2cm and tend to consist of broken clasts rather than intact ones Cross layers are relatively distinct here, light to dark brown. Well ordered, alternating coarse and fine layers on a cm scale.
R=MA-FL, predominantly ma, somewhat less dense juvenile material. Although >5% still present in CA. Fl are pumice. These predominantly occur in diffuse pumice trains rather than as cross layers.

Unit B
40cm dark brown to black crossbedded. Crossbeds are quite distinct, layered on a cm scale cf B-layer from section Ts72. It seems transitional between B and D-type surges

Unit A
3-5 mm. Black, Trace of brown vfa at ice contact. Contact between a and b is unusually indistinct. Massive, frozen, can't tell grain size, but it looks quite fine.

Ts73; 178 cm
64° 24.863' N; 17° 23.087' W
31/07/2007 (TJ)

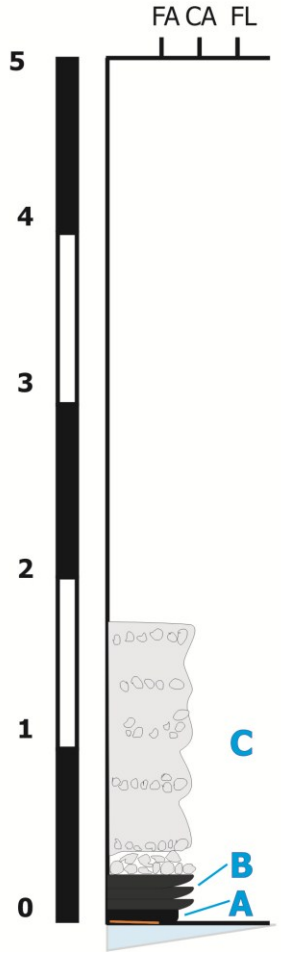

NB this log was taken at the northern end of an extensive (100 m section) where units can be traced laterally.

Unit C
Indistinctly crossbedded. Medium ash to fine lapilli, dark brown to brown, fine lapilli in matrix in surges is generally scoria. Intermittent pumice lenses and trains. Pumice lenses are clast-supported, very localised, up to 20 cm across and 8 cm thick. More commonly pumice bands are more diffuse and matrix supported. There are intermittent pumice lenses at the contact with the B-layer, but the next pumice-rich horizon after that doesn't come in until 35-45 cm above the contact. Above which pumice band or horizons occur on a decimetre scale. In the top 50 cm layering is more distinct, occurring on a cm scale. Two layers at the top: 8-10 cm Brown. Indistinctly crossbedded. Range is medium ash to fine lapilli occurring in diffuse alternating coarse and fine lenses. Medium ash looks like disintegrated pumice. Fine lapilli are pumice and scoria, mostly scoria. Top 7-8 cm, very similar to below but fine lapilli are almost exclusively pumice. Coarse ash fraction less than 5% dense, juvenile scoria. Crossbedding looks indistinct, but when fines are winnowed at the surface distinct coarse lenses can be picked out.

Unit B
10-12 cm, dark brown to black, colour transition at 4cm from black to dark brown, medium ash to fine lapilli, all juvenile scoria material cross-bedded, well-sorted within layers. Coarse and fine lenses are quite discrete.

Unit A
2-3 cm,1mm tan vfa at base, massive, blocky medium to coarse ash.

Ts75; >200 cm
64° 24.285' N; 17° 23.330' W
29/07/2007 (TJ)

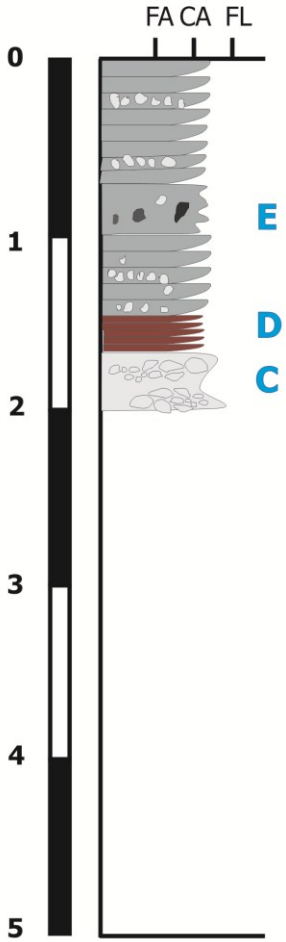

Logged from top down.

Unit E
Very distinctly crossbedded. Moderately sorted. Dark brown medium ash with minor fine lapilli to medium lapilli range from pumice to scoria, predominantly pumice. Coarser fraction occurs in lenses, but these are so diffuse. At the dotted line boundary we can see the introduction of a high proportion of pumice and accidental lithics. Note in the last few sections there have been a lot of recycled clasts principally lithics, but also recycled juveniles. Pumice can be up to 10 cm in diameter and are quite dispersed throughout the area. Diffuse trains at this boundary, the rest of the layer pumice clasts appear sporadically.

Unit D
26-28 cm. Finely laminated. Very low angle cross bedding, almost horizontal laminae. Sharp contact at both boundaries. Distinctive sub-mm, tan very fine ash laminae at contacts and capping each set. Numerous alternating coarse and fine layers. Individual sets are coarsening upwards and are then capped by fine ash laminae. Very well ordered, each set is usually no more than 1 cm thick. Consists of medium ash, grading into very coarse ash. This ash is black, very glassy, shiny, poorly vesicular, angular, platy, blocky plus shard-like clasts all present.

Unit C
30 cm+. Frozen. Brown to black, similar to layer 1 but somewhat more distinctly crossbedded with higher proportion of lithic fragments and pumice. Coarser than layer 1. Coarse ash to fine lapilli.

Ts77; >200 cm
64° 24.205' N; 17° 22.897' W
02/08/2007 (TJ)

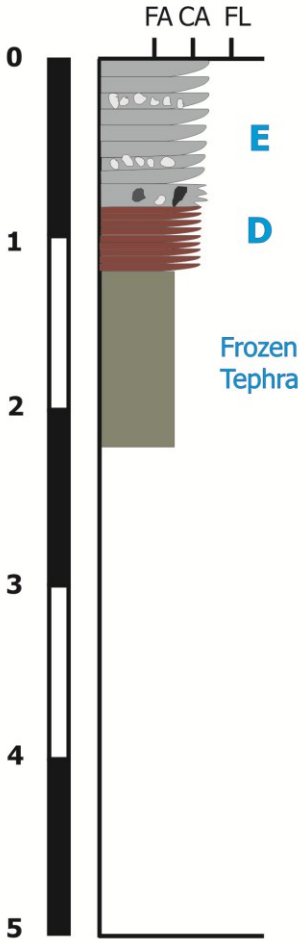

Unit E
80 cm thick to frozen part. Top 48 cm is very similar to top of previous sections (TS81, TS75).

Unit D
Brown, faintly cross-bedded, pumice rich but no actual trains or lenses.
Next 35 cm is banded black and brown layers. The contacts are not very distinct and possibly gradational. The top 15-20 cm of this 35 cm horizon is very finely layered with obvious shiny black fine lapilli horizons.

Ts80; 87 cm
64° 24.468' N; 17° 23.146' W
02/08/2007 (TJ)

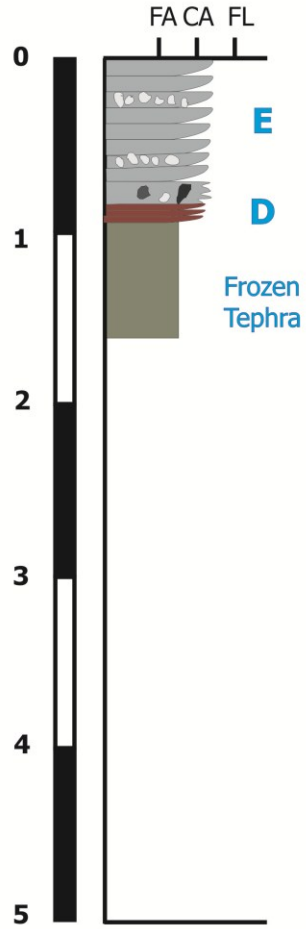

Total exposed thickness is 87 cm, frozen at bottom.

Unit E
80 cm. Indistinctly crossbedded, brown to black banded with alternating black-brown distinctly crossbedded packages plus brown less distinctly crossbedded packages. Less distinctly crossbedded packages are 20-25 cm. Banded horizons 10 cm. Banded horizons appear to be graded with medium ash to fine lapilli in the top browner layer. Fine lapilli are pumice and the black layer is well-sorted coarse ash to very coarse ash which consist of poorly to non-vesicular angular, juvenile fragments. The less distinctly cross-bedded packages consist predominantly of medium ash with 20% fine lapilli. Fine lapilli range from accidental lithics to pumice to poorly vesicular juveniles. Pumice trains are present 20 cm from top and within 10cm of the bottom contact, these are laterally continuous, but quite dispersed with max clast dimaters up to 5 cm.

Unit D
>7 cm: Undulating contact, truncated surface, evidence for erosion, layer seems to pinch and swell but difficult to evaluate as it is by the frozen base. Crossbedded, looks like unit D. Well sorted within layers, predominantly black, coarse ash to very coarse ash. Poorly vesicular, juveniles.

Ts81; 120 cm
64° 24.229' N; 17° 23.209' W
02/08/2007 (TJ)

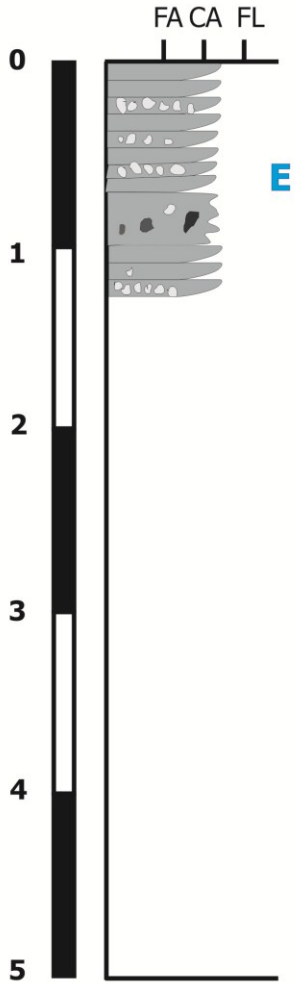

120 cm. Very similar to layer 1 in previous section. Brown to black, indistinct cross-layering, but somewhat more pronounced than in previous section (i.e. TS75). Sporadic pumice, but no real pumice trains. (See diagram on page 122 of field notebook).

Ts82; 75 cm
64° 24.219' N; 17° 22.776' W
02/08/2007 (TJ)

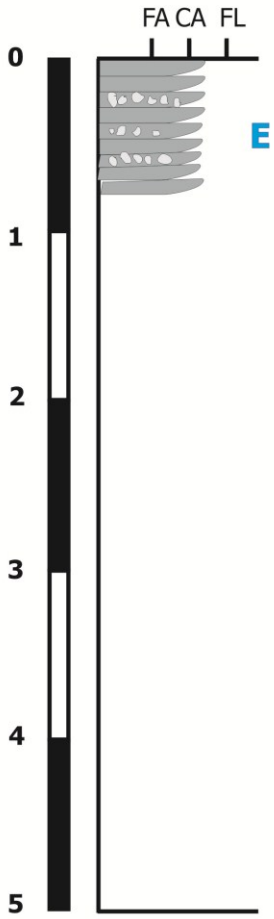

75 cm brown to black. Banded. Banding is particularly prevalent in the bottom 30 cm. Indistinctly cross-bedded throughout. Crossbedding is particularly prevalent in the bottom 30 cm. Sporadic pumice and lithic fragments more than 5-8 cm in diameter throughout. These are not ordered in any way. Some are fines-coated clasts. Moderately sorted, principally MA with a variable proportion of FL in different layers. FL tend to be scoria and up to 1 cm in diameter. Occasional FL pumice are also present. In the lower 30 cm there are alternating coarse and fine layers. Coarse layers are clearly lenses and taper out and have maximum thicknesses of 1-1.5 cm. Fine layers are more continuous with max thicknesses of 4 cm. Fine layers are fining upwards (normal grading).

Ts83; >50 cm
64° 24.175' N; 17° 22.570' W
02/08/2007 (TJ)

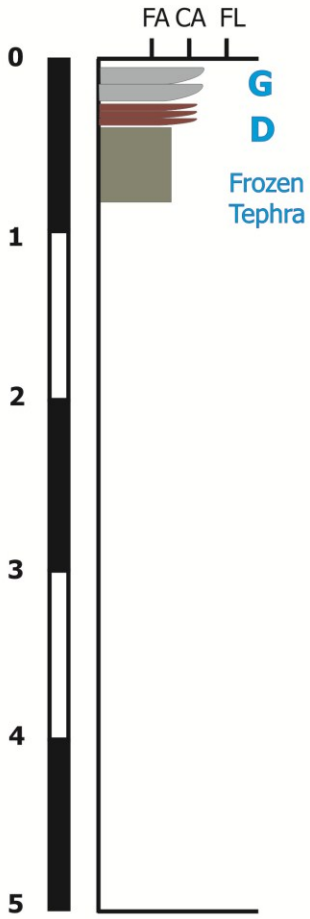

Unit G
Top 20-25 cm is brown and fairly massive but probably indistinctly cross-bedded. Contains sporadic pumice clasts 10cm plus which are discontinuous lenses not more than 10 cm long and one clast thick. FL range from lithics to pumice and scoria. Angular bomb lithic 5x7x11 cm, very dense.

Unit E
Then 10-12 cm max thickness. Upper contact is very undulating. Might even be a lens. Very well sorted FL scoria in a medium ash matrix. Black. Central 3 cm is just matrix with coarser lenses on either side which are browner. Shows classic pinch and swell morphology. Lenses can be traced laterally for 80-100 cm.

Beneath this there appears to be another equivalent layer but structures are less distinct due to freezing. Frozen part appears banded with a distinctive black layer 10-16 cm below the frozen margin.

Ts84; >55 cm
64° 24.139' N; 17° 22.157' W
02/08/2007 (TJ)

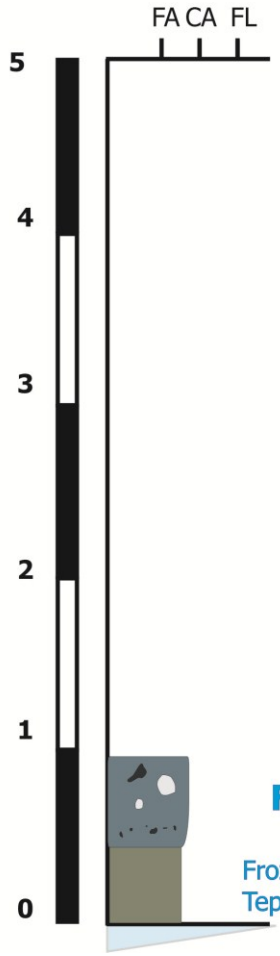

(See diagram on page 126 of field note book)
55cm to frozen. Possibly 1m total thickness. Looks like clean ice and might be the true contact. Top 55cm looks like a typical F layer. Dark brown, massive, and very poorly sorted. It contains abundant lithics and only occasional pumice. It is possible that a very thin A layer is present here but cannot be discerned.

Ts85; >150 cm
64° 24.055' N; 17° 22.362' W
02/08/2007 (TJ)

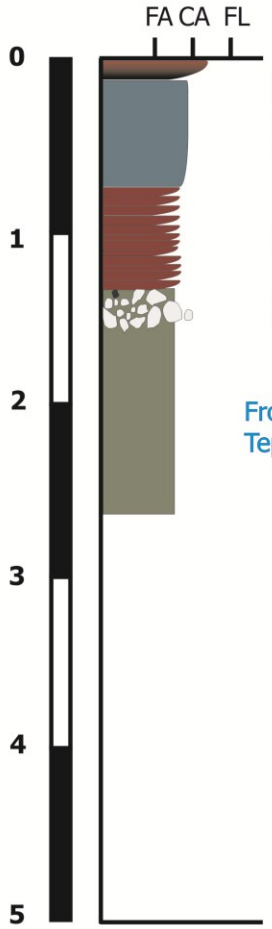

Unit G
10-12cm. Grey/brown. Faintly crossbedded. Brown to black crosslayers which represent alternating coarse and fine, fairly well sorted MA to CA. CA is black, poorly vesicular, juvenile material. Occasional lithic fragments in the FL size fraction.

Unit F
60cm. F layer, as previously, but with a more significant proportion of lithic bombs. Contact with layer beneath is gradational.

Unit F grading into Unit D and C
75cm. Bottom of this is frozen, but it seems like pumice is starting to come in. Could be close to contact with C/D package. This layer could be E, but given its gradational contact, variably distinct crossbedding, and abundance of sporadic lithic pumice fragments, its more likely to be a differentiated base of unit F.

Ts85; >150 cm
64° 24.055' N; 17° 22.362' W
02/08/2007 (TJ)

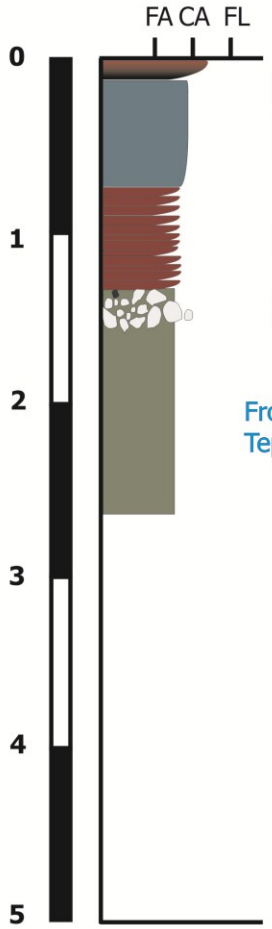

Unit G
10-12cm. Grey/brown. Faintly crossbedded. Brown to black crosslayers which represent alternating coarse and fine, fairly well sorted MA to CA. CA is black, poorly vesicular, juvenile material. Occasional lithic fragments in the FL size fraction.

Unit F
60cm. F layer, as previously, but with a more significant proportion of lithic bombs. Contact with layer beneath is gradational.

Unit F grading into Unit D and C
75cm. Bottom of this is frozen, but it seems like pumice is starting to come in. Could be close to contact with C/D package. This layer could be E, but given its gradational contact, variably distinct crossbedding, and abundance of sporadic lithic pumice fragments, its more likely to be a differentiated base of unit F.

Ts86; 180 cm
64° 24.026' N; 17° 22.581' W
02/08/2007 (TJ)

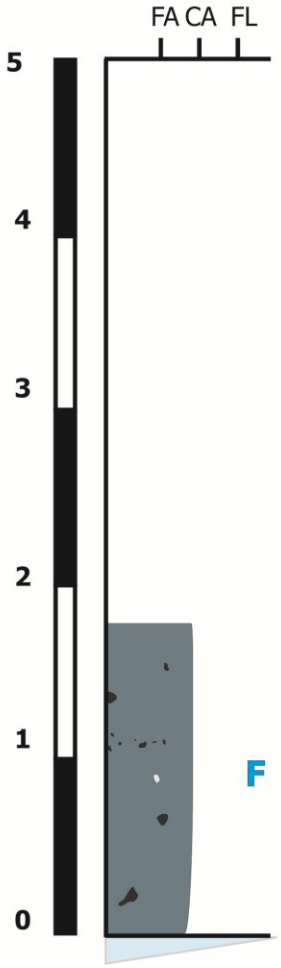

Unit F
180cm. F, all of it. G doesn't seem to be present here. However, there is 20cm in another section close by which looks like it could be G. It is the same as what F looks like elsewhere, but its very fines rich. Predominantly FA to MA. Brown. Matrix supported. Poorly sorted. Abundant lithics. Full range of componentry but appears to lack pumice.

Ts90; >595 cm
64° 24.482' N; 17° 23.448' W
31/08/2007 (TJ)

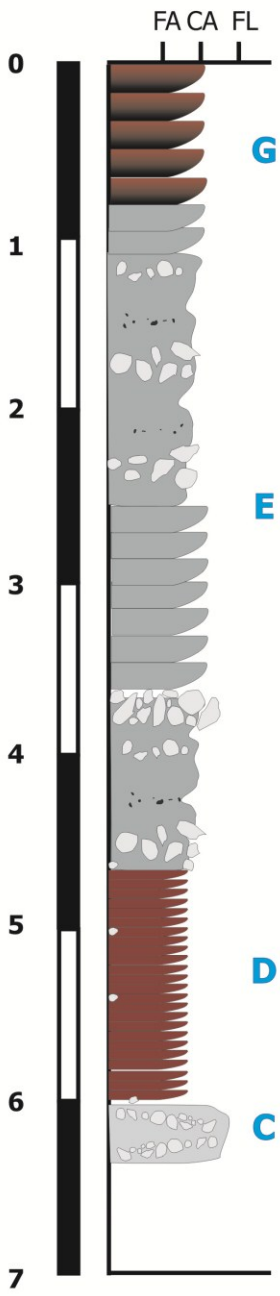

Logged from top down
25-26 cm. Black, faintly crossbedded, well-sorted medium to coarse ash. Occasional fine lapilli which are concentrated into lenses. Poorly to non-vesicular juvenile fragments.
26 cm. Dark brown to black crossbedded. Similar to layer above but less well sorted. Higher proportion of fine lapilli. Range of components from poorly to highly vesicular juvenile fragments.
20 cm. Sharp contact with layer above but relatively indistinct or gradational contact below. Light brown with numerous mm to sub-mm very fine ash laminae similar to what is usually seen at the base of sections, interspersed with occasional coarse lenses up to 1 cm thick more commonly less than 1 cm. These coarse layers consist of black, shiny, poorly to non-vesicular coarse ash to very coarse ash.
10-12 cm. Dark brown to black, alternating dark and light/coarse and fine layers. Very well-sorted within layers. Fine layers are fine ash, coarse layers are coarse ash. Again, this is full of moderately vesicular juvenile scoria. NB this whole section is characterised by a lack of lithic bombs unlike G5 nearby which contains abundant ballistics and other lithics.
380 cm E layer. Exactly the same as seen in hole G5 and in similat packages/sections elsewhere (e.g. G10/11; TS6; TS60).
Bottom 140 cm: Very distinctly crossbedded. Medium ash is dark brown and comprises 60% of the layer, while the coarse ash is black, angular, poorly to non- vesicular fragments. There are sporadic fine lapilli pumice fragments. The next 5 cm is quite compact and the scraper grates against it. It exhibits very distinct low angle crossbedding see more detailed diagram on page 106 of fieldbook. Very well-sorted within layers. These layers are a few mm to up to 1 cm thick. Most commonly 5-7 mm. They consist of alternating coarse lenses which are exclusively black, shiny, blocky, poorly vesicular juvenile material with diameters in the range of 1-3 mm. The finer layers are medium to coarse ash of the same composition and are capped by tan brown sub-mm very fine ash laminae.
The next 45-47 cm is almost identical to the first layer, however it appears to have a slightly higher proportion (although still <5%) of fine lapilli pumice and lithics. There are also occasional lithic and pumice clasts about half way through this layer up to 8cm in diameter. These are far too sporadic to be considered a train, but are confined within a 10cm horizon in the middle of this layer. These pumices are also whole clasts not broken fragments.
The next 8 cm are the same as the second layer within this package, but the layers are a little bit less well-defined. This is principally because the fine ash laminae are not present and the layering is somewhat more diffuse. For both of these finely layered sequences the top contact is sharp while the bottom contact is gradational.
The next layer to the bottom of the section is indistinctly/diffusely layered. It is brown and poorly sorted and consists of a medium ash matrix with abundant fine lapilli fragments dispersed throughout.

APPENDIX II

CODE FOR BALLISTIC CALCULATIONS

(WRITTEN IN R)

```
#### Ballistic problem with application to volcanic bombs ####

### Written by Mark Naylor
### University of Edinburgh
### School of GeoSciences

###################################
#### Define the problem
### Constants
#!!! Copy parameters into R at start

dt=0.00001
radius_1 =1.07
radius_2 =0.70
radius_3 =0.53
g=9.81
dragCoefficient = 1.0
densityOfAir = 1.3

mass = 1135.33
crossSectionalArea = pi * radius_1 * radius_2 /4
```

```
K1=0.000

K2= 0.5 * densityOfAir * dragCoefficient * crossSectionalArea / mass


### Targets

observedRange= 1170

minVelWithNoDrag = sqrt(observedRange*g)    ### Assumes no resistance theta=45 and initial/final height the same


### Variables

V0=minVelWithNoDrag

theta=45*pi/180


thetaList=seq(30,60,5)*pi/180

range=c()


############################################################

#### Case 0: Plot a trajectory

angle=45*pi/180

findRange(V0=100,theta=angle, K1=0, K2=0, plotTrajectory=TRUE)


############################################################

#### Case 1: Loop over angles to find range for constant vel


for(l in 1:length(thetaList)){

print(l)

theta=thetaList[l]

range[l]=findRange(V0,theta, K2=K2)

}
```

```
par(mfrow=c(1,1))
plot(thetaList*180/pi,range, type="l", xlab="Launch angle", ylab="Range")
title(paste("V0 = ",V0, sep=""))

############################################################
### Case 2: Optimise the velocity for a given angle and range
velLimit=c(50,450)
opVelList=c()
minVel=10000

for(l in 1:length(thetaList)){
print(l)
theta=thetaList[l]
optimisedVel <- optimise(getRangeDifference,velLimit,theta=theta,observedRange=observedRange, K1=K1, K2=K2, tol=0.1)
opVelList[l]=optimisedVel$minimum
if (optimisedVel$minimum<minVel) {minVel=optimisedVel$minimum}
}

par(mfrow=c(1,1))
plot(thetaList*180/pi,opVelList, type="l", xlab ="Launch angle", ylab="Initial velocity", ylim=c(floor(minVelWithNoDrag), max(opVelList)) )
abline(h=minVelWithNoDrag , col=2)
title(paste("Target range = ",observedRange, sep=""))

minVel

##########################################
```

```
##########################################
### Required Functions For the Above #####
#!!! Copy below into R at start

getRangeDifference = function(V0, theta, observedRange, K1, K2){

trialRange=findRange(V0,theta, K1=K1, K2=K2)
rangeDifference = (trialRange-observedRange)^2
rangeDifference
}

#########################################################
### Ballistic forward model

findRange = function(V0, theta, K1=0, K2=0, dt=0.001, g=9.81, plotTrajectory=FALSE){
### Initial conditions

y=c(0)
x=c(0)

vx=c(V0*cos(theta))
vy=c(V0*sin(theta))

### Run forward model
i=1
while (y[i]>=0){

x[i+1]=x[i]+vx[i]*dt
y[i+1]=y[i]+vy[i]*dt
```

```
## Non-linear component
v2 = (vx[i]^2+vy[i]^2)
v = sqrt(v2)
cosTheta = vx[i]/v

sinTheta = vy[i]/v

vx[i+1]=vx[i]        - K1*vx[i]*dt - K2*v2*cosTheta*sign(vx[i])*dt
vy[i+1]=vy[i] - g*dt  - K1*vy[i]*dt - K2*v2*sinTheta*sign(vy[i])*dt

i=i+1
}

range=x[i-1]

if(plotTrajectory){
par(mfrow=c(2,1))
plot(x,y,type="l")
abline(h=0, col=3)
plot(vx,type="l", ylim=c(min(vx,vy), max(vx,vy)))
points(vy, type="l", col=2)
}
range
}
```

APPENDIX III

GRAIN-SIZE DATA

THIS STUDY

UNIT A

Φ	μm	G1	S1	TT01	TT02	TS26	TS40	TS48	TS71	TS72
-5.0	32000	0.00	0.00	0.00	0.00	0.00	0.00	0.00	0.00	0.00
-4.5	24000	0.00	0.00	0.00	7.05	0.00	0.00	0.00	0.00	0.00
-4.0	16000	0.00	0.00	0.00	0.00	0.00	0.00	0.00	0.00	0.00
-3.5	12000	0.93	0.00	0.00	0.20	0.00	0.00	0.00	0.00	0.00
-3.0	8000	2.18	0.00	0.74	1.12	0.98	0.61	0.00	0.00	0.00
-2.5	6000	7.89	0.00	1.58	4.72	0.38	0.22	0.42	0.00	0.98
-2.0	4000	8.22	0.16	3.25	6.06	1.87	0.61	0.81	0.01	1.11
-1.5	3000	6.84	0.71	5.14	6.79	2.42	1.26	2.26	0.41	2.22
-1.0	2000	7.63	1.33	6.73	9.72	3.47	2.10	3.57	1.24	3.27
-0.5	1500	7.76	2.97	8.84	10.20	5.56	4.44	7.25	2.51	4.59
0.0	1000	7.50	5.05	8.96	9.51	6.75	4.68	10.15	3.52	5.29
0.5	750	7.21	6.90	9.29	8.02	9.89	6.26	12.06	3.29	6.19
1.0	500	6.37	8.56	9.18	6.84	8.24	9.61	10.91	6.81	6.53
1.5	375	5.93	10.04	7.73	5.13	9.90	9.98	9.45	8.27	6.56
2.0	250	5.69	8.57	5.46	4.67	6.28	7.21	9.01	8.85	8.21

Φ	µm	G1	S1	TT01	TT02	TS26	TS40	TS48	TS71	TS72
3.0	125	4.53	9.62	6.67	4.18	8.54	10.64	7.77	11.58	11.33
3.5	94	3.55	7.27	4.64	2.36	5.87	7.22	5.09	9.43	6.96
4.0	63	3.10	8.64	4.99	2.52	6.73	7.92	5.01	10.14	7.30
4.5	47	1.99	6.76	3.52	1.92	5.50	6.32	3.43	8.03	5.71
5.0	31	1.79	4.84	2.34	1.29	4.05	4.51	2.14	5.64	4.26
5.5	23	1.21	2.47	1.23	0.63	2.13	2.33	1.12	2.90	2.42
6.0	16	0.96	2.12	1.08	0.52	1.91	2.09	0.98	2.50	2.34
6.5	12	0.56	1.29	0.74	0.31	1.26	1.41	0.65	1.53	1.75
7.0	8	0.49	0.80	0.53	0.20	0.87	0.98	0.46	0.98	1.35
7.5	6	1.32	0.40	0.29	0.11	0.47	0.54	0.26	0.52	0.79
8.0	4	0.40	0.32	0.16	0.06	0.40	0.35	0.22	0.57	0.70
8.5	3	0.00	0.26	0.11	0.05	0.35	0.25	0.19	0.57	0.56
9.0	2	0.00	0.15	0.17	0.02	0.25	0.11	0.11	0.24	0.44
9.5	1.5	0.00	0.11	0.07	0.02	0.17	0.09	0.07	0.13	0.37
10.0	1	0.00	0.97	0.79	0.36	0.94	1.90	0.54	0.80	1.44
Totals		100.00	100.00	100.00	100.00	100.00	100.00	100.00	100.00	100.00
Thickness (cm)		29.00	2.00	41.00	20.00	5.00	4.00	10.00	0.75	0.40
Location		N 64.39972 W 17.37583	N 64.40072 W 17.39975	N64.40187 W17.37842	N 64.40215 W 17.38530	N 64.39797 W 17.37389	N 64.42757 W 17.39230	N 64.41418 W 17.38433	N 64.41213 W 17.39038	N 64.41457 W 17.38922

UNIT B

Φ	µm	G1	G2	S1	TT01	TT02	TT02-B	TS18	TS26	TS30	TS40	TS45	TS61
-5.0	32000	0.00	0.00	0.00	0.00	0.00	0.00	0.00	0.00	0.00	0.00	0.00	0.00
-4.5	24000	0.00	0.00	0.00	0.00	0.00	0.00	0.00	0.00	0.00	0.00	0.00	0.00
-4.0	16000	0.00	0.00	0.00	0.00	0.44	0.00	0.00	0.00	0.00	0.00	0.00	0.00
-3.5	12000	0.00	0.00	0.87	0.00	0.65	2.37	0.00	0.00	0.00	0.00	0.00	0.00
-3.0	8000	0.04	0.00	1.03	1.02	1.10	1.64	0.00	0.45	0.66	0.00	0.54	1.44
-2.5	6000	0.40	0.00	2.41	3.08	3.64	4.30	0.00	0.00	0.20	0.00	0.55	1.29
-2.0	4000	1.27	0.88	6.81	8.12	4.16	5.78	0.16	0.19	4.59	0.01	0.67	3.20
-1.5	3000	3.00	2.33	5.99	7.61	5.63	5.79	0.37	4.72	4.82	0.09	1.99	5.90
-1.0	2000	4.62	4.06	7.23	7.05	7.92	7.00	0.77	1.96	5.83	0.35	3.83	7.80
-0.5	1500	7.36	6.15	8.64	7.90	8.71	6.82	1.42	6.58	7.39	1.22	6.69	9.56
0.0	1000	9.61	7.59	7.43	9.23	9.96	7.56	2.55	5.72	7.37	3.06	9.19	9.94
0.5	750	10.49	8.92	8.32	7.34	8.83	5.96	4.41	8.03	11.57	6.52	9.80	9.74
1.0	500	10.23	8.98	7.67	7.55	8.29	5.36	6.20	6.78	7.55	10.68	8.94	7.99
1.5	375	9.70	8.76	6.87	6.61	7.13	5.17	7.13	8.36	9.23	11.09	7.61	6.67
2.0	250	8.85	9.24	6.29	5.57	6.21	5.19	9.12	5.49	2.87	8.02	7.55	6.22
2.5	188	9.49	7.02	5.95	4.80	7.32	6.70	7.85	0.00	4.89	7.06	5.51	4.59
3.0	125	8.08	9.63	5.91	5.56	5.85	6.30	12.49	8.35	8.45	11.83	7.56	6.26
3.5	94	4.31	6.13	4.15	4.24	3.03	4.68	9.79	6.75	5.60	8.02	5.24	4.31
4.0	63	4.32	6.36	4.57	4.52	2.91	4.58	10.38	7.67	6.02	8.81	5.80	4.53
4.5	47	3.13	4.72	3.49	3.34	2.04	3.22	7.67	6.66	4.65	7.03	4.98	3.48
5.0	31	2.01	3.13	2.38	2.24	1.41	2.35	5.42	5.14	3.11	5.01	3.79	2.37
5.5	23	0.92	1.57	1.15	1.12	0.79	1.43	3.04	2.91	1.50	2.59	2.08	1.22
6.0	16	0.70	1.33	0.92	0.94	0.84	1.67	2.91	2.79	1.24	2.33	1.99	1.05
6.5	12	0.40	0.85	0.53	0.58	0.70	1.47	2.09	2.78	0.72	1.56	1.42	0.67

Φ	µm	G1	G2	S1	TT01	TT02	TT02B	TS18	TS26	TS30	TS40	TS45	TS61
7.0	8	0.25	0.58	0.34	0.39	0.60	1.26	1.54	1.89	0.44	1.09	1.04	0.46
7.5	6	0.13	0.32	0.18	0.21	0.42	0.79	0.87	1.73	0.23	0.61	0.59	0.24
8.0	4	0.10	0.21	0.11	0.18	0.36	0.70	0.66	1.57	0.11	0.47	0.47	0.2
8.5	3	0.06	0.14	0.06	0.11	0.29	0.61	0.46	1.28	0.07	0.36	0.36	0.18
9.0	2	0.05	0.05	0.03	0.09	0.17	0.56	0.38	1.03	0.05	0.27	0.26	0.08
9.5	1.5	0.03	0.06	0.03	0.08	0.09	0.37	0.24	0.89	0.04	0.18	0.17	0.07
10.0	1	0.46	0.99	0.66	0.46	0.51	0.36	2.09	0.29	0.80	1.72	1.36	0.53
		100.00	100.00	100.00	99.95	100.00	100.00	100.00	100.00	100.00	100.00	100.00	100.00
Thickness (cm)		43.00	6.00	40.00	61.00	80.00	70.00	37.00	33.00	30.00	6.00	12.5	90
Location		N64.39972 W 17.37583	N 64.39972 W 17.37361	N 64.40072 W 17.39975	N 64.40187 W 17.37842	N 64.40215 W 17.38530	N 64.40235 W 17.38615	N 64.40448 W 17.39537	N 64.39797 W 17.37389	N 64.39839 W 17.37331	N 64.42757 W 17.39230	N 64.41718 W 17.39422	N 64.40233 W 17.38780

UNIT C

Φ	μm	G1	S1	TT01	TT02-B	TS18	TS19	TS25	TS40	TS45	TS60	TS71	TS72
-5.0	32000	0.00	3.35	0.00	1.23	0.00	0.00	0.00	0.00	0.00	0.00	0.00	0.00
-4.5	24000	0.00	2.57	1.18	2.20	0.00	0.00	0.00	0.00	0.00	0.00	0.00	0.00
-4.0	16000	0.00	4.40	1.16	1.86	0.00	2.56	0.00	0.00	3.45	0.00	0.00	0.00
-3.5	12000	0.00	2.69	1.16	6.69	0.00	0.44	0.00	0.00	0.44	0.00	0.00	0.00
-3.0	8000	0.00	3.93	2.83	4.34	0.45	0.77	0.16	0.00	1.27	1.52	0.23	0.60
-2.5	6000	0.28	3.01	1.50	9.56	1.24	1.21	2.01	0.00	4.78	1.56	0.71	1.56
-2.0	4000	1.42	8.50	4.51	7.57	2.12	1.60	5.69	0.00	6.20	5.15	3.20	0.32
-1.5	3000	3.83	6.79	5.50	7.84	3.82	3.93	7.93	0.07	9.05	6.19	3.78	2.88
-1.0	2000	7.00	6.36	5.37	7.99	5.67	5.12	8.53	0.59	11.18	8.06	4.38	5.10
-0.5	1500	9.77	6.86	6.40	6.92	7.42	7.83	10.50	1.93	10.03	10.18	6.48	7.76
0.0	1000	11.78	5.49	7.28	6.01	8.19	8.58	8.75	4.30	8.37	5.97	7.03	8.75
0.5	750	12.65	5.14	4.99	4.61	8.41	8.42	7.75	7.92	6.49	5.72	6.67	9.30
1.0	500	9.39	4.05	5.12	3.87	7.47	7.50	5.06	12.15	4.64	4.85	6.89	8.63
1.5	375	8.03	3.40	4.03	3.09	5.72	6.13	5.29	11.67	3.40	4.28	6.07	6.76
2.0	250	9.02	2.76	4.05	2.76	5.67	5.75	4.31	9.01	3.16	3.69	5.33	7.36
2.5	188	6.32	2.71	4.18	3.23	4.17	3.93	2.89	7.83	2.20	3.73	4.83	5.42
3.0	125	5.35	4.36	6.47	3.13	6.49	5.53	5.97	12.00	3.32	5.20	6.54	7.44
3.5	94	3.68	3.31	5.94	3.42	5.24	4.45	4.44	7.43	2.89	5.37	6.44	4.55
4.0	63	3.86	4.37	7.18	3.26	6.33	5.77	5.41	7.20	3.89	6.64	7.74	5.39
4.5	47	2.84	4.19	6.09	2.23	5.59	5.46	4.61	5.23	3.81	5.92	6.60	4.78
5.0	31	1.82	3.37	4.45	1.59	4.43	4.28	3.55	3.68	3.18	4.45	4.92	3.57
5.5	23	0.85	1.87	2.43	0.97	2.47	2.39	1.99	1.96	1.85	2.46	2.69	1.93
6.0	16	0.67	1.78	2.25	1.14	2.34	2.24	1.91	1.87	1.76	2.36	2.54	1.83
6.5	12	0.39	1.24	1.57	1.03	1.69	1.57	1.33	1.31	1.23	1.68	1.79	1.36
7.0	8	0.25	0.87	1.12	0.90	1.24	1.14	0.93	0.92	0.87	1.23	1.29	1.06

Φ	µm	G1	S1	TT01	TT02-B	TS18	TS19	TS25	TS40	TS45	TS60	TS71	TS72
7.5	6	0.13	0.48	0.62	0.58	0.71	0.64	0.51	0.51	0.48	0.69	0.72	0.63
8.0	4	0.11	0.37	0.54	0.5	0.68	0.47	0.26	0.43	0.34	0.66	0.52	0.46

Φ	μm	G1	S1	TT01	TT02-B	TS18	TS19	TS25	TS40	TS45	TS60	TS71	TS72
8.5	3	0.06	0.29	0.47	0.45	0.58	0.38	0.07	0.26	0.20	0.49	0.30	0.31
9.0	2	0.03	0.16	0.37	0.32	0.44	0.27	0.05	0.18	0.17	0.30	0.21	0.24
9.5	1.5	0.04	0.09	0.22	0.21	0.37	0.21	0.03	0.06	0.08	0.26	0.16	0.12
10.0	1	0.44	1.27	1.03	0.51	1.02	1.43	0.07	1.49	1.27	1.41	1.94	1.88
		100.00	100.00	100.00	100.00	100.00	100.00	99.99	100.00	100.00	100.00	100.00	100.00
Thickness (cm)		48.00	265.00	70.00	420.00	118.00	110.00	80.00	20.00	22.00	350	254	105
Location		N 64.39972 W 17.37583	N 64.40072 W 17.39975	N 64.40187 W 17.37842	N 64.40235 W 17.38615	N 64.40448 W 17.39537	N 64.40765 W 17.39583	N 64.39797 W 17.37389	N 64.42757 W 17.39230	N 64.41718 W 17.39422	N 64.40097 W 17.38732	N 64.41213 W 17.39038	N 64.41457 W 17.38922

UNIT D

Φ	µm	COR4	G1	G7	GH9	S1	TT01	TT02B	TS43B	TS60	TS71	TS72	TS73
-5.0	32000	0.00	0.00	0.00	0.00	0.00	0.00	0.00	0.00	0.00	0.00	0.00	0.00
-4.5	24000	0.00	0.00	0.00	0.00	0.00	0.00	0.00	0.00	0.00	0.00	0.00	0.00
-4.0	16000	0.00	0.00	0.00	0.00	0.40	0.14	3.88	0.00	0.00	0.00	0.00	0.00
-3.5	12000	0.00	0.00	0.00	0.00	0.45	0.00	3.64	0.00	0.00	0.00	0.67	0.00
-3.0	8000	0.00	0.00	0.60	0.00	0.83	0.35	5.15	0.00	0.00	0.65	1.46	2.54
-2.5	6000	0.00	0.16	6.30	3.04	0.61	0.19	12.26	0.10	0.27	1.86	2.41	1.64
-2.0	4000	0.67	1.29	8.78	2.22	1.92	1.28	7.41	0.52	0.67	4.20	2.56	1.90
-1.5	3000	1.43	4.00	11.67	3.55	2.09	2.51	8.67	1.06	1.03	11.20	3.68	2.95
-1.0	2000	2.76	8.06	13.67	3.85	3.45	4.54	6.94	1.98	1.76	17.34	4.90	3.62
-0.5	1500	5.72	11.85	12.70	5.47	6.42	6.84	5.19	5.12	3.32	17.00	6.41	4.82
0.0	1000	6.85	13.71	10.49	5.88	5.40	8.55	4.50	5.73	4.28	5.90	7.27	5.25
0.5	750	7.17	15.41	7.84	6.76	9.44	8.76	3.68	6.73	6.67	13.04	7.73	5.70
1.0	500	6.28	10.15	5.46	7.22	8.70	9.24	3.31	13.46	8.15	9.52	6.90	6.14
1.5	375	5.73	7.98	3.87	6.24	9.55	8.75	3.05	12.70	8.89	5.82	6.07	5.20
2.0	250	6.20	7.70	3.34	6.96	8.26	6.57	2.74	9.98	8.69	3.58	6.10	5.72
2.5	188	4.88	4.72	2.20	5.63	7.71	6.50	3.22	6.85	8.39	2.37	4.51	4.63
3.0	125	7.59	4.50	2.88	8.31	8.15	8.11	4.03	8.33	9.76	1.91	6.31	8.20
3.5	94	6.81	2.94	2.18	6.24	4.93	6.52	4.16	5.07	6.59	1.12	4.78	6.64
4.0	63	8.39	2.81	2.34	7.06	5.43	6.41	4.19	5.28	7.29	1.18	6.37	7.93
4.5	47	7.68	1.90	1.81	5.80	4.38	4.90	3.01	4.20	6.31	0.95	5.89	6.94
5.0	31	6.16	1.15	1.26	4.37	3.33	3.29	2.23	3.26	5.05	0.69	4.65	5.40
5.5	23	3.46	0.52	0.65	2.49	1.86	1.88	1.38	1.87	2.88	0.37	2.56	3.13
6.0	16	3.25	0.38	0.57	2.39	1.78	1.30	1.62	1.90	2.77	0.35	2.37	3.04
6.5	12	2.29	0.20	0.37	1.68	1.25	0.89	1.43	1.40	1.94	0.24	1.65	2.20
7.0	8	1.66	0.12	0.26	1.23	0.89	0.63	1.22	1.04	1.37	0.17	1.19	1.61
7.5	6	0.92	0.06	0.14	0.69	0.50	0.35	0.76	0.60	0.76	0.10	0.67	0.90
8.0	4	0.75	0.06	0.10	0.60	0.35	0.27	0.56	0.45	0.67	0.08	0.52	0.57

Φ	µm	COR4	G1	G7	GH9	S1	TT01	TT02B	TS43B	TS60	TS71	TS72	TS73
9.0	2	0.45	0.04	0.06	0.32	0.19	0.16	0.37	0.20	0.46	0.04	0.32	0.29
9.5	1.5	0.27	0.05	0.07	0.21	0.07	0.11	0.21	0.11	0.32	0.03	0.22	0.11
10.0	1	2.02	0.16	0.31	1.32	1.45	0.77	0.75	1.76	1.18	0.22	1.36	2.56
		100.00	100.00	100.00	100.00	100.00	100.00	100.00	100.00	100.00	100.00	100.00	100.00
Thickness (cm)		8.00	56.00	15.00	30.00	7.00	152.00	24.00	6.00	22.00	7.00	13.00	30.00
Location		N 64.41205 W 17.37848	N 64.39972 W 17.37583	N 64.39889 W 17.37389	N 64.39750 W 17.37472	N 64.40072 W 17.39975	N 64.40187 W 17.37842	N 64.40235 W 17.38615	N 64.42072 W 17.38568	N 64.40097 W 17.38732	N 64.41213 W 17.39038	N 64.41457 W 17.38922	N 64.41438 W 17.38478

UNIT E

Φ	μm	COR4	G5	TT01	TT02B	TS6	TS48	TS60
-5.0	32000	0.00	0.00	0.00	0.00	0.00	0.00	0.00
-4.5	24000	0.00	0.00	0.00	0.00	0.00	0.00	0.32
-4.0	16000	0.00	0.00	1.01	2.64	0.00	0.00	0.15
-3.5	12000	0.00	0.00	0.20	2.07	0.00	0.00	0.40
-3.0	8000	0.00	0.90	1.98	3.50	1.13	0.00	1.00
-2.5	6000	0.32	0.88	1.49	9.28	2.14	0.47	1.02
-2.0	4000	1.24	1.24	5.25	7.32	2.27	0.37	3.63
-1.5	3000	2.04	3.22	5.05	7.49	4.11	0.56	4.73
-1.0	2000	3.27	4.90	6.50	6.69	5.88	1.57	5.56
-0.5	1500	5.98	6.60	6.82	5.45	7.41	4.54	7.47
0.0	1000	7.65	7.46	6.27	4.96	7.13	7.64	5.90
0.5	750	8.17	7.31	4.29	4.01	7.11	9.14	6.51
1.0	500	7.38	6.43	4.34	3.77	6.27	8.55	6.27
1.5	375	6.24	5.46	5.50	3.61	5.14	7.08	5.81
2.0	250	6.13	5.76	4.43	3.56	5.11	6.96	5.26
2.5	188	4.58	4.42	3.99	5.27	3.64	5.08	5.18
3.0	125	6.84	7.18	6.41	5.51	5.74	7.66	6.47
3.5	94	5.95	6.01	5.82	4.56	4.70	6.61	5.40
4.0	63	7.46	7.31	7.43	4.59	6.49	8.62	6.59
4.5	47	7.01	6.59	6.66	3.32	6.37	7.56	5.82
5.0	31	5.55	5.00	5.02	2.50	5.18	5.48	4.49
5.5	23	3.17	2.80	2.72	1.56	3.01	2.86	2.53
6.0	16	3.00	2.67	2.49	1.85	2.92	2.56	2.45
6.5	12	2.07	1.93	1.69	1.63	2.10	1.75	1.77
7.0	8	1.49	1.44	1.18	1.38	1.53	1.25	1.31
7.5	6	0.83	0.82	0.65	0.85	0.86	0.70	0.74
8.0	4	0.68	0.78	0.46	0.77	0.69	0.66	0.56

Φ	µm	COR4	G5	TT01	TT02B	TS6	TS48	TS60
8.5	3	0.55	0.62	0.31	0.63	0.55	0.52	0.42
9.0	2	0.46	0.47	0.26	0.49	0.38	0.49	0.38
9.5	1.5	0.27	0.38	0.14	0.37	0.29	0.34	0.22
10.0	1	1.65	1.40	1.63	0.37	1.84	0.97	1.65
		100.00	100.00	100.00	100.00	100.00	100.00	100.00
Thickness (cm)		50.00	320.00	185.00	115.00	300.00	8.00	265.00
Location		N 64.41205 W 17.37848	N 64.40806 W 17.38806	N 64.40187 W 17.37842	N 64.40235 W 17.38615	N 64.40050 W 17.38762	N 64.41418 W 17.38433	N 64.40097 W 17.38732

UNIT F

Φ	μm	G1	G2	G3	GH3	GH4	TT01	TS26
-5.0	32000	0.00	0.00	0.00	0.00	0.00	0.00	0.00
-4.5	24000	0.00	0.00	0.00	0.00	0.00	0.00	0.00
-4.0	16000	1.03	0.00	0.00	0.00	0.00	0.00	0.00
-3.5	12000	0.07	0.00	1.45	1.45	0.00	0.52	0.00
-3.0	8000	0.66	3.17	1.65	1.65	0.00	1.18	0.13
-2.5	6000	1.11	0.87	0.94	0.94	0.72	1.20	1.67
-2.0	4000	2.31	5.75	4.29	4.29	1.32	4.87	4.71
-1.5	3000	3.76	7.60	4.96	4.96	3.31	5.27	6.56
-1.0	2000	4.59	8.41	6.08	6.08	5.11	5.81	7.06
-0.5	1500	5.60	8.05	6.98	6.98	6.91	6.37	8.69
0.0	1000	6.25	7.83	6.29	6.29	7.49	6.34	7.25
0.5	750	9.12	8.23	7.44	7.44	7.54	4.95	7.40
1.0	500	6.06	4.54	4.47	4.47	7.30	4.86	4.79
1.5	375	5.20	5.88	6.87	6.86	8.57	5.13	5.75
2.0	250	5.10	3.15	3.98	4.50	4.82	4.46	3.49
2.5	188	4.10	2.73	3.71	4.38	4.05	4.21	2.55
3.0	125	7.88	5.23	6.83	7.73	7.11	7.41	6.30
3.5	94	5.67	4.24	5.12	5.59	5.42	5.66	4.96
4.0	63	7.08	5.51	6.33	6.54	6.90	7.14	6.44
4.5	47	6.22	4.98	5.66	5.52	6.22	6.39	5.87
5.0	31	4.90	3.82	4.45	4.16	4.79	4.89	4.46
5.5	23	2.80	2.08	2.52	2.26	2.63	2.74	2.50
6.0	16	2.71	2.01	2.50	2.14	2.53	2.63	2.41
6.5	12	1.95	1.45	1.85	1.49	1.81	1.92	1.75
7.0	8	1.42	1.07	1.36	1.06	1.32	1.44	1.29
7.5	6	0.80	0.61	0.76	0.58	0.74	0.82	0.73
8.0	4	0.61	0.40	0.66	0.47	0.69	0.71	0.66

Φ	µm	G1	G2	G3	GH3	GH4	TT01	TS26
9.0	2	0.46	0.27	0.34	0.19	0.41	0.58	0.45
9.5	1.5	0.39	0.18	0.27	0.15	0.28	0.35	0.22
10.0	1	1.56	1.62	1.67	1.51	1.43	1.47	1.32
		100.00	100.00	100.00	100.00	100.00	100.00	100.00
Thickness (cm)		226.00	200.00	26.00	48.00	74.00	139.00	150.00
Location		N 64.39972 W 17.37583	N 64.39972 W 17.37361	N 64.40000 W 17.37028	N 64.40111 W 17.36500	N 64.39972 W 17.36861	N 64.40187 W 17.37842	N 64.39797 W 17.37389

UNIT G

Φ	μm	COR4	G1	S1	TT01	TT02B	TS19	TS45	TS60	TS71
-5.0	32000	0.00	0.00	0.00	0.00	0.00	0.00	0.00	0.00	0.00
-4.5	24000	0.00	0.00	0.00	0.00	0.36	0.00	0.00	0.00	0.00
-4.0	16000	0.00	0.00	0.00	0.00	3.55	0.00	0.00	0.00	0.00
-3.5	12000	0.00	0.00	0.00	0.00	5.59	0.00	0.00	0.73	0.00
-3.0	8000	0.00	0.00	0.62	1.08	3.42	0.00	0.00	0.22	0.91
-2.5	6000	0.27	0.78	0.48	2.14	8.15	0.62	0.27	0.65	1.03
-2.0	4000	1.09	8.78	1.84	4.71	7.13	0.83	1.09	3.91	2.12
-1.5	3000	3.22	3.30	2.55	4.89	6.53	1.56	3.22	4.21	3.50
-1.0	2000	5.73	3.58	3.77	5.47	6.61	2.82	5.73	5.21	4.12
-0.5	1500	8.46	5.52	6.02	7.18	5.74	4.87	8.46	6.62	5.69
0.0	1000	8.19	7.04	6.15	7.26	6.27	6.82	8.19	5.16	6.24
0.5	750	7.21	7.59	8.54	6.81	4.90	7.84	7.21	6.04	6.75
1.0	500	6.15	10.21	7.82	6.41	5.26	8.09	6.15	5.96	6.97
1.5	375	5.34	7.67	7.82	6.11	4.21	7.65	5.34	5.69	7.30
2.0	250	5.81	7.72	6.88	4.57	3.61	7.40	5.81	5.05	7.06
2.5	188	4.91	5.75	5.66	4.67	4.12	6.25	4.91	4.61	6.59
3.0	125	7.97	3.31	7.89	6.49	4.19	6.90	7.97	6.49	7.81
3.5	94	6.08	6.04	5.50	4.89	3.67	6.72	6.08	5.75	5.72
4.0	63	7.03	4.06	6.65	6.10	3.67	7.65	7.03	7.38	6.55
4.5	47	5.98	4.79	5.73	5.51	2.65	6.45	5.98	6.87	5.54
5.0	31	4.50	4.06	4.42	4.32	1.99	4.85	4.50	5.30	4.26
5.5	23	2.55	3.00	2.47	2.45	1.25	2.67	2.55	2.98	2.43
6.0	16	2.44	1.63	2.39	2.31	1.51	2.54	2.44	2.85	2.38
6.5	12	1.73	1.50	1.71	1.64	1.36	1.84	1.73	2.05	1.74
7.0	8	1.28	1.03	1.24	1.20	1.17	1.37	1.28	1.52	1.29
7.5	6	0.73	1.73	0.69	0.68	0.74	0.78	0.73	0.86	0.73
8.0	4	0.62	0.67	0.48	0.37	0.67	0.62	0.67	0.69	0.71

Φ	µm	COR4	G1	S1	TT01	TT02B	TS19	TS45	TS60	TS71
9.0	2	0.34	0.08	0.36	0.19	0.48	0.31	0.43	0.51	0.52
9.5	1.5	0.27	0.05	0.27	0.09	0.33	0.25	0.36	0.45	0.44
10.0	1	1.54	0.00	1.70	2.29	0.31	1.77	1.30	0.38	0.28
									1.24	0.62
		100.00	100.01	100.00	100.00	100.00	100.00	100.00	100.00	100.00
Thickness (cm)		35.00	30.00	47.00	65.00	10.00	15.00	35.00	45.00	50.00
Location		N 64.41205 W 17.37848	N 64.39972 W 17.37583	N 64.40072 W 17.39975	N 64.40187 W 17.37842	N 64.40235 W 17.38615	N 64.40765 W 17.39583	N 64.41718 W 17.39422	N 64.40097 W 17.38732	N 64.41213 W 17.39038

FROM ODDSON, 2007

Φ	µm	BO_03	BO_05	Kq_02	Ks_02	Ks_05	Kt_02	Kt_04	Ku_03	Ku_05
-5.0	32000	0.00	0.00	0.00	0.00	0.00	0.00	0.00	0.00	0.00
-4.5	24000	0.00	0.00	0.00	0.00	0.00	0.00	0.00	0.00	0.00
-4.0	16000	0.00	0.00	0.00	0.00	0.00	0.00	0.00	0.00	0.00
-3.5	12000	0.00	0.00	0.00	0.00	0.00	0.00	0.00	0.20	0.10
-3.0	8000	0.00	0.00	0.00	0.00	0.00	0.05	0.07	0.18	0.21
-2.5	6000	0.31	0.18	0.00	0.17	0.00	0.16	0.14	0.54	0.28
-2.0	4000	0.05	0.23	2.29	0.22	0.00	0.35	0.21	0.82	0.32
-1.5	3000	0.51	0.71	0.00	0.66	0.12	0.48	0.84	1.82	1.06
-1.0	2000	0.67	0.83	0.82	0.91	0.33	1.19	1.72	2.79	1.98
-0.5	1500	1.49	2.48	2.02	2.54	0.66	2.80	3.16	4.80	3.39
0.0	1000	3.74	3.85	3.49	4.10	2.03	3.91	5.24	5.60	4.60
0.5	750	6.47	5.71	5.48	5.89	5.09	5.07	7.79	5.91	6.07
1.0	500	8.35	7.95	5.78	7.19	8.39	6.38	8.79	5.64	7.04

Φ	µm	BO_03	BO_05	Kq_02	Ks_02	Ks_05	Kt_02	Kt_04	Ku_03	Ku_05
1.5	375	8.85	9.26	6.22	7.94	9.19	8.02	8.76	5.64	7.72
2.5	188	8.42	8.68	7.99	8.38	8.35	10.09	7.43	6.85	8.28
3.0	125	12.32	12.33	13.73	12.24	13.01	13.57	10.81	11.34	12.33
3.5	94	9.40	9.16	11.42	9.44	10.08	9.33	8.71	9.96	9.17
4.0	63	8.78	8.92	10.38	9.41	11.58	8.23	8.39	9.71	9.39
4.5	47	7.90	4.95	6.25	7.36	8.57	6.14	6.30	7.45	9.43
5.0	31	4.75	3.66	5.03	4.61	5.04	3.96	4.00	4.74	4.45
5.5	23	2.83	2.71	4.04	2.97	2.98	2.61	2.61	3.04	2.18
6.0	16	1.73	2.01	3.20	1.96	1.78	1.75	1.74	1.96	1.10
6.5	12	1.07	1.48	1.64	1.31	1.06	1.18	1.18	1.27	0.58
7.0	8	0.67	1.10	0.50	0.90	0.64	0.81	0.81	0.83	0.31
7.5	6	0.44	0.81	0.28	0.62	0.39	0.56	0.57	0.55	0.15
8.5	3	0.06	0.53	0.09	0.29	0.12	0.32	0.31	0.26	0.03
9.0	2	0.05	0.45	0.06	0.18	0.09	0.21	0.27	0.13	0.02
9.5	1.5	0.03	0.24	0.08	0.08	0.07	0.16	0.18	0.09	0.01
10.0	1	0.40	0.17	0.61	0.36	0.15	0.35	0.14	0.25	0.01

		BO_03	BO_05	Kq_02	Ks_02	Ks_05	Kt_02	Kt_04	Ku_03
	100.00	100.00	100.00	100.00	100.00	100.00	100.00	100.00	100.00
Thickness (cm)	1.27	0.34	0.01	1.37	0.17	5.12	3.67	13.33	6.20
Location	N 64.56333 W 17.20001	N 64.64666 W 17.41666	N 64.60833 W 17.08334	N 64.52083 W 17.23333	N 64.53833 W 17.43334	N 64.48516 W 17.40000	N 64.47500 W 17.28333	N 64.44667 W 17.35001	N 64.44733 W 17.40000

APPENDIX IV

METHOD FOR DETERMING GRAIN-SIZE DISTRIBUTION OF PUMICE LENSES

The size distribution of pumice layers was determined from photographs according to the number density of clasts within a given size range per 100 cm^2. A selection of photographs of G2004 pumice lenses were imported into drafting software (Corel™) where the image was scaled to a 10 x 10 cm grid and grain boundaries were manually outlined. The maximum diameter of each clast was then measured in order to create a grain-size frequency distribution. If all clasts are assumed to be spherical and of equivalent density then the frequency distribution according to clast diameter will be equivalent to the conventional mass frequency distribution used for grain-size analysis.

Figure A4.1: Photographs of pumice lenses in units C and E. Clast outlines are manually traced and thresholded. The maximum diameter of each clast is then measured to create an area-normalised frequency distribution of clast sizes. Unit E, Section TS60.

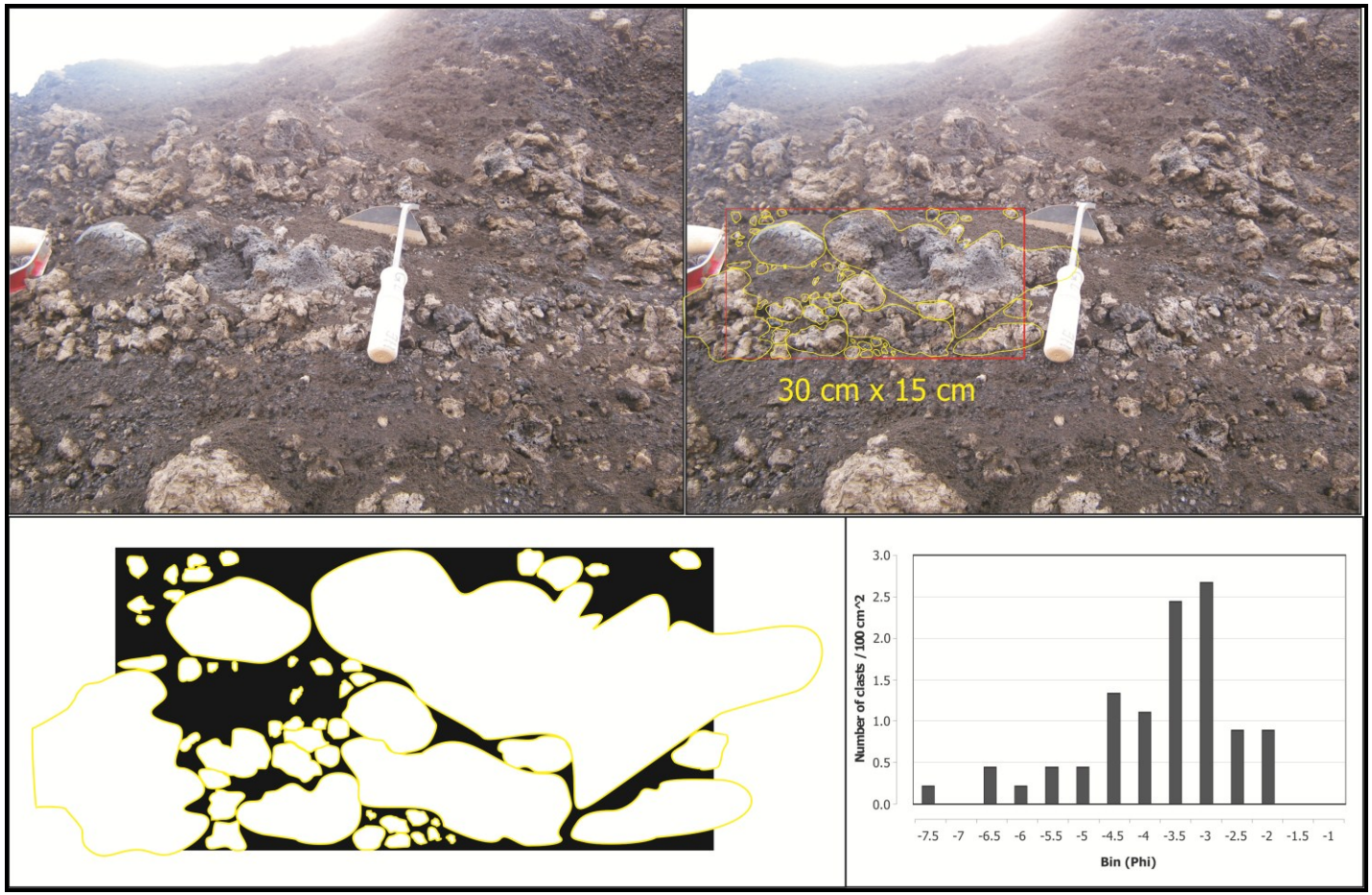

Figure A4.2: Photographs of pumice lenses in units C and E. Clast outlines are manually traced and thresholded. The maximum diameter of each clast is then measured to create an area-normalised frequency distribution of clast sizes. Unit C, Section TS48.

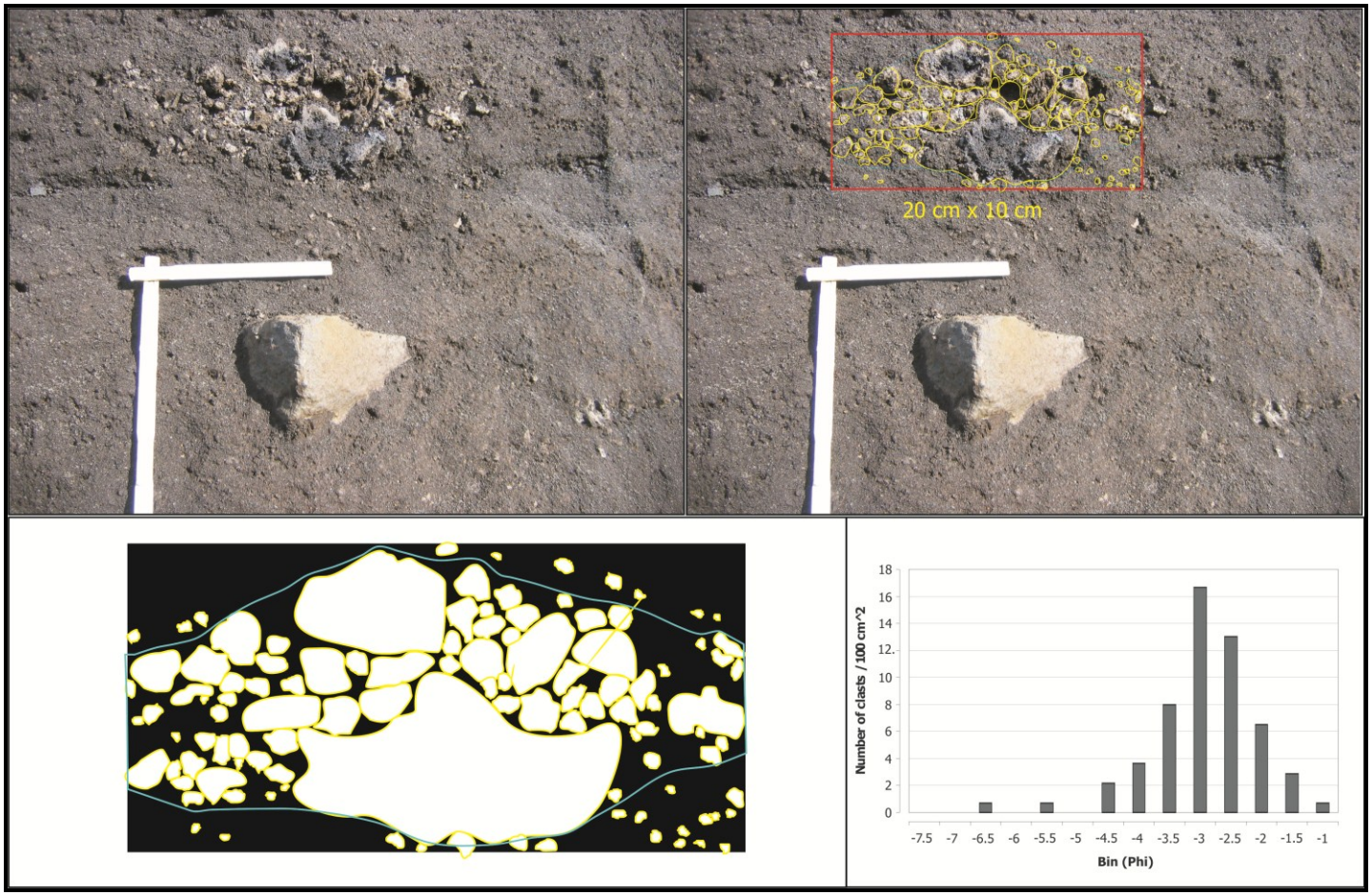

Figure A4.3: Photographs of pumice lenses in units C and E. Clast outlines are manually traced and thresholded. The maximum diameter of each clast is then measured to create an area-normalised frequency distribution of clast sizes. Unit C, Section GH7.

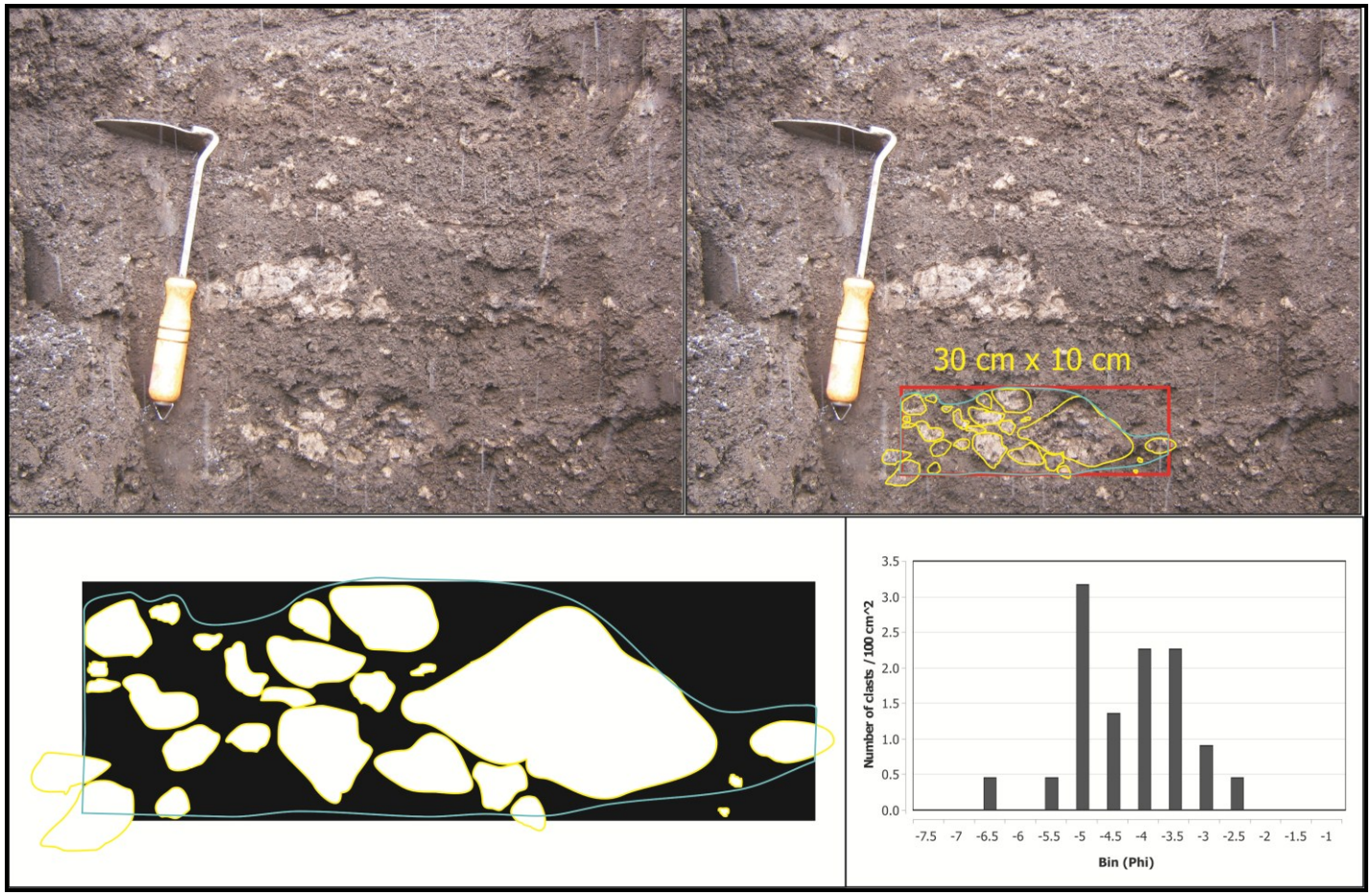

Figure A4.4: Photographs of pumice lenses in units C and E. Clast outlines are manually traced and thresholded. The maximum diameter of each clast is then measured to create an area-normalised frequency distribution of clast sizes. Unit E, Section TS71.

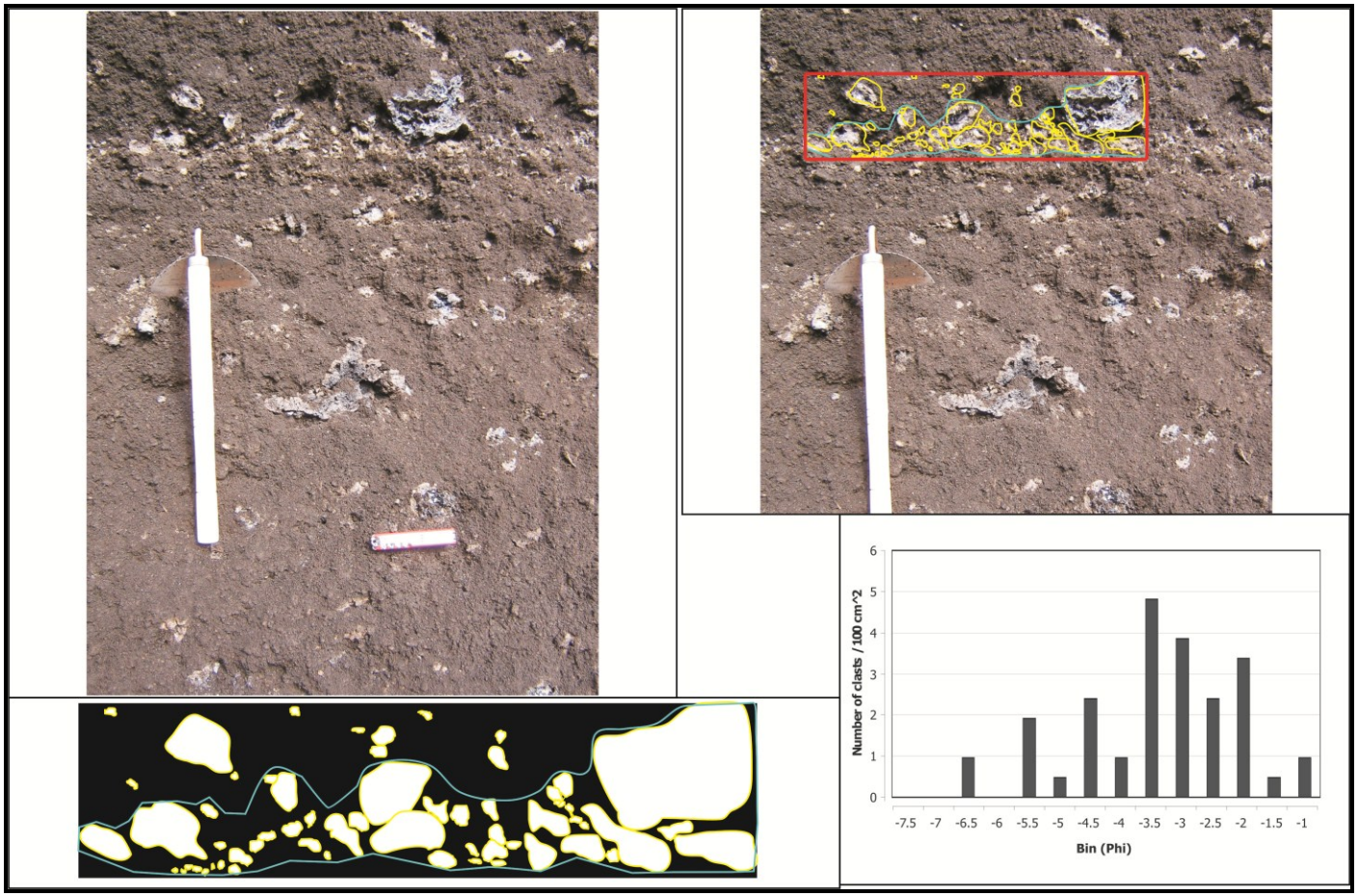

Figure A4.5: Photographs of pumice lenses in units C and E. Clast outlines are manually traced and thresholded. The maximum diameter of each clast is then measured to create an area-normalised frequency distribution of clast sizes. Unit C, Section TT02.

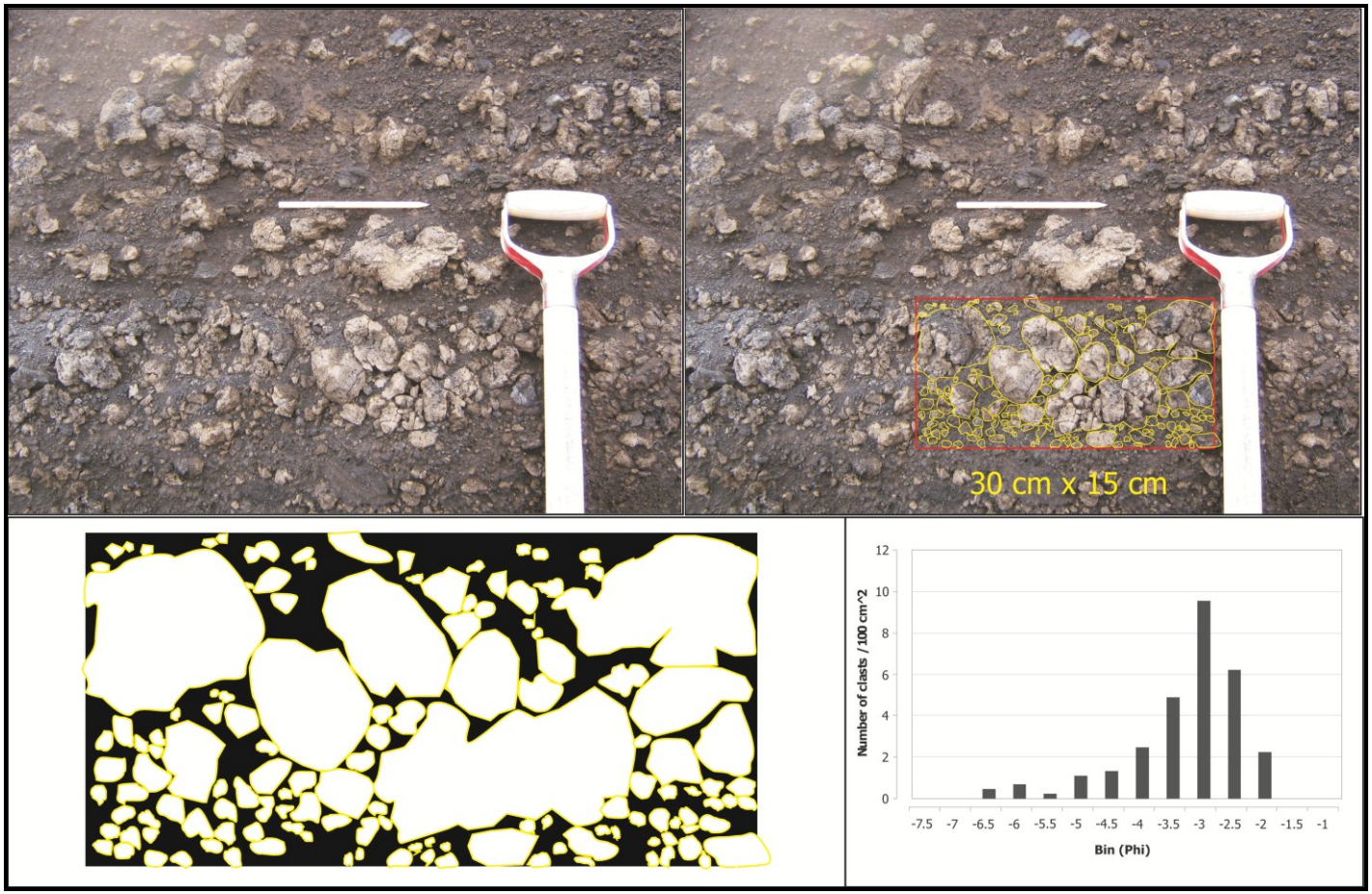

APPENDIX V

COMPONENT DATA

UNIT A					**UNIT B**			
Proximal	**-2.0**	**-1.0**	**0.5**	**2.5**	**Proximal**	**-2.0**	**-1.0**	**0.5**
Free crystals	0	0	1	2	Free crystals	0	0	0
Accidental lithics	0	0	2	1	Accidental lithics	2	0	3
Juvenile highly vesicular	3	1	0	0	Juvenile highly vesicular	0	0	0
Juvenile moderately vesicular	97	99	86	95	Juvenile moderately vesicular	98	100	81
Juvenile non-vesicular	0	0	11	2	Juvenile non-vesicular	0	0	16

UNIT A					UNIT B			
Ropy	0	0	2	23	Ropy	0	0	4
Ragged	0	0	1	0	Ragged	0	0	0
Blocky	100	100	97	76	Blocky	100	100	96
Cuspate	0	0	0	2	Cuspate	0	0	0
Distal	**-2.0**	**-1.0**	**0.5**	**2.5**	**Distal**	**-2.0**	**-1.0**	**0.5**
Free crystals	0	0	2	23	Free crystals	0	0	0
Accidental lithics	0	0	1	0	Accidental lithics	0	3	2
Juvenile highly vesicular	100	100	97	76	Juvenile highly vesicular	0	0	0
Juvenile moderately vesicular	0	0	0	2	Juvenile moderately vesicular	67	15	7
Juvenile non-vesicular	0	0	0	0	Juvenile non-vesicular	33	82	91
Ropy	2	0	3	1	Ropy	0	1	0

UNIT A					**UNIT B**			
Ragged	0	7	7	10	Ragged	0	3	7
Blocky	95	93	90	88	Blocky	100	96	93
Cuspate	3	1	0	1	Cuspate	0	1	0

UNIT C					**UNIT D**			
Proximal	**-2.0**	**-1.0**	**0.5**	**2.5**	**Proximal**	**-1.0**	**0.5**	**2.5**
Free crystals	0	0	0	0	Free crystals	0	0	0
Accidental					Accidental			
lithics	1	0	1	0	lithics	0	0	0
Juvenile highly					Juvenile highly			
vesicular	61	55	29	32	vesicular	2	1	5
Juvenile moderately					Juvenile moderately			
vesicular	38	45	70	68	vesicular	91	93	95
Juvenile					Juvenile			
non-vesicular	0	0	0	0	non-vesicular	6	5	0
Ropy	0	4	10	0	Ropy	0	1	3
Ragged	0	11	16	32	Ragged	0	0	0
Blocky	100	84	74	67	Blocky	98	98	73
Cuspate	0	1	0	1	Cuspate	2	1	24

UNIT C					**UNIT D**			
Distal	**-2.0**	**-1.0**	**0.5**	**2.5**	**Distal**	**-1.0**	**0.5**	**2.5**
Free crystals	0	0	3	2	Free crystals	0	0	0
Accidental lithics	12	11	14	8	Accidental lithics	9	6	0
Juvenile highly vesicular	0	5	2	0	Juvenile highly vesicular	13	9	14
Juvenile moderately vesicular	46	58	14	0	Juvenile moderately vesicular	77	85	86
Juvenile non-vesicular	42	26	67	90	Juvenile non-vesicular	0	0	0
Ropy	0	5	0	0	Ropy	0	4	1
Ragged	6	4	2	0	Ragged	14	7	0
Blocky	79	90	98	87	Blocky	83	88	68
Cuspate	15	1	0	13	Cuspate	3	1	30

UNIT E				**Unit F**			
Proximal	**-0.5**	**-1.5**	**2.5**	**Proximal**	**-2.0**	**-1.0**	**0.5**
Free crystals	2	1	2	Free crystals	0	0	0
Accidental lithics	0	3	1	Accidental lithics	5	3	2
Juvenile highly vesicular	0	13	20	Juvenile highly vesicular	17	26	13
Juvenile moderately vesicular	98	76	40	Juvenile moderately vesicular	79	70	85
Juvenile non-vesicular	0	7	38	Juvenile non-vesicular	0	0	0
Ropy	0	5	2	Ropy	10	7	4
Ragged	0	9	18	Ragged	0	4	5
Blocky	98	85	74	Blocky	90	86	91
Cuspate	2	1	5	Cuspate	0	3	1

UNIT E				**Unit F**			
Distal	**-0.5**	**-1.5**	**2.5**	**Distal**	**-2.0**	**-1.0**	**0.5**
Free crystals	0	1	0	Free crystals	0	0	0
Accidental lithics	1	1	1	Accidental lithics	13	4	7
Juvenile highly vesicular	0	0	0	Juvenile highly vesicular	33	5	7
Juvenile moderately vesicular	70	39	40	Juvenile moderately vesicular	54	90	86
Juvenile non-vesicular	29	59	59	Juvenile non-vesicular	0	0	0
Ropy	0	1	0	Ropy	19	1	3
Ragged	4	12	38	Ragged	0	4	4
Blocky	96	85	58	Blocky	81	95	93
Cuspate	0	1	4	Cuspate	0	0	0

UNIT G				
Proximal	**-2.0**	**-1.0**	**0.5**	**2.5**
Free crystals	0	0	0	4
Accidental lithics	17	5	2	1
Juvenile highly vesicular	34	95	21	0
Juvenile moderately vesicular	49	0	77	12
Juvenile non-vesicular	0	0	0	83
Ropy	0	2	2	5
Ragged	2	0	17	11
Blocky	96	98	80	83
Cuspate	1	0	1	2
Distal	**-2.0**	**-1.0**	**0.5**	**2.5**
Free crystals	0	0	1	0
Accidental lithics	0	9	2	0
Juvenile highly vesicular	80	0	0	0

UNIT G				
Juvenile moderately vesicular	10	28	23	28
Juvenile non-vesicular	10	63	75	72
Ropy	0	0	2	0
Ragged	0	0	10	25
Blocky	100	98	87	70
Cuspate	0	2	1	5

APPENDIX VI

THE 1998 GRÍMSVÖTN ERUPTION

ERUPTION CHRONOLOGY

Prior to the 1998 eruption, vigorous micro-earthquake activity at depths between 1 and 4 km along the western and southern caldera rim were detected during a seismic survey conducted between May and August of that year (Alfaro, 2001). This local seismicity was interpreted to result from a combination of geothermal activity and the inflation of a shallow (~4 km depth) magma chamber (Alfaro et al., 2007).

The following overview of the 1998 Grímsvötn (G1998) eruption is based upon contemporary observations, as described by Guðmundsson et al. (1999), Sturkell et al. (2003) and F. Sigmundsson

(http://www.norvol.hi.is/html/geol/grimsvotn1998/photos98.html).

The Grímsvötn 1998 eruption commenced on December 18th and lasted for ten days. The eruption site was located on the southern caldera fault directly beneath the nunatak Svíahnúkur Vestri (also the location of the 1983 and 1934 eruptions; Fig. A6.1). The eruption site was inspected by aircraft each day during the first three days of the eruption, and then again on the penultimate day of activity. A selection of photographs is provided to accompany the verbal descriptions (Fig. A6.2).

Figure A6.1: Location of recent eruptions at Grímsvötn.

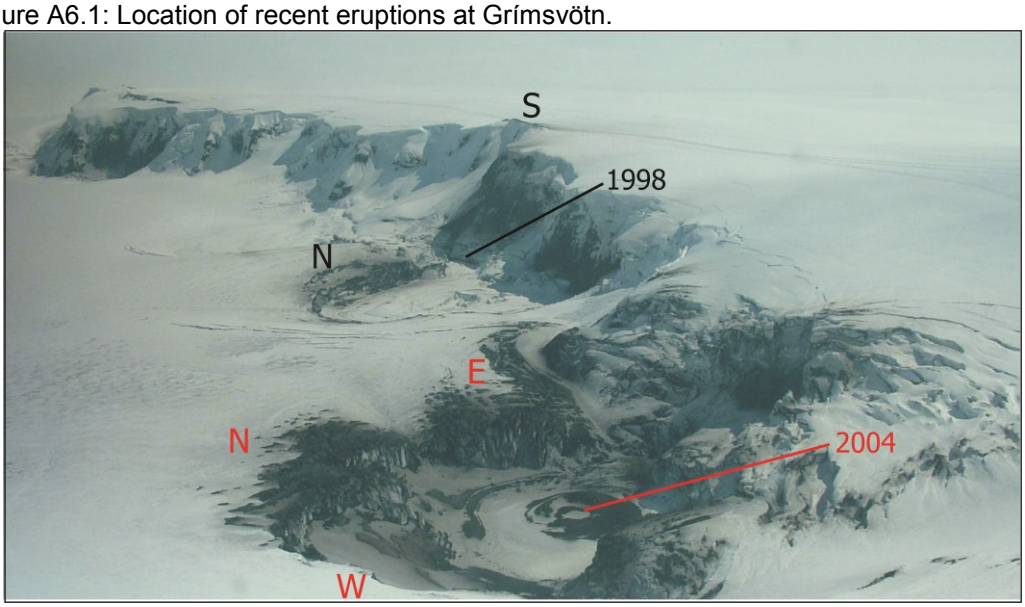

DAY 1

Eruption onset was marked by continuous seismic tremor at 10:20 GMT. Within ten minutes of onset, a subaerial plume was established, attaining up to 10 km elevation. Prior to the eruption, the ice was between 50 and120 m thick at this location. The initial phase of the eruption opened a 1.1 km long and 200 m wide fissure, aligned along the caldera edge. Along the fissure up to five eruptive centres were observed. Tephra jets from the thrust region of the eruption column reached as high as the top of the Grímsfjall ridge (300 m). Shortly thereafter, activity concentrated towards the centre of fissure segment and the base of the eruption column was estimated to be 400 m wide. Tephra was dispersed to the ESE.

DAY 2

Although the level of activity was sufficient to sustain a continuous plume at between 7 and 8 km elevation, the eruption was slightly less vigorous on the second day. Mild westerly winds resulted in tephra fall towards the SE. A portion of the Grímsvötn ice shelf was observed to have melted, but this did not significantly change the water level in the Grímsvötn lake.

DAY 3

A variety of different styles of activity were observed on the third day. The maximum plume height was 7 km; however this plume was not consistently maintained. Initially the plume was light-coloured (steam rich), but later the ash content of the plume increased, turning the plume black. Eventually it collapsed by approximately 1-2 km, generating a pyroclastic density current (PDC). Occasionally the eruption featured continuous uprush style activity. From the December 20th onwards, tephra was dispersed towards the north. Eruptive activity changed little over the next few days.

DAY 10

Activity was intermittent, resulting in a discontinuous plume. The plume attained a maximum altitude of up to 4.5 km, but disappeared entirely for periods in between. Ash was deposited in the near vicinity of the crater itself, with bombs up to 0.5 m in diameter occasionally ejected onto Grímsfjall. Continued melting of the ice shelf resulted in water ponding NE of the eruption site. At this stage a tephra ring within the lake, but also lying partly on the ice surface, had been created. This cone was estimated to be tens of metres thick, compared to the most proximal region of the tephra pile, which was estimated to be 20 m thick.

After G1998 an increase in geothermal output was observed, which was interpreted to result from shallow dyke intrusion associated with the eruption itself. There was no jökulhlaup associated with this event. Alfaro (2007) has estimated the erupted volume to be on the order of 0.1 km3.

STRATIGRAPHY

A representative section 350 m north of the 1998 crater (within the Grímsvötn caldera) was logged and sampled by Th. Thorðarson in 2007. This section was created as crevasses opened in the ice beneath, dissecting the tephra pile. In 2009, a further two sections were dug and logged south of the eruption site, along the Grímsfjall ridge, by M. T. Guðmundsson. The stratigraphy was identical at these two sites, hence only one location was sampled at ten centimetre intervals (on Svíahnúkur Vestri). Together, these sections record much of the material deposited during this event (Fig. A6.3). Sections to the south are logged from the underlying contact with 1934 scoria up to the surface, recording the opening phases of the eruption. Conversely, the northern section is logged from the top down and record material deposited during the middle and final phases of activity. Snowfall occurred during deposition of the tephra layer towards the south. However, as a consequence of geothermal activity beneath the ridge (a temperature of 77°C was recorded at the bottom of the logged hole), no intercalated snow/ice layers remain. Furthermore, any snow that may have initially covered the top of the deposit has since melted away. Samples were collected for grain size and geochemical analysis. Geochemical results are evaluated in Chap. 5, while grain size distributions are presented at the end of this appendix (Figs. A6.6 and A6.7).

Figure A6.2: Eruption photo panel illustrating the variability in styles of activity during the G1998 event. (A); (B); (C); (D); (E). Photos courtesy of M. T. Gudmundsson.

SOUTHERN SECTIONS

Two layers were identified, measured from the bottom contact up. The corresponding layer thickness at Hole 2, 50 m to the west of Hole 1, is given in square brackets (Fig. A6.4).

UNIT A1 - 75 CM [145 CM]

This layer is brown to greyish brown in appearance and consists almost entirely of juvenile, predominantly fine, ash with no apparent bedding or internal architecture. Layer 1 also contains some very rare coarse lapilli sized scoria fragments.

UNIT A2 – 45 CM [80 CM]

This layer consists of predominantly medium to coarse ash. Grain sizes range from fine ash to scoria lapilli clasts up to 10 cm in diameter (typically 2-3 cm). Unit 2 is diffusely and finely layered on a centimetre to sub-centimetre scale.

Figure A6.3: Composite stratigraphy of the G1998 tephra pile, with sample names and locations.

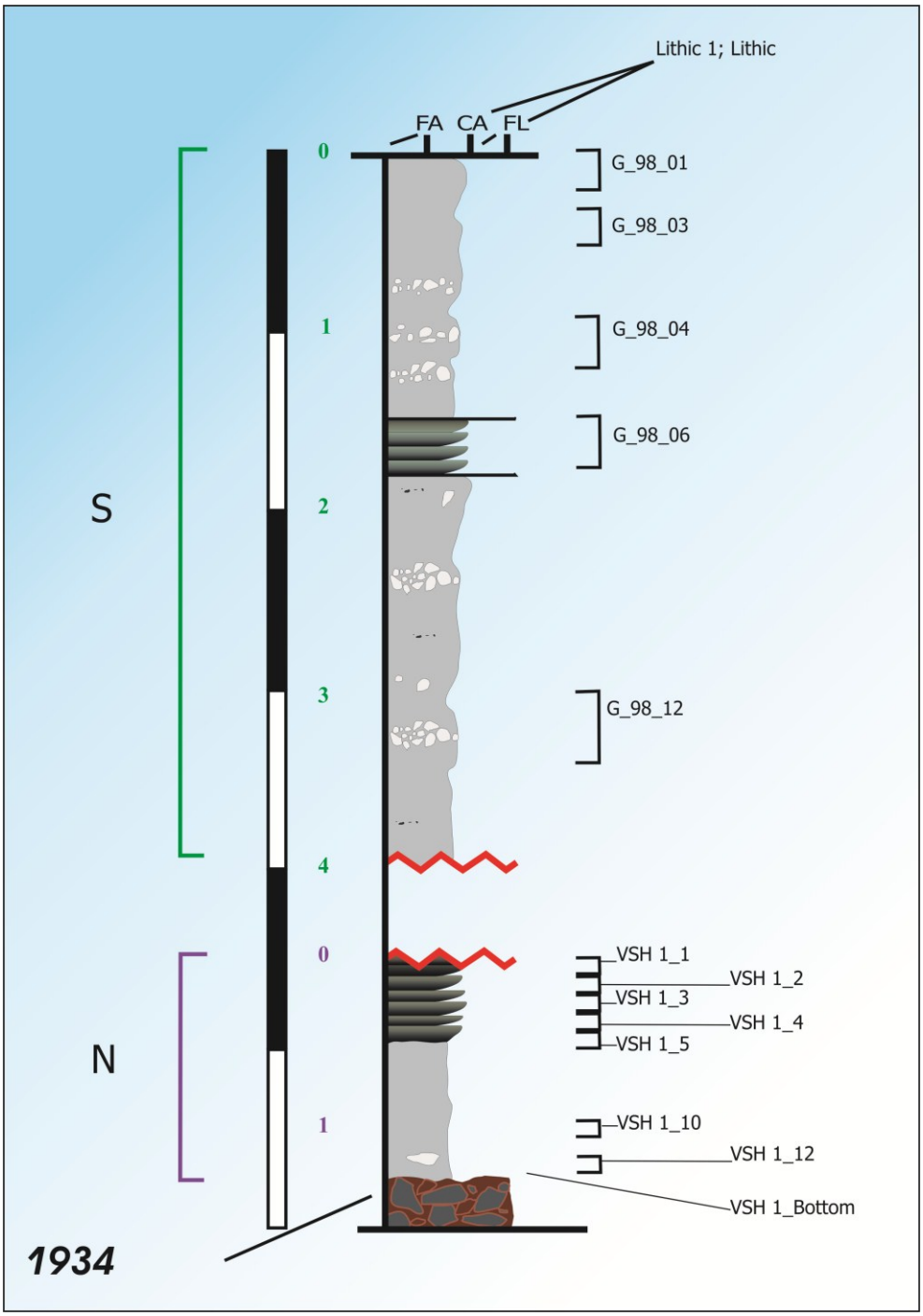

Figure A6.4: Sample locations (A) and stratigraphy (B) of tephra deposited on Svíahnúkur Vestri.

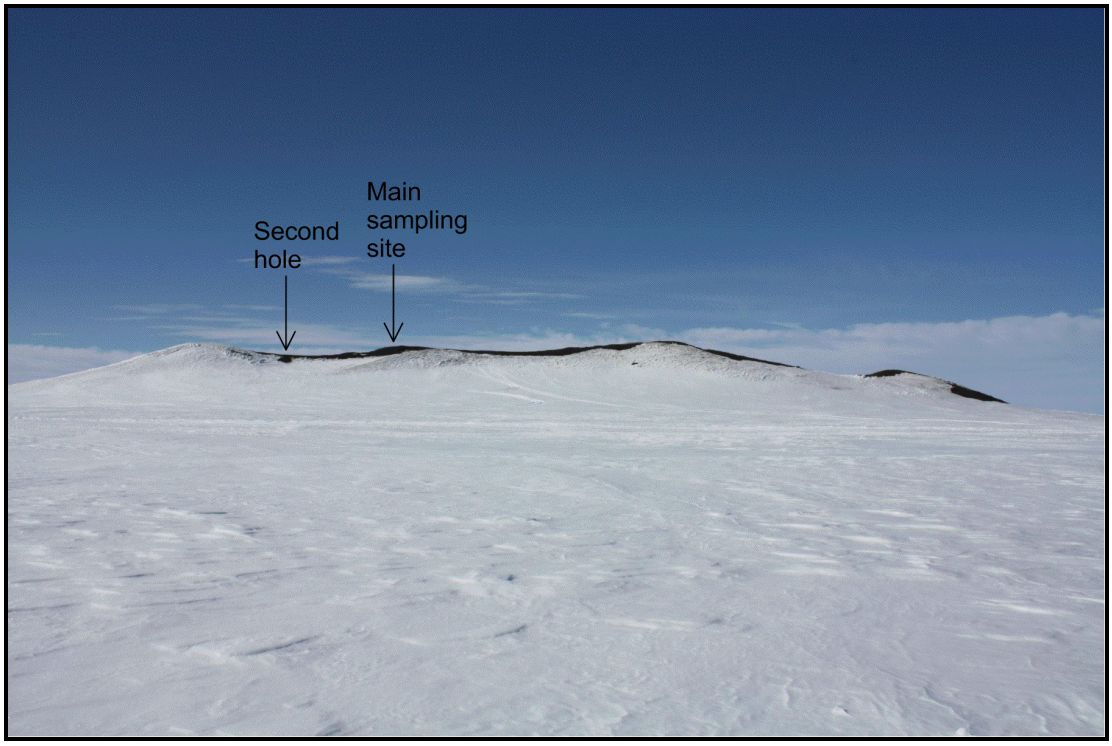

NORTHERN SECTION

UNIT B1 – 152 CM

Unit B1 is fines-abundant and poorly sorted, yet diffusely layered, consisting largely of brown to greyish brown fine ash to medium lapilli tephra. It is supported by a fine to medium ash matrix, hosting trains and, more rarely, lenses and floating clasts of pumice. Lenses and trains consist of medium to coarse lapilli sized fragments, while floating clasts are generally in the coarse ash to medium lapilli range. The lenses and trains consist of basaltic pumice, along with black, poorly to moderately vesicular scoria and an assortment of lithic fragments - moberg, altered basalt and basaltic vein fragments. Cross-bedding in this layer is relatively indistinct, but becomes apparent due to the presence of fine lapilli trains.

Unit B1 features a number of pumice trains, lenses and layers. The first pumice lens appears at 10 cm below the surface. It is 40 cm long and consists of fine to coarse lapilli basaltic pumice. Although clast-supported, large grains are coated with fine ash up to 1-2 mm thick. There are three more relatively continuous pumice layers spaced at intervals of between 20 and 50 cm through this layer. These consist of clast-supported, inversely graded, fine to coarse lapilli sized whole and broken pumice clasts. The pumice layers are fines-poor and individual clasts here are not coated by fine ash. These pumice layers are generally 3-7 cm thick.

UNIT B2 – 27 CM

This unit has an overall grey-brown to grey-black colour and is clast-supported but fines rich. It is poorly sorted. The dominant size fractions are coarse ash to medium lapilli sized clasts, which are largely black, poorly vesicular fragments. Unit B2 is internally cross-bedded (Fig. A6.5). Coarse cross-lenses consist of 20-40 cm long and 1-5 cm thick inversely graded sets, separated by 1-5 mm thick bands of fine ash which mantle the coarse sets. Coarser clasts are likewise coated with 1-2 mm thick layers of fine ash. Lithic fragments and rare basaltic pumice are also present, and are up to 30 mm in diameter.

UNIT B3 – >212 CM

Unit B3 is almost identical in character to Unit B1. The two units differ slightly in that (1) the interval between pumice layers/lenses is smaller in Unit B3 (10-20 cm in places) than in Unit B1; (2) some pumice horizons within the middle third of the unit are less distinct/discrete with respect to the rest of the layer (i.e. they are more diffuse trains rather than clast supported layers) than those of Unit B1; (3) towards the bottom of the logged portion of the tephra pile occasional pumice bombs have been identified.

Figure A6.5: Detailed stratigraphy within the northern dispersal area.

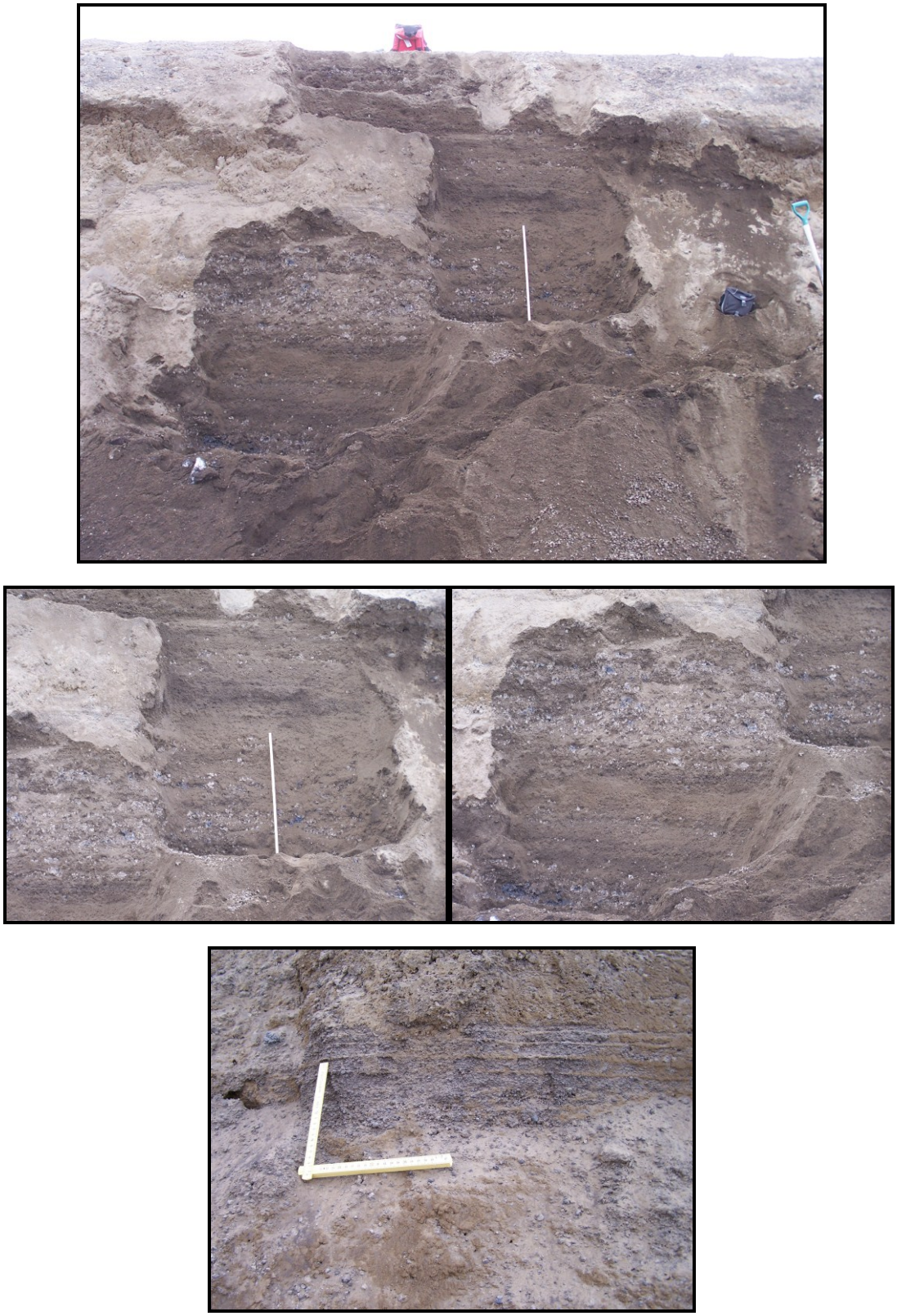

Figure A6.6: Grain size distributions for samples taken from the southern dispersal area.

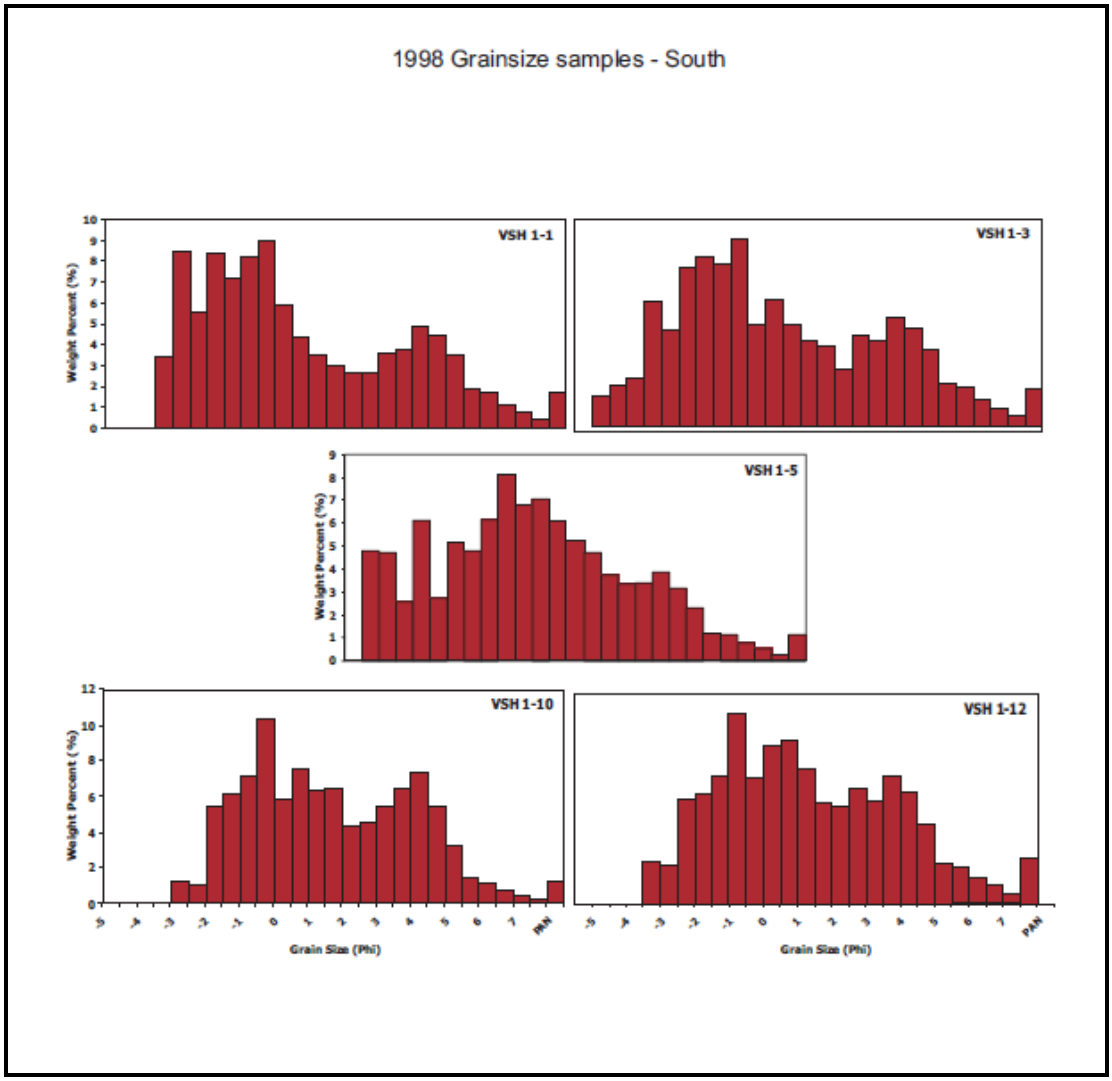

Figure A6.7: Grain size distributions for samples taken from the northern dispersal area.

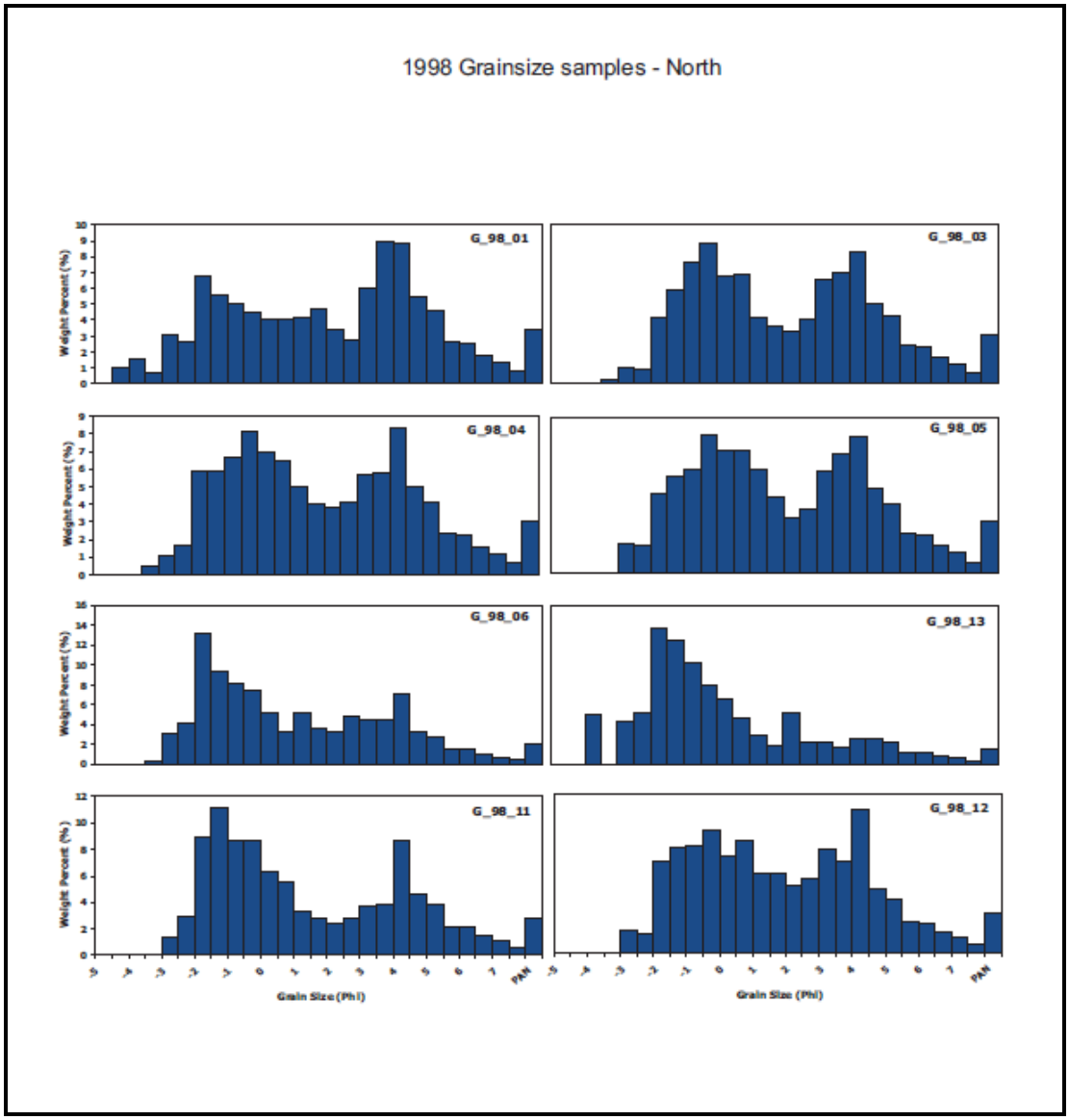

APPENDIX VII

XRF ANALYSES

MAJOR OXIDES

Event	Coordinates	Location	Section	Unit	Type	Sample #	SiO_2	TiO_2	Al_2O_3	Fe_2O_3	MnO	MgO	CaO	Na_2O	K_2O	P_2O_5	TOTAL
1934	64˚ 23.698' N; 17˚ 18.991' W	Sviahnhukur Vestri	VSH 1	n/a	Scoria	VSH1_13	53.57	2.837	13.76	14.9	0.213	4.97	8.93	2.71	0.661	0.323	102.874
Gjalp 1996	64˚ 30.642' N; 17˚ 22.385' W	Gjálp	Gjalp	n/a	Bulk Tephra	Gjalp	53.45	2.523	12.18	16.69	0.301	3.03	7.36	3.22	0.839	1.079	100.67
1998	64˚ 23.698' N; 17˚ 18.991' W	Sviahnhukur Vestri	VSH 1	n/a	Bulk Tephra	VSH 1 BOTTOM	50.93	2.76	12.99	13.24	0.21	4.79	8.43	2.62	0.65	0.32	96.93
1998	64˚ 23.698' N; 17˚ 18.991' W	Sviahnhukur Vestri	VSH 1	n/a	Bulk Tephra	VSH1_12	51.17	2.76	13.01	13.27	0.21	4.85	8.58	2.69	0.64	0.31	97.49
1998	64˚ 23.698' N; 17˚ 18.991' W	Sviahnhukur Vestri	VSH 1	n/a	Bulk Tephra	VSH 1_10	51.68	2.495	13.88	13.53	0.215	5.63	9.82	2.59	0.527	0.278	100.65
1998	64˚ 23.698' N; 17˚ 18.991' W	Sviahnhukur Vestri	VSH 1	n/a	Bulk Tephra	VSH 1_5	51.63	2.454	13.63	13.46	0.209	5.63	9.84	2.42	0.527	0.279	100.08
1998	64˚ 23.698' N; 17˚ 18.991' W	Sviahnhukur Vestri	VSH 1	n/a	Bulk Tephra	VSH1_4	50.40	2.43	12.26	13.40	0.21	5.63	9.86	2.42	0.52	0.28	97.41

Event	Coordinates	Location	Section	Unit	Type	Sample #	SiO_2	TiO_2	Al_2O_3	Fe_2O_3	MnO	MgO	CaO	Na_2O	K_2O	P_2O_5	TOTAL
1998	64˚ 24.056' N; 17˚ 20.031' W	Sviahnhukur Vestri	VSH 1	n/a	Bulk Tephra	VSH 1_2	49.76	2.42	12.18	13.37	0.20	5.57	9.74	2.49	0.51	0.27	96.51
1998	64˚ 23.698' N; 17˚ 18.991' W	Sviahnhukur Vestri	VSH 1	n/a	Bulk Tephra	VSH 1_1	51.28	2.418	13.55	13.42	0.21	5.55	9.62	2.47	0.53	0.277	99.33
1998	64˚ 24.056' N; 17˚ 20.031' W	Grímsvötn Caldera	G1998	n/a	Bulk Tephra	G_98_12	51.72	2.444	13.68	13.55	0.208	5.71	9.89	2.64	0.518	0.27	100.63
1998	64˚ 24.056' N; 17˚ 20.031' W	Grímsvötn Caldera	G1998	n/a	Bulk Tephra	G98_06	50.06	2.432	13.58	13.39	0.205	5.65	9.72	2.63	0.52	0.27	
1998	64˚ 24.056' N; 17˚ 20.031' W	Grímsvötn Caldera	G1998	n/a	Bulk Tephra	G_98_04	51.69	2.442	13.64	13.59	0.209	5.78	9.96	2.63	0.515	0.271	100.73
1998	64˚ 24.056' N; 17˚ 20.031' W	Grímsvötn Caldera	G1998	n/a	Bulk Tephra	G98_03	50.38	2.385	13.35	13.21	0.207	5.53	9.59	2.55	0.513	0.268	97.98
1998	64˚ 24.056' N; 17˚ 20.031' W	Grímsvötn Caldera	G1998	n/a	Bulk Tephra	G_98_01	49.38	2.321	13.1	14.41	0.201	5.39	9.32	2.45	0.508	0.261	97.34
1998	64˚ 24.056' N; 17˚ 20.031' W	Grímsvötn Caldera	n/a	n/a	Lithic	Lithic 1	53.57	2.837	14.9	13.76	0.213	4.97	8.93	2.71	0.661	0.323	102.87
1998	64˚ 24.056' N; 17˚ 20.031' W	Grímsvötn Caldera	n/a	n/a	Lithic	Lithic 2	50.91	2.898	15.28	13.5	0.23	5.11	9.68	2.7	0.484	0.306	101.10
2004	64˚ 24.129' N; 17˚ 23.118' W	Grímsvötn Caldera	TT02	A	Bulk Tephra	TT02-01	50.00	2.74	13.44	14.70	0.22	5.38	9.92	2.75	0.48	0.30	99.93
2004	64˚ 24.129' N; 17˚ 23.118' W	Grímsvötn Caldera	TT02	A	Bulk Tephra	TT02-02	49.93	2.84	13.45	15.00	0.23	5.25	9.65	2.68	0.51	0.28	99.82
2004	64˚ 24.129' N; 17˚ 23.118' W	Grímsvötn Caldera	TT02	A	Vesicular Tephra	TT02-04 VSC	50.36	2.73	13.63	14.67	0.22	5.48	9.84	2.72	0.48	0.30	100.43
2004	64˚ 24.129' N; 17˚ 23.118' W	Grímsvötn Caldera	TT02	A	Dense Tephra	TT02-04 DNS	50.54	3.03	13.24	15.69	0.24	5.09	9.30	2.90	0.52	0.35	100.89

Event	Coordinates	Location	Section	Unit	Type	Sample #	SiO_2	TiO_2	Al_2O_3	Fe_2O_3	MnO	MgO	CaO	Na_2O	K_2O	P_2O_5	TOTAL
2004	64˚ 24.129' N; 17˚ 23.118' W	Grímsvötn Caldera	TT02	A	Bulk Tephra	TT02-05 (1)	49.86	3.01	13.01	15.53	0.24	4.95	9.20	2.83	0.52	0.35	99.49
2004	64˚ 24.129' N; 17˚ 23.118' W	Grímsvötn Caldera	TT02	A	Bulk Tephra	TT02-05 (3)	49.92	2.79	13.45	14.84	0.22	5.20	9.74	2.67	0.48	0.28	99.59
2004	64˚ 24.129' N; 17˚ 23.118' W	Grímsvötn Caldera	TT02	B	Bulk Tephra	TT02-06	50.52	2.99	13.21	15.60	0.24	5.12	9.40	2.89	0.52	0.34	100.83
2004	64˚ 24.141' N; 17˚ 23.169' W	Grímsvötn Caldera	TT02B	B	Bulk Tephra	TT02B-01	50.21	2.80	13.31	15.01	0.23	5.37	9.75	2.61	0.48	0.28	100.05
2004	64˚ 24.141' N; 17˚ 23.169' W	Grímsvötn Caldera	TT02B	B	Bulk Tephra	TT02B-02	50.25	2.81	13.41	14.94	0.23	5.34	9.74	2.67	0.49	0.28	100.15
2004	64˚ 24.141' N; 17˚ 23.169' W	Grímsvötn Caldera	TT02B	C	Dense Tephra	TT02B-3ADNS	50.21	2.85	13.24	15.16	0.23	5.26	9.72	2.62	0.49	0.29	100.07
2004	64˚ 24.141' N; 17˚ 23.169' W	Grímsvötn Caldera	TT02B	C	Vesicular Tephra	TT02B-3AVSC	49.90	2.81	13.19	14.94	0.22	5.26	9.62	2.63	0.49	0.28	99.34
2004	64˚ 24.141' N; 17˚ 23.169' W	Grímsvötn Caldera	TT02B	C	Bulk Tephra	TT02B-3B (1)	49.67	2.82	13.27	15.06	0.23	5.17	9.76	4.28	0.54	0.32	101.12
2004	64˚ 24.141' N; 17˚ 23.169' W	Grímsvötn Caldera	TT02B	C	Bulk Tephra	TT02B-3B (2)	50.24	2.76	13.49	14.77	0.22	5.43	9.97	2.65	0.47	0.27	100.28
2004	64˚ 24.141' N; 17˚ 23.169' W	Grímsvötn Caldera	TT02B	C	Bulk Tephra	TT02B-3C	50.48	2.83	13.52	15.05	0.23	5.35	9.76	2.80	0.49	0.32	100.82
2004	64˚ 24.141' N; 17˚ 23.169' W	Grímsvötn Caldera	TT02B	C	Bulk Tephra	TT02B-04	50.19	2.83	13.25	15.07	0.23	5.30	9.68	2.63	0.49	0.29	99.95
2004	64˚ 24.141' N; 17˚ 23.169' W	Grímsvötn Caldera	TT02B	C	Bulk Tephra	TT02B-07 (1)	50.43	2.84	13.58	15.04	0.22	5.29	9.72	2.80	0.49	0.32	100.73
2004	64˚ 24.141' N; 17˚ 23.169' W	Grímsvötn Caldera	TT02B	C	Bulk Tephra	TT02B-07 (2)	50.01	3.03	14.40	15.66	0.24	4.93	9.23	3.02	0.54	0.32	101.37

Event	Coordinates	Location	Section	Unit	Type	Sample #	SiO_2	TiO_2	Al_2O_3	Fe_2O_3	MnO	MgO	CaO	Na_2O	K_2O	P_2O_5	TOTAL
2004	64˚ 24.141' N; 17˚ 23.169' W	Grímsvötn Caldera	TT02B	C	Bulk Tephra	TT02B-08	47.68	2.65	12.79	14.14	0.21	5.13	9.32	2.61	0.46	0.30	95.29
2004	64˚ 24.141' N; 17˚ 23.169' W	Grímsvötn Caldera	TT02B	C	Bulk Tephra	TT02B-10	50.21	2.83	13.44	15.02	0.22	5.33	9.79	2.83	0.49	0.32	100.48
2004	64˚ 24.141' N; 17˚ 23.169' W	Grímsvötn Caldera	TT02B	C	Bulk Tephra	TT02B-11(2)	49.49	2.98	12.74	15.48	0.23	4.96	9.16	2.63	0.52	0.31	98.49
2004	64˚ 24.141' N; 17˚ 23.169' W	Grímsvötn Caldera	TT02B	C	Bulk Tephra	TT02B-12	50.14	2.84	13.34	15.07	0.23	5.24	9.67	2.75	0.49	0.32	100.09
2004	64˚ 24.141' N; 17˚ 23.169' W	Grímsvötn Caldera	TT02B	C	Bulk Tephra	TT02B-13A	49.87	2.87	13.28	15.11	0.22	5.21	9.62	2.76	0.49	0.32	99.76
2004	64˚ 24.141' N; 17˚ 23.169' W	Grímsvötn Caldera	TT02B	C	Bulk Tephra	TT02B-13B	49.98	2.75	13.77	14.70	0.22	5.40	9.88	2.70	0.47	0.27	100.14
2004	64˚ 24.141' N; 17˚ 23.169' W	Grímsvötn Caldera	TT02B	D	Bulk Tephra	TT02B-14 (1)	50.09	2.75	13.51	14.68	0.22	5.46	9.98	2.68	0.47	0.30	100.14
2004	64˚ 24.141' N; 17˚ 23.169' W	Grímsvötn Caldera	TT02B	D	Bulk Tephra	TT02B-14 (2)	49.87	2.87	13.28	15.12	0.22	5.20	9.61	2.76	0.49	0.32	99.75
2004	64˚ 24.141' N; 17˚ 23.169' W	Grímsvötn Caldera	TT02B	E	Bulk Tephra	TT02B-15A	49.85	2.88	13.27	15.13	0.22	5.19	9.59	2.76	0.50	0.32	99.72
2004	64˚ 24.141' N; 17˚ 23.169' W	Grímsvötn Caldera	TT02B	E	Bulk Tephra	TT02B-15B	49.96	2.76	13.45	14.78	0.22	5.39	9.86	2.71	0.48	0.31	99.92
2004	64˚ 24.141' N; 17˚ 23.169' W	Grímsvötn Caldera	TT02B	E	Bulk Tephra	TT02B-16	49.84	2.88	13.26	15.14	0.22	5.18	9.58	2.76	0.50	0.32	99.70
2004	64˚ 24.141' N; 17˚ 23.169' W	Grímsvötn Caldera	TT02B	E	Bulk Tephra	TT02B-17	49.92	2.73	13.61	14.69	0.22	5.46	9.74	2.75	0.48	0.30	99.90

Event	Coordinates	Location	Section	Unit	Type	Sample #	SiO_2	TiO_2	Al_2O_3	Fe_2O_3	MnO	MgO	CaO	Na_2O	K_2O	P_2O_5	TOTAL
2004	64˚ 24.141' N; 17˚ 23.169' W	Grímsvötn Caldera	TT02B	G	Bulk Tephra	TT02B-19	49.83	2.89	13.25	15.15	0.22	5.18	9.57	2.76	0.50	0.32	99.68
2004	64˚ 24.141' N; 17˚ 23.169' W	Grímsvötn Caldera	TT02B	G	Bulk Tephra	TT02B-20	50.33	2.87	13.31	15.17	0.23	5.26	9.71	2.67	0.49	0.29	100.32
2004	64˚ 24.141' N; 17˚ 23.169' W	Grímsvötn Caldera	TT02B	C	Bulk Tephra	TT02B-D	50.29	2.85	13.47	15.04	0.23	5.42	9.79	2.65	0.49	0.33	100.56
2004	64˚ 24.141' N; 17˚ 23.169' W	Grímsvötn Caldera	TT02B	C	Bulk Tephra	TT02B-E	49.82	2.89	13.25	15.16	0.22	5.17	9.56	2.76	0.50	0.32	99.66
2004	64˚ 23.983' N; 17˚ 22.550' W	Grímsvötn Caldera	G1	A	Bulk Tephra	03/08/06/G1/A1	50.17	2.99	13.17	15.55	0.23	5.11	9.50	2.77	0.52	0.34	100.34
2004	64˚ 23.983' N; 17˚ 22.550' W	Grímsvötn Caldera	G1	A	Bulk Tephra	05/08/06/G1/A5	49.88	2.98	13.07	15.50	0.23	5.09	9.46	2.77	0.51	0.34	99.83
2004	64˚ 23.983' N; 17˚ 22.550' W	Grímsvötn Caldera	G1	B	Bulk Tephra	01-08-06/G1/B2	49.80	2.90	13.23	15.18	0.22	5.15	9.54	2.77	0.50	0.32	99.62
2004	64˚ 23.983' N; 17˚ 22.550' W	Grímsvötn Caldera	G1	C	Bulk Tephra	31-07-06/G1/C	49.79	2.90	13.23	15.19	0.22	5.15	9.54	2.77	0.50	0.32	99.61
2004	64˚ 23.983' N; 17˚ 22.550' W	Grímsvötn Caldera	G1	C	Bulk Tephra	01-08-06/G1/C2	49.94	2.90	13.25	15.24	0.23	5.25	9.67	2.80	0.49	0.32	100.09
2004	64˚ 23.983' N; 17˚ 22.550' W	Grímsvötn Caldera	G1	C	Bulk Tephra	01-08-06/G1/D1	50.10	2.92	13.28	15.33	0.23	5.23	9.60	2.75	0.50	0.33	100.27
2004	64˚ 23.983' N; 17˚ 22.550' W	Grímsvötn Caldera	G1	C	Bulk Tephra	01-08-06/G1/D2	49.34	2.89	13.04	15.14	0.23	5.13	9.42	2.72	0.50	0.32	98.72
2004	64˚ 23.983' N; 17˚ 22.550' W	Grímsvötn Caldera	G1	D	Bulk Tephra	31-07-2006/G1/E	50.03	2.88	13.30	15.15	0.23	5.27	9.70	2.72	0.49	0.32	100.09

Event	Coordinates	Location	Section	Unit	Type	Sample #	SiO_2	TiO_2	Al_2O_3	Fe_2O_3	MnO	MgO	CaO	Na_2O	K_2O	P_2O_5	TOTAL
2004	64˚ 23.983' N; 17˚ 22.550' W	Grímsvötn Caldera	G1	F	Bulk Tephra	01-08-06/G1/F1	49.84	2.86	13.24	15.09	0.23	5.23	9.64	2.72	0.49	0.32	99.66
2004	64˚ 23.983' N; 17˚ 22.550' W	Grímsvötn Caldera	G1	F	Bulk Tephra	01-08-06/G1/F2	49.89	2.86	13.34	15.11	0.23	5.18	9.63	2.75	0.50	0.32	99.81
2004	64˚ 23.983' N; 17˚ 22.550' W	Grímsvötn Caldera	G1	F	Bulk Tephra	01-08-06/G1/F3	49.80	2.83	13.29	14.98	0.22	5.25	9.67	2.69	0.48	0.31	99.53
2004	64˚ 23.983' N; 17˚ 22.550' W	Grímsvötn Caldera	G1	G	Bulk Tephra	01-08-06/G1/G1	49.81	2.76	13.48	14.73	0.22	5.35	9.87	2.70	0.48	0.31	99.70
2004	64˚ 24.728' N; 17˚23.423' W	Grímsvötn Caldera	TS71	E	Bulk Tephra	TS71-01	49.14	2.71	13.27	14.55	0.22	5.29	9.72	2.70	0.47	0.30	98.36
2004	64˚ 24.728' N; 17˚23.423' W	Grímsvötn Caldera	TS71	E	Bulk Tephra	TS71-03	50.00	2.76	13.42	14.75	0.22	5.39	9.91	2.67	0.48	0.30	99.91
2004	64˚ 24.728' N; 17˚23.423' W	Grímsvötn Caldera	TS71	B	Bulk Tephra	TS71-06	50.01	2.97	13.16	15.44	0.23	5.10	9.44	2.82	0.51	0.34	100.01
2004	64˚ 24.058' N; 17˚ 23.239' W	Grímsvötn Caldera	TS60	G	Bulk Tephra	TS60-01	49.75	2.73	13.49	14.64	0.22	5.37	9.82	2.72	0.47	0.30	99.52
2004	64˚ 24.058' N; 17˚ 23.239' W	Grímsvötn Caldera	TS60	E	Bulk Tephra	TS60-02	50.58	2.80	13.84	14.90	0.23	5.48	10.02	2.70	0.48	0.30	101.33
2004	64˚ 24.058' N; 17˚ 23.239' W	Grímsvötn Caldera	TS60	E	Bulk Tephra	TS60-06	49.49	2.74	13.43	14.71	0.22	5.42	9.82	2.69	0.48	0.30	99.29
2004	64˚ 24.058' N; 17˚ 23.239' W	Grímsvötn Caldera	TS60	E	Bulk Tephra	TS60-07	49.56	2.72	13.51	14.55	0.22	5.45	9.86	2.71	0.47	0.29	99.34
2004	64˚ 24.058' N; 17˚ 23.239' W	Grímsvötn Caldera	TS60	C	Bulk Tephra	TS60-08	50.00	2.86	13.45	15.07	0.22	5.26	9.70	2.78	0.49	0.31	100.14

Event	Coordinates	Location	Section	Unit	Type	Sample #	SiO_2	TiO_2	Al_2O_3	Fe_2O_3	MnO	MgO	CaO	Na_2O	K_2O	P_2O_5	TOTAL
2004	64˚ 24.058' N; 17˚ 23.239' W	Grímsvötn Caldera	TS60	C	Bulk Tephra	TS60-11	50.09	2.79	13.44	14.85	0.23	5.27	9.75	2.74	0.50	0.31	99.96
2004	64˚ 24.058' N; 17˚ 23.239' W	Grímsvötn Caldera	TS60	C	Bulk Tephra	TS60-12	49.86	2.79	13.44	14.84	0.22	5.28	9.70	2.68	0.49	0.30	99.60
2004	64˚ 23.878' N; 17˚ 22.433' W	Grímsvötn Caldera	TS25	C	Bulk Tephra	TS25-01	50.01	2.85	13.39	15.06	0.22	5.28	9.66	2.74	0.49	0.31	100.01
2004	64˚ 23.878' N; 17˚ 22.433' W	Grímsvötn Caldera	TS26	C	Bulk Tephra	TS26-02	49.63	2.86	13.24	15.12	0.23	5.22	9.62	2.73	0.50	0.31	99.45
2004	64˚ 23.878' N; 17˚ 22.433' W	Grímsvötn Caldera	TS26	C	Bulk Tephra	TS26-03	49.58	2.97	13.04	15.41	0.23	5.07	9.37	2.81	0.52	0.33	99.31
2004	64˚ 23.878' N; 17˚ 22.433' W	Grímsvötn Caldera	TS26	B	Bulk Tephra	TS26-04	46.31	2.66	12.40	14.02	0.21	4.91	8.99	2.50	0.46	0.29	92.74
2004	64˚ 23.878' N; 17˚ 22.433' W	Grímsvötn Caldera	TS30	B	Bulk Tephra	TS30-01	50.04	2.98	13.25	15.51	0.23	5.15	9.55	2.79	0.51	0.33	100.34
2004	64˚ 24.043' N; 17˚ 23.985'W	Grímsvötn Caldera	S1	E	Pumice	10-08-05/07	53.62	3.01	9.74	16.04	0.23	5.36	9.21	2.04	0.46	0.21	99.92
2004	64˚ 24.483' N; 17˚ 23.283' W	Grímsvötn Caldera	G5	C	Pumice	G5-3	50.57	2.76	13.74	14.76	0.22	5.60	9.98	2.79	0.48	0.32	101.22
2004	64˚ 23.933' N; 17˚ 22.433' W	Grímsvötn Caldera	G7	C	Pumice	G7-5	50.04	2.74	13.48	14.62	0.22	5.53	9.93	2.60	0.48	0.32	99.95
2004	64˚ 23.877' N; 17˚ 23.062' W	Grímsvötn Caldera	TS1	n/a	Pumice	TS1-01	50.25	2.75	13.43	14.73	0.22	5.47	10.09	2.58	0.49	0.32	100.35
2004	64˚ 23.871' N; 17˚ 23.008' W	Grímsvötn Caldera	TS12	n/a	Pumice	TS12-05	50.55	2.81	13.52	14.92	0.22	5.44	9.83	2.66	0.50	0.33	100.78

Event	Coordinates	Location	Section	Unit	Type	Sample #	SiO_2	TiO_2	Al_2O_3	Fe_2O_3	MnO	MgO	CaO	Na_2O	K_2O	P_2O_5	TOTAL
2004	64˚ 24.459' N; 17˚ 23.750' W	Grímsvötn Caldera	TS19	E	Pumice	TS19-04	50.35	2.84	13.48	15.02	0.23	5.38	9.81	2.70	0.49	0.33	100.63

TRACE ELEMENTS

Event	Coordinates	Location	Section	Unit	Sample #	Ba	Rb	Sr	Cu	Cr	Ni	Nb	V	Y	Zn	Zr	Sc
1934	64° 23.698' N; 17° 18.991' W	Sviahnhukur Vestri	VSH 1	n/a	VSH1_13	117.1	11.3	222.7	96.15	52.5	38.55	20.7	369.1	42.4	127.5	212.2	39.4
Gjalp 1996	64° 30.642' N; 17° 22.385' W	Gjálp	Gjalp	n/a	Gjalp	169.25	18.1	207.1	26.15	n.d.	1.75	39.5	71.15	88.8	190.7	430.9	33.3
1998	64° 23.698' N; 17° 18.991' W	Sviahnhukur Vestri	VSH 1	n/a	VSH 1 BOTTOM	142	14.4	212.4	97.5	20.1	38.1	23.4	415.3	48.3	141.2	248.7	37.5
1998	64° 23.698' N; 17° 18.991' W	Sviahnhukur Vestri	VSH 1	n/a	VSH1_12	143.5	13.8	216.1	99.7	17.3	37	23.6	408	47.9	139.3	248.2	37.7
1998	64° 23.698' N; 17° 18.991' W	Sviahnhukur Vestri	VSH 1	n/a	VSH 1_10	117.40	10.90	223.7	96.00	56.50	38.95	20.70	117.40	41.70	128.65	209.30	40.80
1998	64° 23.698' N; 17° 18.991' W	Sviahnhukur Vestri	VSH 1	n/a	VSH 1_5	117.85	10.80	221.6	98.20	56.80	39.95	20.60	361.90	42.00	128.05	209.10	40.45
1998	64° 23.698' N; 17° 18.991' W	Sviahnhukur Vestri	VSH 1	n/a	VSH1_4	123.5	11.1	221.5	99.1	55.4	43.6	20.6	371.5	41.8	126.7	210.2	40.7
1998	64° 24.056' N; 17° 20.031' W	Sviahnhukur Vestri	VSH 1	n/a	VSH1_3	122.3	11.3	224	96.7	58	44.1	20.9	370.1	43.1	127.9	215.3	39.9
1998	64° 24.056' N; 17° 20.031' W	Sviahnhukur Vestri	VSH 1	n/a	VSH 1_2	126.5	10.5	222	102.1	57.2	43.8	20.5	370	42	127.8	210.1	40.7
1998	64° 23.698' N; 17° 18.991' W	Sviahnhukur Vestri	VSH 1	n/a	VSH 1_1	118.60	10.90	222.2	97.55	54.00	39.10	20.80	373.55	42.30	127.60	210.70	40.35
1998	64° 24.056' N; 17° 20.031' W	Grímsvötn Caldera	G1998	n/a	G_98_12	112.75	10.70	222.9	90.20	378.55	39.55	20.40	378.55	41.20	126.60	204.00	40.35
1998	64° 24.056' N; 17° 20.031' W	Grímsvötn Caldera	G1998	n/a	G98_06	119.4	10.9	223.5	90.2	57.8	42.1	20.6	377.9	42.3	123.2	210.3	39.9
1998	64° 24.056' N; 17° 20.031' W	Grímsvötn Caldera	G1998	n/a	G_98_04	113.45	10.40	223.4	92.40	65.75	41.10	20.30	376.70	41.00	125.90	203.00	39.60
1998	64° 24.056' N; 17° 20.031' W	Grímsvötn Caldera	G1998	n/a	G98_03	115.05	10.9	223.2	88.5	59.2	39.35	20.7	378.55	41.6	128.4	207.1	40.1
1998	64° 24.056' N; 17° 20.031' W	Grímsvötn Caldera	G1998	n/a	G_98_01	112.00	10.70	221.2	89.80	59.10	39.55	20.70	112.00	41.50	127.35	206.30	39.75

Event	Coordinates	Location	Section	Unit	Sample #	Ba	Rb	Sr	Cu	Cr	Ni	Nb	V	Y	Zn	Zr	Sc
1998	64° 24.056' N; 17° 20.031' W	Grímsvötn Caldera	n/a	n/a	Lithic 1	117.1	11.3	222.7	96.15	52.5	38.55	20.7	369.1	42.4	127.5	212.2	39.4
2004	64° 24.129' N; 17° 23.118' W	Grímsvötn Caldera	TT02	Unit A	TT02-01	94.20	9.50	231.5	102.6	41.50	38.60	21.20	43.80	42.90	138.60	204.50	43.80
2004	64° 24.129' N; 17° 23.118' W	Grímsvötn Caldera	TT02	Unit A	TT02-02	127.30	10.90	229.9	88.00	24.10	37.10	24.10	44.10	47.90	151.80	232.90	44.10
2004	64° 24.129' N; 17° 23.118' W	Grímsvötn Caldera	TT02	Unit A	TT02-04 VSC	96.20	9.50	230.2	102.5	42.10	38.00	21.20	43.00	42.70	135.40	203.90	43.00
2004	64° 24.129' N; 17° 23.118' W	Grímsvötn Caldera	TT02	Unit A	TT02-04 DNS	99.60	10.60	230.2	83.70	8.00	28.20	23.70	42.60	47.20	146.60	229.30	42.60
2004	64° 24.129' N; 17° 23.118' W	Grímsvötn Caldera	TT02	Unit A	TT02-05 (1)	110.50	10.90	232.0	85.00	9.50	27.90	24.20	42.00	47.60	146.00	231.70	42.00
2004	64° 24.129' N; 17° 23.118' W	Grímsvötn Caldera	TT02	Unit A	TT02-05 (2)	120.60	10.90	230.3	88.10	24.90	38.40	24.00	43.60	47.70	151.40	232.10	43.60
2004	64° 24.129' N; 17° 23.118' W	Grímsvötn Caldera	TT02	Unit A	TT02-05 (3)	111.40	9.40	230.4	97.50	59.00	43.50	21.30	44.70	42.30	138.50	205.20	44.70
2004	64° 24.129' N; 17° 23.118' W	Grímsvötn Caldera	TT02	Unit B	TT02-06	102.00	10.10	232.9	90.90	13.50	30.30	22.50	43.20	44.50	146.30	212.40	43.20
2004	64° 24.141' N; 17° 23.169' W	Grímsvötn Caldera	TT02B	Unit B	TT02B-01	111.40	10.10	231.2	98.70	59.00	43.50	22.30	44.70	44.50	143.70	212.70	44.70
2004	64° 24.141' N; 17° 23.169' W	Grímsvötn Caldera	TT02B	Unit B	TT02B-02	118.00	9.80	230.9	101.1	55.40	49.00	21.80	44.50	44.30	142.50	212.50	44.50
2004	64° 24.141' N; 17° 23.169' W	Grímsvötn Caldera	TT02B	Unit C	TT02B-3ADNS	110.80	9.70	229.8	100.6	45.40	44.50	22.00	45.10	44.00	141.10	209.90	45.10
2004	64° 24.141' N; 17° 23.169' W	Grímsvötn Caldera	TT02B	Unit C	TT02B-3AVSC	114.60	9.90	232.0	98.70	49.90	44.40	21.80	44.00	43.60	140.60	209.90	44.00
2004	64° 24.141' N; 17° 23.169' W	Grímsvötn Caldera	TT02B	Unit C	TT02B-3B (1)	91.90	9.90	231.7	97.50	30.10	34.60	22.00	42.90	43.80	135.30	212.50	42.90
2004	64° 24.141' N; 17° 23.169' W	Grímsvötn Caldera	TT02B	Unit C	TT02B-3B (2)	120.90	9.80	230.3	101.3	46.40	44.30	21.90	44.50	44.10	141.30	212.20	44.50
2004	64° 24.141' N; 17° 23.169' W	Grímsvötn Caldera	TT02B	Unit C	TT02B-3C	97.00	9.90	231.2	100.3	29.80	35.50	21.80	42.80	43.90	141.60	212.00	42.80
2004	64° 24.141' N; 17° 23.169' W	Grímsvötn Caldera	TT02B	Unit C	TT02B-04	116.70	9.40	230.6	98.00	41.80	43.20	22.10	43.40	44.70	143.90	215.00	43.40
2004	64° 24.141' N; 17° 23.169' W	Grímsvötn Caldera	TT02B	Unit C	TT02B-07 (1)	93.00	9.50	230.9	95.00	29.70	35.70	21.80	42.90	43.90	137.50	211.10	42.90
2004	64° 24.141' N; 17° 23.169' W	Grímsvötn Caldera	TT02B	Unit C	TT02B-07 (2)	116.60	10.00	230.5	95.90	45.50	46.10	22.10	44.30	44.80	144.10	214.40	44.30
2004	64° 24.141' N; 17° 23.169' W	Grímsvötn Caldera	TT02B	Unit C	TT02B-08	93.60	9.80	230.6	102.3	31.80	36.20	21.70	43.10	43.40	139.20	210.30	43.10

Event	Coordinates	Location	Section	Unit	Sample #	Ba	Rb	Sr	Cu	Cr	Ni	Nb	V	Y	Zn	Zr	Sc
2004	64˚ 24.141' N; 17˚ 23.169' W	Grímsvötn Caldera	TT02B	Unit C	TT02B-10	87.80	9.60	230.1	99.00	27.50	35.40	21.90	43.80	44.00	139.90	210.70	43.80

Event	Coordinates	Location	Section	Unit	Sample #	Ba	Rb	Sr	Cu	Cr	Ni	Nb	V	Y	Zn	Zr	Sc
2004	64˚ 24.141' N; 17˚ 23.169' W	Grímsvötn Caldera	TT02B	Unit C	TT02B-11(2)	114.80	9.90	229.7	96.60	41.30	41.50	22.00	43.80	44.40	142.50	214.00	43.80
2004	64˚ 24.141' N; 17˚ 23.169' W	Grímsvötn Caldera	TT02B	Unit C	TT02B-12	96.90	9.90	231.1	101.6	34.60	37.50	22.20	42.90	44.10	139.60	213.10	42.90
2004	64˚ 24.141' N; 17˚ 23.169' W	Grímsvötn Caldera	TT02B	Unit C	TT02B-13A	94.60	9.70	230.3	92.80	30.30	33.60	21.60	41.30	43.20	133.30	209.80	41.30
2004	64˚ 24.141' N; 17˚ 23.169' W	Grímsvötn Caldera	TT02B	Unit C	TT02B-13B	108.10	9.80	233.1	97.20	59.40	44.40	21.20	43.60	42.70	138.60	205.30	43.60
2004	64˚ 24.141' N; 17˚ 23.169' W	Grímsvötn Caldera	TT02B	Unit D	TT02B-14 (1)	94.00	9.60	230.4	96.20	50.00	37.00	20.90	43.90	42.10	134.70	203.20	43.90
2004	64˚ 24.141' N; 17˚ 23.169' W	Grímsvötn Caldera	TT02B	Unit D	TT02B-14 (2)	91.80	9.40	230.6	95.30	39.50	37.10	21.00	43.50	42.40	137.70	203.40	43.50
2004	64˚ 24.141' N; 17˚ 23.169' W	Grímsvötn Caldera	TT02B	Unit E	TT02B-15A	91.80	9.30	230.7	95.30	39.50	37.10	21.30	43.50	42.50	137.70	205.20	43.50
2004	64˚ 24.141' N; 17˚ 23.169' W	Grímsvötn Caldera	TT02B	Unit E	TT02B-15B	98.70	9.40	230.2	95.60	37.90	36.10	21.30	42.60	42.50	135.80	206.10	42.60
2004	64˚ 24.141' N; 17˚ 23.169' W	Grímsvötn Caldera	TT02B	Unit E	TT02B-16	95.00	9.20	231.5	95.30	43.20	37.50	21.50	43.20	42.90	136.40	206.60	43.20
2004	64˚ 24.141' N; 17˚ 23.169' W	Grímsvötn Caldera	TT02B	Unit E	TT02B-17	94.20	9.70	230.6	96.80	37.10	34.80	21.30	43.00	42.30	136.10	206.00	43.00
2004	64˚ 24.141' N; 17˚ 23.169' W	Grímsvötn Caldera	TT02B	Unit G	TT02B-19	93.70	9.50	230.2	98.10	43.60	38.20	21.50	42.40	42.40	136.90	205.30	42.40
2004	64˚ 24.141' N; 17˚ 23.169' W	Grímsvötn Caldera	TT02B	Unit G	TT02B-20	110.00	9.10	230.3	100.1	58.00	47.30	21.20	44.30	42.90	139.90	204.30	44.30
2004	64˚ 24.141' N; 17˚ 23.169' W	Grímsvötn Caldera	TT02B	Unit C	TT02B-D	98.30	9.80	230.8	99.80	30.60	36.00	21.90	43.00	43.70	140.20	211.40	43.00
2004	64˚ 24.141' N; 17˚ 23.169' W	Grímsvötn Caldera	TT02B	Unit C	TT02B-E	91.50	9.60	231.3	100.5	30.30	35.40	21.90	43.10	43.90	139.00	210.50	43.10
2004	64˚ 23.983' N; 17˚ 22.550' W	Grímsvötn Caldera	G1	Unit A	03/08/06/G1/A1	94.10	10.00	229.3	85.60	13.00	28.50	23.10	41.10	45.70	133.50	222.50	41.10
2004	64˚ 23.983' N; 17˚ 22.550' W	Grímsvötn Caldera	G1	Unit A	05/08/06/G1/A5	102.70	10.40	231.3	88.40	13.20	31.00	23.30	43.10	46.00	145.70	223.70	43.10
2004	64˚ 23.983' N; 17˚ 22.550' W	Grímsvötn Caldera	G1	Unit B	01-08-06/G1/B2	104.90	10.70	231.2	90.20	14.10	31.90	23.30	42.90	45.90	145.00	222.80	42.90

Event	Coordinates	Location	Section	Unit	Sample #	Ba	Rb	Sr	Cu	Cr	Ni	Nb	V	Y	Zn	Zr	Sc
2004	64˚ 23.983' N; 17˚ 22.550' W	Grímsvötn Caldera	G1	Unit C	31-07-06/G1/C	99.70	9.90	231.0	99.50	28.70	38.60	21.70	43.60	43.80	140.50	212.20	43.60
2004	64˚ 23.983' N; 17˚ 22.550' W	Grímsvötn Caldera	G1	Unit C	01-08-06/G1/C2	102.20	10.00	231.4	94.00	22.40	34.00	22.50	42.10	44.70	139.90	216.40	42.10

Event	Coordinates	Location	Section	Unit	Sample #	Ba	Rb	Sr	Cu	Cr	Ni	Nb	V	Y	Zn	Zr	Sc
2004	64˚ 23.983' N; 17˚ 22.550' W	Grímsvötn Caldera	G1	Unit C	01-08-06/G1/D2	99.80	10.30	230.0	88.30	34.70	36.70	22.80	41.20	45.20	137.10	219.20	41.20
2004	64˚ 23.983' N; 17˚ 22.550' W	Grímsvötn Caldera	G1	Unit D	31-07-2006/G1/E	98.40	9.60	231.3	91.30	22.60	32.50	22.20	41.00	44.30	136.30	213.40	41.00
2004	64˚ 23.983' N; 17˚ 22.550' W	Grímsvötn Caldera	G1	Unit F	01-08-06/G1/F1	98.80	10.10	229.8	97.10	30.40	36.10	22.30	43.00	44.50	141.00	213.60	43.00
2004	64˚ 23.983' N; 17˚ 22.550' W	Grímsvötn Caldera	G1	Unit F	01-08-06/G1/F2	98.20	10.30	230.6	94.70	28.20	35.80	22.50	43.80	44.50	141.60	215.90	43.80
2004	64˚ 23.983' N; 17˚ 22.550' W	Grímsvötn Caldera	G1	Unit F	01-08-06/G1/F3	100.30	9.70	231.1	97.30	26.20	33.40	22.00	42.30	44.20	138.20	211.80	42.30
2004	64˚ 23.983' N; 17˚ 22.550' W	Grímsvötn Caldera	G1	Unit G	01-08-06/G1/G1	100.90	9.10	230.5	96.80	43.00	37.60	21.20	42.90	42.60	132.60	205.40	42.90
2004	64˚ 24.728' N; 17˚23.423' W	Grímsvötn Caldera	TS71	Unit E	TS71-01	97.40	9.60	230.7	99.40	39.80	36.70	21.20	42.20	43.10	135.10	205.20	42.20
2004	64˚ 24.728' N; 17˚23.423' W	Grímsvötn Caldera	TS71	Unit E	TS71-03	100.00	9.50	230.1	96.10	47.40	37.30	21.10	42.60	42.30	135.10	205.10	42.60
2004	64˚ 24.728' N; 17˚23.423' W	Grímsvötn Caldera	TS71	Unit C	TS71-04	91.40	9.90	231.0	97.30	27.10	34.00	22.00	42.50	43.70	132.80	212.20	42.50
2004	64˚ 24.728' N; 17˚23.423' W	Grímsvötn Caldera	TS71	Unit B	TS71-06	99.30	10.10	230.7	100.7	33.10	38.20	23.00	43.20	45.50	141.80	221.20	43.20
2004	64˚ 24.058' N; 17˚ 23.239' W	Grímsvötn Caldera	TS60	Unit G	TS60-01	95.50	9.60	229.5	97.80	23.70	35.50	21.20	43.20	42.40	140.10	204.60	43.20
2004	64˚ 24.058' N; 17˚ 23.239' W	Grímsvötn Caldera	TS60	Unit E	TS60-02	92.50	9.40	231.6	101.0	38.20	36.40	21.10	43.60	42.70	137.20	205.50	43.60
2004	64˚ 24.058' N; 17˚ 23.239' W	Grímsvötn Caldera	TS60	Unit E	TS60-06	98.70	9.70	231.1	94.60	22.70	34.30	21.20	43.20	42.90	143.60	205.60	43.20
2004	64˚ 24.058' N; 17˚ 23.239' W	Grímsvötn Caldera	TS60	Unit E	TS60-07	100.00	9.30	230.2	96.10	47.40	37.30	20.90	42.60	42.40	135.10	203.30	42.60
2004	64˚ 24.058' N; 17˚ 23.239' W	Grímsvötn Caldera	TS60	Unit C	TS60-08	101.30	9.60	230.0	95.80	25.10	34.20	22.20	42.80	44.10	140.70	213.00	42.80
2004	64˚ 24.058' N; 17˚ 23.239' W	Grímsvötn Caldera	TS60	Unit C	TS60-11	99.30	9.90	231.4	100.7	33.10	38.20	22.20	43.20	44.40	141.80	213.70	43.20

Event	Coordinates	Location	Section	Unit	Sample #	Ba	Rb	Sr	Cu	Cr	Ni	Nb	V	Y	Zn	Zr	Sc
2004	64˚ 24.058' N; 17˚ 23.239' W	Grímsvötn Caldera	TS60	Unit C	TS60-12	107.60	9.90	230.7	89.80	14.10	30.50	21.60	42.60	43.70	146.10	210.50	42.60
2004	64˚ 23.878' N; 17˚ 22.433' W	Grímsvötn Caldera	TS25	Unit C	TS25-01	106.60	9.60	230.0	92.30	19.00	33.90	22.10	43.60	44.00	143.50	212.50	43.60
2004	64˚ 23.878' N; 17˚ 22.433' W	Grímsvötn Caldera	TS26	Unit C	TS26-02	109.50	9.90	231.6	96.40	12.60	29.90	22.10	42.90	44.40	142.00	214.60	42.90

Event	Coordinates	Location	Section	Unit	Sample #	Ba	Rb	Sr	Cu	Cr	Ni	Nb	V	Y	Zn	Zr	Sc
2004	64˚ 23.878' N; 17˚ 22.433' W	Grímsvötn Caldera	TS26	Unit B	TS26-04	98.60	9.70	230.9	101.7	35.50	37.60	22.00	44.40	44.70	137.00	213.90	44.40
2004	64˚ 23.878' N; 17˚ 22.433' W	Grímsvötn Caldera	TS30	Unit B	TS30-01	101.40	10.30	229.5	100.7	70.40	47.60	22.90	43.90	45.60	134.50	221.90	43.90
2004	64˚ 24.043' N;17˚ 23.985' W	Grímsvötn Caldera	S1	Unit E	10-08-05/07	109.50	10.50	231.9	96.40	12.60	29.90	23.20	42.90	46.90	142.00	226.20	42.90
2004	64˚ 23.996' N; 17˚ 22.222' W	Grímsvötn Caldera	G3	Unit C	G3-C5	98.60	9.70	228.6	101.7	35.50	37.60	21.10	44.40	43.00	137.00	206.80	44.40
2004	64˚ 24.483' N; 17˚ 23.283' W	Grímsvötn Caldera	G5	Unit C	G5-3	97.40	3.70	86.90	101.9	48.60	40.40	6.70	44.50	14.30	135.00	74.40	44.50
2004	64˚ 23.933' N; 17˚ 22.433' W	Grímsvötn Caldera	G7	Unit C	G7-5	101.40	5.00	119.3	100.7	70.40	47.60	9.20	43.90	20.50	134.50	100.40	43.90
2004	64˚ 23.877' N; 17˚ 23.062' W	Grímsvötn Caldera	TS1	n/a	TS1-01	101.00	3.90	88.10	100.4	27.80	33.80	6.80	40.90	14.60	134.70	77.90	40.90
2004	64˚ 23.871' N; 17˚ 23.008' W	Grímsvötn Caldera	TS12	n/a	TS12-05	100.10	2.60	53.90	106.3	32.30	35.00	4.20	41.10	8.10	136.00	46.40	41.10
2004	64˚ 24.459' N; 17˚ 23.750' W	Grímsvötn Caldera	TS19	Unit E	TS19-04	104.20	9.60	234.2	101.4	32.60	35.10	21.20	43.40	43.50	138.00	209.00	43.40

APPENDIX VIII

CIPW NORMS

Sample	Qz	Or	Ab	An	Di	Hy	Ol	Il	Ap	IUGS Classification
100805-07	0.43	3.07	23.75	22.41	19.14	24.65		5.73	0.76	THOLEIITIC BASALT
G5_3		2.89	23.67	23.57	20.12	22.55	1.20	5.25	0.70	BASALT
G7_5	0.43	2.89	22.32	24.05	20.02	24.05		5.29	0.70	THOLEIITIC BASALT
TS1_01	0.57	2.95	22.06	23.85	20.68	23.81		5.31	0.72	THOLEIITIC BASALT
TS12_05	0.65	2.95	22.65	23.65	19.57	24.37		5.38	0.72	THOLEIITIC BASALT
TT02B_D	0.47	2.95	22.65	23.59	19.54	24.33		5.48	0.72	THOLEIITIC BASALT
TT02B_E	0.11	3.01	23.84	22.66	19.77	24.23		5.61	0.72	THOLEIITIC BASALT
G1_A1	0.43	3.07	23.67	22.26	19.58	24.43		5.75	0.74	TRACHYBASALT or HAWAIITE
G1_A5	0.26	3.07	23.84	22.09	19.77	24.42		5.76	0.74	TRACHYBASALT or HAWAIITE

Sample	Qz	Or	Ab	An	Di	Hy	Ol	Il	Ap	IUGS Classification
G1_C	0.15	3.01	23.84	22.64	19.72	24.25		5.63	0.72	THOLEIITIC BASALT
G1_C2		2.95	24.01	22.44	20.25	23.43	0.56	5.59	0.72	BASALT
G1_D1	0.19	3.01	23.58	22.66	19.69	24.46		5.63	0.72	THOLEIITIC BASALT
G1_D2	0.24	2.95	23.67	22.57	19.65	24.50		5.65	0.72	THOLEIITIC BASALT
G1_E	0.28	2.89	23.33	22.96	19.93	24.28		5.55	0.72	THOLEIITIC BASALT
G1_F1	0.27	2.95	23.41	22.89	19.91	24.24		5.55	0.72	THOLEIITIC BASALT
G1_F2	0.16	2.95	23.67	22.97	19.76	24.17		5.54	0.72	THOLEIITIC BASALT
G1_F3	0.37	2.89	23.16	23.25	19.82	24.26		5.50	0.70	THOLEIITIC BASALT
G1_G1		2.83	23.41	23.68	20.14	23.62	0.27	5.21	0.68	BASALT
TS25_01	0.13	2.95	23.50	23.12	19.77	24.28		5.52	0.68	THOLEIITIC BASALT
TS26_02		3.01	23.58	22.85	20.05	24.02	0.19	5.55	0.68	BASALT
TS26_03		3.13	24.26	21.94	19.73	24.28	0.11	5.76	0.72	TRACHYBASALT or HAWAIITE
TS26_04	0.15	3.01	23.16	23.24	19.74	24.42		5.53	0.70	THOLEIITIC BASALT

Sample	Qz	Or	Ab	An	Di	Hy	Ol	Il	Ap	IUGS Classification
TT02_01		2.83	23.58	23.30	20.72	23.19	0.33	5.31	0.68	BASALT
TT02_02	0.29	3.07	23.07	23.52	19.58	23.52		5.50	0.63	THOLEIITIC BASALT
TT02_04	0.19	2.83	23.25	23.80	19.70	24.25		5.25	0.68	THOLEIITIC BASALT
TT02_04 DNS	0.26	3.13	24.68	18.93	18.93	24.69		5.80	0.76	TRACHYBASALT or HAWAIITE
TT02_05	0.60	3.13	24.43	21.69	18.65	24.73		5.84	0.76	TRACHYBASALT or HAWAIITE
TT02_06	0.21	3.07	24.60	21.71	19.36	24.49		5.74	0.76	TRACHYBASALT or HAWAIITE
TT02B_01	0.77	2.89	22.40	23.51	19.93	24.43		5.42	0.61	THOLEIITIC BASALT
TT02B_02	0.52	2.95	22.91	23.43	19.91	24.21		5.40	0.61	THOLEIITIC BASALT
TT02B_3A VSC	0.86	2.95	22.48	23.22	20.01	24.27		5.52	0.63	THOLEIITIC BASALT
TT02B_3A DNS	0.78	2.95	22.74	23.22	19.88	24.30		5.46	0.63	THOLEIITIC BASALT
TT02B_3B	0.03	2.89	23.84	23.02	19.88	24.17		5.42	0.70	THOLEIITIC BASALT
TT02B_04	0.85	2.95	22.57	23.26	19.85	24.38		5.46	0.63	THOLEIITIC BASALT
TT02B_07	0.11	2.89	23.84	23.24	19.57	24.16		5.44	0.70	THOLEIITIC BASALT

Sample	Qz	Or	Ab	An	Di	Hy	Ol	Il	Ap	IUGS Classification
TT02B_09	0.07	2.89	23.41	23.38	19.83	24.34		5.35	0.68	THOLEIITIC BASALT
TT02B_09 VSC	0.07	2.89	23.41	23.38	19.83	24.34		5.35	0.68	THOLEIITIC BASALT
TT02B_10		2.95	24.17	22.73	20.37	22.59	1.00	5.44	0.70	BASALT
TT02B_11		2.95	24.26	22.77	20.09	23.25	0.53	5.40	0.70	BASALT
TT02B_12	0.28	2.95	23.58	22.91	19.90	24.13		5.48	0.70	THOLEIITIC BASALT
TT02B_13A	0.16	2.95	23.67	22.84	19.83	24.22		5.55	0.72	THOLEIITIC BASALT
TT02B_13B		2.83	23.16	24.37	19.75	23.48		5.31	0.59	BASALT
TT02B_14	0.05	2.83	22.99	23.72	20.54	23.86		5.29	0.66	THOLEIITIC BASALT
TT02B_15A	0.13	2.95	23.75	22.77	19.81	24.24		5.57	0.72	THOLEIITIC BASALT
TT02B_16	0.12	3.01	23.75	22.73	19.79	24.22		5.59	0.72	THOLEIITIC BASALT
TT02B_17		2.83	23.58	23.79	19.55	23.56	0.68	5.27	0.68	BASALT
TT02B_18	0.23	2.83	22.99	23.83	20.12	23.96		5.31	0.68	THOLEIITIC BASALT
TS19_04	0.36	2.95	22.99	23.41	19.78	24.27		5.46	0.72	THOLEIITIC BASALT

Sample	Qz	Or	Ab	An	Di	Hy	Ol	Il	Ap	IUGS Classification
TS60_06	7.95	2.65	21.33	21.71	18.57	22.25		4.89	0.62	BASALTIC TRACHYANDESITE
TS60_07		2.83	23.41	23.79	20.30	22.53	1.14	5.27	0.66	BASALT
TS60_08		2.95	23.84	23.07	19.94	23.58	0.38	5.52	0.68	BASALT
TS60_11	0.19	3.01	23.50	23.25	20.03	23.90		5.38	0.68	THOLEIITIC BASALT
TS60_12	0.33	2.95	23.07	23.64	19.66	24.22		5.40	0.68	THOLEIITIC BASALT
TS71_01		2.83	23.50	23.56	20.26	23.24	0.55	5.33	0.68	BASALT
TS71_03	0.25	2.83	22.91	23.60	20.43	23.90		5.35	0.68	THOLEIITIC BASALT
TS71_04	0.30	2.95	23.50	23.15	19.99	23.92		5.44	0.70	THOLEIITIC BASALT
TS71_06	0.17	3.07	24.18	22.07	19.61	24.36		5.73	0.74	TRACHYBASALT or HAWAIITE
VSH1_BOTTOM	3.82	3.95	22.82	23.17	15.02	25.03		5.40	0.72	THOLEIITIC BASALT
VSH1_12	3.43	3.84	23.33	22.82	15.78	24.66		5.38	0.70	THOLEIITIC BASALT
VSH1_10	2.25	3.13	22.06	23.90	19.53	23.68		4.77	0.61	THOLEIITIC BASALT
VSH1_5	3.25	3.13	20.71	24.65	19.22	23.64		4.74	0.61	THOLEIITIC BASALT

Sample	Qz	Or	Ab	An	Di	Hy	Ol	Il	Ap	IUGS Classification
VSH1_3	1.55	3.25	22.40	24.31	19.24	23.81		4.76	0.63	THOLEIITIC BASALT
VSH1_2	1.36	3.13	21.81	24.64	19.73	23.90		4.76	0.61	THOLEIITIC BASALT
VSH1_1	3.05	3.19	21.30	24.46	18.76	23.87		4.71	0.61	THOLEIITIC BASALT
G98_12	2.00	3.07	22.48	23.76	19.97	23.38		4.71	0.59	THOLEIITIC BASALT
G98_06	2.06	3.12	22.28	24.22	19.31	23.65		4.69	0.61	THOLEIITIC BASALT
G98_04	1.80	3.07	22.40	23.89	20.10	23.42		4.68	0.59	THOLEIITIC BASALT
G98_03	1.55	3.07	22.57	24.15	19.84	23.52		4.66	0.59	THOLEIITIC BASALT
G98_01	2.46	3.19	21.89	24.21	19.10	23.84		4.66	0.61	THOLEIITIC BASALT

APPENDIX IX

EMP DATA

UNIT A

Sample #	Section	SiO_2	TiO_2	Al_2O_3	FeO	MnO	MgO	CaO	Na_2O	K_2O	P_2O_5	SO_2	F	Cl	Total
C2_1_2	G1	49.84	2.83	13.15	14.08	0.23	5.25	9.83	2.86	0.47	0.32	0.086	0.060	0.018	99.02
C2_1_3	G1	50.15	2.88	13.33	13.80	0.23	5.54	9.82	2.91	0.48	0.33	0.092	0.037	0.016	99.60
C2_2_2	G1	49.85	3.16	13.19	14.31	0.24	4.94	9.46	3.02	0.54	0.37	0.136	0.056	0.019	99.29
C2_3_1	G1	50.18	3.19	13.12	14.65	0.25	5.16	9.75	2.52	0.53	0.35	0.154	0.037	0.020	99.92
C2_3_2	G1	50.25	3.19	12.85	14.77	0.24	5.15	9.48	2.29	0.48	0.35	0.149	0.041	0.018	99.26
C2_3_3	G1	50.14	3.15	13.03	14.22	0.25	5.21	9.57	2.46	0.51	0.36	0.140	0.019	0.018	99.08
C2_4_1	G1	50.04	2.98	12.84	14.20	0.23	5.04	9.49	2.98	0.54	0.35	0.140	0.043	0.017	98.89
C2_4_2	G1	50.34	2.98	13.11	13.78	0.24	5.01	9.34	2.84	0.53	0.36	0.127	0.052	0.018	98.74
D9_1	TS71	50.27	3.03	13.20	14.18	0.23	5.13	9.52	2.96	0.54	0.33	0.139	0.076	0.022	99.63

Sample #	Section	SiO_2	TiO_2	Al_2O_3	FeO	MnO	MgO	CaO	Na_2O	K_2O	P_2O_5	SO_2	F	Cl	Total
D9_2	TS71	49.76	3.05	12.86	13.77	0.23	5.20	9.49	2.91	0.54	0.34	0.139	0.061	0.017	98.36
D9_3	TS71	49.51	3.04	13.08	14.29	0.24	5.13	9.56	2.89	0.49	0.36	0.133	0.041	0.017	98.78

Sample #	Section	SiO_2	TiO_2	Al_2O_3	FeO	MnO	MgO	CaO	Na_2O	K_2O	P_2O_5	SO_2	F	Cl	Total
D9_4	TS71	49.61	2.87	13.32	13.97	0.24	5.05	9.33	2.97	0.47	0.33	0.131	0.075	0.011	98.37
D9_5	TS71	49.78	2.98	13.05	14.00	0.23	5.19	9.21	2.91	0.48	0.34	0.124	0.059	0.020	98.37
D9_6	TS71	50.04	2.90	13.30	13.76	0.24	5.32	9.48	3.05	0.48	0.32	0.145	0.069	0.022	99.13
D9_7	TS71	49.89	2.90	13.07	13.92	0.22	4.99	9.30	2.99	0.55	0.34	0.129	0.051	0.018	98.36
D9_8	TS71	49.60	3.24	12.97	14.20	0.24	4.72	8.90	3.13	0.52	0.35	0.123	0.043	0.019	98.06
D9_9	TS71	50.02	3.21	12.90	14.33	0.24	4.86	8.99	3.11	0.48	0.36	0.127	0.056	0.023	98.71
D9_10	TS71	49.76	3.04	13.31	13.96	0.24	4.90	9.34	3.02	0.47	0.33	0.159	0.060	0.018	98.62
D9_12	TS71	50.21	3.03	13.23	13.42	0.23	5.07	9.25	2.81	0.55	0.33	0.151	0.062	0.014	98.36
D9_13	TS71	49.92	2.96	12.48	13.92	0.23	5.04	9.32	2.99	0.55	0.33	0.159	0.065	0.019	98.01
D9_14	TS71	49.73	3.06	13.03	13.70	0.23	4.89	9.41	2.98	0.45	0.36	0.174	0.049	0.016	98.07
D9_15	TS71	50.55	2.79	13.19	13.89	0.24	5.18	9.53	2.99	0.59	0.32	0.142	0.056	0.016	99.48
D9_16	TS71	49.89	2.98	13.33	13.74	0.23	5.01	9.39	2.88	0.44	0.32	0.129	0.081	0.016	98.43
D9_17	TS71	50.18	2.81	13.19	13.90	0.24	5.18	9.39	2.96	0.43	0.33	0.136	0.063	0.019	98.82
D9_18	TS71	49.45	2.86	13.55	13.74	0.24	5.23	9.61	2.89	0.48	0.33	0.157	0.068	0.021	98.63
D9_19	TS71	51.08	2.90	13.03	13.79	0.23	5.11	9.71	3.05	0.50	0.33	0.139	0.037	0.022	99.92

UNIT B

Sample #	Section	SiO_2	TiO_2	Al_2O_3	FeO	MnO	MgO	CaO	Na_2O	K_2O	P_2O_5	SO_2	F	Cl	Total
A5_1_2	TT02	50.23	3.10	12.84	14.31	0.24	4.82	9.01	2.85	0.58	0.40	0.115	0.046	0.018	98.56
A5_2_1	TT02	50.40	3.12	12.98	13.62	0.25	4.99	9.51	2.81	0.54	0.35	0.115	0.044	0.018	98.75
A5_2_2	TT02	50.41	3.14	12.93	13.48	0.25	4.99	9.29	2.80	0.54	0.36	0.113	0.038	0.018	98.34
A5_3_1	TT02	50.21	3.17	12.90	14.46	0.26	4.81	9.15	2.89	0.57	0.38	0.126	0.082	0.020	99.02
A5_3_2	TT02	50.73	3.12	12.79	14.38	0.24	5.02	9.08	3.01	0.53	0.39	0.131	0.073	0.019	99.50
A5_4_2	TT02	49.78	2.94	13.13	13.18	0.24	5.36	9.80	2.75	0.44	0.32	0.143	0.059	0.015	98.15
A5_5_1	TT02	50.45	3.01	12.73	13.59	0.24	5.09	9.57	2.89	0.49	0.34	0.142	0.032	0.020	98.60
A5_5_2	TT02	49.66	3.16	13.22	13.61	0.23	5.02	9.62	2.85	0.49	0.35	0.146	0.046	0.019	98.44
A6_1_1	TT02	50.20	2.96	13.01	13.76	0.25	5.16	9.61	2.83	0.47	0.35	0.155	0.046	0.018	98.81
A6_1_2	TT02	49.46	2.99	13.35	13.90	0.23	5.15	9.43	2.95	0.50	0.35	0.144	0.063	0.018	98.55
A6_2_1	TT02	49.96	3.13	12.87	13.79	0.23	4.83	9.24	2.93	0.49	0.37	0.123	0.039	0.019	98.01
A6_2_2	TT02	49.91	3.14	12.81	14.25	0.23	4.81	9.15	3.05	0.52	0.37	0.122	0.042	0.020	98.43
A6_3_2	TT02	50.34	2.96	13.14	13.99	0.23	4.75	9.46	2.92	0.56	0.38	0.140	0.054	0.019	98.94
A6_3_1	TT02	50.23	3.05	12.68	13.90	0.24	4.95	9.46	2.87	0.49	0.34	0.126	0.043	0.020	98.40

Sample #	Section	SiO_2	TiO_2	Al_2O_3	FeO	MnO	MgO	CaO	Na_2O	K_2O	P_2O_5	SO_2	F	Cl	Total
A6_4_2	TT02	49.57	3.01	13.21	13.85	0.22	5.15	9.34	2.94	0.49	0.34	0.145	0.063	0.016	98.34
A6_5_1	TT02	50.31	2.96	13.54	13.74	0.24	4.94	9.52	2.97	0.50	0.35	0.138	0.047	0.020	99.28

Sample #	Section	SiO_2	TiO_2	Al_2O_3	FeO	MnO	MgO	CaO	Na_2O	K_2O	P_2O_5	SO_2	F	Cl	Total
A6_5_2	TT02	49.99	2.99	13.12	13.80	0.24	5.06	9.36	2.88	0.51	0.36	0.138	0.080	0.021	98.56
B1_1_1	TT02	51.14	2.99	12.82	13.82	0.23	5.16	9.67	3.09	0.52	0.34	0.127	0.048	0.018	99.96
B1_1_2	TT02	49.70	2.86	13.09	13.61	0.22	5.04	9.66	2.95	0.49	0.34	0.118	0.060	0.015	98.16
B1_2_1	TT02	49.54	2.95	12.90	13.44	0.22	5.39	9.78	3.03	0.47	0.33	0.106	0.072	0.018	98.26
B1_2_1	TT02	50.27	3.01	13.31	13.73	0.24	5.44	9.65	2.81	0.50	0.33	0.116	0.041	0.016	99.45
B1_3_1	TT02	49.89	2.96	13.03	13.70	0.23	5.30	9.73	2.93	0.48	0.33	0.142	0.047	0.020	98.79
B1_3_2	TT02	50.18	2.92	12.91	13.41	0.23	5.40	9.84	2.75	0.45	0.34	0.161	0.047	0.017	98.67
B1_4_1	TT02	50.31	3.02	13.04	14.06	0.24	4.93	9.40	2.90	0.52	0.36	0.152	0.071	0.014	99.03
B1_5_1	TT02	50.61	2.86	13.04	13.63	0.23	5.20	9.55	2.87	0.51	0.33	0.099	0.037	0.018	98.99
B1_5_2	TT02	51.23	2.95	13.06	13.69	0.22	5.26	9.59	2.87	0.51	0.36	0.104	0.046	0.017	99.90
A5_1_2	TT02	50.23	3.10	12.84	14.31	0.24	4.82	9.01	2.85	0.58	0.40	0.115	0.046	0.018	98.56
A5_2_1	TT02	50.40	3.12	12.98	13.62	0.25	4.99	9.51	2.81	0.54	0.35	0.115	0.044	0.018	98.75
A5_2_2	TT02	50.41	3.14	12.93	13.48	0.25	4.99	9.29	2.80	0.54	0.36	0.113	0.038	0.018	98.34
A5_3_1	TT02	50.21	3.17	12.90	14.46	0.26	4.81	9.15	2.89	0.57	0.38	0.126	0.082	0.020	99.02
A5_3_2	TT02	50.73	3.12	12.79	14.38	0.24	5.02	9.08	3.01	0.53	0.39	0.131	0.073	0.019	99.50
A5_4_2	TT02	49.78	2.94	13.13	13.18	0.24	5.36	9.80	2.75	0.44	0.32	0.143	0.059	0.015	98.15

Sample #	Section	SiO_2	TiO_2	Al_2O_3	FeO	MnO	MgO	CaO	Na_2O	K_2O	P_2O_5	SO_2	F	Cl	Total
A5_5_1	TT02	50.45	3.01	12.73	13.59	0.24	5.09	9.57	2.89	0.49	0.34	0.142	0.032	0.020	98.60
A5_5_2	TT02	49.66	3.16	13.22	13.61	0.23	5.02	9.62	2.85	0.49	0.35	0.146	0.046	0.019	98.44
A6_1_1	TT02	50.20	2.96	13.01	13.76	0.25	5.16	9.61	2.83	0.47	0.35	0.155	0.046	0.018	98.81
A6_1_2	TT02	49.46	2.99	13.35	13.90	0.23	5.15	9.43	2.95	0.50	0.35	0.144	0.063	0.018	98.55
A6_2_1	TT02	49.96	3.13	12.87	13.79	0.23	4.83	9.24	2.93	0.49	0.37	0.123	0.039	0.019	98.01
A6_2_2	TT02	49.91	3.14	12.81	14.25	0.23	4.81	9.15	3.05	0.52	0.37	0.122	0.042	0.020	98.43
A6_3_2	TT02	50.34	2.96	13.14	13.99	0.23	4.75	9.46	2.92	0.56	0.38	0.140	0.054	0.019	98.94
A6_3_1	TT02	50.23	3.05	12.68	13.90	0.24	4.95	9.46	2.87	0.49	0.34	0.126	0.043	0.020	98.40
A6_4_1	TT02	49.77	3.06	13.11	14.20	0.24	4.80	9.45	2.92	0.49	0.37	0.145	0.040	0.016	98.61
A6_4_2	TT02	49.57	3.01	13.21	13.85	0.22	5.15	9.34	2.94	0.49	0.34	0.145	0.063	0.016	98.34
A6_5_1	TT02	50.31	2.96	13.54	13.74	0.24	4.94	9.52	2.97	0.50	0.35	0.138	0.047	0.020	99.28
A6_5_2	TT02	49.99	2.99	13.12	13.80	0.24	5.06	9.36	2.88	0.51	0.36	0.138	0.080	0.021	98.56
B1_1_1	TT02-B	51.14	2.99	12.82	13.82	0.23	5.16	9.67	3.09	0.52	0.34	0.127	0.048	0.018	99.96
B1_1_2	TT02-B	49.70	2.86	13.09	13.61	0.22	5.04	9.66	2.95	0.49	0.34	0.118	0.060	0.015	98.16
B1_2_1	TT02-B	49.54	2.95	12.90	13.44	0.22	5.39	9.78	3.03	0.47	0.33	0.106	0.072	0.018	98.26
B1_2_1	TT02-B	50.27	3.01	13.31	13.73	0.24	5.44	9.65	2.81	0.50	0.33	0.116	0.041	0.016	99.45
B1_3_1	TT02-B	49.89	2.96	13.03	13.70	0.23	5.30	9.73	2.93	0.48	0.33	0.142	0.047	0.020	98.79

Sample #	Section	SiO_2	TiO_2	Al_2O_3	FeO	MnO	MgO	CaO	Na_2O	K_2O	P_2O_5	SO_2	F	Cl	Total
B1_3_2	TT02-B	50.18	2.92	12.91	13.41	0.23	5.40	9.84	2.75	0.45	0.34	0.161	0.047	0.017	98.67
B1_4_1	TT02-B	50.31	3.02	13.04	14.06	0.24	4.93	9.40	2.90	0.52	0.36	0.152	0.071	0.014	99.03
B1_5_1	TT02-B	50.61	2.86	13.04	13.63	0.23	5.20	9.55	2.87	0.51	0.33	0.099	0.037	0.018	98.99
B1_5_2	TT02-B	51.23	2.95	13.06	13.69	0.22	5.26	9.59	2.87	0.51	0.36	0.104	0.046	0.017	99.90
TS26-02_01	TS26	50.01	2.94	13.39	13.88	0.24	4.88	9.39	2.98	0.51	0.32	0.187	0.061	0.020	98.82

Sample #	Section	SiO_2	TiO_2	Al_2O_3	FeO	MnO	MgO	CaO	Na_2O	K_2O	P_2O_5	SO_2	F	Cl	Total
TS26-02_02	TS26	50.09	3.05	13.12	13.76	0.24	5.13	9.73	2.93	0.51	0.32	0.184	0.053	0.018	99.14
TS26-02_03	TS26	49.49	2.98	13.14	13.91	0.23	5.03	9.53	2.91	0.52	0.32	0.132	0.074	0.017	98.29
TS26-02_04	TS26	50.15	3.05	13.25	13.66	0.23	5.14	9.64	2.94	0.47	0.32	0.169	0.050	0.014	99.09
TS26-02_05	TS26	49.59	2.92	13.24	13.35	0.24	5.36	9.88	2.92	0.45	0.32	0.180	0.037	0.023	98.50
TS26-02_06	TS26	49.34	2.83	13.77	13.36	0.22	5.48	9.85	2.78	0.53	0.31	0.172	0.063	0.019	98.72
TS26-02_07	TS26	49.98	2.92	13.66	13.30	0.21	5.33	9.84	2.85	0.42	0.32	0.180	0.050	0.020	99.07
TS26-02_08	TS26	49.87	2.97	13.25	13.76	0.22	5.47	9.81	2.82	0.44	0.32	0.157	0.079	0.014	99.19
TS26-02_09	TS26	49.45	2.88	13.42	13.33	0.22	5.40	9.79	2.81	0.50	0.31	0.161	0.088	0.017	98.37
TS26-02_10	TS26	49.56	2.82	12.90	13.56	0.22	5.44	9.66	2.90	0.51	0.32	0.152	0.069	0.014	98.13
TS26-02_11	TS26	50.16	3.01	13.02	13.92	0.24	4.95	9.23	3.07	0.59	0.35	0.139	0.053	0.018	98.75
TS26-02_12	TS26	49.33	3.08	13.18	14.22	0.24	5.09	9.49	3.11	0.54	0.36	0.139	0.065	0.015	98.87
TS26-02_13	TS26	49.74	3.00	13.08	13.56	0.24	5.02	9.40	2.96	0.49	0.34	0.139	0.082	0.018	98.07
TS26-02_14	TS26	50.26	2.94	13.05	13.67	0.23	4.89	9.34	3.01	0.58	0.33	0.146	0.065	0.020	98.53
TS26-02_15	TS26	49.78	3.04	12.89	13.68	0.24	5.01	9.28	3.00	0.50	0.38	0.134	0.077	0.017	98.02
TS26-02_16	TS26	49.76	3.11	13.32	14.44	0.24	5.07	9.32	2.92	0.51	0.34	0.117	0.064	0.022	99.23
TS26-02_17	TS26	50.39	3.02	12.76	13.93	0.24	5.10	9.44	3.03	0.52	0.32	0.131	0.042	0.016	98.93

Sample #	Section	SiO_2	TiO_2	Al_2O_3	FeO	MnO	MgO	CaO	Na_2O	K_2O	P_2O_5	SO_2	F	Cl	Total
TS26-02_18	TS26	50.07	3.07	12.72	13.68	0.24	5.11	9.29	3.01	0.53	0.34	0.131	0.039	0.020	98.24
TS26-02_19	TS26	50.14	3.06	12.79	13.84	0.24	5.07	9.19	2.98	0.52	0.35	0.137	0.071	0.021	98.41

UNIT C

Sample #	Section	SiO_2	TiO_2	Al_2O_3	FeO	MnO	MgO	CaO	Na_2O	K_2O	P_2O_5	SO_2	F	Cl	Total
B3b_1_1	TT02-B	50.16	3.20	12.77	14.26	0.50	4.96	9.37	2.92	0.50	0.37	0.173	0.037	0.021	99.24
B3b_1_2	TT02-B	50.22	3.10	12.78	14.01	0.50	4.93	9.42	2.79	0.50	0.35	0.162	0.027	0.020	98.80
B3b_1_3	TT02-B	50.48	3.22	13.12	14.83	0.49	4.87	9.41	2.90	0.49	0.33	0.165	0.043	0.018	100.37
B3b_2_1	TT02-B	49.85	3.18	12.94	14.09	0.55	4.90	9.17	3.07	0.55	0.36	0.126	0.060	0.017	98.86
B3b_2_2	TT02-B	50.52	3.17	13.14	14.31	0.51	4.91	9.00	3.07	0.51	0.37	0.118	0.067	0.020	99.71
B3b_3_1	TT02-B	49.66	2.98	13.26	13.76	0.49	5.09	9.65	2.90	0.49	0.33	0.127	0.058	0.016	98.80
B3b_3_2	TT02-B	49.95	3.04	12.88	13.78	0.53	5.23	9.82	3.09	0.53	0.32	0.118	0.061	0.019	99.36
B3b_3_3	TT02-B	50.00	2.97	12.86	13.86	0.50	5.21	9.65	2.97	0.50	0.34	0.120	0.035	0.021	99.05
B3b_4_1	TT02-B	50.72	2.97	13.21	13.38	0.49	5.22	9.54	2.95	0.49	0.33	0.113	0.038	0.016	99.46
B3b_4_2	TT02-B	50.31	3.00	13.15	13.48	0.53	5.22	9.53	2.97	0.53	0.33	0.101	0.041	0.017	99.19
B12_1_1	TT02-B	50.20	2.84	13.27	13.62	0.45	5.17	9.66	2.81	0.45	0.33	0.109	0.048	0.014	98.97
B12_1_2	TT02-B	49.88	2.92	13.01	13.50	0.48	5.31	9.70	2.85	0.48	0.32	0.106	0.029	0.019	98.61
B12_2_1	TT02-B	49.00	2.90	13.17	13.94	0.51	5.33	9.71	2.86	0.51	0.31	0.151	0.081	0.020	98.47
B12_3_2	TT02-B	49.43	2.91	13.51	13.76	0.51	5.13	9.66	3.01	0.51	0.34	0.112	0.028	0.017	98.92

Sample #	Section	SiO_2	TiO_2	Al_2O_3	FeO	MnO	MgO	CaO	Na_2O	K_2O	P_2O_5	SO_2	F	Cl	Total
B12_3_3	TT02-B	49.64	2.97	13.24	13.88	0.49	5.27	9.65	3.15	0.49	0.34	0.119	0.033	0.017	99.28
B12_4_1	TT02-B	49.80	3.12	12.51	14.73	0.48	5.22	9.33	2.86	0.48	0.34	0.147	0.066	0.021	99.10

Sample #	Section	SiO_2	TiO_2	Al_2O_3	FeO	MnO	MgO	CaO	Na_2O	K_2O	P_2O_5	SO_2	F	Cl	Total
B12_4_2	TT02-B	49.43	3.16	12.87	14.38	0.54	5.00	9.38	2.82	0.54	0.36	0.137	0.070	0.015	98.71
B12_4_3	TT02-B	49.55	3.11	12.75	14.49	0.50	4.93	9.51	3.02	0.50	0.35	0.141	0.036	0.021	98.91
B5_1_1	TT02-B	49.87	2.98	12.84	13.43	0.48	5.18	9.58	2.88	0.48	0.36	0.143	0.063	0.020	98.32
B5_3_1	TT02-B	49.87	2.82	13.42	13.38	0.47	5.46	10.02	2.83	0.47	0.34	0.113	0.037	0.017	99.24
B5_3_2	TT02-B	49.98	2.88	13.17	13.55	0.47	5.46	9.88	2.86	0.47	0.32	0.113	0.032	0.016	99.19
B5_2_1	TT02-B	50.53	2.84	13.18	13.55	0.51	5.22	9.78	3.05	0.51	0.32	0.113	0.053	0.022	99.69
B5_2_2	TT02-B	49.75	2.86	13.24	13.38	0.51	5.36	9.83	2.85	0.51	0.33	0.094	0.043	0.015	98.78
B10_1_1	TT02-B	50.42	3.31	12.44	14.58	0.59	4.54	9.34	2.83	0.59	0.38	0.111	0.059	0.021	99.21
B10_1_2	TT02-B	49.37	3.25	12.74	14.84	0.59	4.72	9.35	2.94	0.59	0.36	0.118	0.057	0.019	98.93
B10_1_3	TT02-B	49.52	3.24	12.30	14.60	0.56	4.60	9.35	2.96	0.56	0.39	0.121	0.048	0.019	98.27
B10_2_1	TT02-B	49.86	2.89	13.27	13.82	0.44	5.17	9.66	2.94	0.44	0.36	0.094	0.070	0.018	99.04
B10_2_2	TT02-B	50.04	2.88	12.75	13.29	0.52	5.17	9.71	3.00	0.52	0.34	0.091	0.041	0.018	98.38
B10_4_2	TT02-B	50.15	2.91	13.07	13.52	0.47	5.44	9.73	2.80	0.47	0.31	0.175	0.024	0.015	99.08
B10_4_3	TT02-B	50.55	2.83	12.59	13.42	0.43	5.25	9.83	3.04	0.43	0.32	0.133	0.027	0.019	98.86
B7_1_1	TT02-B	49.53	2.88	12.93	13.59	0.47	5.43	9.86	2.86	0.47	0.34	0.124	0.054	0.018	98.55
B7_1_2	TT02-B	50.40	2.87	13.21	13.57	0.45	5.45	9.92	2.87	0.45	0.33	0.130	0.053	0.018	99.73

Sample #	Section	SiO_2	TiO_2	Al_2O_3	FeO	MnO	MgO	CaO	Na_2O	K_2O	P_2O_5	SO_2	F	Cl	Total
B7_2_1	TT02-B	49.69	3.09	13.26	13.81	0.53	4.96	9.30	3.02	0.53	0.36	0.111	0.050	0.020	98.74
B7_2_2	TT02-B	49.89	3.12	13.29	13.80	0.48	4.91	9.25	2.98	0.48	0.36	0.112	0.058	0.019	98.75
B7_2_3	TT02-B	49.80	2.99	13.51	13.99	0.51	4.81	9.25	2.91	0.51	0.35	0.120	0.041	0.016	98.81
B7_1_3	TT02-B	50.33	2.91	13.09	13.46	0.47	5.36	9.67	2.84	0.47	0.34	0.124	0.068	0.016	99.15
B3b_1_1	TT02-B	50.16	3.20	12.77	14.26	0.24	4.96	9.37	2.92	0.50	0.37	0.173	0.037	0.021	98.98
B3b_1_2	TT02-B	50.22	3.10	12.78	14.01	0.24	4.93	9.42	2.79	0.50	0.35	0.162	0.027	0.020	98.55
B3b_1_3	TT02-B	50.48	3.22	13.12	14.83	0.25	4.87	9.41	2.90	0.49	0.33	0.165	0.043	0.018	100.13
B3b_2_1	TT02-B	49.85	3.18	12.94	14.09	0.23	4.90	9.17	3.07	0.55	0.36	0.126	0.060	0.017	98.55
B3b_2_2	TT02-B	50.52	3.17	13.14	14.31	0.25	4.91	9.00	3.07	0.51	0.37	0.118	0.067	0.020	99.45
B3b_3_1	TT02-B	49.66	2.98	13.26	13.76	0.24	5.09	9.65	2.90	0.49	0.33	0.127	0.058	0.016	98.55
B3b_3_2	TT02-B	49.95	3.04	12.88	13.78	0.24	5.23	9.82	3.09	0.53	0.32	0.118	0.061	0.019	99.07
B3b_3_3	TT02-B	50.00	2.97	12.86	13.86	0.23	5.21	9.65	2.97	0.50	0.34	0.120	0.035	0.021	98.78
B3b_4_1	TT02-B	50.72	2.97	13.21	13.38	0.24	5.22	9.54	2.95	0.49	0.33	0.113	0.038	0.016	99.21
B3b_4_2	TT02-B	50.31	3.00	13.15	13.48	0.23	5.22	9.53	2.97	0.53	0.33	0.101	0.041	0.017	98.90
B12_1_1	TT02-B	50.20	2.84	13.27	13.62	0.23	5.17	9.66	2.81	0.45	0.33	0.109	0.048	0.014	98.75
B12_1_2	TT02-B	49.88	2.92	13.01	13.50	0.23	5.31	9.70	2.85	0.48	0.32	0.106	0.029	0.019	98.36
B12_2_1	TT02-B	49.00	2.90	13.17	13.94	0.24	5.33	9.71	2.86	0.51	0.31	0.151	0.081	0.020	98.20

Sample #	Section	SiO_2	TiO_2	Al_2O_3	FeO	MnO	MgO	CaO	Na_2O	K_2O	P_2O_5	SO_2	F	Cl	Total
B12_3_2	TT02-B	49.43	2.91	13.51	13.76	0.22	5.13	9.66	3.01	0.51	0.34	0.112	0.028	0.017	98.64
B12_3_3	TT02-B	49.64	2.97	13.24	13.88	0.22	5.27	9.65	3.15	0.49	0.34	0.119	0.033	0.017	99.01
B12_4_1	TT02-B	49.80	3.12	12.51	14.73	0.25	5.22	9.33	2.86	0.48	0.34	0.147	0.066	0.021	98.87
B12_4_2	TT02-B	49.43	3.16	12.87	14.38	0.23	5.00	9.38	2.82	0.54	0.36	0.137	0.070	0.015	98.39
B12_4_3	TT02-B	49.55	3.11	12.75	14.49	0.25	4.93	9.51	3.02	0.50	0.35	0.141	0.036	0.021	98.65

Sample #	Section	SiO_2	TiO_2	Al_2O_3	FeO	MnO	MgO	CaO	Na_2O	K_2O	P_2O_5	SO_2	F	Cl	Total
B5_1_1	TT02-B	49.87	2.98	12.84	13.43	0.22	5.18	9.58	2.88	0.48	0.36	0.143	0.063	0.020	98.06
B5_3_1	TT02-B	49.87	2.82	13.42	13.38	0.23	5.46	10.02	2.83	0.47	0.34	0.113	0.037	0.017	99.00
B5_3_2	TT02-B	49.98	2.88	13.17	13.55	0.24	5.46	9.88	2.86	0.47	0.32	0.113	0.032	0.016	98.96
B5_2_1	TT02-B	50.53	2.84	13.18	13.55	0.24	5.22	9.78	3.05	0.51	0.32	0.113	0.053	0.022	99.41
B5_2_2	TT02-B	49.75	2.86	13.24	13.38	0.24	5.36	9.83	2.85	0.51	0.33	0.094	0.043	0.015	98.50
B10_1_1	TT02-B	50.42	3.31	12.44	14.58	0.25	4.54	9.34	2.83	0.59	0.38	0.111	0.059	0.021	98.87
B10_2_1	TT02-B	49.86	2.89	13.27	13.82	0.24	5.17	9.66	2.94	0.44	0.36	0.094	0.070	0.018	98.83
B10_2_2	TT02-B	50.04	2.88	12.75	13.29	0.24	5.17	9.71	3.00	0.52	0.34	0.091	0.041	0.018	98.09
B10_4_1	TT02-B	50.54	3.37	14.03	13.51	0.19	5.28	9.75	3.20	0.38	0.36	0.005	-0.009	0.003	100.60
B10_4_2	TT02-B	50.15	2.91	13.07	13.52	0.23	5.44	9.73	2.80	0.47	0.31	0.175	0.024	0.015	98.84
B10_4_3	TT02-B	50.55	2.83	12.59	13.42	0.24	5.25	9.83	3.04	0.43	0.32	0.133	0.027	0.019	98.66
B7_1_1	TT02-B	49.53	2.88	12.93	13.59	0.23	5.43	9.86	2.86	0.47	0.34	0.124	0.054	0.018	98.31
B7_1_2	TT02-B	50.40	2.87	13.21	13.57	0.22	5.45	9.92	2.87	0.45	0.33	0.130	0.053	0.018	99.51
B7_2_1	TT02-B	49.69	3.09	13.26	13.81	0.23	4.96	9.30	3.02	0.53	0.36	0.111	0.050	0.020	98.44
B7_2_2	TT02-B	49.89	3.12	13.29	13.80	0.22	4.91	9.25	2.98	0.48	0.36	0.112	0.058	0.019	98.50
B7_2_3	TT02-B	49.80	2.99	13.51	13.99	0.25	4.81	9.25	2.91	0.51	0.35	0.120	0.041	0.016	98.55

Sample #	Section	SiO_2	TiO_2	Al_2O_3	FeO	MnO	MgO	CaO	Na_2O	K_2O	P_2O_5	SO_2	F	Cl	Total
B7_1_3	TT02-B	50.33	2.91	13.09	13.46	0.23	5.36	9.67	2.84	0.47	0.34	0.124	0.068	0.016	98.91
C7_1	G1	49.71	2.97	13.51	13.73	0.22	5.31	9.63	2.72	0.47	0.34	0.133	0.065	0.016	98.83
C7_2	G1	50.28	3.06	13.21	14.10	0.22	5.25	9.71	2.88	0.48	0.34	0.136	0.068	0.015	99.74
C7_3	G1	49.42	2.96	13.24	13.77	0.24	5.08	9.81	2.95	0.49	0.33	0.139	0.073	0.015	98.54
C7_4	G1	49.96	2.89	13.40	13.68	0.23	5.28	9.40	2.99	0.44	0.30	0.134	0.048	0.023	98.77
C7_5	G1	50.41	2.98	13.20	13.28	0.23	5.40	9.52	3.03	0.55	0.32	0.139	0.060	0.015	99.12
C7_6	G1	49.83	2.84	13.34	13.82	0.23	5.29	9.57	2.81	0.42	0.32	0.146	0.055	0.017	98.69
C7_7	G1	50.33	2.88	13.20	13.73	0.23	5.30	9.82	2.91	0.52	0.32	0.147	0.060	0.017	99.45
C7_8	G1	50.13	2.86	13.13	13.64	0.23	5.24	9.45	2.94	0.51	0.34	0.142	0.084	0.017	98.72
C7_9	G1	50.22	2.95	13.73	13.68	0.23	5.23	9.66	2.95	0.50	0.31	0.142	0.065	0.018	99.70
C8_1	G1	50.01	2.88	13.43	13.84	0.22	5.41	9.65	2.82	0.45	0.31	0.126	0.068	0.022	99.25
C8_2	G1	49.64	2.89	13.59	13.78	0.22	5.39	9.78	2.98	0.44	0.32	0.141	0.049	0.018	99.25
C8_3	G1	50.33	2.89	13.35	13.61	0.23	5.36	9.77	2.88	0.49	0.34	0.141	0.025	0.013	99.42
C8_4	G1	49.95	2.76	13.16	13.49	0.23	5.40	9.75	2.83	0.50	0.29	0.126	0.061	0.013	98.57
C8_5	G1	50.48	2.81	12.81	13.57	0.23	5.37	9.61	2.89	0.48	0.32	0.137	0.075	0.017	98.79
C8_6	G1	50.56	2.94	13.31	13.48	0.22	5.44	9.88	2.90	0.43	0.31	0.145	0.056	0.015	99.71
C8_7	G1	49.90	2.90	13.80	13.18	0.22	5.47	9.82	2.93	0.39	0.31	0.135	0.034	0.017	99.11

Sample #	Section	SiO_2	TiO_2	Al_2O_3	FeO	MnO	MgO	CaO	Na_2O	K_2O	P_2O_5	SO_2	F	Cl	Total
C8_8	G1	49.79	2.78	13.63	13.50	0.22	5.60	9.65	2.95	0.47	0.31	0.135	0.051	0.017	99.09
E12_1	TS60	50.72	2.89	13.11	13.46	0.23	5.45	9.58	2.77	0.47	0.30	0.150	0.050	0.018	99.20
E12_2	TS60	49.99	2.93	13.63	13.24	0.22	5.52	9.85	2.87	0.48	0.32	0.137	0.069	0.021	99.27
E12_3	TS60	49.89	2.79	13.33	13.73	0.23	5.47	9.85	2.91	0.49	0.30	0.139	0.081	0.013	99.23
E12_4	TS60	50.07	2.70	13.46	13.53	0.24	5.57	9.90	2.80	0.45	0.31	0.156	0.032	0.023	99.24

Sample #	Section	SiO_2	TiO_2	Al_2O_3	FeO	MnO	MgO	CaO	Na_2O	K_2O	P_2O_5	SO_2	F	Cl	Total
E12_6	TS60	50.37	2.92	13.55	13.58	0.23	5.41	9.36	2.97	0.54	0.31	0.139	0.046	0.014	99.43
E12_7	TS60	50.10	2.86	13.53	13.22	0.22	5.43	9.61	2.88	0.41	0.32	0.134	0.059	0.022	98.81
E12_8	TS60	50.23	2.81	13.22	13.77	0.24	5.42	9.77	2.91	0.48	0.32	0.143	0.079	0.020	99.41
E12_9	TS60	49.77	2.83	13.11	13.27	0.23	5.35	9.68	2.95	0.46	0.33	0.135	0.065	0.016	98.21
E12_10	TS60	50.46	2.82	13.04	13.23	0.23	5.40	9.88	2.93	0.44	0.31	0.129	0.090	0.017	98.96
E12_11	TS60	50.07	2.84	13.20	13.39	0.22	5.43	9.90	2.83	0.50	0.30	0.130	0.060	0.021	98.89
E12_12	TS60	50.47	2.83	13.52	13.43	0.23	5.43	9.80	2.85	0.48	0.33	0.115	0.064	0.019	99.57
E12_13	TS60	50.13	2.87	13.35	13.32	0.23	5.55	9.92	2.73	0.47	0.29	0.126	0.034	0.019	99.03
E12_14	TS60	50.03	2.80	13.06	13.38	0.22	5.37	9.76	2.86	0.41	0.32	0.132	0.047	0.019	98.42
E12_15	TS60	49.71	2.85	12.85	13.35	0.25	5.57	9.84	2.98	0.53	0.30	0.117	0.056	0.016	98.41
E12_16	TS60	50.40	2.86	13.30	13.07	0.22	5.52	9.94	2.78	0.49	0.32	0.117	0.057	0.014	99.09
E12_17	TS60	50.76	2.84	13.53	13.74	0.23	5.70	10.07	1.48	0.47	0.30	0.130	0.079	0.019	99.34
E12_18	TS60	50.25	2.91	13.33	13.15	0.23	5.35	9.68	3.04	0.49	0.31	0.130	0.046	0.017	98.93
E12_19	TS60	49.56	2.90	13.19	13.60	0.23	5.24	9.51	2.95	0.55	0.33	0.150	0.054	0.015	98.29
E12_20	TS60	49.78	2.88	13.15	13.34	0.23	5.44	9.81	3.02	0.49	0.30	0.126	0.076	0.013	98.68
E12_21	TS60	49.90	2.83	13.17	13.52	0.23	5.35	9.71	3.04	0.54	0.32	0.139	0.084	0.012	98.85

Sample #	Section	SiO_2	TiO_2	Al_2O_3	FeO	MnO	MgO	CaO	Na_2O	K_2O	P_2O_5	SO_2	F	Cl	Total
E12_22	TS60	49.48	2.95	13.59	13.46	0.23	5.22	9.75	2.93	0.50	0.33	0.133	0.078	0.014	98.67
E12_23	TS60	51.12	2.80	13.26	14.13	0.22	5.46	9.81	3.03	0.51	0.30	0.132	0.083	0.023	100.89
E12_24	TS60	50.13	2.94	13.50	13.48	0.22	5.22	9.62	2.84	0.53	0.32	0.137	0.057	0.019	99.01
TS25-01	TS25	49.81	2.89	13.01	13.55	0.23	5.37	9.51	2.85	0.49	0.33	0.128	0.080	0.016	98.26
TS25-01	TS25	49.98	2.83	12.92	13.48	0.24	5.26	9.64	2.84	0.51	0.31	0.118	0.071	0.016	98.21
TS25-01	TS25	50.19	3.05	13.41	13.26	0.21	5.03	9.49	2.82	0.46	0.34	0.138	0.029	0.016	98.43
TS25-01	TS25	49.27	3.08	13.33	14.12	0.23	5.00	9.20	2.95	0.56	0.33	0.131	0.066	0.022	98.30
TS25-01	TS25	49.99	2.99	13.09	14.24	0.24	5.15	9.49	2.97	0.55	0.35	0.123	0.081	0.018	99.28
TS25-01	TS25	49.76	3.09	13.38	13.82	0.23	5.07	9.33	3.07	0.53	0.34	0.125	0.056	0.017	98.82
TS25-01	TS25	49.26	3.01	13.49	13.30	0.22	5.33	9.69	2.95	0.42	0.30	0.108	0.076	0.017	98.17
TS25-01	TS25	50.09	2.82	13.12	13.45	0.22	5.54	9.63	2.99	0.47	0.31	0.110	0.056	0.018	98.83

UNIT D

Sample #	Section	SiO_2	TiO_2	Al_2O_3	FeO	MnO	MgO	CaO	Na_2O	K_2O	P_2O_5	SO_2	F	Cl	Total
C9_1	G1	50.29	3.00	13.00	14.24	0.24	4.89	9.26	2.84	0.52	0.35	0.130	0.037	0.018	98.82
C9_2	G1	49.54	2.94	13.28	13.97	0.25	5.12	9.13	2.95	0.53	0.34	0.128	0.068	0.017	98.27
C9_3	G1	50.05	3.01	13.11	13.92	0.24	4.93	9.17	2.97	0.46	0.36	0.139	0.073	0.021	98.46
C9_4	G1	50.08	3.13	13.34	13.98	0.24	4.77	9.32	2.95	0.46	0.35	0.137	0.089	0.020	98.85
C9_5	G1	50.29	3.01	12.85	13.54	0.23	4.98	9.28	3.06	0.49	0.36	0.128	0.056	0.018	98.27
C9_6	G1	50.15	2.98	12.72	13.88	0.23	4.92	9.41	2.99	0.56	0.35	0.135	0.057	0.019	98.40
C9_7	G1	50.34	3.03	12.93	14.12	0.25	4.97	9.18	2.97	0.46	0.36	0.140	0.078	0.014	98.85
C9_8	G1	50.38	2.99	13.08	13.84	0.23	5.13	9.18	2.98	0.53	0.34	0.137	0.074	0.017	98.90
C9_9	G1	50.02	3.03	13.52	13.83	0.24	5.08	9.34	2.86	0.53	0.34	0.141	0.064	0.017	99.01
C9_10	G1	50.14	3.08	13.07	13.97	0.24	5.04	9.15	2.99	0.48	0.38	0.133	0.042	0.020	98.72
E9_1	TS60	50.39	2.79	13.14	13.51	0.21	5.54	9.73	2.92	0.46	0.32	0.135	0.071	0.016	99.25
E9_2	TS60	49.33	2.79	13.22	13.57	0.23	5.63	9.68	3.08	0.48	0.31	0.130	0.068	0.017	98.53
E9_3	TS60	50.11	2.82	13.20	12.97	0.24	5.48	9.80	2.93	0.52	0.32	0.128	0.066	0.019	98.59
E9_4	TS60	49.84	2.84	13.13	13.66	0.23	5.52	9.93	2.82	0.50	0.31	0.124	0.063	0.015	99.00

Sample #	Section	SiO_2	TiO_2	Al_2O_3	FeO	MnO	MgO	CaO	Na_2O	K_2O	P_2O_5	SO_2	F	Cl	Total
E9_5	TS60	50.16	2.81	13.34	13.13	0.22	5.52	9.71	2.97	0.53	0.31	0.121	0.062	0.018	98.90
E9_6	TS60	50.13	2.78	13.48	13.08	0.23	5.48	9.86	2.88	0.46	0.31	0.115	0.070	0.019	98.89

Sample #	Section	SiO_2	TiO_2	Al_2O_3	FeO	MnO	MgO	CaO	Na_2O	K_2O	P_2O_5	SO_2	F	Cl	Total
E9_7	TS60	50.20	2.89	13.53	13.35	0.22	5.46	9.84	2.75	0.46	0.31	0.127	0.055	0.018	99.21
E9_8	TS60	49.43	2.85	13.67	13.66	0.22	5.37	10.02	2.96	0.48	0.30	0.129	0.050	0.017	99.16
E9_9	TS60	51.06	2.84	13.51	13.00	0.24	5.31	9.80	2.95	0.49	0.30	0.116	0.069	0.016	99.70
E9_10	TS60	50.18	2.72	13.42	13.33	0.22	5.43	9.57	3.09	0.49	0.31	0.112	0.062	0.018	98.96
E11_1	TS60	50.50	2.90	13.23	13.76	0.23	5.33	9.67	2.90	0.46	0.32	0.136	0.050	0.016	99.50
E11_2	TS60	49.82	2.97	13.27	14.07	0.24	5.21	9.43	3.04	0.49	0.34	0.138	0.072	0.019	99.10
E11_3	TS60	50.18	2.88	13.08	13.40	0.23	5.33	9.67	3.19	0.42	0.34	0.125	0.065	0.016	98.94
E11_4	TS60	51.07	3.00	13.56	13.80	0.24	5.28	9.39	2.99	0.52	0.32	0.129	0.068	0.019	100.40
E11_5	TS60	50.97	2.92	13.41	13.56	0.22	5.22	9.56	2.96	0.50	0.33	0.129	0.056	0.021	99.87
E11_6	TS60	50.48	3.01	12.95	13.56	0.21	5.28	9.37	2.96	0.53	0.34	0.131	0.051	0.021	98.91
E11_7	TS60	50.90	2.87	13.24	13.54	0.23	5.22	9.66	3.00	0.48	0.32	0.136	0.062	0.020	99.67
E11_8	TS60	50.23	2.95	13.48	13.50	0.23	5.33	9.65	3.01	0.49	0.33	0.136	0.081	0.021	99.44
E11_9	TS60	50.16	2.91	13.30	13.65	0.22	5.35	9.42	2.97	0.50	0.35	0.140	0.087	0.017	99.06
E11_10	TS60	49.57	3.03	13.13	13.69	0.23	5.25	9.43	2.92	0.52	0.33	0.129	0.071	0.021	98.33

UNIT E

Sample #	Section	SiO_2	TiO_2	Al_2O_3	FeO	MnO	MgO	CaO	Na_2O	K_2O	P_2O_5	SO_2	F	Cl	Total
B_15a_2_1	TT02B	49.76	2.98	13.21	13.58	0.22	5.27	9.75	2.92	0.51	0.33	0.135	0.047	0.017	98.73
B_15a_2_2	TT02B	49.80	2.87	13.11	13.40	0.23	5.30	9.72	3.00	0.49	0.35	0.140	0.064	0.018	98.47
B_15a_4_2	TT02B	50.06	2.82	13.06	13.42	0.23	5.44	9.96	2.76	0.41	0.31	0.106	0.027	0.017	98.62
B18_2_1	TT02B	50.70	2.88	13.01	12.85	0.23	5.45	9.94	2.94	0.48	0.32	0.115	0.037	0.017	98.96
B18_2_2	TT02B	49.76	2.94	13.90	12.95	0.23	5.26	9.61	2.81	0.48	0.35	0.118	0.060	0.020	98.49
B18_2_3	TT02B	49.56	2.78	13.55	13.52	0.24	5.43	9.80	2.95	0.48	0.32	0.124	0.069	0.017	98.84
B18_3_1	TT02B	49.51	2.82	13.07	13.80	0.22	5.56	9.88	2.96	0.49	0.32	0.115	0.053	0.021	98.82
B18_3_2	TT02B	49.75	2.96	12.92	13.75	0.23	5.43	10.02	2.84	0.47	0.32	0.106	0.055	0.021	98.87
B18_3_3	TT02B	49.23	2.86	12.96	13.51	0.23	5.47	10.13	2.95	0.47	0.33	0.224	0.036	0.030	98.43
B16_2_1	TT02B	49.68	3.02	12.50	14.59	0.24	5.67	10.01	2.79	0.48	0.35	0.142	0.032	0.018	99.54
B16_2_2	TT02B	49.92	2.93	12.78	13.46	0.23	5.44	9.64	2.74	0.52	0.32	0.109	0.083	0.015	98.18
E7_1	TS60	49.99	2.73	12.97	13.36	0.23	5.57	9.71	2.94	0.47	0.30	0.155	0.076	0.015	98.51
E7_2	TS60	49.36	2.76	13.38	13.30	0.23	5.44	10.02	3.02	0.44	0.31	0.169	0.043	0.018	98.49
E7_3	TS60	49.91	2.84	13.33	13.37	0.22	5.47	10.00	2.96	0.41	0.31	0.173	0.036	0.017	99.05

Sample #	Section	SiO_2	TiO_2	Al_2O_3	FeO	MnO	MgO	CaO	Na_2O	K_2O	P_2O_5	SO_2	F	Cl	Total
E7_4	TS60	50.25	2.79	13.33	13.73	0.24	5.46	10.00	2.88	0.43	0.29	0.160	0.082	0.013	99.66
E7_5	TS60	50.73	2.86	13.04	13.33	0.23	5.42	9.50	2.82	0.41	0.33	0.141	0.066	0.021	98.92

Sample #	Section	SiO_2	TiO_2	Al_2O_3	FeO	MnO	MgO	CaO	Na_2O	K_2O	P_2O_5	SO_2	F	Cl	Total
E7_6	TS60	49.81	2.95	13.36	14.11	0.24	5.00	9.35	2.96	0.52	0.33	0.132	0.072	0.016	98.85
E7_7	TS60	49.61	2.80	13.44	13.41	0.23	5.41	9.80	2.92	0.53	0.32	0.145	0.091	0.016	98.72
E7_8	TS60	50.58	2.72	13.73	13.26	0.24	5.32	9.76	2.97	0.43	0.30	0.158	0.048	0.017	99.54
E7_9	TS60	50.15	2.73	13.24	13.36	0.22	5.55	9.82	2.99	0.47	0.30	0.124	0.078	0.019	99.05
E8_1	TS60	49.69	2.94	12.99	13.82	0.22	5.47	9.66	3.00	0.43	0.32	0.116	0.045	0.017	98.73
E8_2	TS60	49.00	2.98	13.29	13.88	0.24	5.42	9.70	3.00	0.46	0.32	0.133	0.033	0.017	98.47
E8_4	TS60	50.85	2.96	13.07	13.88	0.23	5.50	9.79	2.85	0.51	0.31	0.126	0.060	0.017	100.15
E8_5	TS60	49.60	2.79	13.24	13.25	0.22	5.58	9.64	2.83	0.48	0.32	0.100	0.074	0.017	98.14
E8_6	TS60	50.02	2.85	13.18	13.30	0.23	5.41	9.71	3.01	0.45	0.31	0.103	0.056	0.019	98.66
E8_7	TS60	50.27	2.71	13.51	13.75	0.23	5.51	9.72	2.83	0.49	0.32	0.103	0.063	0.019	99.53
E8_8	TS60	50.58	2.76	13.16	13.43	0.23	5.40	9.67	3.03	0.39	0.32	0.106	0.089	0.020	99.18
E8_9	TS60	50.35	2.79	13.25	13.39	0.22	5.48	9.74	3.03	0.50	0.30	0.095	0.046	0.018	99.20
E8_10	TS60	49.88	2.84	13.12	13.20	0.21	5.29	9.90	2.90	0.50	0.32	0.101	0.079	0.016	98.36
E5_1	TS60	50.58	2.88	13.17	13.73	0.23	5.23	9.81	2.82	0.49	0.30	0.136	0.071	0.020	99.47
E5_2	TS60	49.65	2.79	13.18	13.40	0.23	5.36	9.69	2.82	0.43	0.31	0.141	0.057	0.010	98.06
E5_3	TS60	49.08	2.88	13.57	13.61	0.22	5.16	9.61	2.83	0.48	0.33	0.144	0.062	0.017	98.00

Sample #	Section	SiO_2	TiO_2	Al_2O_3	FeO	MnO	MgO	CaO	Na_2O	K_2O	P_2O_5	SO_2	F	Cl	Total
E5_4	TS60	50.26	2.83	13.44	13.09	0.23	5.39	9.93	3.05	0.50	0.32	0.141	0.037	0.018	99.25
E5_5	TS60	50.40	2.86	13.32	13.44	0.23	5.34	9.93	2.98	0.47	0.31	0.133	0.094	0.015	99.51
E5_6	TS60	49.42	2.87	13.18	13.48	0.23	5.43	9.69	2.84	0.49	0.32	0.131	0.063	0.019	98.17
E5_7	TS60	50.18	2.71	13.30	13.10	0.23	5.48	9.72	2.87	0.50	0.31	0.131	0.074	0.014	98.61
E5_8	TS60	50.51	2.70	13.45	13.57	0.24	5.27	9.73	2.88	0.46	0.30	0.132	0.097	0.016	99.34
E5_9	TS60	50.50	2.73	13.45	12.77	0.23	5.40	9.71	3.02	0.51	0.29	0.097	0.068	0.013	98.80
E5_10	TS60	49.93	2.78	13.55	13.19	0.23	5.36	9.48	3.02	0.53	0.31	0.125	0.084	0.017	98.59
E6_1	TS60	50.45	2.86	12.91	14.00	0.24	5.34	9.51	2.88	0.52	0.33	0.129	0.057	0.021	99.25
E6_2	TS60	50.08	2.92	13.14	13.27	0.24	5.25	9.50	2.89	0.48	0.33	0.146	0.053	0.019	98.33
E6_3	TS60	50.01	2.87	13.35	13.78	0.22	5.31	9.63	2.95	0.53	0.30	0.137	0.083	0.021	99.20
E6_4	TS60	49.90	2.91	13.46	13.52	0.23	5.38	9.68	3.01	0.43	0.30	0.132	0.067	0.017	99.04
E6_5	TS60	50.59	2.92	13.13	13.52	0.23	5.36	9.40	2.90	0.45	0.34	0.136	0.041	0.015	99.04
E6_6	TS60	49.74	2.94	13.13	13.76	0.22	5.37	9.52	2.90	0.48	0.32	0.143	0.082	0.016	98.63
E6_7	TS60	49.51	2.95	13.11	13.98	0.22	5.29	9.50	2.99	0.45	0.31	0.136	0.081	0.019	98.55
E6_8	TS60	49.66	3.00	13.03	14.29	0.24	5.61	9.57	2.85	0.50	0.34	0.141	0.087	0.015	99.32
E6_9	TS60	50.21	2.84	13.29	13.31	0.23	5.48	9.65	2.96	0.44	0.31	0.147	0.047	0.018	98.93
E6_10	TS60	49.32	2.83	13.43	13.52	0.23	5.38	9.39	3.05	0.44	0.32	0.143	0.039	0.018	98.10

Sample #	Section	SiO_2	TiO_2	Al_2O_3	FeO	MnO	MgO	CaO	Na_2O	K_2O	P_2O_5	SO_2	F	Cl	Total
E4_1	TS60	49.91	2.91	13.04	13.50	0.24	5.53	9.77	2.88	0.51	0.31	0.129	0.070	0.019	98.81
E4_2	TS60	50.51	2.96	13.60	13.50	0.23	5.42	10.20	1.51	0.50	0.30	0.117	0.075	0.019	98.93
E4_3	TS60	49.76	3.02	12.98	13.65	0.22	5.51	9.71	2.90	0.44	0.30	0.124	0.069	0.015	98.70
E4_4	TS60	50.84	2.81	12.89	13.61	0.22	5.47	9.55	2.94	0.48	0.28	0.105	0.070	0.017	99.29
E4_5	TS60	49.96	2.91	13.06	13.75	0.22	5.25	9.48	2.87	0.50	0.34	0.140	0.064	0.017	98.55

Sample #	Section	SiO_2	TiO_2	Al_2O_3	FeO	MnO	MgO	CaO	Na_2O	K_2O	P_2O_5	SO_2	F	Cl	Total
E4_7	TS60	49.85	2.96	13.12	13.54	0.23	5.25	9.23	3.04	0.48	0.34	0.148	0.077	0.020	98.27
E4_8	TS60	49.86	2.82	13.22	13.18	0.23	5.37	9.49	3.09	0.52	0.33	0.125	0.042	0.018	98.27
E4_9	TS60	50.20	2.86	12.87	13.43	0.22	5.36	9.39	2.93	0.45	0.31	0.143	0.051	0.014	98.23
E4_10	TS60	49.98	2.85	12.92	13.32	0.24	5.56	9.75	3.03	0.46	0.29	0.137	0.054	0.019	98.61
E4_11	TS60	49.45	2.86	13.14	13.11	0.23	5.58	9.99	2.74	0.47	0.29	0.188	0.056	0.021	98.12
E4_12	TS60	50.05	2.89	13.09	13.41	0.22	5.48	9.79	2.89	0.46	0.31	0.145	0.047	0.020	98.81
E4_13	TS60	49.62	2.82	13.23	13.11	0.24	5.64	9.82	2.83	0.46	0.31	0.156	0.076	0.019	98.33
E4_14	TS60	49.75	2.76	13.26	13.24	0.23	5.57	9.78	2.89	0.57	0.30	0.157	0.067	0.017	98.60
E4_15	TS60	49.45	2.84	13.29	13.58	0.21	5.53	9.55	2.89	0.46	0.31	0.157	0.053	0.017	98.34
E4_16	TS60	49.85	2.82	13.64	13.42	0.21	5.54	9.69	2.92	0.50	0.31	0.143	0.075	0.019	99.13

UNIT F

Sample #	Section	SiO_2	TiO_2	Al_2O_3	FeO	MnO	MgO	CaO	Na_2O	K_2O	P_2O_5	SO_2	F	Cl	Total
C`12_1_1	G1	49.88	2.91	12.93	13.40	0.23	5.37	9.65	2.92	0.23	0.32	0.132	0.047	0.012	98.04
C`12_1_2	G1	49.81	3.02	13.25	13.68	0.23	5.46	9.87	2.85	0.23	0.32	0.129	0.062	0.019	98.93
C`12_1_3	G1	49.44	2.86	13.37	13.45	0.23	5.33	9.76	2.90	0.23	0.34	0.128	0.056	0.017	98.11
C`12_1_1	G1	49.88	2.92	12.93	13.40	0.23	5.37	9.65	2.91	0.51	0.32	0.132	0.047	0.012	98.32
C`12_1_2	G1	49.81	2.85	13.25	13.68	0.23	5.46	9.87	3.02	0.52	0.32	0.129	0.062	0.019	99.22
C`12_1_3	G1	49.44	2.90	13.37	13.45	0.23	5.33	9.76	2.86	0.48	0.34	0.128	0.056	0.017	98.36
C10_1	G1	49.91	2.95	13.02	13.58	0.24	4.96	9.34	3.00	0.59	0.34	0.133	0.087	0.018	98.16
C10_2	G1	50.20	2.99	13.13	14.04	0.24	4.98	9.27	3.15	0.52	0.34	0.126	0.089	0.016	99.08
C10_3	G1	49.70	2.95	13.21	13.84	0.23	4.84	9.39	2.80	0.53	0.34	0.133	0.063	0.021	98.04
C10_4	G1	50.08	2.96	13.52	13.83	0.24	5.07	9.62	2.77	0.47	0.33	0.136	0.078	0.019	99.11
C10_5	G1	50.18	2.89	13.18	13.46	0.22	5.42	9.71	2.84	0.43	0.31	0.144	0.077	0.017	98.88
C10_6	G1	49.50	2.92	13.41	13.37	0.23	5.25	9.66	2.98	0.49	0.31	0.141	0.046	0.015	98.32
C10_7	G1	50.14	2.90	13.52	13.28	0.23	5.43	9.54	3.06	0.42	0.31	0.153	0.028	0.019	99.02
C10_8	G1	50.44	2.86	13.45	13.10	0.23	5.42	9.76	2.73	0.45	0.32	0.137	0.066	0.017	98.98

Sample #	Section	SiO_2	TiO_2	Al_2O_3	FeO	MnO	MgO	CaO	Na_2O	K_2O	P_2O_5	SO_2	F	Cl	Total
C11_1	G1	50.34	2.96	13.61	13.46	0.23	5.28	9.52	3.01	0.54	0.34	0.134	0.073	0.016	99.52
C11_2	G1	49.74	2.88	13.18	13.76	0.21	5.31	9.69	3.01	0.49	0.31	0.139	0.053	0.017	98.81

Sample #	Section	SiO_2	TiO_2	Al_2O_3	FeO	MnO	MgO	CaO	Na_2O	K_2O	P_2O_5	SO_2	F	Cl	Total
C11_3	G1	49.46	2.98	13.36	13.37	0.24	5.25	9.83	2.87	0.52	0.32	0.125	0.060	0.017	98.39
C11_4	G1	50.18	2.94	13.52	13.85	0.24	5.27	9.55	3.14	0.50	0.35	0.120	0.060	0.017	99.73
C11_5	G1	51.12	3.07	13.72	14.11	0.24	5.46	9.59	0.99	0.56	0.33	0.121	0.059	0.018	99.39
C11_6	G1	50.22	2.99	13.16	13.78	0.24	5.19	9.58	2.89	0.54	0.33	0.128	0.076	0.018	99.12
C11_7	G1	49.92	2.93	13.35	13.41	0.24	4.99	9.63	2.82	0.51	0.33	0.144	0.059	0.019	98.37
C11_8	G1	49.76	3.07	13.21	13.78	0.24	5.18	9.38	2.90	0.51	0.33	0.118	0.085	0.017	98.57
C11_9	G1	50.11	3.05	13.15	13.76	0.24	5.19	9.24	2.91	0.48	0.34	0.139	0.057	0.019	98.67
C11_10	G1	50.52	3.03	13.27	13.76	0.22	5.28	9.62	2.85	0.55	0.33	0.124	0.103	0.021	99.67
Ts26-01	TS26	49.91	3.00	13.02	13.94	0.23	5.05	9.26	2.87	0.55	0.33	0.139	0.066	0.019	98.40
Ts26-01	TS26	50.00	2.87	12.91	13.91	0.24	5.29	9.59	2.77	0.51	0.31	0.166	0.066	0.018	98.65
Ts26-01	TS26	50.48	2.95	13.27	13.75	0.24	5.39	9.66	2.80	0.46	0.32	0.153	0.083	0.017	99.57
Ts26-01	TS26	50.13	2.96	13.56	13.70	0.22	5.34	9.77	2.97	0.52	0.31	0.152	0.072	0.014	99.71
Ts26-01	TS26	50.24	2.91	13.32	13.35	0.23	5.45	9.63	2.81	0.46	0.29	0.153	0.067	0.019	98.92
Ts26-01	TS26	50.23	2.86	13.43	13.50	0.24	5.44	9.69	2.95	0.48	0.30	0.156	0.037	0.019	99.33
Ts26-01	TS26	50.44	2.87	13.43	13.42	0.23	5.52	9.84	2.77	0.45	0.30	0.164	0.053	0.013	99.50
Ts26-01	TS26	51.28	2.93	13.57	14.18	0.22	5.39	10.24	0.88	0.47	0.31	0.182	0.096	0.015	99.77

Sample #	Section	SiO_2	TiO_2	Al_2O_3	FeO	MnO	MgO	CaO	Na_2O	K_2O	P_2O_5	SO_2	F	Cl	Total
Ts26-01	TS26	49.51	2.88	13.00	13.77	0.24	5.36	9.84	2.99	0.47	0.32	0.153	0.080	0.015	98.63
Ts26-01	TS26	50.90	2.89	13.40	13.45	0.24	5.45	9.72	3.14	0.52	0.30	0.158	0.084	0.014	100.27

UNIT G

Sample #	Section	SiO_2	TiO_2	Al_2O_3	FeO	MnO	MgO	CaO	Na_2O	K_2O	P_2O_5	SO_2	F	Cl	Total
C`13_1_1	G1	49.19	2.98	12.96	14.49	0.25	5.12	9.74	2.53	0.25	0.34	0.125	0.093	0.019	98.08
C`13_1_2	G1	50.01	2.86	13.52	13.48	0.24	4.94	9.76	2.77	0.24	0.33	0.118	0.079	0.020	98.38
C`13_3_1	G1	49.56	2.90	13.39	13.09	0.23	5.40	9.88	2.92	0.23	0.32	0.117	0.049	0.016	98.11
C`13_3_2	G1	49.92	2.86	12.98	13.86	0.23	5.27	9.99	2.77	0.23	0.30	0.115	0.042	0.016	98.58
C`13_3_3	G1	50.76	2.89	12.98	13.62	0.22	5.35	9.76	3.07	0.22	0.33	0.110	0.016	0.014	99.36
C13_4_1	G1	49.51	3.11	13.21	14.20	0.23	4.97	9.43	2.90	0.23	0.34	0.135	0.044	0.016	98.34
C13_4_2	G1	50.14	3.10	13.04	14.03	0.24	4.97	9.23	2.91	0.24	0.34	0.155	0.055	0.016	98.47
C13_4_3	G1	48.49	2.79	12.91	13.36	0.23	5.38	9.66	2.97	0.23	0.31	0.259	0.037	0.026	96.64
C`13_1_1	G1	49.19	2.98	12.96	14.49	0.25	5.12	9.74	2.53	0.49	0.34	0.125	0.093	0.019	98.32
C`13_1_2	G1	50.01	2.86	13.52	13.48	0.24	4.94	9.76	2.77	0.50	0.33	0.118	0.079	0.020	98.64
C`13_3_1	G1	49.56	2.90	13.39	13.09	0.23	5.40	9.88	2.92	0.46	0.32	0.117	0.049	0.016	98.33
C`13_3_2	G1	49.92	2.86	12.98	13.86	0.23	5.27	9.99	2.77	0.50	0.30	0.115	0.042	0.016	98.84
C`13_3_3	G1	50.76	2.89	12.98	13.62	0.22	5.35	9.76	3.07	0.47	0.33	0.110	0.016	0.014	99.60
C13_4_1	G1	49.51	3.11	13.21	14.20	0.23	4.97	9.43	2.90	0.52	0.34	0.135	0.044	0.016	98.63

Sample #	Section	SiO_2	TiO_2	Al_2O_3	FeO	MnO	MgO	CaO	Na_2O	K_2O	P_2O_5	SO_2	F	Cl	Total
C13_4_2	G1	50.14	3.10	13.04	14.03	0.24	4.97	9.23	2.91	0.51	0.34	0.155	0.055	0.016	98.74
E1_1	TS60	50.15	3.05	12.80	13.91	0.23	5.07	9.30	3.18	0.50	0.35	0.133	0.069	0.022	98.74

Sample #	Section	SiO_2	TiO_2	Al_2O_3	FeO	MnO	MgO	CaO	Na_2O	K_2O	P_2O_5	SO_2	F	Cl	Total
E1_2	TS60	49.32	3.17	12.69	13.75	0.25	5.09	9.19	3.02	0.51	0.35	0.146	0.062	0.016	97.58
E1_3	TS60	49.18	3.10	12.75	13.96	0.24	4.94	9.13	3.11	0.55	0.33	0.137	0.064	0.019	97.50
E1_4	TS60	49.34	3.04	12.79	14.03	0.23	5.01	9.25	3.02	0.52	0.34	0.126	0.079	0.018	97.79
E1_5	TS60	49.76	3.07	12.65	13.34	0.25	4.90	9.11	2.90	0.47	0.33	0.125	0.067	0.015	96.98
E1_6	TS60	49.02	3.02	12.91	13.83	0.23	4.95	9.21	3.00	0.48	0.33	0.132	0.060	0.019	97.20
E1_7	TS60	50.04	2.96	13.35	14.21	0.25	5.11	9.35	2.96	0.51	0.33	0.140	0.058	0.020	99.30
E1_8	TS60	49.03	3.03	12.73	14.29	0.21	5.08	9.28	2.92	0.54	0.34	0.133	0.088	0.016	97.69
E1_9	TS60	49.27	2.96	13.08	13.93	0.22	5.09	9.22	2.90	0.55	0.32	0.142	0.070	0.020	97.77
E1_10	TS60	49.40	3.06	13.20	14.05	0.24	5.18	9.38	3.04	0.50	0.32	0.152	0.040	0.017	98.59
E2_1	TS60	49.73	2.87	13.16	12.98	0.23	5.55	9.79	2.99	0.55	0.31	0.136	0.024	0.015	98.34
E2_2	TS60	49.90	2.86	13.22	13.39	0.23	5.19	9.76	2.80	0.54	0.33	0.145	0.105	0.020	98.50
E2_3	TS60	49.55	2.91	12.70	13.69	0.23	5.27	9.78	2.91	0.49	0.33	0.134	0.072	0.014	98.06
E2_4	TS60	49.47	2.87	12.93	13.49	0.23	5.28	9.52	2.84	0.52	0.31	0.133	0.052	0.020	97.67
E2_5	TS60	50.09	2.89	13.39	13.94	0.22	5.29	9.81	2.93	0.44	0.32	0.130	0.069	0.017	99.52
E2_6	TS60	49.35	2.87	13.11	13.53	0.22	5.34	9.68	2.87	0.48	0.32	0.134	0.070	0.017	97.98
E2_7	TS60	49.55	3.00	13.04	13.81	0.23	5.41	9.73	2.87	0.47	0.32	0.127	0.039	0.016	98.61

Sample #	Section	SiO_2	TiO_2	Al_2O_3	FeO	MnO	MgO	CaO	Na_2O	K_2O	P_2O_5	SO_2	F	Cl	Total
E2_8	TS60	49.55	2.84	12.94	13.56	0.22	5.54	9.81	2.88	0.44	0.32	0.130	0.061	0.018	98.31
E2_9	TS60	49.79	2.95	12.95	13.80	0.23	5.44	9.74	2.86	0.41	0.32	0.138	0.063	0.017	98.69
E2_10	TS60	48.96	2.90	12.86	13.91	0.24	5.35	9.57	2.82	0.48	0.32	0.132	0.072	0.016	97.63

PUMICE

Sample #	Section	SiO_2	TiO_2	Al_2O_3	FeO	MnO	MgO	CaO	Na_2O	K_2O	P_2O_5	SO_2	F	Cl	Total
TS1205 P1	TS12	49.14	3.24	12.28	14.84	0.22	4.86	9.70	2.84	0.59	0.34	0.068	0.079	0.013	98.21
TS1205 P2	TS12	50.43	3.15	12.58	14.14	0.24	4.86	9.38	2.89	0.57	0.35	0.056	0.073	0.017	98.73
TS1205 P3	TS12	50.47	3.22	12.43	14.31	0.23	5.05	9.62	2.91	0.56	0.33	0.075	0.076	0.019	99.30
TS1205 P4	TS12	49.42	3.30	13.13	14.99	0.25	4.96	9.39	2.90	0.54	0.35	0.081	0.076	0.019	99.41
TS1205 P5	TS12	50.05	3.31	12.66	14.64	0.25	4.69	9.36	2.97	0.61	0.37	0.070	0.066	0.018	99.06
TS1205 P6	TS12	50.31	3.23	12.54	14.18	0.23	4.91	9.45	2.92	0.59	0.36	0.069	0.039	0.018	98.86
TS1205 P7	TS12	50.03	3.16	12.62	14.88	0.25	4.87	9.38	2.91	0.55	0.34	0.063	0.093	0.018	99.16
TS1205 P8	TS12	50.12	3.21	12.93	14.52	0.24	4.90	9.43	3.01	0.63	0.34	0.084	0.086	0.020	99.51
TS1205 P9	TS12	49.80	3.29	12.67	14.49	0.23	4.90	9.53	2.93	0.57	0.33	0.101	0.053	0.016	98.91
TS1205 P10 New	TS12	51.23	3.31	12.72	14.08	0.25	4.94	9.54	2.83	0.56	0.35	0.094	0.089	0.017	100.00
TS12-05-58_01	TS12	50.78	3.31	12.63	15.26	0.25	4.84	9.46	2.67	0.48	0.34	0.098	0.101	0.019	100.24

Sample #	Section	SiO_2	TiO_2	Al_2O_3	FeO	MnO	MgO	CaO	Na_2O	K_2O	P_2O_5	SO_2	F	Cl	Total
TS12-05-58_01	TS12	50.65	3.34	12.63	14.35	0.27	4.10	9.68	3.03	0.60	0.34	0.110	0.087	0.021	99.20
TS12-05-58_01	TS12	50.19	3.19	12.62	14.63	0.23	4.74	9.44	2.78	0.53	0.34	0.091	0.104	0.018	98.90
TS12-05-58_01	TS12	50.05	3.29	12.88	14.52	0.25	4.76	9.36	2.91	0.54	0.33	0.070	0.056	0.017	99.02
TS12-05-58_01	TS12	50.56	3.26	12.48	14.55	0.25	4.96	9.35	2.89	0.53	0.34	0.089	0.090	0.022	99.38
TS12-05-58_01	TS12	50.82	3.35	12.96	14.26	0.25	4.18	9.90	3.21	0.37	0.35	0.077	0.093	0.016	99.85
TS12-05-58_01	TS12	51.37	3.31	12.83	14.59	0.25	4.64	9.27	3.07	0.53	0.35	0.074	0.079	0.016	100.38
TS12-05-58_01	TS12	50.27	3.28	12.67	15.01	0.26	4.91	9.37	2.93	0.57	0.35	0.081	0.080	0.020	99.80
TS12-05-58_01	TS12	50.72	3.33	12.74	14.47	0.25	4.85	9.50	2.80	0.59	0.36	0.086	0.063	0.022	99.78
TS12-05-58_01	TS12	50.59	3.30	12.48	14.52	0.25	4.81	9.47	2.89	0.52	0.35	0.076	0.081	0.014	99.34
TTB-98_1	TT02-B	50.41	3.09	12.87	13.92	0.24	4.88	9.15	2.84	0.45	0.36	0.134	0.076	0.019	98.42
TTB-98_2	TT02-B	50.12	3.06	12.77	13.73	0.24	4.98	9.20	3.06	0.51	0.35	0.122	0.089	0.016	98.25
TTB-98_3	TT02-B	50.12	3.15	13.07	13.99	0.26	4.95	9.10	2.92	0.48	0.34	0.124	0.059	0.020	98.58
TTB-98_4	TT02-B	49.18	3.09	13.01	14.15	0.24	4.96	9.32	2.93	0.58	0.34	0.128	0.089	0.022	98.04

Sample #	Section	SiO_2	TiO_2	Al_2O_3	FeO	MnO	MgO	CaO	Na_2O	K_2O	P_2O_5	SO_2	F	Cl	Total
TTB-98_5	TT02-B	50.19	3.10	13.10	14.12	0.23	5.01	9.27	3.03	0.58	0.35	0.127	0.073	0.019	99.21
TTB-98_6	TT02-B	49.73	3.00	13.31	14.09	0.23	5.01	9.26	3.09	0.55	0.36	0.113	0.078	0.015	98.83
TTB-5_1	TT02-B	49.99	3.10	12.85	14.26	0.23	4.92	9.04	3.08	0.51	0.36	0.131	0.083	0.020	98.57

Sample #	Section	SiO_2	TiO_2	Al_2O_3	FeO	MnO	MgO	CaO	Na_2O	K_2O	P_2O_5	SO_2	F	Cl	Total
TTB-5_2	TT02-B	50.35	3.16	12.89	14.05	0.24	4.94	9.01	3.17	0.55	0.37	0.126	0.080	0.017	98.97
TTB-5_3	TT02-B	50.04	3.09	12.89	14.27	0.22	4.83	9.19	3.07	0.52	0.34	0.129	0.092	0.016	98.68
TTB-5_4	TT02-B	50.39	3.03	12.87	14.24	0.24	4.88	9.01	3.17	0.55	0.36	0.120	0.066	0.016	98.96
TTB-5_5	TT02-B	50.37	3.19	12.84	14.02	0.23	4.82	8.90	3.03	0.47	0.36	0.124	0.103	0.025	98.48
TTB-5_6	TT02-B	50.42	3.10	12.98	14.32	0.24	4.86	9.07	3.11	0.59	0.36	0.133	0.056	0.020	99.24
TTB-5_7	TT02-B	50.34	3.25	13.05	14.31	0.24	4.75	9.16	3.01	0.53	0.36	0.113	0.057	0.021	99.18
TTB-5_8	TT02-B	51.25	3.18	13.11	14.43	0.25	4.93	9.26	0.91	0.57	0.36	0.147	0.109	0.019	98.53
TTB-5_9	TT02-B	49.95	3.20	13.18	14.43	0.24	4.94	8.96	3.12	0.60	0.34	0.123	0.058	0.022	99.16

TTB37-2	TT02-B	50.55	3.21	13.35	14.14	0.24	4.88	8.92	3.17	0.51	0.35	0.133	0.082	0.021	99.55
TTB37-3	TT02-B	49.96	3.12	13.44	14.69	0.25	4.89	8.99	3.08	0.50	0.36	0.126	0.048	0.018	99.47
TTB37-4	TT02-B	50.56	3.19	12.82	14.19	0.25	4.89	9.06	2.87	0.49	0.35	0.129	0.056	0.020	98.87
TTB37-4	TT02-B	49.48	3.27	13.17	14.25	0.24	4.65	9.24	3.17	0.51	0.34	0.128	0.098	0.021	98.56
TTB37-6	TT02-B	50.45	3.16	12.96	14.13	0.25	4.85	9.12	3.35	0.57	0.34	0.130	0.084	0.022	99.42
TTB37-7	TT02-B	50.38	3.23	13.24	13.99	0.25	4.95	9.01	3.09	0.52	0.35	0.138	0.054	0.019	99.22

Sample #	**Section**	**SiO_2**	**TiO_2**	**Al_2O_3**	**FeO**	**MnO**	**MgO**	**CaO**	**Na_2O**	**K_2O**	**P_2O_5**	**SO_2**	**F**	**Cl**	**Total**
TTB37-8	TT02-B	50.01	3.21	13.47	14.69	0.24	4.75	9.16	2.95	0.53	0.35	0.170	0.087	0.019	99.63
TTB37-9	TT02-B	50.04	3.06	13.11	14.04	0.23	4.78	9.01	2.92	0.53	0.36	0.133	0.080	0.022	98.33
TTB37-10	TT02-B	50.58	3.20	12.92	13.80	0.24	4.92	9.23	3.07	0.55	0.37	0.138	0.082	0.018	99.11

APPENDIX X

PETROLOGIC MODELLING

Table A10.1: Modelling (using MELTS software: Ghiorso and Sack, 1995; Asimow and Ghiorso, 1998) of expected feldspar composition crystallising from a melt of the most primitive, median, and most evolved compositions measured for the Laki, G1998, and G2004 eruptions at 1200°C and 1kbar . Laki data are from Grönvold, 1984; and Métrich et al., 1991.

	LAKI				**G1998**				**G2004**		
	PRIMITIVE	**MEDIAN**	**EVOLVED**		**PRIMITIVE**	**MEDIAN**	**EVOLVED**		**PRIMITIVE**	**MEDIAN**	**EVOLVED**
SiO_2	50.25	50.34	50.40		52.02	52.49	53.01		50.90	50.95	50.81
TiO_2	1.71	3.03	3.65		2.46	2.48	2.81		3.07	2.90	2.78
Al_2O_3	13.88	13.02	11.79		13.68	13.74	13.62		13.28	13.43	13.69
FeO	12.30	14.05	16.41		12.35	12.48	13.27		14.28	13.85	13.36
MnO	0.26	0.23	0.41		0.21	0.21	0.21		0.24	0.23	0.22
MgO	7.02	5.45	4.64		5.82	5.68	4.92		5.05	5.34	5.61
CaO	11.86	10.35	9.53		10.02	9.85	8.84		9.39	9.86	10.08
Na_2O	2.53	2.68	2.74		2.65	2.53	2.68		2.89	2.66	2.64
K_2O	0.19	0.48	0.42		0.52	0.54	0.65		0.53	0.50	0.49
P_2O_5	n.d.	0.37	n.d.		0.27	0.28	0.32		0.35	0.29	0.32
Albite	0.27	0.31	0.33		0.31	0.30	0.34		0.34	0.31	0.31
Anorthite	0.71	0.66	0.64		0.65	0.65	0.61		0.62	0.65	0.65
Sanidine	0.02	0.03	0.03		0.04	0.05	0.05		0.04	0.04	0.04

APPENDIX XI

MELT INCLUSION DATA

Table A11.1: Major oxide and volatile content of measured melt inclusions

	Sample #	Section	SiO_2 (wt. %)	TiO_2 (wt. %)	Al_2O_3 (wt. %)	FeO (wt. %)	MnO (wt. %)	MgO (wt. %)	CaO (wt. %)	Na_2O (wt. %)	K_2O (wt. %)	P_2O_5 (wt. %)	SO_2 (wt. %)	F (wt. %)	Cl (wt. %)	Total
Pristine/ Near Pristine	F13_1_2	G5	50.24	2.90	12.85	12.88	0.22	5.70	9.95	2.80	0.51	0.29	0.298	0.075	0.017	98.73
	F13_1_1	G5	49.50	3.00	12.77	13.30	0.24	5.63	9.53	2.57	0.57	0.30	0.306	0.063	0.019	97.79
	F13_1_3	G5	50.01	2.99	13.00	13.60	0.24	5.74	9.85	2.43	0.61	0.30	0.305	0.090	0.021	99.18
	F13_1_4	G5	49.82	3.01	12.97	13.87	0.24	5.58	9.84	2.83	0.50	0.32	0.295	0.050	0.016	99.34
	TS12_2_1	TS12	50.20	3.31	12.16	14.92	0.24	5.21	9.60	2.90	0.52	0.35	0.230	0.041	0.019	99.70
	TS12_3_1	TS12	49.57	3.26	12.10	14.76	0.24	5.27	9.50	2.76	0.50	0.33	0.220	0.057	0.020	98.59
	F13_3_3	G5	49.29	3.29	11.73	14.83	0.29	5.79	9.75	2.58	0.57	0.34	0.301	0.053	0.023	98.83
	TS12_3_1	TS12	49.80	3.19	12.08	15.23	0.24	5.66	9.43	2.79	0.67	0.33	0.228	0.042	0.018	99.71
	TS12_4_3	TS12	49.55	3.52	11.60	16.85	0.27	5.31	9.81	2.56	0.50	0.38	0.196	0.078	0.022	100.62
	TS12_5_2	TS12	49.36	3.43	10.93	16.13	0.27	5.54	9.49	2.57	0.68	0.35	0.207	0.099	0.020	99.02
Affected	TS12_6_1	TS12	48.99	3.55	9.88	17.64	0.28	6.26	9.23	2.21	0.75	0.37	0.254	0.082	0.031	99.49
	T9B_2_1	TT02-B	48.10	3.47	9.37	18.46	0.30	5.96	9.24	1.95	0.66	0.35	0.268	0.123	0.025	98.27
	TS12_5_4	TS12	47.42	3.80	8.03	19.54	0.30	6.52	9.65	1.61	0.63	0.38	0.296	0.097	0.046	98.28
	TS12_4_4	TS12	47.64	4.00	8.37	19.89	0.31	6.85	10.10	1.79	0.58	0.42	0.299	0.104	0.042	100.35
	TS12_5_3	TS12	49.47	3.61	10.53	16.81	0.27	6.01	9.46	1.32	0.81	0.38	0.288	0.107	0.025	99.05
	TS12_3_2	TS12	48.64	3.57	9.22	18.23	0.27	5.76	9.37	2.01	0.60	0.36	0.202	0.129	0.032	98.37
	TS12_3_4	TS12	48.52	3.79	10.01	18.25	0.27	5.92	9.75	1.99	0.55	0.37	0.198	0.068	0.024	99.67
	TS12_4_5	TS12	48.72	4.06	7.90	19.66	0.31	6.20	9.18	1.83	0.78	0.44	0.299	0.087	0.034	99.47
	TS58_1_4	TS58	48.46	3.99	9.80	17.25	0.29	4.52	10.01	2.09	0.66	0.37	0.284	0.090	0.036	97.84
	F13_2_1	G5	50.01	2.99	13.00	13.60	0.24	5.74	9.85	2.43	0.61	0.30	0.305	0.090	0.021	99.18

	Sample #	Section	SiO_2 (wt. %)	TiO_2 (wt. %)	Al_2O_3 (wt. %)	FeO (wt. %)	MnO (wt. %)	MgO (wt. %)	CaO (wt. %)	Na_2O (wt. %)	K_2O (wt. %)	P_2O_5 (wt. %)	SO_2 (wt. %)	F (wt. %)	Cl (wt. %)	Total
Unit A (avg)	-	-	50.04	3.00	13.08	13.78	0.23	5.10	9.50	2.92	0.51	0.34	0.17	0.06	0.02	98.74
Unit B (avg)	-	-	50.08	3.01	13.06	13.79	0.23	5.09	9.49	2.91	0.51	0.35	0.17	0.05	0.02	98.76
Unit C (avg)	-	-	49.99	2.96	13.14	13.74	0.31	5.22	9.62	2.91	0.49	0.33	0.16	0.05	0.02	98.95
Unit D (avg)	-	-	50.20	2.93	13.24	13.64	0.23	5.25	9.52	2.96	0.49	0.33	0.16	0.06	0.02	99.03
Unit E (avg)	-	-	49.97	2.86	13.21	13.50	0.23	5.41	9.71	2.90	0.48	0.32	0.16	0.06	0.02	98.84
Unit F (avg)	-	-	50.12	2.94	13.30	13.65	0.23	5.28	9.63	2.79	0.50	0.32	0.17	0.07	0.02	99.01
Unit G (avg)	-	-	49.61	2.97	13.01	13.78	0.23	5.19	9.53	2.92	0.50	0.33	0.16	0.06	0.02	98.31
Pumice (avg)	-	-	50.27	3.20	12.88	14.35	0.24	4.84	9.28	2.94	0.54	0.35	0.14	0.08	0.02	99.13

Table A11.2: Original and corrected volatile compositions of G2004 melt inclusions hosted in plagioclase phenocrysts.

	Sample #	Section	SO_2 (ppm)	S (ppm)	F (ppm)	Cl (ppm)	Al/Na	Factor	S (corr) (ppm)	F (corr) (ppm)	Cl (corr) (ppm)	An # (core)	An # (rim)
Pristine/Near Pristine	F13_1_2	G5	2979	1490	746	165	4.59	-	-	-	-	77	72
	F13_1_1	G5	3062	1531	631	190	4.97	1.10	1683	694	209	77	72
	F13_1_3	G5	3054	1527	898	214	5.34	1.18	1804	1061	253	77	72
	F13_1_4	G5	2945	1473	500	163	4.58	-	-	-	-	77	72
	TS12_2_1	TS12	2296	1148	412	194	4.19	0.93	1064	382	180	82	-
	TS12_3_1	TS12	2200	1100	570	204	4.39	-	-	-	-	81	80
	F13_3_3	G5	3010	1505	526	232	4.54	-	-	-	-	81	80
	TS12_3_1	TS12	2279	1140	422	182	4.32	0.96	1089	403	174	74	66
	TS12_4_3	TS12	1964	982	775	222	4.53	-	-	-	-	69	67
	TS12_5_2	TS12	2068	1034	988	199	4.26	0.94	974	931	187	-	-
Affected	TS12_6_1	TS12	2541	1271	819	306	4.47	-	-	-	-	82	70
	TT9B_2_1	TT02-B	2681	1341	1232	249	4.82	1.07	1429	1313	265	-	-
	TS12_5_4	TS12	2962	1481	969	463	4.98	1.10	1633	1069	511	74	66
	TS12_4_4	TS12	2993	1497	1039	417	4.67	-	-	-	-	82	70
	TS12_5_3	TS12	2883	1442	1073	253	7.97	1.76	2540	1891	446	74	66
	TS12_3_2	TS12	2020	1010	1288	321	4.58	-	-	-	-	69	67
	TS12_3_4	TS12	1979	990	682	244	5.02	1.11	1099	757	271	69	67
	TS12_4_5	TS12	2994	1497	870	342	4.31	0.95	1427	829	326	81	80
	TS18_1_4	TS18	2835	1418	896	361	4.68	-	-	-	-	64	63
Unit A (avg)	-	-	1695	847	563	180	4.48	-	-	-	-	-	-
Unit B (avg)	-	-	1662	831	547	180	4.49	-	-	-	-	-	-
Unit C (avg)	-	-	1581	790	538	178	4.52	-	-	-	-	-	-
Unit D (avg)	-	-	1604	802	647	181	4.47	-	-	-	-	-	-
Unit E (avg)	-	-	1636	818	617	177	4.55	-	-	-	-	-	-
Unit F (avg)	-	-	1707	853	673	172	4.77	-	-	-	-	-	-
Unit G (avg)	-	-	1624	812	615	173	4.46	-	-	-	-	-	-
Pumice (avg)	-	-	1376	688	774	188	4.38	-	-	-	-	-	-

Table A11.3: EMP analyses of G2004 phenocrysts.

Sample #	Section	Unit	SiO_2	TiO_2	Al_2O_3	FeO	MnO	MgO	CaO	Na_2O	K_2O	Total	Moles Na	Moles Ca	% Na	% Ca	An #
TS12-05-58_Plag 1	TS12	-	53.22	0.11	29.11	0.97	0.01	0.19	12.51	4.39	0.11	100.61	0.07	0.14	34	66	66
TS12-05-58_Plag 2_1 (Core)	TS12	-	53.04	0.13	28.87	1.05	0.00	0.23	12.85	4.19	0.10	100.45	0.07	0.14	32	68	68
TS12-05-58_Plag 2_2 (Core)	TS12	-	53.11	0.15	29.11	1.06	0.01	0.22	12.50	4.42	0.11	100.68	0.07	0.14	34	66	66
TS12-05-58_Plag 2_3 (Core)	TS12	-	53.45	0.12	29.13	1.06	0.01	0.20	12.52	4.33	0.11	100.93	0.07	0.14	34	66	66
TS12-05-58_Plag 2_4 (Core)	TS12	-	53.47	0.13	29.15	1.08	0.00	0.20	12.42	4.25	0.11	100.82	0.07	0.14	33	67	67
TS12-05-58_Plag 2_6 (Rim)	TS12	-	53.02	0.30	29.26	1.72	0.01	0.42	12.58	4.31	0.14	101.76	0.07	0.14	34	66	66
TS12-05-58_Plag 2_8 (Rim)	TS12	-	53.06	0.41	25.04	2.03	0.02	0.56	11.91	4.27	0.15	97.46	0.07	0.13	35	65	65
TS12-05-58 Plag 3_1	TS12	-	53.19	0.11	29.22	0.91	0.00	0.23	12.90	4.28	0.10	100.94	0.07	0.14	33	67	67
TS12-05-58 Plag 4_1 (Core)	TS12	-	53.59	0.10	29.04	0.90	0.01	0.20	12.51	4.41	0.11	100.87	0.07	0.14	34	66	66
TS12-05-58 Plag 4_2 (Rim)	TS12	-	54.14	0.12	28.81	1.11	0.00	0.21	12.16	4.57	0.11	101.22	0.07	0.13	36	64	64
TS12-05-58 Plag 2 (Core)	TS12	-	48.46	0.06	32.77	0.80	0.00	0.15	16.02	2.41	0.06	100.73	0.04	0.18	18	82	82
TS12-05-58 Plag 3 (Core 1)	TS12	-	47.46	0.06	32.48	0.88	0.01	0.14	16.52	2.28	0.02	99.86	0.04	0.18	17	83	83
TS12-05-58 Plag 3 (Core 2)	TS12	-	49.15	0.06	32.48	0.83	0.00	0.15	16.11	2.37	0.05	101.22	0.04	0.18	18	82	82
TS12-05-58 Plag 3 _1 (Rim)	TS12	-	52.25	0.09	29.61	0.82	0.01	0.18	13.18	4.05	0.10	100.29	0.07	0.14	31	69	69
TS12-05-58 Plag 3_2 (Rim)	TS12	-	51.99	0.09	29.52	0.68	0.01	0.21	13.22	3.85	0.14	99.71	0.06	0.15	30	70	70
TS12-05-58 Xtal 3_ 3 (Rim)	TS12	-	53.21	0.12	29.26	1.05	0.01	0.23	12.61	4.41	0.10	101.00	0.07	0.14	34	66	66
TS12-05-58 Plag 3_4 (Core)	TS12	-	52.44	0.09	29.24	0.81	0.00	0.16	13.16	4.15	0.05	100.10	0.07	0.14	32	68	68
TS12-05-58 Plag 4_3 (Rim)	TS12	-	53.90	0.13	29.04	1.08	0.01	0.18	12.16	4.65	0.12	101.26	0.08	0.13	36	64	64
TS12-05-58 Plag 4_4 (Core)	TS12	-	53.12	0.11	28.87	0.98	0.02	0.17	12.82	4.34	0.11	100.54	0.07	0.14	33	67	67
TS12-05-58 Plag 5_1 (Core)	TS12	-	50.01	0.08	31.30	0.78	0.01	0.15	14.52	3.33	0.06	100.25	0.05	0.16	25	75	75

TS12-05-58 Plag 5_2 (Rim)	TS12	-	53.18	0.12	28.63	1.27	0.00	0.15	12.36	4.66	0.15	100.52	0.08	0.14	36	64	64
TS12-05-41 Plag 2 (Core)	TS12	-	53.29	0.12	28.87	1.04	0.00	0.23	12.61	4.28	0.11	100.54	0.07	0.14	33	67	67
TS12-05-41 Plag 2 (Rim)	TS12	-	53.05	0.11	29.00	1.03	0.01	0.21	12.64	4.38	0.11	100.55	0.07	0.14	34	66	66
TS12-05-41 Plag 3 (Core)	TS12	-	52.32	0.09	29.86	0.87	0.01	0.18	13.56	3.95	0.09	100.92	0.06	0.15	30	70	70
TS12-05-41 Plag 3 (Core 2)	TS12	-	52.78	0.10	29.19	0.91	0.01	0.19	12.92	4.20	0.10	100.40	0.07	0.14	32	68	68
TS12-05-41 Plag 3 (Rim 1)	TS12	-	52.75	0.12	29.02	0.92	0.02	0.19	12.85	4.27	0.10	100.23	0.07	0.14	33	67	67
TS12-05-41 Plag 3 (Rim 2)	TS12	-	53.13	0.12	29.56	0.93	0.01	0.17	12.52	4.37	0.11	100.92	0.07	0.14	34	66	66
TS12-05-41 Plag 4 (Core)	TS12	-	48.42	0.07	32.45	0.80	0.01	0.20	16.36	2.40	0.04	100.75	0.04	0.18	18	82	82
TS12-05-41 Plag 4 (Rim)	TS12	-	52.19	0.13	29.94	1.00	0.00	0.25	13.32	3.84	0.11	100.79	0.06	0.15	30	70	70
TS12-05-41 Plag 5 (Core)	TS12	-	51.22	0.09	30.52	0.93	0.00	0.20	14.29	3.45	0.07	100.77	0.06	0.16	26	74	74
TS12-05-41 Plag 5 (Rim)	TS12	-	53.68	0.12	29.22	0.86	0.00	0.18	12.58	4.40	0.11	101.16	0.07	0.14	34	66	66
TS12-05-41 Plag 6 Core 1	TS12	-	53.23	0.10	28.58	0.99	0.01	0.21	12.40	4.47	0.11	100.10	0.07	0.14	35	65	65
TS12-05-41 Plag 6 Core 2	TS12	-	53.09	0.11	28.94	0.93	0.02	0.20	12.69	4.44	0.11	100.53	0.07	0.14	34	66	66
TS12-05-41 Plag 6 Rim 1	TS12	-	53.36	0.12	28.59	0.99	0.00	0.21	12.30	4.49	0.12	100.19	0.07	0.14	35	65	65
TS12-05-41 Plag 6 Rim 2	TS12	-	53.48	0.11	28.55	0.99	0.00	0.20	12.28	4.50	0.12	100.23	0.07	0.13	35	65	65
TS12-05-47 Plag Core 1	TS12	-	53.25	0.11	28.78	0.95	0.02	0.16	12.58	4.48	0.07	100.40	0.07	0.14	34	66	66
TS12-05-47 Plag Core 2	TS12	-	53.23	0.12	29.42	1.16	0.02	0.17	12.56	4.30	0.10	101.06	0.07	0.14	33	67	67
TS12-05-47 Plag Rim 1	TS12	-	51.99	0.10	29.19	1.03	0.00	0.14	13.35	3.89	0.09	99.80	0.06	0.15	30	70	70
TS12-05-41 Plag 4 Cor 2	TS12	-	48.99	0.12	31.74	1.12	0.01	0.23	15.48	2.89	0.08	100.68	0.05	0.17	22	78	78
TS12-05-41 Plag 4 Rim 2	TS12	-	53.47	0.13	29.00	1.12	0.01	0.20	12.58	4.37	0.11	101.00	0.07	0.14	34	66	66
TS12-05-58 Plag 20_1 (Core)	TS12	-	53.49	0.14	28.52	1.12	0.01	0.23	12.29	4.39	0.12	100.30	0.07	0.13	34	66	66
TS12-05-58 Plag 20_2 (Core)	TS12	-	53.65	0.13	28.67	1.14	0.02	0.22	12.24	4.61	0.11	100.81	0.07	0.13	36	64	64
TS12-05-58 Plag 20_3 (Rim)	TS12	-	53.75	0.13	28.63	1.11	0.01	0.23	12.12	4.56	0.12	100.65	0.07	0.13	36	64	64
TS12-05-58 Plag 20_4 (Rim)	TS12	-	53.71	0.14	28.82	1.07	0.00	0.20	12.44	4.56	0.12	101.06	0.07	0.14	35	65	65
TTB-9B Plag 1 (Core)	TT02-B	C	48.97	0.07	31.39	0.84	0.00	0.14	15.18	2.54	0.06	99.19	0.04	0.17	20	80	80
TTB-9B Plag 1 (Rim)	TT02-B	C	48.19	0.06	32.09	0.78	0.02	0.14	15.90	2.43	0.04	99.65	0.04	0.17	18	82	82
TTB-9B Plag 2 (Core)	TT02-B	C	48.53	0.05	32.53	0.71	0.01	0.16	16.17	2.34	0.04	100.54	0.04	0.18	18	82	82
TTB-9B Plag 2 (Rim)	TT02-B	C	47.92	0.08	31.11	0.86	0.00	0.14	15.41	2.31	0.06	97.89	0.04	0.17	18	82	82
TT100 Plag 2 (Core 1)	TT02B	E	49.74	-	31.97	0.80	0.05	0.18	15.66	2.74	0.05	101.20	0.04	0.17	20	80	80
TT100 Plag 2 (Core 2)	TT02B	E	48.28	-	32.65	0.78	0.06	0.17	16.28	2.40	0.04	100.66	0.04	0.18	18	82	82

Sample #	Section	Unit	SiO_2	TiO_2	Al_2O_3	FeO	MnO	MgO	CaO	Na_2O	K_2O	Total	Moles Na	Moles Ca	% Na	% Ca	An #
TT100Plag 2 (Rim 1)	TT02B	E	51.12	-	30.80	0.84	0.07	0.20	13.97	3.56	0.08	100.64	0.06	0.15	27	73	73
TT100 Plag 2 (Rim 2)	TT02B	E	51.28	-	30.23	0.86	0.09	0.20	13.82	3.67	0.08	100.23	0.06	0.15	28	72	72
TT100 Plag 3 (Core)	TT02B	E	48.67	-	31.87	0.91	0.06	0.13	15.78	2.55	0.05	100.01	0.04	0.17	19	81	81
TT100 Plag 3 (Rim)	TT02B	E	52.46	-	29.46	0.91	0.09	0.17	12.94	4.20	0.09	100.33	0.07	0.14	32	68	68
TT100 Plag 4 (Core)	TT02B	E	52.98	-	29.36	1.07	0.11	0.19	12.72	4.34	0.11	100.88	0.07	0.14	33	67	67
TT100 Plag 4 (Core 2)	TT02B	E	49.21	-	31.90	1.17	0.13	0.25	15.75	2.50	0.06	100.97	0.04	0.17	19	81	81
TT100 Plag 5 (Core 1)	TT02B	E	53.77	-	28.62	1.04	0.12	0.18	12.15	4.63	0.11	100.63	0.07	0.13	36	64	64
TT100 Plag 5 (Core 2)	TT02B	E	53.68	-	28.73	1.03	0.12	0.19	12.25	4.51	0.11	100.61	0.07	0.13	35	65	65
TT100 Plag 5 (Rim 1)	TT02B	E	52.90	-	29.43	1.08	0.11	0.20	12.77	4.26	0.10	100.84	0.07	0.14	33	67	67
TT100_Plag 5 (Rim 2)	TT02B	E	53.15	-	29.35	1.05	0.11	0.19	12.76	4.31	0.10	101.03	0.07	0.14	33	67	67
F13 Plag_1_1 (Rim)	G5	E	51.65	0.10	30.19	0.79	0.00	0.20	13.85	3.62	0.08	100.49	0.06	0.15	28	72	72
F13 Plag_1_2 (Core)	G5	E	51.23	0.08	30.56	0.75	0.01	0.17	14.16	3.54	0.08	100.58	0.06	0.16	27	73	73
F13 Plag 1_3 (Core)	G5	E	50.24	0.07	31.38	0.78	0.00	0.16	14.92	3.05	0.07	100.67	0.05	0.16	23	77	77
F13 Plag_1_4 (Rim)	G5	E	50.11	0.08	31.27	0.88	0.02	0.16	15.13	3.02	0.07	100.74	0.05	0.17	23	77	77
F13 Plag_1_5 (Rim)	G5	E	50.34	0.07	31.25	0.87	0.01	0.16	14.65	3.14	0.07	100.57	0.05	0.16	24	76	76
TS58_1_4 (Rim)	TS18	C	53.65	0.11	29.35	0.99	0.02	0.18	12.62	4.41	0.12	101.45	0.07	0.14	34	66	66
TS58_1_4 (Core)	TS18	C	53.83	0.12	28.42	1.09	0.01	0.18	12.03	4.63	0.12	100.44	0.07	0.13	36	64	64
TS58-01_2_1 (Core)	TS18	C	53.61	0.13	28.34	1.11	0.01	0.20	12.04	4.77	0.13	100.32	0.08	0.13	37	63	63
TS58-01_2_2 (Rim)	TS18	C	53.69	0.13	28.85	1.22	0.01	0.19	12.12	4.64	0.12	100.97	0.07	0.13	36	64	64

A DREAM DEFERRED,

BY LANGSTON HUGHES

What happens to a dream deferred?

Does it dry up
like a raisin in the sun?
Or fester like a sore--
And then run?
Does it stink like rotten meat?
Or crust and sugar over--
like a syrupy sweet?

Maybe it just sags
like a heavy load.

Or does it explode?